Convection-diffusion models for distillation columns : application to estimation and control of cryogenic air separation processes

Stéphane Dudret

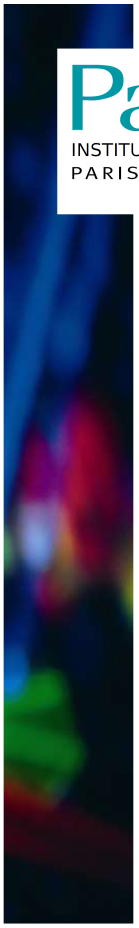

ParisTech
INSTITUT DES SCIENCES ET TECHNOLOGIES
PARIS INSTITUTE OF TECHNOLOGY

MINES ParisTech

École doctorale n°432 : Sciences des Métiers de l'ingénieur

Doctorat ParisTech

T H È S E

pour obtenir le grade de docteur délivré par

l'École nationale supérieure des mines de Paris

Spécialité « Mathématiques appliquées et automatique »

présentée et soutenue publiquement par

Stéphane DUDRET

le 11 Juin 2013

Titre

Modèles de convection-diffusion pour les colonnes de distillation : application à l'estimation et au contrôle des procédés de séparation cryogénique des gaz de l'air

Directeur de thèse : **Pierre ROUCHON**
Co-encadrement de la thèse : **Fouad AMMOURI**

Jury

M. Yann LE GORREC, Professeur, ENSMM	Rapporteur
M. Joachim RUDOLPH, Univ.-Prof. Dr. Ing. habil., Universität des Saarlandes	Rapporteur
M. Hugues MOUNIER, Professeur, Université Paris Sud	Président
M. Fouad AMMOURI, Ph.D., Expert International en Transferts Thermiques en Milieux Industriels, Air Liquide CRCD	Examinateur
M. Georges BASTIN, Professeur Emérite, Université Catholique de Louvain	Examinateur
M. Athanasios KONTOPOULOS, Ph.D., Directeur du Core Global Lab Mathématiques Appliquées, Air Liquide	Examinateur
M. Pierre ROUCHON, Professeur, MINES-ParisTech	Examinateur

T H È S E

MINES ParisTech
Mathématiques et Systèmes
60-62 Boulevard Saint-Michel, 75272 PARIS cedex 06, France

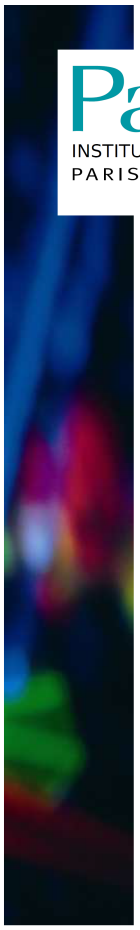

ParisTech
INSTITUT DES SCIENCES ET TECHNOLOGIES
PARIS INSTITUTE OF TECHNOLOGY

MINES ParisTech

École doctorale n°432 : Sciences des Métiers de l'ingénieur

ParisTech Doctorate

T H E S I S

to obtain the

Doctor's degree from the Ecole nationale supérieure des Mines de Paris

Speciality « Mathematics and control »

defended in public by

Stéphane DUDRET

June, 11^{th} 2013

Title

Convection-diffusion models for distillation columns : application to estimation and control of cryogenic air separation processes

Advisor : **Pierre ROUCHON**
Co-advisor : **Fouad AMMOURI**

Jury

M. Yann LE GORREC, Professor, ENSMM	Referee
M. Joachim RUDOLPH, Univ.-Prof. Dr. Ing. habil., Universität des Saarlandes	Referee
M. Hugues MOUNIER, Professor, Université Paris Sud	Chair
M. Fouad AMMOURI, Ph.D., International Expert in Heat Transfer in Industrial Media Air Liquide CRCD	Examiner
M. Georges BASTIN, Professor Emeritus, Université Catholique de Louvain	Examiner
M. Athanasios KONTOPOULOS, Ph.D., Applied Mathematics Core Global Lab Director, Air Liquide	Examiner
M. Pierre ROUCHON, Professor, MINES-ParisTech	Examiner

THÈSE

MINES ParisTech
Mathématiques et Systèmes
60-62 Boulevard Saint-Michel, 75272 PARIS cedex 06, France

Acknowledgments

I would like to thank my advisors Pierre Rouchon and Fouad Ammouri for their expertise and support throughout this work. I am also grateful to Karine Beauchard for her fruitful collaboration .

I express my gratitude to Yann Le Gorrec and Joachim Rudolph for accepting to be my referees, as well as to Georges Bastin, Hugues Mounier and Athanasios Kontopoulos for accepting to join the jury.

I am grateful to my successive managers at Air Liquide, Florence Dessertine, Vincent Gourlaouen and Claude Weber, as well as Jonathan Macron, for their involvment in the set-up and defense of this industrial research project. I am furthermore in debt to all my former coworkers of the Process Control and Logistics team, and to my current colleagues in Applied Mathematics, for their support and the friendly working environment. Special yet non exclusive thanks go to Lionel for the drawings, Mehdi for the sandwich, and Amélie for the pirate ship. I would not forget to also express my gratitude to the members of the Centre Automatique et Systèmes at MINES-ParisTech, especially Nicolas Petit, Jean Lévine, and Florent, Hadis, Nadège and Paul.

I have a very special and grateful thought for my longstanding friend Adrien and his beloved Lucile, whose indefectible care and support during those bizarre days was truly fantastic. Thank you for never stopping telling stories and making us part of the myth.

I also thank the lifelong-or-so companions, Jean-Philippe, Nina, Louise and their relatives, Céline, Cyrille and Kévin, as well as the actually-not-that-recent newcomers Antoine, Grazielli, Mathilde, Edouard, Cécile, Martin, Caroline and Anne-Claire.

To conclude, I give my vote to all the members of the *L.I.M.A.S.S.* and *Alunissons!* improvisation teams, for the great moments shared on stage and besides.

Résumé

Cette thèse s'intéresse au problème de la modélisation dynamique des profils de compositions le long d'une colonne de distillation. L'approche de modélisation retenue est orientée vers des applications au contrôle du procédé, plutôt que vers la simulation intensive pour le design des installations. La validation et la discussion autour du modèle sont menées tant du point de vue théorique de l'automatique, que du point de vue expérimental, *via* des comparaisons avec des données issues d'installations réelles.

Premièrement, nous proposons une introduction aux principes de base de la distillation et au fonctionnement d'une unité de séparation des gaz de l'air (ASU en anglais). Nous conduisons une étude bibliographique des techniques de modélisation et contrôle des colonnes de distillation. Nous détaillons en particulier le modèle d'onde (dont la thèse est inspirée), dans lequel la dynamique des profils de compositions est expliquée comme le glissement d'ondes de compositions de forme fixée, piloté par le taux de reflux dans la colonne.

Deuxièmement, nous proposons un modèle à deux fluides simplifié, où la dynamique des compositions résulte des effets couplés de transports convectifs à contre-courant dans les phases liquide et vapeur le long de l'axe de la colonne, et d'un échange radial piloté par des inhomogénéités de concentrations dans ces deux phases. Nous réduisons ce modèle en une équation aux dérivées partielles (EDP) de convection-diffusion associée à des sorties statiques, en utilisant une technique de réduction variété centre. Cette réduction repose sur une séparation d'échelles de temps. Le modèle réduit obtenu est adapté à un nombre quelconque de constituants dans le mélange à distiller. Nous discutons ses propriétés, et en particulier comment il permet de dépasser l'hypothèse de forme fixe dans le modèle d'onde, et traduit la dépendance de l'efficacité du garnissage vis-à-vis des flux internes. Puis, considérant le phénomène de convection seul, nous adaptons des résultats issus du domaine de la chromatographie, pour construire des ensembles de constituants propagés de manière cohérente comme des ondes de choc, suivant des règles simples.

Troisièmement, nous étudions le modèle EDP réduit du point de vue de l'automatique. Nous prouvons l'existence, l'unicité et la stabilité locale d'une solution stationnaire. Nous proposons des observateurs asymptotiques localement convergents pour les profils de composition, qui s'accomodent d'une hydraulique instationnaire. Des simulations semblent indiquer que les propriétés démontrées s'étendent globalement dans la pratique. En parallèle, nous construisons un modèle linéarisé tangent de fonctions de transfert pour un segment de colonne, qui relie les variations des flux et compositions d'alimentation aux variations des compositions en sortie. Ce modèle de transfert est à base de gains statiques et de retards purs uniquement. Il dépend explicitement de paramètres liés au design du procédé ou à son opération, qui peuvent être mesurés ou estimés en ligne.

Quatrièmement, nous implantons numériquement le modèle EDP afin de reproduire le comportement d'une colonne de séparation binaire réelle. Le modèle est d'abord comparé à

des simulations statiques de référence, puis à des scénarios réels de fonctionnement dynamique. Dans les deux cas, le modèle est en bon accord avec les données de référence. Nous étudions des explications partielles à certains écarts constatés entre les valeurs attendues des paramètres du modèle et les valeurs finales adoptées empiriquement. Nous vérifions aussi le comportement du modèle linéarisé tangent, qui s'avère capable de reproduire les petites oscillations de compositions autour d'un point de fonctionnement.

Cinquièmement, nous étendons la validation du modèle EDP à la simulation d'une cascade de deux colonnes séparant un mélange ternaire, couplées à une troisième traitée de façon simplifiée. Une fois encore, cette configuration correspond à une réalité du terrain. Les comparaisons avec des données statiques de référence montrent un bon comportement du modèle. Celui-ci est cependant très sensible aux erreurs d'estimation des flux internes de gaz et de liquide, ce qui dégrade la qualité des simulations dynamiques. À l'aide des résultats obtenus pour la propagation des ondes de choc de compositions, nous montrons que la forme des profils de compositions est structurée par des ondes de vitesse nulle, qui restent immobiles au milieu des sections de la colonne. De petites erreurs d'estimation sur les flux leur confèrent une vitesse non-nulle, et leur glissement modifie significativement les profils reconstitués.

Abstract

This thesis addresses the problem of modeling the dynamics of continuous composition profiles along a distillation column. The modeling approach is control-oriented, in opposition with numerically intensive models used for designing the columns. Validation and discussion on the model are both considered from a theoretical, control theory point of view, and from an experimental viewpoint, using real plant data for comparisons.

First, we provide an introduction to the basics of distillation and the functioning of a cryogenic air separation unit (ASU). We propose a literature review regarding the techniques for modeling and controlling distillation columns. We detail in particular the wave-model (from which the thesis is inspired), where the dynamics of the composition profiles are explained as the drift of composition waves of fixed shape, driven by the column's internal reflux rate.

Second, we propose a simplified two-flows model in which the compositions dynamics result from countercurrent convection in the liquid and gas phase along the column axis, together with radial exchange driven by inhomogeneous concentrations in the liquid and gas phase. We reduce this model into a non-linear, convection-diffusion partial differential equation (PDE) with static outputs, using the Centre Manifold reduction technique. This technique relies on a time-scale separation. The obtained reduced model is for any number of components in the separated mixture. We discuss its properties, in particular how it relaxes the fixed shape assumption of the wave-model and makes the packing efficiency dependent from the internal flows. Then focusing on the convection phenomenon only, we adapt results from the field of chromatography, to construct coherent sets of components which propagate as shockwaves following simple rules.

Third, we investigate the reduced PDE model from the point of view of control theory. We prove the existence, uniqueness and local stability of the stationary solution. We propose local asymptotic observers for the composition profiles, which can cope with unsteady hydraulics. Some simulations indicate that the demonstrated properties could be global in practice. In parallel, we construct a tangent linearized transfer function model for a column segment, which connects the variations of the inlet flows and compositions with the variations of the outlet compositions. The transfer model consists of static gains and pure delays only. It explicitly depends on process or design data, which can be measured or estimated on-site.

Fourth, we numerically implement the PDE model to reproduce the behavior of a real plant binary separation column. The model is first checked and tuned using static reference simulation cases, then compared against real dynamic operation scenarios. In both cases the model is in good agreement with the reference data. We investigate partial explanations for the discrepancies between the empirically tuned parameters and the expected values. We also check the performances of the linear tangent model, which proves able to reproduce small composition oscillations around a set-point.

Fifth, we extend the experimental validation of the PDE model to reproduce the behavior

of two cascaded columns with ternary mixture, coupled to a simplified third one. This corresponds again to a real plant configuration. Comparisons are made against static reference cases with good agreement. Yet the PDE model turns out to be highly sensitive to estimation errors on the internal liquid and gas flows, which decreases the accuracy of the dynamic simulations. Applying the results obtained for the composition shock-waves, we find that the composition profiles' shape is structured by waves with null-speed, which stay balanced between the column's segments boundaries. Small estimation errors on the flows cause them to drift and significantly impact the estimated profiles.

Contents

Introduction (version française)

> Cette colonne, je suis jamais retourné la voir, même pas de l'extérieur [...] C'est bête, et je le sais bien que c'est bête, mais j'ai plus été capable de redevenir comme avant.
>
> Primo Levi
> La clef à molette

On estime que les installations de séparation des gaz de l'air sont responsables d'environ 0.1 % de la consommation mondiale d'électricité. Ce chiffre illustre à lui seul l'importance, pour la société opérant une telle installation, d'une bonne gestion de l'efficacité énergétique de l'usine. Une part importante de l'effort de réduction de la consommation énergétique est concentrée sur l'amélioration de l'intégration énergétique de l'installation et de son isolation (pour diminuer l'énergie nécessaire à son maintien en froid), ainsi que sur la réduction des pertes de charge dans les colonnes de distillation et les échangeurs thermiques (pour réduire la charge de travail des compresseurs de l'unité). Cependant, des améliorations complémentaires peuvent être apportées en optimisant la conduite du procédé de séparation. Avec cette dernière approche, on cherche essentiellement à traiter les points suivants :

les marges de pureté : une Unité de Séparation des gaz de l'Air (ASU en anglais) produit des liquides et des gaz pratiquement purs. La société opérant l'unité garantit à ses clients que le taux d'impuretés dans les produits n'excédera jamais un seuil donné. Le cas échéant, les produits pollués sont mis à l'air et perdus, ainsi que l'énergie dépensée pour la séparation. Si le point de fonctionnement de l'unité est trop proche du seuil contractuel, et la conduite du procédé peu précise, de petites perturbations peuvent mener à des dépassements intempestifs de ce seuil. En conséquence, on choisit généralement un point de fonctionnement qui éloigne l'unité du seuil critique, ce qui conduit à une surpurification inutile des produits. Ce gain en pureté est coûteux, puisqu'il requiert des flux de gaz et de liquide plus importants dans les colonnes de distillation, et donc, une charge de travail plus grande des compresseurs, pour la même quantité de produit en sortie. Améliorer le rejet de perturbations peut participer à réduire les coûts associés.

la stabilisation : une ASU comporte une succession d'étapes de distillation, réalisées par des colonnes en cascade. Schématiquement, chacune sépare un composant du mélange initial. On récupère donc, pour chaque colonne, un produit purifié qui est vendu aux clients, et un sous-produit, impur, qui alimente la colonne suivante. Une mauvaise stabilisation de la colonne au début de la cascade, même si elle doit n'avoir aucune conséquence sur son produit pur, peut se répercuter sur les colonnes suivantes à travers les sous-

produits, et pénaliser leur fonctionnement. Un travail de purification supplémentaire et coûteux peut devenir nécessaire à la fin de la cascade, qu'une meilleure stabilisation des premières colonnes aurait pu éviter. L'amélioration de la conduite du procédé passe donc aussi par la stabilisation de la qualité des sous-produits dès les premières colonnes, avec une répercussion sur la performance énergétique de l'installation complète.

la flexibilité : la dérégulation des marchés de l'électricité est à la fois une opportunité et un défi pour qui opère un parc d'ASU. Pour réduire le coût global de la production d'un gaz, il est préférable d'en produire plus lorsque l'électricité est bon marché, et de réduire la production quand les prix de l'énergie montent. Cependant, la loi du marché vaut aussi pour les clients de l'ASU, lesquels vont adapter la conduite de leurs propres procédés. Le besoin d'un client peut donc évoluer fortement au sein d'une même journée. Le raisonnement devient plus complexe encore lorsque l'on envisage le fonctionnement coopératif de plusieurs ASU par le biais de réseaux de distribution, et si l'on considère que le stockage de gaz ou de liquide obéit aussi à ses propres règles d'optimisation énergétique. L'idée générale, c'est le changement du mode opératoire des ASU : d'un fonctionnement stabilisé, on passe à une production constamment en régime transitoire. Or, pour ne pas dépasser les seuils de pureté contractuels durant ces transitoires, il est tentant d'opérer par de lentes variations d'un point de fonctionnement, et de rester autour d'un régime quasi-stationnaire sécurisant. Cela génère des temps morts, pendant lesquels la production peut ne pas être adaptée aux prix de l'énergie ou à la demande client, avec pour conséquences possibles : des opportunité manquées d'économie d'énergie, une surproduction, ou au contraire des demandes insatisfaites. Une conduite améliorée du procédé devrait donc permettre des transitoires plus rapides, plus agressifs, tout en respectant les seuils de pureté, en utilisant au mieux les capacités de l'usine qui découlent de son design.

La question sous-jacente est celle des modèles de contrôle à utiliser dans les systèmes de pilotage de l'unité de séparation. En simplifiant à l'extrême, nous pouvons distinguer deux grandes catégories de modèles.

D'une part, les modèles linéaires de fonctions de transfert, à base de gains statiques, de constantes de temps et de retards purs. Ces modèles sont souvent du type 'boîte noire', ce qui suppose leur calage sur site. De plus, leur précision est limitée à un petit voisinage du point stationnaire utilisé pour ce calage, puisque la dynamique des colonnes de distillation et des échangeurs thermiques est hautement non-linéaire. Or les ASU opèrent de moins en moins fréquement en régime stationnaire. Ainsi, si les modèles boîtes-noires sont réglés alors que l'unité est en production, ce qui est régulièrement le cas puisqu'interrompre la production pour le réglage a un coût immédiat, le résulat est l'indentification d'un point de fonctionnement fantôme ; on obtient un modèle d'une sorte de dynamique moyenne, dont la justesse est sujette à caution. De tels modèles sont bien entendu inadaptés au contrôle de grands transitoires. En outre, la nature même de ces boîtes noires rend délicat leur pré-réglage à partir de données de design, lequel permettrait de réduire la charge de travail pour le réglage sur site, ou encore l'estimation de leur pertinence.

D'autre part, nous trouvons des modèles de grande taille, où chaque sous-fonction ou élément constitutif du procédé (compresseur, échangeur, plateau de distillation, condenseur...) est représentée par des équations physiques détaillées. De tels modèles peuvent compter des centaines ou des milliers de variables et de paramètres, ce qui complique leur réglage, et pose la question de leur stabilité numérique, ainsi que celle des ressources de calcul et de mémoire

nécessaires pour une utilisation temps-réel. De plus, ces modèles impliquant de nombreux sous-systèmes, il devient difficile d'extraire l'information nécessaire, complète mais non superflue, dont on a besoin pour le contrôle : ces modèles n'offrent pas nécessairement un aperçu clair des variables, phénomènes et dynamiques à considérer.

L'interrogation qui sous-tend ce travail est donc la suivante : quel serait le prochain modèle de contrôle pour une unité de séparation des gaz de l'air, ayant une complexité minimale, qui pourrait être à la fois concis comme un modèle de fonctions de transfert, tout en allant au-delà des seuls gains, constantes de temps et retards purs, et devrait éclairer les dynamiques non-linéaires critiques qui sont parfois cachées dans les gros modèles physiques ?

Pour apporter des éléments de réponse, nous proposons l'approche suivante. Du point de vue du contrôle, les éléments critiques dans une ASU sont les colonnes de distillation et les échangeurs, puisque leurs dynamiques sont hautement non-linéaires, avec des retards importants, et que ces sous-ensembles sont peu instrumentés. Nous axons ce travail sur les colonnes, qui sont au cœur du procédé. Notre objectif est de modéliser la dynamique de ces colonnes, l'une après l'autre. Une colonne, prise seule, comporte plusieurs segments, qui diffèrent par leur taille, les traffics internes de liquide et de gaz, et les compositions typiques en entrée et en sortie. Le plus petit sous-système de notre étude sera donc un segment homogène de colonne. Nous construisons pour un tel segment un modèle physique simple basé sur des bilans, que nous réduirons afin d'obtenir un modèle concis qui montrera clairement les phénomènes à l'œuvre dans la dynamique des colonnes. Nous construirons alors un modèle réduit d'une première colonne en combinant plusieurs segments. En itérant, on peut obtenir ainsi un modèle pour une cascade de colonnes. Dans cette étude, nous nous limiterons à deux colonnes en cascade, connectées de manière simplifiée à une troisième. Du point de vue du procédé, ceci permet d'étudier la séparation N_2/O_2, tout en tenant compte de manière simplifiée de la première étape d'extraction d'argon. Nous validerons les modèles de colonnes grâce à des cas de référence (des simulations) en régime stationnaire, et des données d'exploitation provenant d'une ASU réelle. Le modèle que nous proposons est adapté à l'observation, sur le temps long, de colonnes de distillation. Mais sur la base du même modèle, nous dériverons des fonctions de tranfert qui pourraient s'intégrer dans des lois de stabilisation des colonnes. Nous proposerons également une interprétation de la sensibilité de notre modèle (par rapport aux flux internes de gaz et de liquide) en termes d'ondes de compositions. Notons pour finir que dans le cadre de cette étude, nous ne nous préoccupons pas de la question du temps de calcul (quoique les simulations avec nos modèles soient nettement plus rapides que le temps réel).

Plan du manuscrit

Le Chapitre 1 introduit le lecteur aux principes de base de la distillation et du fonctionnement d'une Unité de Séparation des gaz de l'Air, ainsi qu'à l'état de l'art en modélisation et contrôle des procédés de distillation.

Partant d'un modèle de cornue, nous montrons comment une succession d'étapes d'équilibre liquide-vapeur permet la séparation d'un mélange. Nous présentons ensuite les technologies (plateaux de distillation et garnissages) qui réalisent ces étapes dans une colonne de distillation, leurs avantages et inconvénients. Nous poursuivons avec le schéma général d'une ASU, et donnons quelques détails sur ses principales fonctions : compression, purification, production de froid, échanges thermiques et distillation.

La deuxième partie du chapitre, qui est une revue de modèles de contrôle pour la distillation, débute avec l'exploitation des unités en régime stabilisé, comme il était d'usage

par le passé. Nous évoquons le choix des variables de contrôle, la robustesse du régime stationnaire vis-à-vis de certaines perturbations. Nous familiarisons le lecteur avec les modèles à plateaux, les non-linéarités du régime stationnaire et les problèmes de conditionnement des modèles. Nous montrons ensuite comment la dynamique des colonnes de distillations est traitée avec de tels modèles. Nous évoquons un modèle en particulier, le modèle d'onde, qui exprime la dynamique des profils de composition dans la colonne par le déplacement d'une onde de composition, de forme fixée, le long de la colonne. Nous traitons également de quelques modèles et techniques de contrôle heuristiques, à base de réseaux de neurones ou de logique floue par exemple. La section suivante est dédiée au problème du temps de calcul et aux techniques permettant de réduire la charge de calcul et de mémoire nécessaire aux stratégies de contrôle prédictives utilisant des modèles complexes. Comme on l'a dit précédemment, les colonnes de distillation sont couplées entre elles et aux échangeurs thermiques dans leur fonctionnement ; une section traite des possibles problèmes de couplage causés par la forte intégration énergétique du procédé. Les échangeurs thermiques en eux-mêmes sont hors du cadre de ce travail ; nous présentons cependant brièvement quelques modèles adaptés aux échangeurs multiphasiques. Nous concluons cette revue de la littérature par quelques problèmes ouverts, rappelons le cadre de notre travail et ses objectifs par rapport à cet état de l'art, et donnons pour terminer les orientations de la recherche chez les grands acteurs industriels de la séparation des gaz de l'air.

Le présent travail étant directement inspiré du modèle d'onde, la dernière section de ce chapitre revient plus en détail sur ce dernier.

Le Chapitre 2 commence par l'écriture d'un modèle d'équations bilans pour un segment de colonne de distillation, qui est ensuite réduit en un modèle non-linéaire de convection-diffusion. Le chapitre se clôt par une adaptation d'un modèle de propagation d'ondes, du cadre de la chromatographie vers celui de la distillation.

Nous décrivons la distillation comme le résultat d'un échange de matière entre une phase liquide équivalente et une phase gazeuse équivalente, à travers une unique surface de contact. Le flux d'échange de matière est imposé par une inhomogénéité de compositions dans chacune des phases, lesquelles ne sont pas instantanément à l'équilibre thermodynamique dans leur ensemble. L'échelle de ce flux d'échange est donnée par un terme en $\frac{1}{\epsilon}$, $0 < \epsilon << 1$; nous relions qualitativement ϵ à l'efficacité du garnissage.

Nous faisons une tentative pour réduire, en régime stationnaire, notre premier modèle, en distingant deux échelles en espace, à connecter par la technique des développements asymptotiques raccordés. Nous montrons comment le jeu entre des conditions aux limites particulières et un profil de composition exponentiellement raide rend caduque cette approche.

Nous nous tournons alors vers la réduction du système dynamique initiale en tirant parti de deux échelles de temps distinctes, à l'aide de techniques de réduction variété centre (nous donnons une introduction à ces techniques). Nous menons rigoureusement la réduction d'une version discrète du modèle d'équations bilans, dans le cas d'un mélange binaire. Nous appliquons ensuite formellement la même technique de réduction à la version du modèle de dimension infinie (toujours pour un mélange binaire). Ceci est motivé par la similarité entre les structures des deux modèles (discret et continu) réduits obtenus. Le modèle réduit comprend :

– une équation aux dérivées partielles (EDP) de convection-diffusion pour la dynamique

d'une variable interne X, qui est assimilée à la composition moyenne d'une espèce sur les phases liquide et gaz,
– des sorties statiques pour récupérer les compositions phase par phase à partir de la variable interne X.

Nous discutons ce modèle, et notamment la dépendance du terme de diffusion en ϵ et en les conditions opératoires de la colonne. Nous étendons ensuite ce modèle à un nombre quelconque de composants.

Si l'on néglige la diffusion, notre modèle EDP se réduit à un modèle de convection pure. La question naturelle est : quelles sont les quantités qui se progagent, et à quelle vitesse ? Nous donnons des éléments de réponse en adaptant des résultats originellement obtenus pour la chromatographie : nous rapprochons la circulation à contre-courant de gaz et de liquide dans la colonne de la circulation d'un mélange analysé sur un lit (fixe) de chromatographie. Nous montrons que pour un mélange à $N + 1$ composants, il existe N^2 invariants de Riemann qui permettent de construire N combinaisons de composants, chacune convectée comme une seule entité. Dans ces ensembles, les compositions n'ont pas de réalité physique (elles pourraient être négatives, par exemple). Nous donnons les relations permettant d'obtenir ces ensembles à partir des compositions réelles, physiques, dans la colonne, et vice-versa. Concernant les vitesses de propagation, nous donnons une condition suffisante pour n'obtenir dans la colonne que des ondes de chocs, sans interactions entre elles. On verra que cette condition est vérifiée dans les colonnes que nous considérons en applications. Nous donnons les vitesses de choc correspondantes.

Le Chapitre 3 comprend l'analyse du modèle EDP du point de vue de la théorie des systèmes dynamiques et du contrôle, ainsi que le développement d'un modèle linéarisé tangent de fonctions de transfert pour un segment de colonne.

Nous considérons une configuration de colonne simplifiée, analogue à un segment unique. Nous établissons un ensemble d'hypothèses portant sur les flux de liquide et de gaz, les compositions d'alimentation et la relation d'équilibre thermodynamique, sous lesquelles nous prouvons les résultats suivants : pourvu que les données initiales soient dans $(0, 1)$, la composition moyenne X reste dans le même intervalle pour tout temps positif ; pour toute valeur positive du paramètre de diffusion ϵ, il existe une solution stationnaire unique et monotone au système dynamique considéré ; la composition au sommet de la colonne a, en régime stationnaire, une dépendance monotone en ϵ ; la solution stationnaire est localement exponentiellement stable. Ce dernier résultat est donné au moyen d'une fonction de Lyapunov.

Partant du modèle EDP, nous proposons une famille d'observateurs asymptotiques avec injection de sortie réglable. La même fonction de Lyapunov que précédemment nous permet de prouver que ces observateurs sont localement exponentiellement convergents, même si l'hydraulique de la colonne n'est pas en régime stationnaire.

Nos simulations semblent indiquer que ces propriétés locales peuvent, en pratique, être considérées comme globales.

La deuxième partie du chapitre est dédiée à la dérivation d'un modèle linéaire tangent, partant du modèle EDP. L'EDP linéarisée est réécrite comme une équation aux dérivées ordinaires dans le domaine de Laplace. Les racines de l'équation homogène associée s'expriment, l'une comme une série entière en ϵ, l'autre comme une série de Laurent en ϵ. En manipulant ces racines sous forme symbolique, nous obtenons via un développement asymptotique non-standard, l'expression des variations de compositions au sommet et

en pied de colonne, comme des séries entières en ϵ, à des termes exponentiellement précis près. En tronquant les expressions des racines, nous obtenons une approximation des variations de composition des sorties en $O(\epsilon)$. Deux cas doivent être distingués, suivant la direction de convection des compositions.

Le Chapitre 4 concerne l'implémentation numérique et le test des modèles EDP et linéaire par rapport à des simulations de référence en régime stationnaire et des données issues d'une ASU réelle. On se focalise sur la première colonne (la colonne Moyenne Pression) de l'unité.

Nous rappelons d'abord le fonctionnement de cette colonne, puis présentons les schémas numériques utilisés pour le modèle EDP (nous nous limitons ici à la séparation binaire N_2/O_2 en négligeant l'argon). Nous tentons d'estimer *a priori* certains des paramètres du modèle par des considérations élémentaires sur la géométrie du garnissage.

Nous comparons ensuite les estimations du modèle EDP avec des cas de référence en régime stationnaire obtenus avec le logiciel Hysys . Les profils de composition simulés sont en bon accord avec Hysys , et résistent à des simplifications du modèle, dans une certaine mesure. On note cependant que les paramètres estimés empiriquement pour obtenir ces résultats diffèrent significativement de leurs estimations *a priori*.

Le modèle EDP est ensuite testé à l'aide de données de fonctionnement (en régime dynamique) provenant de l'ASU. Plusieurs scénarios sont testés, que le lecteur pourra retrouver en Annexe C. Dans le corps du chapitre, nous nous concentrons sur un scénario en particulier. Nous montrons qu'en boucle ouverte, notre modèle EDP reproduit de manière satisfaisante les mesures de compositions sur l'unité, avec des paramètres directement repris des tests en régime stationnaire. Seule la vitesse de descente du liquide doit être significativement modifiée pour synchroniser le modèle avec l'unité. La dynamique des compositions est peu sensible aux changements sur les rétentions liquide et vapeur, ce qui semble indiquer que c'est en fait l'hydraulique, plutôt que la dynamique de séparation elle-même, qui prédomine dans l'unité de séparation.

Nous montrons qu'une simple adaptation en ligne du paramètre de diffusion ϵ permet au modèle de rester cohérent avec les mesures sur plusieurs dizaines d'heures, et sur plusieurs scénarios. Sur certains cependant, notre modèle est incapable de reproduire les compositions mesurées, ce qui constitue une limite à son domaine de validité actuel.

Sur un scénario distinct et sur des intervalles de temps plus courts, nous testons aussi le modèle de fonctions de transfert développé au Chapitre 3. Malgré un biais lentement variable, ce modèle reproduit les oscillations de composition observées.

Le Chapitre 5 poursuit la validation expérimentale du modèle. La seconde colonne (la colonne Basse Pression) est simulée en utilisant le modèle EDP (la première colonne est simulée simultanément, et l'ensemble est couplé à une troisième colonne de manière simplifiée). Les résultats sont comparés à des cas de référence statiques et des données issues de l'unité réelle.

Comme dans le chapitre précédent, nous rappelons le fonctionnement de la colonne Basse Pression. Nous la considérons d'abord comme une colonne de séparation d'un mélange pseudobinaire. Cependant, cette colonne étant connectée à la première colonne d'extraction d'argon, une seconde étape consiste à simuler la séparation du mélange ternaire $N_2/O_2/Ar$. Nous présentons le schéma numérique utilisé pour ce mélange ternaire.

Le modèle EDP binaire est comparé aux cas statiques HYSYS . Les résultats indiquent le profil de composition O_2, qui comporte un grand front de changement de composition, est très sensible aux erreurs d'estimation sur les flux de liquide et de gaz, et sur la volatilité des composants. La comparaison du modèle ternaire avec HYSYS mène aux mêmes constatations.

Nous comparons ensuite le modèle EDP pour les colonnes couplées avec les données issues de l'unité. Pour ces simulations, nous envisageons plusieurs modèles simplifiés pour tenir compte du couplage avec la première colonne argon, sans avoir à la simuler elle aussi. Trois mesures de composition O_2 sont disponibles pour les comparaisons, au sommet de la colonne Basse Pression (quelques pourcents d'oxygène), à son pied (presque 100 %) et au niveau de la connection avec la première colonne argon (environ 90%). Nous nous concentrerons sur cette dernière, critique pour la bonne marche du procédé argon. Notre modèle est en accord avec la composition O_2 moyenne à cet endroit, et reproduit certaines de ses variations. Mais la sensibilité du modèle aux petites variations des flux internes de liquide et de gaz est telle que notre estimation diverge fréquemment de la mesure.

Dans la dernière partie du chapitre, nous étudions cette sensibilité à l'aide du modèle d'ondes de choc adapté au Chapitre 2. Nous montrons que dans la colonne Basse Pression, en régime stationnaire, certaines ondes de compositions sont immobiles. Elle se maintiennent au milieu d'un segment de colonne, isolées des effets de bord. Un petit changement sur les flux de liquide ou de gaz leur confère une vitesse non-nulle. L'onde glisse alors dans le segment avant d'être stoppée par les effets de bord, ce qui change significativement le profil de compositions correspondant.

Des Conclusions et perspectives closent le manuscrit.

L'Annexe A regroupe des schémas de l'ASU considérée et des colonnes étudiées.

L'Annexe B résume les notations utilisées dans nos modèles pour les différents flux de gaz et de liquide.

L'Annexe C regroupe, sous une forme résumée, les comparaisons modèle-ASU sur 17 scénarios de fonctionnement de la colonne Moyenne Pression.

L'Annexe D complète la première partie du Chapitre 5 avec des comparaisons supplémentaires en régime stationnaire, entre le modèle EDP et des cas HYSYS de référence, pour la colonne Basse Pression.

L'Annexe E expose succinctement les performances des schémas numériques et de possibles améliorations.

Publications et brevets

Ce travail a conduit à une communication [22] à l'American Control Conference (ACC) 2012 (conférence internationale avec actes et comité de lecture). Cette communication traite de l'obtention d'un modèle dynamique réduit pour une colonne de distillation binaire, pour lequel on donne des résultats de stabilité et d'observabilité, similaires à ceux présentés en première section du Chapitre 3. La réduction est menée formellement dans [22] ; le Chapitre 2 justifie cette réduction en appliquant rigoureusement la technique correspondante à une version discrète du sytème, et l'étend également à un nombre quelconque de composants.

Le modèle linéaire tangent présenté en deuxième section du Chapitre 3, et testé en fin du Chapitre 4, a été soumis pour publication à l'Annual Conference on Decision and Control (CDC) 2013.

En marge de ces publications, cette thèse a mené à trois demandes de brevets (enregistrés mais non encore publiés) :

- FR-1254802 qui couvre l'intégration d'un modèle de convection-diffusion tel que développé au Chapitre 2 dans un capteur logiciel, pour l'estimation et la prédiction des profils de composition sur site,
- FR-1255974 qui couvre l'utilisation d'un tel modèle à des fins de détection de défaillances de capteurs physiques,
- FR-1256782 qui couvre l'utilisation d'un tel modèle pour prévenir le désamorçage du condenseur en tête de la première colonne d'argon, en détectant des tendances potentiellement problématiques dans la dynamique des profils de compositions.

Introduction

Air separations plants are responsible for about 0.1 % of the worldwide electricity consumption. That goes to show the importance of the plants' energy efficiency management for the plant operating companies. A large fraction of the energy consumption reduction effort is focused on the plant's energy integration and insulation (to decrease the required cooling power) and the pressure drops inside the distillation columns and heat exchangers (to decrease the compressors' duty). Yet another, complementary energy optimization approach focuses on enhanced process control. This approach essentially addresses the three following issues:

Purity margins: an Air Separation Unit produces almost pure liquids and gases. The plant operating company guarantees its customers that impurities will not exceed a certain concentration in the products. Whenever the threshold is exceeded, the products are vented and lost. If the plant set-point is too close to the threshold and the process control too loose, small perturbations can yield untimely exceeding of the critical limit. Consequently, the chosen set-point is often far below the contractual threshold and the products are unnecessary over-purified. This additional purification is costly, since it requires increased liquid and gas traffic inside the distillation columns, that is, additional compression power, for the same amount of final product. Enhanced disturbance rejection shall help reducing these costs.

Stabilization: air separation plants are a chain of distillation steps, where columns operate in a cascade manner. In broad outline, each of them separates a component of the initial mixture. The results for each column are a pure product which is sold to the customers, and by-products which feed the next column in the cascade. Loose stabilization of a column at the beginning of the cascade, even if it has no consequence on its pure product, can be passed to the next columns via the by-products, and dramatically impede their functioning. Additional, costly purification duty will thus be necessary at the end of the cascade, because of disturbances which could have been damped at its beginning. Enhanced process control shall thus focus also on the stabilization of the by-products composition in the first columns, to improve the energy efficiency of the global process.

Flexibility: deregulation of the electricity markets offers both new opportunities and challenges for the plant operating companies. To reduce the overall production cost of a gas, it is preferable to produce more of it when the electricity is cheap, and to decrease the production when prices increase. Yet the deregulation also plays for the plants' customers, which adapt their own processes. Thus the customer demand can radically vary during a day. The reasoning gets even more intricate when considering that air separation plants can operate in a cooperative manner via pipeline networks, and that

liquid and gas storage for buffering purpose also obeys its own energy optimization rules. Yet the big picture is that ASU operation has switched from steady-state to frequent large transients. In order not to exceed the purity thresholds during the transients, it is tempting to slow down the set-point changes, so as to always operate near the steady-state. Yet this leads to dead-times during which the production is possibly not adapted to the energy prices and to the customers demands, which results in lost spares, wasted products or unsatisfied orders. Enhanced process control shall then allow accelerated transients, while respecting the purity limits, by pushing the plant to the edge of its design.

The underlying question regards the control models to be embedded in the plants' control system. In a simplified manner, we can distinguish two main modeling approaches.

On the one hand, linear transfer function models consisting of static gains and time constant for small order transfers, and pure delays. These models are often of black-box type, which supposes tuning them on-site. In addition, they are accurate only in a small vicinity of a steady-state, since distillation columns and heat-exchangers show highly non-linear dynamics. And it just so happens that a distillation plant almost never operates at steady state. If the black-box models are tuned during regular operation, which is often the case since interrupting the production for testing purposes has an immediate cost, the result is the identification of a ghostly, floating set-point; one obtains the model of a mean dynamics, whose accuracy can be problematic. Such models are of course unadapted to large transients control in particular. In addition, the black-box nature makes it difficult to estimate *a priori* the model parameters from design data, in order to reduce the on-site tuning time or assess their relevance.

One the other hand, we find large models where each step and device of the plant (be it a compressor, an exchanger, a distillation tray, a condenser ...) are represented with first-principles physics equations. Such models can count hundreds or thousands of parameters and variables, which makes their tuning complicated, and sets the question of their numerical stability as well as the required CPU resources for real-time applications. In addition, the numerous sub-systems involved in these models make it hard to extract the right, necessary and non-superfluous information for control; they offer no clear view of the critical variables, physical effects and dynamics to be considered.

The question which subtends this work is then: what is the next control model of minimal complexity for air separation plants, which should be concise as the transfer functions models, yet go beyond the gain / time constant / pure delay framework, and give a clear view of the critical non-linear dynamic phenomena which are somehow hidden in the large first principle models?

We propose the following approach to make a start on providing answers to this question. The very critical elements of a distillation plant regarding the control purposes are the distillation columns and the heat-exchangers, for they show highly non-linear dynamics, important delays, and are only little instrumented. We focus in this work on the distillation columns, which are the core of the process. Our goal is to model the dynamics of the multiple chemical species molar fraction profiles along the column. As said previously, the column operate in a cascade manner. We will address the columns one after the other. A single column comprises several subsections, which essentially differ by their size, the internal liquid and gas flows, and the typical magnitude of their inlet and outlet compositions. The smallest sub-system in our study will then be an homogeneous subsection. For such a subsection, we will build a simple

first-principle physics model, which we will reduce to obtain a concise form clearly displaying the critical phenomena which structure the dynamics of distillation. We will then build the reduced model of the plant's first column by combining several subsections. Ultimately, one would so obtain the model of the whole cascade. Yet in this study, we will limit ourselves to two cascaded columns, interacting in a simplified manner with a third one. From the process point of view, this is addressing the N_2/O_2 separation process, with a glance at the first argon extraction step. We will validate the columns models using static reference simulation cases, and against real dynamic plant data (from an Air Liquide Air Separation Unit). The model we propose is essentially adapted to the long-term observation of the distillations columns. On this basis, we will derive a linearized transfer function model which could be part of a stabilization strategy. We will also propose an interpretation of the sensitivity of our model to the liquid and gas internal flows, in term of traveling composition waves. Note that in this work, we do not focus on the computation time issue regarding our models (which yet run faster that the real-time).

Organization of the manuscript

Chapter 1 introduces the reader to the basic principles of distillation, the functioning of an Air Separation Unit, and with the state of the art regarding the modeling and control of distillation processes.

Starting with the retort model, we show how a succession of biphasic equilibrium stages separates a mixture. We then present the technologies (distillation trays and packing) which realize this stages in a distillation column, their advantages and drawbacks. We continue with the general scheme of an Air Separation unit, and give some insights into the main functions: compression, purification, cold production, heat-exchange and distillation.

The second part of the chapter, an overview on control models for distillation, begins with the steady-state exploitation of the plants, which was the rule in the past. We broach the choice of control variables, the robustness of the steady-state with respect to some disturbances. We introduce the reader to the stage-by-stage models, the non-linearities in the static gains and the conditioning issues. We then show how the dynamics of distillations columns are addressed with linear models or tray models. We cite a particular model, the wave-model, in which the composition profiles dynamics are explained as the move of fixed-shape composition waves along the column. We also deal with some heuristic modeling and control techniques, based on neuron networks or fuzzy logic for instance. The next section is dedicated to the computation time issue, and techniques to reduce the CPU and memory resources required for predictive control strategies using large models. As mentioned earlier, distillations columns and heat-exchangers operate in a coupled manner in the plant: a section addresses the possible coupling issues resulting from the high energy-integration of the process. Heat-exchangers are out of the scope of this work, yet we briefly present some modeling techniques applied to multiphasic exchanger. We conclude the literature review by mentioning some pending issues, recalling the scope and goals of the thesis with respect to the state of the art, and giving the research orientations of the major air separation industrials.

Since our work is inspired by the wave-model, the last section of the chapter returns

with more detail to its development.

Chapter 2 begins with the writing of a first-principles physics model for a distillation column subsection, which is then reduced into a non-linear convection-diffusion partial differential equation model, and ends with adaption of a traveling composition waves model from the field of chromatography to distillation.

We describe distillation as the result of a mass-exchange between an equivalent liquid phase and an equivalent gas phase through a single contact interface. The mass-exchange flow is driven by composition inhomogeneities in each phase, where the thermodynamic equilibrium is not instantly reached everywhere. This exchange flow is scaled by a term in $\frac{1}{\epsilon}$, $0 < \epsilon << 1$, and we qualitatively connect ϵ with the packing efficiency.

We present a tentative to reduce, in steady state, this first principle model using two space scales and the matched asymptotic development technique. We show how the interplay between specific boundary conditions and an exponentially stiff composition profile impedes this reduction.

We then switch to a reduction of the dynamic system using two time scales, based on the Centre Manifold reduction techniques, to which we introduce the reader. We rigorously reduce a discrete version of the first-principles models using this technique, in the case of a binary mixture separation. Then we formally apply the same reduction to the infinite dimension version of the model, still with binary mixture, motivated by the similarity of the reduced models structures. The resulting reduced model comprises:

- a dynamic convection-diffusion partial differential equation (PDE) for an internal variable X, which corresponds to the lumped composition of a species over the liquid and gas phase.
- static outputs to retrieve the actual composition in each phase from the internal variable X.

We discuss this model, notably the dependence of the diffusion term in ϵ and in the column's operating conditions. We then extend the model to take any number of components into account.

Neglecting the diffusion, our PDE model reduces to a pure convection model. The arising questions are: which quantities are convected, and at which speeds ? We give some answers by adapting results from the field of chromatography: we analogize the counter-current circulation of gas and liquid with the circulation of an analyzed mixture along a fixed chromatography bed. We show that for an $N+1$ components mixture, there are N^2 Riemann invariants which allows forming N multicomponent sets convected in a coherent manner. In these bundles, the compositions are non-physical (they can be negative, for instance). We give the equation to obtain the bundles composition from the physical compositions, and vice-versa. Regarding the convection speeds, we give a sufficient condition for the composition bundles to propagate as non-interacting shock-waves. This condition will be fulfilled in the investigated distillation columns. We give the corresponding shock-speeds.

Chapter 3 comprises the theoretical analyze of the PDE model from the point of view of dynamic systems and control theory, and the development of a tangent linearized

transfer functions model for a single subsection.

We consider a simplified column configuration, with only one subsection. We establish a set of hypotheses regarding the liquid and gas flows, the inlet compositions and the thermodynamic equilibrium relation, under which we prove the following results: provided that initial data is within $(0, 1)$, the lumped composition remains within the same interval for any positive time; for each value of the diffusion parameter ϵ, there exists a unique, monotone stationary solution for the considered dynamic system; the stationary composition at the top of the column has a monotone dependence on ϵ; the stationary solution is locally exponentially stable. This last result is obtained by the mean of a Lyapunov function.

Based on the PDE model, we propose a family of asymptotic observers with tunable output injection. The same Lyapunov function allows us to prove that the observers are locally exponentially convergent, even if the internal liquid and gas flows are unsteady.

Some simulations seem to indicate that the local nature of the enunciated properties could in practice turn into a global one.

The second part of the chapter is dedicated to the derivation of a linear tangent model from the PDE model. The linearized PDE model is rewritten as an ordinary differential equation in the Laplace domain. The roots of the corresponding homogeneous equation are a power series and a Laurent series in the diffusion parameter ϵ. Using symbolic calculations to handle these roots, we obtain an expression of the top and bottom outlet compositions variations, *via* non-standard asymptotic expansion, as a power series in ϵ, up to exponentially small residuals. Truncating the expansions of the roots, we obtain an approximation of the outlet composition variations in $O(\epsilon)$. Two cases have to be distinguished, depending on the direction of the compositions convection.

Chapter 4 is dedicated to the implementation and test of the PDE and linear models against reference steady-state simulations and real plant data regarding the first column (the High Pressure column) of the plant.

We first recall the functioning of the High Pressure column, then present the numerical schemes used to implement the PDE model (here we limit ourselves to the binary N_2/O_2 separation, neglecting the argon concentration). We pre-estimate some of the model parameters based on simple considerations on the packing geometry.

We then check the PDE model estimations against reference steady-state simulations obtained with the Hysys software. The simulated molar fraction profiles are in satisfying agreement with Hysys , and robust to the simplification of some parameters, to a certain extent. Yet the results are obtained using empirical parameters which significantly differ from the pre-estimated ones.

The PDE model is then tested against real dynamic data gathered from the Air Separation Unit. Several scenarios are tested, which the reader can find in Appendix C. We focus in the chapter on only one scenario. We show that, in open loop, the PDE model satisfyingly reproduces the compositions measurements with parameters borrowed from the steady state tests. Only the liquid theoretical speed had to be significantly changed to synchronize the model with the plant. The compositions dynamics are only little sensitive to changes on the hold-ups, which seems to indicate that the column's hydraulics dominate the distillation dynamics.

We show that a simple on-line adaption of the diffusion parameter ϵ allows the model to cope with the measurements over several dozens hours, on several scenarios. Yet on some scenarios, our model in unable to reproduce the measured compositions, which limits its range of validity for the moment.

On a different scenario and on shorter time intervals, we also test the transfer functions model developed in Chapter 3. Up to a time-varying bias, it reproduces the composition oscillations at the chosen location.

Chapter 5 continues the model testing: the second column (the Low Pressure column) is simulated using the PDE model (simultaneously to the first one, and coupled with a third one in a simplified manner), and the results are compared against static reference cases and real plant data.

As for the previous chapter, we recall the functioning of the Low Pressure column. We first consider it as a binary mixture separation column. Yet this column is connected to the first argon extraction column, thus in a second step we will simulate the separation of the ternary mixture $N_2/O_2/Ar$. We present the numerical scheme used for this ternary mixture.

The binary PDE model is tested against Hysys steady-state cases. The results show that the O_2 molar fractions profile, which comprises a huge front, is highly sensitive to estimation errors on the internal liquid and gas flows, and on the components volatility. Similar results are obtained when comparing the ternary model against Hysys .

Then we test the PDE model of the coupled High Pressure and Low Pressure columns against real plant data. For these simulations, we investigate simple models to handle the coupling with the first argon column, without actually simulating it. Three O_2 molar fraction measurements are available for comparisons: at the top of the High Pressure column (some percents), at its bottom (almost 100%), and at the location of the connection with the first argon column (about 90%). The latter is a critical measure for the functioning of the argon process, so we focus on it. Our model is in agreement with the mean O_2 molar fraction at this location, and reproduces some of its oscillations. Yet the sensitivity to small changes on the internal flows is such that our estimation frequently diverges from the measurements.

In the last part of this chapter, we make use of the shock-waves model adapted in Chapter 2 to investigate this sensitivity. We show that, in the Low Pressure column, in steady-state, some composition shock-waves are motionless. They stand in the middle of a subsection, far from end effects. A small change on the internal flows makes their speed non-null, and causes them to drift along the subsection before the end effects stop them, significantly changing the resulting molar fraction profiles.

Conclusion and perspectives regarding this work close the study.

Appendix A contains schemes of the Air Separation Unit, and flowcharts of the investigated columns.

Appendix B summarizes the notations used to represent the numerous liquid and gas flows involved in our models.

Appendix C summarizes the results of plant-model comparisons on 17 scenarios, regarding the High Pressure column transient operation.

Appendix D completes the first part of Chapter 5 with additional steady-state comparisons between our non-linear model and a reference HYSYS model of the Low Pressure column.

Appendix E gives some information regarding the computational performances of the numerical schemes and how they could be improved.

Publications and patents

This work has led to a presentation [22] to the American Control Conference (ACC) 2012 (international conference with reviewing committee and proceedings). This communication deals with the obtention of a reduced dynamic model for a binary mixture distillation column, for which stability and observability results are given, similar to those presented in the first section of Chapter 3. The reduction is made formally in [22]; Chapter 2 justifies this reduction by rigorously applying the technique to a discrete version of the considered system, and also extends it to multicomponent mixtures.

The tangent linear model presented in the second section of Chapter 3 and tested at the end of Chapter 4 has been submitted for publication to the Annual Conference on Decision and Control (CDC) 2013.

Apart from the publications, the thesis yielded three patent applications (not published yet):

- FR-1254802 on embedding the convection-diffusion model developed in Chapter 2 in a soft-sensor for on-site composition profiles estimation and prediction,
- FR-1255974 on using the same model for physical sensor failure detection purposes,
- FR-1256782 on using the same model to avoid the deactivation of the condenser at the top of the first argon column, by detecting risky trends in the composition profiles dynamics.

Chapter 1

State of the art

On rencontre des procédés de distillation dans une large gamme d'applications, ce qui conduit à une grande diversité dans la réalisation du procédé. Même en se restreignant à la séparation des gaz de l'air, on trouve presque autant de designs différents qu'il y a d'installations. Les mêmes lois physiques fondamentales sont cependant à l'œuvre, et les diverses réalisations du procédé ont les mêmes sous-fonctions critiques en commun. Ce chapitre se veut une introduction aux principes généraux et partagés des procédés de distillation.

La première section commence par la séparation d'un mélange par des équilibres diphasiques successifs. Nous présentons ensuite les techniques qui permettent de réaliser ces équilibres diphasiques dans une colonne de distillation. Une telle colonne n'est qu'un maillon de la chaîne de séparation : la section se clôt par la présentation des autres sous-fonctions critiques et de leurs interactions.

En lien avec l'aspect contrôle de cette étude, la section suivante est un aperçu des techniques de modélisation pour le contrôle des unités de séparations, qu'elles soient éprouvées ou en développement. Partant du problème initial de l'exploitation en régime stationnaire, nous nous intéressons au besoin croissant de modèles et contrôleurs pour les régimes transitoires. De nombreux modèles sont de grande dimension, et leur utilisation en temps réel pose le problème des ressources de calcul nécessaires. Nous examinons quelques solutions à ce problème, testées sur site ou en simulation. Comme mentionné plus haut, une colonne de distillation fait partie d'un ensemble plus complexe ; notre revue se termine par un examen des couplages entre les divers sous-systèmes de l'unité de séparation, et en particulier les échangeurs thermiques.

Après cette revue bibliographique, nous évoquons quelques points qui nous semblent ne pas faire consensus dans la littérature. Nous présentons également les axes de recherche de grands groupes industriels dans le domaine de la séparation de l'air, et rappelons le positionnement de cette thèse par rapport à la littérature.

Nous concluons ce chapitre par une présentation plus détaillée d'un modèle de colonne de distillation en particulier, dont cette étude est dérivée : le modèle d'onde de W. Marquardt [74].

Distillation processes are encountered in a broad variety of applications, and thus present a vast diversity in their implementation. Even regarding only air separation, there are almost as many different implementations of the process as plants. Yet the same fundamental physics are at work, and the many process realizations gather the same critical subfunctions. The present

chapter then aims to provide the reader with basic perspective on the shared fundamentals of distillation processes.

The first section begins with the separation of a mixture using successive steps of biphasic equilibrium. Then we present the techniques to maintain and exploit these biphasic states in a distillation column. Such a column is only a link in the separation chain: the section then ends in presenting the other critical subsystems of an air separation plant, and how they interact.

In-line with the control orientation of the thesis, the next section is an overview of well-tried or in development modeling and control techniques for separation plants. Starting from the initial steady-state exploitation issues, we pursue with the increasing need for dynamic models and transient-oriented control systems. Many models are of large dimension, and the need for faster-than-real-time computation rises the issue of CPU resources. We examine some solutions which have been tested on-site or in simulations. As mentioned earlier, a distillation column is part of a more complex system; our overview thus ends by examining the interactions between the various plant's subsystems, focusing in particular on the heat-exchangers.

Following this state-of-the-art, we point out some concepts which do not seem to make consensus in the literature. We also present some research axes of the major gas industries in the field of air separation, and recall the positioning of this work with respect to the literature review.

We conclude this chapter with a more detailed presentation of a distillation column model in particular, from which our work is inspired: the wave-model of W. Marquardt [74].

1.1 Cryogenic air separation technology

In current cryogenic distillation plant design and control, several important concepts inherit from classical[1] separation technology history, which is therefore to be recalled for the sake of comprehension. Yet air distillation rules are also dictated by some peculiarities of cryogenics, which sometimes makes it difficult to transpose results and methods directly from classical distillation processes. These particularities will also be enlightened in the following. Information regarding the distillation principles and the columns technology can be found in [64], [92] and [1]. Information regarding the general functioning of an air separation plant are from [1] and [2].

1.1.1 Principles

Distillation is defined as an operation aiming to separate the components of a mixture by taking advantage of their different volatilities, that is, their preferential accumulation in the liquid or gas phase when the mixture is at biphasic thermodynamic equilibrium. The most elementary distillation device is then provided by a retort as depicted in Fig. 1.1. When heated, the exiting vapor will be enriched in the most volatile components of the mixture, while the less volatile will be concentrated in the remaining liquid. This illustrates an unsteady batch process: compositions of the gas and liquid will vary over time, and one ultimately will have to refill the retort. A continuous process with constant product compositions is

[1] In a somehow circular manner, we will use the word 'classical' to refer to non-cryogenic operations - such as oil separation processes, water-methanol pilot devices...

obtained by continuously feeding the retort and continuously drawing gas and liquid out, as on Fig. 1.2. Thermodynamic equilibrium and mass conservation principle impose the product compositions. Thus at fixed operating pressure and temperature, further enrichment requires cascading several elementary steps, or stages. In a staged process as depicted on Fig. 1.3, the gas leaving stage $n-1$ and the liquid exiting stage $n+1$ serve as feed for stage n. Additionally, gas from stage $n-1$ provides heating power to stage n, while liquid from stage $n+1$ provides cooling power. A top condenser and a bottom vaporizer ensure constant countercurrent circulation of liquid and gas - which yields to the denomination of reflux distillation. The section of the process ensuring enrichment of the feed with the most volatile components is called the rectification section; the other one is referred to as the stripping section.

Let us see how successive stages allow the mixture separation, by a simplified use of the McCabe and Thiele method. Consider a staged process as on Fig. 1.4, with N stages, liquid production at the bottom and gas production at top. The mixed liquid-gas feed flow is F, internal liquid and gas flows L and V are supposed constant along the column (Lewis hypothesis). Let us note them with a subscript r in the rectifying section, s in the stripping section. Consider the separation of a binary mixture, and choose the less volatile component. Let x^i (resp. y^i) be its fraction in the liquid (resp. gas) leaving stage i. The mass balance in the rectification section writes:

$$y^{i+1} = \frac{V_{prod}}{V_r} y^{prod} + \frac{L_r}{V_r} x^i,$$

and in the stripping section:

$$y^i = -\frac{L_{prod}}{L_s} x^{prod} + \frac{L_s}{V_s} x^{i-1},$$

where y^{prod} is the fraction of the chosen component in the gaseous product, and x^{prod} its fraction in the liquid product. On Fig. 1.5 we plot the corresponding lines (namely the rectification line and the stripping line) together with the liquid-gas biphasic equilibrium curve. Starting with the feed stage liquid fraction x_f, we find the fraction y_{f-1} in the gas leaving the stage below using the stripping curve. On the stage $f-1$, we suppose that the liquid and gas are at thermodynamic equilibrium, thus the equilibrium curve gives x_{f-1}. Iterating the procedure along the stripping section, one finds the liquid product fraction x_{prod}, and we indeed have $x_{prod} > x_f$. Proceeding the same way along the rectifying section (see Fig. 1.6), one finds the chosen component fraction $y_{prod} < y_f$ in the gaseous product.

1.1.2 Trays and packings

A stage is efficient if it is as close as possible to the biphasic thermodynamic equilibrium. This supposes maximizing the biphasic mixture homogeneity and the liquid-gas contact surface to enhance phase-to-phase exchanges. Technical solutions to achieve distillation then aim to dissolve as much as possible a phase in the other one. Yet phases will hinder the circulation of each other, causing the energy required to maintain the countercurrent circulation to increase. Almost every distillation column addresses the mixing-circulation trade-off using one of the following solutions: trays or packings.

Trays

A basic tray separation column is depicted on Fig. 1.7. A tray contains a certain amount of liquid through which gas percolates before rising to the superior tray. The liquid leaves the

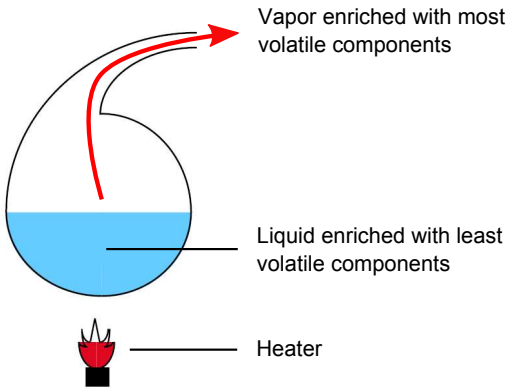

Figure 1.1: A distillation retort

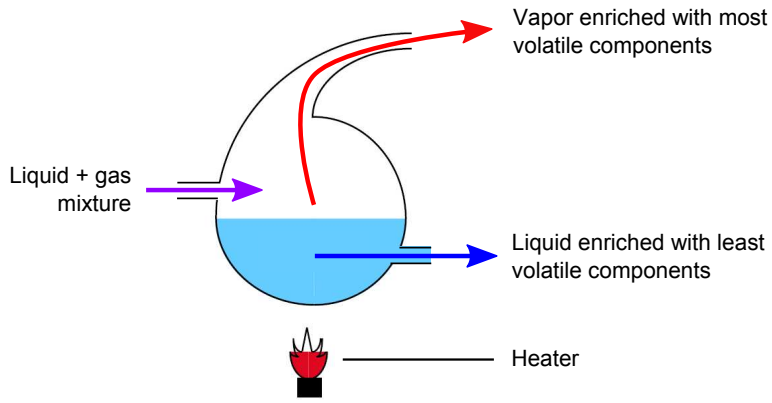

Figure 1.2: A continuously refilled distillation retort

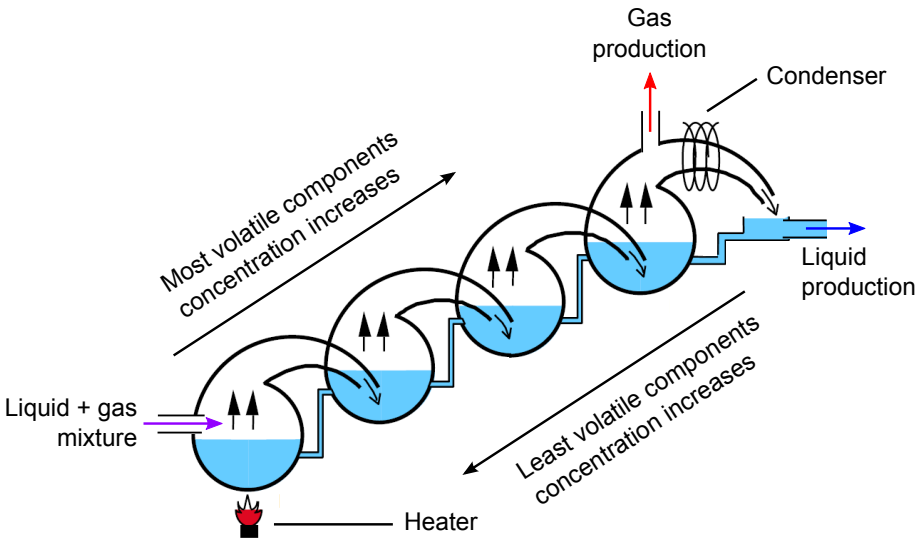

Figure 1.3: Connected retort performing staged reflux distillation steps

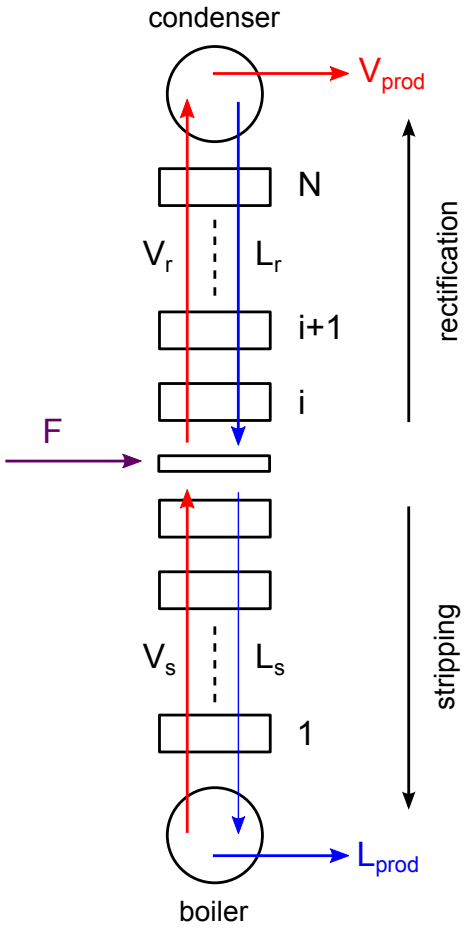

Figure 1.4: Staged separation process.

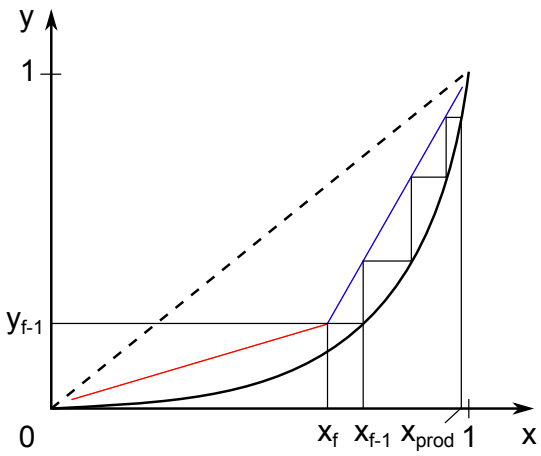

Figure 1.5: Equilibrium curve (solid black), stripping curve (blue) and rectification curve (red). Starting from the feeding stage liquid fraction, one finds the composition of the liquid product.

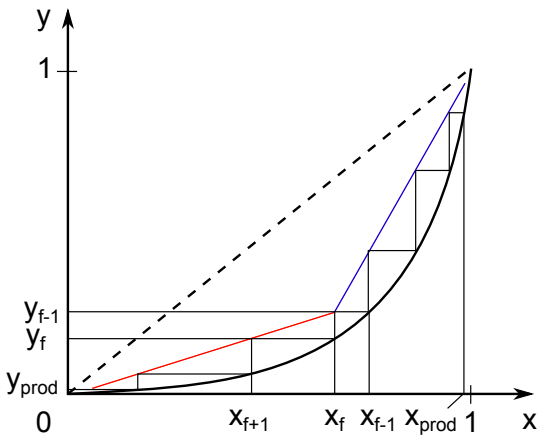

Figure 1.6: Equilibrium curve (solid black), stripping curve (blue) and rectification curve (red). Starting from the feeding stage, one finds the composition of the liquid and gas products.

tray by a draw and falls on the inferior tray. Trays are vertically staged in the column, so that gravity moves the liquid for free. Energy is required to pressurize the gas at the bottom of the column and overcome pressure drop at each tray. A convenient gas-liquid flow rate yields to a foamy biphasic mixture. Too much gas will blow the liquid and decrease the exchange efficiency. On the contrary, a weak gas flow would let the liquid drip through the pinholes, decreasing the foam height as well as the tray efficiency. Variations of the basic tray design (including caps, obturating pinholes ...) exists to widen the range of possible flow rates, yet to the price of increased pressure drops. Trays as depicted on Fig. 1.7 are very sensitive to defects of their planarity (or of the column verticality). Such defect would create preferential regions for the liquid to accumulate, as well as preferential paths for the gas (see Fig. 1.8). To minimize the impact of planarity defects, trays are subdivided into independent volumes using a corrugated geometry termed 'wave' (see Fig. 1.9). Additionally, trays are associated to distributors which ensure homogeneous spreading of the liquid (Fig. 1.10).

Packings

A packing (or structured packing) is a three-dimension structure which defines paths networks for the liquid and gas, and interlocks the circulation channels to maximize the liquid-gas interface. Contrary to tray columns, which are staged systems, packed columns are assimilable to continuous bed processes. The packed section could indeed stretch uninterrupted over the whole column (in practice, it is punctuated with distributors for the sake of robustness towards verticality defects and other causes of inhomogeneous mixing). Depending on the mixture to be separated, packings show various geometries. Random packings (see Fig. 1.11) consist in small sub-structures easy to produce, with which the column is filled. This packings can be made of various materials (plastics, ceramics, metals ...) which also make them suitable for severe operating conditions. In 1977 a low-cost structured packing obtained by juxtaposing corrugated metal sheets as on Fig. 1.12 was introduced. Such structured packings are now widely used, in particular for cryogenic air separation. In these packings, liquid drips in very thin film (about $10\mu m$, similar to the sheets thickness) with direction between vertical and the corrugations direction. Since the gas licks the liquid film instead of forcing its way

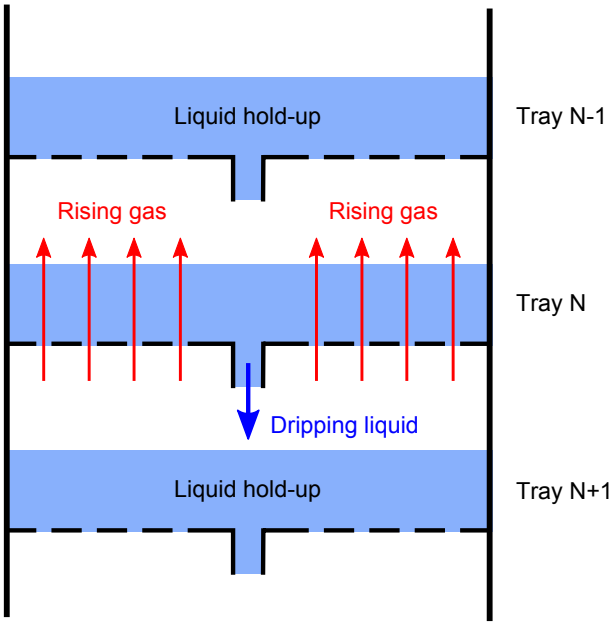

Figure 1.7: Sketch of a tray distillation column

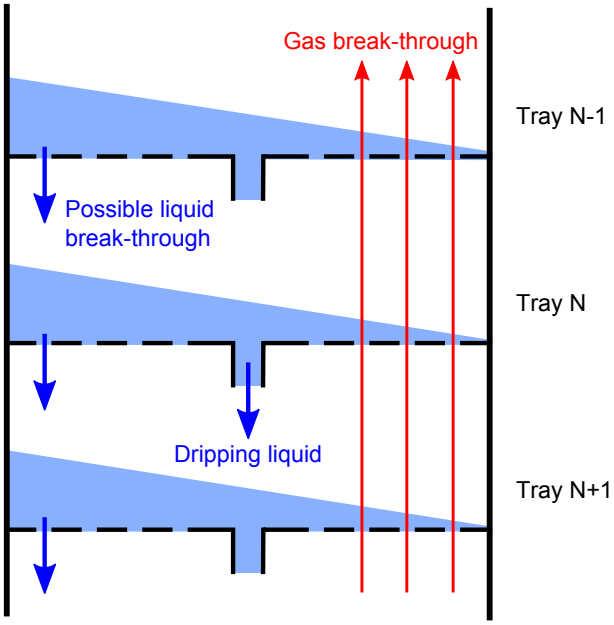

Figure 1.8: A verticality defect of the column causes inhomogeneous distribution on the trays and preferential paths for liquid and gas.

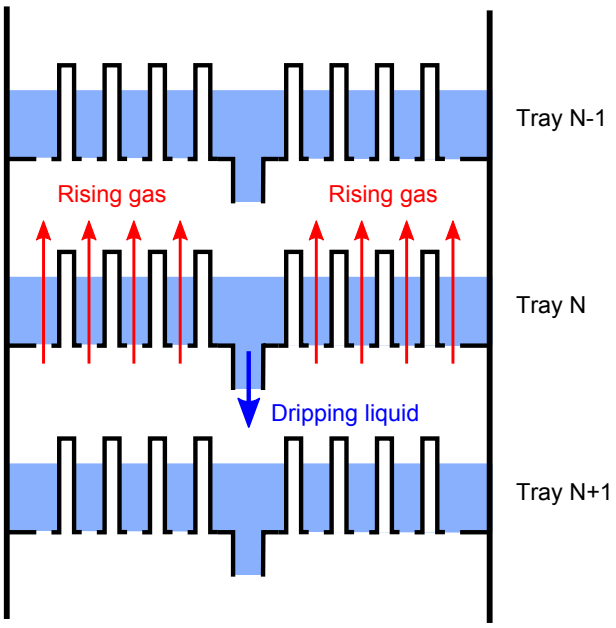

Figure 1.9: A corrugated tray is more robust to planarity defects.

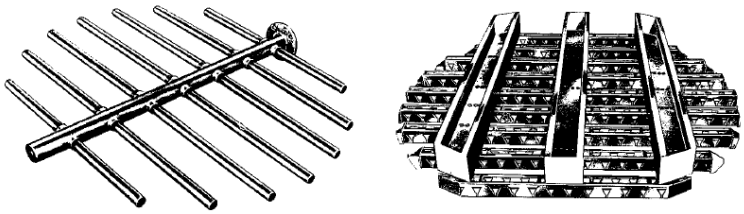

Figure 1.10: Examples of possible liquid distibutors (courtesy of [92]).

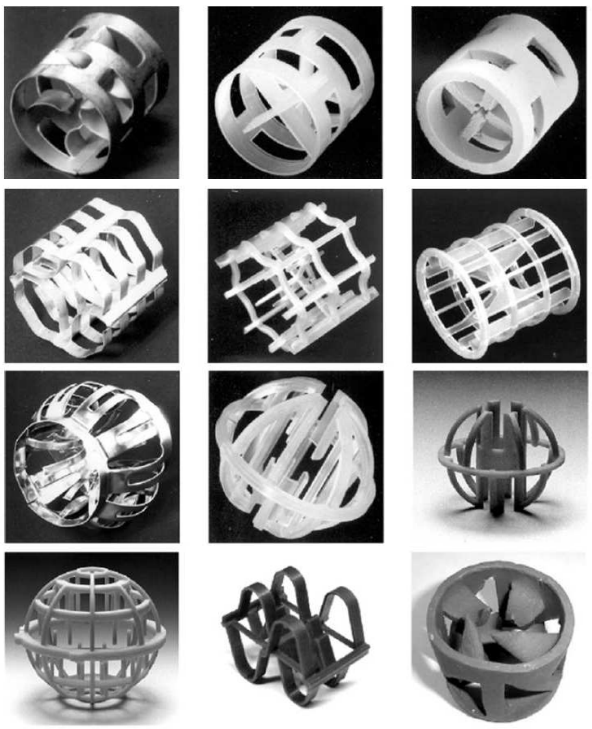

Figure 1.11: A sample of the various shapes taken by casual random packing elements

through, the pressure drops per unit length are dramatically reduced. Structured packings are also promoted for their high mass-transfer efficiency, resulting from the large liquid-gas contact surface. Another advantage is a reduced liquid hold-up compared to the trays, which decreases the process inertia and makes it more flexible.

Other technical solutions

Foliated packings as discussed above do not create real three-dimension channels network, especially for the liquid which is trapped between two sheets. An important part of the liquid paths randomization is thus obtained thanks to distributors and by dividing the packed section into subsections with crossed sheets planes (see Fig. 1.13). Some attempts have been made to develop actual one-piece three-dimension structure, by cutting and folding of the original metal sheet. But manufacturing such a lace is too complex and expensive for industrial applications.

Contrary to the tray technology which tends to dissolve gas in liquid, it was proposed to obtain a mixture of liquid droplets in gas thanks to pulverisers. Yet due to coalescence effect, this solution requires so many successive pulverization steps to maintain the liquid dispersion, that the process is not competitive in terms of energy efficiency.

1.1.3 ASU scheme

Distillation supposes providing a distillation column with raw material (in our case, air) and with the heating/cooling power to maintain biphasic state. Since air liquefaction temperature is about $-190°C$ at atmospheric pressure, a major Air Separation Unit (ASU) design rule is

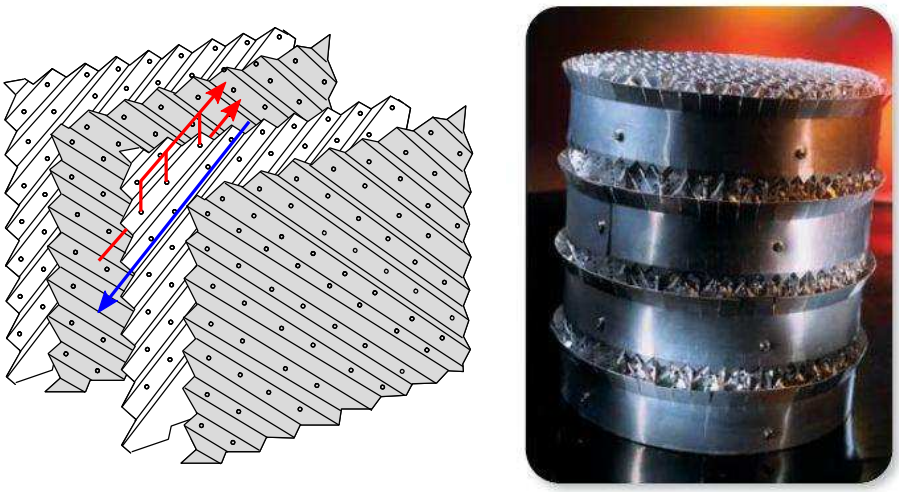

Figure 1.12: Packing as encountered in cryogenic air separation. *Left:* juxtaposed metallic sheets with examples of liquid (blue) and gas (red) paths. *Right:* juxtaposed sheets form staged cylindrical elements in the column.

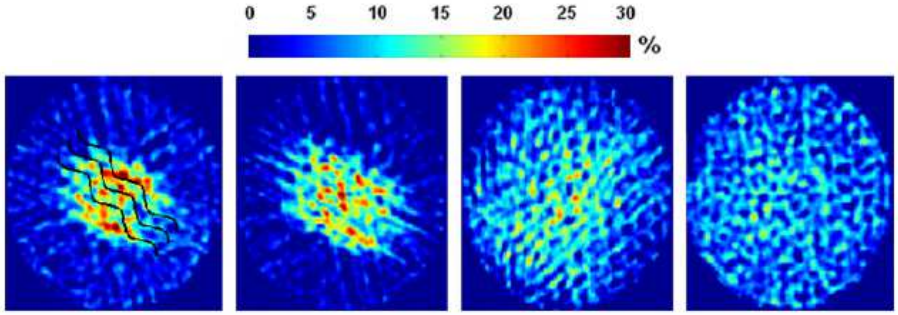

Figure 1.13: Tomography imaging of the radial liquid volume fraction at four locations along a distillation column with structured packing. The column vertical axis is perpendicular to the plane of each figure. The colormap is saturated at 30%. A certain amount of liquid is injected on a disk at the top of the column. The two left figures show that the liquid spreads essentially in the direction of the packing sheets as it drips. Then it enters a section where the packing orientation is rotated by 90°, which changes the spreading preferential direction (third figure from the left). After some alternations of the packing orientation, an homogeneous spreading is obtained (right). Courtesy of [28].

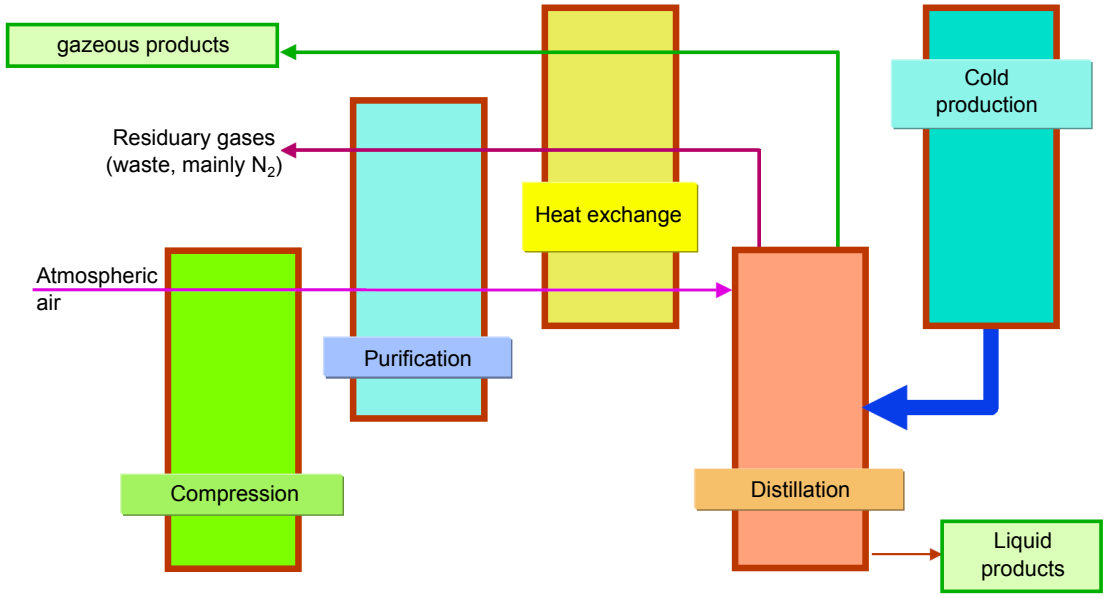

Figure 1.14: The five main functions of an air separation plant.

energy integration : fluids undergo many heat exchanges in order to keep as much frigories as possible inside the cold sections of the process. Many designs have been implemented. Our experimental studies involve a specific ASU design; we will then base our broad explanation of ASU principles on this design.

Five main functions can be distinguished in any ASU: compression, purification, cold production, heat exchange, separation (which we can subdivide into N_2, O_2 and Ar extraction). Interdependence of these functions is depicted on Fig. 1.14.

Compression

Compression is the first link of the chain, and the most energy expensive. Power dedicated to electric air compressors is typically between 1 and $55MW/h$, with typical voltage between 5 and $14kV$. Raw air pressure is increased for two purposes:

- reach the operating pressure of the first distillation column: all the entering air (between 10000 and 20000 Nm^3/h for the ASU we focus on) is thus pressurized to about 6 bar.
- allow further expansions to produce cold: a supercharger pressurizes a fraction of the 6 bar air up to about 40 bar, to be expanded later. Similarly, the pressure difference between column is exploited to create cold by fluid expansion.

After compression, air is cooled down to ambient temperature in water-chilled towers or air-water heat-exchangers.

Purification

Front-end purification step is essentially intended to remove water and carbon dioxide from raw air, since they would freeze inside the distillation columns and cause damage or obstruction. Air goes through a bottle filled with alumina and molecular sieves which adsorb

unwanted components. As the sieve ultimately saturates, it has to be regenerated, that is, vented with dry, unpolluted nitrogen (residual product of the separation step) at high temperature (typically 100 to 300 °C). To maintain continuous air flow to the columns, two purification bottles alternatively operate. Lead-lag control of air flow reduces the disturbance caused by the bottle switches, which occurs about every 3 hours. Due to the heating required for sieves regeneration, the front-end purification is the second most energy expensive step of the process.

Heat exchange

The main heat-exchanger of an air separation unit draws the limit of the cold-box. After this exchanger, the process is enclosed in an insulating casing to maintain cryogenic temperature. Thermal protection measures include white, reflective painting of the casing, vacuum insulation or insulating perlite layers (depending on the unit's size), and inner venting of the casing with cold nitrogen (residual product of the separation step).

The main heat-exchanger's warm-end is about $30°C$, while the cold-end is about $-190°C$. Heat-exchange is achieved along a dozen meters of crossed, counter-current channels separated by wavy aluminium sheets. Every fluid entering or exiting the cold-box flows through this heat exchanger, in order to keep as much frigories as possible inside the casing. In the case of our air separation unit, the main heat exchange also serves to increase part the plant products' pressure up to $40bar$ prior to the injection in a high-pressure distribution network.

A second heat-exchanger (said subcooler) is located between the High and Low Pressure Columns and will be discussed below.

Cold production

In an ASU cold production is equivalent to liquid production. A liquid which is overcooled with respect to the desired biphasic equilibrium serves as a cold source to balance the natural heating of the plant by external sources (sun, atmospheric air, heat losses of the main heat-exchanger at warm-end...). Liquid air is obtained thanks to a turbine-booster device. A fraction of the 40 *bar* gaseous air is cooled in the main-heat exchanger, then expanded in a turbine to the operating pressure of the High Pressure Column, where it serves as gas feed. The mechanical power generated in the turbine is transferred to a booster compressor which increases the pressure of the remaining fraction of the 40 *bar* gaseous air up to 55 *bar*. This high-pressure air is cooled from $70°C$ to cryogenic temperature ($-175°C$) by cooling water and the main heat-exchanger. When in the cold-box, it undergoes a flash to the operating pressure of the High Pressure Column (6 *bar*) and is almost completely liquefied.

Air separation

Air separation takes place in a cascade of four packed distillation columns. The first two columns, namely the High Pressure (HP) and Low Pressure (LP) column, work in a thermally coupled way and are functionally equivalent to a single column with top-condenser and bottom reboiler. Fig. 1.15 illustrates this equivalence. The single column would require cooling power at the top and heating power at the bottom. Here, this equivalent column is split in two, and the halves are arranged upside-down, the top half-column being operated at lower pressure than the other one. Thus cold liquid at the bottom of the LP column provides 'free' cooling

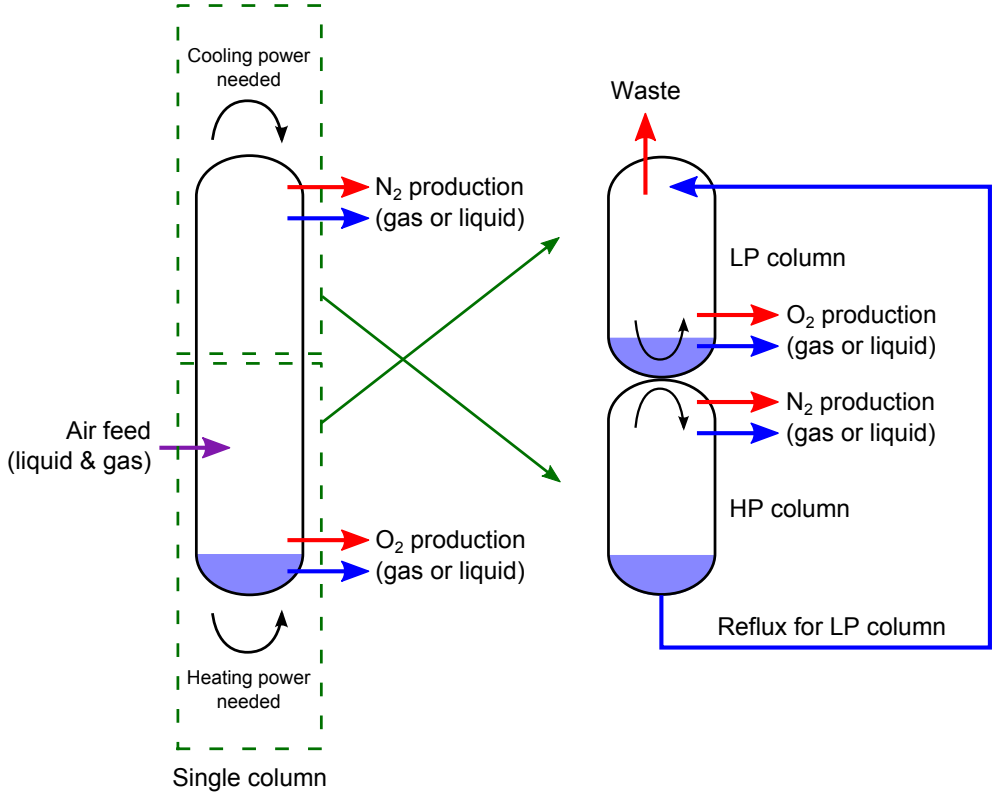

Figure 1.15: Functional equivalence between a single air separation column and two stacked HP and LP columns.

power to condense gas at the top of the HP column. Inversely, gas at the top of the HP column provides 'free' heating power for reboiling at the LP column's bottom.

By equivalence with the single column, it becomes clear that the HP column produces high-purity N_2 (the most volatile air component) at top. The O_2 molar fraction in the pure N_2 is typically maintained below 1 *ppm*. Nitrogen is extracted as a liquid, and can be partially vaporized in the main heat-exchanger to supply the distribution network. The HP column has a second draw located around the 2/3 of its height. The liquid drawn there is called the lean liquid. Its O_2 content is about 2%. Part of the lean liquid serves as cold fluid for Argon condensation in the Argon process; the rest provides reflux at the top of the LP column. All the remaining liquid accumulates at the bottom of the column, where its O_2 content is about 40%. It is withdrawn both to add liquid reflux to the LP column, and to serve for condensation in the Argon process.

The LP column produces high-purity liquid O_2 at its bottom. The O_2 molar fraction there is typically above 99.5%, with less than 100 *ppm* of Nitrogen. As mentioned earlier, liquids drawn off the HP column provide the reflux. A fraction of the liquid obtained by flashing the 55 *bar* air provides an additional reflux. Due to the pressure difference, liquids pumped from the HP to the LP column have to be pre-cooled to prevent excessive vaporization. This is done through the second heat-exchanger, where the cooling power is provided by the residual gas exciting at the top of LP column.

Argon volatility is between O_2 and N_2 volatility. Thus, at the top of LP column, where

N_2 molar fraction is high, Argon behaves as a heavy component and is rejected downwards. Inversely, at the bottom of HP column, O_2 content is high, Argon behaves as a volatile component, and is rejected upwards. This results in an Argon molar fraction peak, called the 'Argon bubble', located at about 1/3 of the HP column's height.

Gaseous Argon is drawn off the LP column thanks to a pipe placed in front of the bubble. This gas feeds a Crude Argon (CA) column, at the top of which one extracts gas almost devoid of oxygen (only some ppm remain). The bottom liquid of the CA column is sent back to the LP column. As the relative volatility of argon with respect to oxygen in close to 1, the separation occurring in the CA column is low and requires a large number of equivalent trays (typically 4 times more than in the LP column). Consequently, the CA column is the highest of the plant (almost $40m$), and the associated liquid hold-ups also make it the slowest (with typical $10h$ time constants).

The gas exiting the CA column at top is condensed to obtain the so-called Crude Argon Liquid (CAL). CAL contains about 99.5% argon; the rest is nitrogen. CAL is then injected into the Pure Argon (PA) column, which achieves the nitrogen-argon separation and furnishes pure liquid Argon (LAR).

One could think that the argon process (CA and PA columns) should be fed with gas drawn off at the very summit of the argon bubble in the LP column. Yet at this location, the N_2 content of the gas would be of about 1%, causing a high nitrogen concentration in the CAL. This would in the end result in a heavy separation burden for the PA column. As a consequence, one preferentially locates the argon draw pipe slightly below the bubble maximum, where nitrogen concentration is about 10 times lower.

1.2 Control models for ASU: an overview

1.2.1 Steady-state exploitation

First analysis of distillation columns for control issues arose from the problem of maintaining stable operation around a given set-point. It seems that consideration of the transitions from a set-point to another one appears quite late in the literature. Papers presented in this part essentially deal with results provided by small excursions of the plant around a given set-point. Historically, stabilized operation was the first way gas industries operated their plants (plate columns used at that time were anyway not suitable for fast and frequent load changes). The main issues to address in that context are:

- Ensuring sufficient product purity;
- Finding proper structures and control to efficiently drive their units;
- Maximizing the profitability of the process despite disturbances or uncertainties on the operating conditions. In this vision, the main dynamic concern is not the proper control of trajectories in the operating conditions space, but rather to obtain interesting stabilization properties or transitions between two operating points, using the simplest feasible control strategy.

Control configurations

From a business point of view, in which economics are strongly related to steady-state operating steps, it is convenient to consider the distillation column as a reactive tank, with only

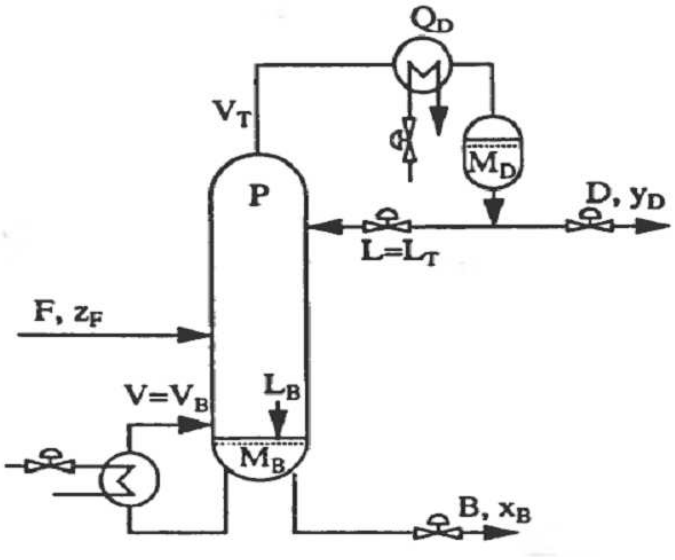

Figure 1.16: Generic business vision of a distillation column. F, V_T, L_T and V_B are vapor and liquid flows, M_D and M_B are condensed liquid accumulations, B and D are drawn-off product flows, Q_D is the top condenser duty, P is the inner column pressure, x_B, y_B and z_F are the concentrations of chemical elements of interest. Courtesy of [100].

little insight into the reaction process. The idea is to focus on the management of the various flows entering or leaving the tank, to ensure profitability in stabilized operating. In [100], Skogestad gives a generic depiction of such a model, which is reproduced on Fig. 1.16 In the following, our notations refer to this figure.

Inner conditions (pressure and liquid levels) must be driven to acceptable values thanks to low-level control loops before one begins to tune the product purity. At the beginning, the trend was to manage each output separately, using single-loop controllers. The pressure P is usually controlled using the exiting flow V_T, while liquid levels are managed through various combinations of remaining vapor and liquid flows. In the end, only two combinations of these flows remain, which are assigned to the control of output concentrations x_B and y_D. This pair of flow combinations is called the 'control configuration'. For instance, if the dripping liquid flow L and the ascending vapor flow V (see Figure 1) are the remaining flow, the term '$L-V$ configuration' is used. The search for a systematic procedure to choose convenient control configuration led to a massive use of the Relative Gain Array (RGA) tool which basically gives information on how the control loops interact with each other. However, distillation was found to be a strongly interactive process, with the consequence that no configuration seemed to provide straightforward decoupling between all the process loops in steady-state. The trend in the industry was to use the easy to implement $L-V$ configuration, which however has the drawback of maintaining interaction between the top and the bottom product purity. This configuration is thus more suitable for one-point purity control (that is, tight control of one product purity, while the remaining one is floating). It was also found [100] that $L-V$ configuration is not the most robust to process disturbances.

Later, with better insight into the dynamics of the process, it was found that the importance of the configuration choice was somehow overestimated, as Skogestad notices himself in [102]:

- First because out of the steady-state, the loops are increasingly uncoupled as frequency increases, due to the propagation delays inside the column.

- Second because it appears that a proper control of the products purity is in practice accomplished only when an additional, fast control loop is added (usually controlling a temperature somewhere inside the column - the choice of its position will be discussed later), which will impact the other control loops.

Self-optimizing techniques

For valuable operation of distillation plants, one has to find the tuning which maximizes the profitability of the process, with respect to several constraints (arising either from the design of the plant, like a maximal admissible flow in the pipes, or from contracts with the customers, like a maximum concentration in the products). Robustness toward disturbances is also taken into account in the tuning. In absence of accurate dynamic models of the process, the optimization has to focus on steady-state exploitation (possibly including some equivalent cost for set-point changes).

The calculation of the optimal tuning for every possible operating condition is computationally expensive, because of the non-linearities of the process and the complexity of the related minimization problem. Plus, it would require very precise knowledge of inner conditions to precisely take into account potential disturbing influences. Self-optimizing techniques offer a mean to approach the steady-state optimum with reduced tuning complexity. By computing off-line the optimal values of the controlled variables for the undisturbed steady-states and slightly disturbed steady-states around them, it is found that many of the variables remain saturated. For these variables, a controller which maintains them to their constrained value is sufficient. To fix the remaining degrees of freedom, one then looks for variables whose optimal value vary little around the undisturbed steady-state ; that is, the loss of optimality is reduced when the system is disturbed whereas the variable is still at its optimal value for undisturbed steady-state. In [102][24], it is found that a temperature loop can be closed on a constant value to achieve nearly-optimal operation around a set-point. On the contrary, variables which show steady-state multiplicities are typically unsuitable for that use.

Stage-by-stage models

Though plant-wide vision may provide interesting optimization results, it has limited performances, and is of course unsuitable for column design, because it gives no insight into the physical phenomenon occurring inside the apparatus. Staged separation columns can be designed according to variants of the famous McCabe & Thiele design method (historically presented in 1925 in the paper 'Graphical Design of Fractionating Columns', in Industrial and Engineering Chemistry). Brief explanation of the method can be found in [40]. Essentially, the distillation process is considered as a succession of thermodynamic flashes in stacked distillation plates, with no transformation phenomenon between the plates. Inspired from this static design method is the dynamic stage-by-stage model (also called equilibrium stage model).

Stage-by-stage model equations are recalled in numerous papers of our literature, notably [88] [61]. They are based on the mass and energy conservation equations around each plate, together with simplified hydraulics to account for flow exchanges between the plates, and with

the idea that the multi-phase equilibrium is always reached on the plates. Besides, implementations of the model often differ in their assumptions on the hydraulics. One usually integrates an efficiency coefficient Eff (empirically determined) in the model, which accounts for non-ideal phase concomitance on the plates: one states that the perfect multiphasic equilibrium hypothesis concerns only $Eff\%$ of the flows passing through a plate, while the remaining $(1 - Eff)\%$ 'ignore' this elementary step. This concept is illustrated in [88]. A drawback of the stage-by-stage model is its large number of state variables. The whole column is represented as a vector of $n \times m$ states, where n is the number of distillation plates, and m is the number of variables (pressure, temperature, molar flows and molar hold-ups, concentrations...) for each plate. Then each stage corresponds to a set of dynamic equations to be solved. Time-scale aggregation technique [70] (see also [90]) proposes differentiating two time scales in the process: the flash on each plate corresponds to a fast dynamics, compared with the dynamics of a large set of plates, which is slow. Using singular perturbation arguments, transient state are supposed to be instantaneous on each plate of the set (transforming the associated ordinary differential equation into costless algebraic equations), whereas a virtual stage inherits the mean transient behavior of the whole set. The trade-off between accuracy and computational cost is managed by tuning the size of the sets of plates, or 'compartments'. As they rely on instantaneous dynamic assumptions, the so-called compartmental (or aggregated) models and stage-by-stage models are strictly equivalent in steady-state anyway. One of the advantages of this order-reduction method is that it avoids losing the physical meaning of modeling (which is a drawback of the methods based on coordinates changes and truncation). More detailed aggregated models for high-purity air separation, including ternary mixture, energy balances and non-ideal liquid-vapor relation have been investigated with support from Praxair recently [9][18]. See also [73] for an extension of [70] to a broader variety of systems. Reduction of the number of variables via aggregation methods also have application in design optimization for distillation systems, such as in [57].

Steady-states properties - Conditioning issues

Without even considering the issues related to accurate dynamic simulation of their behavior, distillation columns show complex static input-output relations. First, given an operating set-point, columns are reported to be highly directional. In the simplified static model where the column is represented by a 2×2 gain matrix between the control flows (say L and V assuming that the classical control configuration is adopted) and the output product purities, purities are much less sensitive to inputs variations in the same direction ($dL = dV$) than in the opposite direction ($dL = -dV$). In [103], Skogestad reports for example impressive condition numbers between 30 and 7000 (at null frequency) for various example columns. Second, the static relation between the purities and the operating conditions is strongly non-linear. This non-linearity is related to several causes, among which the physical boundaries of the concentrations (between 0 and 1), the non-linearity of the liquid-vapor equilibrium relation, and the fluid mechanics. A (partial) palliative to this issue is to express the concentration in log scale, which permits to attenuate the non-linear effects. Illustration of this coordinate rescaling can be found in [103][101]. This method has to be related with the strong exponential dependencies found in the explicit expression of the purities in steady-state given by the use of wave model ([113]) which we will present in Section 1.2.2 and Section 1.4. Moreover, due to these non-linearities, one set of operating conditions can correspond to multiple steady-states. Such degenerations were first reported in 1979 (according to [63]) in the case of heterogeneous,

azeotropic mixture separation. Further, other cases involving mixtures with particular liquid-vapor equilibrium relations or reactive separation processes were reported. Some papers show that the steady-state multiplicity may not only come from intrinsic mixture properties, but also from improper feedback structure (e.g. in [63], Kienle et al. with an approximate conversion of a volumetric flow into a molar flow). Other multiplicities are illustrated in [24].

Conclusion

Plant operation in stabilized conditions, using linear models valid around the reference set-point, emphasizes the importance of non-linearities in the column behavior. This complexity is handled through good practices (use of log scale, choice of control configuration etc.) and by limiting the loss of optimality through proper selection of non-optimized variables ('self-optimizing method'). Models explicitly taking into account the inner physics are necessary in this context for accuracy improvement. Stage-by-stage modeling paves the way for simulation and control of large dynamic excursions, and gives also an insight into some issues connected to the model complexity.

1.2.2 Dynamic modeling and control

Linear dynamic models

The basic context of the first linear dynamic models is still to consider the distillation column as a 2x2 system once the control configuration has been chosen. At the beginning, the main transient behavior was depicted using a first order model with one time constant. This approach remained close to the plant-wide approach previously discussed, and the time constant accounted for the 'mixing-tank' behavior of the column, with little consideration given to the inner phenomena at work. Later, frequency RGA (Relative Gain Array) analysis showed that the huge RGA values collapsed as the frequency increased; this phenomenon was not rendered using only one time constant. In [103] Skogestad then suggested to add a second, shorter time constant to render this influence of the internal flows dynamics, and to tune it to fit RGA curves. Being able to investigate more precisely the initial response of the column, it was found that the logarithmic scale change for purities had an interesting linearizing effect on the first part of the transient step (though being less important as the system gets closer to the steady-state).

This model then has an obvious drawback: it is valid only for a small set of operating conditions centered on the set-point for which the transfer function has been fitted. This has of course important repercussions on model-based control robustness. Yet attempts have been made to extend the range of validity for controllers based on these kinds of model structures. In [19], Christen et al. derive a linear model for both the minimal and the maximal load of the distillation column. They then consider that the actual (uncertain) behavior of the column is a barycenter of these two extreme cases, with uncertain weighings. The framework of structured uncertainties allows taking this partial information into account for the modeling of the actual column behavior, and applying robust controller synthesis techniques (such as μ-synthesis or H_∞-synthesis). 2x2 linear models with two time constants coupled with structured uncertainties have been studied until recently to obtain robust closed-loop performance [83].

First-principles, continuous modeling

Stage-by-stage and compartmental models gave interesting static and dynamic results as far as staged columns were effectively concerned. When packings began to replace copper trays for certain scopes of application (notably air separation), the idea was to find equivalence between the new process and the former models, to apply proved techniques. The link was made stating that a given height of packed column had the same separation performance as stacked trays. The ratio, called the HTU (Height of Transfer Unit) is often used in manufacturer data as a measure of the performance of a particular packing design for a particular separation process. The equivalence is convenient and allows satisfactory static simulation of packed columns with staged models for classical distillation and even for high-purity processes with fine enough tuning. Yet the equivalence leads to important dynamic inaccuracies (as depicted in [61] for example), and is therefore not suitable for high-purity separation simulation and control purposes. In packings, fluids are now subject to continuous thermodynamic transformations along their path, instead of flowing from a located mixing area (a tray) to another one. Stage-by-stage models are consequently not correctly structured to represent the continuum, even if one unreasonably increases the number of trays. There was then a need for a new modeling approach, to catch phenomena at a new level of detail.

Very accurate modeling at the scale of the droplets, involving extensive Computational Fluid Dynamics (CFD), is hardly suitable for off-line simulation of large volumes, and certainly unsuitable for control purposes. Its range of application is limited to the characterization of packings properties by simulating some elementary meshes of the structure. A rougher approach is called the "hydrodynamic analogy" ([59][15][96]). The idea is to replace the actual, extremely complex fluid paths with combinations of more 'academic', geometrically simple flow patterns (typically flat films). This method allows easier simulation of larger volumes (at the scale of the whole column) than the previous one. But the dynamics of these simple flows has to be accurately computed, requiring high calculation costs. Moreover, numerical convergence of such detailed models is slow and hard to ensure. A simplifying approach is then required for control purposes.

In the mid 80s, Marquardt [74] proposes a new, shortcut macroscopic model of the ideal binary distillation process, which accounts for the non-linearity while being computationally cheap enough to allow real-time control applications. The key idea is that matter is continuously transferred from one phase to another, because the constant relative displacements of the fluids maintain them in an unbalanced thermodynamic state. The unbalanced term is given by the difference between the actual concentrations in the gaseous phase and the concentrations at the equilibrium with concomitant liquid phase (which has the largest time constant in the process). Note that the relations connecting the matter transfer flow and the unbalance are dependant on the packings properties, and can be experimentally estimated, such as in [23]. Through these unbalanced terms and using mass conservation principle, material balances on the liquid and on the vapor around an infinitesimal slice of the column are connected to each other. Integrating these balances along the whole column, one obtains a continuous formulation of the concentration profile for the elements in the mixture, which shows a marked front in steady state. Marquardt's idea for model reduction is to assume that the system dynamics is essentially caused by the propagation of this front, and not by changes in its shape (see Fig. 1.17). Using mass conservation principle on the whole column, he derives an approximation of the front speed; he can then simulate the distillation dynamics by propagating the non-linear concentration wave. Marquardt's work relies on several simpli-

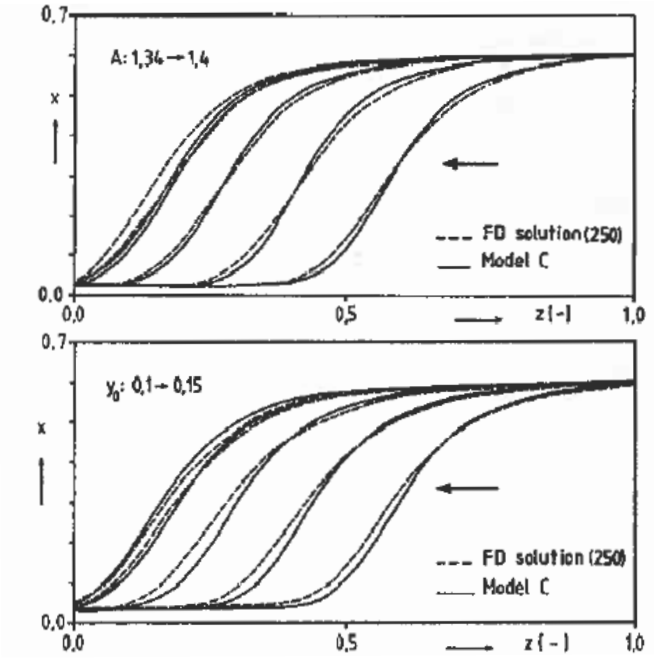

Figure 1.17: Illustration of Marquardt's wave model results. Solid lines represent the concentration profiles along the column (normalized abscissa from 0 to 1) as operating conditions vary, according to the wave model. Dotted lines correspond to finite differences solution of Marquardt basis equations. One can see how the wave model profile 'slides' without distortion. Courtesy of [74].

fications of the process, such as constant pressure, molar flows and relative volatilities of the components along the column. Relaxation of these hypotheses have been considered in later works, energy balances have been taken into account, and the principles of the wave model have also been extended to multi-component distillation [36][62].

Under the main hypothesis of the wave-model (constancy of the wave front shape), concentration control is now possible in a cascade manner, through wave-front position control. The later is made through wave-speed control based on material balances. Yet this crucial hypothesis has been questioned. Discrepancies between the wave-model predictions and the detailed simulations (made with the engineering tool Aspen Custom Modeler or similar software applications) have been pointed out and related to not-rendered front shape variations when operating conditions vary [113][60]. Proper front rendering becomes then a key issue in the context of product purity estimation and control. The most common answer to that problem is to dynamically adjust the modeled profile shape thanks to online state estimation techniques (typically using Extended Kalman Filters, [113][7][8]).

Additional measurements are required for front re-localization. Concentration measurements are the first possibility. However, since concentration, temperature, pressure and molar flows fronts are correlated (because they correspond to the same area where large mass transfers occur between phases), temperature measurements are a good alternative: they are cheaper, almost not delayed, and more robust. As it is not possible to monitor the whole column to reconstruct the whole concentration profile, research efforts have aimed to find proper sensor locations. They are most often determined by setting a large amount of potential loca-

tions, constructing the sensitivity matrix between these candidate measures and the observed variables through accurate simulations around a set-point. Then the candidate measurements are ranked according to the information amount they provide, by applying Principal Component Analysis techniques. Finally, the sets of location which remain high-ranked for various set-points are selected. The ranking of the candidates can be modified to favor measurements which are the less correlated with each other [7][8]. One can also cite [99] where the sensors location problem is addressed with the mean of empirical observability gramians to deal with the process non-linearities over its range of operation. As one can expect, selected measurements are often located close to the front (where they provide important sensitivity at the beginning of the transients, when the front moves) and at the column ends (where static gain is exploited at best). Connection between temperatures, concentrations and locations are often written through Taylor expansions around the front inflexion point, assuming that partial derivatives can be approximated by constant coefficients or finite differences between sensors-provided data [87]. One can also mention inferential formulas, whose coefficients are determined by Partial Least Square based methods on collections of static data or time series [87][58][77]. The inferential approach has the advantage of being computationally fast, as it only requires the evaluation of a simple function of the measurements. Yet the structure of this function (e.g. polynomial) is chosen to provide easy-to-fit coefficients rather than physical significance, with obvious drawbacks on its range of accuracy. The inflexion point of the profile is the location where it is best approximated by a regular slope. Yet during load changes, the front may move far enough from its initial position, so that the measurement locations are too distant from the inflexion point to provide relevant information. In some papers, a weighting function is then applied on these measures, to maximize the influence of those which are close to the current inflexion point [97][33].

In fact, the reason for the inaccuracy of the constant front shape hypothesis is closely connected to the simplified treatment of the boundary conditions in the wave-model. In Marquardt's model, the column ends are considered as infinitely distant from the concentration front, and have thus no effect on it. In a real column, of finite length, at the top and the bottom, partial recycling of the distillates creates a repelling effect on the concentration wave, which prevents a sharp shock-wave to reach the column boundaries, and modifies the shape of the concentration profile when the front moves. This effect is typically not taken into account by the wave-model [36][9], and seems to have been only little addressed [62].

Wave-modeling is not yet the most widespread approach in classical distillation (possibly because several distillation processes still use staged columns). It seems however much more classical in processes involving reaction-diffusion or reaction-convection phenomena, such as reactive distillation or on-bed chromatography, which are often referred by documents related to coherence or partial coherence theory (process description where sets of physical variables travel as perennial waves, mentioned in justification of the wave-model approach), as illustrated e.g. in [37][32]. Stage-by-stage models are then still widely used, for example to address the issue of Input-Output Linearization (IOL) of the distillation columns. In [54][53][55][52], input-output linearization techniques are illustrated with various complexity of the staged model. These papers emphasize the advantages in using a shortcut state observer with measurement feedback rather than a complex state estimator in open loop. The need for such a feedback was expressed in an earlier paper [67], which also pointed out issues regarding input saturations. Even though later works proposed palliative, constraints and uncertainties handling (e.g. [66][11][10]), results of the IOL approach remain very poor as far as output purity control is concerned. In fact, this method focuses on the column top

and bottom stages, therefore losing the 'forward' information provided by the consideration of the whole profile. In [94], Seliger et al. establish a link between wave models and stage models, in their analysis of the dynamics behavior of a plate column. They distinguish the short-term and the long-term responses. The first one is explained to be mainly driven by hydraulics and mass and energy balances along the column, as in the classical stage-by-stage model. The long-term concerns only concentration changes, and is explained using a wave framework. The paper notably illustrates the asymmetric dynamics of the column, which is also predicted by wave models [36].

'Intelligent' modeling and control

In parallel with research on analytical, comprehensive models and control laws for distillation operation, several attempts have been made in the field of black-box modeling to address the issue of separation process control. Given their ability to approximate complex, non-linear behaviors with simple structures, neural networks have been used as output composition predictors for column model predictive control [95], with notable inherent drawbacks connected to their learning sets: it can be long and difficult to construct them with diversity and significance enough. Other classifiers such as Support Vector Machines (SVM) have been tested ([50]) yet are only slightly better than the best linear models. To compensate for the lack of confidence in neural networks outside their training area, it has been proposed [65] to associate them with more robust (although less accurate) wide-range models; with a suitable confidence estimator, a progressive switch is done between the neural network and the robust model, so that the most adapted to the current situation has the preeminence. On the control side, intelligent techniques do not appear directly as control generators, but rather in supervisory layers; one finds occurrence of fuzzy-logic layers performing on-line tuning of the low-level PID controllers, reproducing the know-how of human plant operators [85].

A more interesting application of these intelligent techniques can be the automated startup of the distillation plants. In that particular phase, several steps of relatively short duration can be distinguished, wherein various physical phenomenon successively occur and drive the process. As a consequence, a detailed white-box modeling of each step may be an unsuitable approach, given that the accuracy requirements for the models may be less stringent than for optimized plant operation. Plus, operating conditions are *a priori* less subject to change. Thus, a black-box approach can be relevant, provided minimum comprehension of the system to determine proper structure and objectives for each step, such as in [25].

Conclusion

Models containing a set of static gains, time constants and delays are not sufficient for dynamic behavior simulation. Even if they were associated with robust controllers synthesis techniques, the resulting system would hardly match high-purity accuracy requirements. Stage-by-stage models have the decisive advantage of being close to the physics of the staged columns. Yet it is proven that their accuracy is decreased as far as packed columns are concerned. Wave-models result in a new continuous modeling of the distillation, which matches the rate-based phenomena occurring in the packings. They allow a very concise modeling of the columns, but still lack of accuracy because of neglected end-effects. Numerous methods exist to estimate the concentration profiles without monitoring the whole column. They emphasize the usefulness of reduced models with feedbacks. Alternative approaches exist, such as fuzzy logic or neural

networks, but seems more suitable for low-purity processes or start-up steps.

1.2.3 The computation time issue

As illustrated by the previous paragraphs, the reduction of the computational effort required both by the simulation and the computation of the optimal commands is an underlying issue as soon as the modeling approach is non-explicit. Computational effort reduction can be made through model reductions or simplifications, which are then closely related to the physics of the actual process. Conversely, several general mathematical or algorithmic methods provide interesting results when applied to distillation, and are therefore more frequently applied or studied. As far as dynamics are concerned, the main problem is to reduce the computation time, to perform reasonably fast simulation and ultimately to comply with process control (and even predictive control) requirements. A possibility is to replace on-line computation with off-line pre-calculation. To improve the computational performance of the aggregated model, instead of computing the numerous algebraic equations on the fly, one can express them as functions of the reflux rate and of the concentrations whose dynamics are explicitly depicted by ODEs (Ordinary Differential Equations). Then, off-line, one maps the values of these functions all over their (bounded) parameter space. On-line model computation is thus reduced to approximation of ODEs solutions through look-up in these pre-calculated data. Skogestad and Linhart present the method in [72]. On a test case, they announce 5 to 10 time faster computations, without optimized storage structure for pre-calculated data.

In the field of optimized operation, and particularly when predictive control is used, the main objective is to reduce the on-line computational effort required for the minimization problem, which generates the optimal control. Here the aim of the computation is then not to simulate the system, but to generate this appropriate control (which however possibly necessitates simulating the system). Several possibilities exist to quicken the task. An approach consists in roughly simplifying the control model, through local linearization for example. Thus in [18], Chen et al. test a simplified linear model predictive controller (LMPC) versus a non-linear model predictive controller (NMPC) on a column simulator. The LMPC causes no computation time issue, but is too simplistic to reach the optimization problem constraints, with notable over-purification as a result. The NMPC requires several computation-time reduction strategies to be implemented to converge fast enough (computation time is reduced by 95%). But it manages the constraints better.

To obtain both accurate and fast predictions and control, the idea is then to preserve the original model structure. One can improve the computations using the existing knowledge of the system and using the available time differently. As previously, one can export most of the computations off-line, using a mapping technique. The system is located in a multidimensional space using appropriate coordinates (state variables, constraints of the problem...). This space is split into several areas, on which a specific parametric control law is pre-defined (hence the term 'multi-parametric model predictive control'). The key is to define the pairs area, control law so that the control laws remain optimal or quasi-optimal on their dedicated area (and, on their dedicated area, at least as efficient as any other areas's dedicated law). The possibility of constructing these critical areas and the corresponding control laws depends on the properties of the underlying global optimization problem [80]. Once the areas have been defined, solving the optimization problem at each time-step is transformed into retrieving the area which corresponds to the current coordinates of the system. The appropriate control to be applied is then directly given as a function of these coordinates. As no optimization task is therefore

performed on-line, the controller can ultimately be embedded in a simple electronic chip. The technique and related issues are presented in [81][20]. In the latter, application of the technique to a small air separation unit (similar to Air Liquide small nitrogen production units called APSA - Advanced Product Supply Approach) is mentioned. On-chip controller uses 8 coordinates and 578 areas and specific control laws. The apparatus is driven closer to its contractual limit, with energy savings estimated to be around 3%. Alternative techniques are proposed to solve only some optimization problems over a relevant domain, and to interpolate the solution of the actual problem from stored nearby data, such as in [41].

Another approach consists of an improved use of the interval between two sampling times, which can be used to anticipate the incoming optimization problem. Classically, when a sample time t occurs, the controller computes and generates the optimal control (with a certain computation lag), and then must wait for the following sampling instant t+1 to begin computation on a new optimization problem. The principle of the advanced step non-linear model predictive control (asNMPC [46][111][110]) is to shift the computation sequence forward. At instant t, the state of the system is known (estimated), as well as the generated control. Consequently, one can compute the theoretical future state of the system at $t+1$ (which will occur only if the models are perfect, if no disturbance occurs, etc). Therefore, one knows the theoretical optimization problem that would have to be solved at $t+1$. One can solve this problem (in a feedforward manner, because these 'background' computations occur between t and $t+1$) and obtain the theoretical optimal control to be generated at $t+1$. To deal with model inaccuracies and disturbances, an additional background computation is made to obtain the sensitivity matrix of the optimal solution with respect to local variations of the optimization problem around its theoretical $t+1$ value. Then at instant $t+1$, the actual optimization problem is known, as well as its variations with respect to the theoretical pre-solved problem (which should be close enough to the actual problem, so that local considerations remain acceptable). Adding the proper complement to the theoretical optimal command to obtain the actual quasi-optimal command to be generated is then computationally cheap. Once this command has been generated, the method can be iterated. In [46], the CPU time requested for on-line computation steps is reduced by a factor of 100, while maintaining quasi-identical performances in comparison with the original NMPC algorithm.

Of course, none of these methods is perfect, and each has its drawbacks:

- Multi-parametric approach supposes a convenient subjacent optimization problem.
- Mappings may be memory consuming, and require efficient look-up techniques overall.
- The asNMPC approach requires no off-line storage, but supposes that all the background computations can be done during the sampling time.

They however remain promising, with the noticeable advantage that they do not denature the physics-based structure of the underlying models.

1.2.4 Plant-wide issues

Couplings

Until now, the distillation column has been considered as a stand-alone device. In fact, columns are in general part of a complex production plant, and consequently, interactions between various components have to be considered. Their importance may grow with the

energy-integration of the process. The less energy is wasted, the more the process involves recycles and thermal coupling between the columns outputs and inputs. Consequently, these interactions are particularly important in the field of cryogenic distillation, which is a highly energy-integrated process. Quite simultaneously with Skogestad contributions on control configurations, [31] investigated the choice of a SISO (Single-Input-Single Output) control scheme for a set of coupled distillations columns, and its impact on the whole plant controllability. In [93], a study on several possible configurations for a sequence of (non-cryogenic) distillation columns shows that their controllability is decreased when operating at the minimum energy consumption set point, which makes them less robust regarding disturbances. Ultimately, choosing a non-optimal set-point (with respect to energy consumption in undisturbed conditions) can improve the plant profit margin (in real disturbed operating conditions). Considering the coupling effects in the whole plant through detailed simulations (using Aspen Custom Modeler or similar software), or even through a shortcut plate-model approach [115], obviously makes the choice of optimal values for inner variables more complex. Even in steady-state, when a set-point change occurs, the new static optimum can be too far from the previous one to allow classical Newton-based solvers to find it. Alternative techniques can then be used, such as homotopy-based approach. This method will continuously transform the optimization problem from a hypothetical simple one to the actual one, thus 'smoothing' the shift of the optimum [114]. Couplings at the scale of the plant are also addressed for optimal design purposes. In [116], non-linear interior point algorithm with barrier functions is used to find a set of design parameters and static control references. The goal is to allow the plant to satisfy several scenarios, which account for uncertainties in the process modeling and exploitation. The results of the numerical experiments, involving 8000 to 675 000 variables (in spite of rather simple modeling), illustrate well the long-range effects of the couplings: a +/- 20% uncertainty on the argon demand (that is, on the last step of the process) requires 26% supplementary horsepower for the main air compressor (i.e. on the first step of the process).

Note that, starting from the original problem of plant controllability around an optimized set-point, plant design and control strategies optimization increasingly tends to focus on dynamic operation, in response to fast varying econometrics (energy cost and customer demands, essentially). For instance, [16] investigates ASU optimization for fast set-point changes, considering control inputs together with the possibility of assisting the plant with additional storages. In [47], [48] and [49], economic objectives are directly integrated in the process control problem, where electricity cost is assumed to obey a periodic pattern.

Heat-exchangers modeling

As the couplings in cryogenic distillation are essentially caused by thermal exchanges in the plant heat-exchangers, it is reasonable to view them as critical devices to be modeled. The aim is to ensure that the heat exchange network control prevents a destabilizing feedback from happening, which would partially recycle output disturbances as input disturbances. A lot of literature deals with detailed, computationally intensive numerical simulations (in steady-state as well as in transient), and fast solvers and reduced models are quite common for steady-state modeling ([5][12] for example). On the contrary, dynamic heat-exchangers simulation for real-time applications seems less mature , though the need for reduced heat-exchangers models and concerns regarding their relevance are expressed in various industrial fields (see e.g. [98]). Spatial discretization of first-principles equations may be used [86], but remains computationally costly. Solving the modeling problem in Laplace or frequency do-

main can provide the explicit solution in time domain, but the drawback lies in the numerical computation of the inverse transform [82]. Shortcut models provide costless expressions of exchanger transient behavior. They derive from a globally acknowledged assumption of first order transition from the initial steady-state temperature distribution to the final one. The time constant however varies along the fluids propagation direction. Thus the model renders the delay observed between temperature changes at the inlet and the outlet. This framework is used in [109][3]. Experimental validation is quite satisfying, though it suggests that a second-order model should be used to take fluid propagation effects into account. The first-order model also has been used to apply Kalman filtering framework to the heat-exchanger problem in [6]. Note that the shortcut approach is here only applied to 2-fluids exchangers. Moreover, the authors associate each kind of disturbance with a transient response, but give no clue on how to combine them together. Note also that an important issue is to take into account single-phase to two-phase transitions (or vice versa) in the fluids. The latter issue is addressed by the moving-boundary framework (see Pettit et al. papers: [108] for a general model, and [79] for a resulting application on an evaporator). In this framework, each fluid channel in the exchanger is divided into several successive zones (one zone for liquid phase, one for concomitant liquid-vapor, and one for vapor phase). The locations of the boundaries between zones are handled as dynamic variables. In start-up or shut-downs operations, phase boundaries will move off the exchanger. As for distillation columns start-up operation, switching models [71] may address transitions with these specific regimes. The resulting models are of reduced order, but use mean values for the different zones, rather than real space-dependant values. Notably, the model has a strong dependency in the slip velocity (the ratio between gas and liquid velocities in a same channel), as shown in [75]. The framework also makes the assumption that the exchange wall temperature is constant on a zone. This may cause problematic discontinuities at the boundaries, as explained in [112]. Note that in the presented papers, the authors seem to focus more on the management of a variable number of zones (notably, as stressed above, in the case of phase boundary moving off the exchanger) than on the modeling assumptions. In addition, they do not address the case of heat exchange between several multi-phase fluids (which would increase the complexity of the management of the zones).

Conclusion

The distillation columns are considered as the heart of the distillation plants. Though they will not modify the phenomena occurring inside the columns, interactions with other components have an impact on the benefits one can expect from the renewal of the control strategy. Such couplings are notably thermal exchanges in the heat-exchangers of the cryogenic plants. A commonly admitted framework exists for shortcut dynamic modeling of fluid-fluid heat exchangers, but the issue of phase change is not addressed in this context. This issue is addressed in the moving-boundary framework by tracking the interfaces between 1-phase and 2-phases regions in the exchanger channels.

1.3 Pending issues and current research

Pending issues

Only few papers among those presented in the literature deal with what gas industry nowadays regards as high-purity distillation in cryogenic processes. Many of our examples show impurities concentrations around or above 10^{-4} (100 ppm), whereas Air Liquide and competitors usually use 1 ppm as order of magnitude for oxygen concentration in produced nitrogen. Therefore, we have little information on how to deal with probably sharpened non-linear and asymmetry phenomena or end-effects. Concerning end-effects, we can mention that the importance of delays induced by the condensers and boilers has been pointed out in [36], but seems never taken into account in shortcut modeling.

Beside, it seems difficult to derive general rules for modeling the thermodynamics and the hydraulics of the columns. The only commonly admitted simplification is to neglect the vapor hold-up for our applications (illustrations of the impact of this hypothesis can be found in [88]). Another frequent assumption in the field of air separation is to consider that a binary mixture (nitrogen-oxygen) is a good approximation of actual air as far as nitrogen and oxygen production are considered. This approach has been questioned: regarding the very low oxygen concentration atop the columns in high-purity processes, one could take other gases into account, introducing at least a ternary mixture (nitrogen-oxygen-argon) [61]. Similarly, there is no clear consensus on the accuracy of the thermodynamic models: inner enthalpy balance is not always taken into account, or may be simplified in a static balance [88]. The components in the mixture may have similar or different heats of vaporization. The equilibrium relation between the liquid and vapor phases is often considered either as driven by the liquid (mass transfer occurs between the phases because the vapor tends to reach the equilibrium state corresponding to the actual liquid state) or endogenous (mass transfer occurs inside each phase because of non-homogeneous local concentration and a mass transfer flow appears between the phases because they are constantly at the equilibrium wherever they are in contact). Plus, these various approaches are combined either with the stage-model or wave-model point of view.

Industrial involvement

Current industrial research seems to focus on computational issue and existing models improvement, without apparent novelty in the modeling approach. Air Liquide and Air Products (among others) indirectly support theses at the U.S Process Science & Technology Center (PSTC) in the field of cryogenic and non-cryogenic distillation. Investigated themes are data sets selection for model parameters estimation, reduction of non-linear models consisting of differential and algebraic equations (similar to stage-by-stage models), optimization of ASU dynamic operation and control through reduced order non-linear models [34]. Air Products also has publicly addressed the challenge of High Performance Process Control (HPPC) it its 2006 White Paper [107]. This firm has supported recent research on multi-parametric model-based control [80][20] with London Imperial College. In comparison, Praxair has been widely involved in compartmental model and wave-model studies ([61][9][18][113][74][60][7][8]) but is not mentioned in our recent papers. Surprisingly, the most recent control related paper [18] makes no use of the wave approach. This paper involves compartmented models and rather classical non-linear predictive control. Praxair also seems to have shown interest in fastened heat-exchanger simulation [12]. Others companies sometimes appear in recent pub-

lications, such as Dow Chemical (credited with support in wave-model study in [36] through its subsidiary Union Carbide Corporation, and involved with others in a funding consortium in an asNMPC study [46]), Siemens AG in a dynamic study of air separation plants [94], and Carrier Corporation in moving-boundary framework development [112].

1.3.1 Position of the thesis

This work is part of the research regarding a broader issue: air separation plants energy optimization, by the mean of tighter composition stabilization systems, and increased flexibility of the production. In this thesis, we address the dynamic modeling of the air distillation columns, as the core of the separation process. As emphasized in the state of the art, heat exchangers modeling would deserve a dedicated in-depth study, which is yet out of our scope. Regarding the columns, we proceed by building the column's network step-by-step: first the modeling focuses on an uninterrupted column; the we address a real column configuration with intermediary feeds and draws. Finally, we envisage several coupled columns. Our modeling approach is an attempt to answer the question: what should be the minimal dynamic model to obtain performances beyond those of linear gain/time constant/delay control model, which are nowadays widely used on real plants?

Consequently, the first steps of the modeling are close to Marquardt's approach [74], at an intermediary scale between the too simple tank models and the numerically expensive detailed tray models. We propose a refined description of the composition profiles dynamics and of the column's end-effects, which are counted amongst the drawbacks of the wave-model when applied to high-purity separation. We proceed by reducing a first set of equation using Centre Manifold reduction techniques; to our knowledge, these techniques have never been applied to the distillation modeling problem. The wave-model sets the question of the drift velocity of the composition waves, and of the interaction between the different components in the separated mixture. We investigate this aspect of our problem in line with [37], [32] and especially [84] which we closely follow, using coherent waves sets and Riemann invariants.

The reduced distillation dynamic model we obtain is observed from the point of view of control theory: it essentially consists of a non-linear hyperbolic partial-differential equation, to which a small diffusion term is added. For this mathematical object, we propose some results regarding the uniqueness and the properties of its solution. Then, we investigate the stability of the steady-state, by the mean of Lyapunov functions; the same tool is used to prove the local observability of a binary mixture composition profile, with or without output injection.

Our model performances are checked against steady state profiles obtained using the Hysys model (essentially a tray model similar to those presented above) of a real Air Liquide plant. Then, and contrary to many paper reviewed in the state of the art, we present the results obtained with our model together with real plant data (from the same ASU). Thus we challenge its performances and meaning within a context of realistic, noisy, or deteriorated input data and uncertain parameters. Also, we briefly investigate the possibility to derive linearized control models from the reduced PDE model.

Note that the numerical implementation of the model, though leading to faster than real-time simulations, is not intended for on-site use and direct control application. Thus, contrary to some of the presented papers which were focusing on dramatically reducing the computation time, no particular attempt has been made here in this direction.

1.4 Marquardt's wave models

Our work being partially inspired by the wave model, we give here a more detailed introduction than in the previous state of the art. This will also allow to draw parallels further in the text.

In the original Marqardt's contribution [74], modeling starts with two partial-differential equations arising from mass-balances over an infinitesimal slice of column, separately in the gas and in the liquid phase:

$$\begin{aligned} \frac{\partial x}{\partial t} - \frac{\partial x}{\partial z} &= -B\left(y^*(x) - y\right), \\ \epsilon_\sigma \frac{\partial y}{\partial t} + \frac{1}{A}\frac{\partial y}{\partial z} &= B\left(y^*(x) - y\right). \end{aligned} \tag{1.1}$$

Notations have been changed with respect to [74] for the sake of homogeneity with our notation system. In the previous dimensionless system, t is the time and z is the space variable (t and z have been scaled to absorb the hold-up coefficients). x (resp. y) is the molar fraction of the component of interest in the liquid (resp. gas) phase of the studied binary mixture. ϵ_σ is the ratio of the gas hold-up with respect to the liquid hold-up. A is the ratio of the liquid and gas flows, that is, the reflux rate. $y^*(x)$ indicates the thermodynamic equilibrium relation, and B is a dimensionless transfer coefficient. One can here notice that the system is driven by the liquid phase. Indeed, the state the gas must reach to stop the transfer flow $B\left(y^*(x) - y\right)$ is defined with respect to the liquid only, through $y^*(x)$. In addition, the ratio ϵ_σ is thought to be small.

With the idea that the distillation dynamics is mostly due to a sliding wave phenomenon, the previous system is rewritten using a moving space coordinate $\xi = z - z' = z - \int w dt$, where w is the wave speed. With the assumption $\epsilon_\sigma = 0$ (neglected gas hold-up), one has:

$$\begin{aligned} \frac{\partial x}{\partial t} - (1+w)\frac{\partial x}{\partial \xi} &= -B\left(y^*(x) - y\right), \\ \frac{\partial y}{\partial \xi} &= AB\left(y^*(x) - y\right). \end{aligned} \tag{1.2}$$

Boundary conditions are given by $x(1 - z', t) = x_1(t)$ (at top) and $y(-z', t) = y_0(t)$ (at the bottom). Dropping the time derivative (one reduces the dynamics to the movement along ξ of a fixed-shape wave) one obtains:

$$\begin{aligned} y &= A(1+w)x - C_1, \\ \xi &= \int \frac{(1+w)dx}{B\left(C_1 + y^*(x) - A(1+w)x\right)} + C_2, \end{aligned}$$

that is (if the integral is analytically solvable): $\xi = F\left(x(\xi)\right)$. F(.) depends here on A, B, w, the integration constants C_1 and C_2, and on the equilibrium relation $y^*(x)$. In some cases (quadratic equilibrium relation in [74]) the implicit relation can be solved, leading to a profile $x(\xi)$ given by:

$$x(\xi) = x_{-\infty} + \frac{x_{+\infty} - x_{-\infty}}{1 + e^{\gamma(x_{+\infty} - x_{-\infty})(\xi(t) - \xi_0)}}, \tag{1.3}$$

where γ (the main shape parameter) is connected to the maximum slope of the profile, and $\xi_0 = \xi(t = 0)$. The profile is defined over the column physical boundaries: $x_{+\infty}$ stands for the virtual value of x at the top of a virtually infinite column, and $x_{-\infty}$ is the virtual value of

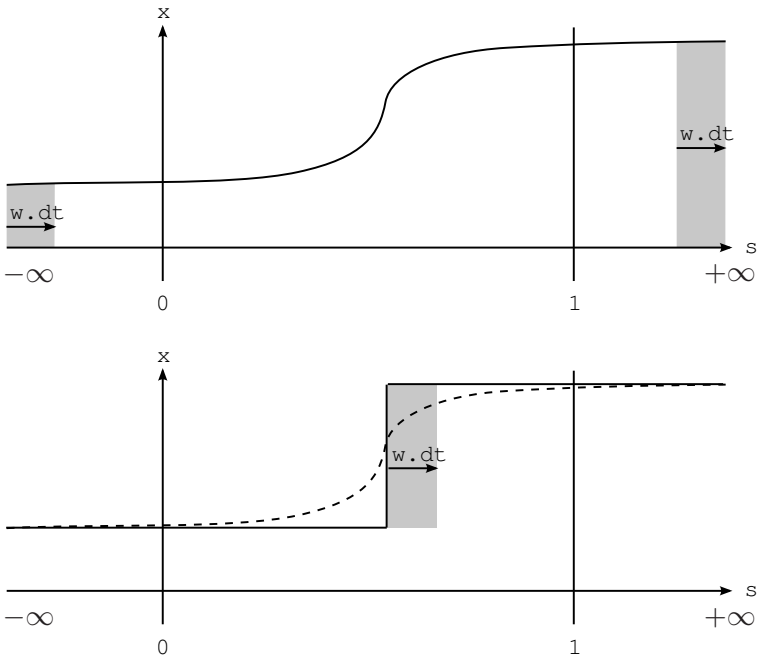

Figure 1.18: *Top:* material balance over the virtual infinite column is made of the contributions at $s = -\infty$ ($Lx_{-\infty} - Vy^*(x_{-\infty})$) and at $s = +\infty$ ($Vy^*(x_{+\infty}) - Lx_{+\infty}$). *Bottom:* alternatively, one can approximate the profile with a discontinuity whose speed is obtained using the same contributions.

x at the bottom of such a column. The wave motion is given by: $\frac{dz'}{dt} = w$. At this moment, the model ignores the physical boundaries of the column: whatever the position of the wave-front with respect to the top or bottom end, the dynamics are unchanged. As a consequence, the boundaries' influence on the composition profile, which are recognized to be important, especially for high-purity operation, are not rendered. Wavefront location and shape, as well as the compositions at the infinite, are thus considered as time-varying state variables of the system, to be estimated using available data, as mentioned in the state of the art. [8] notably illustrates the importance of these estimations to recover the pinching end-effects.

When not considered as a purely estimated state-variable, the wave-speed w is generally obtained through the material balance of the whole column (that is, the virtual infinite column), or over the wave-front approximated by a discontinuity (see Fig. 1.18). One has

$$\sigma(x_{+\infty} - x_{-\infty})w = V\left(y^*(x_{+\infty}) - y^*(x_{-\infty})\right) - L\left(x_{+\infty} - x_{-\infty}\right)$$
$$\sigma w = \frac{V\left(y^*(x_{+\infty}) - y^*(x_{-\infty})\right)}{L\left(x_{+\infty} - x_{-\infty}\right)} - L,$$

where σ accounts for the (constant) liquid and gas hold-ups. In [74], σ and L are absorbed by the scaling of t and z, which yields the formula:

$$w = \frac{y^*(x_{+\infty}) - y^*(x_{-\infty})}{A\left(x_{+\infty} - x_{-\infty}\right)} - 1. \tag{1.4}$$

Chapter 2

Reduced dynamic model for packed distillation columns

Le modèle d'onde de Marquardt, brièvement décrit au chapitre précédent, est structurellement simple et adapté pour le contrôle, mais n'est pas assez complet pour être utilisé en distillation à haute pureté. En suivant l'approche du modèle d'onde, nous proposons un modèle d'échange non-linéaire, continu, entre le gaz et le liquide, qui ne suppose pas l'homogénéisation instantanée des compositions dans chaque phase à une hauteur de colonne donnée. En celà, le modèle à deux fluides proposé ressemble aux modèle de taux de transfert tels que dans [91], [14] ou [13], qui traitent cependant de colonnes à plateaux (ou modélisées ainsi). Notre modèle utilise des coefficients de tranfert entre le liquide et le gaz, que nous relions qualitativement à la notion d'efficacité de plateau.

Nous présentons ensuite une tentative de réduction du modèle pour une colonne de distillation binaire en régime stationnaire, par application d'une technique de développements asymptotiques raccordés (DAR), brièvement présentée, à notre modèle à deux fluides. En supposant une relation linéaire pour l'équilibre thermodynamique liquide-gaz (qui rend le modèle à deux fluides linéaire), nous montrons que la méthode des DAR ne fonctionne pas, car elle requiert le développement asymptotique de la solution (le profil de compositions) en un terme en $\frac{1}{\epsilon}$, $0 < \epsilon << 1$ *(le coefficient d'échange liquide-gaz), en un point où elle est exponentiellement raide (en* $e^{\frac{1}{\epsilon}}$*). Nous étendons qualitativement cette constatation au cas non-linéaire.*

Dans le cadre des DAR, la perturbation singulière introduite dans le modèle à deux fluides par le petit ϵ *est traitée en établissant deux échelles de longueur. Alternativement, nous considérons que le modèle représente un système dynamique à deux échelles de temps différentes. La réduction d'un tel système renvoie aux techniques de perturbations singulières, et plus précisément ici, à la réduction variété centre. Celle-ci est d'abord présentée, dans le cadre des systèmes de dimension finie. L'intérêt de la technique de réduction est ici de préserver le régime lent de la colonne (son bilan matière, indépendamment des variations de compositions). Nous l'appliquons dans un premier temps rigoureusement à une version discrète du modèle à deux fluides. L'application à la version continue n'est menée que formellement ; nous observons cependant que la structure du modèle réduit obtenu est inchangée : il est équivalent de réduire le modèle discret, ou de discrétiser après réduction du modèle continu. Nous étendons les résultats à un nombre quelconque de constituants dans le mélange à séparer. Jusqu'à ce point, ce chapitre constitue une extension aux parties modélisation et réduction de [22], où nous n'avions traité la réduction que formellement.*

Le modèle dynamique réduit que nous obtenons consiste en :

- *une équation aux dérivées partielles, 1-D, non-linéaire, de convection diffusion, pour une variable assimilée à une composition moyenne, décrivant la dynamique du système au voisinage de sa variété centre,*
- *des sorties statiques permettant d'exprimer les distributions de compositions réelles, dans les phases liquide et vapeur, partant de la composition moyenne sur les deux phases.*

Nous observons que le terme de convection, pris seul, renvoie au modèle d'onde, alors que le terme de diffusion introduit des effets de bord répulsifs, et rend l'efficacité de la distillation localement dépendante des flux de liquide et de gaz. Dans le langage du modèle d'onde, il correspondrait à un facteur de forme variant dans le temps et l'espace. Cette caractéristique nouvelle du modèle motive la proposition qui est faite dans les demandes de brevets FR-1254802, FR-1255974 et FR-1256782, de l'utiliser au sein d'un capteur logiciel pour l'estimation et la prédiction des profils de compositions dans une colonne de distillation industrielle.

Dans la dernière partie du chapitre, nous ne nous intéressons plus qu'au seul phénomène de convection. En effet, le transport d'espèces chimiques dans un liquide et un gaz circulant à contre-courant peut être rapproché de la chromatographie sur lit fixe, pour laquelle la propagation cohérente de certaines quantités (des paquets de constituants) a été largement étudiée. En suivant de près [84], nous trouvons les invariants de Riemann de notre problème de convection, ainsi qu'un homéomorphisme entre l'espace des compositions réelles et un espace Ω transformé, dans lequel l'évolution des ondes de compositions est régie par des règles simples. Nous nous limitons au cas des ondes de choc. Ces ondes sont, comme nous le montrons, les seules existantes dans les colonnes de distillation considérées dans cette étude.

Marquardt's wave model, briefly described in the previous chapter, is structurally simple and suited for control applications, yet not complete enough to be applied to real high-purity separation processes. Following the wave model approach, we propose a non-linear continuous liquid-gas exchange model, which yet does not suppose the instant homogenization of the composition in a phase at a given height. In that, the proposed two-flows model resembles the rate-based models such as in [91], [14] or [13], which are for tray columns though (or packed columns modeled with successive non-equilibrium stages). Our model makes use of liquid-gas transfer coefficients, which we qualitatively relate to the notion of tray efficiency.

We then present an attempt to obtain a reduced formulation of a binary distillation column's steady-state composition profile, by application of the Matched Asymptotic Development (MAD) technique, briefly presented, to our two-flows model. The non-linearity in the two flow model arises from the liquid-gas thermodynamic equilibrium relation. Supposing a simplified linear equilibrium relation, we show that the MAD approach fails, since it requires the asymptotic expansion of the solution (the composition profile) in the exchange coefficient ($\frac{1}{\epsilon}$, $0 < \epsilon << 1$), at a point of exponential stiffness (in $e^{\frac{1}{\epsilon}}$). We extend qualitatively this explanation to the non-linear case.

Within the framework of MAD, the singular perturbation introduced by ϵ in the two-flows model was handled by introducing two different space-scales. An alternative is to consider the two-flows model as a dynamic system mixing two highly different time-scales. The reduction of this system then connects with the singular perturbation reduction techniques. More precisely, we address the problem using the Centre Manifold theory, to ensure that the system's slow dynamics (the column's mass balance, regardless of the composition variations) is unmodified by the reduction. We first introduce the reader to the Centre Manifold theory for finite

dimension systems; then, we apply the reduction technique, in a rigorous manner, on a discretized formulation of the two flow-model in the binary mixture case. The application to the continuous model is done formally only, yet we observe that the structure of the resulting reduced model is unchanged: it is equivalent to reduce the discrete two-flows model and to discretize the reduced infinite dimension two-flows model. We also extend the results to any number of components in the separated mixture. So far this chapter is an extension to the modeling part of [22], where only the formal infinite dimension reduction was dealt with.

The reduced dynamic model we obtain consists of:

- a 1-D non-linear convection-diffusion partial differential equation for a lumped composition variable, describing the dynamics of the system in the vicinity of it's centre manifold,
- static outputs to express the actual composition distributions in gas and liquid phase, out of the lumped composition variable.

We observe that the convection term alone connects with the wave-model, whereas the diffusion term introduces repelling end-effects, and makes the distillation efficiency depend locally on the liquid and gas flows. In the context of the wave-model, this would be a naturally time- and space-depending shape parameter. This interesting and new property motivates us to propose in the patent applications FR-1254802, FR-1255974 and FR-1256782 this new model structure as the heart of a soft-sensor for composition profiles estimation and prediction inside a distillation column.

In the last part of the chapter, we consider the convection phenomenon only. Indeed, transport of chemical species in countercurrent liquid and gas flows can be analogized to the fixed bed chromatography, for which the formation of coherent convected bundles of components has been extensively studied. Closely following [84], we find Riemann invariants for our convection problem, as well as an homeomorphism between the physical composition space and a transformed Ω-space, where the evolution of composition waves is described by simple rules. We limit ourselves to the case of shockwaves, since we can show that only that type of wave exists in the distillation columns we consider in this study.

2.1 Two-flows model

In this section we consider a continuous, packed section of a distillation column. As depicted on Fig. 2.1, we define the column's vertical axis s orientated downwards. t will stand for the time of the system. We address the complex intricate geometry of liquid and gas flows by considering only one equivalent liquid flow $L(s,t) > 0$, and one equivalent gas flow $V(s,t) > 0$. $L(s,t)$ (resp. $V(s,t)$) is the sum of all elementary liquid (resp. gas) flows crossing the column's section $S(s)$. L and V flows share a unique contact interface, which is an equivalent model for the actual contact surface between elementary liquid and gas paths. An elementary column's slice holds a certain amount of liquid $\sigma_L(s,t) > 0$. We define similarly the gas hold-up $\sigma_V(s,t) > 0$.

Let us consider the separation of mixture with components C_i, $i = 1...N$. Considering that the column achieves perfect mixing, we assume that the components' molar fractions are independent from the considered packing channel. We will denote the molar fractions of C_i, $i = 1...N$ by $0 \leq x_i(s,t) \leq 1$ in the liquid, and by $0 \leq y_i(s,t) \leq 1$ in the gas. Since $\sum_{i=1}^{N+1} x_i(s,t) = \sum_{i=1}^{N+1} y_i(s,t) = 1$, we can restrict the modeling to the reduced collection

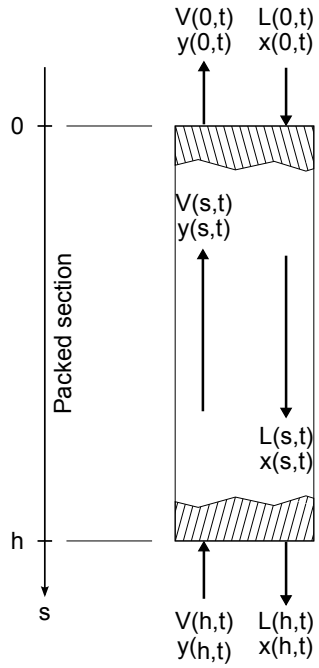

Figure 2.1: Scheme of the considered packed section.

$C_1, \cdots, C_N$. For the sake of simplicity, we will order the components by increasing volatility, so that C_{N+1} is the most volatile component of the mixture.

We define the relative volatility of the components with respect to component $N+1$. Thus

$$0 < \alpha_i(s,t) = \frac{\frac{y_i(s,t)}{x_i(s,t)}}{\frac{y_{N+1}(s,t)}{x_{N+1}(s,t)}} < 1, \quad i = 1...N,$$
$$\alpha_{N+1} = 1.$$

A superscript '*' will indicate molar fractions at the thermodynamic equilibrium of the mixture. For $i = 1...N$ we introduce the equilibrium applications

$$\begin{array}{rccc} k_i : & [0,1]^N & \to & [0,1] \\ & (x_1, ..., x_N) & \mapsto & k_i(x_1, ..., x_N). \end{array} \tag{2.1}$$

to set $y_i^* = k_i(x_1^*, ..., x_N^*)$.

Unless otherwise stated, we will use

$$k_i(x_1, ..., x_N) = \frac{\sum_{i=1}^N \alpha_i x_i}{1 + \sum_{i=1}^N (\alpha_i - 1) x_i}, \quad i = 1...N, \tag{2.2}$$

following in this many authors of the reviewed literature.

As depicted on Fig. 2.2, thanks to the use of equivalent flows, the molar fraction profiles now only depends on two space coordinates: vertical position s and distance from the equivalent contact interface. The contact interface is the locus of phase change, thus liquid and gas are there at thermodynamic equilibrium. Farther from the interface, the thermodynamic

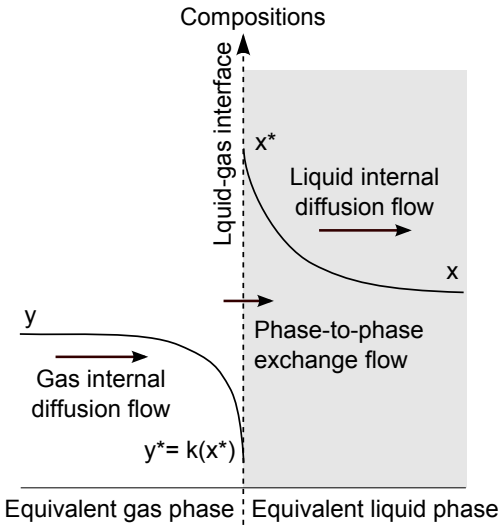

Figure 2.2: An equivalent liquid phase and an equivalent gas phase are in contact through a single liquid-gas equivalent interface. Here the column's vertical axis would be perpendicular to the plane of the figure. Non-instant diffusion in the liquid and the gas causes composition inhomogeneities to appear in the direction perpendicular to the contact interface.

coupling between liquid and gas is expected to weaken, whereas the influence of upcoming gas flows and descending liquid flows strengthens. This results in inhomogeneous molar fraction distributions in the cross-interface direction. We simplify the geometry of the problem in this direction using two layers in each phase, as illustrated in Fig. 2.3:

- a boundary layer close to the interface, where instant thermodynamic equilibrium is maintained; there, $y_i^* = k_i(x_1^*, \cdots, x_N^*)$. This layer has null thickness and no inertia.
- a main layer where molar fractions x_i or y_i are free from thermodynamic coupling. This layer accounts for the whole thickness and hold-up of the corresponding phase.

At a given altitude s, diffusion inside each phase generates molar flows from the boundary layer to the main layer, which we write for $i = 1...N$:

$$\begin{aligned} \Phi_{L_i} &= \Lambda_L(x_i^* - x_i) \quad \text{in the liquid,} \\ \Phi_{V_i} &= \Lambda_V(y_i^* - y_i) \quad \text{in the gas.} \end{aligned}$$

where the dimension of $\Lambda_{L,V}$ is $mol.m^{-1}.s^{-1}$. These coefficients are the equivalents, for a two-layers model, of the actual diffusion coefficients $D_{L,V}$ of the components in the liquid and gas phase. More specifically, Λ_L should be approximately $\frac{D_L \sigma_L}{\delta_L e_L}$ where δ_L is a characteristic diffusion length in the liquid (thickness of the boundary layer) and e_L the thickness of a liquid channel. Replacing L with V in the latter gives the approximation for D_V. Here, we suppose that the diffusion coefficient in a phase is the same for each species.

A mass balance in each phase's main layer gives:

$$\frac{\partial \sigma_L x_i}{\partial t} = -\frac{\partial L x_i}{\partial s} + \Lambda_L(x_i^* - x_i), \tag{2.3}$$

$$\frac{\partial \sigma_V y_i}{\partial t} = \frac{\partial V y_i}{\partial s} + \Lambda_V(y_i^* - y_i), \ i = 1...N. \tag{2.4}$$

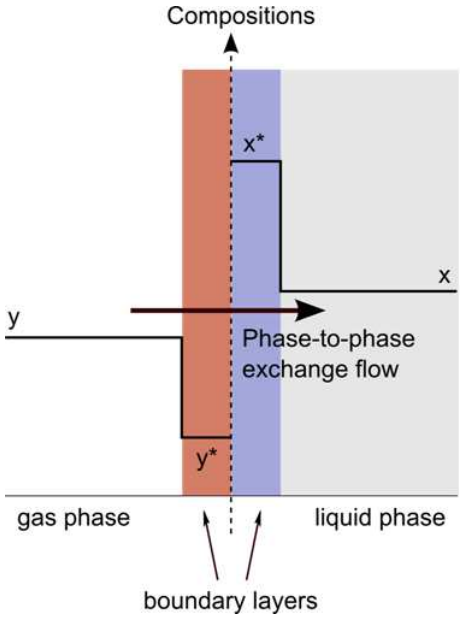

Figure 2.3: Only the axial dimension of the model is kept, by separating each equivalent phase into two layers: a boundary layer with no inertia, at the thermodynamic equilibrium, and another layer which accounts for all the hold-up, possibly not at the equilibrium. The column's vertical axis is perpendicular to the plane of the figure.

In addition, the mass conservation principle at the interface gives:

$$\Lambda_L(x_i^* - x_i) + \Lambda_V(y_i^* - y_i) = 0.$$

For air separation application, we will consider that the latent heat of vaporization is the same for the three handled components. For Ar and O_2, this is almost true since $\Delta H_{Ar} \approx 0.94\Delta H_{N_2}$ at pressure and temperature encountered in an ASU. Regarding N_2 and O_2, the hypothesis is less accurate ($\Delta H_{N_2} \approx 0.78\Delta H_{O_2}$); we have to expect that a fraction of the columns internal flow will not be taken into account by the model, since the enthalpy balance is loosely handled. The effect on the ASU HP column should yet be limited, for the amplitude of O_2 and N_2 molar fractions variations is limited.

This assumption dramatically simplifies the equations since the enthalpy balance has no more to be handled. The differential-algebraic dynamic model consequently reads

$$\left\{\begin{array}{rcl} \sigma_L \frac{\partial x_i}{\partial t} & = & -L\frac{\partial x_i}{\partial s} + \Lambda_L(x_i^* - x_i), \\ \sigma_V \frac{\partial y_i}{\partial t} & = & V\frac{\partial y_i}{\partial s} + \Lambda_V(y_i^* - y_i), \\ 0 & = & \Lambda_L(x_i^* - x_i) + \Lambda_V(y_i^* - y_i), \\ y_i^* & = & k_i(x_1^*, \cdots, x_N^*), \end{array}\right. \tag{2.5}$$

for $i = 1...N$, with

$$\frac{\partial \sigma_L}{\partial t} = -\frac{\partial L}{\partial s},$$
$$\frac{\partial \sigma_V}{\partial t} = \frac{\partial V}{\partial s}.$$

2.1.1 Transfer coefficients

Distillation efficiency is maximized with large components exchange flows between liquid and gas. This means that a small deviation from the biphasic equilibrium shall generate huge compensating flows across the interface. For a plate column, in the way of [88], one can define e_V, the tray efficiency regarding the gas, such that a fraction $1-e$ of the gas is not affected by the thermodynamic coupling when passing through a plate. A similar definition holds for e_L regarding the liquid. Thus in steady state, one has on plate n:

$$\begin{aligned} x_{n,i}^{out} &= (1-e_L)x_{n-1,i}^{out} + e_L x_{n,i}, \\ y_{n,i}^{out} &= (1-e_V)y_{n+1,i}^{out} + e_V k_i(x_{n,1},\cdots,x_{n,N}) \quad i=1...N. \end{aligned}$$

Rewriting the PDEs of (2.5) in a discrete manner and in steady state, assuming that a height Δs corresponds to one tray, yields:

$$\begin{aligned} x_{n,i}^{out} &= \frac{L}{L+\Delta s\Lambda_L}x_{n-1,i}^{out} + \frac{\Delta s\Lambda_L}{L+\Delta s\Lambda_L}x_{n,i}^{*}, \\ y_{n,i}^{out} &= \frac{V}{V+\Delta s\Lambda_V}y_{n+1,i}^{out} + \frac{\Delta s\Lambda_V}{V+\Delta s\Lambda_V}k_i(x_{n,1}^{*},\cdots,x_{n,N}^{*}) \quad i=1...N, \end{aligned}$$

which leads to the identification

$$e_L = \frac{\Delta s\Lambda_L}{L+\Delta s\Lambda_L}, \quad e_V = \frac{\Delta s\Lambda_V}{V+\Delta s\Lambda_V}. \tag{2.6}$$

An efficient column corresponding to e_L and e_V close to 1, is it reasonable to consider large Λ_L, Λ_V in our model. We thus let:

$$\Lambda_L = \frac{\lambda_L}{\epsilon}, \quad \Lambda_V = \frac{\lambda_V}{\epsilon}, \quad 0<\epsilon<<1.$$

Note that we make no assumption about the size of λ_L with respect to λ_V. Yet it would seem plausible to consider $\lambda_V > \lambda_L$, even if gas channels are much larger than liquid channels, since diffusion is far easier in the gas.

Note also that according to (2.6), $\frac{\Delta s}{\epsilon} \to +\infty \Rightarrow \frac{\Delta s\Lambda_V}{V} \to +\infty \Rightarrow e_V \to 1$. The same holds for e_L. Consequently arbitrary small sections of packing achieve perfect separation in case of vanishing ϵ. For such a limit case, s is not the proper length scale. This example introduces the scaling $\epsilon S = s$ we use in the next section.

2.2 Matched asymptotic developments with vanishing ϵ

We present here an attempt to distinguish the behavior of the steady-state solution of the two-flows distillation model in the high- and low-purity regions of a column. Though unsuccessful, it provides a motivation for further use of various scales to address the modeling problem.

2.2.1 Introduction

Matched asymptotic developments were introduced in the 50's to approximate solutions to differential equations perturbed by a small term. More precisely, the technique deals with problems where different scales can be separated in the solution. Let us consider as a toy

example the problem proposed by Friedrichs [29] and treated by Van Dyke ([105], to which we refer the reader for more in-depth presentation) :

$$\epsilon \frac{d^2 f}{ds^2} + \frac{df}{ds} = \frac{1}{2},\ f(0) = 0,\ f(1) = 1, \tag{2.7}$$

where ϵ is a small positive parameter. The exact solution is:

$$f(s) = \frac{1}{2}\left(\frac{1 - e^{-\frac{s}{\epsilon}}}{1 - e^{-\frac{1}{\epsilon}}} + s\right).$$

It appears that, for $s >> \epsilon$, the exponential term of the solution is in its flat region, and the solution is little dependent in ϵ. On the contrary, when s is comparable to ϵ, $f(s)$ varies fast with s due to the stiffness of the exponential, and the solution is highly sensitive to changes on ϵ. Thus one can distinguish two domains on the s-axis: for large s, the term in ϵ in (2.7) is indeed negligible; for small s, its impact on the solution is of the same order of magnitude that the remainders. Such problems with two successive domains arise for example from the fields of fluid mechanics (boundary layer problems) or electromagnetism (distinction between the near- and far-field depending on the distance to an emitter).

Let us first consider the large s domain (the outer domain); here we can rewrite (2.7) into:

$$\frac{df}{ds} = \frac{1}{2},\ f(0) = 0,\ f(1) = 1,$$

Obviously, one of the boundary conditions can not be satisfied. Since the simplification $\epsilon = 0$ we have made on the singularly perturbed problem (2.7) is not valid for small s (or, otherwise speaking, since the boundary condition at $s = 0$ is outside the outer domain), we choose the so-called outer solution: $f(s) = \frac{s+1}{2}$.

To investigate the behavior of the solution in the inner domain where s does not dominate ϵ anymore, s is not properly scaled to allow using the approximation $\epsilon = 0$. Let us rescale the problem with $s = aS$; dropping the boundary condition which belongs to the outer domain, we have:

$$\epsilon \frac{d^2 \tilde{f}}{a^2 dS^2} + \frac{d\tilde{f}}{adS} = \frac{1}{2},\ \tilde{f}(0) = 0. \tag{2.8}$$

The gauge a is a function of ϵ, which is chosen such that going to the limit $\epsilon = 0$ preserves as much terms as possible in (2.8). Here we take $a = \epsilon$ and passing to the limit yields:

$$\frac{d^2 \tilde{f}}{dS^2} + \frac{d\tilde{f}}{dS} = 0,\ \tilde{f}(0) = 0, \tag{2.9}$$

thus the inner solution $\tilde{f} = A\left(1 - e^{-S}\right)$. Constant A is undetermined for the moment.

The last step consists in connecting (matching) the inner and outer solution. The inner, microscopic scale $S = \frac{s}{\epsilon}$ overlaps the outer, large scale s for $S \to +\infty$. Conversely, the outer scale matches the magnitude of the inner scale when $s \to 0$. Thus (see Fig. 2.4) the matching is made by choosing A such that:

$$\lim_{S \to +\infty} \tilde{f}(S) = A = \frac{1}{2} = \lim_{s \to 0} f(s).$$

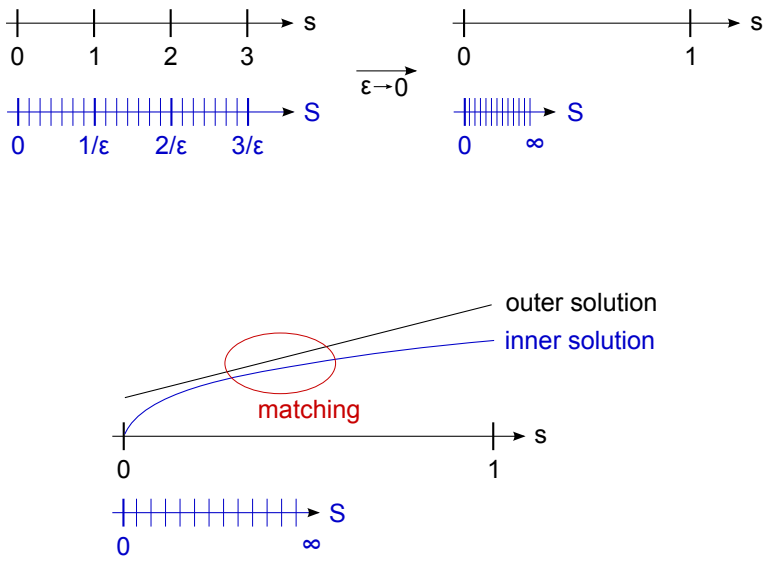

Figure 2.4: *Top left:* the natural scale s is suitable for slowly varying solution. The new scale S allows catching faster variations. *Top right:* at the limit $\epsilon \to 0$, the two scales define an inner and outer domains which match for $s \to 0$, $S \to +\infty$. *Bottom:* Integration constants in the inner and outer solutions are adjusted to match them at the limit of the two domains.

The result of the procedure is a composite solution (entirely written in the natural, outer scale s):

$$f_c(s) = \frac{s+1}{2} + \frac{1}{2}\left(1 - e^{-\frac{s}{\epsilon}}\right) - \frac{1}{2},$$

in which the outer solution progressively replaces the inner one, as one leaves the inner domain for the outer one.

2.2.2 Application

Application of the matched asymptotic development method to our problem is limited to the steady state. Restricting ourselves to the separation of a binary mixture ($N+1=2$) we can drop the component related subscripts i in the equations. In addition, we use a linear thermodynamic equilibrium relation $y^* = \alpha x^*$, $0 < \alpha < 1$. Thus (2.5) yields:

$$\left\{\begin{array}{rcl} L\frac{\partial x}{\partial s} & = & \frac{\lambda_L}{\epsilon}(x^*(s) - x(s)), \\ V\frac{\partial y}{\partial s} & = & -\frac{\lambda_V}{\epsilon}(y^*(s) - y(s)), \\ 0 & = & \lambda_L(x^*(s) - x(s)) + \lambda_V(y^*(s) - y(s)), \\ y^*(s) & = & \alpha x^*(s), \end{array}\right. \tag{2.10}$$

for $s \in (0, h)$. Let $x(0) = y(0) = x_{(0)}$, $x(h) = x_{(1)}$ and $y(h) = y_{(1)}$.

Let us consider an asymptotic development of the stationary solution versus ϵ, up to an

arbitrary order $n \geq 1$. We set:

$$\overline{x}(s) = \sum_{k=0}^{n} \epsilon^k \overline{x}_k(s) + o(\epsilon^n), \quad \overline{y}^*(s) = \sum_{k=0}^{n} \epsilon^k \overline{y}^*_k(s) + o(\epsilon^n),$$
$$\overline{y}(s) = \sum_{k=0}^{n} \epsilon^k \overline{y}_k(s) + o(\epsilon^n), \quad \overline{y}^*(s) = \sum_{k=0}^{n} \epsilon^k \overline{y}^*_k(s) + o(\epsilon^n)$$

the outer solution, for $s \in (0, h)$. (2.10) yields

$$\overline{x}_k(s) = \overline{x}^*_k(s), \qquad \overline{y}_k(s) = \overline{y}^*_k(s),$$
$$\frac{\partial \overline{x}_k}{\partial s} = 0, \qquad \frac{\partial \overline{y}_k}{\partial s} = 0$$

for $k = 0...n$. Using boundary conditions at $s = h$, one obtains:

$$\overline{x}_0(s) \equiv \overline{x}^*_0(s) \equiv x_{(1)}, \qquad \overline{y}_0(s) = \overline{y}^*_0(s) \equiv y_{(1)} = \alpha x_{(1)},$$
$$\overline{x}_k(s) \equiv \overline{x}^*_k(s) \equiv 0, \qquad \overline{y}_k(s) = \overline{y}^*_k(s) \equiv 0, \ k = 1...n.$$

The outer solution $\overline{x}(s), \overline{y}(s), \overline{x}^*(s), \overline{y}^*(s)$ is obtained using the natural scale s. For $\epsilon = 0$, (2.10) yields

$$\overline{x}(s) = \overline{x}^*(s), \qquad \overline{y}(s) = \overline{y}^*(s),$$
$$\frac{\partial \overline{x}}{\partial s} = 0, \qquad \frac{\partial \overline{y}}{\partial s} = 0,$$

for $s \in (0, h)$. Thus $\overline{x}(s) \equiv \overline{x}^*(s) \equiv x_1$ and $\overline{y}(s) \equiv \overline{y}^*(s) \equiv y_1 = \alpha x_1$. As mentioned before, s is too large a scale to catch the non-ideal efficiency of the column for vanishing ϵ; the approximate solution corresponds to the thermodynamic equilibrium over the whole domain.

To obtain the inner solution, we introduce the small scale S such that $\epsilon S = s$. We set

$$\tilde{x}(S) = \sum_{k=0}^{n} \tilde{x}_k(S), \quad \tilde{y}^*(S) = \sum_{k=0}^{n} \tilde{y}^*_k(S),$$
$$\tilde{y}(S) = \sum_{k=0}^{n} \tilde{y}_k(S), \quad \tilde{y}^*(S) = \sum_{k=0}^{n} \tilde{y}^*_k(S)$$

the inner solution for $S \in (0, +\infty)$. (2.10) yields

$$L\frac{\partial \tilde{x}_k}{\partial S} = \lambda_L(\tilde{x}^*_k(S) - \tilde{x}_k(S)),$$
$$V\frac{\partial \tilde{y}_k}{\partial S} = -\lambda_V(\tilde{y}^*_k(S) - \tilde{y}_k(S)),$$
$$0 = \lambda_L(\tilde{x}^*_k(S) - \tilde{x}_k(S)) + \lambda_V(\tilde{y}^*_k(S) - \tilde{y}_k(S)),$$
$$\tilde{y}^*_k(S) = \alpha \tilde{x}^*_k(S),$$

for $k = 0...n$. Thus for any k one obtains

$$\tilde{y}_k(S) \equiv r\tilde{x}_k(S) + \tilde{x}_k(0)(1 - r),$$
$$\tilde{x}^*_k(S) \equiv \frac{\lambda_L + r\lambda_V}{\lambda_L + \alpha\lambda_V}\tilde{x}_k(S) + \frac{\lambda_V(1 - r)\tilde{x}_k(0)}{\lambda_L + \alpha\lambda_V},$$

with the reflux rate $r = \frac{L}{V} \in (0,1)$, and eventually

$$\frac{\partial \tilde{x}_k}{\partial S} = \frac{\lambda_L \lambda_V (r-\alpha)}{L(\lambda_L + \lambda_V \alpha)} \tilde{x}_k + \frac{\lambda_L \lambda_V (1-r)}{L(\lambda_L + \lambda_V \alpha)} \tilde{x}_k(0).$$

Case $\mathbf{r > \alpha}$: since $\tilde{x}(S)$ shall not diverge for $S \to +\infty$, the only feasible solution corresponds to $\tilde{x} \equiv \frac{1-r}{\alpha - r}\tilde{x}(0)$. Then $\tilde{x} \equiv 0$ and $\tilde{x} \equiv \tilde{x}^* \equiv \tilde{y} \equiv \tilde{y}^* \equiv 0$. Matching the inner and outer solutions using $\lim_{S \to +\infty} \tilde{x}(S) = \lim_{s \to 0} \overline{x}(s)$ gives $x_{(1)} = y_{(1)} = 0$.

Case $\mathbf{r = \alpha}$: for any k $\tilde{x}_k(S)$ does not diverge for $S \to +\infty$ only if $\tilde{x}_k(0) = 0$. Again, one obtains $\tilde{x} \equiv \tilde{x}^* \equiv \tilde{y} \equiv \tilde{y}^* \equiv 0$ and $x_{(1)} = y_{(1)} = 0$.

Case $\mathbf{r < \alpha}$: one has, for any k, $\lim_{S \to +\infty} \tilde{x}_k(S) = \frac{1-r}{\alpha - r}\tilde{x}_k(0)$. Matching $\lim_{S \to +\infty} \tilde{x}(S)$ with $\lim_{S \to 0} \overline{x}(s)$ yields

$$\tilde{x}_0(0) = \frac{\alpha - r}{1 - r} x_{(1)}, \quad \tilde{x}_k(0) = 0, \ k = 1...n.$$

One can check that $\tilde{y}$, $\tilde{x}^*$ and $\tilde{y}^*$ then automatically match with their outer equivalents.

Thus, according to the matched asymptotic development, regardless of the order k, the compound solution $x_{\text{comp}}(s) = \tilde{x}(\frac{s}{\epsilon}) + \overline{x}(s) - \lim_{s \to 0} \overline{x}$ reduces to the inner solution $\tilde{x}(\frac{s}{\epsilon})$ and one has

$$\begin{cases} x_{\text{comp}} \equiv 0, & \text{if } r \geq \alpha; \\ x_{\text{comp}}(s) = x_{(1)} \left(1 - \frac{1-\alpha}{1-r} e^{\frac{-\theta s}{\epsilon}}\right), \ \theta = \frac{\lambda_V \lambda_L (\alpha - r)}{L(\lambda_L + \alpha \lambda_V)} & \text{if } r < \alpha. \end{cases}$$

But since $x_{\text{comp}}(h) = x_{(1)} = x_{(1)} \left(1 - \frac{1-\alpha}{1-r} e^{\frac{-\theta h}{\epsilon}}\right)$, the only solution matching the boundary corresponds to $x_{\text{comp}} \equiv 0$, $x_{(1)} = 0$.

2.2.3 Analysis

For the chosen binary linear example, we dispose of the explicit exact solution $x(s, \epsilon)$, which is:

$$x(s, \epsilon) = \frac{1 - \frac{1-\alpha}{1-r} e^{-\frac{\theta s}{\epsilon}}}{1 - \frac{1-\alpha}{1-r} e^{-\frac{\theta h}{\epsilon}}} x_{(1)}, \quad s \in (0, h).$$

For the limit $\epsilon = 0$, when $r \neq \alpha$, $x(s, \epsilon)$ degenerates into a discontinuous solution:

$$\begin{aligned} &x(0,0) = 0, && x(s,0) = x_{(1)}, \ s \in (0,h), \text{ if } r > \alpha (i.e.) \theta < 0, \\ &x(0,0) = \frac{\alpha - r}{1 - r} x_{(1)}, && x(s,0) = x_1, \ s \in (0,h), \text{ if } r < \alpha (i.e.) \theta > 0. \end{aligned}$$

In addition, due to exponential dependence on $1/\epsilon$, all the derivatives $\frac{\partial^n x(s,\epsilon)}{\partial \epsilon^n}$, $n > 0$ vanish for $\epsilon = 0$, $s \in (0, h)$. Consequently, any asymptotic development of the exact solution $x(s, \epsilon)$ around $\epsilon = 0$ reduces to the term of order 0. Because of the discontinuity of the later, the asymptotic development is then accurate only if

$$\begin{aligned} &x(0,0) = 0 = \frac{\frac{\alpha - r}{1-r} x_{(1)}}{1 - \frac{1-\alpha}{1-r} e^{-\frac{\theta h}{\epsilon}}}, && \text{i.e. } x_{(1)} = 0 \text{ if } r > \alpha, \\ &x(0,0) = \frac{\alpha - r}{1 - r} x_{(1)} = \frac{\frac{\alpha - r}{1-r} x_{(1)}}{1 - \frac{1-\alpha}{1-r} e^{-\frac{\theta h}{\epsilon}}}, && \text{i.e. } x_{(1)} = 0 \text{ if } r < \alpha. \end{aligned}$$

For $r = \alpha$, i.e. $\theta = 0$, $x(s,\epsilon)$ grows no more discontinuity when $\epsilon \to 0$. All the derivatives $\frac{\partial^n x(s,\epsilon)}{\partial \epsilon^n}$, $n > 0$ vanish for $\epsilon = 0$, thus any asymptotic development of $x(s,\epsilon)$ in ϵ reduces to $x(s,0) \equiv x_{(1)}$. The development is accurate only if

$$x(0,0) = x_{(1)} = x\frac{\frac{\alpha-r}{1-r}x_{(1)}}{1-\frac{1-\alpha}{1-r}e^{-\frac{\theta h}{\epsilon}}}$$

that is $x_{(1)} = 0$ as previously.

2.2.4 Generalization

Consider now the binary stationary problem, where the equilibrium relation is now non-linear. We have:

$$\left\{\begin{array}{rcl} L\frac{\partial x}{\partial s} & = & \frac{\lambda_L}{\epsilon}(x^*(s)-x(s)), \\ V\frac{\partial y}{\partial s} & = & -\frac{\lambda_V}{\epsilon}(y^*(s)-y(s)), \\ 0 & = & \lambda_L(x^*(s)-x(s))+\lambda_V(y^*(s)-y(s)), \\ y^*(s) & = & k(x^*(s)), \end{array}\right. \tag{2.11}$$

for $s \in (0,h)$. We still have $x(0) = y(0) = x_{(0)}$, $x(h) = x_{(1)}$ and $y(h) = y_{(1)}$. To the limit $\epsilon \to 0$, (2.11) yields:

$$\left\{\begin{array}{rcl} \frac{\partial x}{\partial s} & = & 0, \\ y(s) & = & k(x(s)) \propto \frac{L}{V}y(s). \end{array}\right.$$

Since $y(0) = x_{(0)} = k(x_{(0)})$, one has $x(0) = y(0) = 0$ or 1. For $x_{(1)} \neq 0$ or 1, a solution exists only if one allows $x(s)$ to be discontinuous. Then any $x(s)$ which is a step from 0 or 1 to $x_{(1)}$ satisfies to the limit problem. Additionally, the position $\tilde{s}$ of the discontinuity along s must be stationary. Let $w = \frac{ds}{dt}$. Then a mass balance around the discontinuity yields:

$$\begin{aligned} w &= \frac{L(x(\tilde{s}_+)-x(\tilde{s}_-))-V(y(\tilde{s}_+)-y(\tilde{s}_-))}{\sigma_L(x(\tilde{s}_+)-x(\tilde{s}_-))+\sigma_V(y(\tilde{s}_+)-y(\tilde{s}_-))} \\ &= \frac{L(x(\tilde{s}_+)-x(\tilde{s}_-))-V(k(x(\tilde{s}_+))-k(x(\tilde{s}_-)))}{\sigma_L(x(\tilde{s}_+)-x(\tilde{s}_-))+\sigma_V(y(\tilde{s}_+)-y(\tilde{s}_-))}. \end{aligned}$$

Given $\frac{L}{V} \leq 1$, $w = 0$ is achievable only with $x(\tilde{s}_-) \leq x(\tilde{s}_+)$. Thus allowed discontinuous solutions $x(s)$ are increasing steps from 0 to $x_{(1)}$, with arbitrary position of the jump.

For such piecewise constant solutions, standard matched asymptotic developments will face the same problem as illustrated with the linear example. Non-standard asymptotic approaches may provide results, yet it seems that defining two successive space scales, one for the high-purity phenomena at one end of the column, and another for higher concentrations in the rest of the column, is not the simplest reduction approach. Be it in steady-state or above all in dynamics. In the next section, we then investigate a different approximation technique. This technique is directly for the dynamic solution of (2.5), but we will show that it also matches the stationary solution to the chosen order.

2.3 Reduction

2.3.1 Introduction to the centre manifold theory

In the analysis of singularly perturbed dynamic systems, a difficulty arises from the various timescales involved (say, a slow and a fast timescale). Rewriting the system in each timescale yields slow and fast systems which are no more equivalent at the limit. Centre manifold theory offers tools to approximate the dynamics of the original system as a regular perturbation of the limit slow system, recovering information from the fast one. The fundamental set of theorems is due to Fenichel (see [26] which is beyond the single case of singular perturbations, and [27] which specifically addresses them). Introduction to the theory and its applications have been given in [56] and [17], both of which we follow. We also refer the interested reader to [106].

Consider a dynamic system of the form

$$\left\{ \begin{array}{rcl} \frac{\partial x_1}{\partial t} & = & f_1(x_1, x_2, \epsilon) \\ \frac{\partial x_2}{\partial t} & = & \epsilon f_2(x_1, x_2, \epsilon) \end{array} \right. \tag{2.12}$$

where f_1, f_2 have *ad hoc* regularity, and ϵ is a real, small yet non-null parameter. Introducing $\tau = \epsilon t$, the system rewrites

$$\left\{ \begin{array}{rcl} \epsilon \frac{\partial x_1}{\partial \tau} & = & f_1(x_1, x_2, \epsilon) \\ \frac{\partial x_2}{\partial \tau} & = & f_2(x_1, x_2, \epsilon). \end{array} \right. \tag{2.13}$$

As long as $\epsilon \neq 0$, systems (2.12) and (2.13) are strictly equivalent. Yet their limit dynamic behavior differ when $\epsilon \to 0$. One has:

$$\left\{ \begin{array}{ll} \frac{\partial x_1^0}{\partial t} & = f_1(x_1^0(t), x_2^0, 0) \\ \frac{\partial x_2^0}{\partial t} & = 0 \end{array} \right. \qquad \left\{ \begin{array}{ll} 0 & = f_1(x_1^0(\tau), x_2^0(\tau), 0) \\ \frac{\partial x_2^0}{\partial \tau} & = f_2(x_1^0(\tau), x_2^0(\tau), 0) \end{array} \right.$$

Using t as the time variable, x_2^0 becomes constant and uncoupled from the limit dynamic behavior of $x_1^0(t)$. t is the appropriate time scale for the dynamics of x_1. Yet the dynamics of x_2 are much slower (roughly, $\frac{1}{\epsilon}$ times slower) and seem ultimately to be frozen for $\epsilon \to 0$. $\tau = \epsilon t$ defines a slow time scale which is much more suited for x_2 dynamics (to the expense of x_1 which seems instantaneous at the limit).

The limit dynamics using the fast and slow time scale provides each a simplified yet restricted focus on the original system. With the fast time scale, the dynamics of the slow variable x_2 is lost, and the limit behavior shows artificial critical points for the subset $f_1(x_1^0, x_2^0, 0) = 0$. Using the slow time scale, one both retrieves the system dynamics on this subset, and restricts the dynamics to this subset. Namely, one has no information on how (2.12) reaches or leaves (a neighborhood of) that subset. The Singular Perturbation theory provides tools to reconciliate the various time scales.

Let us first recall the definition of an invariant manifold. Consider the dynamic system

$$\frac{dx}{dt} = f(x), \quad x \in \mathbb{R}^n. \tag{2.14}$$

The associated flow Φ defines $\Phi_t(x_0)$ as the state $x(t)$ reached by (2.14) after time t (not necessarily positive) with initial condition x_0.

Definition 2.1. A manifold M is *locally invariant* by (2.14) if $\exists T > 0$ such that $\forall t \in (-T, T)$, $\forall x_0 \in M$, $\Phi_t(x_0) \in M$. If one can make $T \to \infty$, the manifold M is *invariant* by (2.14).

We shall now consider specific manifolds of (2.14), namely its stable, unstable and centre manifolds. Suppose that the system admits an equilibrium point x_*. Let $A = \frac{\partial f}{\partial x}(x_*)$. One can define

- E^- the stable eigenspace of A, associated with eigenvalues whose real part is < 0;
- E^+ the unstable eigenspace of A, associated with eigenvalues whose real part is > 0;
- E^0 the centre eigenspace of A, associated with pure imaginary eigenvalues.

E^+, E^- and E^0 are supplementary ($E^+ \oplus E^- \oplus E^0 = \mathbb{R}^n$) and invariant by $\frac{dx}{dt} = Ax$. If A is hyperbolic, the centre eigenspace vanishes and we have the

Theorem 2.2 (from Hartman-Grobman theorem, see for instance [38], [39], [30])**.** *There exists $W^-_{loc}(x_*)$ and $W^+_{loc}(x_*)$, respectively locally invariant stable and unstable manifolds of f at x_*, with dim $W^-_{loc}(x_*)$ = dim E^- and dim $W^+_{loc}(x_*)$ = dim E^+, respectively tangent to E^- and E^+ at x_*, and having the same regularity as f.*

In the non-hyperbolic case, the centre eigenspace gives rise to a centre manifold, as stated by the

Theorem 2.3 (from Shoshitaishvili's theorem in [4])**.** *If f is C^r, it admits locally invariant stable, unstable and centre manifolds noted $W^-_{loc}(x_*)$, $W^+_{loc}(x_*)$ and $W^0_{loc}(x_*)$, which are C^r, C^r and C^{r-1} respectively, and tangent at x_* to E^-, E^+ and E^0 respectively. $W^-_{loc}(x_*)$ and $W^+_{loc}(x_*)$ are uniquely defined, which is not necessarily the case for $W^0_{loc}(x_*)$.*

Furthermore, with $x_* = (x_{1*}, x_{2*})^T$ the centre manifold can be, at least locally, represented as a graph:

$$W^0_{loc}(x_*) = \{(x_1, x_2) \in \mathbb{R}^n : x_2 = h(x_1)\} \tag{2.15}$$

for $|x_1 - x_{1*}|$ small enough, with $h(x_{1*}) = x_{2*}$ and $\frac{dh(x_1)}{dx_1}(x_{1*}) = 0$.

Let us go back to the singularly perturbed dynamic system (2.12). We now know that for small excursions around the equilibrium, the trajectories of the system will stay close to its centre manifold (assuming its existence). Yet its calculation is not straightforward for $\epsilon \neq 0$. We review here two ways of approximating it.

The first way is from [56]. Making $\epsilon \to 0$ in (2.12) yields the limit system

$$\begin{aligned} \frac{\partial x_1^0}{\partial t} &= f_1(x_1^0(t), x_2^0, 0) \\ \frac{\partial x_2^0}{\partial t} &= 0. \end{aligned}$$

According to the previous theorems, the limit system admits a centre manifold W_0^0 (the subscript 0 indicates value of ϵ for which it is obtained). W_0^0 is given by $f_1(x_1^0, x_2^0, 0) = 0$, that is $x_1^0 = h_0(x_2)$ for some function h_0 around the equilibrium. To go on, we need an additional theorem.

Theorem 2.4 (Fenichel's Invariant Manifold first theorem)**.** *For $\epsilon > 0$ sufficiently small, there exists a manifold M_ϵ that lies within $O(\epsilon)$ from W_0^0 and is diffeomorphic to W_0^0. Moreover, M_ϵ is locally invariant by (2.12), has the same regularity as W_0^0 in x_1, x_2, and is C^∞ in ϵ.*

As previously, the manifold M_ϵ can be represented, at least locally, as a graph:

$$M_\epsilon = \{(x_1, x_2) \in \mathbb{R}^n : x_1 = h_\epsilon(x_2)\}$$

where h_ϵ has the same regularity in x_2 than h_0 and is C^∞ in ϵ.

Using the smoothness of h_ϵ in ϵ, one can expand $x_1 = h_\epsilon(x_2)$ in ϵ:

$$x_1 = h_0(x_2) + \epsilon h_1(x_2) + O(\epsilon^2),$$

where the zero-order term is immediately given by the fact that M_ϵ is close to W_0^0 to $O(\epsilon)$, according to theorem 2.4. The 1^{st} order term will be calculated to guarantee the local invariance of M_ϵ in (2.12). Using the first equation of (2.12), one has

$$\begin{aligned}
\frac{dx_1}{dt} &= f_1(h_0(x_2) + \epsilon h_1(x_2) + O(\epsilon^2), x_2, \epsilon) \\
&= f_1(h_0(x_2), x_2, 0) + \epsilon \frac{\partial f_1}{\partial x_1}(h_0(x_2)), x_2, 0) h_1(x_2) + \epsilon \frac{\partial f_1}{\partial \epsilon}(h_0(x_2)), x_2, 0) + O(\epsilon^2) \\
&= \epsilon \frac{\partial f_1}{\partial x_1}(h_0(x_2)), x_2, 0) h_1(x_2) + \epsilon \frac{\partial f_1}{\partial \epsilon}(h_0(x_2)), x_2, 0) + O(\epsilon^2)
\end{aligned}$$

since $f_1(h_0(x_2), x_2, 0) = 0$ by the definition of h_0. On the other hand, the second equation of (2.12) yields

$$\begin{aligned}
\frac{dx_1}{dt} &= \left(\frac{dh_0}{dx_2} + \epsilon \frac{dh_1}{dx_2} + O(\epsilon^2) \right) \frac{dx_2}{dt} \\
&= \left(\epsilon \frac{dh_0}{dx_2} + \epsilon^2 \frac{dh_1}{dx_2} + O(\epsilon^3) \right) f_2(h_0(x_2) + \epsilon h_2(x_2) + O(\epsilon^2), x_2, \epsilon) \\
&= \epsilon \frac{dh_0}{dx_2} f_2(h_0(x_2), x_2, 0) + O(\epsilon^2).
\end{aligned}$$

Equalizing the terms of order 1 in ϵ leads to

$$h_1 = \left(\frac{\partial f_1}{\partial x_1} \right)^{-1} \left(\frac{dh_0}{dx_2} f_2(h_0(x_2), x_2, 0) - \frac{\partial f_1}{\partial \epsilon} \right) (h_0(x_2), x_2, 0).$$

The manifold M_ϵ approximated by $h_0 + \epsilon h_1$ is called the *slow manifold*. The Second Fenichel's Invariant Manifold theorem ensures that M_ϵ, as well as its approximation, permits tracking the dynamics of (2.12) for small ϵ and small excursions around the equilibrium.

Theorem 2.5 (Fenichel's Invariant Manifold second theorem)**.** *If $\epsilon > 0$ is sufficiently small, there exists manifolds $W^s(M_\epsilon)$ and $W^u(M_\epsilon)$ that lie within $O(\epsilon)$ of, and are diffeomorphic to, the stable and unstable invariant manifolds of the limit system ($W^-(M_0)$ and $W^+(M_0)$), respectively. Moreover, they are each locally invariant by (2.12), have the same regularity in x_1, x_2 than $W^-(M_0)$ and $W^+(M_0)$, and are C^∞ in ϵ.*

The following theorem justifies the terminologies 'stable' and 'unstable' for the perturbed manifolds $W^s(M_\epsilon)$ and $W^u(M_\epsilon)$.

Theorem 2.6. *Let $\Phi_t(x)$ the flow associated to (2.12). There exist $K_s > 0$, $\alpha_s < 0$ and a neighborhood D of M_ϵ such that if $v \in W^s(M_\epsilon)$ and $\Phi_t(v) \in D$ with $t > 0$, then*

$$d(\Phi_t(v), M_\epsilon) \leq K_s e^{\alpha_s t},$$

where $d(.,.)$ is the Euclidian distance.

Furthermore, there exists $K_u > 0$, $\alpha_u > 0$ such that if $v \in W^s(M_\epsilon)$ and $\Phi_t(v) \in D$ with $t < 0$, then

$$d(\Phi_t(v), M_\epsilon) \leq K_u e^{\alpha_u t}.$$

Thus, provided that the trajectories of (2.12) remain in the appropriate neighborhood of M_ϵ, they exponentially converge towards M_ϵ, either forward or backward in time. This is formulated by the

Lemma 2.7 (Shadow Lemma)**.** *For every initial conditions in the neighborhood of M_ϵ, the integral curves fast converge towards M_ϵ, without necessary entering in it, but are approximated by trajectories remaining in M_ϵ (the shadows[1]) to which they converge.*

For small ϵ, small excursions around the equilibrium, it may then be sufficient to limit the study of (2.12) to its restriction to the approximation of M_ϵ.

A slightly different approach is proposed in [17]. Instead of perturbing the centre manifold M_0 of the limit system to approximate the dynamics of (2.12), this approach directly addresses a centre manifold for (2.12). Around an equilibrium point $x_* = (x_{1*}, x_{2*})$ the linearization of (2.12) reads

$$\begin{aligned}
\frac{d\delta x_1}{dt} &= D_{x_1} f_1 \delta x_1 + D_{x_2} f_1 \delta x_2, \\
\frac{d\delta x_2}{dt} &= \epsilon D_{x_1} f_2 \delta x_1 + \epsilon D_{x_2} f_2 \delta x_2.
\end{aligned}$$

If f_1 and f_2 are such that

$$\begin{pmatrix} D_{x_1} f_1 & D_{x_2} f_1 \\ \epsilon D_{x_1} f_2 & \epsilon D_{x_2} f_2 \end{pmatrix}$$

is hyperbolic at x_*, the conditions of theorem 2.3 are not fulfilled; there is no centre manifold. The key point, which also re-introduces the vision of (2.12) as a perturbation of the limit system for $\epsilon = 0$, consists in extending the state space to include ϵ as a constant:

$$\begin{aligned}
\frac{dx_1}{dt} &= f_1(x_1, x_2, \epsilon), \\
\frac{dx_2}{dt} &= \epsilon f_2(x_1, x_2, \epsilon), \\
\frac{d\epsilon}{dt} &= 0.
\end{aligned}$$

The equilibrium point around which we consider the system is extended as well: $x_* = (x_{1*}, x_{2*}, 0)$. The linearization now writes

$$\begin{aligned}
\frac{d\delta x_1}{dt} &= D_{x_1} f_1 \delta x_1 + D_{x_2} f_1 \delta x_2 + D_\epsilon f_1 \delta\epsilon, \\
\frac{d\delta x_2}{dt} &= \epsilon D_{x_1} f_2 \delta x_1 + \epsilon D_{x_2} f_2 \delta x_2 + \epsilon D_\epsilon f_2 \delta\epsilon + f_2(x_1, x_2, \epsilon)\delta\epsilon \\
\frac{d\delta\epsilon}{dt} &= 0,
\end{aligned}$$

[1] not to be confounded with projections of the trajectories on M_ϵ

which turns at x_* in

$$\begin{aligned}\frac{d\delta x_1}{dt} &= D_{x_1} f_1 \delta x_1 + D_{x_2} f_1 \delta x_2 + D_\epsilon f_1 \delta\epsilon,\\ \frac{d\delta x_2}{dt} &= 0\\ \frac{d\delta\epsilon}{dt} &= 0.\end{aligned}$$

The conditions of theorem 2.3 are now fulfilled; there exists a centre manifold W_ϵ for the extended system, which can be locally defined by

$$x_1 = h(x_2, \epsilon)$$

for some function h. Yet this existence result does not define W_ϵ. Its approximation is made possible by use of the

Theorem 2.8. [2] *For functions $\Psi : \mathbb{R}^{k+1} \to \mathbb{R}^m$ which are C^1 in a neighborhood of $(x_{2*}, 0)$ define*

$$(M\Psi)(x_2, \epsilon) = D\Psi(x_2, \epsilon) f_2(\Psi(x_2, \epsilon), x_2, \epsilon) - f_1(\Psi(x_2, \epsilon), x_2, \epsilon).$$

Note that $(Mh)(x_2, \epsilon) = 0$.

Let now Ψ be a C^1 mapping of a neighborhood of the (new) equilibrium x_* in $\mathbb{R}^{k+1}$ into $\mathbb{R}^m$ with $\Psi(x_{2*}, 0) = x_{1*}$ and $D\Psi(x_{2*}, 0) = 0$. Suppose that as $(x_2, \epsilon) \to (x_{2*}, 0)$, $(M\Psi)(x_2, \epsilon) = O(|(x_2 - x_{2*}, \epsilon)|^q)$ for some $q > 1$. Then as $(x_2, \epsilon) \to (x_{2*}, 0)$, $|h(x_2, \epsilon) - \Psi((x_2, \epsilon))| = O(|(x_2 - x_{2*}, \epsilon)|^q)$.

It is thus possible to approximate the function h defining W_ϵ locally around x_* by a function Ψ, which can be determined order by order, by choosing its component such that $(M\Psi)(x_2, \epsilon) = O(|(x_2 - x_{2*}, \epsilon)|^q)$ for increasing $q > 1$ up to the desired precision.

2.3.2 Application to the discrete distillation dynamics

The tools we presented in the previous section are for finite-dimension systems; our basis distillation column model (2.5) is of infinite dimension. In a first time, we will handle it as if it were discrete in space, to approximate the dynamics on the center manifold in a rigorous manner. The calculation will be done for a binary mixture for the sake of readability, and in the way of [56]. In the next sections, we will formally extend the results to the infinite-dimension case, and to the M-components mixtures, $M > 2$.

Discretizing the original model (2.5) yields, for a binary mixture

$$\left\{\begin{array}{rcl}\sigma_L \frac{\partial x_p}{\partial t} &=& -L\frac{x_p - x_{p-1}}{\Delta s} + \frac{\lambda_L}{\epsilon}(x_p^* - x_p),\\ \sigma_V \frac{\partial y_p}{\partial t} &=& V\frac{y_{p+1} - y_p}{\Delta s} + \frac{\lambda_V}{\epsilon}(y_p^* - y_p),\\ 0 &=& \Lambda_L(x_p^* - x_p) + \Lambda_V(y_p^* - y_p),\\ y_p^* &=& k(x_p^*),\end{array}\right. \tag{2.16}$$

[2] Note that this theorem also explains why the non-uniqueness of the centre manifold is not a problem in practice: two centre manifolds become arbitrary close to each other when approaching the equilibrium point, and each approximation of the first centre manifold is also an approximation of the second one, to the same degree of precision.

where $\Delta s > 0$ is the space-step and the subscript $0 < p < P+1$ indicates a variable evaluated at $s = p\Delta s$. Multiplying the two ODEs by ϵ shows that the model is formulated as a slow system:

$$\left\{\begin{array}{rcl} \epsilon\sigma_L \frac{\partial x_p}{\partial t} & = & -\epsilon L \frac{x_p - x_{p-1}}{\Delta s} + \lambda_L(x_p^* - x_p), \\ \epsilon\sigma_V \frac{\partial y_p}{\partial t} & = & \epsilon V \frac{y_{p+1} - y_p}{\Delta s} + \lambda_V(y_p^* - y_p), \\ 0 & = & \lambda_L(x_p^* - x_p) + \lambda_V(y_p^* - y_p), \\ y_p^* & = & k(x_p^*), \end{array}\right. \tag{2.17}$$

The time scale separation is more appearing through the coordinate change[3]

$$Z_p = \frac{\sigma_L x_p + \sigma_V y_p}{\sigma}, \quad \sigma = \sigma_L + \sigma_V.$$

Physically, Z_p corresponds to a lumped concentration at point p, in the sense that Z_p does not indicate if the component is mostly located in the gas or liquid phase. In (x, Z) coordinates the system rewrites

$$\epsilon\sigma_L \frac{\partial x_p}{\partial t} = -\epsilon L \frac{x_p - x_{p-1}}{\Delta s} + \lambda_L(x_p^* - x_p), \tag{2.18}$$

$$\sigma \frac{\partial Z_p}{\partial t} = -L \frac{x_p - x_{p-1}}{\Delta s} - \frac{V\sigma_L}{\sigma_V} \frac{x_{p+1} - x_p}{\Delta s} + \frac{V\sigma}{\sigma_V} \frac{Z_{p+1} - Z_p}{\Delta s}, \tag{2.19}$$

$$x_p = \left[\lambda_L x_p^* + \lambda_V \left(y_p^* - \frac{\sigma}{\sigma_V} Z_p\right)\right] \left(\lambda_L - \lambda_V \frac{\sigma_L}{\sigma_V}\right)^{-1}, \tag{2.20}$$

$$y_p^* = k(x_p^*), \tag{2.21}$$

Now it is clear that the Z_p are pure slow variables, whose dynamics are driven by liquid and gas transport. This is coherent with the physical meaning of Z_p, which ignores the notion of phase. On the contrary, the x_p are mixed slow-fast variables. The slow dynamics are driven by transport in the liquid phase only, whereas the fast dynamics are dictated by phase-to-phase exchanges.

The natural time of the system t is thus here a fast time scale. To obtain the system in the fast formulation, let $\theta = \frac{t}{\epsilon}$ to define a slow time scale. One obtains (we do not repeat the algebraic equation anymore since they are not impacted):

$$\left\{\begin{array}{rcl} \sigma_L \frac{\partial x_p}{\partial \theta} & = & -\epsilon L \frac{x_p - x_{p-1}}{\Delta s} + \lambda_L(x_p^* - x_p), \\ \sigma \frac{\partial Z_p}{\partial \theta} & = & -\epsilon \left[L \frac{x_p - x_{p-1}}{\Delta s} + \frac{V\sigma_L}{\sigma_V} \frac{x_{p+1} - x_p}{\Delta s} - \frac{V\sigma}{\sigma_V} \frac{Z_{p+1} - Z_p}{\Delta s}\right], \end{array}\right. \tag{2.22}$$

The limit fast system for $\epsilon \to 0$ is

$$\left\{\begin{array}{rcl} \sigma_L \frac{\partial x_p}{\partial \theta} & = & \lambda_L(x_p^* - x_p), \\ \sigma \frac{\partial Z_p}{\partial \theta} & = & 0, \end{array}\right. \tag{2.23}$$

The equilibrium point corresponds to the thermodynamic equilibrium of the whole column, since it is defined by $x_{p*} = x_{p*}^* \ \forall p$. Using equations (2.20) and (2.21) one has

$$\sigma_V k(x_{p*}) + \sigma_L x_{p*} = \sigma Z_{p*} \quad \forall p. \tag{2.24}$$

[3]Note that the centre manifold reduction is a geometric method, hence independent from the chosen coordinates. The same calculations could be done with the natural coordinates (x_p, y_p), to the expense of the readability.

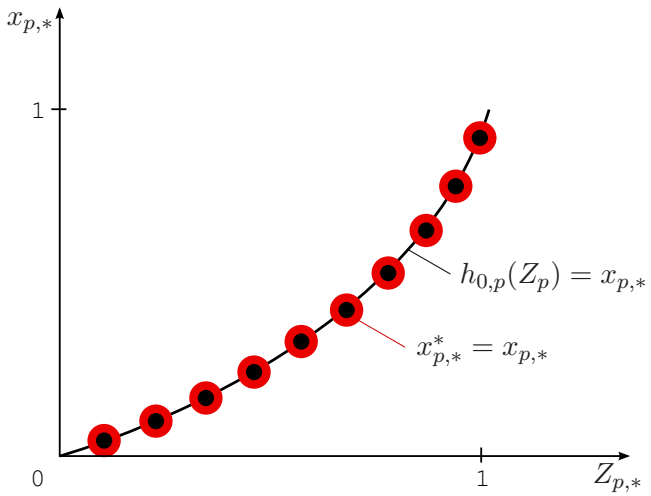

Figure 2.5: Locus of the thermodynamic equilibriums of the fast limit system, which also corresponds to its center manifold

For each p, we can, at least locally, define the continuum of equilibrium points as the graph

$$x_{p*} = h_{0,p}(Z_{p*}),$$
$$x^*_{p*} = h_{0,p}(Z_{p*}),$$

with $h_{0,p}$ s.t. $\sigma_V k(h_{0,p}(Z_{p*})) + \sigma_L h_{0,p}(Z_{p*}) = \sigma Z_{p*}$ as illustrated on Fig. 2.5.

Let $x_* = (x_{1*}, \cdots, x_{P*})$, $Z_* = (Z_{1*}, \cdots, Z_{P*})$. It turns out that the graphs of the $h_{0,p}$ functions correspond (together) to the centre manifold $W^0_{0,(x_*,Z_*)}$ of the limit fast system[4], whatever the equilibrium (x_*, Z_*). Indeed, for any p, one has:

$$\frac{\partial x^*_p}{\partial x_p}(x_{p*}, Z_{p*}) = 1 - \frac{\lambda_V \sigma_L}{\lambda_L \sigma_V} - \frac{\lambda_V}{\lambda_L}\left[\frac{dk(x^*_p)}{dx^*_p}\frac{\partial x^*_p}{\partial x_p} - \frac{\sigma_L}{\sigma_V}\frac{dZ_p}{dx_p}\right](x_{p*}, Z_{p*}),$$
$$\left[\frac{\partial x^*_p}{\partial x_p}\left(1 + \frac{\lambda_V}{\lambda_L}\frac{dk(x^*_p)}{dx^*_p}\right)\right](x_{p*}, Z_{p*}) = 1 - \frac{\lambda_V \sigma_L}{\lambda_L \sigma_V} + \frac{\lambda_V}{\lambda_L}\frac{\sigma_L}{\sigma_V}\frac{dZ_p}{dx_p}(x_{p*}, Z_{p*}). \tag{2.25}$$

If $x_p = h_{0,p}(Z_p)$, that is $\sigma_V k(x_p) + \sigma_L x_p = \sigma Z_p$, then

$$\begin{aligned}\frac{dZ_p}{dx_p}(x_{p*}, Z_{p*}) &= \frac{\sigma_V}{\sigma}\frac{dk(x_p)}{dx_p}(x_{p*}, Z_{p*}) + \frac{\sigma_L}{\sigma} \\ &= \frac{\sigma_V}{\sigma}\frac{dk(x^*_p)}{dx^*_p}(x^*_{p*}, Z_{p*}) + \frac{\sigma_L}{\sigma}.\end{aligned}$$

Reporting in (2.25) yields

$$\left[\frac{\partial x^*_p}{\partial x_p}\left(1 + \frac{\lambda_V}{\lambda_L}\frac{dk(x^*_p)}{dx^*_p}\right)\right](x_{p*}, Z_{p*}) = \left(1 + \frac{\lambda_V}{\lambda_L}\frac{dk(x^*_p)}{dx^*_p}\right)(x_{p*}, Z_{p*})$$

that is

$$\frac{\partial x^*_p}{\partial x_p}(x_{p*}, Z_{p*}) = 1.$$

[4]More precisely, they are a local approximation of a centre manifold (possibly not unique) of the limit fast system, which can be made arbitrarily accurate by getting closer to the equilibrium point.

Consequently, we have in system (2.23), for any p:

$$\left\{\begin{array}{rcl} x_{p*}(h_{0,p}(Z_p),Z_p)-h_{0,p}(Z_p) & = & 0 \text{ for } Z_p=Z_{p*},\\ \frac{d}{dZ_p}\left(x_{p*}(h_{0,p}(Z_p),Z_p)-h_{0,p}(Z_p)\right) & = & 0 \text{ at } Z_p=Z_{p*},\end{array}\right.$$

which matches the requirements of (2.15). Reporting $\sigma_V k(x_p)-\sigma_L x_p=\sigma Z_p$ in (2.20) one also obtains

$$x_p^*+\frac{\lambda_V}{\lambda_L}k(x_p^*)=x_p+\frac{\lambda_V}{\lambda_L}k(x_p)$$

which yields the conclusion that, for any p, for any equilibrium $(h_0(Z_{p*}),Z_{p*})$, one has

$$\begin{aligned} x_p&=h_{0,p}(Z_p),\\ x_p^*&=h_{0,p}(Z_p),\end{aligned}$$

on the centre manifold $W^0_{0,(x_*,Z_*)}$.

The trajectories of the limit fast system (2.23) converge with constant Z_p towards the centre manifold, as illustrated on Fig. 2.6. Conversely, the trajectories of the slow limit system

$$\begin{aligned} x_p^* =& x_p=h_{0,p}(Z_p),\\ \sigma\frac{\partial Z_p}{\partial t} =& -L\frac{h_{0,p}(Z_p)-h_{0,p-1}(Z_p-1)}{\Delta s}-\frac{V\sigma_L}{\sigma_V}\frac{h_{0,p+1}(Z_{p+1})-h_{0,p}(Z_p)}{\Delta s}+\frac{V\sigma}{\sigma_V}\frac{Z_{p+1}-Z_p}{\Delta s},\end{aligned} \tag{2.26}$$

slide on the centre manifold. To get rid of h_0, which is here only implicitly defined, it is useful to rewrite (2.26) in x_p using $\sigma_V k(x_p)+\sigma_L x_p=\sigma Z_p$ on the centre manifold. One must though keep in mind that Z_p enslaves x_p through $x_p=h_0(Z_p)$, and not the contrary. One obtains

$$\left(\sigma_L+\sigma_V k'(x_p)\right)\frac{\partial x_p}{\partial t}=-L\frac{x_p-x_{p-1}}{\Delta z}+V\frac{k(x_{p+1})-k(x_p)}{\Delta z}. \tag{2.27}$$

The trajectories thus slide on the centre manifold converging, for any p, towards $(h_0(Z_{p,eq}),Z_{p,eq})$ with

$$h_0(Z_{p,eq})=x_{p,eq} \text{ such that } Lx_{p,eq}+Vk(x_{p,eq})=Lx_{p-1}+Vk(x_{p+1})$$

as illustrated on Fig. 2.7. Note that, for $(x_{p-1},x_{p+1})\in[0,1]^2$, $x_{p,eq}$ exists in $[0,1]$ since k is continuous bijective from $[0,1]$ to $[0,1]$.

According to the theorem 2.4, the centre manifold $W^0_{0,(x_*,Z_*)}$ of the limit system (2.23) lies within $O(\epsilon)$ of the slow manifold M_ϵ of the original system (2.22), for ϵ small enough. We will now perturb $W^0_{0,(x_*,Z_*)}$ to obtain an approximation of M_ϵ. Using the local graph representation, this is equivalent to perturb all the $h_{0,p}(Z_p)$ to obtain the $h_{\epsilon,p}(Z_p)$ such that $x_p=h_{\epsilon,p}(Z_p)$ on the slow manifold. Once again, not to deal with the implicitly defined function h_0 (and so will be h_ϵ), we will instead perturb the relation $\sigma_V k(x_p)+\sigma_L x_p=\sigma Z_p$. The previous reminder on the actual order of enslaving is still to be kept in mind.

Let, on the slow manifold and for any p:

$$x_p(Z_p)=X_{0,p}(Z_p)+\epsilon X_{1,p}(Z_p)+O(\epsilon^2). \tag{2.28}$$

One has

$$\sigma Z_p=\sigma_V k(X_{0,p}(Z_p))+\epsilon\sigma_V k'(X_{0,p}(Z_p))X_{1,p}(Z_p)+\sigma_L X_{0,p}(Z_p)+\epsilon\sigma_L X_{1,p}(Z_p)+O(\epsilon^2).$$

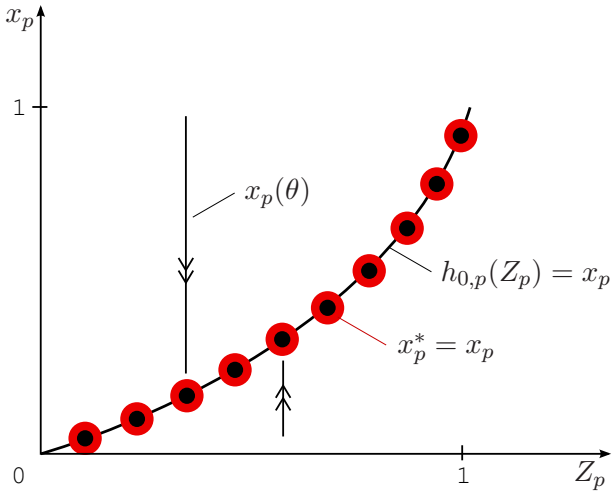

Figure 2.6: The fast limit system converge with constant Z_p towards the center manifold

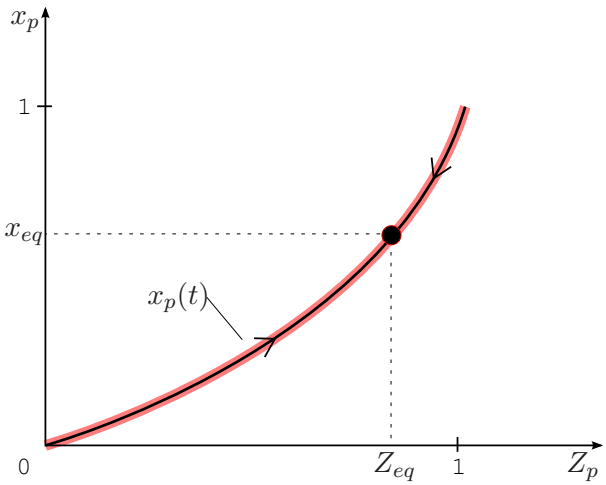

Figure 2.7: The slow limit system converges on the manifold of thermodynamic equilibrium (defined for p) towards the dynamic equilibrium (impacted by $p+1$, $p-1$)

The manifolds $W^0_{0,(x_*,Z_*)}$ and M_ϵ being close up to $O(\epsilon)$, the terms $X_{0,p}(Z_p)$ are immediately given:

$$X_{0,p}(Z_p) = h_0(Z_p),$$

that is, $X_{0,p}(Z_p)$ is s.t. $\sigma Z_p = \sigma_V k(X_{0,p}(Z_p)) + \sigma_L X_{0,p}(Z_p)$. The terms $X_{1,p}(Z_p)$ will be obtained by ensuring the local invariance of (2.28) by (2.22). One must have, for any p:

$$\begin{aligned}\frac{dx_p}{d\theta} &= \left(\frac{dX_{0,p}}{d\theta} + \epsilon\frac{dX_{1,p}}{d\theta} + O(\epsilon^2)\right)\\ &= \frac{dx_p}{dZ_p}\frac{dZ_p}{d\theta},\end{aligned}$$

that is

$$\begin{aligned}&\frac{\epsilon}{\sigma_L}L(x_p - x_{p-1}) - \frac{\lambda_L}{\sigma_L}(x^*_p - x_p)\Delta s\\ &\quad= \epsilon\frac{\left(1+\epsilon\frac{dX_1}{dZ_p}\right)\left(L(x_p - x_{p-1}) + V\frac{\sigma_L}{\sigma_V}(x_{p+1}-x_p) - V\frac{\sigma}{\sigma_V}(Z_{p+1}-Z_p)\right)}{(\sigma_L + k'(X_0)\sigma_V)} + O(\epsilon^2). \quad (2.29)\end{aligned}$$

Since for any p

$$x^*_p = x_p\left(1 - \frac{\sigma_L\lambda_V}{\sigma_V\lambda_L}\right) - \frac{\lambda_V}{\lambda_L}\left(k(x^*_p) - \frac{\sigma Z_p}{\sigma_V}\right)$$

according to equations (2.20) and (2.21), the perturbation of the x_p also affects the x^*_p, which rewrite

$$x^*_p = X^*_{0,p} + \epsilon X^*_{1,p} + O(\epsilon^2)$$

with

$$X^*_{0,p} = X_{0,p}, \quad X^*_{1,p}\left(1 + \frac{\lambda_V}{\lambda_L}k'(X_{0,p})\right) = X_{1,p}\left(1 - \frac{\sigma_L\lambda_V}{\sigma_V\lambda_L}\right).$$

Thus, in equation (2.29) one can replace $\lambda_L(x^*_p - x_p)$ by

$$-\epsilon\lambda_V\frac{\frac{\sigma_L}{\sigma_V} + k'(X_{0,p})}{1 + \frac{\lambda_V}{\lambda_L}k'(X_{0,p})}X_{1,p}.$$

Furthermore, since

$$\begin{aligned}&L(x_p - x_{p-1}) + V\frac{\sigma_L}{\sigma_V}(x_{p+1}-x_p) - V\frac{\sigma}{\sigma_V}(Z_{p+1}-Z_p)\\ &\qquad= L(X_{0,p} - L(X_{0,p-1})) - V(k(X_{0,p+1}) - k(X_{0,p}) + O(\epsilon),\end{aligned}$$

equation (2.29) reduces to the order 1 versus ϵ to:

$$\begin{aligned}&\frac{L}{\sigma_L}(X_{0,p} - X_{0,p-1}) + \frac{\lambda_V}{\sigma_V}\frac{\sigma_L + \sigma_V k'(X_{0,p})}{1 + \frac{\lambda_V}{\lambda_L}k'(X_{0,p})}X_{1,p}\Delta s\\ &\qquad= \frac{L(X_{0,p} - L(X_{0,p-1})) - V(k(X_{0,p+1}) - k(X_{0,p}))}{\sigma_L + k'(X_0)\sigma_V}.\end{aligned}$$

Finally, one obtains

$$X_{1,p} = -\sigma_V J_p \left(\sigma_V L k'(X_{0,p}) \frac{X_{0,p} - X_{0,p-1}}{\Delta s} + \sigma_L V \frac{k(X_{0,p+1}) - k(X_{0,p})}{\Delta s} \right), \tag{2.30}$$

$$J_p = \frac{\frac{1}{\lambda_V} + \frac{k'(X_{0,p})}{\lambda_L}}{\left(\sigma_L + \sigma_V k'(X_{0,p})\right)^2}. \tag{2.31}$$

One can now express the dynamics (in $O(\epsilon^2)$) of the system on the slow manifold, with the natural (slow) time scale t. Again, we write it using the x_p to get rid of the implicit functions $h_{\epsilon,p}$. Yet to cope with the enslaving principe, x_p should here be though of as coordinates, say Ξ_p, built on Z_p such that $\Xi_p = h_{\epsilon,p}(Z_p) + O(\epsilon^2)$ rather than as actual molar fractions. Rewriting (2.19) yields:

$$\left(\sigma_L + \sigma_V k'(X_{0,p})\right) \frac{dX_{0,p}}{dt} = -L \frac{x_p - x_{p-1}}{\Delta s} - \frac{V\sigma_L}{\sigma_V} \frac{x_{p+1} - x_p}{\Delta s} + \frac{V\sigma}{\sigma_V} \frac{Z_{p+1} - Z_p}{\Delta s} + O(\epsilon^2)$$

since $Z_p = \sigma_L X_{0,p} + \sigma_V k(X_{0,p}) + O(\epsilon^2)$ by construction. Replacing the x_p and Z_p one has:

$$\begin{aligned}\left(\sigma_L + \sigma_V k'(X_{0,p})\right) \frac{dX_{0,p}}{dt} \Delta s = {} & V\left(k(X_{0,p}) - k(X_{0,p+1})\right) - L\left(X_{0,p} - X_{0,p-1}\right) \\ & + \epsilon \left[V\left(k'(X_{0,p}) X_{1,p} - k'(X_{0,p+1} X_{1,p+1}\right) - L\left(X_{1,p} - X_{1,p-1}\right) \right] + O(\epsilon^2).\end{aligned}$$

One only needs $O(\epsilon)$ precision for the square bracketed term, thus one can use

$$\epsilon \sigma_V k'(X0,p) X_{1,p} + \epsilon \sigma_L X_{1,p} = O(\epsilon^2) \tag{2.32}$$

(because of $Z_p = \sigma_L X_{0,p} + \sigma_V k(X_{0,p}) + O(\epsilon^2)$) to get:

$$\begin{aligned}\left(\sigma_L + \sigma_V k'(X_{0,p})\right) \frac{dX_{0,p}}{dt} = {} & V \frac{k(X_{0,p}) - k(X_{0,p+1})}{\Delta s} - L \frac{X_{0,p} - X_{0,p-1}}{\Delta s} \\ & - \epsilon \left[\frac{\sigma_L V}{\sigma_V} \frac{X_{1,p+1} - X_{1,p}}{\Delta s} + L \frac{X_{1,p} - X_{1,p-1}}{\Delta s} \right] + O(\epsilon^2),\end{aligned}$$

in which we replace the $X_{1,p}$ using the formula (2.30). The dynamics on the slow manifold reads for any p:

$$\begin{aligned}& \left(\sigma_L + \sigma_V k'(X_{0,p})\right) \frac{dX_{0,p}}{dt} = \\ & - L \frac{X_{0,p} - X_{0,p-1}}{\Delta s} + V \frac{k(X_{0,p}) - k(X_{0,p+1})}{\Delta s} \\ & + \epsilon \sigma_L V J_{p+1} \left(\sigma_V L k'(X_{0,p+1}) \frac{X_{0,p+1} - X_{0,p}}{\Delta s^2} + \sigma_L V \frac{k(X_{0,p+2}) - k(X_{0,p+1})}{\Delta s^2} \right) \\ & - \epsilon \sigma_L V J_p \left(\sigma_V L k'(X_{0,p}) \frac{X_{0,p} - X_{0,p-1}}{\Delta s^2} + \sigma_L V \frac{k(X_{0,p+1}) - k(X_{0,p})}{\Delta s^2} \right) \\ & + \epsilon \sigma_V L J_p \left(\sigma_V L k'(X_{0,p}) \frac{X_{0,p} - X_{0,p-1}}{\Delta s^2} + \sigma_L V \frac{k(X_{0,p+1}) - k(X_{0,p})}{\Delta s^2} \right) \\ & - \epsilon \sigma_V L J_{p-1} \left(\sigma_V L k'(X_{0,p-1}) \frac{X_{0,p-1} - X_{0,p-2}}{\Delta s^2} + \sigma_L V \frac{k(X_{0,p}) - k(X_{0,p-1})}{\Delta s^2} \right) \\ & + O(\epsilon^2).\end{aligned} \tag{2.33}$$

Back to the natural coordinates x_p, y_p, we have the approximations, for any p:

$$x_p = X_{0,p} - \epsilon\sigma_V J_p \left(\sigma_V L k'(X_{0,p}) \frac{X_{0,p} - X_{0,p-1}}{\Delta s} + \sigma_L V \frac{k(X_{0,p+1}) - k(X_{0,p})}{\Delta s} \right) + O(\epsilon^2), \tag{2.34}$$

$$y_p = k(X_{0,p}) + \epsilon\sigma_L J_p \left(\sigma_V L k'(X_{0,p}) \frac{X_{0,p} - X_{0,p-1}}{\Delta s} + \sigma_L V \frac{k(X_{0,p+1}) - k(X_{0,p})}{\Delta s} \right) + O(\epsilon^2), \tag{2.35}$$

where each $X_{0,p}$ obeys the previous dynamics (2.33).

2.3.3 Reduced infinite-dimension distillation dynamics

We address now the centre manifold reduction of the continuous distillation column model. This reduction will be conducted in a formal way only, using the rigorous discrete reduction as a guideline. Again, we are here only interested in the binary mixture distillation model

$$\left\{ \begin{array}{rcl} \sigma_L \frac{\partial x}{\partial t} & = & -L \frac{\partial x}{\partial s} + \frac{\lambda_L}{\epsilon} (x^* - x), \\ \sigma_V \frac{\partial y}{\partial t} & = & V \frac{\partial y}{\partial s} + \frac{\lambda_V}{\epsilon} (y^* - y), \\ 0 & = & \lambda_L (x^* - x) + \lambda_V (y^* - y), \\ y^* & = & k(x^*). \end{array} \right. \tag{2.36}$$

Let us define as previously the lumped variable

$$Z(s,t) = \frac{\sigma_L x(s,t) + \sigma_V y(s,t)}{\sigma}, \quad \sigma = \sigma_L + \sigma_V. \tag{2.37}$$

In order to manipulate the centre manifold through its local graph formulation, let $X(s,t)$ such that

$$Z(s,t) = \frac{\sigma_L X(s,t) + \sigma_V k(X(s,t))}{\sigma}. \tag{2.38}$$

With the notation $k'(X) = \frac{dk(X)}{dX}$, one has:

$$\frac{\partial Z}{\partial t} = \frac{\sigma_L + \sigma_V k'(X)}{\sigma} \frac{\partial X}{\partial t}. \tag{2.39}$$

We shall now write the state variables of the system as functions of X, regularly perturbed by ϵ:

$$x = x_0(X) + \epsilon x_1(X) + O(\epsilon^2), \qquad x^* = x_0^*(X) + \epsilon x_1^*(X) + O(\epsilon^2),$$
$$y = y_0(X) + \epsilon y_1(X) + O(\epsilon^2), \qquad y^* = y_0^*(X) + \epsilon y_1^*(X) + O(\epsilon^2).$$

Limiting ourselves to the limit system, that is, to the case $\epsilon \to 0$ in (2.36), yields:

$$x_0^* \equiv x_0, \quad y_0^* \equiv y_0, \quad y_0^* \equiv k(x_0^*), \quad Z = \frac{\sigma_L x_0(X) + \sigma_V y_0(X)}{\sigma},$$

then

$$x_0(X) = X, \tag{2.40}$$
$$y_0(X) = k(X), \tag{2.41}$$
$$\frac{\partial X}{\partial t} = \frac{-L + V k'(X)}{\sigma_L + \sigma_V k'(X)} \frac{\partial X}{\partial s}, \tag{2.42}$$

the PDE being exactly the limit of (2.27) when $\Delta z \to 0$.

Reporting the expansions of x, x^*, y, y^* with the known 0^{th}-order terms in System (2.36) yields:

$$\sigma_L \frac{\partial X}{\partial t} = -L\frac{\partial X}{\partial s} + \lambda_L \left(x_1^* - x_1\right) + O(\epsilon), \tag{2.43}$$

$$\sigma_V k'(X)\frac{\partial X}{\partial t} = Vk'(X)\frac{\partial X}{\partial s} + \lambda_V \left(y_1^* - y_1\right) + O(\epsilon), \tag{2.44}$$

$$0 = \lambda_L \left(x_1^* - x_1\right) + \lambda_V \left(y_1^* - y_1\right) + O(\epsilon), \tag{2.45}$$

$$y_1^* = k'(X)x_1^* + O(\epsilon). \tag{2.46}$$

Doing the same in (2.37) gives

$$Z = \frac{\sigma_L X + \epsilon\sigma_L x_1(X) + \sigma_V k(X) + \epsilon\sigma_V y_1(X)}{\sigma} + O(\epsilon^2).$$

Confronting to (2.38) one obtains the infinite-dimension equivalent of (2.32):

$$\epsilon\sigma_L x_1 \equiv -\epsilon\sigma_V y_1 + O(\epsilon^2). \tag{2.47}$$

The first-order terms in the expansions can now be determined to match the invariance principle: x_1 and x_1^* are so that the trajectories of (2.40) and (2.43) are the same (up to $O(\epsilon)$); similarly, y_1 and y_1^* are so that the trajectories of (2.40) and (2.44) are the same. One must have:

$$k'(X)\frac{\sigma_V L + \sigma_L V}{\sigma_L + \sigma_V k'(X)}\frac{\partial X}{\partial s} = \lambda_L \left(x_1^* - x_1\right) + O(\epsilon), \tag{2.48}$$

$$-k'(X)\frac{\sigma_V L + \sigma_L V}{\sigma_L + \sigma_V k'(X)}\frac{\partial X}{\partial s} = \lambda_V \left(y_1^* - y_1\right) + O(\epsilon). \tag{2.49}$$

According to (2.46),(2.45) and (2.47) one has:

$$\lambda_V \left(y_1^* - y_1\right) = -\lambda_L \left(x_1^* - x_1\right) = \lambda_V \left(k'(X)x_1^* + \frac{\sigma_L}{\sigma_V}x_1\right) + O(\epsilon),$$

then multiplying (2.48) by $\frac{\lambda_V}{\lambda_L}k'(X)$ and subtracting (2.49) yields

$$x_1 = -\sigma_V \frac{\frac{k'(X)^2}{\lambda_L} + \frac{k'(X)}{\lambda_V}}{\left(\sigma_L + \sigma_V k'(X)\right)^2}\left(\sigma_L V + \sigma_V L\right)\frac{\partial X}{\partial s} + O(\epsilon), \tag{2.50}$$

$$y_1 = \sigma_L \frac{\frac{k'(X)^2}{\lambda_L} + \frac{k'(X)}{\lambda_V}}{\left(\sigma_L + \sigma_V k'(X)\right)^2}\left(\sigma_L V + \sigma_V L\right)\frac{\partial X}{\partial s} + O(\epsilon). \tag{2.51}$$

Note that the zero-order approximation of x_1 is exactly the limit of (2.30) when $\Delta z \to 0$. For the sake of concision let

$$G(X) = \frac{\frac{k'(X)^2}{\lambda_L} + \frac{k'(X)}{\lambda_V}}{\left(\sigma_L + \sigma_V k'(X)\right)^2}\left(\sigma_L V + \sigma_V L\right)^2. \tag{2.52}$$

Injecting the known terms of the expansions in the first equation of System (2.36) leads to the following convection-diffusion equation for the dynamics of X on the system's slow manifold:

$$\left(\sigma_L + \sigma_V k'(X)\right) \frac{\partial X}{\partial t} = \frac{\partial}{\partial s}\left(-LX + Vk(X) + \epsilon G(X)\frac{\partial X}{\partial s}\right) + O(\epsilon^2). \tag{2.53}$$

The actual molar fractions are given as static outputs:

$$\begin{aligned} x(s,t) &= x_0(X(s,t)) + \epsilon x_1(X(s,t)) + O(\epsilon^2) \\ &= X(s,t) - \epsilon\sigma_V \frac{G(X(s,t))}{\sigma_V L + \sigma_L V}\frac{\partial X}{\partial s}(s,t) + O(\epsilon^2), \end{aligned} \tag{2.54}$$

$$\begin{aligned} y(s,t) &= y_0(X(s,t)) + \epsilon y_1(X(s,t)) + O(\epsilon^2) \\ &= k(X(s,t)) + \epsilon\sigma_L \frac{G(X(s,t))}{\sigma_V L + \sigma_L V}\frac{\partial X}{\partial s}(s,t) + O(\epsilon^2), \end{aligned} \tag{2.55}$$

where $X(s,t)$ obeys the dynamics described by (2.53).

Note that the infinite-dimension static outputs correspond exactly to the limit of the discrete static outputs (2.34),(2.35) for $\Delta z \to 0$, as well as the PDE (2.53) which corresponds to the limit when $\Delta z \to 0$ of the discrete dynamics on the slow manifold (2.33).

2.4 Discussion

Dynamic equation (2.53) reduces for our purpose to its terms in $O(1)$ and $O(\epsilon)$:

$$\left(\sigma_L + \sigma_V k'(X)\right) \frac{\partial X}{\partial t} = \frac{\partial}{\partial s}\left(-LX + Vk(X) + \epsilon G(X)\frac{\partial X}{\partial s}\right), \tag{2.56}$$

as well as the static outputs:

$$\begin{aligned} x(s,t) &= x_0(X(s,t)) + \epsilon x_1(X(s,t)) + O(\epsilon^2) \\ &= X(s,t) - \epsilon\sigma_V \frac{G(X(s,t))}{\sigma_V L + \sigma_L V}\frac{\partial X}{\partial s}(s,t), \end{aligned} \tag{2.57}$$

$$\begin{aligned} y(s,t) &= y_0(X(s,t)) + \epsilon y_1(X(s,t)) + O(\epsilon^2) \\ &= k(X(s,t)) + \epsilon\sigma_L \frac{G(X(s,t))}{\sigma_V L + \sigma_L V}\frac{\partial X}{\partial s}(s,t). \end{aligned} \tag{2.58}$$

Equation (2.56) is a parabolic convection-diffusion equation, which in the vanishing diffusion limit ($\epsilon \to 0$) reduces to the hyperbolic convection equation

$$\left(\sigma_L + \sigma_V k'(X)\right) \frac{\partial X}{\partial t} = \frac{\partial}{\partial s}\left(-LX + Vk(X)\right). \tag{2.59}$$

Let us consider the case of a binary mixture $\{N_2,O_2\}$, with X the lumped oxygen molar fraction, in a distillation column such as the HP column. At the top, gas and liquid are almost devoid of oxygen, thus as soon as the reflux is large enough ($L > Vk'(X_{(z=0)} \approx V\alpha_{O_2}$), the composition information travels downwards. Conversely, at the bottom, when the reflux is not too large, ($L < Vk'(X_{(z=h)})$), the composition information travels upwards. With the reflux between this margins, the composition wave speed changes sign inside the column, at the location where $L = Vk'(X)$. The composition profile degenerates into a discontinuous

profile. With the assumption $\sigma_V << \sigma_L$ made in Marqardt's wave model, the speed w of this discontinuity is given by:

$$w = \frac{-L + V\frac{k(X_\oplus)-k(X_\ominus)}{X_\oplus - X_\ominus}}{\sigma_L}$$

where $\oplus$ and $\ominus$ subscripts respectively indicate the downward and the upward side of the discontinuity. In Marquardt's model, $x(z,t)$ identifies to $X(z,t)$ and $y_(z,t)$ to $k(X(z,t))$, thus the equation rewrites:

$$w = \frac{-L + V\frac{y_\oplus - y_\ominus}{x_\oplus - x_\ominus}}{\sigma_L}$$

or, changing the timescale to absorb σ_L and the space-scale to absorb L:

$$w = -1 + \frac{V}{L}\frac{y_\oplus - y_\ominus}{x_\oplus - x_\ominus}$$

which matches (1.4).

The diffusion term in $O(\epsilon)$ prevents the apparition of the discontinuity. Notice that this term is not introduced in the equation *a priori*, in order to get rid of the shock; it naturally emerges from the original balance equations during the reduction procedure. This is a notable difference with the wave-model, where a regular composition wave is set *a priori*, and its motion treated as for a shock-wave a *posteriori*. Note also that this small, axial diffusion term originates from a large, radial (in a cross-s direction) exchange term (in $\frac{1}{\epsilon}$ in the original balance equations).

We have seen in Section 2.1.1 subsection that a large $\frac{1}{\epsilon}$ term in the coupling equation between liquid and gas phase indicates an efficient packing. Then an efficient column should produce stiff $X(s,t)$ profiles, whereas this profiles should be smooth for an inefficient column. And it just so happens that our diffusion term has an in-built dependence on $X(s,t)$, the internal flows $L(s,t)$, $V(s,t)$, and the hold-ups σ_L and σ_V. Thus we obtain a formulation of a packing efficiency depending on operating conditions.

Once again, there is a difference with the original wave-model, where the smoothness of the profile (and so the tray or packing efficiency) is tuned by the shape parameter γ. In our model, the efficiency depends *locally* on the operating conditions; a global tuning is yet still possible using ϵ.

One may be surprised to see that the holds-ups σ_L, σ_V intervene in the diffusion term and in the $O(\epsilon)$ term of the static outputs. Indeed, according to the original balance equations (2.5), the hold-ups should not impact the steady-state. In steady-state, we have (it is useful to reintroduce the $O(\epsilon^2)$ residual term):

$$0 = \frac{d}{ds}\left(-LX + Vk(X) + \epsilon G(X)\frac{dX}{ds}\right) + O(\epsilon^2),$$

thus

$$\begin{aligned} 0 &= \frac{d}{ds}\left(-Lx + Vy + \epsilon G(X)\left(1 - \frac{\sigma_L V}{\sigma_L V + \sigma_V L} - \frac{\sigma_V L}{\sigma_L V + \sigma_V L}\right)\frac{dx}{ds}\right) + O(\epsilon^2) \\ &= \frac{d}{ds}\left(Lx + Vy\right) + O(\epsilon^2), \end{aligned}$$

and:

$$y = k(x) + \epsilon \frac{\sigma_L G}{\sigma_V L + \sigma_L V} \frac{dx}{ds} + \epsilon k'(x) \frac{\sigma_V G}{\sigma_V L + \sigma_L V} \frac{dx}{ds} + O(\epsilon^2).$$

Yet the considered steady-state is a perturbation, by ϵ, of the steady-state limited to the order $O(1)$, that is, the steady-state of the purely convective equation (2.59). One then has $-L + Vk'(X) = O(\epsilon)$ and consequently the previous equation rewrites:

$$\begin{aligned} y &= k(x) + \epsilon \frac{G}{\sigma_V L + \sigma_L V} \left(\sigma_L + \frac{L}{V} \right) \frac{dx}{ds} + O(\epsilon^2) \\ &= k(x) + \epsilon \frac{G}{V} \frac{dx}{ds} + O(\epsilon^2). \end{aligned}$$

In addition, G has become independent from the hold-ups since, according to (2.52):

$$G(X) = \frac{\frac{k'(X)^2}{\lambda_L} + \frac{k'(X)}{\lambda_V}}{(\sigma_L + \sigma_V k'(X))^2} (\sigma_L V + \sigma_V L)^2 = \frac{\frac{k'(X)^2}{\lambda_L} + \frac{k'(X)}{\lambda_V}}{V^2} + O(\epsilon).$$

Consequently, the steady-state of the reduced dynamic system is indeed independent from σ_L, σ_V up to the chosen reduction order.

One can also notice that the right-hand terms of (2.56), (2.57), (2.58) are invariant by the changes on σ_L, σ_V which preserve the ratio $\frac{\sigma_L}{\sigma_V}$.

2.5 Extension to non-binary mixtures

The methodology used in subsections 2.3.2, 2.3.3 easily extends to M-components mixtures, $M = N + 1 > 2$. We briefly illustrate here the extension to the infinite-dimension problem.

First let us rewrite the original system (2.5) with vector notations. With:

$$\begin{aligned} \mathbf{x} &= (x_1, \dots, x_N)^T, & \mathbf{x}^* &= (x_1^*, \dots, x_N^*)^T, \\ \mathbf{y} &= (y_1, \dots, y_N)^T, & \mathbf{y}^* &= (y_1^*, \dots, y_N^*)^T, \end{aligned}$$

the system reads:

$$\left\{ \begin{array}{rcl} \sigma_L \frac{\partial \mathbf{x}}{\partial t} &=& -L \frac{\partial \mathbf{x}}{\partial s} + \frac{\lambda_L}{\epsilon} (\mathbf{x}^* - \mathbf{x}), \\ \sigma_V \frac{\partial \mathbf{y}}{\partial t} &=& V \frac{\partial \mathbf{y}}{\partial s} + \frac{\lambda_V}{\epsilon} (\mathbf{y}^* - \mathbf{y}), \\ 0 &=& \lambda_L (\mathbf{x}^* - \mathbf{x}) + \lambda_V (\mathbf{y}^* - \mathbf{y}), \\ \mathbf{y}^* &=& \mathbf{K}(\mathbf{x}^*), \end{array} \right. \tag{2.60}$$

where $\mathbf{K}(\mathbf{x}) = (k_1(x_1, \dots, x_N), \dots, k_N(x_1, \dots, x_N))^T$. Let us define the lumped compositions vector

$$\mathbf{Z} = \frac{\sigma_L \mathbf{x} + \sigma_V \mathbf{y}}{\sigma}, \quad \sigma = \sigma_L + \sigma_V,$$

and $\mathbf{X}(\mathbf{s}, \mathbf{t})$ such that

$$\mathbf{Z} = \frac{\sigma_L \mathbf{X} + \sigma_V \mathbf{K}(\mathbf{X})}{\sigma}.$$

With $J_K(\mathbf{X})$ the Jacobian matrix of application $\mathbf{K}$ at $\mathbf{X}$, and I_N the identity matrix of size $N \times N$ one has:

$$\sigma \frac{\partial \mathbf{Z}}{\partial t} = (\sigma_L I_N + \sigma_V J_K(\mathbf{X})) \frac{\partial \mathbf{X}}{\partial t}.$$

Setting as previously:

$$\begin{aligned}
\mathbf{x} &= \mathbf{x_0}(\mathbf{X}) + \epsilon \mathbf{x_1}(\mathbf{X}) + O(\epsilon^2), & \mathbf{x}^* &= \mathbf{x_0^*}(\mathbf{X}) + \epsilon \mathbf{x_1^*}(\mathbf{X}) + O(\epsilon^2), \\
\mathbf{y} &= \mathbf{y_0}(\mathbf{X}) + \epsilon \mathbf{y_1}(\mathbf{X}) + O(\epsilon^2), & \mathbf{y}^* &= \mathbf{y_0^*}(\mathbf{X}) + \epsilon \mathbf{y_1^*}(\mathbf{X}) + O(\epsilon^2),
\end{aligned}$$

one obtains, to the order zero versus ϵ:

$$\mathbf{x_0^*} \equiv \mathbf{x_0}, \quad \mathbf{y_0^*} \equiv \mathbf{y_0}, \quad \mathbf{y_0^*} \equiv \mathbf{K}(\mathbf{x_0^*}), \quad \mathbf{Z} = \frac{\sigma_L \mathbf{x_0}(\mathbf{X}) + \sigma_V \mathbf{y_0}(\mathbf{X})}{\sigma},$$

then:

$$\begin{aligned}
&\mathbf{x_0}(\mathbf{X}) = \mathbf{X}, \quad \mathbf{y_0}(\mathbf{X}) = \mathbf{K}(\mathbf{X}), \\
&\frac{\partial \mathbf{X}}{\partial t} = \left(\sigma_L I_N + \sigma_V J_K(\mathbf{X})\right)^{-1} \left(-L I_N + V J_K(\mathbf{X})\right) \frac{\partial \mathbf{X}}{\partial s}.
\end{aligned}$$

The first-order terms of the expansions are then dictated by the invariance principle; one must have:

$$\begin{aligned}
\left(\sigma_L I_N + \sigma_V J_K(\mathbf{X})\right)^{-1} \left(\sigma_V L + \sigma_L V\right) J_K(\mathbf{X}) &= \lambda_L \left(\mathbf{x_1^*} - \mathbf{x_1}\right) + O(\epsilon), \\
-\left(\sigma_L I_N + \sigma_V J_K(\mathbf{X})\right)^{-1} \left(\sigma_V L + \sigma_L V\right) J_K(\mathbf{X}) &= \lambda_V \left(\mathbf{y_1^*} - \mathbf{y_1}\right) + O(\epsilon).
\end{aligned}$$

One also has

$$\lambda_V \left(\mathbf{y_1^*} - \mathbf{y_1}\right) = -\lambda_L \left(\mathbf{x_1^*} - \mathbf{x_1}\right) = \lambda_V \left(J_K(\mathbf{X}) \mathbf{x_1^*} + \frac{\sigma_L}{\sigma_V} \mathbf{x_1}\right) + O(\epsilon),$$

and since we only manipulate linear combinations of $J_K(\mathbf{X})$ and I_N, the matrix commute freely in the calculations, yielding:

$$\mathbf{x_1} = -\sigma_V \frac{\frac{J_K(\mathbf{X})^2}{\lambda_L} + \frac{J_K(\mathbf{X})}{\lambda_V}}{\left(\sigma_L I_N + \sigma_V J_K(\mathbf{X})\right)^2} \left(\sigma_L V + \sigma_V L\right) \frac{\partial \mathbf{X}}{\partial s} + O(\epsilon), \tag{2.61}$$

$$\mathbf{y_1} = -\sigma_L \frac{\frac{J_K(\mathbf{X})^2}{\lambda_L} + \frac{J_K(\mathbf{X})}{\lambda_V}}{\left(\sigma_L I_N + \sigma_V J_K(\mathbf{X})\right)^2} \left(\sigma_L V + \sigma_V L\right) \frac{\partial \mathbf{X}}{\partial s} + O(\epsilon). \tag{2.62}$$

Defining

$$\mathbf{G}(\mathbf{X}) = \left(\frac{J_K(\mathbf{X})^2}{\lambda_L} + \frac{J_K(\mathbf{X})}{\lambda_V}\right) \left(\sigma_L I_N + \sigma_V J_K(\mathbf{X})\right)^{-2} \left(\sigma_L V + \sigma_V L\right)^2, \tag{2.63}$$

which this time is a matrix, we obtain the static outputs

$$\begin{aligned}
\mathbf{x}(s,t) &= \mathbf{x_0}(\mathbf{X}(s,t)) + \epsilon \mathbf{x_1}(\mathbf{X}(s,t)) + O(\epsilon^2) \\
&= \mathbf{X}(s,t) - \epsilon \sigma_V \frac{\mathbf{G}(\mathbf{X}(s,t))}{\sigma_V L + \sigma_L V} \frac{\partial \mathbf{X}}{\partial s}(s,t) + O(\epsilon^2), \qquad (2.64) \\
\mathbf{y}(s,t) &= \mathbf{y_0}(\mathbf{X}(s,t)) + \epsilon \mathbf{y_1}(\mathbf{X}(s,t)) + O(\epsilon^2) \\
&= \mathbf{K}(\mathbf{X}(s,t)) + \epsilon \sigma_L \frac{\mathbf{G}(\mathbf{X}(s,t))}{\sigma_V L + \sigma_L V} \frac{\partial \mathbf{X}}{\partial s}(s,t) + O(\epsilon^2), \qquad (2.65)
\end{aligned}$$

where $\mathbf{X}(s,t)$ obeys the following dynamics:

$$(\sigma_L I_N + \sigma_V J_K(\mathbf{X}))\frac{\partial \mathbf{X}}{\partial t} = \frac{\partial}{\partial s}\left(-L\mathbf{X} + V\mathbf{K}(\mathbf{X}) + \epsilon \mathbf{G}(\mathbf{X})\frac{\partial \mathbf{X}}{\partial s}\right) + O(\epsilon^2). \tag{2.66}$$

It is interesting to notice that the matrix $\mathbf{G}(\mathbf{X}(s,t))$ in the diffusion term is generally non-antisymmetric, since $J_K(\mathbf{X})$ is non-antisymmetric itself. For example, for $\mathbf{K}(\mathbf{X})$ defined according to (2.2):

$$\begin{aligned}\frac{\partial k_i}{\partial x_j} &= -\frac{\alpha_i(\alpha_j - 1)x_i}{\left(1 + \sum_{l=1}^{N}(\alpha_l - 1)x_l\right)^2}, \quad i \neq j \\ &= \frac{\alpha_i\left(1 + \sum_{l=1,\, l\neq i}^{N}(\alpha_l - 1)x_l\right)}{\left(1 + \sum_{l=1}^{N}(\alpha_l - 1)x_l\right)^2}, \quad i = j.\end{aligned}$$

Thus the diffusion term does not respect Onsager's reciprocity relations, despite the fact that it has been developed in the vicinity of the equilibrium $\mathbf{y_0} = \mathbf{K}(\mathbf{x_0})$.

2.6 Riemann invariants approach for non-binary mixture

Despite the importance of the diffusive effect on the molar fraction profile, thinking in terms of wave-fronts may increase the comprehensibility of both the static and dynamic regimes of the distillation column. As mentioned above, the intuitive notion of wave-front, which is a single step in binary distillation, is lost for a larger number of components. In this section, we seek to adapt the results of [84] from the field of multicomponent chromatography on fixed bed to multicomponent distillation. Note that similar results, notably regarding (2.80) and (2.87) can also be adapted from the work of Helfferich (see [43] and [42] for instance). In agreement with the review [51], it seems that approaches similar to the one we present have only been little used for distillation with more than 2 components. [32] mentions how $N-1$ composition fronts will appear in an N components mixture reactive distillation, but does not calculate the corresponding velocities. In [36] the author deals with ternary mixture distillation in a more complex case than ours (including effects on the fluids distribution and temperature profiles) using coherent waves and gives a formula for their velocities. Yet he does not provide relations similar to (2.80) and (2.87) to calculate the intermediate composition between two consecutive composition waves. On the contrary, results similar to the one we present can be found in [76] and [104], which are for plate distillation columns. The latter in addition compares the theoretical coherent waves compositions and speeds against experimental dynamic data (whereas we will be limited to comparison with steady-state simulation cases); note that this data were obtained using an experimental, non-cryogenic column with a ternary mixture of methanol, 1-propanol, 1-pentanol.

Let us reduce the distillation dynamic model to the transport equation

$$\sigma\frac{\partial \mathbf{X}}{\partial t} = \frac{\partial}{\partial s}\left(-L\mathbf{X} + V\mathbf{K}(\mathbf{X})\right), \tag{2.67}$$

where we take σ a constant scalar coefficient. This is a rough simplification, since σ should depend on $\mathbf{X}$ according to the centre manifold reduction. Yet it has the advantage of dramatically simplifying the following calculations. Moreover, we will see that we have only to

deal with piecewise constant molar fraction profiles, for which σ is actually constant on each branch of the discontinuity.

According to the first step of the (finite dimension) centre manifold reduction, $\mathbf{X} = (X_1, \dots, X_N)^T$ is here confounded with $\mathbf{x} = (x_1, \dots, x_N)^T$ the actual molar fraction vector in the liquid phase. Thus equation (2.67) can be seen as describing transport phenomena in the liquid phase, impacted by interaction with the gas phase. The liquid phase plays here the role of the solute phase in chromatography, whereas the gas phase behaves as the adsorbent. The only differences are that the adsorbent is a fixed bed whereas the gas is moving, and that the equilibrium relation between the two 'beds' is now defined by (2.2) instead of the Langmuir isotherm.

Let us reformulate (2.67) as

$$\sigma \frac{\partial \mathbf{X}}{\partial t} + \frac{\partial r(\mathbf{X})}{\partial s} = 0, \quad r(\mathbf{X}) = L\mathbf{X} - V\mathbf{K}(\mathbf{X}) \tag{2.68}$$

and suppose that we dispose of a coherent molar fractions profile $\mathbf{X}(z,t)$, that is, a profile which propagates along the (unbounded) column with no deformation. Then $\forall i = 1, .., N$, X_i depends only on $\omega = \frac{t}{\sigma} - s$ and, using the initial data, X_i is mapped to any X_j by a relation $X_j = g_{i,j}(X_i)$. Such a profile in the molar fractions space is called a Γ-curve, which is parameterized with ω.

We define $\mathcal{D}$ the infinitesimal variation along the Γ-curve, that is, the variation between the points of the curve corresponding to w and $w + dw$. Let $r_i = LX_i - Vk_i(\mathbf{X})$. Along the Γ-curve, one has:

$$\begin{aligned}
\frac{\mathcal{D}r_i}{\mathcal{D}X_i} &= \sum_{j=1}^{N} \frac{\partial r_i}{\partial X_j} \frac{dX_j}{dX_i} \\
&= \sum_{j=1}^{N} \frac{\partial r_i}{\partial X_j} \frac{dg_{j,i}(X_j)}{\partial X_i} \\
&= \sum_{j=1}^{N} r_{i,j} \frac{dg_{j,i}(X_j)}{\partial X_i},
\end{aligned}$$

thus (2.68) rewrites

$$\sigma \frac{\partial X_i}{\partial t} + \frac{\mathcal{D}r_i}{\mathcal{D}X_i} \frac{\partial X_i}{\partial z} = 0, \quad \forall i \in [1, N].$$

Let $\nu := \frac{\mathcal{D}r_i}{\sigma \mathcal{D}X_i} = \sigma \left(\frac{dz}{\sigma dt}\right)_\omega$. ν (in $m.s^{-1}$) corresponds to the propagation speed of our coherent composition profile, and thus does not depend on i. This imposes

$$\frac{\mathcal{D}r_i}{\mathcal{D}X_i} = \frac{\mathcal{D}r_j}{\mathcal{D}X_j} \quad \forall i, j \in [1, N]. \tag{2.69}$$

Under this condition, we have

$$\begin{aligned}\frac{\partial X_i}{\partial t}+\nu\frac{\partial X_i}{\partial Z} &= \frac{\partial X_i}{\partial t}+\frac{\mathcal{D}r_i}{\sigma\mathcal{D}X_i}\frac{\partial X_i}{\partial z}=0\\ &= -\nu\frac{\partial X_i}{\partial z}+\frac{\mathcal{D}r_i}{\sigma\mathcal{D}X_i}\frac{\partial X_i}{\partial z}\\ &= -\sigma\nu\frac{\partial X_i}{\partial z}+\sum_{j=1}^{M} r_{i,j}\frac{dg_{i,j}}{dX_i}\frac{\partial X_i}{\partial z}\\ &= -\sigma\nu\frac{\partial X_i}{\partial z}+\sum_{j=1}^{M} r_{i,j}\frac{\partial X_j}{\partial z}=0 \quad \forall i,j\in[1,N].\end{aligned} \tag{2.70}$$

In the matrix form, the last equality rewrites as the following eigenvalues problem:

$$\left(\nabla_c\mathbf{r}-\sigma\nu\mathbf{I}\right)\frac{d\mathbf{X}}{dw}=0, \tag{2.71}$$

where ∇_c stands for the gradient operator with respect to the molar fractions.

The equilibrium relation we use has some similarity with the Langmuir isotherm used in [84]. Similarly to the paper, let

$$\Phi_i=(\alpha_i/\mu_i)X_i=(\alpha_i-1)X_i, \quad D=1+\sum_{j=1}^{M}\Phi_j, \tag{2.72}$$

with $\mu_i=(\alpha_i)/(\alpha_i-1)$ for commodity. With the relations $r_{i,j}$, the Φ_i and X_i can be expressed as functions of D only, then:

$$k_i=\frac{\mu_i\Phi_i(D)}{D}. \tag{2.73}$$

Infinitesimal displacements along the Γ-curve can thus be expressed in terms of variations with respect to D. One has with $\mathcal{D}=\frac{d}{dD}$:

$$\frac{\mathcal{D}r_i}{\mathcal{D}X_i}=\frac{L\frac{dX_i}{dD}-V\frac{dk_i}{dD}}{\frac{dX_i}{dD}}=L-V(\alpha_i-1)\frac{\frac{dk_i}{dD}}{\frac{d\Phi_i}{dD}}, \quad i=1...N,$$

thus equation (2.69) rewrites

$$\alpha_i\frac{dk_i/dD}{d\Phi_i/dD}=\alpha_j\frac{dk_j/dD}{d\Phi_j/dD}, \quad \forall i,j\in[1,N].$$

Injecting (2.73) yields

$$\frac{\alpha_i}{D}-\frac{\alpha_i\Phi_i}{D^2\frac{d\Phi_i}{dD}}=\frac{\alpha_j}{D}-\frac{\alpha_j\Phi_j}{D^2\frac{d\Phi_j}{dD}}, \tag{2.74}$$

and differentiating once again with respect to D leads $\forall i,j\in[1,N]$ to:

$$2\left(\frac{\alpha_i}{D^2}-\frac{\Phi_i\alpha_i}{D^3\frac{d\Phi_i}{dD}}\right)-\frac{\alpha_i\Phi_i\frac{d^2\Phi_i}{dD^2}}{D^2\left(\frac{d\Phi_i}{dD}\right)^2}=2\left(\frac{\alpha_j}{D^2}-\frac{\Phi_j\alpha_j}{D^3\frac{d\Phi_j}{dD}}\right)-\frac{\alpha_j\Phi_j\frac{d^2\Phi_j}{dD^2}}{D^2\left(\frac{d\Phi_j}{dD}\right)^2}.$$

This equation is simplified using (2.74) into

$$\frac{\frac{d^2\Phi_i}{dD^2}}{\frac{1}{\alpha_i\Phi_i}\left(\frac{d\Phi_i}{dD}\right)^2} = \frac{\frac{d^2\Phi_j}{dD^2}}{\frac{1}{\alpha_j\Phi_j}\left(\frac{d\Phi_j}{dD}\right)^2} \quad \forall i,j \in [0,1],$$

and thus one obtains:

$$\frac{\sum_{j=1}^{N}\frac{d^2\Phi_j}{dD^2}}{\sum_{j=1}^{N}\frac{1}{\alpha_j\Phi_j}\left(\frac{d\Phi_j}{dD}\right)^2} = \frac{\frac{d^2\Phi_i}{dD^2}}{\frac{1}{\alpha_i\Phi_i}\left(\frac{d\Phi_i}{dD}\right)^2} \quad \forall i \in [1,N]. \tag{2.75}$$

Yet given the definition of D in (2.72):

$$0 = \frac{d^2D}{dD^2} = \sum_{j=1}^{N}\frac{d^2\Phi_j}{dD^2}.$$

Consequently, any solution to (2.75) satisfies one of the following conditions:

1. $\frac{d^2\Phi_j}{dD^2} = 0 \quad \forall j \in [1,N]$,
2. $\sum_{j=1}^{N}\alpha_j\Phi_j\left(\frac{d\Phi_j}{dD}\right)^2$.

The second condition would require that not all the Φ_j have the same sign. Since we have chosen to order the components by increasing volatility, the unexpressed component C_{N+1} is the most volatile, and one has

$$0 < \alpha_1 < \alpha_2 < ... < \alpha_N < 1,$$

which ensures that the sign of the Φ_j does not change. The solution must necessarily fulfill the 1^{st} condition, whose integration yields:

$$\Phi_i - \Phi_i^0 = J_i\left(D - D^0\right) \quad \forall i \in [1,N], \tag{2.76}$$

where Φ_i^0 and D^0 correspond to initial conditions and J_i is an integration constant to be now determined.

Summing (2.76) over i gives

$$\sum_{i=1}^{N}\Phi_i - \sum_{i=1}^{N}\Phi_i^0 = (D - D^0)\sum_{i=1}^{N}J_i = \left(\sum_{i=1}^{N}\Phi_i - \sum_{i=1}^{N}\Phi_i^0\right)\sum_{i=1}^{N}J_i,$$

thus

$$\sum_{j=1}^{N}J_i = 1. \tag{2.77}$$

One can now inject (2.76) in (2.74) to get

$$\frac{\alpha_i}{D} - \frac{\alpha_i\Phi_i}{D^2J_i} = \frac{\alpha_j}{D} - \frac{\alpha_j\Phi_j}{D^2J_j} \quad \forall i,j \in [1,N],$$

Table 2.1: Sign of Riemann invariants $J_i^{(k)}$

$J_i^{(k)}$	J_1	J_2	J_3	$\cdots$	J_{N-2}	J_{N-1}	J_N
$J^{(1)}$	+	-	-	$\cdots$	-	-	-
$J^{(2)}$	+	+	-	$\cdots$	-	-	-
$J^{(3)}$	+	+	+	$\cdots$	-	-	-
$\vdots$	$\vdots$	$\vdots$	$\vdots$	$\ddots$	$\vdots$	$\vdots$	$\vdots$
$J^{(N-2)}$	+	+	+	$\cdots$	+	-	-
$J^{(N-1)}$	+	+	+	$\cdots$	+	+	-
$J^{(N)}$	+	+	+	$\cdots$	+	+	+

that is, using (2.73)

$$(\alpha_i - 1)\left(\frac{\mu_i}{D} - \frac{k_i}{DJ_i}\right) = (\alpha_j - 1)\left(\frac{\mu_j}{D} - \frac{k_j}{DJ_j}\right) \quad \forall i, j \in [1, N].$$

Let us define:

$$\omega = (\alpha_i - 1)\left(\mu_i - \frac{k_i}{J_i}\right) \quad \forall i \in [1, N]. \tag{2.78}$$

The summation over i of

$$J_i = \frac{k_i}{\mu_i - \frac{\omega}{\alpha_i - 1}} = \frac{k_i(\alpha_i - 1)}{\alpha_i - \omega} \quad \forall i \in [1, N] \tag{2.79}$$

yields an implicit equation to determine ω:

$$\sum_{i=1}^{N} \frac{k_i(\alpha_i - 1)}{\alpha_i - \omega} = 1. \tag{2.80}$$

This equation has N real roots, which furthermore satisfy

$$0 < \alpha_1 \leq \omega_{(1)} \leq \alpha_2 \leq ... \leq \alpha_k \leq \omega_{(k)} \leq \alpha_{k+1} \leq ... \leq \alpha_N \leq \omega_{(N)} \leq 1. \tag{2.81}$$

Reasoning backwards, each possible ω gives rise to a set of integration constants J_i, $i = 1...N$, each being associated to a solution to our transport problem. For all $i \in [1, N]$, there are N associated Riemann invariants J_i, which we note

$$J_i^{(k)} = \frac{k_i}{\mu_i - \frac{\omega_{(k)}}{\alpha_i - 1}} = \frac{k_i(\alpha_i - 1)}{\alpha_i - \omega_{(k)}} \quad \forall i, k \in [1, N]. \tag{2.82}$$

We will name $\Gamma^{(k)}$ the Γ-curve corresponding to the set of invariants $\{J_i^{(k)}\}$.

The ordering of the $\omega_{(k)}$ gives a triangular structure to the sign of the $J_i^{(k)}$, as shown on in Table 2.1. One can also notice that

$$0 < J_1^{(1)} < J_1^{(2)} < ... < J_1^{(N-1)} < J_1^{(N)}. \tag{2.83}$$

Replacing k_i with $\mu_i \Phi_i / D$ in (2.78), one can define

$$\Lambda_{(k)} := D\omega_{(k)} = \alpha_i \left(D - \frac{\Phi_i}{J_i^{(k)}}\right) \quad \forall i, k \in [1, N]. \tag{2.84}$$

Note that due to (2.81):

$$0 < \Lambda_{(1)} \leq \Lambda_{(1)} \leq ... \leq \Lambda_{(N-1)} \leq \Lambda_{(N)}. \tag{2.85}$$

Using (2.76), one has

$$\Lambda_{(k)} = \alpha_i \left(D^0 - \frac{\Phi_i^0}{J_i^{(k)}} \right).$$

As $\{J_i^{(k)}\}$ is the family of integration constants defining $\Gamma^{(k)}$, it comes that $\Lambda_{(k)}$ is constant along the corresponding $\Gamma^{(k)}$. Inversely, one can show that $w_{(m)}$ remains constant on any $\Gamma^{(k)}$, $k \neq m$. Indeed, from (2.77) one has:

$$\sum_{i=1}^{N} \frac{k_i(\alpha_i - 1)}{\alpha_i - \omega_{(m)}} = \sum_{i=1}^{N} J_i^{(k)}, \quad \forall m \neq k.$$

Yet according to (2.82):

$$\frac{k_i(\alpha_i - 1)}{\alpha_i - \omega_{(m)}} = \frac{\alpha_i - \omega_{(k)}}{\alpha_i - \omega_{(m)}} J_i^{(k)},$$

and thus one obtains

$$\left(\omega_{(m)} - \omega_{(k)}\right) \sum_{i=1}^{N} \frac{J_i^{(k)}}{\alpha_i - \omega_{(m)}} = 0, \quad \forall m \neq k. \tag{2.86}$$

With equation (2.80) we dispose of a continuous mapping from the physical molar fractions space $\Phi(N)$ to the $\Omega(N)$-space where live the $\omega_{(k)}$. The inverse mapping is given by:

$$\Phi_i = \left(\frac{\alpha_i}{\omega_{(i)}} - 1 \right) \prod_{j=1, j\neq i}^{N} \left(\frac{\frac{\alpha_i}{\omega_{(j)}} - 1}{\frac{\alpha_i}{\alpha_j} - 1} \right) \tag{2.87}$$

Suppose a Γ^k-curve; to each point of it is associated a characteristic speed ν_k. If

$$\frac{d\nu_k}{ds} < 0 \tag{2.88}$$

then the characteristics overlap and the Γ^k-curve degenerates into a discontinuous profile, and the composition wave into a shockwave. Since

$$\frac{d\nu_k}{ds} < 0 \Leftrightarrow \frac{d\nu_k}{dD}\frac{dD}{ds} < 0$$

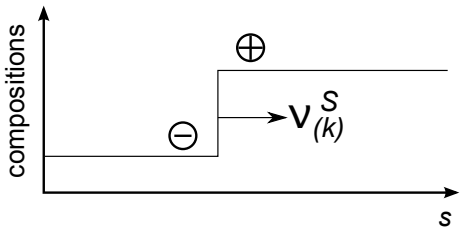

Figure 2.8: A discontinuity traveling along the s-axis.

and

$$\begin{aligned}
\frac{d\nu_k}{dD} &= \frac{1}{\sigma}\frac{d}{dD}\left(\frac{\mathcal{D}r_i}{\mathcal{D}X_i}\right) = \frac{1}{\sigma}\frac{d}{dD}\left(L - V(\alpha_i - 1)\frac{\frac{dk_i}{dD}}{\frac{d\Phi_i}{dD}}\right) \\
&= -\frac{V(\alpha_i - 1)}{\sigma}\frac{d}{dD}\left(\frac{\mu_i}{D} - \frac{\Phi_i\mu_i}{D^2\frac{d\Phi_i}{dD}}\right) \text{ (using } k_i = \frac{\mu_i\Phi_i}{D}\text{)} \\
&= -\frac{V(\alpha_i - 1)}{\sigma}\frac{d}{dD}\left(\frac{\mu_i}{D} - \frac{\Phi_i\mu_i}{D^2 J_i^k}\right) \\
&= -\frac{V\alpha_i}{\sigma}\frac{d}{dD}\left(\frac{1}{D} - \frac{\Phi_i}{D^2 J_i^k}\right) \\
&= -\frac{V\alpha_i}{\sigma}\frac{d}{dD}\left(\frac{\Lambda_k}{D^2}\right) \text{ (according to (2.84))} \\
&= \frac{2V\alpha_i\Lambda_k}{\sigma D^3} \text{ (since } \Lambda_k \text{ is constant along the } \Gamma^{(k)}\text{)} \\
&> 0 \text{ (according to (2.85))} ,
\end{aligned}$$

condition (2.88) is equivalent to:

$$\frac{dD}{ds} < 0. \tag{2.89}$$

As we will see in Chapter 5, this condition is fullfilled in both the High and Low Pressure columns. Thus we restrict ourselves to the case where all existing wave are shockwaves. Let us consider a discontinuous composition profile. As for the wave-model, the shock-speed ν^S of the wavefront is now dictated by the mass conservation principle across the discontinuity. Let the subscripts $_\ominus$ and $_\oplus$ respectively designate the upstream and the downstream sides of the discontinuity (see Fig. 2.8).

One has:

$$\nu^S = \frac{L - V\frac{k_{i,\oplus} - k_{i,\ominus}}{X_{i,\oplus} - X_{i,\ominus}}}{\sigma} \tag{2.90}$$

for $i = 1...N$, which notably implies:

$$\frac{k_{i,\oplus} - k_{i,\ominus}}{X_{i,\oplus} - X_{i,\ominus}} = \frac{k_{j,\oplus} - k_{j,\ominus}}{X_{j,\oplus} - X_{j,\ominus}} \quad \forall i,k \in [1,N].$$

Yet these conservation relations across the discontinuity do not indicate whether it is increasing or decreasing. This information is retrieved using the previously found shock condition (2.89): one must have $D_\oplus < D_\ominus$. In addition, using (2.76) one has:

$$\Phi_{i,\oplus} - \Phi_{i,\ominus} = J_i^{(k)}\,(D_\oplus - D_\ominus) \quad \forall i \in [1,N]. \tag{2.91}$$

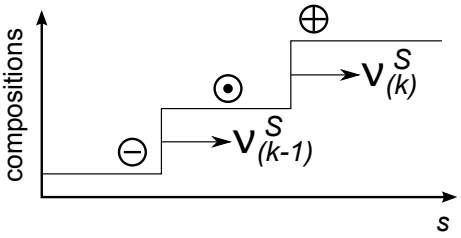

Figure 2.9: Two discontinuities of different kind with their shock-speed.

Note that (2.90) is also

$$\begin{aligned}
\nu^S &= \frac{1}{\sigma}\left(L - V\frac{\left(\frac{\mu_i\Phi_i}{D}\right)_\oplus - \left(\frac{\mu_i\Phi_i}{D}\right)_\ominus}{\left(\frac{\mu_i}{\alpha_i}\Phi_i\right)_\oplus - \left(\frac{\mu_i}{\alpha_i}\Phi_i\right)_\ominus}\right)\\
&= \frac{1}{\sigma}\left(L - V\frac{\alpha_i}{D_\oplus D_\ominus}\frac{D_\ominus\Phi_{i,\oplus} - D_\oplus\Phi_{i,\ominus}}{\Phi_{i,\oplus} - \Phi_{i,\ominus}}\right)\\
&= \frac{1}{\sigma}\left(L - V\frac{\alpha_i}{D_\oplus D_\ominus}\frac{D_\ominus\left(\Phi_{i,\oplus} - \Phi_{i,\ominus}\right) - \Phi_{i,\ominus}\left(D_\oplus - D_\ominus\right)}{\Phi_{i,\oplus} - \Phi_{i,\ominus}}\right)\\
&= \frac{1}{\sigma}\left(L - V\frac{\alpha_i\left(D_\ominus - \frac{\Phi_{i,\ominus}}{J_i^k}\right)}{D_\oplus D_\ominus}\right) \text{ (using (2.91)),}
\end{aligned}$$

thus according to (2.84):

$$\nu^S = \frac{1}{\sigma}\left(L - V\frac{\Lambda_{(k)}}{D_\oplus D_\ominus}\right). \tag{2.92}$$

Thanks to (2.91) we have in addition:

$$\begin{aligned}
\Lambda_{(k)} &= \alpha_i\left(D_\ominus - \frac{\Phi_{i,\ominus}}{J_i^k}\right) = \alpha_i\left(D_\oplus - \frac{\Phi_{i,\oplus}}{J_i^k}\right)\\
\Lambda_{(k)} &= w_{(k),\oplus}D_\oplus = w_{(k),\ominus}D_\ominus.
\end{aligned} \tag{2.93}$$

We now consider two coexisting shocks of different kind, namely $k-1$ and k, as depicted on Fig. 2.9. A subscript $\odot$ will designate the region between the two discontinuities.

Comparing the two shock-speeds yields:

$$\begin{aligned}
\sigma\left(\nu^S_{(k)} - \nu^S_{(k-1)}\right) &= -V\left(\frac{\Lambda_{(k)}}{D_\ominus D_\odot} - \frac{\Lambda_{(k-1)}}{D_\odot D_\oplus}\right)\\
&= -\frac{V}{D_\odot}\left(\alpha_i\left(1 - \frac{\Phi_{i,\ominus}}{D_\ominus J_i^{(k)}}\right) - \alpha_j\left(1 - \frac{\Phi_{j,\oplus}}{D_\oplus J_j^{(k-1)}}\right)\right)
\end{aligned}$$

for any i, j in $[1, N]$. In particular, taking $i = j = k$ yields:

$$\sigma\left(\nu^S_{(k)} - \nu^S_{(k-1)}\right) = -\frac{V\alpha_k}{D_\odot}\left(\frac{\Phi_{k,\oplus}}{D_\oplus J_k^{(k-1)}} - \frac{\Phi_{k,\ominus}}{D_\ominus J_k^{(k)}}\right) < 0$$

since according to Table 2.1, $J_k^{(k)} > 0$ and $J_k^{(k-1)} < 0$, and $\Phi_k < 0$. This holding for any $k \in [1, N]$, one can order the shock-speeds:

$$\nu^S_{(N)} < \nu^S_{(N-1)} < ... < \nu^S_{(2)} < \nu^S_{(1)} < \frac{L}{\sigma}. \tag{2.94}$$

Note that no wave can travel faster than $\frac{L}{\sigma}$ since for any $k \in [1, N]$:

$$\sigma \nu^S_{(k)} = L - V \frac{\Lambda_{(k)}}{D_\oplus D_\ominus} = L - V \frac{\omega_{(k),\oplus}}{D_\ominus} < L$$

according to (2.81).

2.7 Conclusion

We have presented at the beginning of this chapter a simple, 1-D, two-flows model for distillation, with interfacial mass exchange. Contrary to the tray models, ours is continuous; as Marquardt's wave model, it is then naturally suited for packed columns. Contrary to many models (including the original wave-model), we did not suppose that the thermodynamic equilibrium is homogenously reached in each phase. The interfacial exchange flow is indeed driven by compositions inhomogeneities. For the moment, our model does not take energy balance into account. We have qualitatively shown how the interfacial exchange flow and the packing efficiency were related.

We initially thought that, regarding a particular component in a mixture, a good reduction approach was to separate the high-purity region of the column from the region with higher concentrations. We thus attempted to check the validity of this approach in steady-state using a standard matched asymptotic development technique (briefly introduced) to derive simplified steady-state molar fraction profiles from the two-flows model. Using a simplified binary linear case, we have shown that the technique fails due to the exponentially stiff nature of the steady-state profile and the boundary conditions with recycle. This can be qualitatively extended to the non-linear case with any number of components.

This failed attempt suggested not to use successive space-scales to reduce the original system, whether in dynamics or steady-state. An alternative was then to address the two-flows model as a mixed slow-fast system. For such systems, the Centre Manifold reduction techniques appeared to be suitable, since it allows preserving the critical overall mass-balance of the system. The Centre Manifold theory has been introduced within the finite-dimension systems framework. It was then applied to our two-flows model as if it were of finite dimension (that is, to a discretized two-flows model obtained using finite-differences in space). The same technique has then been formally applied to the original continuous model; the structure of the discrete and continuous reduced models are reassuringly similar.

The reduced continuous model we obtained is a non-linear convection-diffusion partial differential equation for an internal variable (a lumped molar fraction over the liquid and gas phase), together with static outputs to derive actual gas and liquid molar fractions from this internal variable. Discussion on this model has shown how the axial diffusion effects arise from the radial interfacial exchange term in the two-flows model; it is thus also related to the distillation efficiency. Interestingly, the diffusion term in our reduced PDE model explicitly depends on the liquid and gas traffic inside the packing, that is, on the operating conditions of the column. We also proved that the PDE model stationary solution is, as the stationary solution to the two-flows model, independent from the liquid and gas hold-ups (up to the chosen reduction order), in spite of their appearance in the diffusion term.

We concluded the model reduction work by extending the PDE model structure to mixtures with any number of components.

In the PDE model, the diffusion term defines the shape of the molar-fractions profiles; yet, most of the profiles dynamics are still driven by convective effects. For binary mixtures, the profile can be, as in the wave-model, described as a sliding discontinuity. To obtain the same kind of model for non-binary mixtures, we inspired ourselves from the field of chromatography ([84] in particular). Neglecting the diffusion effects, we found that the separation of a $(N+1)$ components mixture involves N^2 Riemann invariants, which allows to address the separation dynamics as the convection of N multi-components bundles. Compositions in this bundles can be non-physical; we gave the equations to compute the bundles from the physical concen-

trations, and *vice-versa*. Provided a sufficient condition which will be checked in Chapter 5, the problem reduced to the convection of independent shock-waves. We closed the chapter by computing the (ordered) speeds of these shockwaves.

Chapter 3

Reduced dynamic model analysis

Au chapitre précédent, nous avons développé une équation-modèle non-linéaire aux dérivées partielles pour représenter une section de colonne de distillation à garnissage. Nous allons à présent examiner ce modèle du point de vue de l'automatique. Plus précisément, nous allons considérer ce modèle EDP dans un cas simplifié, mais réaliste, de configuration de colonne : un unique segment homogène, une injection et deux tirages, et un mélange binaire à séparer. Nous montrerons que, pour des données initiales de compositions dans $(0,1)$*, la solution du problème de Cauchy associé reste dans* $(0,1)$*, et donc que la composition moyenne estimée par notre modèle garde un sens physique. Nous prouverons ensuite que le système admet une unique solution stationnaire. Nous étudierons la dépendance de cette solution en le petit coefficient de diffusion* ϵ*. Nous construirons une fonction de Lyapunov pour démontrer la stabilité locale exponentielle de cette solution.*

Sur la base du modèle EDP, nous construirons une famille d'observateurs asymptotiques pour la colonne considérée, avec injection de sortie ajustable. Comme précédemment, une fonction de Lyapunov garantira la convergence asymptotique locale des observations vers le profil de composition dans la colonne, y compris lorsque l'hydraulique est instationnaire.

Ces résultats sont valables sous des hypothèses raisonnables concernant les flux internes, la composition d'alimentation et la relation d'équilibre thermodynamique retenue. La première partie de ce chapitre est une extension des résultats donnés dans [22] et obtenus en collaboration avec Karine Beauchard, avec notamment un traitement plus précis des sorties statiques aux limites du domaine. En lien avec les demandes de brevet FR-1254802, FR-1255974 et FR-1256782, les résultats présentés indiquent que notre modèle a naturellement de bonnes propriétés pour une utilisation comme capteur logiciel.

Dans la seconde partie du chapitre, nous étudierons la réduction du modèle EDP en un modèle de fonctions de transfert linéarisé tangent à entrées et sorties multiples. Un tel modèle est destiné à reproduire les petites dynamiques d'une colonne de distillation autour d'un point de fonctionnement quasi-stationnaire (la reconstruction de la dérive lente de cet état, de même que des grands transitoires soudains, étant plutôt le rôle des observateurs évoqués plus haut). En utilisant des sorties statiques simplifiées, nous considérons l'impact de perturbations des flux liquide et vapeur, et des compositions d'alimentation, sur les compositions de sortie. Nous obtenons nos fonctions de transfert dans deux cas différents : celui d'une convection orientée vers le haut, ou vers le bas. Nous procédons comme suit : le système dynamique linéarisé est réécrit dans le domaine de Laplace comme une équation différentielle ordinaire avec conditions aux deux bouts. Les sorties sont obtenues de manière exacte en manipulant des

représentations symboliques des racines de l'équation homogène associée. Ces racines sont, pour l'une une série entière en ϵ, pour l'autre une série de Laurent en ϵ. En conséquence, moyennant un développement asymptotique non-standard, les sorties s'expriment comme des séries entières en ϵ, à des termes exponentiellement précis près. En tronquant les expressions des racines, nous obtenons les fonctions de transfert recherchées, en $O(\epsilon)$ et $O(\epsilon^2)$. Ces transferts présentent, du point de vue de la conduite du procédé, l'intérêt d'être explicitement paramétrés (via des gains et des retards) par des informations d'exploitation (flux de liquide et de gaz, vitesse du liquide, rétentions, compositions mesurées...) et de design (les dimensions de la colonne). Ils ouvrent donc possiblement une voie vers une forme de programmation de gains dans le système de contrôle de l'unité, basée sur les mesures physiques existantes augmentées de l'estimation en ligne de certaines valeurs critiques.

In the previous chapter, we have developed a non-linear partial-differential equation model to represent a distillation column's packed section. We will now examine this model from the point of view of control systems theory. More precisely, we will consider the PDE model embedded in a simplified yet realistic column configuration: one homogeneous section, one inlet and two outlets, and in the case of binary mixture separation. We will show that provided initial data within $(0, 1)$, the solution of the associated Cauchy problem in time remains within $(0, 1)$, that is, the lumped molar fractions given by our model remain physical. We will then prove that the considered system admits a unique stationary solution. We will also investigate the dependence of this solution with respect to the diffusion coefficient ϵ. We will construct a Lyapunov function, to show that the stationary solution is locally exponentially stable.

Based on the PDE model, we will construct a family of asymptotic observers for the considered column, with tunable output injection. As previously, a Lyapunov function will grant the local asymptotic convergence of the observer towards the actual composition profile, even for time-varying internal flows.

These results hold under a set of reasonable assumptions on the internal reflux rate, the inlet composition and the chosen thermodynamic relation. The first part of this chapter is an extension to the results given in [22] and obtained in collaboration with Karine Beauchard, notably with more precise handling of the static outputs at the boundaries of the column. In connection with the patent applications FR-1254802, FR-1255974 and FR-1256782, the presented results show that the investigated model has in-built good properties for soft-sensor applications.

In the second part of this chapter, we investigate the reduction of the PDE model into a tangent linearized multiple inputs, multiple outputs transfer function model. Such a model is to reproduce the small dynamics of a distillation column around an almost steady-state (the slow, long-term drift of this state, as well as large and sudden dynamics, shall be on the contrary reconstructed using observers). Using simplified static outputs, we consider the impact of perturbations of the liquid and gas flows, and of the top and bottom input compositions, on the top and bottom outlet compositions. The transfer functions are obtained in two different cases: when the composition convection speed is orientated downwards, or upwards. We proceed as follows: the linearized dynamic problem is rewritten is the Laplace domain as an ordinary differential equation with two boundary conditions. The outputs are obtained in an exact way using a symbolic representation of the roots of the corresponding homogeneous differential equation. These roots express, one as a power series in ϵ, the other as a Laurent series in ϵ. As a consequence, after non-standard asymptotic expansion, these

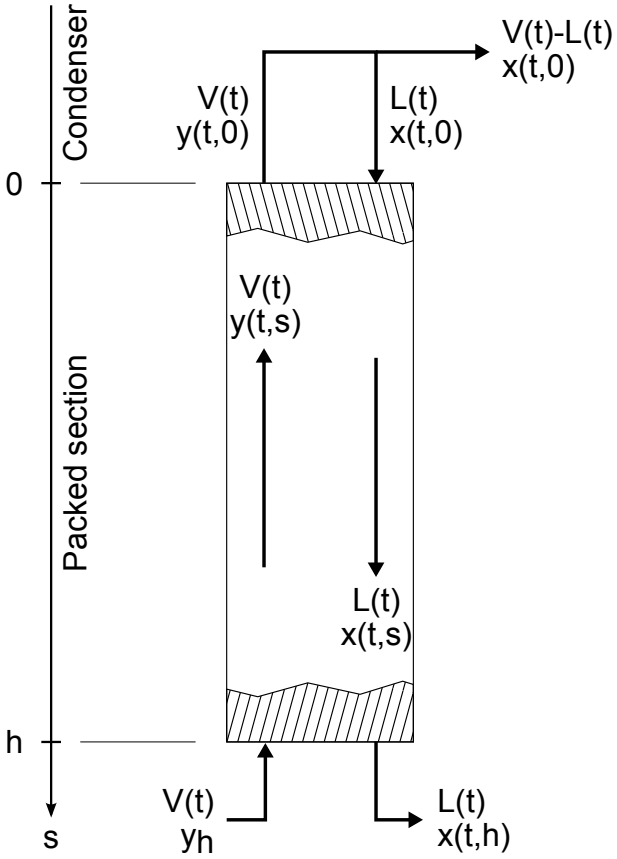

Figure 3.1: The simple column configuration used for this section.

outputs express as power series in ϵ, up to exponentially precise residuals. Truncating the expansion of the roots, we obtain the transfer functions in $O(\epsilon)$ and $O(\epsilon^2)$. The obtained transfers are interesting for process control in that their parameters (gains and delays) explicitly depend on process data (fluid flows, liquid speed, hold-ups, measured compositions) and design data (column's dimensions). Thus they possibly pave the way for gain scheduling in the plant's controller, based on the existing raw measurements plus actualized estimation of some unmeasured critical parameters.

3.1 Stability and observability of the PDE model

The mathematical results will be investigated and given using a simplified column geometry[1]. As depicted on Fig. 3.1 , we consider a single, continuous column with invariant section, fed with gaseous inlet (typically air) at the bottom. Total condensation occurs at top. A fraction of the resulting liquid is drawn off for production. Both the air feed and the top draw may serve as control for the inner reflux rate. In addition, we consider here binary distillation only (N_2/O_2 mixture for instance). Both the gas and the liquid are assumed to propagate with infinite speed, resulting in constant L and V along the vertical s-axis.

[1]Note that such a geometry does not reduce to a toy-model. It is close to the functioning of small (about 10m high) nitrogen production unit type called APSA (Advanced Product Supply Approach).

The generic reduced dynamic model

$$\left(\sigma_L + \sigma_V k'(X)\right) \frac{\partial X}{\partial t} = \frac{\partial}{\partial s}\left(-LX + Vk(X) + \epsilon G(X)\frac{\partial X}{\partial s}\right) \tag{3.1}$$

derived from (2.53) is completed with top and bottom boundary conditions. The top boundary conditions connect the input and output flows, respectively $L(t)x(0,t)$ and $V(t)y(0,t)$ at top under the condition of the total condensation $x(0,t) = y(0,t)$. Neglecting condenser's dynamics and intrinsic hold-up, it reads:

$$LX(t,0) = Lk(X(t,0)) + \epsilon G(X(t,0))\frac{\partial X}{\partial s}(t,0) + (L-V)\epsilon\sigma_L H(X(t,0))\frac{\partial X}{\partial s}(t,0), \tag{3.2}$$

for $t \in (0,+\infty)$. Regarding the bottom boundary condition, we impose the input flow:

$$Vy_h = Vk(X(t,h)) + \epsilon G(X(t,h))\frac{\partial X}{\partial s}(t,h) - \epsilon L\sigma_V H(X(t,0))\frac{\partial X}{\partial s}(t,h), \tag{3.3}$$

where y_h would typically be the oxygen content in air, $t \in (0,\infty)$, and $h > 0$ is the column's packed height. For the sake of simplicity, we will note in the following $f(X) = \sigma_L + \sigma_V k(X)$. The system under study is then

$$\left\{\begin{array}{rcl} f(X)\frac{\partial X}{\partial t} & = & \frac{\partial}{\partial s}\left(-LX + Vk(X) + \epsilon G(X)\frac{\partial X}{\partial s}\right) \\ LX(t,0) & = & Lk(X(t,0)) + \epsilon G(X(t,0))\frac{\partial X}{\partial s}(t,0) \\ & & +(L-V)\epsilon\sigma_L H(X(t,0))\frac{\partial X}{\partial s}(t,0), \\ Vy_h & = & Vk(X(t,h)) + \epsilon G(X(t,h))\frac{\partial X}{\partial s}(t,h) \\ & & -\epsilon L\sigma_V H(X(t,0))\frac{\partial X}{\partial s}(t,h). \end{array}\right. \tag{3.4}$$

We will also make use of the formulation:

$$\left\{\begin{array}{rcl} f(X)\frac{\partial X}{\partial t} & = & \frac{\partial}{\partial s}\left(-LX + Vk(X) + \epsilon G(X)\frac{\partial X}{\partial s}\right) \\ LX(t,0) & = & Lk(X(t,0)) + \epsilon(\sigma_L+\sigma_V)LH(X(t,0))\frac{\partial X}{\partial s}(t,0), \\ Vy_h & = & Vk(X(t,h)) + \epsilon\sigma_L V H(X(t,h))\frac{\partial X}{\partial s}(t,h), \end{array}\right. \tag{3.5}$$

obtained using $G(X) = (\sigma_V L + \sigma_L V)\, H(X)$.

The following set of assumptions is required for the results:

1. $0 < y_h < 1$, $\epsilon > 0$
2. the thermodynamic equilibrium relation $k : [0,1] \leftarrow [0,1]$ is a C^1, strictly increasing function on $[0,1]$, such that

   $$k(0) = 0,\ 0 < k'(0) < 1,\ k(1) = 1,\ 1 < k'(1).$$

   In addition, the function k is extended to the whole line by the following definition:

   $$k(x) := \left\{\begin{array}{ll} k'(0)x & \text{if } x < 0 \\ 1 + k'(1)(x-1) & \text{if } x > 1. \end{array}\right. \tag{3.6}$$

3. the input composition satisfies $y_h > k(y_h)$. It is sufficient working with the heavy component compositions to fulfill this condition.
4. the (possibly time-varying) inner flows L, $V \in \mathbb{R}_+^*$, and satisfy

   $$k'(0)V < L,\ 0 < L < V,\ Vy_h < L \tag{3.7}$$

Note that our usual $k(x) = \frac{\alpha x}{1+(\alpha-1)x}$ matches assumption 1, but other thermodynamic relations may also convene. Notably, assumption 1 does not *a priori* prevent the results from being applied to azeotropic mixtures distillation.

3.1.1 Maximum principle for strong solutions

The existence and uniqueness of strong solutions to the Cauchy problem associated to (3.1), (3.2), (3.3) is a classical result (see [68]): if the initial condition is C^2 versus s, then for $t > 0$, the solution remains C^2 versus s.

With the previously enumerated hypotheses 1 to 4, such solutions also remain inside $(0, 1)$:

Proposition 1. Let k, L, V be as in the previous section. Let $X_0 \in C^2([0, h], \mathbb{R})$ be such that $0 \leq X_0(s) < 1, \forall s \in [0, h]$ and X be the solution of the system (3.4) associated to the initial data $X(0, s) = X_0(s), \quad s \in (0, h)$. Then, $\forall (t, s) \in [0, +\infty) \times [0, h], 0 \leq X(t, s) < 1$.

Proof. The result is obtained by contradiction, applying the maximum principle to the function $Y_\lambda(t, s) := X(t, s)e^{-\lambda t}$, $\lambda > 0$, and limit arguments for $\lambda \to 0$:
First step: Let us prove that, for every $T > 0$,

$$\min_{\overline{Q_T}}(X) \geq 0 \tag{3.8}$$

where $Q_T := (0, T) \times (0, h)$. Let $T > 0$ and $\lambda > 0$. The function $Y_\lambda(t, z) := X(t, z)e^{-\lambda t}$ solves

$$\begin{aligned} f(X)\left(\partial_t Y_\lambda + \lambda Y_\lambda\right) = &[-L + Vk'(X) + \epsilon G'(X)\partial_z X]\partial_z Y_\lambda \\ &+ \epsilon G(X)\partial_z^2 Y_\lambda, \end{aligned} \tag{3.9}$$

on $(0, +\infty) \times (0, h)$. Working by contradiction, we assume that $\min_{\overline{Q_T}}(Y_\lambda) < 0$. Let $(t^*, z^*) \in \overline{Q_T}$ be such that $Y_\lambda(t^*, z^*) = \min_{\overline{Q_T}}(Y_\lambda) < 0$. Since $Y(0, z) = X_0(z) \geq 0$, necessarily $(t^*, z^*) \in (0, T] \times [0, h]$. Let us assume that $z^* \in (0, h)$. Then, we have $\partial_t Y_\lambda(t^*, z^*) \leq 0$, $\partial_z Y_\lambda(t^*, z^*) = 0$ and $\partial_z^2 Y_\lambda(t^*, z^*) \geq 0$. Thus, as $f(X) > 0$ because of (3.6) and the assumption $k'(0) \in (0, 1)$, the equality (3.9) gives

$$\begin{aligned} 0 &> f(X(t^*, z^*))\left(\partial_t Y_\lambda(t^*, z^*) + \lambda Y_\lambda(t^*, z^*)\right) \\ &= \epsilon G(X(t^*, z^*))\partial_z^2 Y_\lambda(t^*, z^*) > 0, \end{aligned}$$

which is a contradiction. Therefore, $z^* = 0$ or h.

Let us assume that $z^* = 0$. From the top boundary condition on X in (3.5), (3.6), and the assumption $k'(0) \in (0, 1)$, we get

$$\epsilon\left(\sigma_L + \sigma_V\right) LH\left(X(t^*, 0)\right)\partial_z Y_\lambda(t^*, 0) = [1 - k'(0)]LY_\lambda(t^*, 0) < 0$$

thus $\partial_z Y_\lambda(t^*, 0) < 0$ which is impossible. Therefore, $z^* = h$.

From the bottom boundary condition on X, (3.6), and the assumption $k'(0) \in (0, 1)$, we get

$$\epsilon\sigma_L V H(X(t^*, h))\partial_z Y_\lambda(t^*, h) = V\left(y_h e^{-\lambda t^*} - k'(0)Y_\lambda(t^*, h)\right) > 0,$$

thus $\partial_z Y_\lambda(t^*, h) > 0$ which is impossible.

We have proved that, for every $\lambda > 0$, $\min_{\overline{Q_T}}(Y_\lambda) \geq 0$. Passing to the limit $\lambda \to 0$, we get (3.8).

Second step: Let us prove that, for every $T > 0$,

$$\max_{\overline{Q_T}}(X) < 1. \tag{3.10}$$

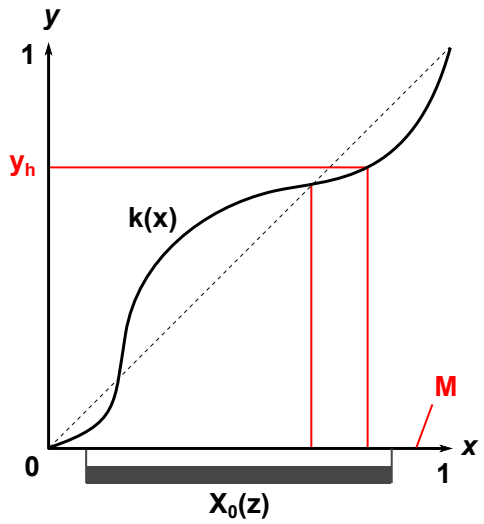

Figure 3.2: Definition of M.

Let $T > 0$ and $\lambda > 0$. Working as in the first step, one may prove that $\max_{\overline{Q_T}}(Y_\lambda)$ is achieved on $\{(0,z); z \in [0,h]\} \cup \{(t,0); t \in [0,T]\} \cup \{(t,h); t \in [0,T]\}$. Thus, passing to the limit $\lambda \to 0$, the same property holds for X. Working by contradiction, we assume that $\max_{\overline{Q_T}}(X) \geq 1$. Let $M \in (0,1)$ be such that $k(x) < x$ on $[M,1)$, $y_h < k(M)$ and $X_0(z) < M, \forall z \in [0,h]$ (see Fig. 3.2). By continuity, we have $X(t,0) < M$ and $X(t,h) < M$ for t small enough. Let $T_1 := \sup\{t \in (0,T); X(\tau,0) < M, X(\tau,h) < M, \forall \tau \in (0,t)\}$. Then $T_1 \in (0,T)$, and $X(T_1,0) = M$ or $X(T_1,h) = M$ (see Fig. 3.3). We know that $\max_{\overline{Q_{T_1}}}(X)$ is achieved on $\{(0,z); z \in [0,h]\} \cup \{(t,0); t \in [0,T_1]\} \cup \{(t,h); t \in [0,T]\}$. Thus $\max_{\overline{Q_{T_1}}}(X) = X(T_1,0)$ or $\max_{\overline{Q_{T_1}}}(X) = X(T_1,h)$.

Let us assume that $\max_{\overline{Q_{T_1}}}(X) = X(T_1,0) = M$. The top boundary condition on X gives

$$\epsilon\,(\sigma_L + \sigma_V)\,LH(X(T_1,0))\partial_z X(T_1,0) = V(M - k(M)) > 0$$

thus $\partial_z X(T_1,0) > 0$, which is impossible. Thus $\max_{\overline{Q_{T_1}}}(X) = X(T_1,h) = M$.

However, the bottom boundary condition on X yields

$$\epsilon\sigma_L V H(X(T_1,h))\partial_z X(T_1,h) = V(y_h - k(M)) < 0$$

thus $\partial_z X(T_1,h) < 0$ which is impossible. We have proved (3.10). □

3.1.2 Stationary solution

Proposition 2. For every $\epsilon > 0$, with the hypotheses 1 to 4 enumerated at the beginning and L, V constant, there exists a unique stationary solution $\overline{X}_\epsilon \in C^\infty([0,h],\mathbb{R})$ to the system (3.4). Moreover, $[0,h] \ni s \mapsto \overline{X}_\epsilon(s)$ is strictly increasing and $0 < \overline{X}_\epsilon(0) < \overline{X}_\epsilon(h) < 1$.

Proof. Let us rewrite system (3.4) in steady-state:

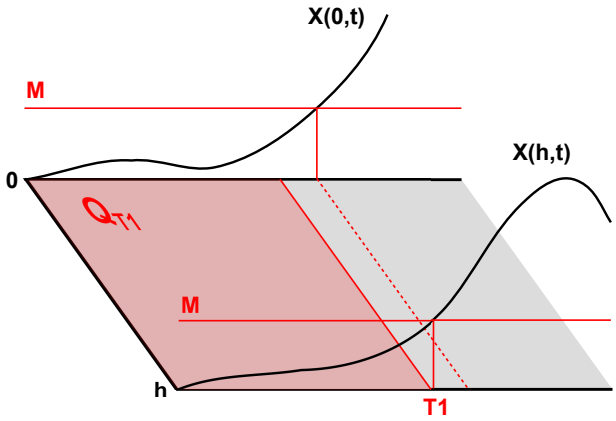

Figure 3.3: Definition of T_1.

$$\begin{cases} C_\epsilon &= -L\overline{X}_\epsilon + Vk(\overline{X}_\epsilon) + \epsilon G(\overline{X}_\epsilon)\frac{d\overline{X}_\epsilon}{ds}, \\ Vy_h &= Vk(\overline{X}_\epsilon(h)) + \epsilon G(\overline{X}_\epsilon(h))\frac{d\overline{X}_\epsilon}{ds}(h) \\ & \quad -\epsilon L\sigma_V H(\overline{X}_\epsilon(h))\frac{d\overline{X}_\epsilon}{ds}(h), \\ L\overline{X}_\epsilon(0) &= Lk(\overline{X}_\epsilon(0)) + \epsilon G(\overline{X}_\epsilon(0))\frac{d\overline{X}_\epsilon}{ds}(0) \\ & \quad +(L-V)\epsilon\sigma_L H(\overline{X}_\epsilon(0))\frac{d\overline{X}_\epsilon}{ds}(0). \end{cases} \tag{3.11}$$

We will prove that for every $\epsilon > 0$, there exists a unique $C_\epsilon \in \mathbb{R}$ such that the system (3.11) has a solution $\overline{X}_\epsilon \in C^\infty([0,h],\mathbb{R})$. Additionally, for every $\epsilon > 0$, we will have

- $0 < C_\epsilon < \frac{V-L}{\sigma_L+\sigma_V}\left(\sigma_L y_h + \sigma_V k(y_h)\right)$,
- $0 < \overline{X}_\epsilon(s) < \overline{X}_\epsilon(h) = \frac{\sigma_L V+\sigma_V L}{L\sigma_L} y_h - \frac{\sigma_V}{\sigma_L}k(\overline{X}_\epsilon(h)) - \frac{C_\epsilon}{L}$,
- $\frac{d\overline{X}_\epsilon}{ds}(s) > 0, \forall s \in [0,h]$.

Notice also that if C_ϵ satisfies (3.11), then

$$\begin{aligned} y_h &= \frac{\sigma_L}{\sigma_L V + \sigma_V L}\left(C_\epsilon + L\overline{X}_\epsilon(h)\right) + \frac{\sigma_V}{\sigma_L V + \sigma_V L}Lk(\overline{X}_\epsilon(h)), \\ \overline{X}_\epsilon(0) &= \frac{C_\epsilon\left(\sigma_L+\sigma_V\right)}{\left(V-L\right)\sigma_L} - k(\overline{X}_\epsilon(0))\frac{\sigma_V}{\sigma_L}. \end{aligned}$$

Indeed, according to the boundary condition at $s = h$ in (3.11):

$$\begin{aligned} Vy_h &= C_\epsilon + L\overline{X}_\epsilon(h) - \epsilon L\sigma_V H(\overline{X}_\epsilon(h))\frac{d\overline{X}_\epsilon}{ds}(h) \\ &= C_\epsilon + L\overline{X}_\epsilon(h) - \frac{L\sigma_V H(\overline{X}_\epsilon(h)}{G(\overline{X}_\epsilon(h))}\left(C_\epsilon + L\overline{X}_\epsilon(h) - Vk(\overline{X}_\epsilon(h))\right), \end{aligned}$$

and $1 - \frac{L\sigma_V H(X)}{G(X)} = \frac{\sigma_L V H(X)}{G(X)}\ \forall X$. The reasoning is the same at $s = 0$.

This being stated, the proof is now in four steps, based on a shooting method.

First step: *Let us define an auxiliary function ϕ.* For every $C \in \mathbb{R}$, there exists a unique solution $X_C \in C^1(\mathbb{R}, \mathbb{R})$ of the Cauchy problem

$$\left\{ \begin{array}{rcl} C & = & -LX_C + Vk(X_C) + \epsilon G(X_C)\frac{dX_C}{ds}, \\ X_C(0) & = & \frac{C(\sigma_L+\sigma_V)}{(V-L)\sigma_L} - k(X_C(0))\frac{\sigma_V}{\sigma_L}. \end{array} \right.$$

Indeed, the ordinary equation may be written $\frac{dX_C}{ds} = F(X_C) + \frac{C}{\epsilon G(X_C)}$, where $F(X) := \frac{LX - Vk(X)}{\epsilon G(X_C)}$. Thus the right hand side is a Lipschitz function of X_C with an affine growth when $|X_C| \to +\infty$. We define the shooting function $\mathbb{R} \ni C \mapsto \phi(C) = \frac{\sigma_L}{\sigma_L V + \sigma_V L}\left(C + L\overline{X}_C(h)\right) + \frac{\sigma_V}{\sigma_L V + \sigma_V L} Lk(\overline{X}_C(h)) \in \mathbb{R}$, which is C^1 and satisfies $\phi(0) = 0$ because $X_0 = 0$ (uniqueness in Cauchy-Lipschitz theorem).

Second step: *Let us prove that ϕ is increasing.* For every $C \in \mathbb{R}$,

$$\phi'(C) = \frac{\sigma_L}{\sigma_L V + \sigma_V L}\left(1 + LY_C(h)\right) + \frac{\sigma_V}{\sigma_L V + \sigma_V L} Lk'(X_C(h))Y_C(h)$$

where $Y_C = \frac{\partial X_C}{\partial C}$ is solution of

$$\left\{ \begin{array}{rcl} \frac{dY_C}{ds} & = & \alpha_C(s)Y_C + \frac{1}{\epsilon G(X_C)}, \\ Y_C(0) & = & \frac{\sigma_L+\sigma_V}{\sigma_L+\sigma_V k'(X_C(0))} > 0, \end{array} \right.$$

and

$$\alpha_C := F'(X_C) - \frac{CG'(X_C)}{\epsilon G(X_C)^2}.$$

Thus

$$Y_C(h) = \left[Y_C(0) + \int_0^h \frac{e^{-\int_0^s \alpha_C(\theta)d\theta}}{\epsilon G(X_C)} ds \right] e^{\int_0^h \alpha_C(\theta)d\theta} > 0, \tag{3.12}$$

and then $\phi'(C) > 0$.

Third step: *Let us prove that $\phi(C_*) > y_h$* for

$$C_* := \frac{V - L}{\sigma_L + \sigma_V}\left(\sigma_L y_h + \sigma_V k(y_h)\right) > 0. \tag{3.13}$$

This particular value is chosen for it implies $X_{C_*}(0) = y_h$. We have

$$\epsilon G(X_{C_*})\frac{dX_{C_*}}{ds} = C_* + LX_{C_*} - Vk(X_{C_*})$$

thus at $s = 0$:

$$\begin{aligned} \epsilon\frac{\sigma_L + \sigma_V}{V - L} G(y_h)\frac{dX_{C_*}}{ds} &= \sigma_L y_h + \sigma_V k(y_h) + L\frac{\sigma_L + \sigma_V}{V - L} y_h - \frac{\sigma_L + \sigma_V}{V - L} k(y_h) \\ &= \frac{\sigma_L V + \sigma_V L}{V - L}\left(y_h - k(y_h)\right) > 0 \end{aligned}$$

thus X_{C_*} is increasing in a neighborhood of 0^+. Let us assume the existence of $s^* \in [0, h]$ such that $\frac{dX_{C_*}}{ds}(s^*) = 0$. Then

$$[L - Vk'(X_{C_*})]\frac{dX_{C_*}}{ds} = \epsilon G'(X_{C_*})\left(\frac{dX_{C_*}}{ds}\right)^2 + \epsilon G(X_{C_*})\frac{d^2X_{C_*}}{ds^2}$$

with $\frac{dX_{C_*}}{ds}(s^*) = 0$. Thus (uniqueness in Cauchy-Lipschitz theorem) $\frac{dX_{C_*}}{ds} \equiv 0$, which contradicts the increasing behavior of X_{C_*} in a neighborhood of 0^+. Therefore, $\frac{dX_{C_*}}{ds}(s^*) > 0, \forall s \in [0,h]$ and $\phi C_* = X_{C_*}(h) > X_{C_*}(0) = y_h$.

Fourth step: *Let us prove the existence and uniqueness of* $\overline{X}_\epsilon$. The function $\phi : [0, C_*] \to \mathbb{R}$ is continuous, increasing and satisfies $\phi(0) = 0$ and $\phi[C_*] > y_h$, thus (intermediate values theorem) there exists a unique $C_\epsilon \in \mathbb{R}$ such that $\phi(C_\epsilon) = y_h$. Moreover, $C_\epsilon \in (0, C_*)$. Then $\overline{X}_\epsilon := X_{C_\epsilon}$ gives the answer.

In a second part, let us prove that $\overline{X}_\epsilon$ is increasing on $[0,h]$. Let us assume the existence of $s^* \in [0,h]$ such that $\frac{d\overline{X}_\epsilon}{ds}(s^*) = 0$. Working as in the previous third step, one deduces that $\overline{X}_\epsilon$ is constant. But this is impossible because $\overline{X}_\epsilon(0) = \overline{X}_\epsilon(1) \Rightarrow C_\epsilon = C_*$. We have proved $\frac{d\overline{X}_\epsilon}{ds}(s) \neq 0, \forall s \in [0,h]$. Necessarily, $\frac{d\overline{X}_\epsilon}{ds}(s) > 0, \forall s \in [0,h]$ and $\forall s \in (0,h)$:

$$0 < \frac{C_\epsilon(\sigma_L + \sigma_V)}{(V-L)\sigma_L} + k(\overline{X}_\epsilon(0))\frac{\sigma_V}{\sigma_L} = \overline{X}_\epsilon(0) < \overline{X}_\epsilon(s),$$
$$\overline{X}_\epsilon(s) < \overline{X}_\epsilon(h) = \frac{\sigma_L V + \sigma_V L}{L\sigma_L} y_h - \frac{\sigma_V}{\sigma_L} k(\overline{X}_\epsilon(h)) - \frac{C_\epsilon}{L}.$$

and $0 < C_\epsilon < C_*$. □

The shooting function defined in the previous proof is also a useful tool to study the dependence of the stationary solution $\overline{X}_\epsilon$ in the parameter ϵ. We have the:

Proposition 3. With the same assumptions than for Proposition 2, the map $\epsilon \mapsto \overline{X}_\epsilon(0)$ is strictly increasing, and the map $\epsilon \mapsto \overline{X}_\epsilon \in L^2(0,h)$ is continuous.

Proof. First, let us prove that the map $\epsilon \mapsto \overline{X}_\epsilon(0)$ is increasing, or, equivalently that the map $\epsilon \mapsto C_\epsilon$ is increasing. Let $0 < \epsilon_1 < \epsilon_2$ and let us prove that $C_{\epsilon_1} < C_{\epsilon_2}$. Let ϕ_1 be the shooting function defined in the first step, associated to $\epsilon = \epsilon_1$. Since ϕ_1 is increasing, it is sufficient to prove that $\phi_1(C_{\epsilon_1}) = y_h < \phi_1(C_{\epsilon_2})$ i.e. that the solution $X(z)$ of

$$\left\{ \begin{array}{rcl} C_{\epsilon_2} & = & -LX + Vk(X) + \epsilon_1 G(X)\frac{dX}{dz}, \\ X(0) & = & \frac{C(\sigma_L+\sigma_V)}{(V-L)\sigma_L} - k(X_C(0))\frac{\sigma_V}{\sigma_L}, \end{array} \right.$$

satisfies $\frac{LX(h)+C_{\epsilon_2}}{V} > y_h$. Let:

$$\gamma(X) := \frac{C_{\epsilon_2} + LX - Vk(X)}{\epsilon_2 G(X)},$$

and $\overline{X}_{\epsilon_2}$ be the solution of the Cauchy problem:

$$\left\{ \begin{array}{rcl} C_{\epsilon_2} & = & -L\overline{X}_{\epsilon_2} + Vk(\overline{X}_{\epsilon_2}) + \epsilon_2 G(\overline{X}_{\epsilon_2})\frac{d\overline{X}_{\epsilon_2}}{dz}, \\ \overline{X}_{\epsilon_2}(0) & = & \frac{C(\sigma_L+\sigma_V)}{(V-L)\sigma_L} - k(\overline{X}_{\epsilon_2}(0))\frac{\sigma_V}{\sigma_L}, \end{array} \right.$$

We have:

$$X' = \frac{\epsilon_2}{\epsilon_1}\gamma(X), \quad \overline{X}'_{\epsilon_2} = \gamma(\overline{X}_{\epsilon_2}), \quad X(0) = \overline{X}_{\epsilon_2}(0).$$

Since $\overline{X}'_{\epsilon_2}(0) > 0$ and $\epsilon_2 > \epsilon_1$, we have $X'(0) > \overline{X}'_{\epsilon_2}(0)$, thus the set $\{z \in [0,h]; X > \overline{X}_{\epsilon_2} \text{ on } (0,z)\}$ is non empty. Let

$$z^* := \sup\{z \in [0,h]; X > \overline{X}_{\epsilon_2} \text{ on } (0,z)\}$$

and let us assume that $z^* < h$. Then $X(z^*) = \overline{X}_{\epsilon_2}(z^*)$. Thus

$$\begin{aligned} X'(z^*) &= \frac{\epsilon_2}{\epsilon_1} g(X(z^*)) \\ &> \gamma(X(z^*)) = \gamma(\overline{X}_{\epsilon_2}(z^*)) = \overline{X}'_{\epsilon_2}(z^*) \end{aligned}$$

because $\overline{X}'_{\epsilon_2}(z^*) > 0$. This is impossible. Therefore $z^* = h$, and $X(h) > \overline{X}_{\epsilon_2}(h)$. As $\frac{L\overline{X}_{\epsilon_2}(h)+C_{\epsilon_2}}{V} = y_h$, one has $\frac{LX(h)+C_{\epsilon_2}}{V} > y_h$.

Now, let us prove that the map $\epsilon \mapsto \overline{X}_\epsilon \in L^2(0,h)$ is continuous. We rename ϕ_ϵ our shooting function to emphasize its dependence on ϵ. Let $\epsilon^* > 0$. In order to prove that $\epsilon \mapsto \overline{X}_\epsilon \in L^2(0,h)$ is continuous at ϵ^*, it is sufficient to prove that $\epsilon \mapsto C_\epsilon$ is continuous at ϵ^* (continuity of the solution of an ODE with respect to a parameter). Let $(\epsilon_n)_{n\in\mathbb{N}}$ be a sequence of $(\epsilon^*/2, 3\epsilon^*/2)$ such that $\epsilon_n \to \epsilon^*$. We know that $C_{\epsilon_n} \in (0, C_*)$ for every $n \in \mathbb{N}$ (C_* has been defined in (3.13)). Let φ be an extraction and $\mathcal{C} \in [0, C_*]$ be such that $C_{\epsilon_{\varphi(n)}} \to \mathcal{C}$ and let us prove that $\mathcal{C} = C_{\epsilon^*}$, or equivalently, that $\phi_{\epsilon^*}(\mathcal{C}) = y_h$. As

$$\phi'_\epsilon(C) = \frac{\sigma_L}{\sigma_L V + \sigma_V L}\left(1 + LY_C(h)\right) + \frac{\sigma_V}{\sigma_L V + \sigma_V L} Lk'(X_C(h))Y_C(h),$$

the explicit formula (3.12) implies the existence of $M > 0$ such that

$$|\phi'_\epsilon(C)| \le M, \forall C \in [0, C_*], \forall \epsilon \in [\epsilon^*/2, 3\epsilon^*/2]$$

(continuous function of (ϵ, C) on a compact subset). Let $\eta > 0$. There exists $n \in \mathbb{N}$ such that $|C_{\epsilon_{\varphi(n)}} - \mathcal{C}| < \eta/(2M)$ and $|\phi_{\epsilon_{\varphi(n)}}(\mathcal{C}) - \phi_{\epsilon^*}(\mathcal{C})| < \eta/2$ (continuity of the solution of an ODE with respect to a parameter). Then for such n,

$$\begin{aligned} |y_h - \phi_{\epsilon^*}(\mathcal{C})| &\le |\phi_{\varphi(\epsilon_n)}(C_{\varphi(\epsilon_n)}) - \phi_{\epsilon_{\varphi(n)}}(\mathcal{C})| + |\phi_{\epsilon_{\varphi(n)}}(\mathcal{C}) - \phi_{\epsilon^*}(\mathcal{C})| \\ &< \eta + O(\eta^2). \end{aligned}$$

This inequality holds for any $\eta > 0$, thus $\phi_{\epsilon^*}(\mathcal{C}) = y_h$. □

3.1.3 Local asymptotic stability

In this section we prove that the unique stationary solution $\overline{X}$ of (3.4) is locally exponentially stable by showing a strict Lyapunov function for the tangent linearized system with at least exponential decay rate.

Let us define $X := \overline{X} + \delta X$. Linearizing (3.5) around the stationary solution $\overline{X}$ one obtains for $t \in (0, +\infty)$

$$\left\{\begin{array}{rcl} f(\overline{X})\partial_t \delta X &=& \partial_s\left[\left(-L + g(\overline{X})\right)\delta X + \epsilon G(\overline{X})\partial_s \delta X\right], \\ \delta X_{(t,0)} &=& Lk'(\overline{X}(0))\overline{X}'\delta X_{(t,0)} + \epsilon\frac{\sigma_L+\sigma_V}{\sigma_L V+\sigma_V L} LG'(\overline{X}(0))\overline{X}'\delta X_{(t,0)} \\ && +\epsilon\frac{\sigma_L+\sigma_V}{\sigma_L V+\sigma_V L} LG(\overline{X}(0))\partial_s \delta X_{(t,0)}, \\ 0 &=& g(\overline{X}(h))\delta X_{(t,h)} - \epsilon\overline{X}'G'(\overline{X}(h))\frac{\sigma_V L}{\sigma_L V+\sigma_V L}\delta X_{(t,h)} \\ && +\epsilon\frac{\sigma_L V G(\overline{X}(h))}{\sigma_L V+\sigma_V L}\partial_s \delta X_{(t,h)}, \end{array}\right. \tag{3.14}$$

where

$$g(\overline{X}) := Vk'(\overline{X}) + \epsilon G'(\overline{X})\overline{X}', \tag{3.15}$$

and with the notations $\overline{X}' = \frac{d\overline{X}}{ds}$, $G' = \frac{dG}{dX}$. Introducing the new variable $\xi = \frac{\delta X}{\overline{X}'}$, (3.14) rewrites:

$$\left\{\begin{array}{rcl} f(\overline{X})\overline{X}'\partial_t\xi & = & \partial_s\left[\epsilon G(\overline{X})\overline{X}'\partial_s\xi\right], \\ \epsilon G(\overline{X}(0))\overline{X}'(0)\partial_s\xi_{(t,0)} & = & \frac{\sigma_L+\sigma_V k'(X)}{\sigma_L+\sigma_V}(V-L)\overline{X}'(0)\xi_{(t,0)}, \\ \epsilon G(\overline{X}(h))\overline{X}'(h)\partial_s\xi_{(t,h)} & = & -L\left(1+\frac{\sigma_L}{\sigma_V}k'(\overline{X})\right)\overline{X}'(h)\xi_{(t,h)}. \end{array}\right. \tag{3.16}$$

We now have the:

Proposition 4. The function

$$\mathcal{V}(\xi) := \int_0^h f(\overline{X}(s))\overline{X}'(s)\xi(s)^2 ds \tag{3.17}$$

is a strict Lyapunov function for (3.16): exists $\lambda_\epsilon > 0$ such that

$$d\mathcal{V}/dt \leq -\lambda_\epsilon \mathcal{V}.$$

Proof. Let

$$f^* := \max_{s\in[0,h]} f(\overline{X}(s))\overline{X}'(s) > 0, \tag{3.18}$$

$$\mu := \min_{s\in[0,h]} G(\overline{X}(s))\overline{X}'(s) > 0. \tag{3.19}$$

We have

$$\frac{1}{2}\frac{d\mathcal{V}}{dt} = \int_0^h \xi(t,s)\partial_s\left[\epsilon G(\overline{X})\overline{X}'\partial_s\xi(t,s)\right] ds.$$

Integrating by part yields

$$\begin{aligned} \frac{1}{2}\frac{d\mathcal{V}}{dt} = & -L\left(1+\frac{\sigma_L}{\sigma_V}k'(\overline{X})\right)\overline{X}'(h)\xi(t,h)^2 \\ & -\frac{\sigma_L+\sigma_V k'(X)}{\sigma_L+\sigma_V}(V-L)\overline{X}'(0)\xi(t,0)^2 \\ & -\epsilon\int_0^h G(\overline{X})\overline{X}'(\partial_s\xi(t,s))^2 ds. \end{aligned} \tag{3.20}$$

Thanks to the formula $\xi(t,s) = \xi(t,h) + \int_h^s \partial_s\xi(t,\theta)d\theta$, one finds a constant $P > 0$ such that

$$\int_0^h \xi(t,s)^2 ds \leq P\left(\xi(t,h)^2 + \int_0^h \left(\partial_s\xi(t,s)\right)^2 ds\right). \tag{3.21}$$

This inequality is proved by contradiction, similarly to the classical Poincaré inequality. Injecting (3.21) in (3.20) and taking

$$m := \min\left(\epsilon\mu\,;\, L\left(1+\frac{\sigma_L}{\sigma_V}k'(\overline{X}(h))\right)\overline{X}'(h)\right) > 0,$$

one obtains:

$$\frac{1}{2}\frac{d\mathcal{V}}{dt} \leq -m\left(\xi(t,h)^2 + \int_0^h \left(\partial_s\xi(t,s)\right)^2 ds\right) \leq -\frac{m}{Pf^*}\mathcal{V}.$$

□

3.1.4 Asymptotic observers for unsteady composition profiles

The molar fraction $y_{\mathrm{M}}(t)$ is supposed to be measured at the top of the column:

$$y_{\mathrm{M}}(t) := k(X(t,0)) + \epsilon\sigma_L \frac{G(X(t,0))}{\sigma_L V(t) + \sigma_V L(t)} \partial_s X(t,0). \tag{3.22}$$

Let $L(t) = \overline{L} + \delta L(t)$, $V(t) = \overline{V} + \delta V(t)$, such that L and V still satisfy (3.7). Let $\overline{X}$ the stationary solution of (3.4) for $L = \overline{L}$, $V = \overline{V}$.

We consider the following 1-parameter family of observers:

$$\left\{\begin{array}{rcl} f(\widehat{X})\partial_t \widehat{X} & = & \partial_s \left[-L\widehat{X} + Vk(\widehat{X}) + \epsilon G(\widehat{X})\partial_s \widehat{X} \right], \\ L\widehat{X}_{(t,0)} & = & -(V-L)\widehat{x}_{(t,0)} + Vk(\widehat{X}_{(t,0)}) + \epsilon G(\widehat{X}_{(t,0)})\partial_s \widehat{X}_{(t,0)}, \\ \widehat{x}_{(t,0)} & = & (1-a)y_{\mathrm{M}}(t) + a\left(k(\widehat{X}_{(t,0)}) + \epsilon\sigma_L H(\widehat{X}_{(t,0)})\partial_s \widehat{X}_{(t,0)} \right), \\ Vy_h & = & Vk(\widehat{X}(t,h)) + \epsilon\sigma_L V H(\widehat{X}(t,h)) \frac{\partial \widehat{X}}{\partial s}(t,h), \end{array}\right. \tag{3.23}$$

where $a \in \mathbb{R}$ *a priori* tunes the output injection.

Let $X = \overline{X} + \delta X$, and $\widehat{X} = \overline{X} + \delta\widehat{X}$. We will note $\delta\widetilde{X}$ the observation error $\delta\widehat{X} - \delta X$.

The partial differential equation is the same in (3.4) and (3.23), thus the linearized dynamics of the observer in the vicinity of $\overline{X}$, $\overline{L}$, $\overline{V}$ is:

$$\begin{aligned} f(\overline{X})\partial_t \delta\widetilde{X} = \partial_s \left[\left(-\overline{L} + g(\overline{X})\right) \delta\widetilde{X} + \epsilon\overline{G}\partial_s \delta\widetilde{X} \right] \\ + \partial_s \left[-\delta L(t)\overline{X} + \epsilon\delta L(t)\overline{X}' \frac{\partial G}{\partial L}_{(\overline{X},\overline{L},\overline{V})} \right] \\ + \partial_s \left[\delta V(t) k'(\overline{X}) + \epsilon\delta V(t)\overline{X}' \frac{\partial G}{\partial V}_{(\overline{X},\overline{L},\overline{V})} \right], \end{aligned} \tag{3.24}$$

where $\overline{G} = G(\overline{X})$ estimated with $L = \overline{L}$, $V = \overline{V}$. Replacing $\delta\widetilde{X}$ by δX in the previous equation yields the linearized dynamics of the system. The linearized dynamics of the observation error is:

$$f(\overline{X})\partial_t \delta\widetilde{X} = \partial_s \left[\left(-\overline{L} + g(\overline{X})\right) \delta\widetilde{X} + \epsilon\overline{G}\partial_s \delta\widetilde{X} \right]. \tag{3.25}$$

The boundary condition of the observer at $s = 0$ rewrites:

$$\begin{aligned} L\widehat{X}_{(t,0)} =& Vk(\widehat{(X)}_{(t,0)}) + a(L-V)k(\widehat{X}_{(t,0)}) + (1-a)(L-V)k(X_{(t,0)}) \\ &+ a\epsilon(L-V)\sigma_L H(\widehat{X}_{(t,0)}, L(t), V(t))\partial_s \widehat{X}_{(t,0)} \\ &+ (1-a)\epsilon(L-V)\sigma_L H(X_{(t,0)}, L(t), V(t))\partial_s X_{(t,0)} \\ &+ \epsilon G(\widehat{X}_{(t,0)}, L(t), V(t))\partial_s \widehat{X}_{(t,0)}. \end{aligned}$$

Comparing with the boundary condition of the observed system under the formulation (3.5), one sees that the terms in $\delta L(t)$, $\delta V(t)$ obtained by linearisation around $\overline{X}$, $\overline{L}$, $\overline{V}$ will be the same. Thus the boundary condition for the observation error at $s = 0$ is:

$$\begin{aligned} \overline{L}\delta\widetilde{X}_{(t,0)} = k'(\overline{X}(0))Q(a)\delta\widetilde{X}_{(t,0)} \\ + \epsilon\frac{\overline{G}}{\sigma_V\overline{L} + \sigma_L\overline{V}} \left(\sigma_V\overline{L} + \sigma_L Q(a)\right) \partial_s \delta\widetilde{X}_{(t,0)} \\ + \epsilon\overline{X}'(0)\frac{\overline{G}'(0)}{\sigma_V\overline{L} + \sigma_L\overline{V}} \left(\sigma_V\overline{L} + \sigma_L Q(a)\right) \delta\widetilde{X}_{(t,0)}, \end{aligned} \tag{3.26}$$

where

$$\overline{G}' := \frac{\partial G(X,L,V}{\partial X}\left(\overline{X},\overline{L},\overline{V}\right),$$
$$Q(a) := (1-a)\overline{V} + a\overline{L}.$$

Similarly, the terms in $\delta L(t)$, $\delta V(t)$ compensate in the linearization of the boundary condition at $s=h$ for the observation error, and one obtains:

$$0 = k'(\overline{X}(h))\delta\widetilde{X}_{(t,\,h)} + \epsilon\frac{\sigma_L\overline{VG}(h)}{\sigma_L\overline{V}+\sigma_V\overline{L}}\partial_s\delta\widetilde{X}_{(t,\,h)} + \epsilon\frac{\sigma_L\overline{VG}(h)}{\sigma_L\overline{V}+\sigma_V\overline{L}}\partial_s\overline{X}(h)\delta\widetilde{X}_{(t,\,h)}. \tag{3.27}$$

Replacing as in the local stability proof $\delta\widetilde{X}$ by $\overline{X}'\xi$ in (3.25), (3.26) and (3.27), we obtain:

$$\left\{\begin{array}{rcl} f(\overline{X})\overline{X}'\partial_t\xi &=& \partial_s\left[\epsilon\overline{GX}'\partial_s\xi\right], \\ \epsilon\overline{G}(0)\overline{X}'(0)\partial_s\xi_{(t,\,0)} &=& \frac{a\overline{L}}{\sigma_V L+\sigma_L Q(a)}\left(\sigma_L + k'(\overline{X}(0))\left(\overline{V}-\overline{L}\right)\overline{X}'(0)\xi_{(t,\,0)}, \\ \epsilon\overline{G}(h)\overline{X}'(h)\partial_s\xi_{(t,\,h)} &=& -L\left(1+\frac{\sigma_V}{\sigma_L}k'(\overline{X}(h))\right)\overline{X}'(h)\xi_{(t,\,h)}. \end{array}\right. \tag{3.28}$$

One can check that for $a=1$ (no use of the measure $y_{\rm M}(t)$, then the observer is a free copy of the original system), the system (3.28) coincides with (3.16).

We can now demonstrate the following result:

Proposition 5. $\forall a \in \left[0, \frac{\sigma_L\overline{V}+\sigma_V\overline{L}}{\sigma_L(\overline{V}-\overline{L})}\right]$, the function $\mathcal{V}$ defined in (3.17) is a strict Lyapunov function of the observation error, with exponential decay rate.

Proof. Integrating $\frac{d\mathcal{V}}{dt}$ by parts yields

$$\begin{aligned}\frac{1}{2}\frac{d\mathcal{V}}{dt} = -L\left(1+\frac{\sigma_V}{\sigma_L}k'(\overline{X}(h))\right)\overline{X}'(h)\xi(t,h)^2 \\ - \frac{a\overline{L}}{\sigma_V L+\sigma_L Q(a)}\left(\sigma_L + k'(\overline{X}(0))\left(\overline{V}-\overline{L}\right)\overline{X}'(0)\xi(t,0)^2 \\ - \epsilon\int_0^h G(\overline{X})\overline{X}'\left(\partial_s\xi(t,s)\right)^2 ds.\end{aligned}$$

For any $a \in \left[0, \frac{\sigma_L\overline{V}+\sigma_V\overline{L}}{\sigma_L(\overline{V}-\overline{L})}\right]$, $\frac{a\overline{L}}{\sigma_V L+\sigma_L Q(a)} \geq 0$. Thus as previously

$$\frac{1}{2}\frac{d\mathcal{V}}{dt} \leq -m\left(\xi(t,h)^2 + \int_0^h\left(\partial_s\xi(t,s)\right)^2\right),$$

where

$$m := min\left(\epsilon\mu\,;\, L\left(1+\frac{\sigma_V}{\sigma_L}k'(\overline{X}(h))\right)\overline{X}'(h)\right) > 0.$$

As in Proposition 4, one finds a constant $P>0$ such that

$$\frac{1}{2}\frac{d\mathcal{V}}{dt} \leq -\frac{m}{Pf^*}\mathcal{V}.$$

□

Time interval	0 to 1h	1 to 2h	2 to 3h	3 to 4h	4 to 5h
Reflux L/V	0.6	0.5	0.6	0.65	0.6

Table 3.1: Reflux step-changes during the simulation.

Consequently, $\forall a \in \left[0, \frac{\sigma_L \overline{V} + \sigma_V \overline{L}}{\sigma_L (\overline{V} - \overline{L})}\right]$, the estimation given by observer (3.23) exponentially converges towards the actual time-varying profile $X(t,s)$, provided that $X(t,s)$ is close enough to the stationary profile $\overline{X}(s)$ associated to $(\overline{L}, \overline{V})$.

Tuning the parameter a allows making $\frac{d\mathcal{V}}{dt}$ more negative, thus fastening the convergence of the observer. It should also allow tuning the observer's robustness to measurement noise, by weighting the internal model effects in the top boundary condition of (3.23).

3.1.5 Simulations

The purpose of the following simulations is to help qualifying the local nature of the previous convergence properties. The simulations will also illustrate some aspects of the concentration profiles dynamics. The results have been obtained with the following parameters: $h = 8m$, $\sigma_L = \sigma_V = 100Nm^3/m$, $\lambda_L = 20Nm^3.s^{-1}.m^{-1}$, $\lambda_V = 10\lambda_L$, $\epsilon = 0.14$, $y_h = 0.21$. We use the thermodynamic equilibrium relation (2.2) with $N = 1$ and $\alpha = 0.42$; thus the simulated binary mixture behaves as air in an APSA or HP column. The inlet air flow is kept constant at $30Nm^3/s$. The column's dynamics are simulated using a finite-difference scheme, with 0.1s time-steps and 0.1m space-steps. The corresponding numerical scheme is similar to the one detailed in the next chapter.

Open-loop convergence of the non-linear model

Figure 3.4 illustrates the uniqueness and stability properties of the stationary solution. The reflux rate undergoes several step-changes, summarized in Table 3.1. Simulations show that the same stationary solution is reached when the original value of the reflux rate is restored, regardless of the previous excursions of the composition profile. Even if such a case is not in the range of the previously given properties, one can check experimentally that a non-instant liquid propagation does not change the uniqueness and stability results. For this test, the liquid speed is $0.02m/s$. One can observe the clear non-symmetrical response of the column to the reflux increases and decreases. The asymmetry is reinforced by the non-instant liquid propagation, which also induces inverse initial responses.

The molar fraction profiles corresponding to the different steady-states are depicted on Fig. 3.5: during the transients, the composition front has traveled all along the column. On the same figure we also plotted snapshots of the transients profiles (in the instant and non-instant liquid propagation cases). This illustrates both the delay and the profile billowing caused by the liquid propagation delay.

Observer convergence around a steady-state

The following simulations illustrate the convergence of observers with various tuning parameters a when the observed system reaches a steady-state (corresponding to a reflux $L/V = 0.6$). The observers were initialized with an O_2 molar fraction of 0.4 everywhere in the column, whereas the observed column's initial profile is linearly increasing from 10^{-9} to 0.4. Results

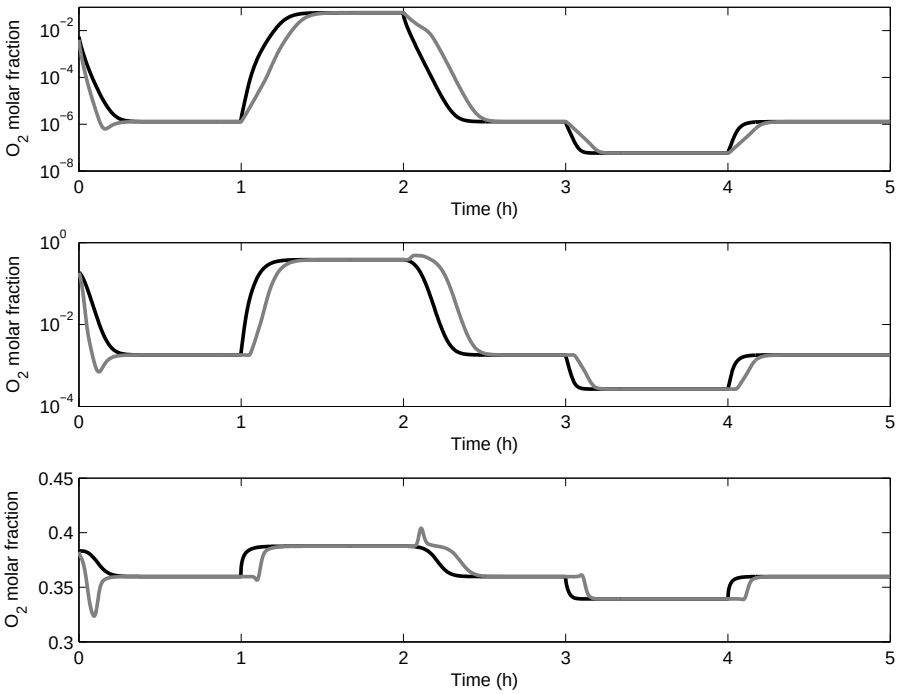

Figure 3.4: O_2 lumped molar fractions at various locations in the column (*Top:* at top, *Center:* at mid-length, *Bottom:* at the bottom). Solid black lines correspond to the instant liquid propagation case. Grey lines are for the non-instant propagation case, where the liquid speed is $0.02m/s$.

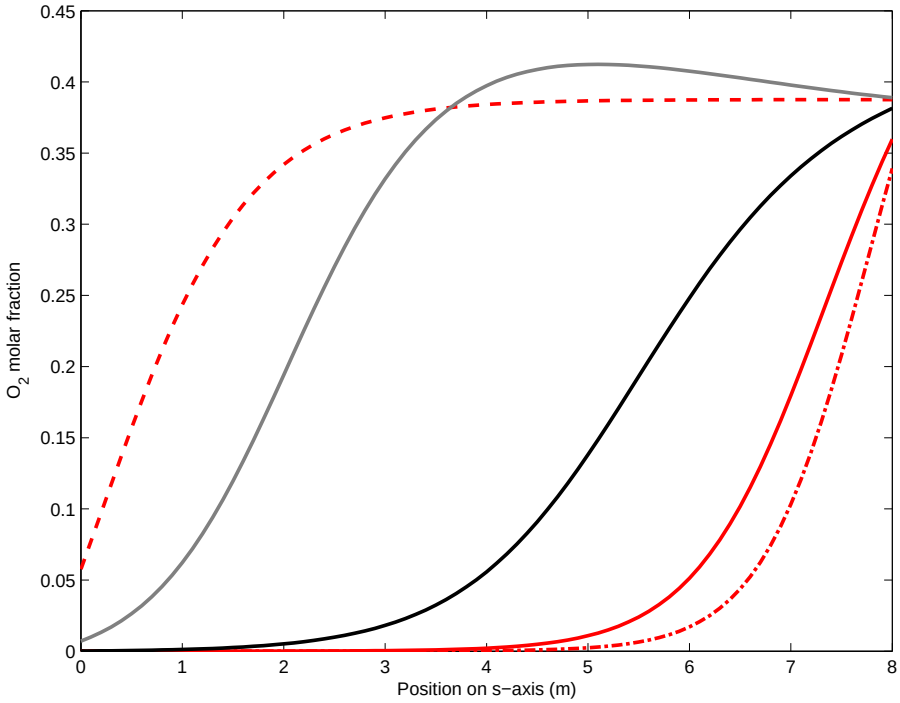

Figure 3.5: Snapshots of the O_2 lumped molar fraction profiles at various instants of the simulation. *Solid red:* stationary profile corresponding to $L/V = 0.6$. *Dashed red:* stationary profile corresponding to $L/V = 0.5$. *Dash-dotted red:* stationary profile corresponding to $L/V = 0.65$. *Solid black:* snapshot at $t = 130min$ for the instant liquid propagation case. *Solid grey:* snapshot at $t = 130min$ for the non-instant liquid propagation case.

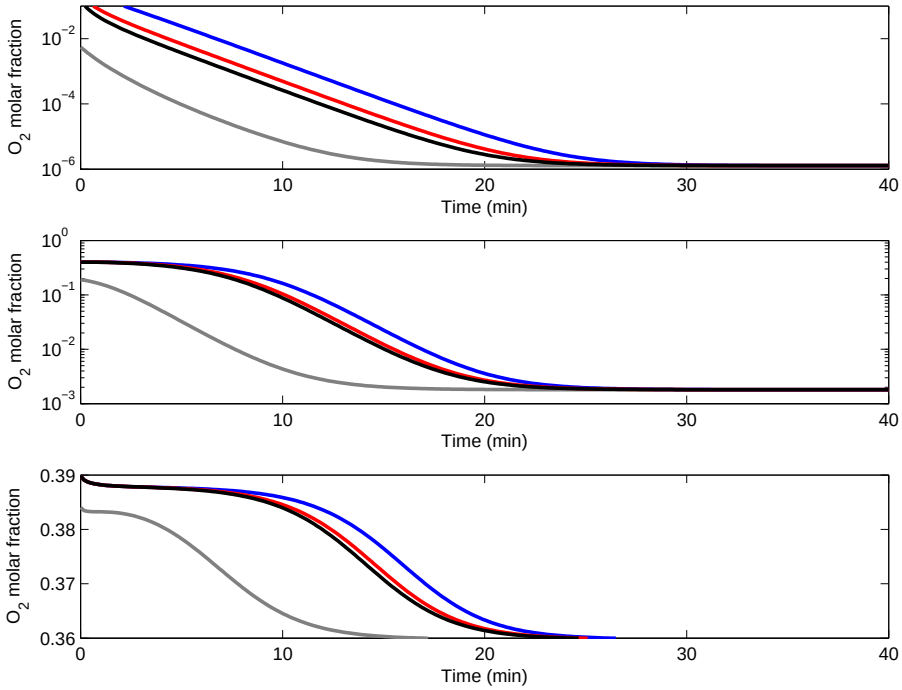

Figure 3.6: Simulated and estimated O_2 lumped molar fractions at various locations in the column (*Top:* at top, *Center:* at mid-length, *Bottom:* at the bottom). *Grey:* simulated column. *Blue:* observer with $a = 0$. *Red:* observer with $a = 0.5$. *Black:* observer with $a = 1$.

are depicted on Fig. 3.6. The convergence is slightly faster for large values of a (that is, when the top measure is rejected). This is coherent with the integration by part in the proof of Proposition 5, where $\frac{a\overline{L}}{\sigma_V L+\sigma_L Q(a)}$ increases with a. Figures 3.7 and 3.8 respectively depicts the evolution of the relative estimation error at the top of the column, and of the L_2 norm of the profile estimation error $||\frac{\tilde{X}-X}{\bar{X}}||_{L_2}$

Observer convergence with a time-periodic L/V

We now consider the case of an unsteady reflux rate L/V which sinusoidally oscillates between 0.43 and 0.725 with a time-period of 1 hour. The inlet air flow is still kept constant at $30Nm^3/s$. The observers and the simulated column are initialized as previously. The observed and estimated compositions are depicted on Fig. 3.9. The corresponding L_2 norms of the profile relative estimation errors are shown on Fig. 3.10. The convergence of the observers takes here less than one oscillation, and is still faster for large a.

One can check that the convergence is still granted when the columns's dynamics are much slower, due to increased hold-ups. On Figures 3.11 and 3.12, we depict the results of the same simulation with $\sigma_L = 1000Nm^3/m$. Several oscillations are required for the estimated molar fractions to match the simulated ones, and the global estimation error decreases much slower.

The same tests can be done with a finite liquid propagation speed (here $0.02m/s$). The results are depicted on Fig. 3.13 and 3.14 for $\sigma_L = 100Nm^3/m$, and Fig. 3.15, 3.16 for $\sigma_L = 1000Nm^3/m$. Even if these tests are out of the range of the demonstrated convergence property, it seems that a finite liquid speed does not impede the observer's performances.

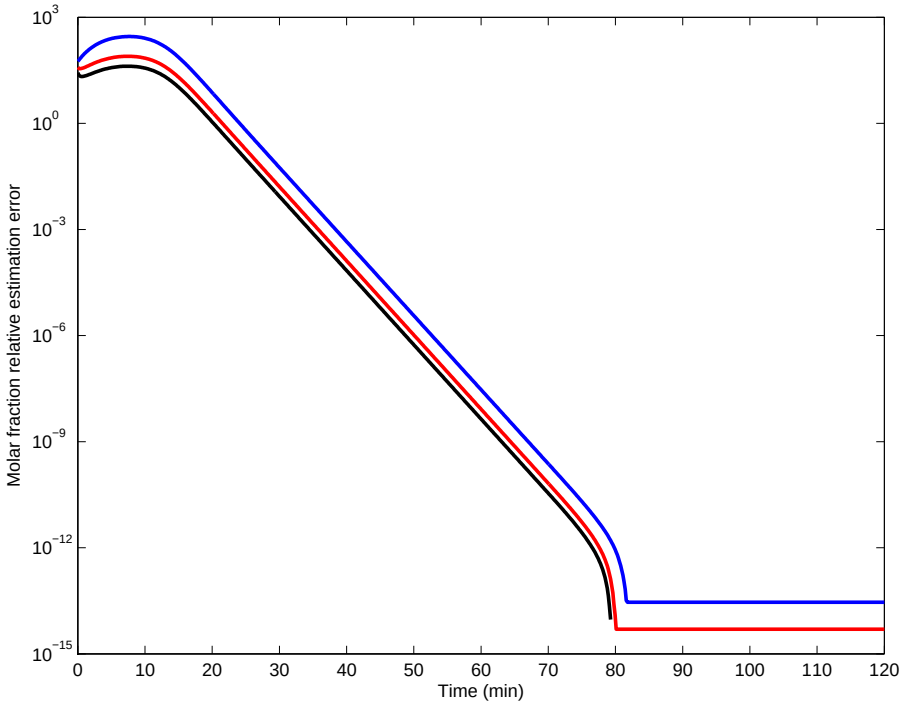

Figure 3.7: Relative estimation error at the top of the column. *Blue:* with $a = 0$. *Red:* with $a = 0.5$. *Black:* with $a = 1$.

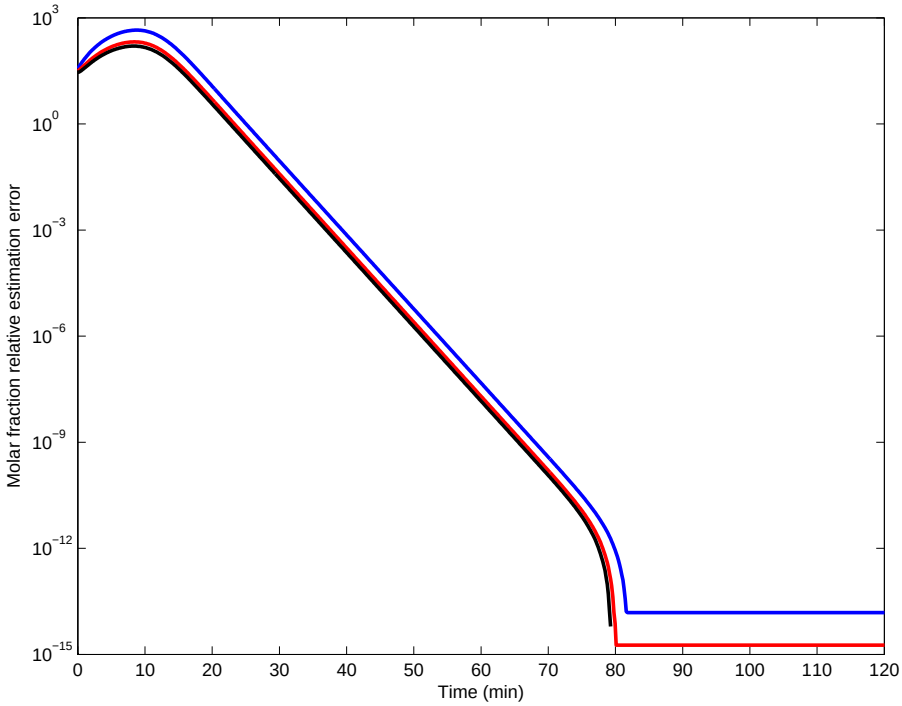

Figure 3.8: L_2-norm of the profile relative estimation error over the whole column. *Blue:* with $a = 0$. *Red:* with $a = 0.5$. *Black:* with $a = 1$.

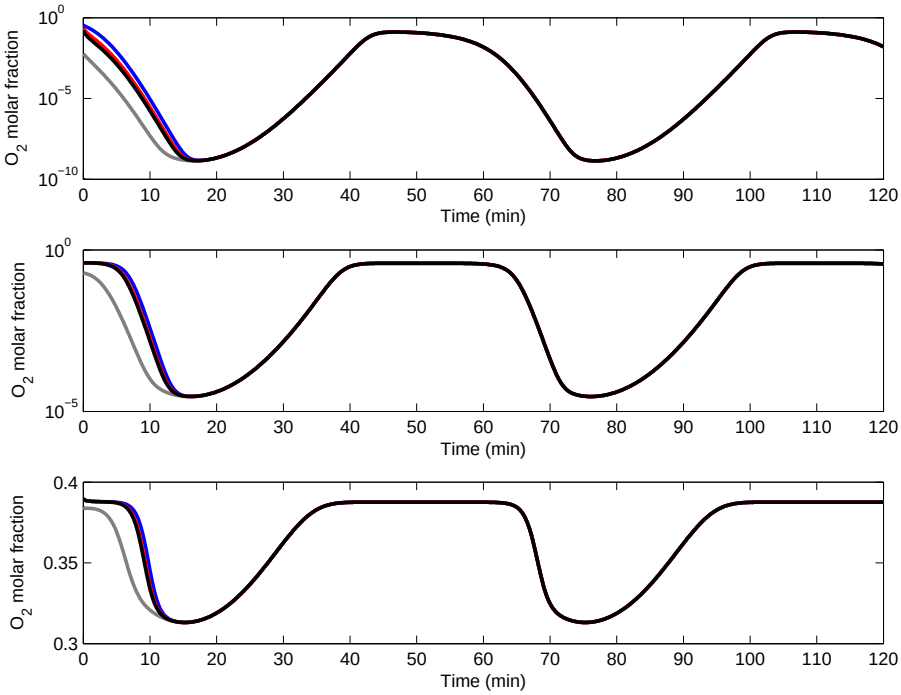

Figure 3.9: Simulated and estimated O_2 lumped molar fractions at various locations in the column (*Top:* at top, *Center:* at mid-length, *Bottom:* at the bottom) with $\sigma_L = 100Nm^3/m$. *Grey:* simulated column. *Blue:* observer with $a = 0$. *Red:* observer with $a = 0.5$. *Black:* observer with $a = 1$.

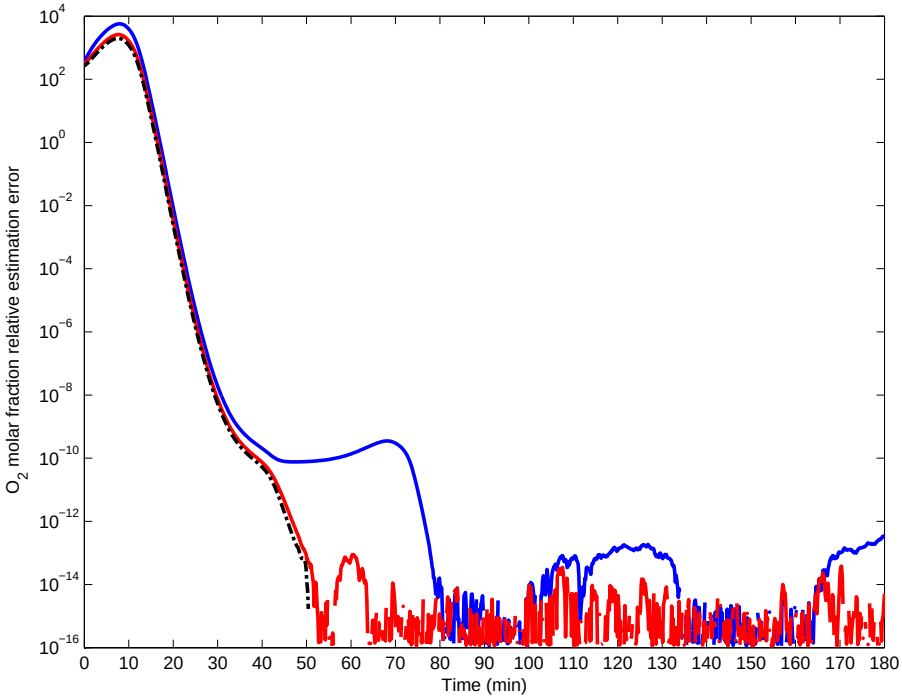

Figure 3.10: L_2-norm of the profile relative estimation error over the whole column $\sigma_L = 100 Nm^3/m$. *Blue:* with $a = 0$. *Red:* with $a = 0.5$. *Black:* with $a = 1$.

These simulations show that the demonstrated stability and convergence properties are experimentally obtained even in the case of large transients. It seems to be an indication that these local properties could be turned in practice into global ones.

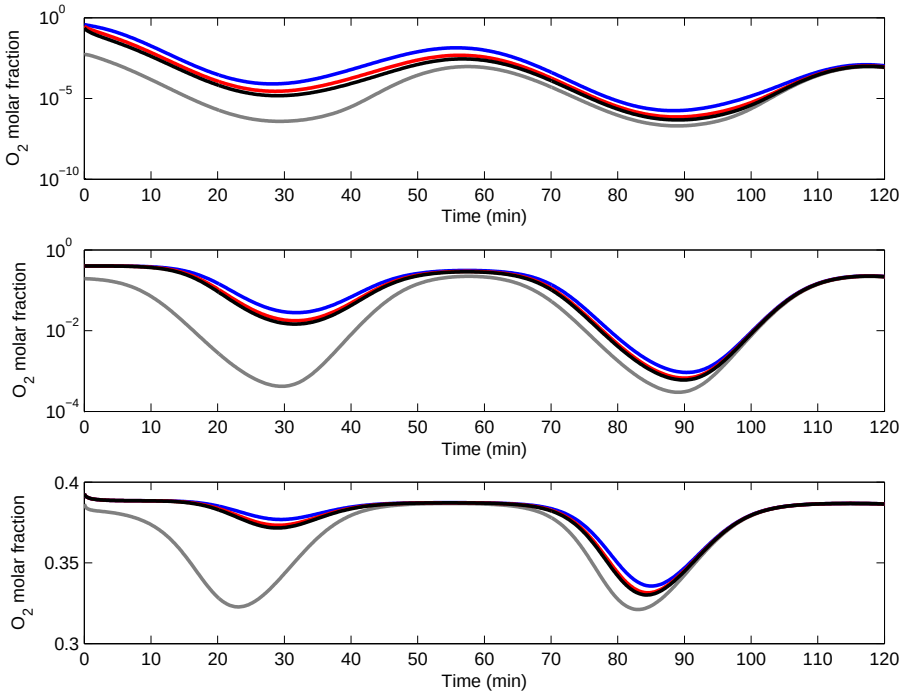

Figure 3.11: Simulated and estimated O_2 lumped molar fractions at various locations in the column (*Top:* at top, *Center:* at mid-length, *Bottom:* at the bottom) with $\sigma_L = 1000Nm^3/m$. *Grey:* simulated column. *Blue:* observer with $a = 0$. *Red:* observer with $a = 0.5$. *Black:* observer with $a = 1$.

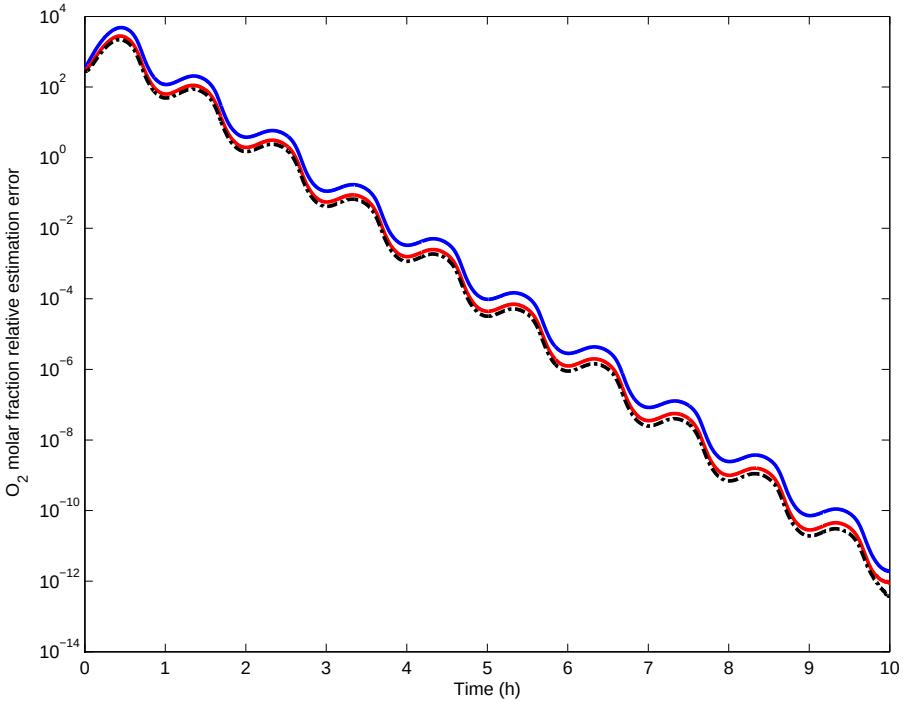

Figure 3.12: L_2-norm of the profile relative estimation error over the whole column with $\sigma_L = 1000 Nm^3/m$. *Blue:* with $a = 0$. *Red:* with $a = 0.5$. *Black:* with $a = 1$.

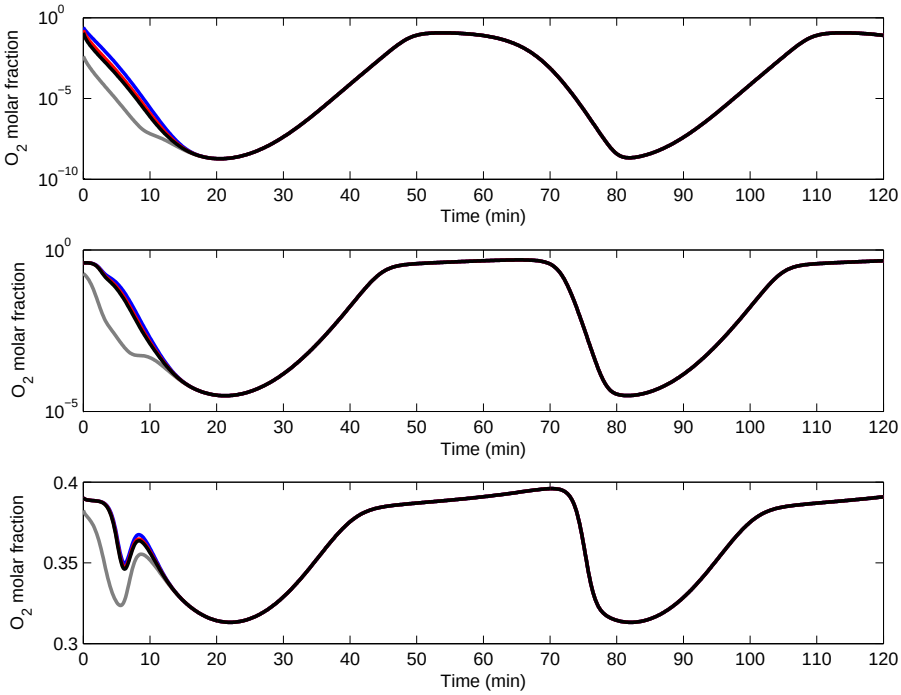

Figure 3.13: Simulated and estimated O_2 lumped molar fractions at various locations in the column (*Top:* at top, *Center:* at mid-length, *Bottom:* at the bottom) with non-instant liquid propagation and $\sigma_L = 100Nm^3/m$. *Grey:* simulated column. *Blue:* observer with $a = 0$. *Red:* observer with $a = 0.5$. *Black:* observer with $a = 1$.

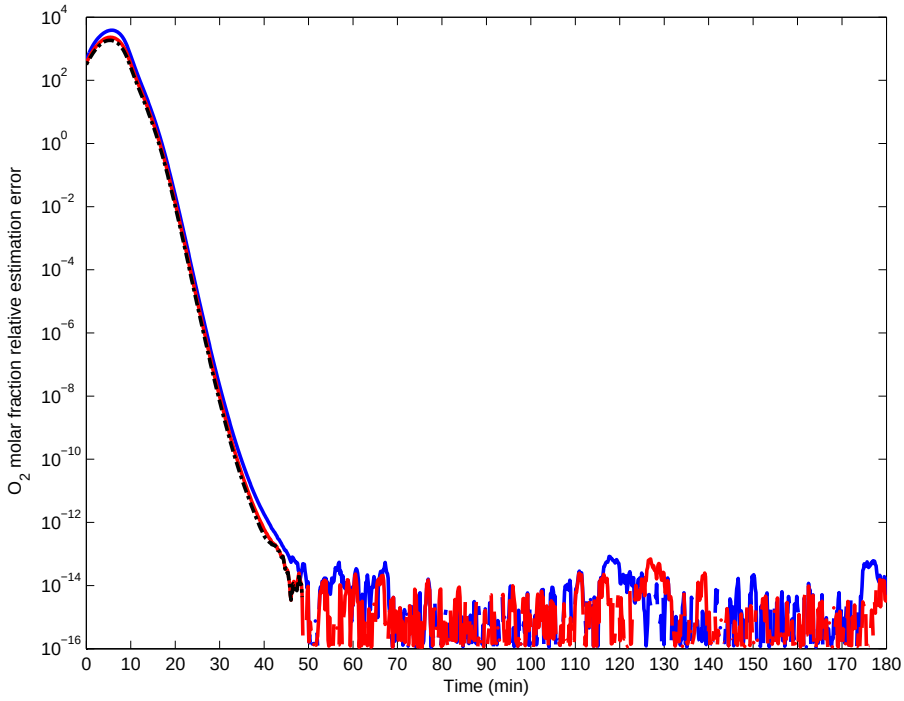

Figure 3.14: L_2-norm of the profile relative estimation error over the whole column with non-instant liquid propagation and $\sigma_L = 100Nm^3/m$. *Blue:* with $a = 0$. *Red:* with $a = 0.5$. *Black:* with $a = 1$.

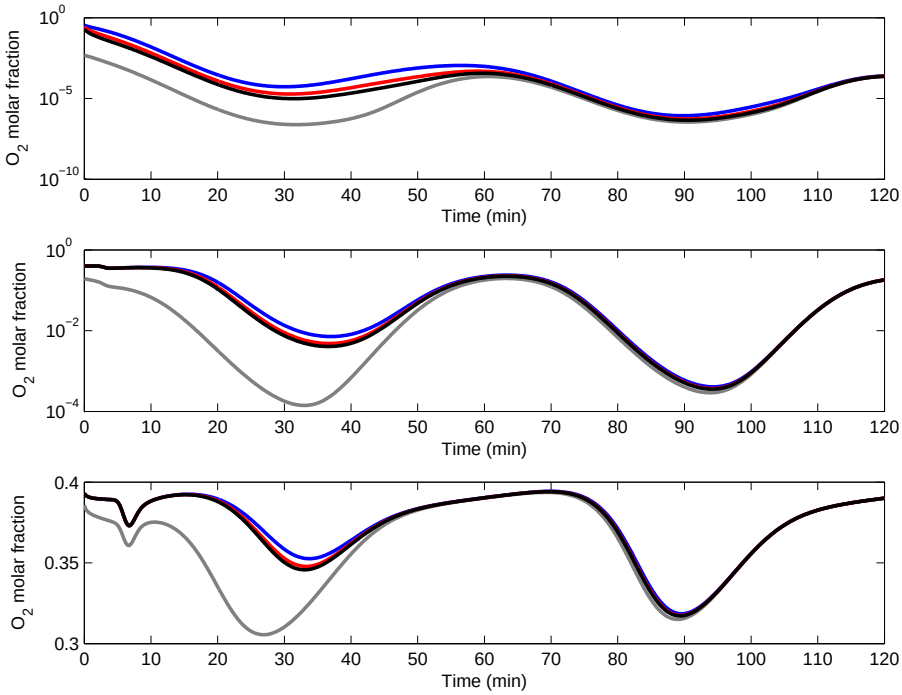

Figure 3.15: Simulated and estimated O_2 lumped molar fractions at various locations in the column (*Top:* at top, *Center:* at mid-length, *Bottom:* at the bottom) with non-instant liquid propagation and $\sigma_L = 1000Nm^3/m$. *Grey:* simulated column. *Blue:* observer with $a = 0$. *Red:* observer with $a = 0.5$. *Black:* observer with $a = 1$.

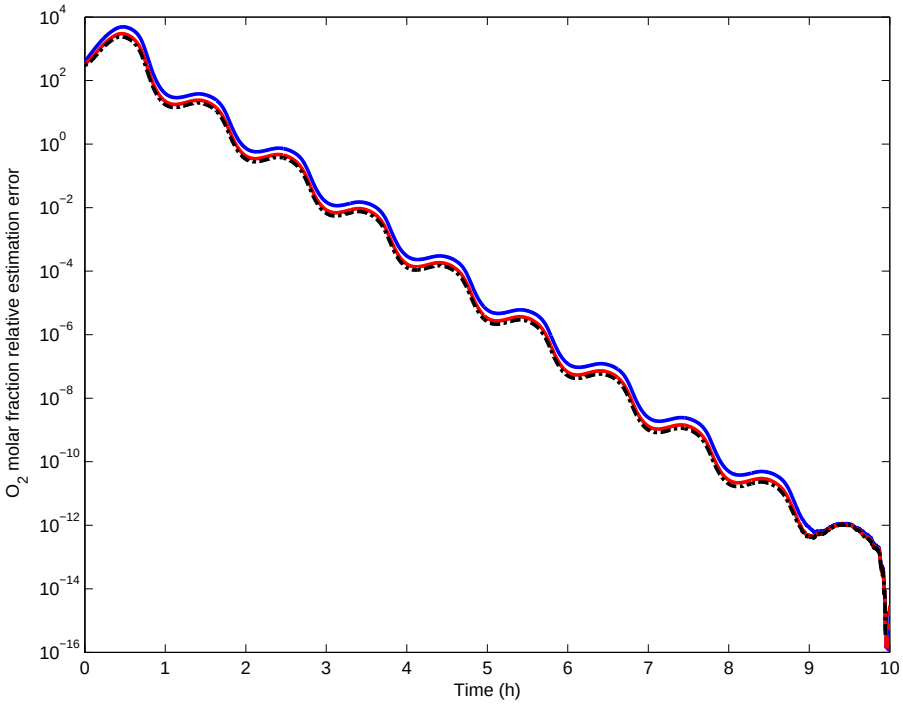

Figure 3.16: L_2-norm of the profile relative estimation error over the whole column with non-instant liquid propagation and $\sigma_L = 1000 N m^3/m$. *Blue:* with $a = 0$. *Red:* with $a = 0.5$. *Black:* with $a = 1$.

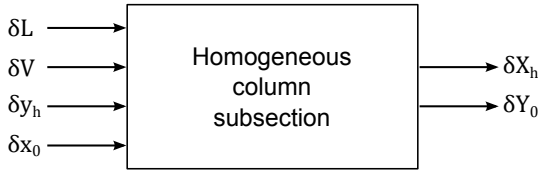

Figure 3.17: Investigated transfers for an homogeneous subsection.

3.2 Linear tangent control model

From the PDE binary distillation model we aim to derive a Multiple Inputs - Multiple Outputs (MIMO) transfer function model for small dynamics in the vicinity of a steady-state (see Fig. 3.17). We first consider an homogeneous column subsection, for which we will write the transfer functions. The complete column transfer will be obtained by chaining the subsections transfers by algebraic relations. On the considered subsection, we will use a linear approximation of the application $k(.)$: $k(X) = \alpha X$, $\alpha \in [0, 1]$, and we will take $G(X, L, V)$ constant, as well as the hold-ups. We also simplify the static outputs by considering that $x(s,t) = X(s,t)$ and $y(s,t) = Y(s,t) = \alpha X(s,t)$.

Thus we consider the following dynamic system:

$$\left\{\begin{array}{rcl} \frac{\partial X}{\partial \tau} & = & -v(s,\tau)\frac{\partial X}{\partial s} + \epsilon G \frac{\partial^2 X}{\partial s^2} \\ Lx_0(\tau) & = & (v_0(\tau) + \alpha V)X_0(\tau) - \epsilon G \frac{\partial X}{\partial s}(0,\tau) \\ -Vy_h(\tau) & = & (v_h(\tau) - L)X_h(\tau) - \epsilon G \frac{\partial X}{\partial s}(h,\tau) \end{array}\right. \tag{3.29}$$

In this system, $x_0(t)$, $y_h(t)$ are the feed compositions respectively at the top and the bottom of the considered subsection and

$$\begin{aligned} v(s,\tau) &= L(s,\tau) - \alpha V(t) = L_0(\tau - \tfrac{s}{\mu_L}) - \alpha V(t), \\ \tau &= \frac{t}{\sigma_L + \sigma_V}, \end{aligned}$$

where $\mu_L = \mathcal{V}_L\,(\sigma_L + \sigma_V)$ is the scaled liquid speed (we assume that the gas flow information propagates instantly along the column). In a first time, we consider the case $v(s,t) > 0$.

Let $\overline{X}$ the stationary solution of (3.29) corresponding to $\overline{L}$, $\overline{V}$, $\overline{x}_0$, $\overline{y}_h$. For small variations around $\overline{X}$, system (3.29) rewrites in the Laplace domain:

$$\left\{\begin{array}{rcl} p\delta X(s,p) & = & -\overline{v}\frac{\partial \delta X}{\partial s}(s,p) - \overline{X}'\delta v(s,p) + \epsilon G \frac{\partial^2 \delta X}{\partial s} \\ \overline{L}\delta x_0(p) & = & (\delta v_0(p) + \alpha \delta V(p))\overline{X}_0 + (\overline{v} + \alpha\overline{V})\delta X_0(p) - \overline{x}_0 \delta L_0(p) \\ & & -\epsilon G \frac{\partial \delta X}{\partial s}(0,p) \\ -\overline{V}\delta y_h(p) & = & (\delta v_h(p) - \delta L(h,p))\overline{X}_h + (\overline{v} - \overline{L})\delta X_h(p) + \overline{y}_h \delta V(p) \\ & & -\epsilon G \frac{\partial \delta X}{\partial s}(h,p), \end{array}\right. \tag{3.30}$$

where p stands for the Laplace variable, $\overline{X}' = \partial_s \overline{X}$ and

$$\begin{aligned} \delta L(s,p) &= \delta L_0(p) e^{-p\frac{s}{\mu_L}}, \\ \delta v(s,p) &= \delta L_0(p) e^{-p\frac{s}{\mu_L}} - \alpha \delta V(p). \end{aligned}$$

Following the constants' variation method, we make the following change of variables:

$$\delta X(s,p) = \lambda_1(s,p)e^{r_1(p)s} + \lambda_2(s,p)e^{r_2(p)s},$$
$$\partial_s \delta X(s,p) = \lambda_1(s,p)r_1(p)e^{r_1(p)s} + \lambda_2(s,p)r_2(p)e^{r_2(p)s},$$

where r_1, r_2 are the solutions of $\epsilon G r_{(1,2)}^2 - v r_{(1,2)} - p = 0$. This yields:

$$\partial_s \lambda_1 e^{r_1 s} + \partial_s \lambda_2 e^{r_2 s} = 0,$$
$$\epsilon G \left(\partial_s \lambda_1 r_1 e^{r_1 s} + \partial_s \lambda_2 r_2 e^{r_2 s}\right) = \overline{X}' \delta v.$$

Let

$$A = \frac{\overline{X}_h - \overline{X}_0}{e^{\frac{vh}{\epsilon G}} - 1}, \quad B = \overline{X}_0 - \frac{\overline{X}_h - \overline{X}_0}{e^{\frac{vh}{\epsilon G}} - 1}$$

such that $\overline{X} = Ae^{\frac{vs}{\epsilon G}} + B$. We have:

$$\partial_s \lambda_1 = \frac{A\overline{v}\delta v(s,\sigma)}{\epsilon G\left(r_1 - r_2\right)} e^{\left(\frac{v}{\epsilon G} - r_1\right)s} = \frac{A\overline{v}\left(\delta L_0 e^{\frac{-sp}{\mu_L}} - \alpha \delta V\right)}{\epsilon G\left(r_1 - r_2\right)} e^{\left(\frac{v}{\epsilon G} - r_1\right)s},$$
$$\partial_s \lambda_2 = \frac{-A\overline{v}\left(\delta L_0 e^{\frac{-sp}{\mu_L}} - \alpha \delta V\right)}{\epsilon G\left(r_1 - r_2\right)} e^{\left(\frac{v}{\epsilon G} - r_2\right)s}$$

thus:

$$\begin{aligned}
\lambda_1(s,p) &= C_1(p) \\
&\quad + \tfrac{A\overline{v}}{\epsilon^2 G^2 (r_1 - r_2)} \left(\tfrac{e^{\left(\frac{\overline{v}}{\epsilon G} - r_1 - \frac{sp}{\mu_L}\right)s} - 1}{\frac{\overline{v}}{\epsilon G} - r_1 - \frac{sp}{\mu_L}} \delta L_0 - \alpha \tfrac{e^{\left(\frac{\overline{v}}{\epsilon G} - r_1\right)s} - 1}{\frac{\overline{v}}{\epsilon G} - r_1} \delta V \right), \\
\lambda_1(s,p) &= C_2(p) \\
&\quad - \tfrac{A\overline{v}}{\epsilon^2 G^2 (r_1 - r_2)} \left(\tfrac{e^{\left(\frac{\overline{v}}{\epsilon G} - r_2 - \frac{sp}{\mu_L}\right)s} - 1}{\frac{\overline{v}}{\epsilon G} - r_2 - \frac{sp}{\mu_L}} \delta L_0 - \alpha \tfrac{e^{\left(\frac{\overline{v}}{\epsilon G} - r_2\right)s} - 1}{\frac{\overline{v}}{\epsilon G} - r_2} \delta V \right),
\end{aligned}$$

where C_1, C_2 are integration constants to be determined with the boundary conditions of (3.30).

We now have:

$$\delta X_0(p) = C_1(p) + C_2(p), \tag{3.31}$$
$$\begin{aligned}
\delta X_h(p) =& C_1(p)e^{r_1 h} + C_2(p)e^{r_2 h} \\
&+ \frac{A\overline{v}e^{\frac{\overline{v}h}{\epsilon G}}}{\epsilon G(r_1 - r_2)} \left(\frac{e^{\frac{-hp}{\mu_L}} - e^{\left(r_1 - \frac{\overline{v}}{\epsilon G}\right)h}}{\overline{v} - \epsilon G r_1 - \epsilon G \frac{p}{\mu_L}} - \frac{e^{\frac{-hp}{\mu_L}} - e^{\left(r_2 - \frac{\overline{v}}{\epsilon G}\right)h}}{\overline{v} - \epsilon G r_2 - \epsilon G \frac{p}{\mu_L}} \right) \delta L_0 \\
&- \alpha \frac{A\overline{v}e^{\frac{\overline{v}h}{\epsilon G}}}{\epsilon G(r_1 - r_2)} \left(\frac{1 - e^{\left(r_1 - \frac{\overline{v}}{\epsilon G}\right)h}}{\overline{v} - \epsilon G r_1} - \frac{1 - e^{\left(r_2 - \frac{\overline{v}}{\epsilon G}\right)h}}{\overline{v} - \epsilon G r_2} \right) \delta V.
\end{aligned} \tag{3.32}$$

Let us now have a look on the roots r_1, r_2. We have:

$$r_1 = \frac{\overline{v}}{\epsilon G} + \frac{p}{\overline{v}} - \epsilon G \frac{p^2}{\overline{v}^3} + O(\epsilon^2), \tag{3.33}$$
$$r_2 = \frac{-p}{\overline{v}} + \epsilon G \frac{p^2}{\overline{v}^3} + O(\epsilon^2).. \tag{3.34}$$

Thus in first approximation, all the right-hand terms in (3.32) but $C_2(p)e^{r_2 h}$ are of the size $e^{\frac{\overline{v}h}{\epsilon G}}$. Yet, since $\overline{X}_h = Ae^{\frac{\overline{v}h}{\epsilon G}} + B$ is finite whatever ϵ, we have necessarily

$$A = \widetilde{A}e^{\frac{-\overline{v}h}{\epsilon G}},$$

where the constant $\widetilde{A}$ admits a classical asymptotic development in ϵ. Thus, in (3.32), only $C_1(p)e^{r_1 h}$ remains of size $e^{\frac{\overline{v}h}{\epsilon G}}$, which contradicts the fact that δX_h should be finite whatever ϵ. We have then to take:

$$C_1(p) = \widetilde{C}_1(p)e^{\frac{-\overline{v}h}{\epsilon G}}$$

to preserve the size of δX_h.

As an immediate consequence, $\delta X_0 = C_2$ with a residual error in $e^{\frac{-\overline{v}h}{\epsilon G}}$. C_2 is straightforward from the boundary condition at $s = 0$ in (3.30):

$$L\delta x_0 = \left(\overline{X}_0 - \overline{x}_0\right)\delta L_0 + C_2\left(\overline{L}_0 - \epsilon G r_2\right) + O\left(e^{\frac{-\overline{v}h}{\epsilon G}}\right),$$

thus, injecting the approximation of r_1:

$$\delta X_0(p) = \frac{\delta x_0(p) - \left(\overline{X}_0 - \overline{x}_0\right)\frac{\delta L_0(p)}{\overline{L}}}{1 + \frac{\epsilon G}{\overline{L}\overline{v}}p} + O(\epsilon^2). \tag{3.35}$$

The obtained transfer function is a simple mixing equation combined with a first-order filter, with time constant (in the actual time-scale t) $\frac{\epsilon G}{\overline{L}\overline{v}}(\sigma_L + \sigma_V)$, which is determined by the local competition between the diffusive and convective effects.

We are now interested in finding $\widetilde{C}_1$ to determine δX_h. Rewriting the symbolic equation (3.32) we have:

$$\begin{aligned}\delta X_h(p) =& \widetilde{C}_1(p)e^{(r_1 - \frac{\overline{v}}{\epsilon G})h} + C_2(p)e^{r_2 h} \\ &+ \frac{\widetilde{A}\overline{v}}{\epsilon G(r_1 - r_2)}\left(\frac{e^{\frac{-hp}{\mu_L}} - e^{(r_1 - \frac{\overline{v}}{\epsilon G})h}}{\overline{v} - \epsilon G r_1 - \epsilon G\frac{p}{\mu_L}} - \frac{e^{\frac{-hp}{\mu_L}} - e^{(r_2 - \frac{\overline{v}}{\epsilon G})h}}{\overline{v} - \epsilon G r_2 - \epsilon G\frac{p}{\mu_L}}\right)\delta L_0 \\ &- \alpha\frac{\widetilde{A}\overline{v}}{\epsilon G(r_1 - r_2)}\left(\frac{1 - e^{(r_1 - \frac{\overline{v}}{\epsilon G})h}}{\overline{v} - \epsilon G r_1} - \frac{1 - e^{(r_2 - \frac{\overline{v}}{\epsilon G})h}}{\overline{v} - \epsilon G r_2}\right)\delta V.\end{aligned} \tag{3.36}$$

Considering the exact expansions of the roots (3.33), (3.34), we see that:

$$\widetilde{C}_1 = \frac{\widetilde{A}}{\epsilon}\sum_{i=0}^{+\infty}\beta_i\epsilon^i + \widetilde{A}e^{-\frac{\overline{v}h}{\epsilon G}}\sum_{i=0}^{+\infty}\gamma_i\epsilon^i,$$

where the β_i and γ_i are some constant or p-depending coefficients. Since $\widetilde{A}$ admits an asymptotic expansion in ϵ, it comes that the Laurent series $\sum_{i=-1}^{J}\widetilde{C}_{1,i}\epsilon^i$ is an approximation of $\widetilde{C}_1$ for in $O(\epsilon^J)$ for any $J \geq -1$. Here we will limit ourselves to the two first terms $\widetilde{C}_{1,-1}$ and $\widetilde{C}_{1,0}$. Considering only the terms in $1/\epsilon$ in (3.36), we obtain:

$$\frac{\widetilde{C}_{1,-1}e^{\frac{ph}{\overline{v}}}}{\epsilon G} = \widetilde{A}\overline{v}\left(\frac{e^{\frac{-hp}{\mu_L}} - e^{\frac{hp}{\overline{v}}}}{\epsilon G p}\left(\frac{\mu_L}{\overline{v} + \mu_L}\right)\delta L_0 - \alpha\frac{1 - e^{\frac{hp}{\overline{v}}}}{\epsilon G p}\delta V\right). \tag{3.37}$$

Now considering the terms of the next order in (3.36), one has:

$$\begin{aligned}\delta X_h =&\frac{-p^2h}{\overline{v}^3}\widetilde{C}_{1,-1}e^{\frac{ph}{\overline{v}}}+\widetilde{C}_{1,0}e^{\frac{ph}{\overline{v}}}+C_2e^{\frac{-ph}{\overline{v}}}\\&+\widetilde{A}\overline{v}\left(T_{\delta L}\delta L_0-\alpha T_{\delta V}\delta V\right)+O(\epsilon),\end{aligned}\tag{3.38}$$

where:

$$\begin{aligned}T_{\delta L}&=\left(\left(\frac{\mu_L}{\overline{v}+\mu_L}\right)^2+\frac{2\mu_L}{\overline{v}+\mu_L}\right)\frac{e^{\frac{-ph}{\mu_L}}-e^{\frac{ph}{\overline{v}}}}{\overline{v}^2}-\frac{ph}{\overline{v}^3}\left(\frac{\mu_L}{\overline{v}+\mu_L}\right)e^{\frac{ph}{\overline{v}}}-\frac{e^{\frac{-ph}{\mu_L}}}{\overline{v}^2},\\T_{\delta V}&=\frac{3}{\overline{v}^2}\left(1-e^{\frac{ph}{\overline{v}}}\right)-\frac{ph}{\overline{v}^3}e^{\frac{ph}{\overline{v}}}-\frac{1}{\overline{v}^2}.\end{aligned}$$

In a symbolic, exact form, boundary condition at $s=h$ in (3.30) reads:

$$\begin{aligned}0=&\overline{V}\delta y_h+\left(\overline{y}_h-\alpha\overline{X}_h\right)\delta V\\&-\widetilde{C}_1\left(\alpha\overline{V}+\epsilon Gr_1\right)e^{\left(r_1-\frac{\overline{v}}{\epsilon G}\right)h}-C_2\left(\alpha\overline{V}+\epsilon Gr_2\right)\\&-\frac{\alpha\overline{V}\widetilde{A}\overline{v}}{\epsilon G(r_1-r_2)}\left(\frac{e^{\frac{-hp}{\mu_L}}-e^{\left(r_1-\frac{\overline{v}}{\epsilon G}\right)h}}{\overline{v}-\epsilon Gr_1-\epsilon G\frac{p}{\mu_L}}-\frac{e^{\frac{-hp}{\mu_L}}-e^{\left(r_2-\frac{\overline{v}}{\epsilon G}\right)h}}{\overline{v}-\epsilon Gr_2-\epsilon G\frac{p}{\mu_L}}\right)\delta L_0\\&+\alpha\frac{\alpha\overline{V}\widetilde{A}\overline{v}}{\epsilon G(r_1-r_2)}\left(\frac{1-e^{\left(r_1-\frac{\overline{v}}{\epsilon G}\right)h}}{\overline{v}-\epsilon Gr_1}-\frac{1-e^{\left(r_2-\frac{\overline{v}}{\epsilon G}\right)h}}{\overline{v}-\epsilon Gr_2}\right)\delta V\\&-\frac{\widetilde{A}\overline{v}}{r_1-r_2}\left(\frac{e^{\frac{-hp}{\mu_L}}-e^{\left(r_1-\frac{\overline{v}}{\epsilon G}\right)h}}{\overline{v}-\epsilon Gr_1-\epsilon G\frac{p}{\mu_L}}r_1-\frac{e^{\frac{-hp}{\mu_L}}-e^{\left(r_2-\frac{\overline{v}}{\epsilon G}\right)h}}{\overline{v}-\epsilon Gr_2-\epsilon G\frac{p}{\mu_L}}r_2\right)\delta L_0\\&+\alpha\frac{\widetilde{A}\overline{v}}{r_1-r_2}\left(\frac{1-e^{\left(r_1-\frac{\overline{v}}{\epsilon G}\right)h}}{v-\epsilon Gr_1}r_1-\frac{1-e^{\left(r_2-\frac{\overline{v}}{\epsilon G}\right)h}}{v-\epsilon Gr_2}r_2\right)\delta V,\end{aligned}\tag{3.39}$$

which becomes, at the same order of magnitude than (3.38):

$$\begin{aligned}0=&\overline{V}\delta y_h+\left(\overline{y}_h-\alpha\overline{X}_h\right)\delta V\\&+\left(\widetilde{C}_{1,-1}\left(\frac{p^2h}{\overline{v}^3}L-\frac{p}{\overline{v}}\right)-L\widetilde{C}_{1,0}\right)e^{\frac{ph}{\overline{v}}}-\alpha VC_2e^{\frac{-ph}{\overline{v}}}\\&-\alpha V\widetilde{A}\overline{v}\left(T_{\delta L}\delta L_0-\alpha T_{\delta V}\delta V\right)\\&-\widetilde{A}\overline{v}^2\left(T_{\delta L}-\frac{\mu_L}{\overline{v}+\mu_L}\left(\frac{e^{\frac{-ph}{\mu_L}}-e^{\frac{ph}{\overline{v}}}}{\overline{v}^2}\right)+\frac{e^{\frac{-ph}{\mu_L}}}{\overline{v}^2}\right)\delta L_0\\&+\alpha\widetilde{A}\overline{v}^2\left(T_{\delta V}-\frac{1-e^{\frac{ph}{\overline{v}}}}{\overline{v}^2}+\frac{1}{\overline{v}^2}\right)\delta V+O(\epsilon),\end{aligned}$$

that is:

$$\begin{aligned}0 =&\overline{V}\delta y_h + \left(\overline{y}_h - \alpha\overline{X}_h\right)\delta V \\ &+ L\left(\widetilde{C}_{1,-1}\frac{p^2 h}{\overline{v}^3} - \widetilde{C}_{1,0}\right)e^{\frac{ph}{\overline{v}}} - \alpha V C_2 e^{\frac{-ph}{\overline{v}}} \\ &- L\widetilde{A}\overline{v}\left(T_{\delta L}\delta L_0 - \alpha T_{\delta V}\delta V\right) \\ &- \widetilde{A}\left(e^{\frac{-ph}{\mu_L}}\delta L_0 - \alpha\delta V\right) + O(\epsilon).\end{aligned}$$

Dividing by L and injecting in (3.38), one obtains:

$$\begin{aligned}\delta X_h(p) =&\frac{\overline{V}}{\overline{L}}\delta y_h + \left(\overline{y}_h - \alpha\overline{X}_h\right)\frac{\delta V}{\overline{L}} \\ &+ \frac{\overline{v}}{\overline{L}}\left(\delta x_0(p) - \left(\overline{X}_0 - \overline{x}_0\right)\frac{\delta L_0(p)}{\overline{L}}\right)e^{\frac{-ph}{\overline{v}}} \\ &- \widetilde{A}e^{\frac{-ph}{\mu_L}}\frac{\delta L_0}{\overline{L}} + \alpha\widetilde{A}\frac{\delta V}{\overline{L}} + O(\epsilon),\end{aligned} \tag{3.40}$$

where C_2 has been replaced with its $O(1)$ approximation. We see that δX_h splits into:

- an instant mixing equation (first line);
- a contribution from the composition variation δX_0 which has reached the other side with composition convection speed $\frac{\overline{v}}{\sigma_L+\sigma_V}$ (second line);
- contributions from the perturbations of the flows as if the composition at $s = 0$ were unchanged, which propagate with finite speed $\mathcal{V}_L$ for the liquid, and infinite speed for the gas (third line).

We shall now consider the case of a composition convection speed $\overline{v}$ orientated upwards (that is, $v(s,t) < 0$). Applying the coordinate change $z = h - s$, (3.30) rewrites:

$$\left\{\begin{array}{rcl} p\delta X(z,p) &=& \overline{v}\frac{\partial\delta X}{\partial z}(z,p) - \overline{X}'\delta v(z,p) + \epsilon G\frac{\partial^2\delta X}{\partial z^2}, \\ \overline{L}\delta x_h(p) &=& (\delta v_h(p) + \alpha\delta V(p))\overline{X}_h \\ & & +(\overline{v} + \alpha\overline{V})\delta X_h(p) - \overline{x}_h\delta L_h(p) \\ & & +\epsilon G\frac{\partial\delta X}{\partial z}(h,p), \\ -\overline{V}\delta y_0(p) &=& (\delta v_0(p) - \delta L(0,p))\overline{X}_0 \\ & & +(\overline{v} - \overline{L})\delta X_0(p) + \overline{y}_0\delta V(p) \\ & & +\epsilon G\frac{\partial\delta X}{\partial z}(0,p), \end{array}\right.$$

which, for a negative $\overline{v}$, corresponds to a fictional downwards system, with switched outlets and inlets with respect to the actual, previously discussed, downward case. For this fictional downward system, one can approximate the downwards transfer functions as previously. Then, the actual upwards transfer functions are obtained by applying the inverse

coordinate change $s = h - z$. This yields:

$$\delta X_h(p) = \frac{\delta y_h(p) + \left(\overline{y}_h - \overline{\alpha}\overline{X}_h\right)\frac{\delta V(p)}{\overline{V}}}{\overline{\alpha}\left(1 - \frac{\epsilon\overline{G}}{\overline{v}\overline{V}\overline{\alpha}}p\right)} + O(\epsilon^2), \tag{3.41}$$

$$\begin{aligned}\delta X_0(p) =& \frac{\overline{L}\delta x_0(p) + \delta L_0(p)\left(\overline{x}_0 - \overline{X}_0\right)}{\overline{\alpha}\overline{V}} \\ & - \frac{\overline{v}}{\overline{\alpha}V}\left(\frac{\delta y_h(p) + \left(\overline{y}_h - \overline{\alpha}\overline{X}_h\right)\frac{\delta V(p)}{\overline{V}}}{\overline{\alpha}}\right)e^{\frac{hp}{\overline{v}}} \\ & + \widetilde{A}\frac{\delta L_0(p)}{\overline{\alpha}\overline{V}}e^{-\frac{hp}{\mu_L}} - \widetilde{A}\frac{\delta V(p)}{\overline{V}} + O(\epsilon),\end{aligned} \tag{3.42}$$

where

$$\widetilde{A} = \frac{\overline{X}_0 - \overline{X}_h}{e^{-\frac{\overline{v}h}{\epsilon\overline{G}}} - 1}e^{-\frac{\overline{v}h}{\epsilon\overline{G}}}.$$

The structure of the transfers is the same as for the downwards case. At the high-purity end ($s = h$), one obtains a mixing equation plus a small filtering effect. Its time constant is determined by the relative influences of the diffusion and the entering gas flow. At $s = 0$, compositions variations are the sum of: an instant mixing, a contribution from the traveling composition wave with speed $\frac{\overline{v}}{\sigma_L + \sigma_V}$, and a contribution from the reflux rate change, which establishes with delay due to the liquid's finite speed.

Tables 3.2 and 3.3 summarize the obtained transfers in $O(\epsilon)$, respectively for the downward and the upward convection case, between dimensionless inputs and outputs. These matrixes will be used in the end of Chapter 4 to construct a model of the plant High Pressure column.

Note that, if we consider only variations of the liquid flow, one has for the downwards convection case:

$$\frac{\delta X_0}{\overline{X}_0} = (\alpha - 1)\frac{\delta L_0}{\overline{L}},$$

supposing that the gas at the top is totally condensed, and (partially) recycled at inlet liquid flow, which yields $\delta x_0 = \alpha\delta X_0$. We find again the phenomenon pointed out in [103] for instance, that the small dynamics expressed in logarithmic scale for the compositions, are almost independent from the initial conditions. The dependence is hidden in $\overline{X}_0$, which is *a priori* small and has an exponential dependence on the (steady-state) reflux. Thus one can drastically modify $\overline{X}_0$ with only a small change on $\overline{L}$.

As said, the obtained transfers consist in static gains and delays only. Thus at the considered order, we do not really leave the classical linear control models framework. It is nevertheless possible that more exotic transfer terms appear at higher order, notably distributed delays which would account for how a perturbation originates at one end of the columns, is convected and spreads at the same time, and in return affects both sides of the column.

Inputs\Outputs	$\frac{\delta X_h(p)}{\overline{X}_h}$	$\frac{\delta X_0(p)}{\overline{X}_0}$
$\frac{\delta L_0(p)}{\overline{L}}$	$\frac{\overline{v}}{\overline{L}}\left(\frac{\overline{x}_0-\overline{X}_0}{\overline{X}_h}e^{\frac{-hp}{\overline{v}}}\right)-\frac{1-\frac{\overline{X}_0}{\overline{X}_h}}{e^{\frac{\overline{v}h}{\epsilon G}}-1}e^{\left(\frac{\overline{v}}{\epsilon G}-\frac{p}{\mu_L}\right)h}$	$\frac{\overline{x}_0}{\overline{X}_0}-1$
$\frac{\delta V(p)}{\overline{V}}$	$\frac{\alpha\overline{V}}{\overline{L}}\left(\frac{\overline{y}_h}{\alpha\overline{X}_h}-1+\frac{1-\frac{\overline{X}_0}{\overline{X}_h}}{e^{\frac{\overline{v}h}{\epsilon G}}-1}e^{\frac{\overline{v}h}{\epsilon G}}\right)$	0
$\frac{\delta x_0(p)}{\overline{x}_0}$	$\frac{\overline{v}}{\overline{L}}\frac{\overline{x}_0}{\overline{X}_h}e^{\frac{-hp}{\overline{v}}}$	$\frac{\overline{x}_0}{\overline{X}_0}$
$\frac{\delta y_h(p)}{\overline{y_h}}$	$\frac{\overline{V}}{\overline{L}}\frac{\overline{y}_h}{\overline{X}_h}$	0

Table 3.2: Dimensionless transfer matrix (in $O(\epsilon)$) for a downwards composition convection speed $\overline{v}=\overline{L}-\alpha\overline{V}>0$.

Inputs\Outputs	$\frac{\delta X_h(p)}{\overline{X}_h}$	$\frac{\delta X_0(p)}{\overline{X}_0}$
$\frac{\delta L_0(p)}{\overline{L}}$	0	$\frac{\overline{L}}{\alpha\overline{V}}\left(\frac{\overline{x}_0}{\overline{X}_0}-1+\frac{1-\frac{\overline{X}_h}{\overline{X}_0}}{e^{\frac{\overline{v}h}{\epsilon G}}-1}e^{\frac{\overline{v}h}{\epsilon G}}\right)$
$\frac{\delta V(p)}{\overline{V}}$	$\frac{\overline{y}_h}{\alpha\overline{X}_h}-1$	$\left(\frac{\overline{y}_h}{\alpha\overline{X}_0}-1\right)\frac{\overline{v}e^{\frac{-hp}{\overline{v}}}}{\alpha\overline{V}}-\frac{1-\frac{\overline{X}_h}{\overline{X}_0}}{e^{\frac{\overline{v}h}{\epsilon G}}-1}e^{\frac{\overline{v}h}{\epsilon G}}$
$\frac{\delta x_0(p)}{\overline{x}_0}$	0	$\frac{\overline{L}}{\alpha\overline{V}}\frac{\overline{x}_0}{\overline{X}_0}$
$\frac{\delta y_h(p)}{\overline{y_h}}$	$\frac{\overline{y}_h}{\alpha\overline{X}_h}$	$\frac{\overline{y}_h}{\alpha\overline{X}_0}\frac{\overline{v}}{\alpha\overline{V}}e^{\frac{-hp}{\overline{v}}}$

Table 3.3: Dimensionless transfer matrix (in $O(\epsilon)$) for an upwards composition convection speed $\overline{v}=\alpha\overline{V}-\overline{L}>0$.

3.3 Conclusion

In the first part of this chapter, a simplified column configuration has been considered to examine our PDE model from the point of view of control theory. We have considered only the case of binary mixture separation. A reasonable set of assumptions has been given, regarding the internal reflux rate, the inlet composition and the chosen thermodynamic relation. Under these assumptions, the following results have been demonstrated:

- provided that the initial data is within $(0, 1)$, the lumped molar fraction $X(s, t)$ remains in the same interval $\forall t > 0$, $\forall s \in [0, h]$.
- for any diffusion coefficient $\epsilon > 0$, there exists a unique stationary composition profile, which is locally exponentially stable.
- The stationary molar fraction at the top of the considered column monotonically increases with the diffusion coefficient ϵ.

Based on the PDE model, we have proposed a family of asymptotic observers for the molar fraction profiles, with tunable output injection. As for the stationary solution, we have constructed a Lyapunov function to prove the local exponential convergence of the observers. This convergence is obtained even with time-varying internal flows. Several simulations results have been presented, which shows that the local nature of the previous propositions seems in practice extensible to a global one. In addition, considering a finite liquid propagation speed, rather than instant propagation as in the proofs, does not affect these results in simulation.

In the second part of the chapter, we have considered the reduction of the PDE model into a MIMO linearized transfer function model. This model connects the perturbations of the internal flows L and V, and of the inlet compositions y_h and x_0 to the variations of the simplified outlet compositions X_h and Y_0, around a steady-state. The outputs are first expressed in an exact, symbolic manner, then are approximated using a truncated expansion of the symbols. The obtained transfer functions are structured as power series in the diffusion coefficient ϵ, after a non-standard asymptotic expansion.

The transfer functions have been given for two cases: when the composition convection speed is downwards or upwards. They are, at the dominating order, composed of direct transfers with delays arising from the composition convection on the one hand, and from the liquid circulation on the other hand. In addition, at this order, no composition information can travel counter the composition convection direction.

Chapter 4

Application to HP column

Au Chapitre 2, nous avons présenté un modèle dynamique réduit pour une colonne de distillation, fondé sur une équation aux dérivées partielles de convection diffusion. Nous avons discuté ce modèle du point de vue de l'automatique au Chapitre 3, dans le cas d'une configuration de colonne idéalisée. Dans le présent chapitre, nous vérifions les performances du modèle en le confrontant à des jeux de données et une configuration de colonne plus complexes. Cette étude se concentre sur la colonne Moyenne Pression (MP) de l'ASU étudiée, que nous décrivons brièvement. Nous présentons ensuite les schémas utilisés pour l'implantation numérique du modèle EDP. En nous basant sur la géométrie de la colonne et les performances attendues du garnissage, nous établissons des valeurs a priori *pour certains paramètres du modèle. Le modèle EDP est comparé à un modèle statique à plateaux* Hysys *de la colonne pour diverses conditions de fonctionnement, ce qui nous permet de raffiner les valeurs des rétentions et du coefficient de diffusion ϵ. Le modèle ainsi réglé est utilisé pour reproduire un scénario de fonctionnement dynamique. Pour ce faire, des données réelles issues de l'ASU étudiée sont utilisées tant comme entrées que comme références. Nous proposons une adaptation en ligne du coefficient de diffusion, et illustrons les performances et limites du modèle sur un total de 680h de fonctionnement de l'unité.*

Partant du modèle linéaire tangent du Chapitre 3, développé pour un segment homogène de colonne, nous construisons un modèle de fonctions de transfert de la colonne MP. Nous vérifions sa capacité à reproduire de petites oscillations de compositions sur des intervalles de temps courts, en comparaison avec des données réelles en provenance de l'unité de séparation.

In Chapter 2 a reduced dynamic model based on convection-diffusion partial differential equations has been presented. This model has been discussed from the point of view of control theory in Chapter 3, based on a idealized column configuration. In this chapter, we check the model performances against more complex configuration and data set. The study is focused on the Air Separation Unit High Pressure (HP) column, which will be briefly described. We then present the numerical scheme used for the PDE model implementation. Based on the column geometry and the packing performances we set *a priori* values for the model parameters. The PDE model is compared to a static Hysys plate model of the column for various operating conditions, which helps us refining the value of the hold-ups and the diffusion coefficient ϵ. The so tuned model is then used to reproduce a dynamic operation scenario. For this test, real data recorded from the air separation plant are used as inputs and targets. On-line adaption of the diffusion coefficient is proposed, and the model performances

and limits are demonstrated over a total of 680 hours of operation.

Based on the linear tangent model written in Chapter 3 for one homogeneous packed subsection, we build a transfer functions model of the HP column. We check its ability to reproduce small composition oscillations over short time intervals, using real data from the plant for the comparison.

4.1 Introduction to the HP column

The High Pressure column[1] is for the production of high-purity nitrogen. It is about 20 m high, with a packed height of about 15 m and an (almost) constant inner diameter of approximately 2.5 m. It consists of three homogeneous sections of packing - the type of packing is the same in each section - and has a total condenser at top. We invite the reader to frequently refer to Fig. A.2 where the tags of sensors and flows used in the following are plotted on the ASU chart.

The HP column is fed by gaseous[2] air. The gas rises up to the top, where a small fraction is drawn to regulate the Argon process. The rest is condensed and falls as liquid on a distributing plate, where the amount required for production is drawn. Oxygen concentration at top must be maintained below 1 ppm to match the contractual requirements. It is typically much lower in operation, as will be seen in the dynamic scenario presentation. The remaining liquid passes through the first packing section down to a second distributor. There about 50% of the liquid is taken out to serve as top reflux in the LP column. Oxygen concentration at this location is about 2%, and Argon concentration should be round 0.5%. Between the second and the third packing section, the remaining liquid mixes with a feed of liquid air, which helps increasing reflux in the last section by compensating the liquid lost at the previous distributor. The liquid air comes from a flash-pot, where a gas fraction has also been obtained. This gas enters the column at the same location and mixes with the existing vapor flow. The internal liquid flow arrives after the last packing section into the HP-column's bottom, whose level reference is function of the ASU entering air flow. The level is manipulated using the drained flow, which is directed towards the LP column (as a reflux) and the Argon process. Thus the bottom serves as a lead-lag buffer to temperate the transient impacts of ASU's set-point changes on the distillation in LP column.

In the HP column, maximum Argon molar fraction is barely above 1%. Since N_2 is the dominant component all along the column, both O_2 and Ar behave as heavy components. Consequently, they can be considered as only one lumped pseudo-component, whose thermochemical properties are close to oxygen's. Alternatively speaking, one can consider that distillation in HP column involves no Argon. We will thus consider in a first time air as a binary mixture in the column. The numerical scheme presented in the next section is for such mixtures. Ternary mixture separation simulation will be dealt with in the next Chapter, regarding the Low Pressure column simulation.

[1] designated in French as the Middle Pressure (MP) column

[2] yet according to some HYSYS simulation cases, a small fraction of liquid may exist in the feed - about 5%.

4.2 Numerical scheme for pseudo-binary simulation

The numerical scheme is to simulate the dynamics of

$$\left(\sigma_L + \sigma_V k'(X)\right) \frac{\partial X}{\partial t} = \frac{\partial}{\partial s}\left(-LX + Vk(X)\right) - \epsilon \frac{\partial}{\partial s}\left(G(X)\frac{\partial X}{\partial s}\right), \tag{4.1}$$

$$x = X - \epsilon\sigma_V \frac{G(X)}{\sigma_V L + \sigma_L V}\frac{\partial X}{\partial s},$$

$$y = k(X) + \epsilon\sigma_L \frac{G(X)}{\sigma_V L + \sigma_L V}\frac{\partial X}{\partial s},$$

according to the centre manifold reduction in Chapter 2. We discretize the dynamics with finite differences in time and space. Time-steps Δt and space-steps Δs will be constant. We note X_k^i the value of X at time $t = i\Delta t$, at $s = k\Delta s$. The same convention is used for other variables.

The finite differences approach has been chosen for this work.

4.2.1 Hydraulics

The liquid flow $L(s,t)$ is considered to propagate according to

$$\frac{\partial L}{\partial t} = -\mathcal{V}_L \frac{\partial L}{\partial s}, \tag{4.2}$$

where $\mathcal{V}_L$ stands for the liquid vertical speed.

Equation (4.2) is discretized with finite differences and implicit Euler scheme:

$$\frac{L_k^{i+1} - L_k^i}{\Delta t_L} = -\mathcal{V}_L \frac{L_k^{i+1} - L_{k-1}^{i+1}}{\Delta s}, \tag{4.3}$$

the finite differences in space being backwards due to the direction of the liquid flow.

We consider that the gas flow $V(s,t)$ establishes instantly over an homogeneous section. Indeed, the gas flow homogenizes because of pressure waves, which travel much faster than matter itself. Consequently, we use only a $V(t)$ and we write: $V_k^i = V^i$.

The liquid hold-up σ_L is considered as a linear function of the liquid flow:

$$\sigma_{L_k^i} = \frac{L_k^i}{\mu_L}.$$

The gas hold-up $\sigma_{V_k^i}$ is a function of the column's inner pressure only, as will be explained in Section 4.3.

4.2.2 General scheme for homogeneous sections

The non-linear transport term in (4.1) is linearized as follows:

$$\frac{\partial}{\partial s}\left(V(t)k(X(s,t)\right) \to \frac{V^i}{\Delta s}\left[\left(\frac{k(X)}{X}\right)_{k+1}^i X_{k+1}^i - \left(\frac{k(X)}{X}\right)_k^i X_k^i\right].$$

The scheme is upwards in space, since the non-linear term corresponds to components convection by the rising gas. This approximation is used to obtain the following, classical finite difference numerical scheme:

$$(\sigma_{L_k}^i + \sigma_{V_k}^i k'(X_k^i))\frac{X_k^{i+1} - X_k^i}{\Delta t} = \frac{1}{\Delta s}\left[L_{k-1}^i X_{k-1}^i - L_k^i X_k^i + \left(V^i \frac{k(X)}{X}\right)_{k+1}^i X_{k+1}^i - \left(V^i \frac{k(X)}{X}\right)_k^i X_k^i\right] + \epsilon G_{k-1/k}\frac{X_{k-1}^i - X_k^i}{\Delta s^2} + \epsilon G_{k/k+1}\frac{X_{k+1}^i - X_k^i}{\Delta s^2}, \quad (4.4)$$

where components transport by liquid is rendered by a backwards finite difference. The varying diffusion term $G(X(s,t))$ is rendered by

$$G_{k-1/k} = 2\frac{G_{k-1}G_k}{G_{k-1} + G_k}, \quad G_{k/k+1} = 2\frac{G_k G_{k+1}}{G_k + G_{k+1}}, \quad (4.5)$$

as recommended in [78]. One easily checks that the scheme (4.4) is conservative, which is an essential property for high-purity numerical simulations. Yet another critical point is to maintain the X_k^i in $(0,1)$, as required by the physics. This is for the moment not granted with the full explicit scheme (4.4). We can transform some terms in the scheme from explicit to implicit:

$$(\sigma_{L_k}^i + \sigma_{V_k}^i k'(X_k^i))\frac{X_k^{i+1} - X_k^i}{\Delta t} = \frac{1}{\Delta s}\left[L_{k-1}^i X_{k-1}^i - L_k^i X_k^{i+1} + \left(V \frac{k(X)}{X}\right)_{k+1}^i X_{k+1}^i - \left(V \frac{k(X)}{X}\right)_k^i X_k^{i+1}\right] + \epsilon G_{k-1/k}\frac{X_{k-1}^i - X_k^{i+1}}{\Delta s^2} + \epsilon G_{k/k+1}\frac{X_{k+1}^i - X_k^{i+1}}{\Delta s^2},$$

which profitably rewrites:

$$\left[\frac{\sigma_{L_k}^i + \sigma_{V_k}^i k'(X_k^i)}{\Delta t} + \frac{1}{\Delta s}\left[L_k^i + \left(V\frac{k(X)}{X}\right)_k^i\right] + \epsilon\frac{G_{k-1/k} + G_{k/k+1}}{\Delta s^2}\right] X_k^{i+1} = \frac{\sigma_k}{\Delta t}X_k^i + \frac{1}{\Delta s}\left[\left(\frac{k(X)}{X}\right)_{k+1}^i + \epsilon\frac{G_{k/k+1}}{\Delta s^2}\right] X_{k+1}^i + \left[\frac{L_{k-1}^i}{\Delta s} + \epsilon\frac{G_{k-1/k}}{\Delta s^2}\right] X_{k-1}^i. \quad (4.6)$$

One observes that X_k^{i+1} is now a barycenter of initial data X_{k-1}^i, X_k^i, X_{k+1}^i, with strictly positive weights. Thus one ensures $X_k^{i+1} > 0$. Additionally, if L is constant (L_k does not depend on k), the sum of the weights is 1. Thus, in that case, X_k^{i+1} remains within the envelope of X_{k-1}^i, X_k^i, X_{k+1}^i: if initial and boundary data are in $(0,1)$, so remains X_k^{i+1} for any $i > 0$ and k. Since this is only true in steady state, we propose in the end of this section an alternative. For the moment, consider that we work with scheme (4.6).

The static outputs x and y are obtained as:

$$x_k^i = X_k^i - \epsilon\sigma_{L_k}^i\frac{G(X_k^i)}{\sigma_{V_k}^i L_k^i + \sigma_{L_k}^i V^i}\frac{X_k^i - X_{k-1}^i}{\Delta s}, \quad (4.7)$$

$$y_k^i = k(X_k^i) + \epsilon\sigma_{V_k}^i\frac{G(X_k^i)}{\sigma_{V_k}^i L_k^i + \sigma_{L_k}^i V^i}\frac{X_{k+1}^i - X_k^i}{\Delta s}. \quad (4.8)$$

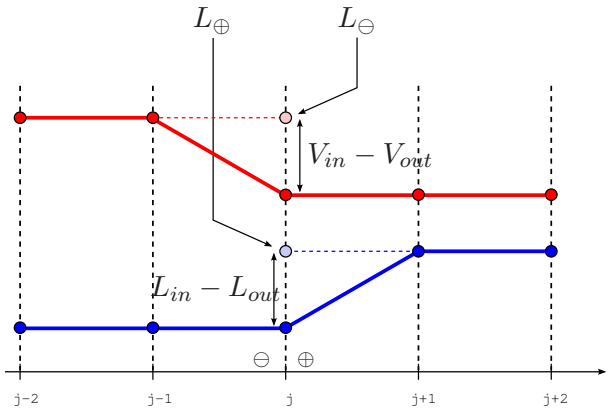

Figure 4.1: Flow grid around a junction

Once again, the finite difference is backwards for x_k^i since it is carried by the dripping liquid, and upwards for y_k^i since it is transported by the rising gas.

4.2.3 Matching conditions

We now consider the junction of two homogeneous sections, where may *a priori* take place one or all of the followings:

- injection of a liquid flow $L_{in}(t)$, with molar fraction $x_{in}(t)$,
- injection of a gas flow $V_{in}(t)$, with molar fraction $y_{in}(t)$,
- withdrawal of a liquid flow $L_{out}(t)$ with molar fraction $x_{out}(t)$ to be determined,
- withdrawal of a gas flow $V_{out}(t)$ with molar fraction $y_{out}(t)$ to be determined.

Let j be the index at which the junction is located. We denote with a subscript $_\oplus$ a variable evaluated at j right below the junction (not at $j+1$), and with a subscript $_\ominus$ a variable evaluated at j right above the junction (not at $j-1$).

Regarding the hydraulics, we have

$$L_\oplus(t) = L_\ominus(t) + L_{in}(t) - L_{out}(t), \quad V_\ominus(t) = V_\oplus(t) + V_{in}(t) - V_{out}(t).$$

We set $L_j^i = L_\ominus^i$, and we have to rewrite (4.3) at $j+1$:

$$\frac{L_{j+1}^{i+(1/d)} - L_{j+1}^{i+1}}{\Delta t_L} = -\mathcal{V}_L \frac{L_{j+1}^{i+(1/d)} - L_j^{i+(1/d)} - L_{in}^i + L_{out}^i}{\Delta s}. \tag{4.9}$$

For the gas, we set $V_j^i = V_\oplus$ and thus $V_{j-1}^i = V_j^i + V_{in}^i - V_{out}^i$. Fig. 4.1 shows how the space grid catches the junction regarding the flows.

Regarding the molar fractions, we have to conserve the flow of component C_1 through the junction. This flow is $Lx + Vy$. Given the expressions of $x(s,t)$ and $y(s,t)$ as static outputs built upon $X(s,t)$, one checks that we have in fact to conserve the flow of $X(s,t)$, that is, $-LX + Vk(X) + \epsilon G(X)\frac{\partial X}{\partial s}$.

The output gas molar fraction y_{out} is calculated with X at j, but using the hydraulics of the $\oplus$ side. Reversely, the output liquid molar fraction x_{out} depends on X at j and of the hydraulics at $\ominus$ side:

$$y^i_{out} = k(X^i_j) + \epsilon\sigma_{L^i_\oplus}\frac{G_{j-1/j}}{\sigma_{L^i_\oplus} + \sigma_{V^i_\oplus}k'(X)}\frac{X^i_{j+1} - X^i_j}{\Delta s},$$
$$x^i_{out} = X^i_j - \epsilon\sigma_{V^i_\ominus}\frac{G_{j/j+1}}{\sigma_{L^i_\ominus} + \sigma_{V^i_\ominus}k'(X)}\frac{X^i_j - X^i_{j-1}}{\Delta s}.$$

In addition, instead of (4.5), we take:

$$G_{j-1/j} = G_{j-1}, \quad G_{j/j+1} = G_{j+1},$$

to circumvent the definition of a G_j. Note that the change must also affect the calculations at $j-1$ and $j+1$ to ensure the conservativeness of the numerical scheme.

This being set, the scheme for X at the junction must ensure:

$$L^i_\ominus X^i_j + V^i_\oplus k(X^i_j) + G_{j+1}\frac{X^i_{j+1} - X^i_j}{\Delta s} + L^i_{in}x^i_{in} + V^i_{in}y^i_{in}$$
$$= L^i_\oplus X^i_j + V^i_\ominus k^i(X^i_j) + G_{j-1}\frac{X^i_j - X^i_j - 1}{\Delta s} + L^i_{out}x^i_{out} + V^i_{out}y^i_{out}.$$

Taking $k(X^i_j) = \frac{k(X^{i-1}_j)}{X^{i-1}_j}X^i_j$ one obtains

$$X^i_j = \frac{L^i_{in}x^i_{in} + V^i_{in}y^i_{in} + X^i_\ominus\left[L^i_\ominus + \frac{G_{j-1} - L^i_{out}\sigma_{V^i_\ominus}H_\ominus}{\Delta s}\right] + X^i_\oplus\left[V^i_\oplus\frac{k(X^{i-1}_j)}{X^{i-1}_j} + \frac{G_{j+1} - V^i_{out}\sigma_{L^i_\oplus}H_\oplus}{\Delta s}\right]}{L^i_\oplus + L^i_{out} + \frac{k(X^{i-1}_j)}{X^{i-1}_j}\left(V^i_\ominus + V^i_{out}\right) + \frac{G_{j+1} + G_{j-1} - \left(V^i_{out}\sigma_{L^i_\oplus}H_\oplus + L^i_{out}\sigma_{V^i_\ominus}H_\ominus\right)}{\Delta s}}. \tag{4.10}$$

where $H_\ominus$ and $H_\ominus$ are defined according to:

$$H_k = \frac{G_k}{\sigma_{L^i_k}V^i_k + \sigma_{V^i_k}L^i_k}.$$

4.2.4 Boundary conditions

HP top boundary condition

Part of the flow Vy exiting the column at top ($s = 0$) is completely condensed and re-injected as a liquid flow Lx. One neglects the condenser's dynamics. Since $x(0,t) = y(0,t)$ (total condensation), the state (liquid or gas) of the drawn-out flow does not affect the balance equation. We chose to write the drawn-out flow as if it were completely liquid, for it helps preserving the positivity of the coefficients in the final, discrete formulation of the boundary condition. One has, as schematized on Fig. 4.2,

$$L(0,t)X(0,t) + (V(0,t) - L(0,t))x(0,t) = V(0,t)k(X(0,t)) + \epsilon G(X(0,t))\frac{\partial X}{\partial s}(0,t),$$

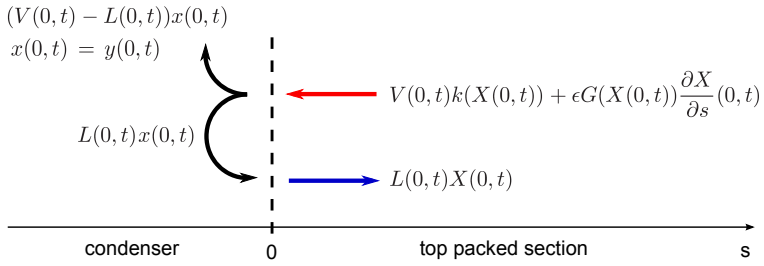

Figure 4.2: Molar flows at the top boundary of HP column.

and thus:

$$V(0,t)X(0,t) = V(0,t)k(X(0,t)) + \epsilon G(X(0,t))\frac{\partial X}{\partial s}(0,t) + \epsilon H(X(0,t))\sigma_V(V(0,t)-L(0,t))\frac{\partial X}{\partial s}(0,t). \quad (4.11)$$

Equation (4.11) is rendered in the numerical scheme by:

$$X_0^i = \frac{\epsilon\frac{\left(G_{0/1}+H_{0/1}\sigma_L\left(V_0^i-L_0^i\right)\right)}{\Delta s}X_1^i}{V_0^i\left(1-\frac{k(X_0^{i-1})}{X_0^{i-1}}\right)+\epsilon\frac{\left(G_{0/1}+H_{0/1}\sigma_L\left(V_0^i-L_0^i\right)\right)}{\Delta s}}. \quad (4.12)$$

Note that, if X_0^{i-1} is small, as expected for O_2, all the coefficients in the previous equation are positive.

HP bottom boundary condition

The flow entering the HP column at the bottom (say, at $s = h$, $k = \kappa$) is the gas flow $V(h,t)y_h$, where y_h is the molar fraction of component C_1 in atmospheric air. Thus one has as in Chapter 3:

$$V(h,t)y_h = V(h,t)k(X(h,t)) + \epsilon\left(G(X(h,t)) - H(X(h,t))\sigma_V L\right)\frac{\partial X}{\partial s}(h,t), \quad (4.13)$$

which discretizes into:

$$X_\kappa^i = \frac{V_\kappa^i y_h + \epsilon\frac{G_{\kappa-1/\kappa}-H_{\kappa-1/\kappa}\sigma_V L_\kappa^i}{\Delta s}X_{\kappa-1}^i}{V\frac{k(X_\kappa^{i-1})}{X_\kappa^{i-1}}+\epsilon\frac{G_{\kappa-1/\kappa}-H_{\kappa-1/\kappa}\sigma_V L_\kappa^i}{\Delta s}}. \quad (4.14)$$

and one takes $L_\kappa^i x_\kappa^i$ as the output flow.

4.2.5 Final regularization

As mentioned before, in transients, the X_k^i may grow beyond 1 with the chosen numerical scheme (yet they can not be negative). For HP column this is not so much a problem, since by choosing the pseudo-component Ar, O_2 as C_1, the maximum value of X_{C_1} will be around 0.4. In the LP column, this is more a concern, because O_2 and N_2 molar fractions span over (0,1).

One can observe that all the previous equations of the numerical scheme could be written as well for the unexpressed component C_2 (to the expression of the function $k(.)$). One can thus dispose of two separated solutions X_{C_1} and X_{C_2}, one for each component. Re-affecting:

$$X_{C_1} \longleftarrow (1 - X_{C_1})X_{C_1} + X_{C_1}(1 - X_{C_2}),$$
$$X_{C_2} \longleftarrow (1 - X_{C_1})(1 - X_{C_1}) + X_{C_1}X_{C_2},$$

one obtains X_{C_1}, X_{C_2} in (0,1), which can be used as initial data for the next iteration. This approach does not seem to degrade the conservativeness of the scheme according to our tests.

Another approach, which would not rise conservativeness issues, is to use a scheme based on C_1 for the part $\mathcal{D}_{C_1}$ of the domain where C_1 is in minority, and a scheme based on C_2 for the remaining $\mathcal{D}_{C_2}$; the junction is made by matching the flow of X_{C1} leaving $\mathcal{D}_{C_1}$ with the flow of $1 - X_{C_2}$ entering $\mathcal{D}_{C_2}$, and *vice-versa*.

4.3 Parameters estimation using design data

In this section we will estimate some of the model parameters, to be used as 'guess values' for the static and dynamic simulations. Namely, we are looking for the liquid flow propagation speed $\mathcal{V}_L$ (we assume the gas flow variations propagates instantly), and the hold-ups σ_L, σ_V.

Let S be the section of the column. The packing's metal sheets occupy only 5% of its volume; the sheets being placed vertically, let $S_p = 0.05S$ the section occupied by the packing. The liquid film's thickness is about half of the sheet's for usual reflux rates. The liquid flowing on both sides of the packing sheets, we take $S_L = S_p = 0.05S$ as the section the liquid flows through. We thus obtain a liquid superficial speed $\frac{L}{\rho S_L}$ where $\rho \simeq 640 Nm^3/m^3$ in the operating conditions of the columns.

The liquid essentially flows following the packing's corrugations with 45° inclination. We only retain the liquid vertical speed

$$\mathcal{V}_L = \frac{L}{\sqrt{2}\rho S_L}$$

($\mathcal{V}_L = 0.08$ m/s with a typical liquid flow $L = 20 Nm^3/s$ at the top of the HP column).

For the simulations, we will use a constant liquid speed $\mathcal{V}_L$ in (4.2), assuming that the liquid film thickness varies with L such that $S_L \propto L$. In the linear relation between the liquid hold-up σ_L and L

$$\sigma_L = \frac{L}{\mu_L},$$

we thus expect $\mu_L = \mathcal{V}_L = 0.08 m/s$ (yielding typically $250 Nm^3/m$ at the top of the HP column).

Note that with a packing specific surface $\mathcal{S} \simeq 500 m^2/m^3$ and a liquid film thickness $e \simeq 10^{-4} m$, one can also estimate

$$\sigma_L = 2e\mathcal{S}S\rho \simeq 350 Nm^3/m$$

which corroborates the previous estimation.

The gas hold-up is given by the perfect gases law:

$$\sigma_V = \frac{P_{HP}}{T_{HP}} \frac{T_{std}}{P_{std}} S_v, \tag{4.15}$$

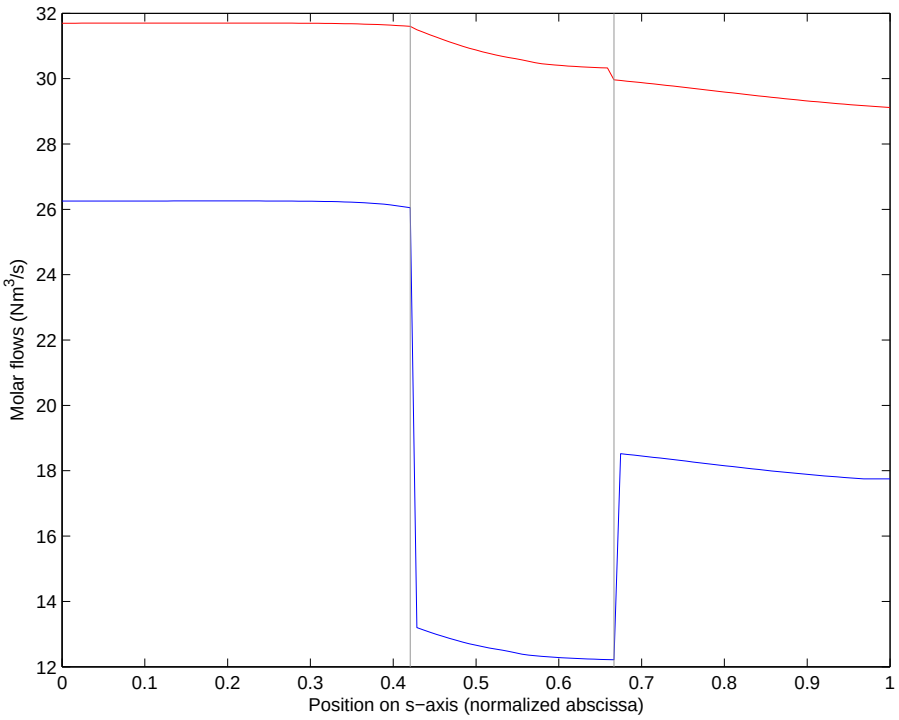

Figure 4.3: Liquid (blue) and gas (red) molar flow profiles in HP column for case A. Vertical grey lines indicate the junctions between homogeneous packed sections.

where $T_{std} = 273K$, $P_{std} = 10^5 Pa$, and typically $T_{HP} = 90K$, $P_{HP} = 5 \times 10^5 Pa$. Thus one expects $\sigma_V \simeq 80 Nm^3.m^{-1}$ in the entire HP column.

4.4 Comparison with static simulation reference cases

We dispose of three static simulation cases from a HYSYS model of the ASU:

Case A (Nominal Nordon) corresponds to nominal operation of the ASU.

Case B (63b) is a variation on the nominal case A, where the lean liquid draw has been increased, with effects on the LP column.

Case C (MAX HPGAN) corresponds to the maximization of the high-pressure gaseous nitrogen production.

The HP column is simulated using a 40-plates model, with air as a ternary mixture. In first approximation, the plate efficiency is constant; thus for each column section, the molar fraction profiles from the HYSYS model are mapped to our space-grid using linear interpolation. The same is done for the relative volatility and the liquid and gas flows. To estimate the hold-ups as discussed previously, we use a linearly increasing temperature profile to interpolate the boundary values given by HYSYS. The pressure varies of only about 1% along the column, thus we consider it as constant. Pressure and temperature values are summarized in Table 4.1. For each case, σ_V is estimated according to (4.15) and the values of this table. The space-step is $10cm$. The value of ϵ is adapted to each case to match the top liquid molar

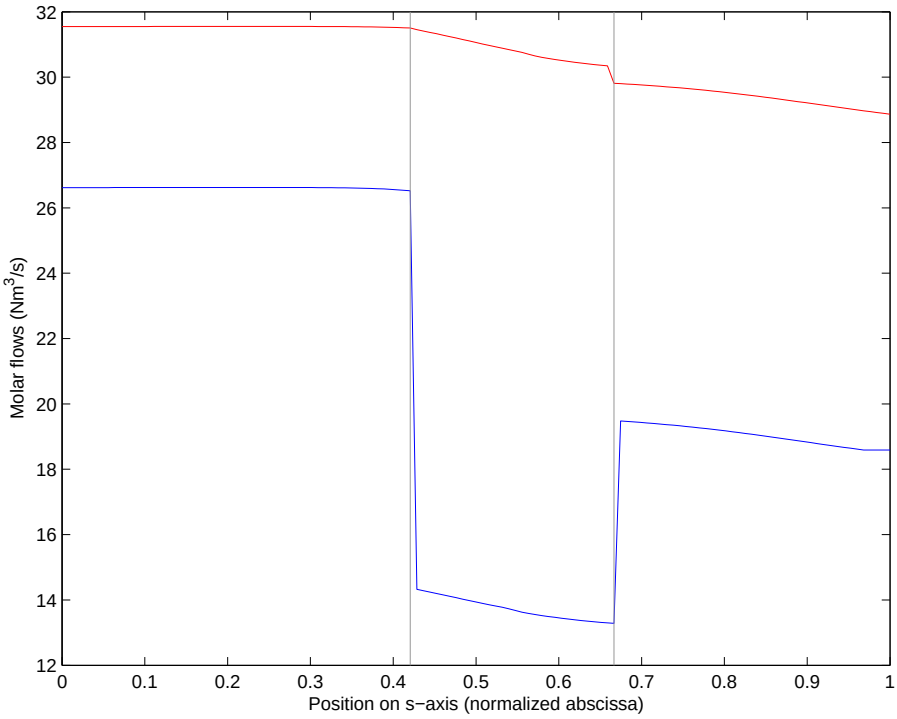

Figure 4.4: Liquid (blue) and gas (red) molar flow profiles in HP column for case B. Vertical grey lines indicate the junctions between homogeneous packed sections.

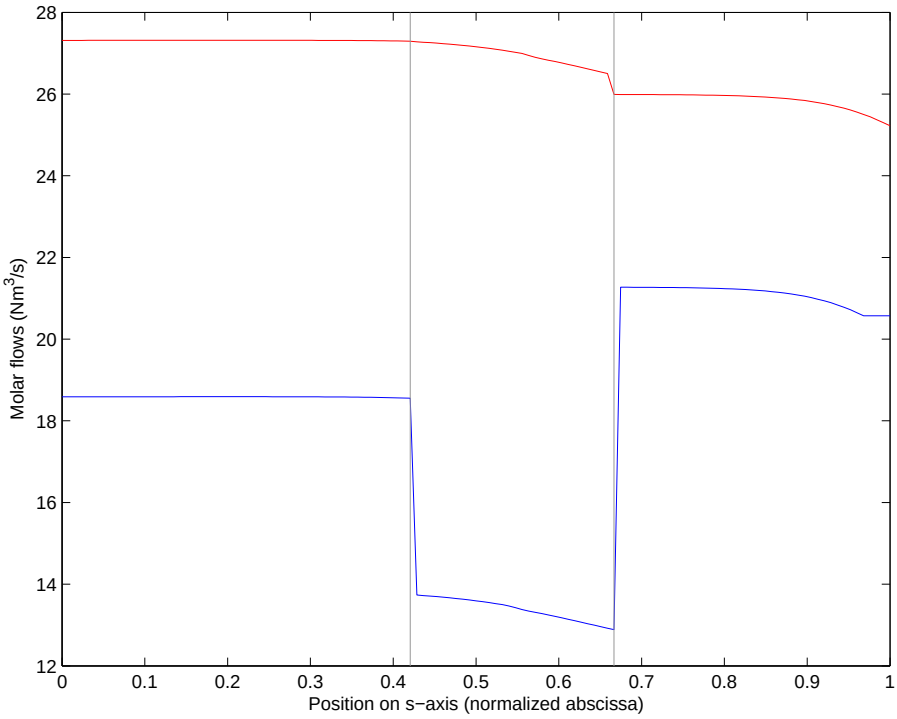

Figure 4.5: Liquid (blue) and gas (red) molar flow profiles in HP column for case C. Vertical grey lines indicate the junctions between homogeneous packed sections.

Case	Pressure (bar)	Bottom temperature (K)	Top temperature (K)
A	5.7	100	95
B	5.67	100	95.5
C	5.4	98.7	95

Table 4.1: Pressure and temperature values used to simulate the static cases with the PDE model

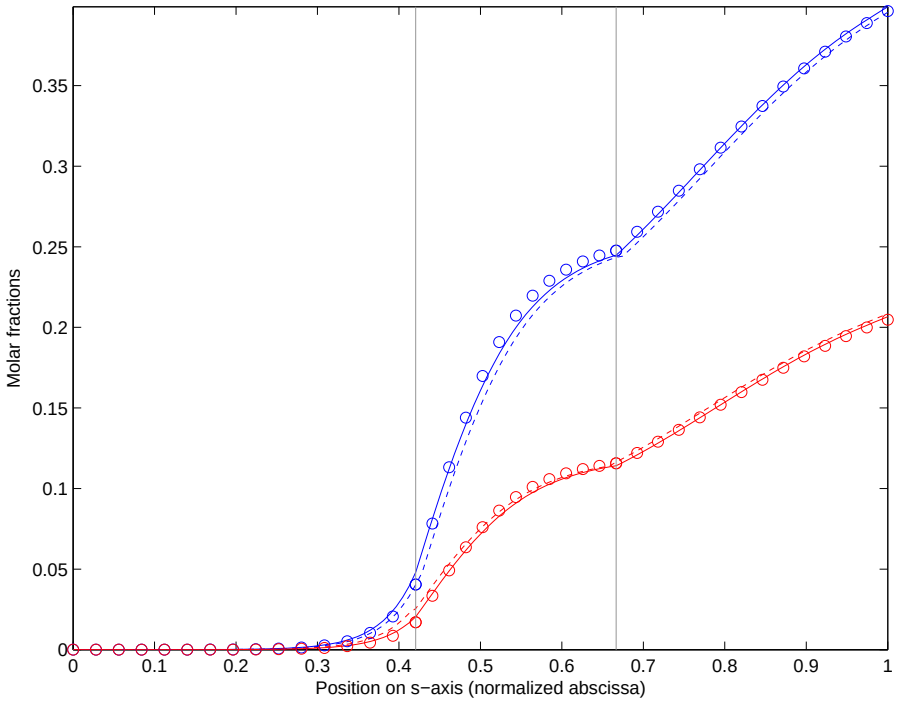

Figure 4.6: Comparison of the lumped component molar fraction profiles in HP column, case A. *Blue:* liquid phase, *red:* gas phase. *Circles:* HYSYS values, *solid:* zero-order term of the static outputs, *dashed:* static-outputs up to order 1 in ϵ. Vertical grey lines indicate the junctions between homogeneous packed sections.

fraction of the lumped component. We take $\sigma_L = \frac{L}{\overline{\mu}_L}$, with the same $\overline{\mu}_L$ for each case. The best fits between HYSYS and the PDE model are obtained with the following values:

$$\overline{\mu}_L = 0.4 \text{ m.s}^{-1}, \quad \begin{cases} \lambda_L = 20 \text{ Nm}^3.\text{s}^{-1}.\text{m}^{-1}, \\ \lambda_V = 10\lambda_L, \end{cases} \qquad \epsilon = \begin{cases} 0.226 & \text{for case A,} \\ 0.225 & \text{for case B,} \\ 0.246 & \text{for case C.} \end{cases}$$

Figures 4.6, 4.7 and 4.8 illustrate the molar fraction profiles obtained with the PDE model for the three cases. Figures 4.9, 4.10 and 4.11 display the same results in log-scale, to illustrate the good match with the HYSYS model also in the high-purity region. Figures 4.12, 4.13 and 4.14 display the liquid and gas hold-up profiles obtained for each case.

Note that the value $\mu_L = 0.4m/s$ is highly different from the expected $0.08m/s$. Here in the static simulations, the liquid speed plays no role; this result might indicate that only a small amount of the liquid hold-up actually participates to the separation process. Note also

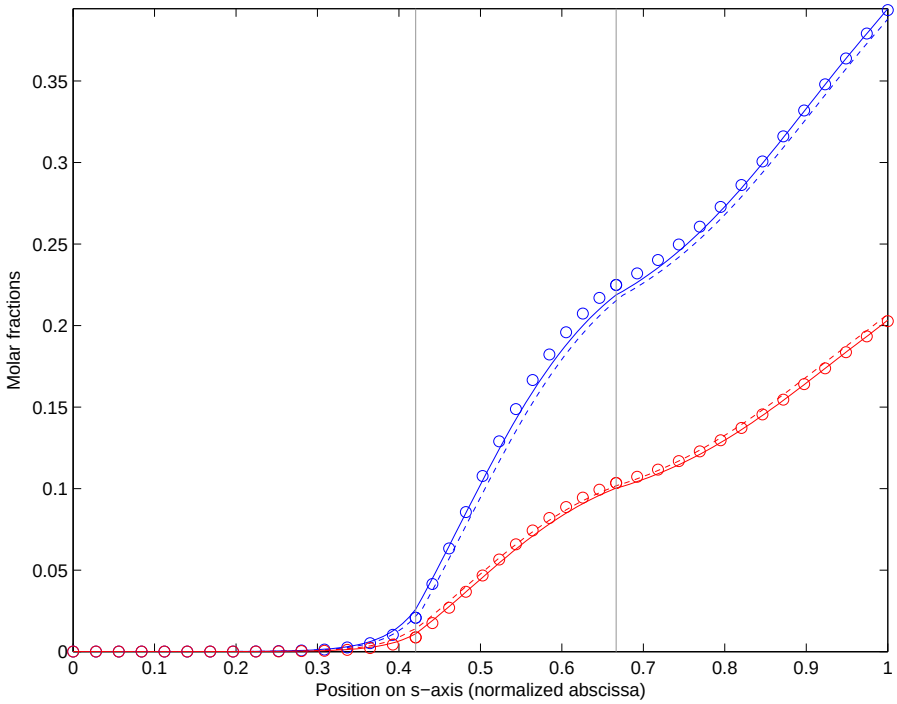

Figure 4.7: Comparison of the lumped component molar fraction profiles in HP column, case B. *Blue:* liquid phase, *red:* gas phase. *Circles:* HYSYS values, *solid:* zero-order term of the static outputs, *dashed:* static-outputs up to order 1 in ϵ. Vertical grey lines indicate the junctions between homogeneous packed sections.

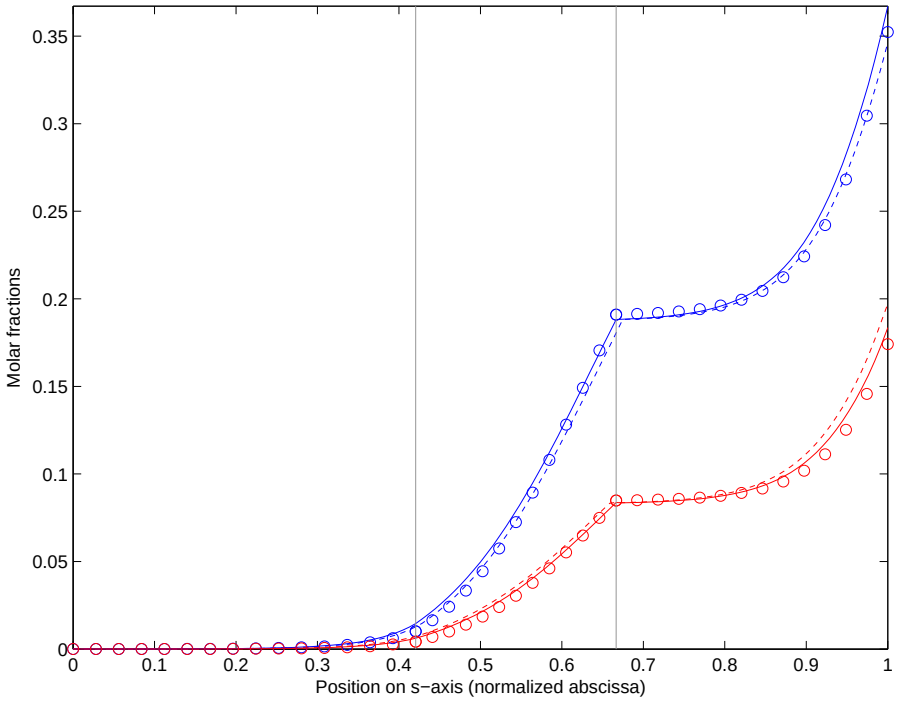

Figure 4.8: Comparison of the lumped component molar fraction profiles in HP column, case C. *Blue:* liquid phase, *red:* gas phase. *Circles:* HYSYS values, *solid:* zero-order term of the static outputs, *dashed:* static-outputs up to order 1 in ϵ. Vertical grey lines indicate the junctions between homogeneous packed sections.

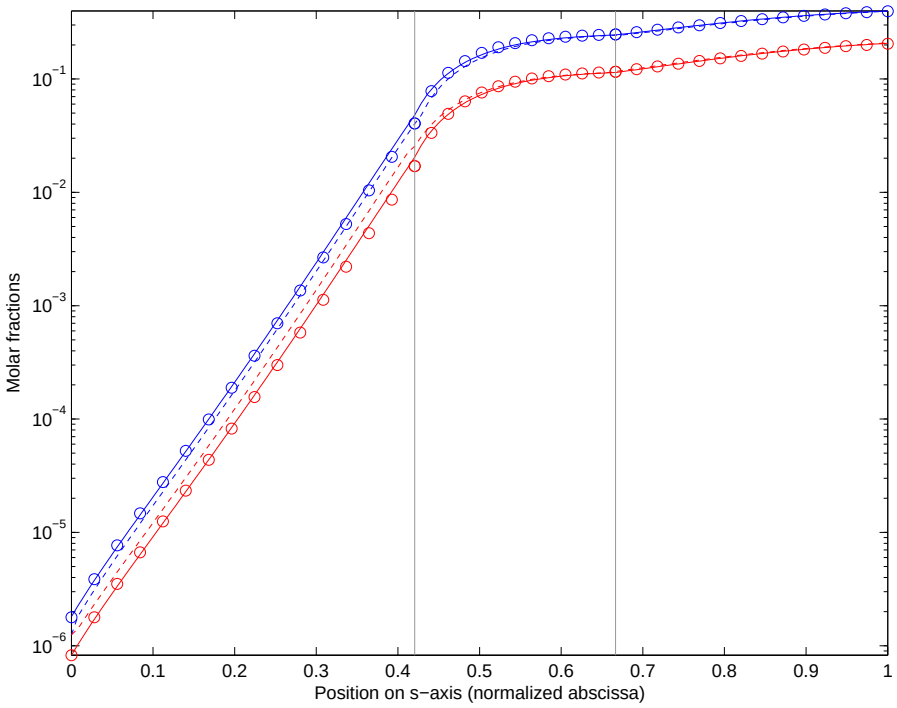

Figure 4.9: Comparison of the lumped component molar fraction profiles (in log scale) in HP column, case A. *Blue:* liquid phase, *red:* gas phase. *Circles:* HYSYS values, *solid:* zero-order term of the static outputs, *dashed:* static-outputs up to order 1 in ϵ. Vertical grey lines indicate the junctions between homogeneous packed sections.

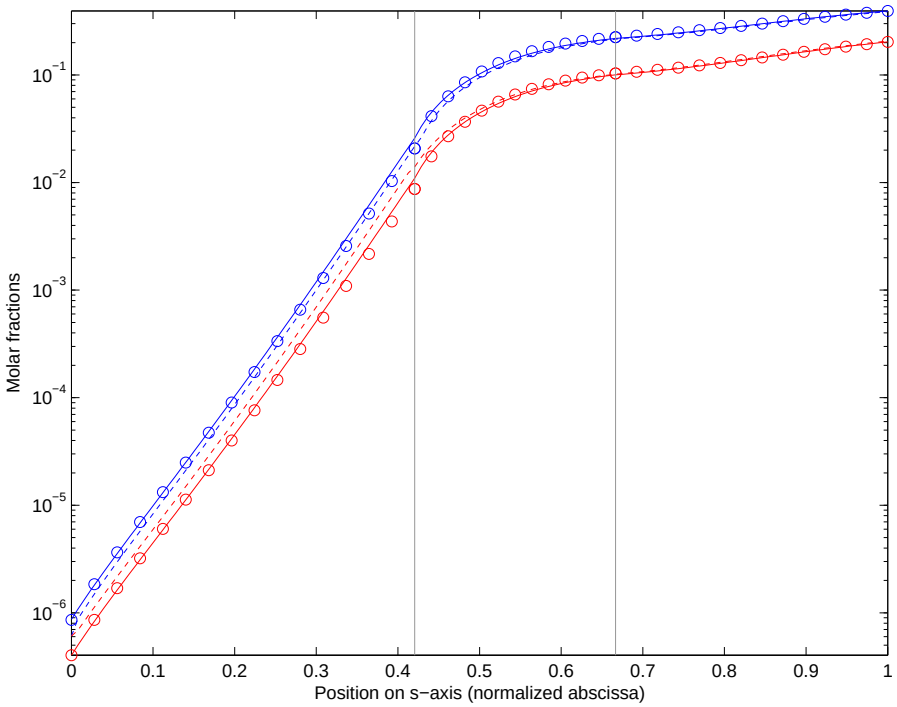

Figure 4.10: Comparison of the lumped component molar fraction profiles (in log scale) in HP column, case B. *Blue:* liquid phase, *red:* gas phase. *Circles:* HYSYS values, *solid:* zero-order term of the static outputs, *dashed:* static-outputs up to order 1 in ϵ. Vertical grey lines indicate the junctions between homogeneous packed sections.

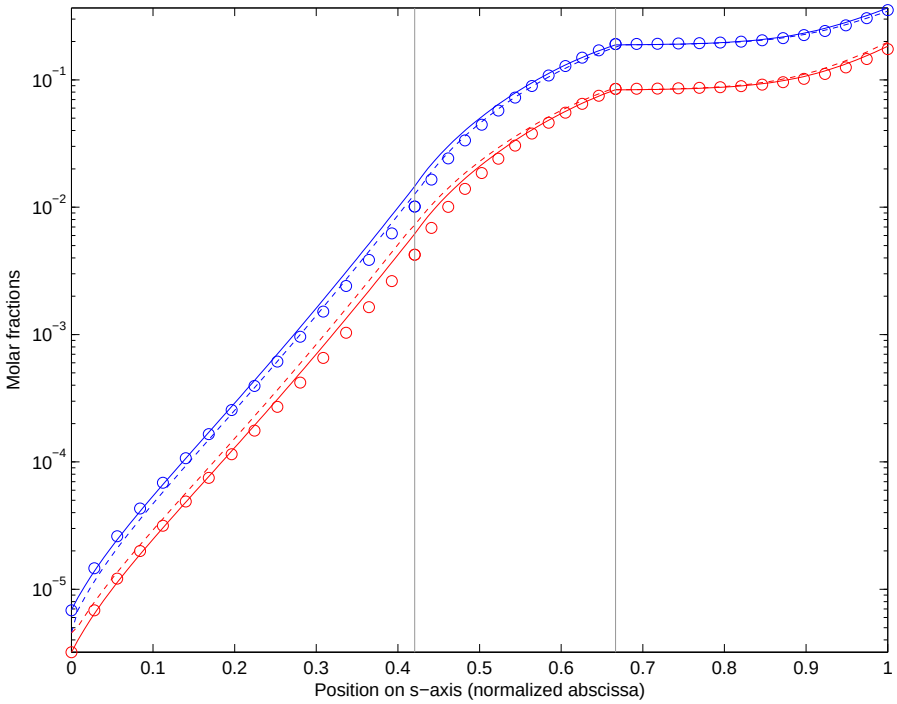

Figure 4.11: Comparison of the lumped component molar fraction profiles (in log scale) in HP column, case C. Blue: liquid phase, *red:* gas phase. *Circles:* HYSYS values, *solid:* zero-order term of the static outputs, *dashed:* static-outputs up to order 1 in ϵ. Vertical grey lines indicate the junctions between homogeneous packed sections.

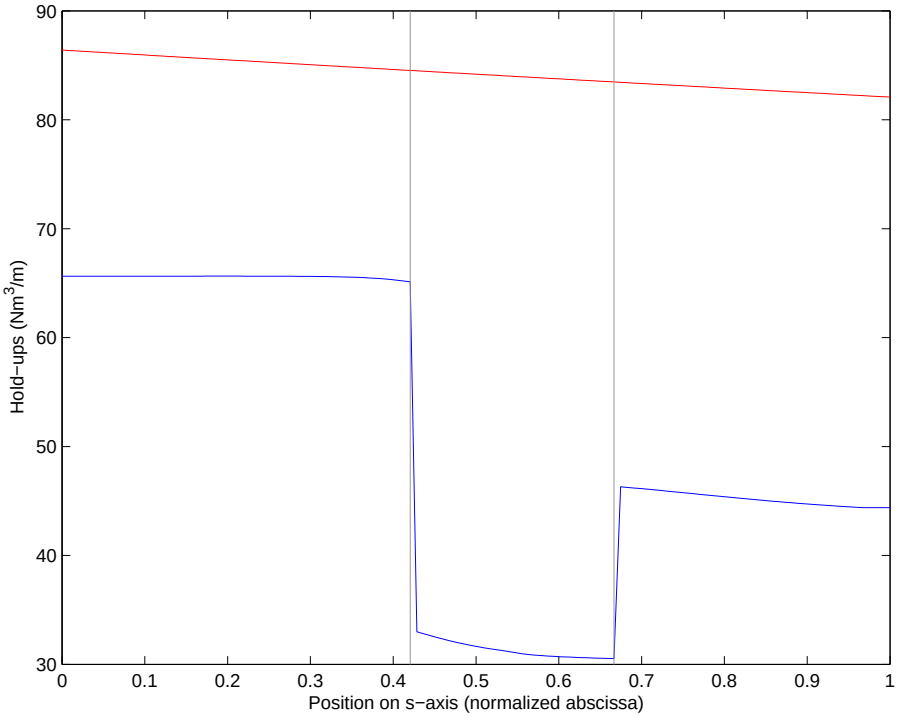

Figure 4.12: Linear molar hold-ups obtained with the PDE model for case A. *Blue:* liquid hold-up σ_L. *Red:* gas hold-up σ_V. Vertical grey lines indicate the junctions between homogeneous packed sections.

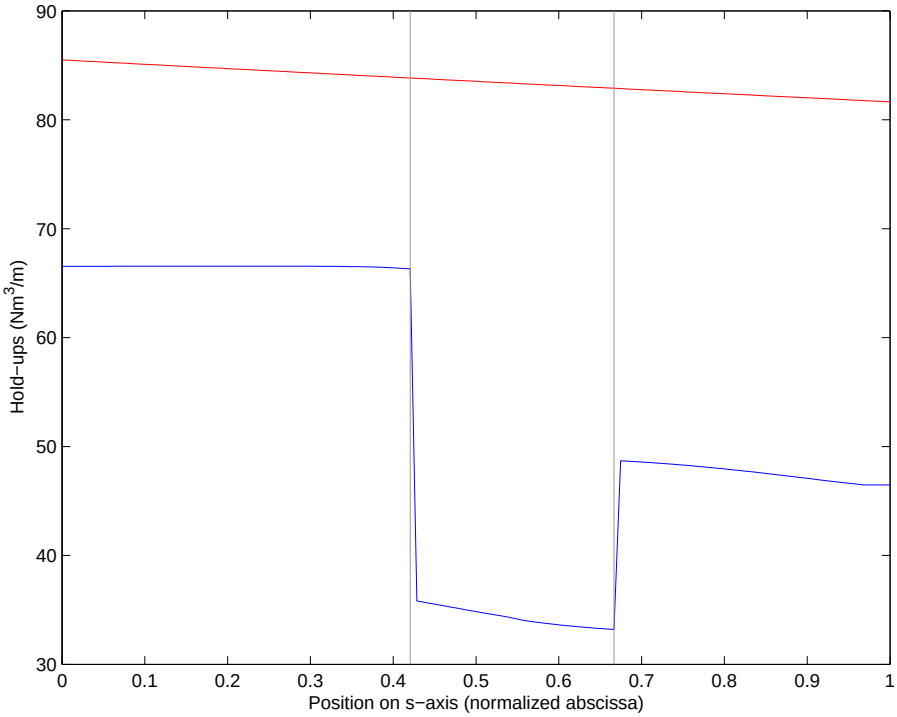

Figure 4.13: Linear molar hold-ups obtained with the PDE model for case B. *Blue:* liquid hold-up σ_L. *Red:* gas hold-up σ_V. Vertical grey lines indicate the junctions between homogeneous packed sections.

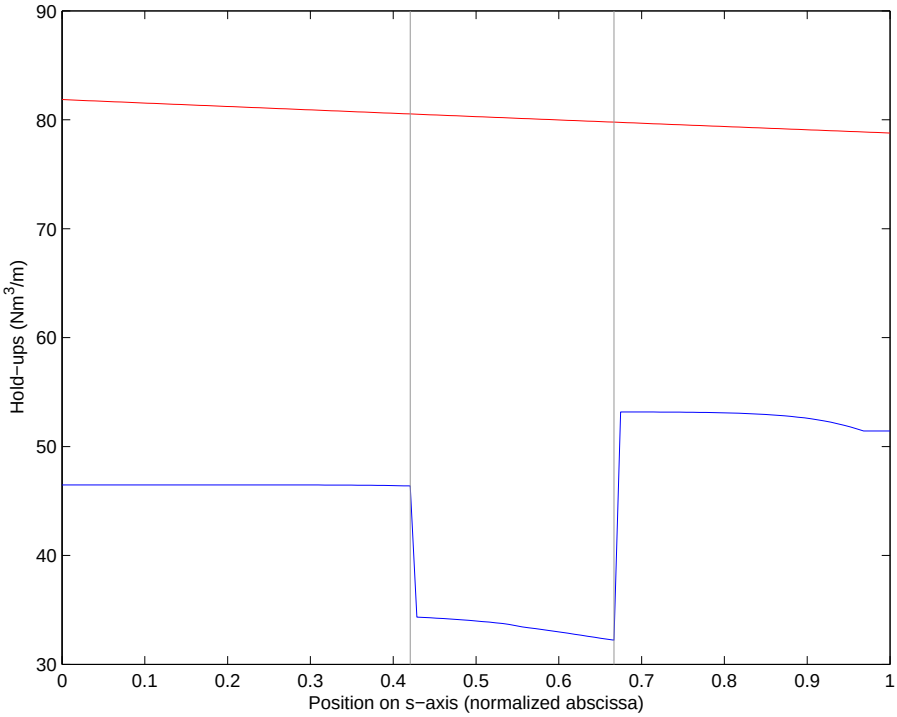

Figure 4.14: Linear molar hold-ups obtained with the PDE model for case C. *Blue:* liquid hold-up σ_L. *Red:* gas hold-up σ_V. Vertical grey lines indicate the junctions between homogeneous packed sections.

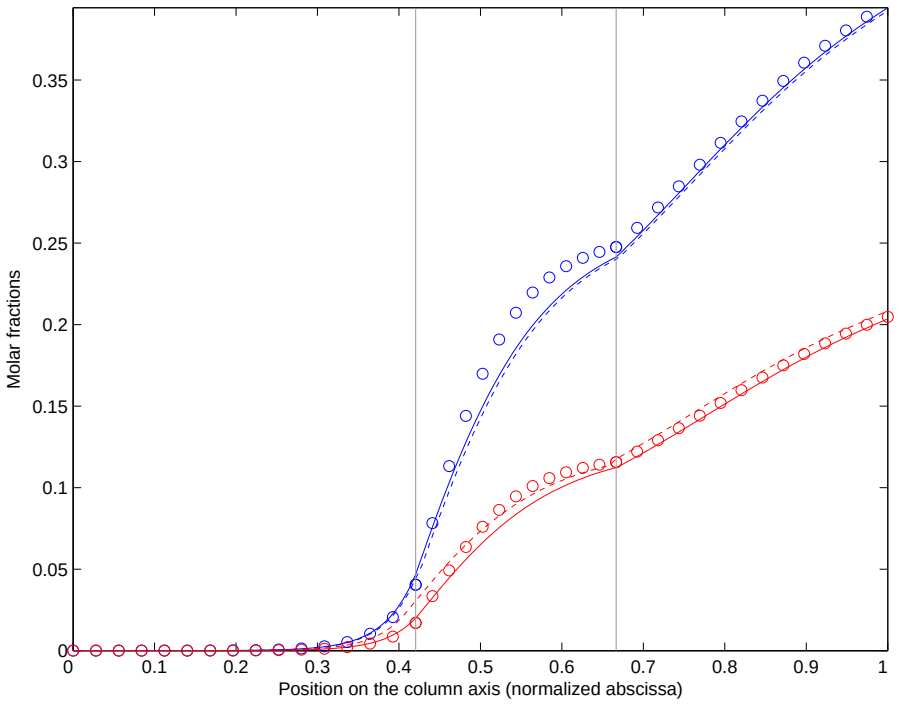

Figure 4.15: Comparison of the lumped component molar fraction profiles in HP column, case A, with the theoretical value $\mu_L = 0.08m/s$. *Blue:* liquid phase, *red:* gas phase. *Circles:* HYSYS values, *solid:* zero-order term of the static outputs, *dashed:* static-outputs up to order 1 in ϵ. Vertical grey lines indicate the junctions between homogeneous packed sections.

that the liquid hold-ups we obtain are comparable to the gas hold-up, which runs counter the frequent assumption $\sigma_V << \sigma_L$. Another explanation could be drawn from Fig. 4.15 showing the obtained composition profiles with $\mu_L = 0.08m/s$ in case A. As one can see, the HYSYS /PDE-model mismatch is essentially located in the middle subsection, where reflux rate is highly different from the top and bottom subsections. This might indicate that the theoretical tray height varies depending on the considered subsection, contrary to our initial assumption. ϵ (here 0.31) is the same for the whole column, so the only subsection-depending parameter we can adjust in the PDE-model is σ_L, by tuning the value of μ_L. Hence the observed discrepancy $\mu_L \neq \mathcal{V}_L = 0.08m/s$. In the following, we keep $\mu_L = 0.4m/s$.

HYSYS simulations use a ternary mixture model, thus the volatility of the lumped pseudo-component depends on a varying proportion of O_2 and Ar. This information is lost when straightly using a binary mixture as we do for the PDE model. Thus we have to check if, without changing the hydraulic estimations, one still obtains a reasonable approximation of the HYSYS profiles with α constant along s. The resulting estimated profiles are depicted on Figures 4.16, 4.17 and 4.18. The value taken for α is the mean of the HYSYS relative volatility over the bottom packed section. One obtains the illustrated results with

$$\alpha = \begin{cases} 0.395, & \text{case A} \\ 0.396, & \text{case B} \\ 0.392, & \text{case C} \end{cases}, \quad \epsilon = \begin{cases} 0.289, & \text{case A} \\ 0.294, & \text{case B} \\ 0.353, & \text{case C} \end{cases}$$

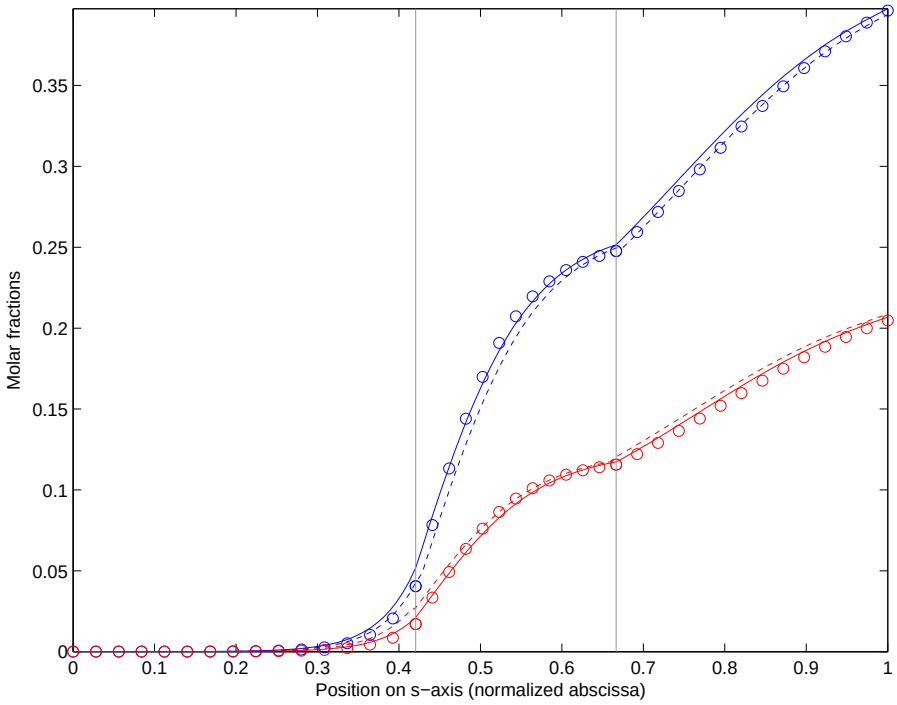

Figure 4.16: Comparison of the lumped component molar fraction profiles in HP column with constant α, case A. *Blue:* liquid phase, *red:* gas phase. *Circles:* HYSYS values, *solid:* zero-order term of the static outputs, *dashed:* static-outputs up to order 1 in ϵ. Vertical grey lines indicate the junctions between homogeneous packed sections.

Note that at the bottom of the column, the oxygen/argon ratio is large and stable, thus the volatility of the pseudo-component is close to the oxygen's and less subject to variations than at the top of the column.

The discrepancy between the HYSYS and PDE models is limited for cases A and B, yet more concerning in case C. This can be easily apprehended in terms of molar-fraction wave-speeds. X being small over the top packed section, one can take $k'(X) = \alpha$ over this region. Thus, neglecting the diffusion for the moment, the molar fractions profile would behave as a traveling wave with speed

$$w_0 = \frac{-L + V\alpha}{\sigma_L + \alpha\sigma_V} < 0.$$

The estimation $\widetilde{\alpha}$ we use is inferior to the α predicted by HYSYS over the top packed section. Thus we obtain in first approximation a speed

$$\widetilde{w} = \frac{-L + V\alpha}{\sigma_L + \alpha\sigma_V} - (\alpha - \widetilde{\alpha})\frac{L + V\frac{\sigma_L}{\sigma_V}}{\sigma_V\left(\frac{\sigma_L}{\sigma_V} + \alpha\right)^2} = w_0 - \Delta w, \quad \Delta w > 0.$$

The wave obtained with the PDE model is then more repelled from the top boundary than in the HYSYS model. This means that the PDE model predicts less undesirable oxygen at the top of the column than HYSYS . We have to compensate by increasing the diffusion, to allow more O_2 to reach the top of the column by diffusion, against the increased downwards convection. This explains the increase of ϵ from 0.246 to 0.353 in case C, for instance. Yet the

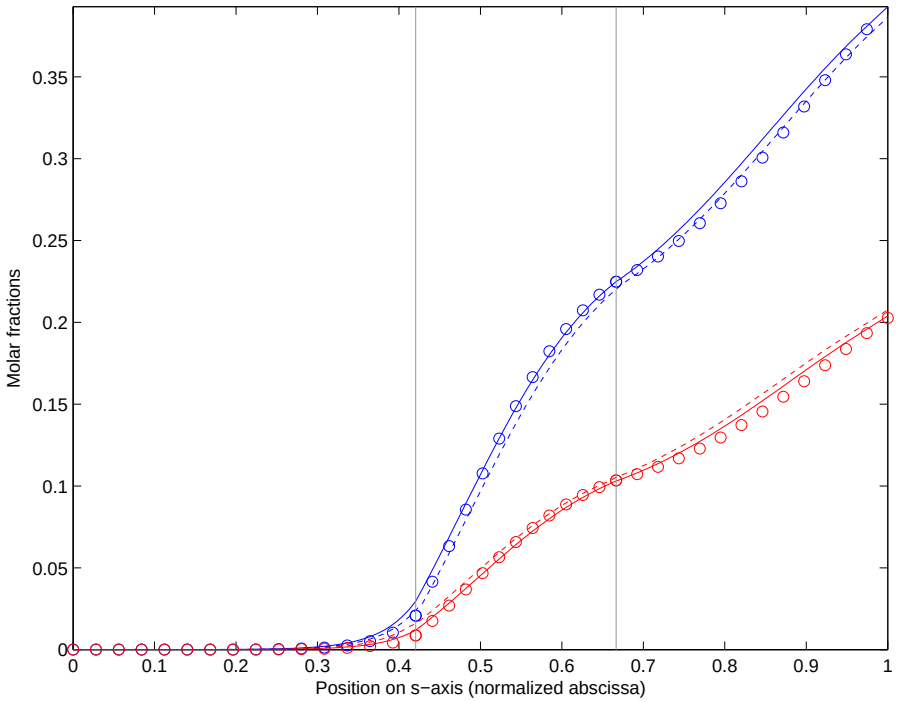

Figure 4.17: Comparison of the lumped component molar fraction profiles in HP column with constant α, case B. *Blue:* liquid phase, *red:* gas phase. *Circles:* HYSYS values, *solid:* zero-order term of the static outputs, *dashed:* static-outputs up to order 1 in ϵ. Vertical grey lines indicate the junctions between homogeneous packed sections.

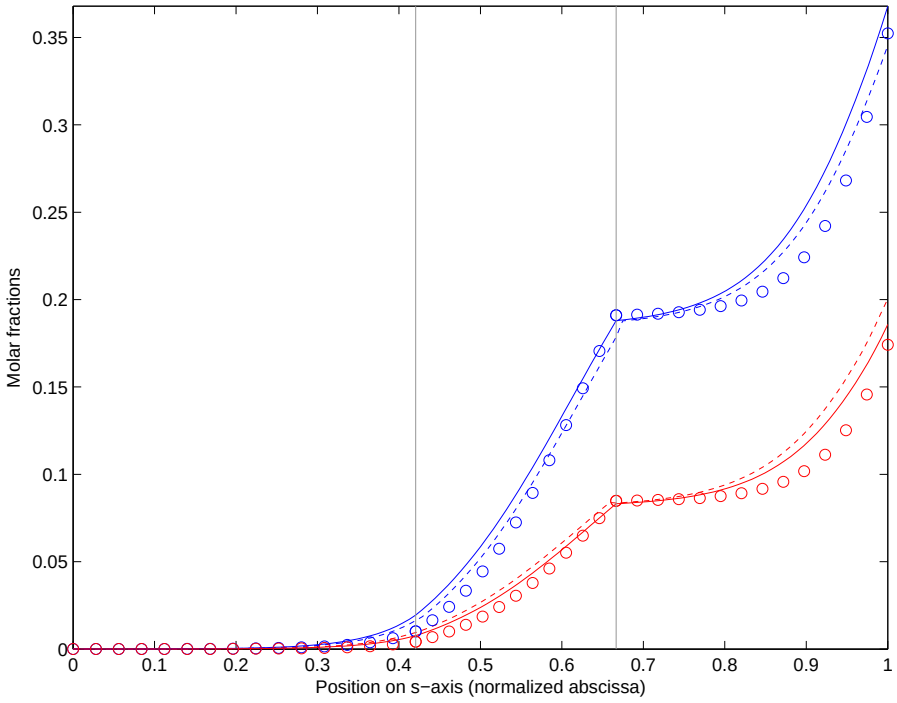

Figure 4.18: Comparison of the lumped component molar fraction profiles in HP column with constant α, case C. *Blue:* liquid phase, *red:* gas phase. *Circles:* HYSYS values, *solid:* zero-order term of the static outputs, *dashed:* static-outputs up to order 1 in ϵ. Vertical grey lines indicate the junctions between homogeneous packed sections.

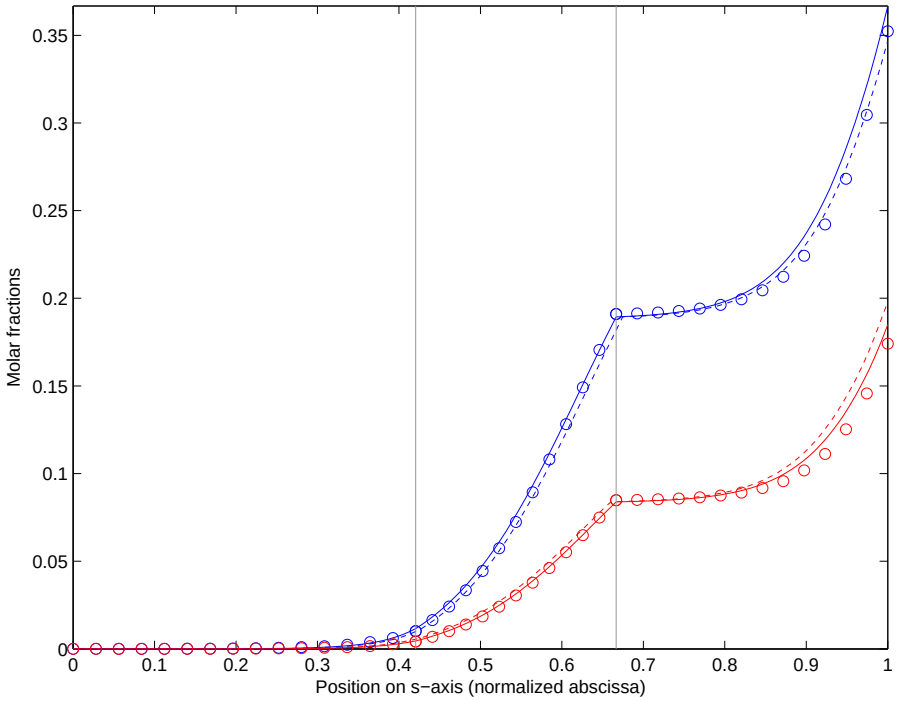

Figure 4.19: In case C, molar fractions in the bottom packed section are correctly estimated with a constant α, if no change is made on ϵ. *Blue:* liquid phase, *red:* gas phase. *Circles:* HYSYS values, *solid:* zero-order term of the static outputs, *dashed:* static-outputs up to order 1 in ϵ. Vertical grey lines indicate the junctions between homogeneous packed sections.

variation of ϵ impacts also the bottom packed sections, where there is less Δw to compensate. Consequently, the oxygen molar fraction will unduly increase in these regions. In addition, since case C has about 30% less liquid than other cases in the top packed section, ϵ has to change more to compensate a bigger Δw. Hence a greater discrepancy in case C in the bottom packed section. Figure 4.19 shows that using the constant α with the value of ϵ previously used for simulation with a s-dependent α allows retrieving a correct estimation of the molar fractions over the bottom packed sections. Yet, at shown on Fig. 4.20, this is at the expense of the accuracy over the high-purity domain.

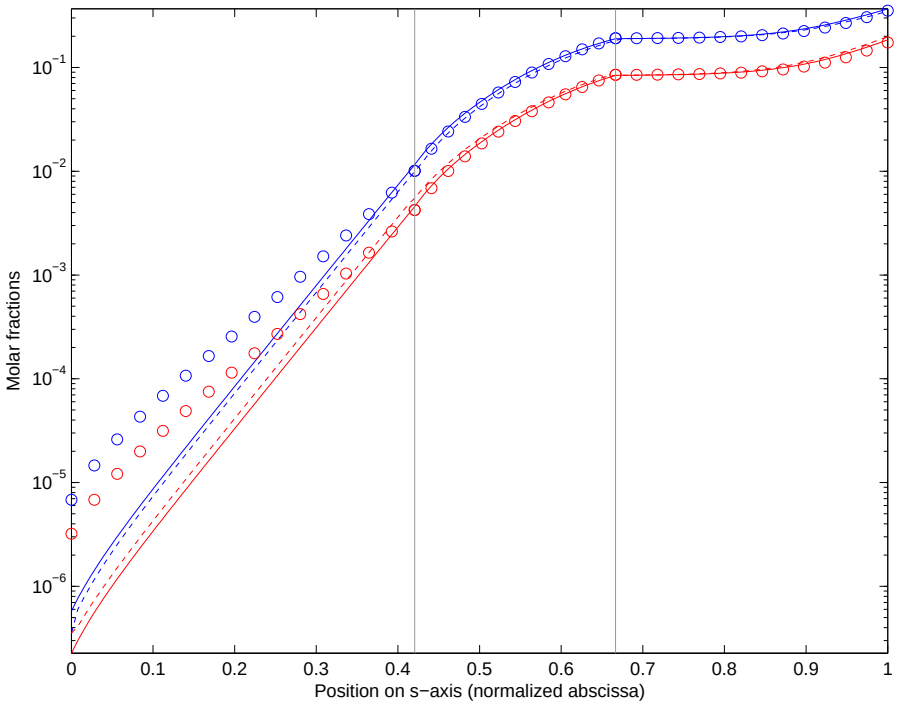

Figure 4.20: In case C, using a constant α, without changing ϵ yields overestimated purification at the top of the HP column. *Blue:* liquid phase, *red:* gas phase. *Circles:* HYSYS values, *solid:* zero-order term of the static outputs, *dashed:* static-outputs up to order 1 in ϵ. Vertical grey lines indicate the junctions between homogeneous packed sections.

4.5 Dynamic operation scenario

The dynamic scenario we use is based on a 10 hours record of the air separation plant operation, on July 4^{th} 2011, from 10 AM to 10 PM. Figure 4.21 shows the input and output flows of the HP column during the scenario. Gas and liquid flows from V03 (as well as the corresponding molar fractions) are obtained by considering an isenthalpic flash (Joule-Thomson expansion) of the incoming liquid air, whose composition, temperature and pressure are known, down to the pressure of the HP column (shown on Fig. 4.22).

Since our model assumes equal heats of vaporization for all the components, the internal re-vaporization of the liquid, which can be seen for example on the HYSYS plots 4.3, 4.4, 4.5, will not appear. To account for the increase of reflux rate due to this effect, we add to V_{air} at the bottom of the column a fictive amount of gas ΔV. An equivalent quantity is subtracted to the liquid at the bottom. We take $\Delta V = 0.07 V_{air}$, which is reasonable according to HYSYS (in case A, the gas flow increases of 7.6% of its value at the bottom because of re-vaporization; in case B, the increase is of 7.4%, in case C, 6.3%). Figure 4.23 shows the internal flows obtained this way. These internal flows are more similar to those obtained for cases A-B, rather than case C. Consequently, when borrowing estimated parameters from the static cases, we will take them from case A.

The column is equipped with a top O_2 concentration analyzer whose span is 0-10 ppm. The typical resolution of such an analyzer is about 0.1 ppm. This analyzer measures the O_2 gas molar fraction at the level of the liquid nitrogen draw. Figure 4.24 shows the estimation given by the analyzer.

The oxygen molar fraction not to be exceeded in operation is 1 ppm at the top of the column. It can hardly be 6×10^{-9} as indicated by the analyzer's signal, because this would require about 2 m of supplementary packing according to Fig. 4.25. Then is is reasonable to consider that the top oxygen molar fraction is only some 0.1 ppm below the 1 ppm threshold; yet the molar fraction of the pseudo-component O_2, Ar, estimated by the binary PDE-model, should be round 1 ppm. It also means that the top analyzer is here of little use for parameter estimation.

A second analyzer is located at the level of the lean liquid draw. It measures the O_2 molar fraction in the gas. The expected molar fraction is only a few percents, which is in the span of the analyzer (0 to 100 %). Figure 4.26 shows the measured molar fraction.

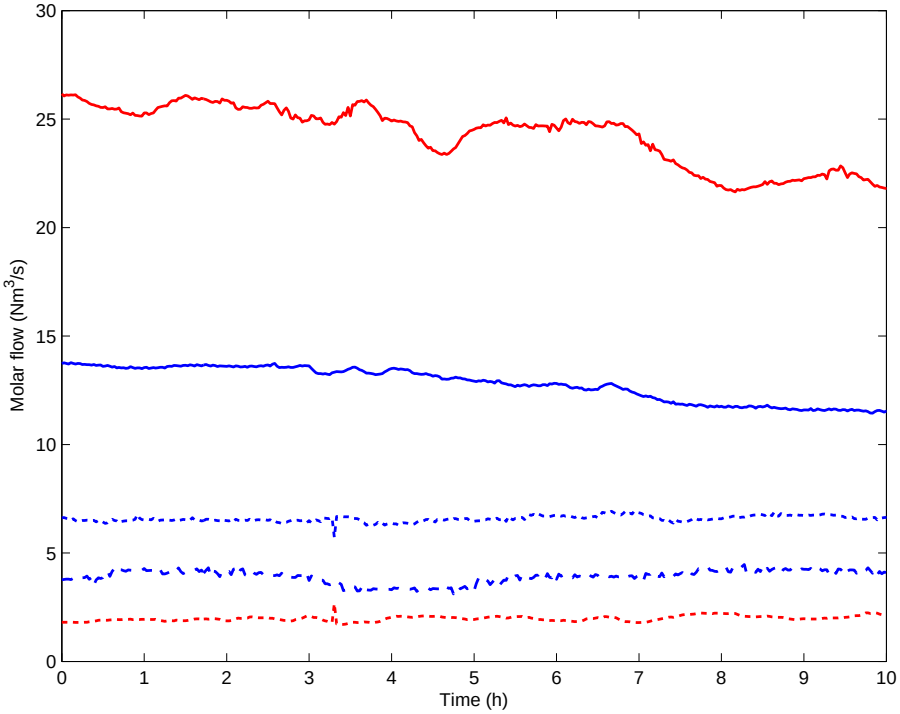

Figure 4.21: Input and output molar flows for the dynamic scenario. *Solid red:* air inlet flows V_{air}, *solid blue:* Lean Liquid draw L_{HP}^{LL}, *dotted blue:* liquid flow from V03 $L_{V03\rightarrow}$, *dashed blue:* liquid drawn on top for production L_{HP}^{prod}, *dotted red:* gas flow from V03 $V_{V03\rightarrow}$.

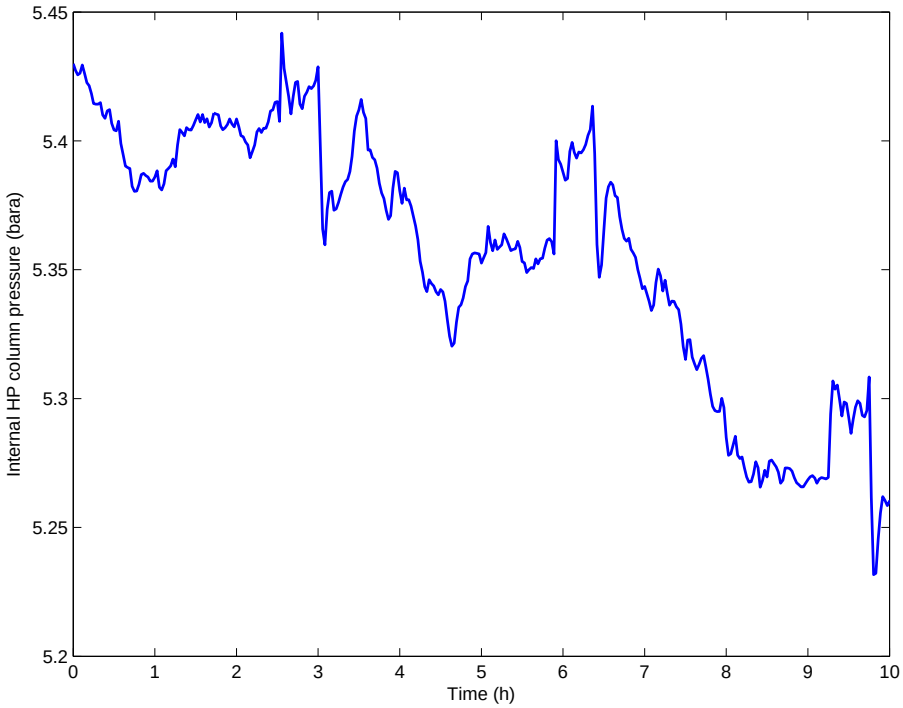

Figure 4.22: Internal pressure of HP column. This pressure is measured at the top of the column, and is assumed to be constant along s since the pressure drop given by HYSYS is only of 5.5 mbar.

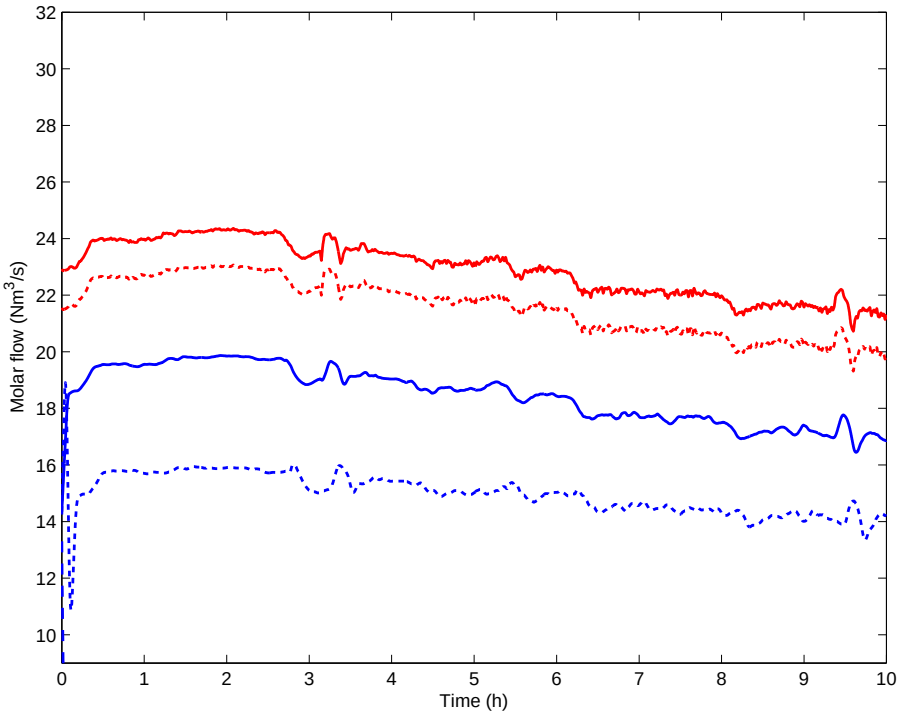

Figure 4.23: Internal gas and liquid molar flows. *Solid blue:* liquid molar flow averaged over the top section. *Dashed blue:* liquid molar flow averaged over the middle section. *Dotted blue:* liquid molar flow averaged over the bottom section. *Solid red:* gas molar flow over the top and middle section. *Dotted red:* gas molar flow over the bottom section.

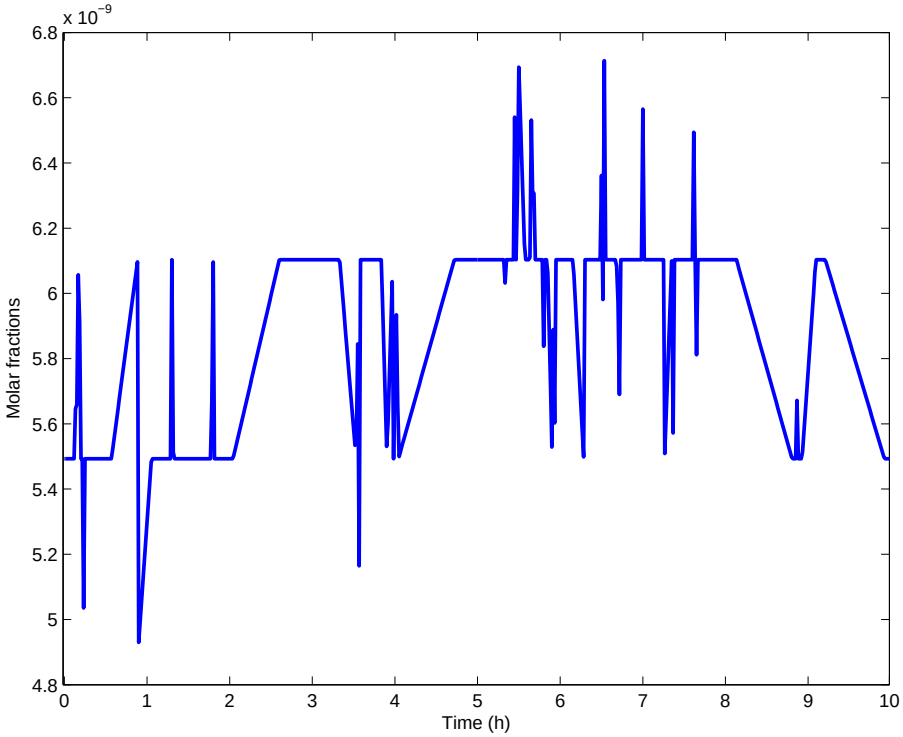

Figure 4.24: Estimation of top O_2 molar fraction given by the corresponding analyzer.

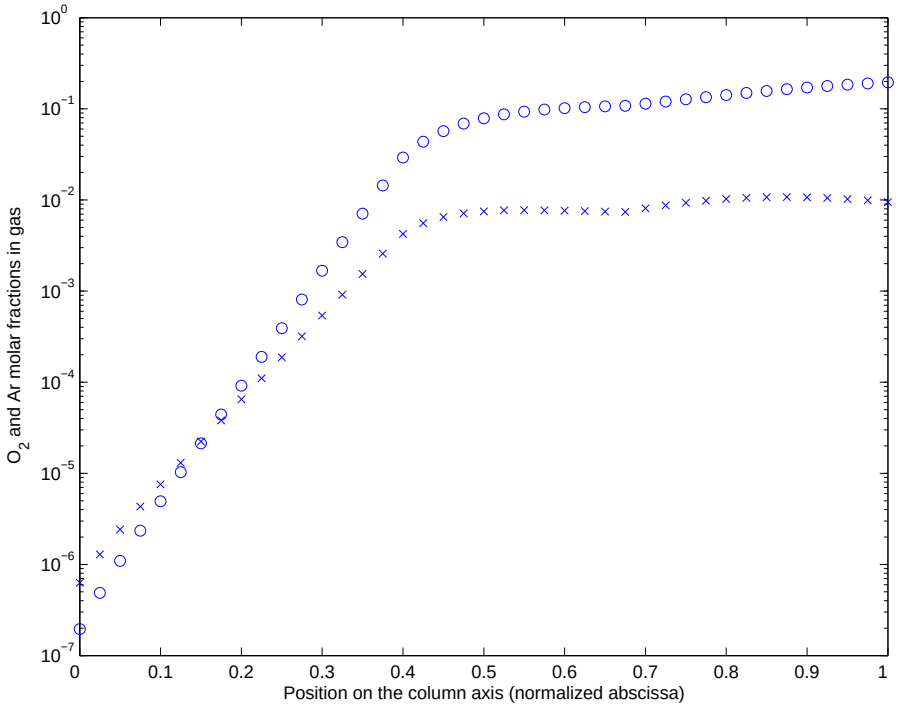

Figure 4.25: Semilog plot of the Oxygen (circles) and Argon (crosses) composition profiles estimated by HYSYS in the static case A. The space-scale is obtained on the basis of an invariant theoretical tray height.

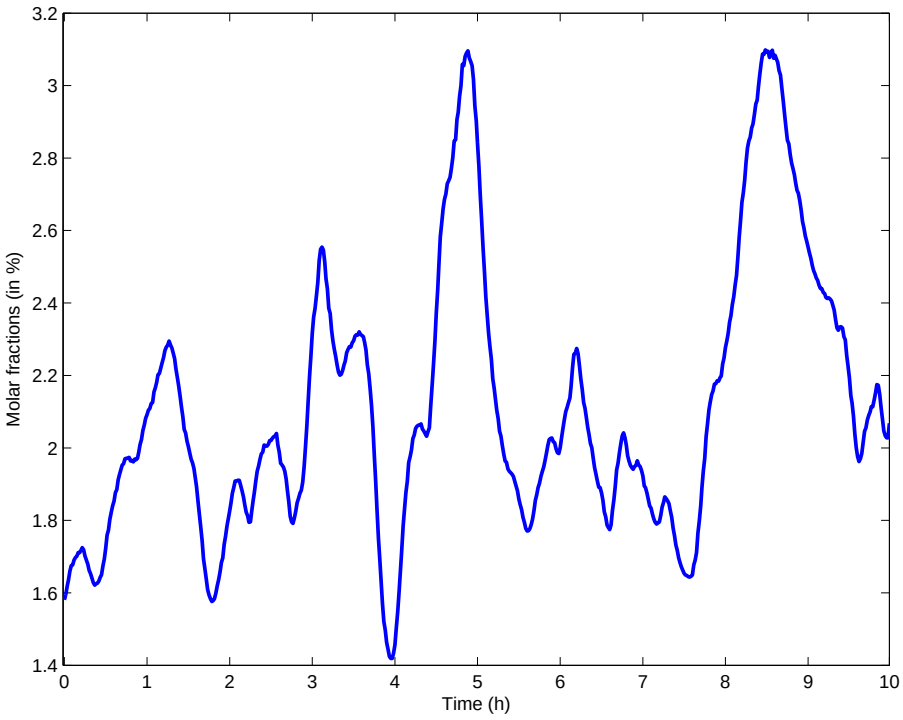

Figure 4.26: Measure of O_2 molar fraction in the gas phase, in front of the lean liquid draw. The molar fraction is in %.

4.6 Dynamic simulation

We play the scenario using a $0.1m$ space-step and a $0.1s$ time-step. The following values are directly borrowed from the simulation of the static case A:

$$\mu_L = 0.4\text{m/s}, \quad \alpha = 0.395, \quad \epsilon = 0.289,$$

In other words, the value of ϵ is the one that preserves the top composition in the static reference case, in spite of the constant α. We take $\mathcal{V}_L = 0.08m/s$ for the liquid speed. Figure 4.27 illustrates the molar fractions estimated by the model at top. The values are close to the 1 ppm threshold, as expected. As shown on Figure 4.28, this estimation at the Lean Liquid draw point coincides with the measurements in terms of magnitude, but with an advance of about 15 min, as visible on the zoomed Fig. 4.29.

The time-shift can be corrected by decreasing the liquid speed to $\mathcal{V}_L = 0.02m/s$, as shown on Fig. 4.30 and 4.31. Comparing these figures with the previous ones, it appears that the change on $\mathcal{V}_L$ slightly affects the shape and the amplitude of the estimated composition variations, since it impacts the constructive or destructive interplay between the various feeds and draws of the column. The same effects apply to the top estimated composition, as shown on Fig. 4.32.

Since our reference signal at the Lean Liquid draw point is provided by an analyzer, one could imagine that the observed 15 min time-shift is partially due to the transport delay of the sample, from the column to the distant analyze bay. In that case, it is not the estimation which is in advance, but the reference which is delayed. It is yet unlikely that this phenomenon

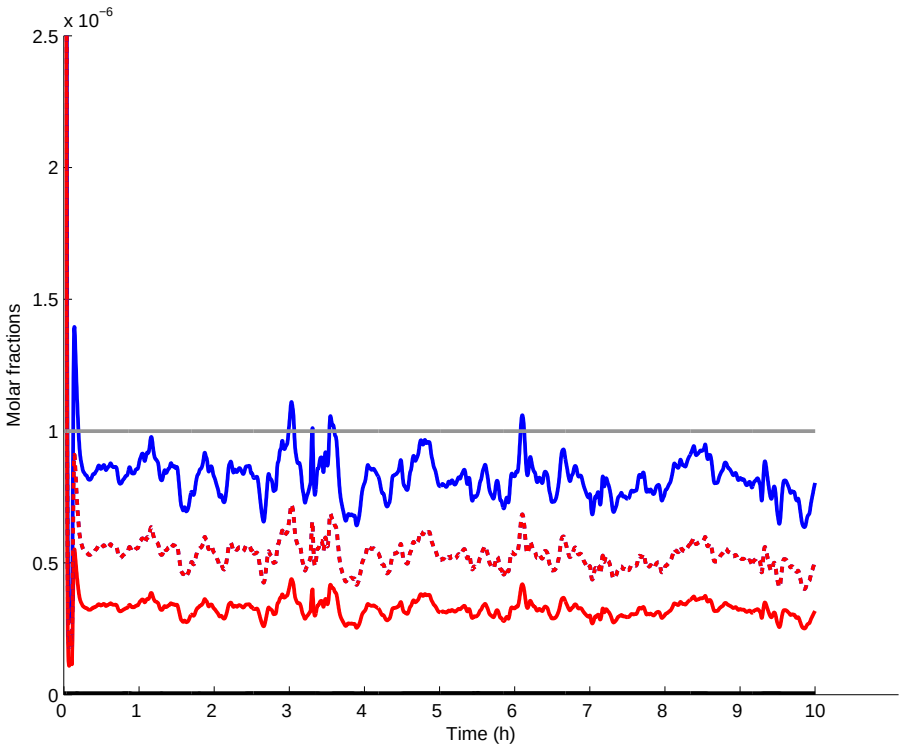

Figure 4.27: Composition estimation at top of the HP column with $\epsilon = 0.289$. *Blue:* X. *Red:* $k(X)$. *Dashed red:* $x = y$. *Grey:* contractual threshold. *Black:* analyzer.

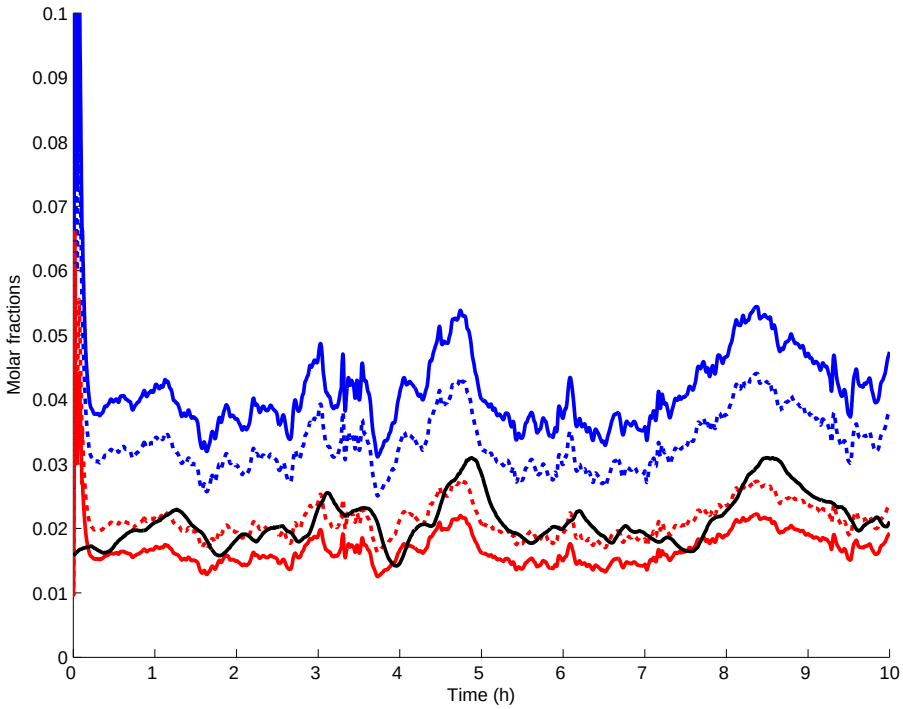

Figure 4.28: Composition estimation at the lean liquid draw point with $\epsilon = 0.289$. *Blue:* X. *Dashed blue:* x. *Red:* $k(X)$. *Dashed red:* y. *Black:* analyzer.

is responsible for the whole delay. In addition, in [21], the liquid descent time is reported to be round 500-700 s for an APSA T7 column (total height: 11m, packed height: 8m). This yields $\mathcal{V}_L \in [0.01, 0.016] m/s$. And yet, this value is found using the liquid level transmitter at the bottom of the column, which introduces no measurement delay. In addition, one shall consider that the liquid flow / column diameter ratio of the APSA is similar to the HP column, so that the scale of the plant plays a limited role. Moreover, both the APSA and the HP column diameter are large enough to limit the impact of the rim on the hydraulics.

Both the APSA and the HP column include three liquid distributors, which could act as liquid buffers, decreasing the liquid average speed over the whole column (the experimental 0.02 m/s) while the liquid speed inside the packing (the theoretical 0.08 m/s) remains large. In [35] a distributor with dimensions and operating conditions similar to the HP column case is reported to hold 0.06 m of liquid. Its diameter is 3.5m, its total height is 0.35 m and the entering liquid flow is about $0.023 m^3/s$ ($15 N m^3/s$). This yields a liquid dwell-time[3]

$$\tau_L = \frac{1}{2} \frac{0.06 * \pi * \frac{3.5^2}{4}}{0.023} \simeq 12.5 s$$

which does not explain the observed time-shift. Sufficient buffering effects are only obtained with unrealistic retention height of the order of 1m. Simulations including simplified distributors dynamics based on Torricelli's relation and the numerical values from [35] yields to the same conclusion.

[3] the factor 1/2 in the calculation arises from the corrugated geometry of the distributor: half of its section holds liquid, while the remaining half is dedicated to gas circulation.

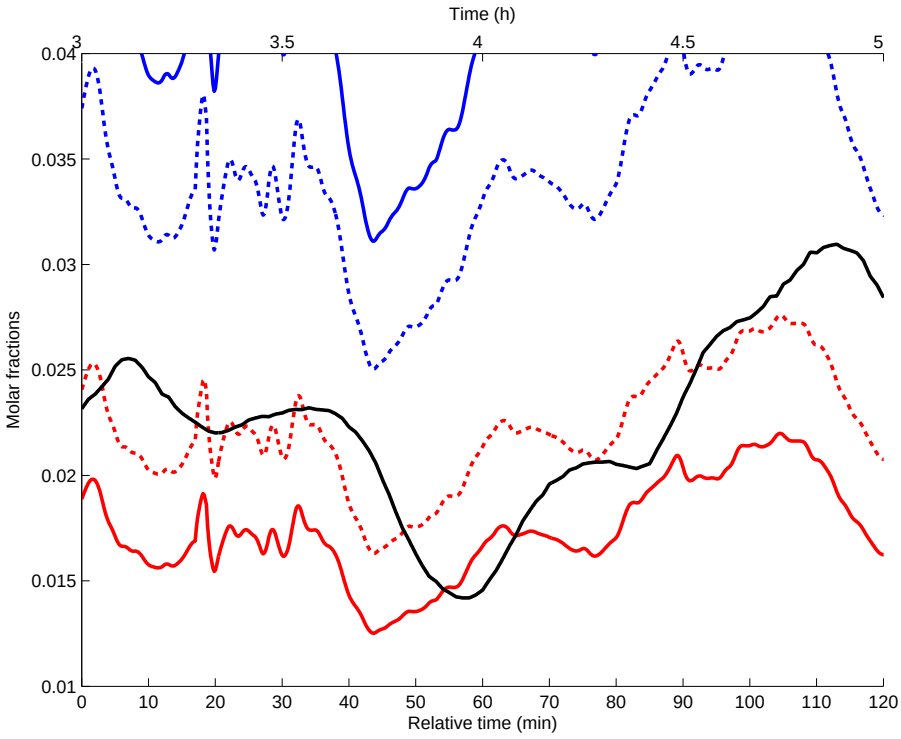

Figure 4.29: Composition estimation at the lean liquid draw point with $\epsilon = 0.289$ (zoom of Fig. 4.28 between 3 and 5 h). *Blue:* X. *Dashed blue:* x. *Red:* $k(X)$. *Dashed red:* y. *Black:* analyzer (almost zero).

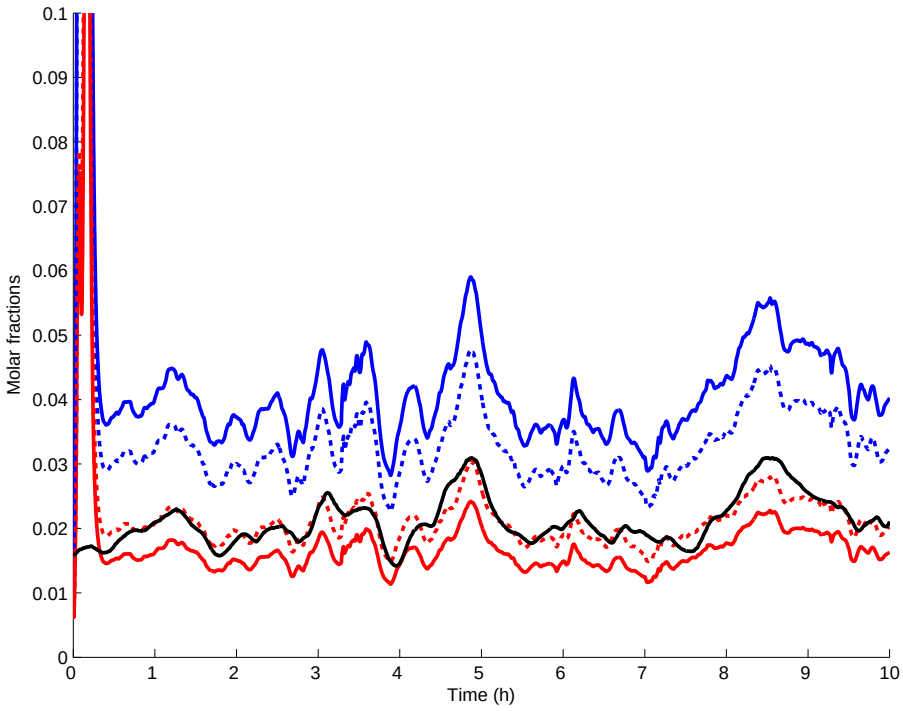

Figure 4.30: Composition estimation at the lean liquid draw point with $\epsilon = 0.289$, $\mathcal{V}_L = 0.02m/s$. *Blue:* X. *Dashed blue:* x. *Red:* $k(X)$. *Dashed red:* y. *Black:* analyzer.

Let us add that a certain dispersion regarding the liquid velocity also exists in the literature. For instance, [94] models a packed column with 19 equivalent trays (the equivalent tray height is 0.3 m). A liquid flow variation at the top of the column is fully transmitted to the bottom in about 75 s, which yields a liquid speed round 0.076 m/s. On the contrary, [46] and [47] use a tray hydraulic equation $L_i = k_d M_i$, where L_i stands for the liquid flow on tray i, M_i is the corresponding hold-up, and $k_d = 0.5min^{-1}$ is tuned from empirical data. Considering a classical equivalent tray height of 0.3 m, one obtains a liquid speed round $0.01m/s$.

In the following, we will use the empirically satisfying value $\mathcal{V}_\mathcal{L} = 0.02\ m/s$. Note yet that a larger liquid speed, as long as it does not excessively distort the composition estimation, may permit to use the PDE-model as a concentration predictor with a significant time advance, which could be of some use for feed-forward control strategies. To the limit, one could envisage instant liquid propagation as illustrated on Fig. 4.33, 4.34.

As for the static simulations, using a smaller ϵ (0.226 according to static case A) dramatically decreases the estimated top composition, whereas the estimation at the lean liquid level draw is little impacted. The corresponding simulations are depicted on Fig. 4.35 and 4.36.

As mentioned earlier, we use a linear relation between the liquid hold-up and the liquid flow: $\sigma_L = \frac{L}{\mu_L}$. Until now, the simulations have been done with $\mu_L = 0.4m/s$, empirically determined with the static simulations. This yields to a typical value $\sigma_L = 50Nm^3/m$ at the top of the column. Using $\mu_L = 0.08m/s$ (the theoretical liquid velocity) yields $\sigma_L = 250Nm^3/m$, which is in accordance with the packing capacity estimation. Finally, taking $\mu_L = 0.02m/s$ (the empirically selected liquid velocity) gives a huge $\sigma_L = 1000Nm^3/m$.

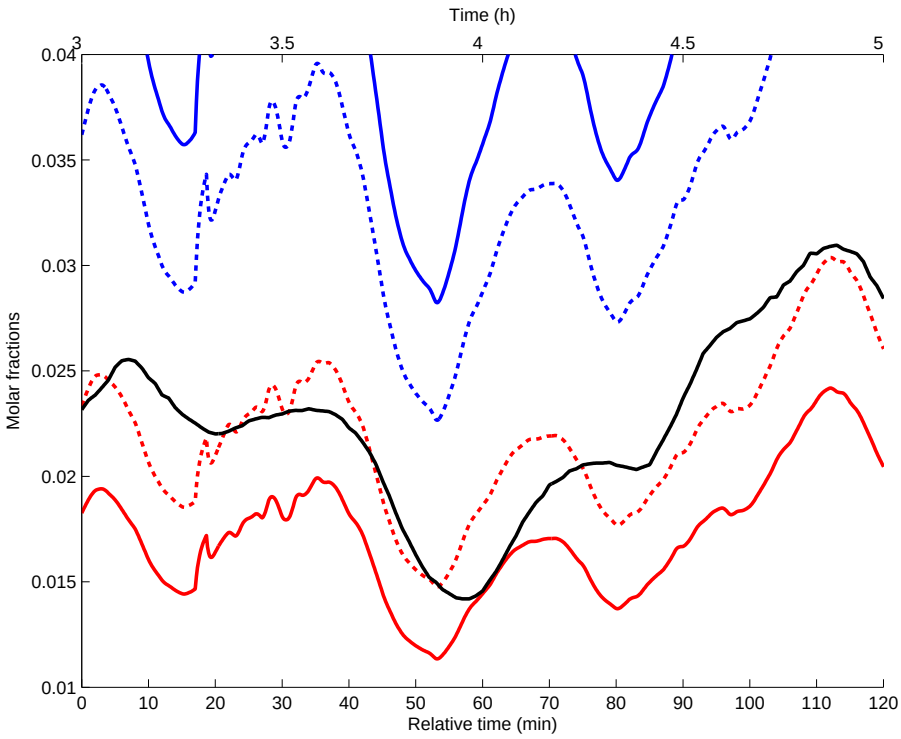

Figure 4.31: Composition estimation at the lean liquid draw point with $\epsilon = 0.289$, $\mathcal{V}_L = 0.02m/s$, (zoom of Fig. 4.30 between 3 and 5 h). *Blue:* X. *Dashed blue:* x. *Red:* $k(X)$. *Dashed red:* y. *Black:* analyzer.

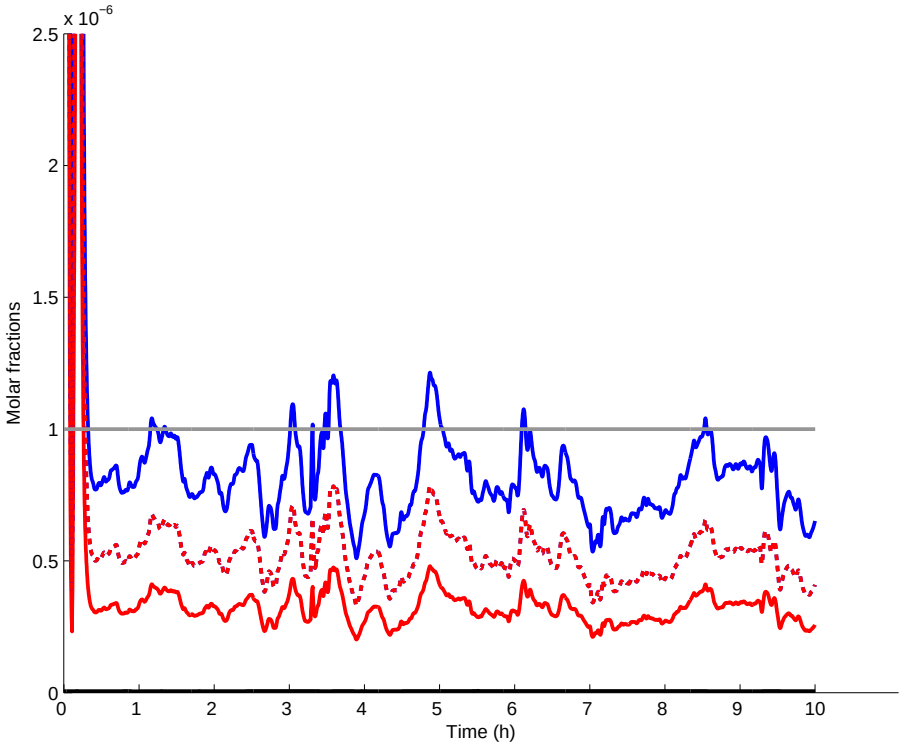

Figure 4.32: Composition estimation at the top of HP column with $\epsilon = 0.289$, $\mathcal{V}_L = 0.02m/s$. *Blue:* X. *Dashed blue:* x. *Red:* $k(X)$. *Dashed red:* y. *Black:* analyzer (almost zero).

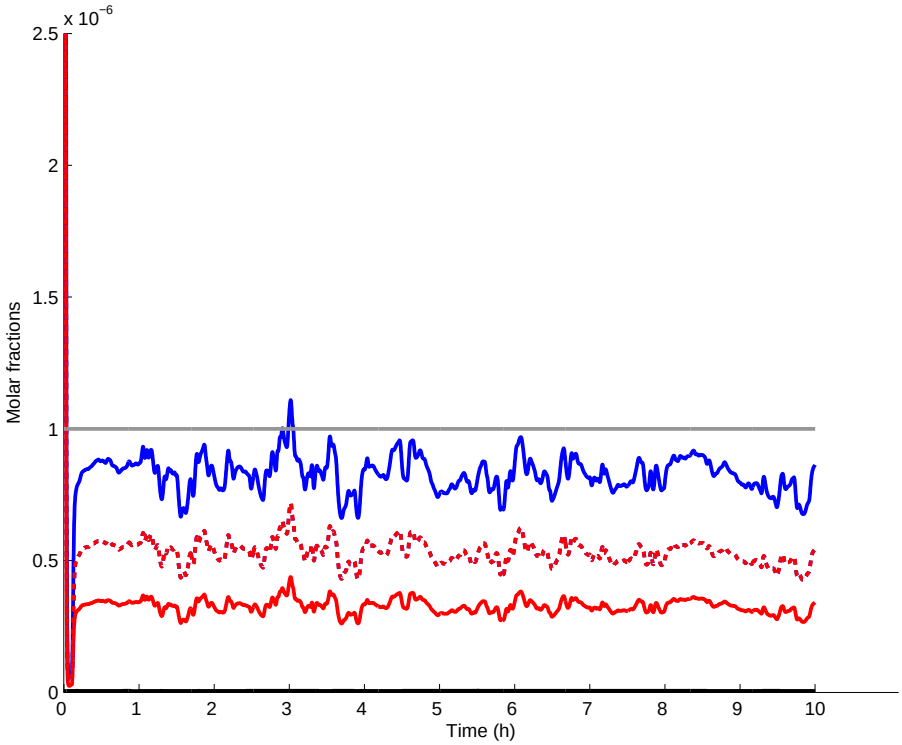

Figure 4.33: Composition estimation at top of the HP column with $\epsilon = 0.289$ and instant liquid propagation. *Blue:* X. *Red:* $k(X)$. *Dashed red:* $x = y$. *Grey:* contractual threshold. *Black:* analyzer (almost zero).

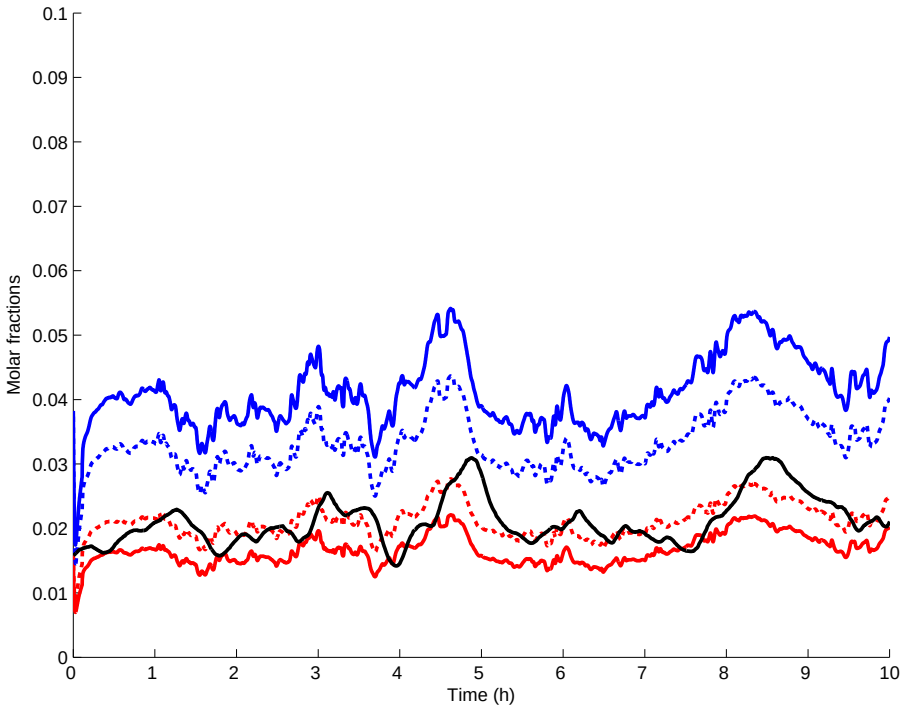

Figure 4.34: Composition estimation at the lean liquid draw point with $\epsilon = 0.289$ and instant liquid propagation. *Blue:* X. *Dashed blue:* x. *Red:* $k(X)$. *Dashed red:* y. *Black:* analyzer.

Figures 4.37, 4.38, 4.39 and 4.40 illustrate the simulation results with these two last values of μ_L. As one can see, taking $\mu_L = 0.4m/s$ or $0.08m/s$ has almost no impact on the composition estimation at the Lean Liquid draw point. On the contrary, $\mu_L = 0.02m/s$ significantly dampens the composition variations at the same point, which leads us to reject this value. At the top of the column, taking $\mu_L = 0.08m/s$ instead of $0.4m/s$ causes a large decrease of the estimated O_2 molar fraction. This makes the simulation more coherent with the top analyzer measures, which yet have to be considered with caution, as said previously. Favoring the static simulation, we will keep using $\mu_L = 0.4m/s$. Again, the results might suggest that the amount of liquid effectively participating to the separation dynamics is different from the total quantity held by the packing.

By the way, the estimated compositions are particularly little sensitive to the changes on σ_L, σ_V which preserve the σ_L/σ_V ratio - provided that the total hold-up $\sigma_L + \sigma_V$ is small enough. Figure 4.41 illustrates the impact of a +/- 50 % variation of the distributed values used for σ_L, σ_V (simultaneously) on the estimated O_2 compositions at the lean liquid draw point. Figures 4.42 depicts the impact of the same variations over the whole composition profiles. Not that the result holds when only one subsection is affected, as depicted on Fig. 4.43 and 4.44, where the changes concern the central subsection only.

This result has to be connected to the discussion in Section 2.4: for such a variation which preserves the σ_L/σ_V ratio, the steady-state solution for X as well as the corresponding static outputs x and y are unchanged (up to $O(\epsilon^2)$). It seems that the system operates in quasi-static regime as far as the separation dynamics are concerned. That is, at any instant t, the composition profiles are close to the steady-state profiles corresponding to (fictional) still-standing

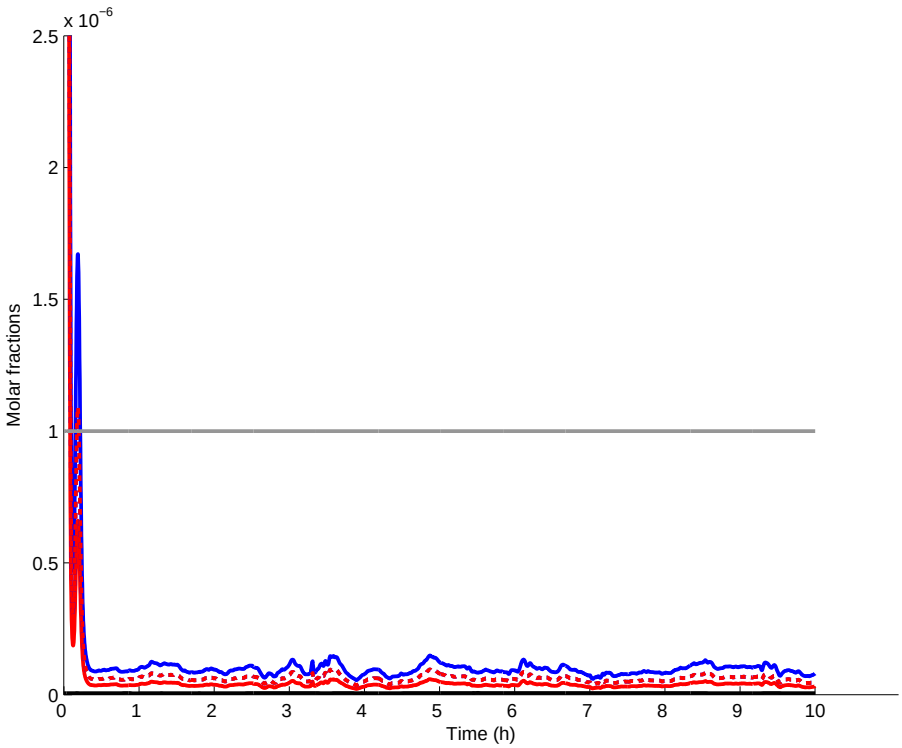

Figure 4.35: Composition estimation at top of the HP column with $\epsilon = 0.226$, $\mathcal{V}_L = 0.02m/s$. *Blue:* X. *Dashed blue:* x. *Red:* $k(X)$. *Dashed red:* y. *Black:* analyzer (almost zero).

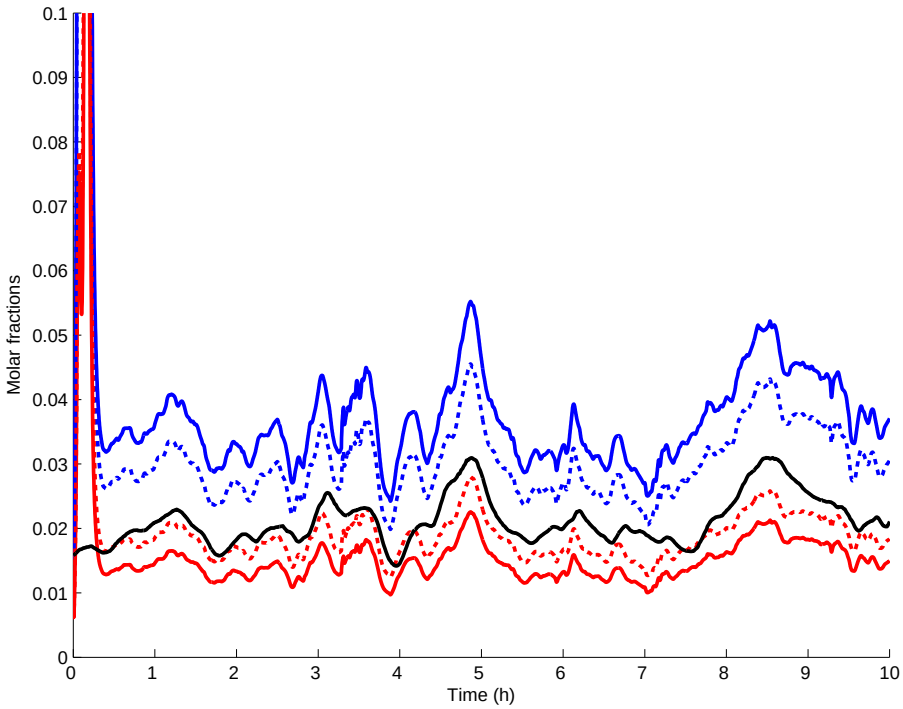

Figure 4.36: Composition estimation at the lean liquid draw point with $\epsilon = 0.226$, $\mathcal{V}_L = 0.02m/s$. *Blue:* X. *Dashed blue:* x. *Red:* $k(X)$. *Dashed red:* y. *Black:* analyzer.

liquid and gas distributions $\overline{L}(s) = L(s,t)$, $\overline{V}(s) = V(s,t)$. The compositions dynamics are thus essentially dictated by the hydraulics. In connection with this, Fig. 4.45(top) shows that with nominal values for the hold-ups, liquid speed mainly dominates the compositions convection speed (we recall that the gas speed is assumed infinite). The same figure (bottom) shows the detectable damping of the estimated composition variation at the Lean Liquid draw point, due to a large variation of σ_L and σ_V, which causes the compositions convection speed to approximate or dominate the liquid speed.

Figure 4.46 displays the envelope of variation of the estimated liquid and gas composition profiles during the 10h scenario[4]. The superimposition of the HYSYS static profiles confirms what was stated at the beginning of the section: the column operates within a region bounded by the static cases A and B. For these cases, the values of ϵ were close one to each other, thus a steady ϵ is sufficient for the dynamic scenario.

For scenarios exploring a broader variety of operating conditions, an adaptive ϵ is of some use. See for instance Fig. 4.47, where the scenario is played on a longer time period (40h instead of 10). Note that after 13h the estimated composition in the gas starts diverging from the analyzer's measures (yet the oscillations are still synchronized and their amplitude remains satisfying).

The diffusion parameter ϵ can be slowly adapted to resorb these divergences. In the

[4]By the way, one clearly sees that the profiles estimated by our model does not behave as wave-model profiles : the envelope is obtained by a combination of translations and billowing, rather than translations only, of the original profile

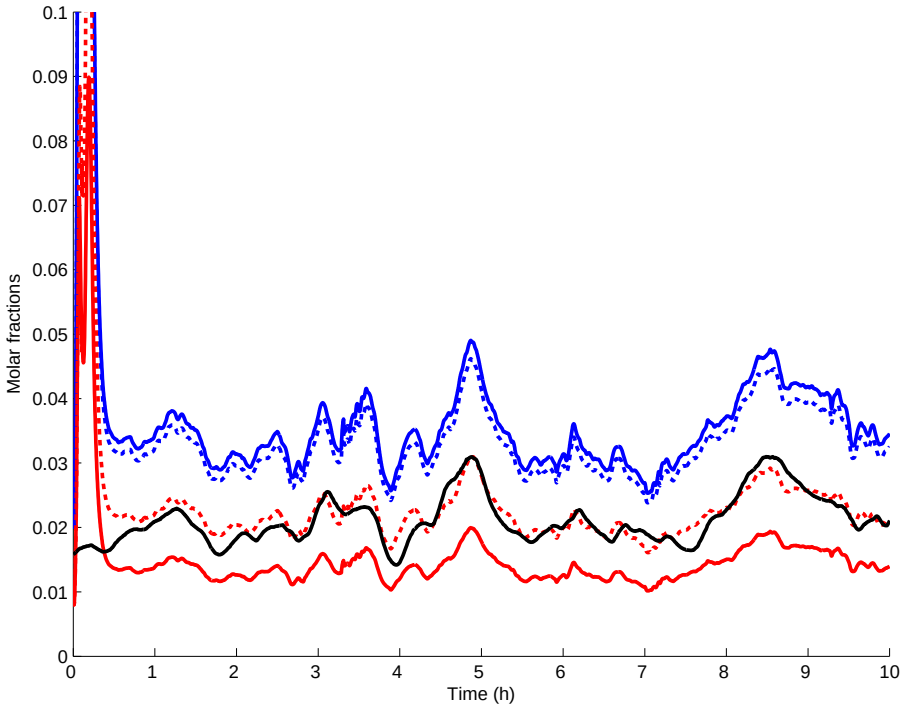

Figure 4.37: Composition estimation at the lean liquid draw point with $\epsilon = 0.289$, $\mathcal{V}_L = 0.02m/s$, and $\mu_L = 0.08m/s$. *Blue:* X. *Dashed blue:* x. *Red:* $k(X)$. *Dashed red:* y. *Black:* analyzer.

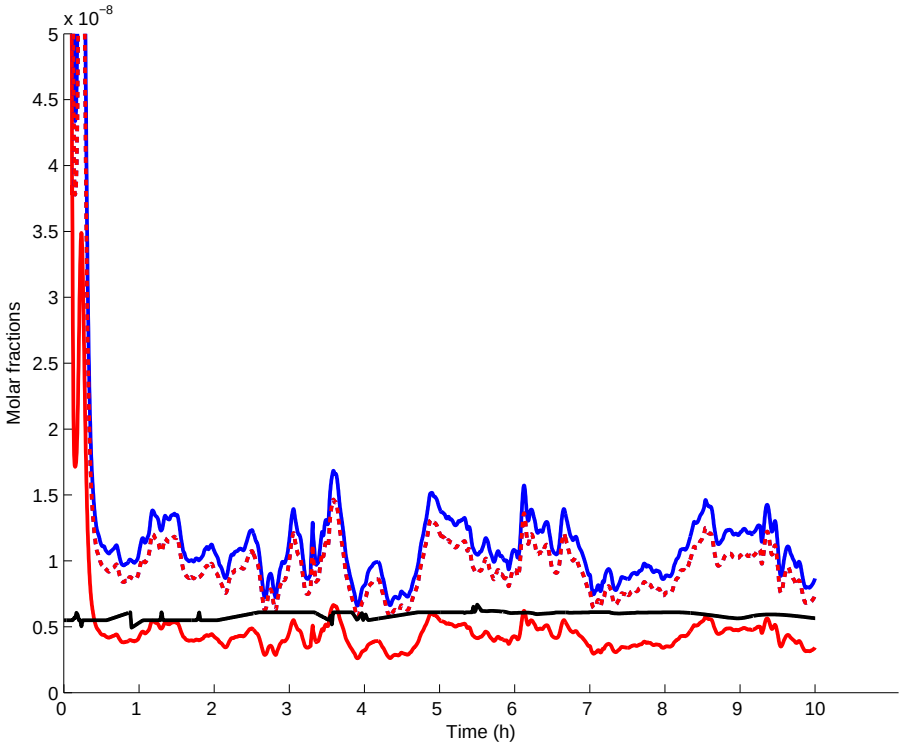

Figure 4.38: Composition estimation at top of the HP column with $\epsilon = 0.289$, $\mathcal{V}_L = 0.02m/s$, and $\mu_L = 0.08m/s$. *Blue:* X. *Dashed blue:* x. *Red:* $k(X)$. *Dashed red:* y. *Black:* analyzer.

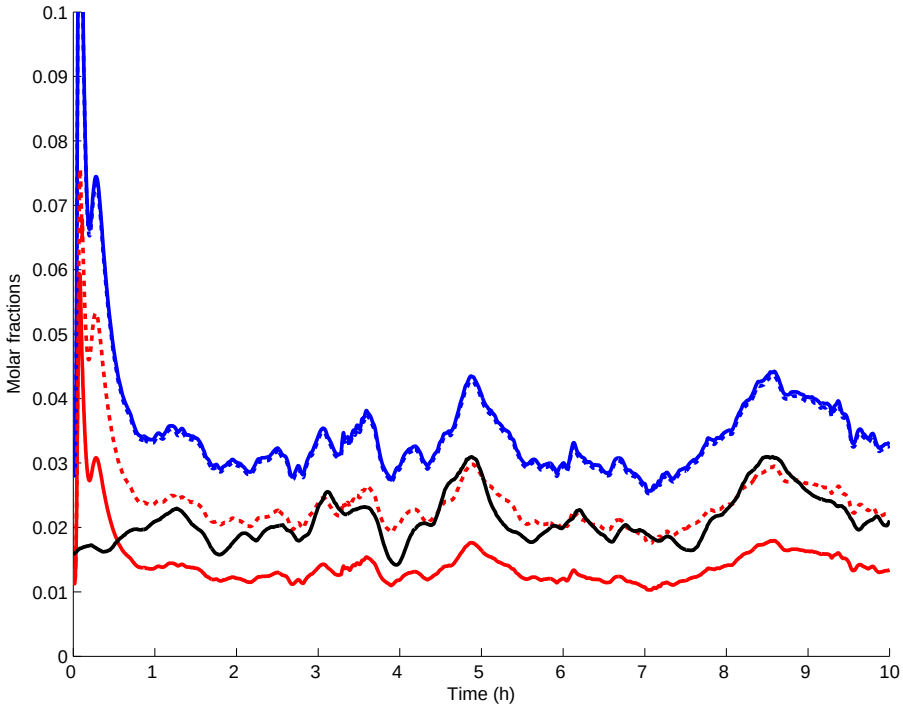

Figure 4.39: Composition estimation at the lean liquid draw point with $\epsilon = 0.289$, $\mathcal{V}_L = 0.02m/s$, and $\mu_L = 0.02m/s$. *Blue:* X. *Dashed blue:* x. *Red:* $k(X)$. *Dashed red:* y. *Black:* analyzer.

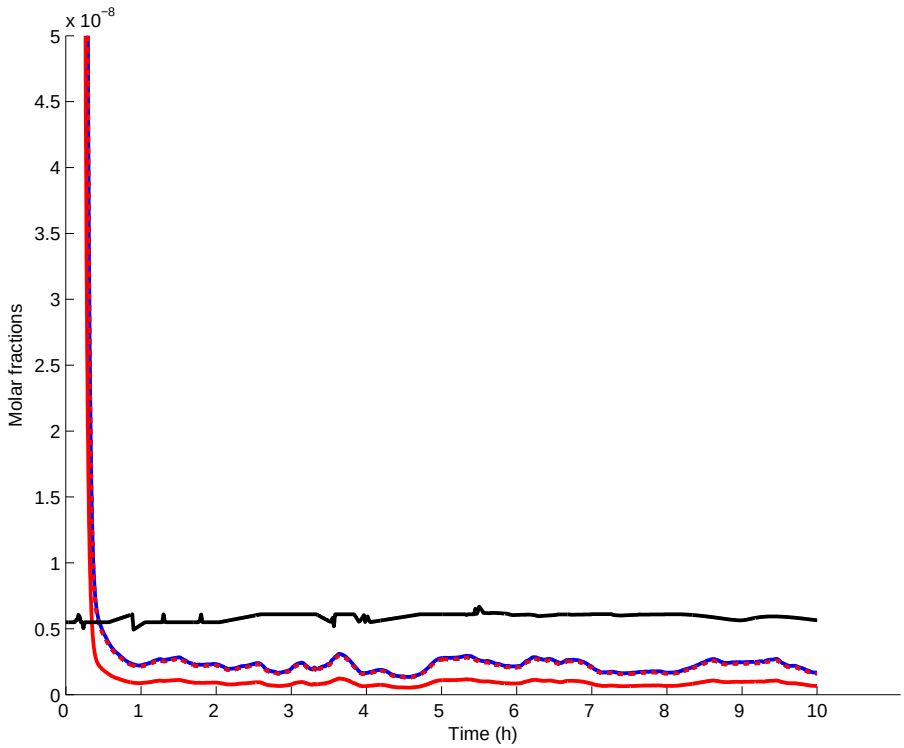

Figure 4.40: Composition estimation at top of the HP column with $\epsilon = 0.289$, $\mathcal{V}_L = 0.02m/s$, and $\mu_L = 0.02m/s$. *Blue:* X. *Dashed blue:* x. *Red:* $k(X)$. *Dashed red:* y. *Black:* analyzer.

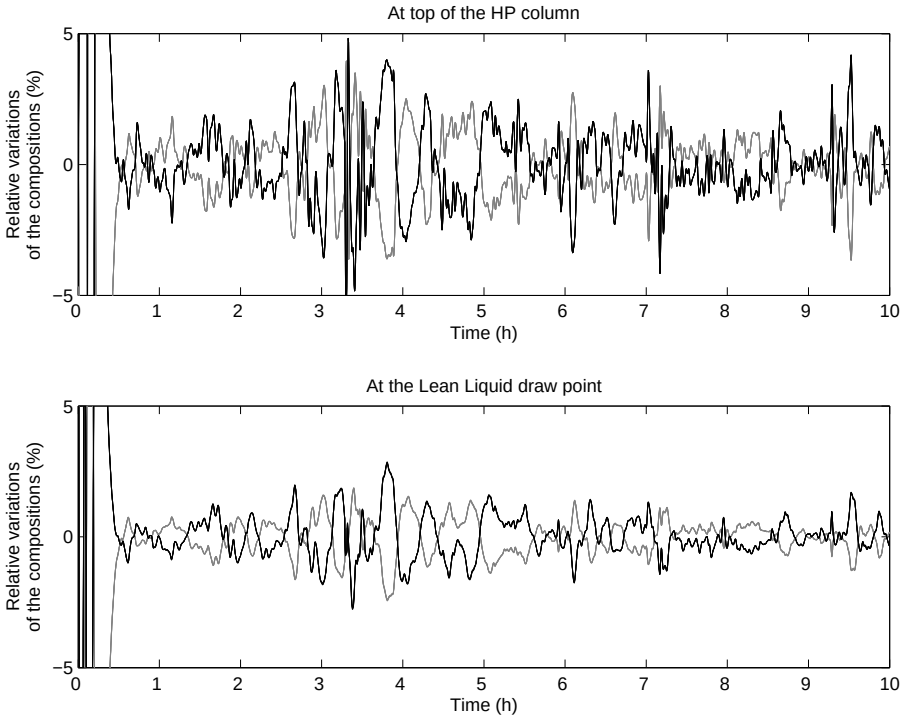

Figure 4.41: Relative variation of the estimated compositions at the top of the column (top) and at the lean liquid draw point (bottom) when σ_L, σ_V vary with respect to their nominal values (obtained using $\mu_L = 0.4m/s$). Simulation with $\epsilon = 0.289$. The black beam corresponds to a - 50 % variation of the hold-ups; the grey beam corresponds to a + 50 % variation.

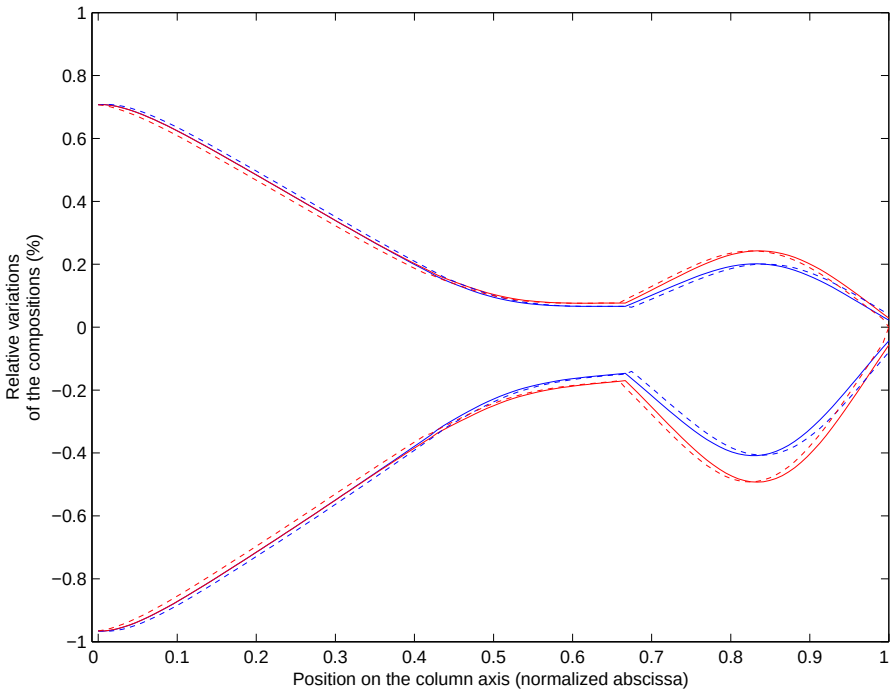

Figure 4.42: Relative variation of the estimated compositions profiles when σ_L, σ_V vary with respect to their nominal values. Simulation with $\epsilon = 0.289$ fixed, snapshot taken at $t = 10h$. The highest beam corresponds to a + 50 % variation of the hold-ups; the lowest beam corresponds to a - 50 % variation. *Solid blue:* X, *solid red:* $k(X)$, *dashed blue:* x, *dashed red:* y.

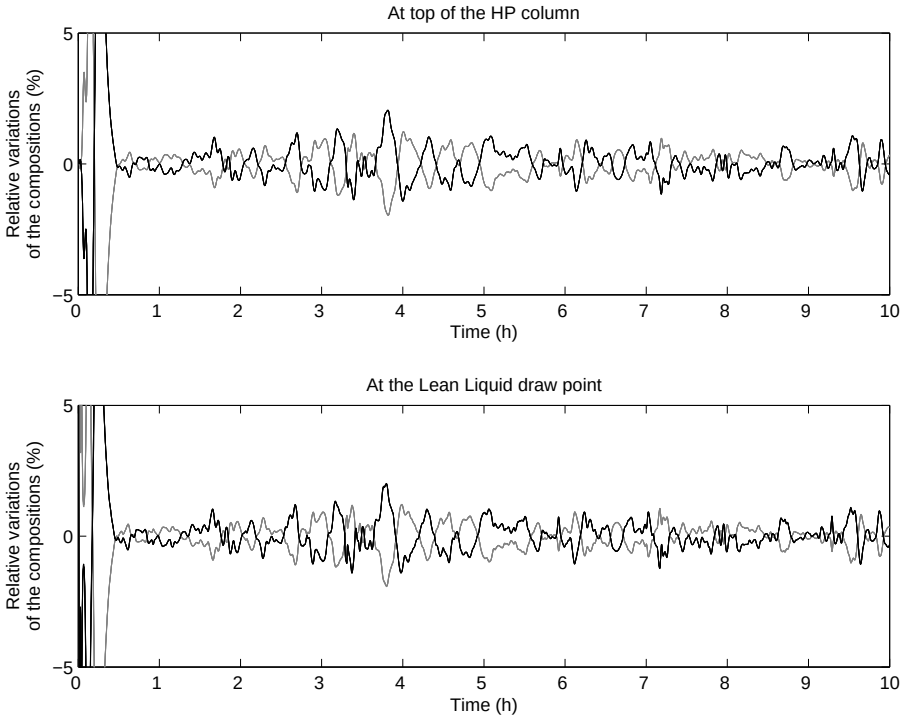

Figure 4.43: Relative variation of the estimated compositions at the top of the column (top) and at the lean liquid draw point (bottom) when σ_L, σ_V vary with respect to their nominal values in the central subsection. Simulation with $\epsilon = 0.289$. The black beam corresponds to a - 50 % variation of the hold-ups; the grey beam corresponds to a + 50 % variation.

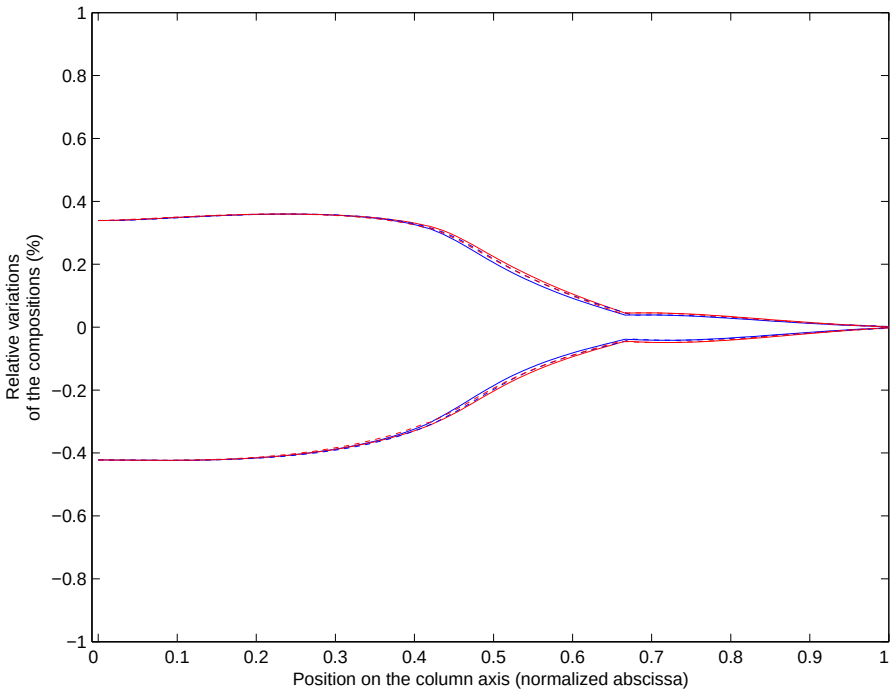

Figure 4.44: Relative variation of the estimated compositions profiles when σ_L, σ_V vary with respect to their nominal values in the central subsection. Simulation with $\epsilon = 0.289$ fixed, snapshot taken at $t = 10h$.The highest beam corresponds to a + 50 % variation of the hold-ups; the lowest beam corresponds to a - 50 % variation. *Solid blue:* X, *solid red:* $k(X)$, *dashed blue:* x, *dashed red:* y.

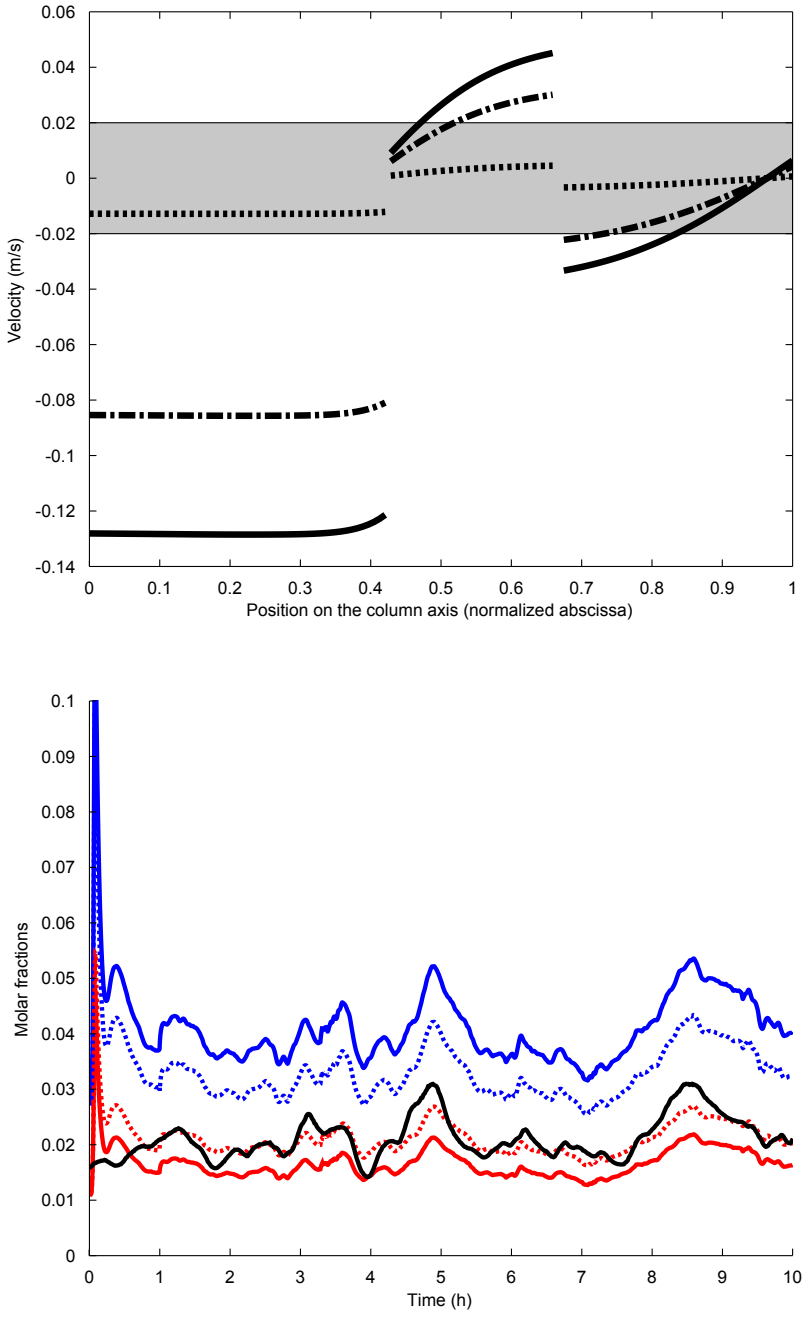

Figure 4.45: *Top*: Comparison of the liquid and composition convection velocity for various hold-ups, at $t = 10h$. *Solid:* σ_L and σ_V at their nominal values. *Dash-dotted:* σ_L and σ_V at 1.5 times their nominal values. *Dotted:* σ_L and σ_V at 10 times their nominal values. The grey band bounds are $-\mathcal{V}_L$, $+\mathcal{V}_L$. *Bottom*: Damped composition variations obtained with σ_L and σ_V at 10 times their nominal values. *Blue:* X. *Dashed blue:* x. *Red:* $k(X)$. *Dashed red:* y. *Black:* analyzer.

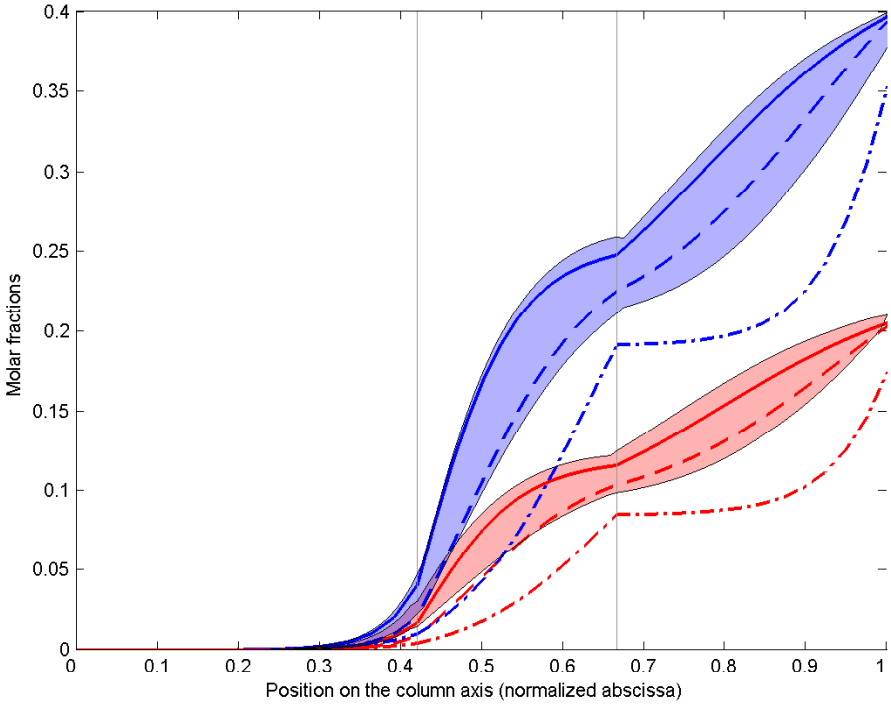

Figure 4.46: Envelope of variations of the liquid (pale blue) and gas (pale red) oxygen molar fraction profiles during the dynamic scenario with $\epsilon = 0.289$. Static HYSYS profiles for cases A (solid), B (dashed), C (dash-dotted) are superimposed. Vertical gray lines indicate the junctions between packed sections.

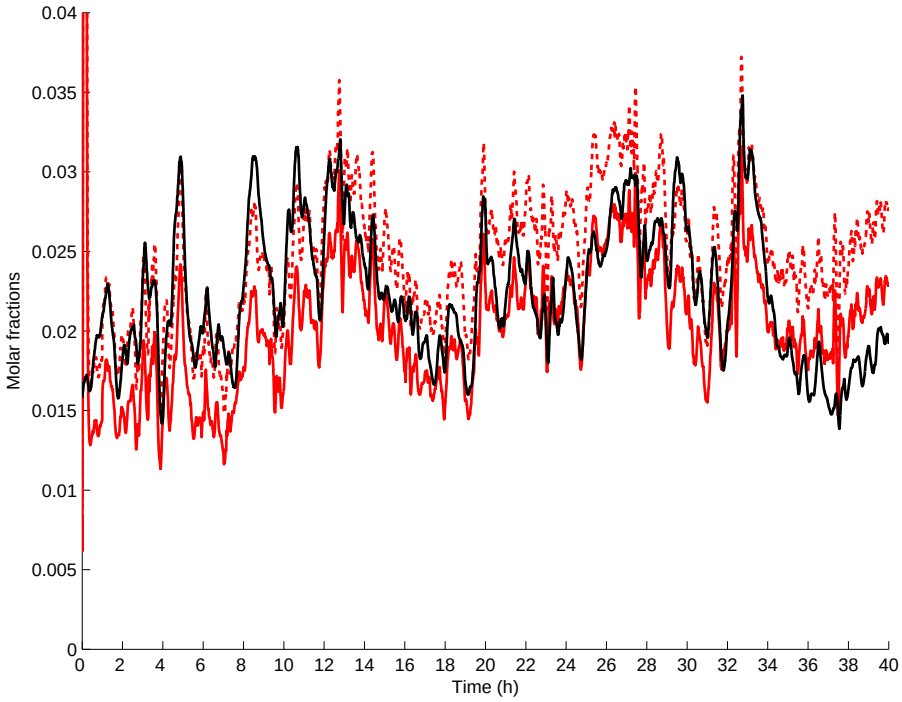

Figure 4.47: Composition estimation at the lean liquid draw point with $\epsilon = 0.289$ for the 40h scenario. Only the gas compositions are displayed. *Red:* $k(X)$. *Dashed red:* y. *Black:* analyzer.

following, we dynamicly adapt ϵ using:

$$\frac{d\epsilon}{dt} = \frac{1}{T_i} \frac{\widehat{y}_{O_2}(t) - \overline{y}_{O_2}(t)}{\overline{y}_{O_2}(t)}, \tag{4.16}$$

where $\widehat{y}_{O_2}(t)$ is the estimation given by the model at the lean liquid draw point and $\overline{y}_{O_2}(t)$ is given by the analyzer. The time constant is set at $T_i = 1h$, which is fast enough to correct the estimations, as shown on Fig. 4.48, while remaining coherent with the timescale of the plant operating conditions. Figure 4.49 shows the adaptive diffusion parameter; one can observe that ϵ is also continuously struggling to compensate for small time-shifts between the measure and the estimation (hence the variations in the 0 - 10h interval, whereas we have seen that a constant ϵ was satisfying there). A better handling of the time-shifts between the various inputs of the model, and a time-varying liquid speed may help reducing this effect. As shown on Fig. 4.50, the variations of ϵ are at the expense of large transients in the top composition estimation.

Figure 4.51 displays the envelope of variation of the estimated liquid and gas composition profiles during the 40h scenario with adaptive ϵ. The envelope is effectively broader than in the non-adaptive 10h scenario; the closed-loop estimation ensures robustness towards a broader range of operating conditions.

This robustness can be checked on a number of dynamic scenarios, but also proves limited for some others. For the sake of brevity, the figures and statistics related to these multiple scenarios are moved in Appendix C. It turns out that three main clusters can be distinguished in the scenario pool (see Table 4.2). The first one corresponds to a high level of production,

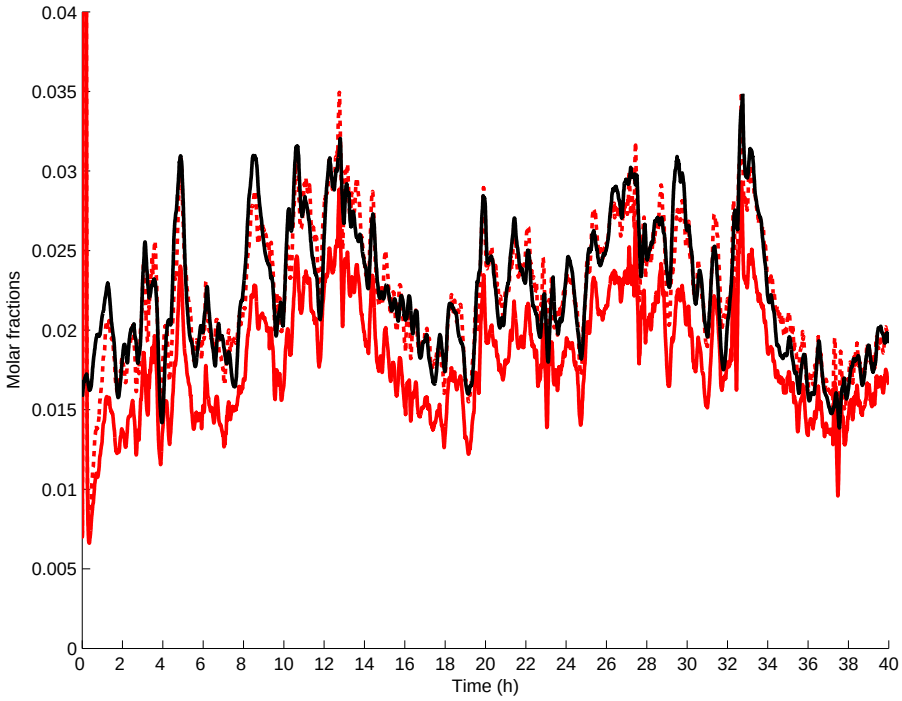

Figure 4.48: Composition estimation at the lean liquid draw point with adaptive epsilon. Only the gas compositions are displayed. *Red:* $k(X)$. *Dashed red:* y. *Black:* analyzer.

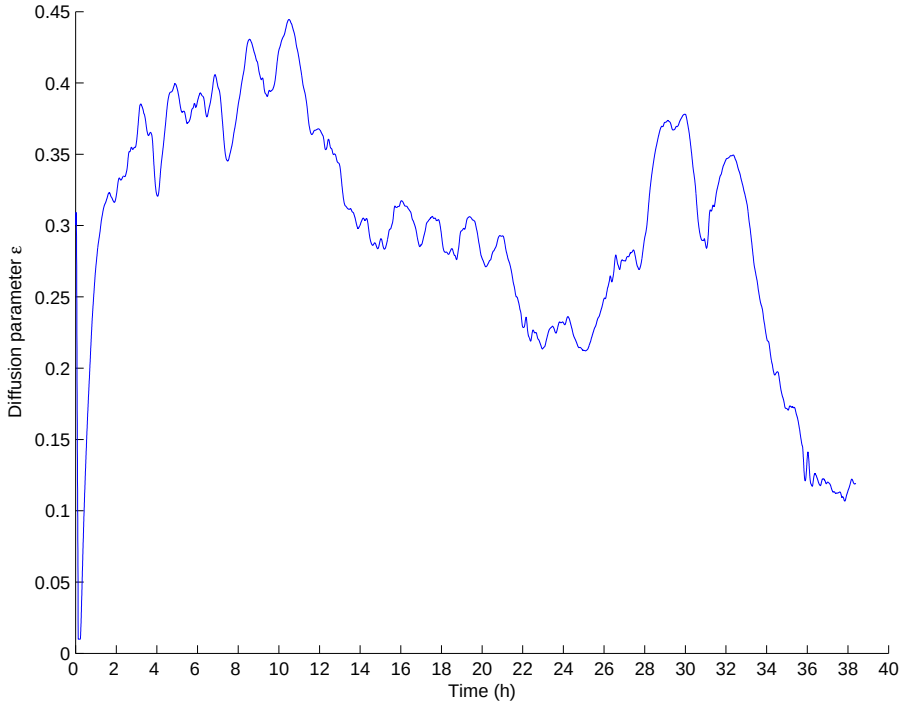

Figure 4.49: Adaptive diffusion parameter during the 40h scenario.

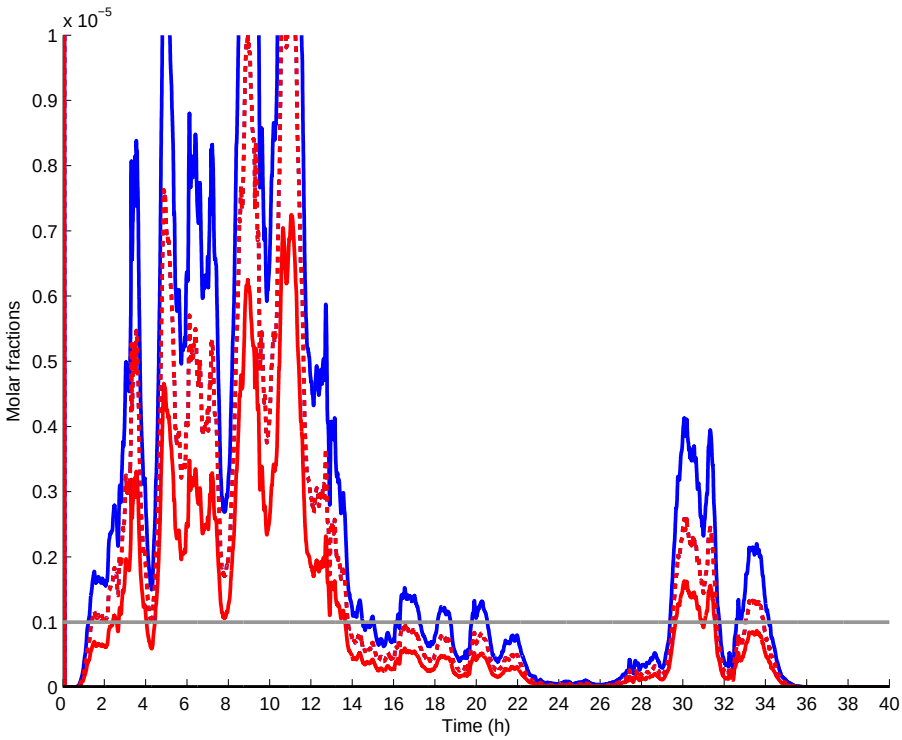

Figure 4.50: Composition estimation at the top of the column with adaptive epsilon. *Blue:* X. *Dashed blue:* x. *Red:* $k(X)$. *Dashed red:* y. *Black:* analyzer.

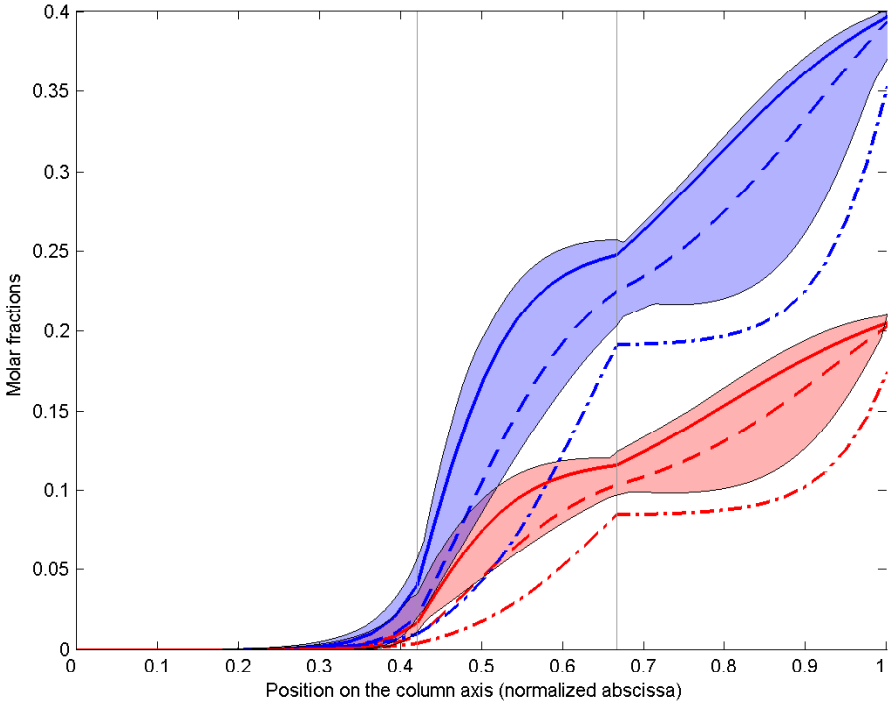

Figure 4.51: Envelope of variations of the liquid (pale blue) and gas (pale red) oxygen molar fraction profiles during the 40h dynamic scenario with adaptive ϵ. Static HYSYS profiles for cases A (solid), B (dashed), C (dash-dotted) are superimposed. Vertical gray lines indicate the junctions between packed sections.

Cluster	Scenarios
1	1, 2, 3, 4, 5, 6, 7, 8, 9, 10, 11
2	12, 13, 14, 17
3	15, 16

Table 4.2: Classifications of the dynamic scenarios in three clusters

with operating conditions comparable to the static cases A and B. For this cluster, the model shows satisfying results, similar to those discussed in this chapter. The second cluster corresponds to a reduced operation mode, where the plant was operated at low production level with one air compressor only. For this cluster, the model is unable to render the composition measured at the Lean Liquid draw point, in spite of a dramatically decreased ϵ. It yet still renders the composition oscillations, in a synchronized, though damped, manner. The third cluster is between the previous ones: the unit is operated with two compressors as in cluster 1, yet with lower production rates. For this cluster, the estimations may be satisfying, but are at the price of a small ϵ parameter, and ultimately some divergences will appear as in the cluster 2.

An overestimation by 10% has been reported for the measurements given by one of the plant's flowmeters. The presented simulations take the correction into account; yet it seems legitimate to investigate the sensitivity of the HP column simulation to changes of the same magnitude on the input and output flows. All the more that the flowmeters installation is reported to be an issue on the investigated plant (the straight pipe section on the upward side of some flowmeters is not long enough, which can make the measured flow turbulent and deteriorate the result). We choose one of the problematic scenarios in the 3^{rd} cluster as an example. Indeed, we obtain for this scenario a reflux rate of about 0.25 in subsection 2, which seems too little. And one clearly sees on the envelopes plotted on Fig. C.15 or C.16 that the simulated profiles seems pushed too strongly against the junction between subsections 2 and 3. One tries to compensate by decreasing ϵ, making the profile very stiff, whereas changing the composition wave speed in subsection 2 seems more reasonable. We focus on the lean liquid draw flow, since it seems to have the more impact on the composition profile. In the case of scenario 15, it turns out that one can not recover the expected composition at the lean liquid draw point with less than a 40% diminution of the lean liquid flow (with this correction, we obtain a reasonable 0.4 reflux rate in subsection 2). Results with this correction are depicted on Fig. 4.52 (composition at the lean liquid draw location), 4.53 (adaptive parameter ϵ) and 4.54 (envelopes of variation of the profiles). Consequently, the decreased model performances for cluster 2 or 3 can hardly be explained by flow measurement biases only. For the moment, we have no satisfying alternative explanation to propose.

4.7 Transfer functions model

We have developed in Chapter 3 a linear tangent model connecting the composition variations at both ends of an homogeneous packed section to the variations of the inlet compositions and flows. We have seen that we have to distinguish the cases where the composition convection speed is upwards or downwards.

Based on this model, we aim to build a complete representation of the HP column, in order to reproduce the small oscillations of the Lean Liquid composition around an almost

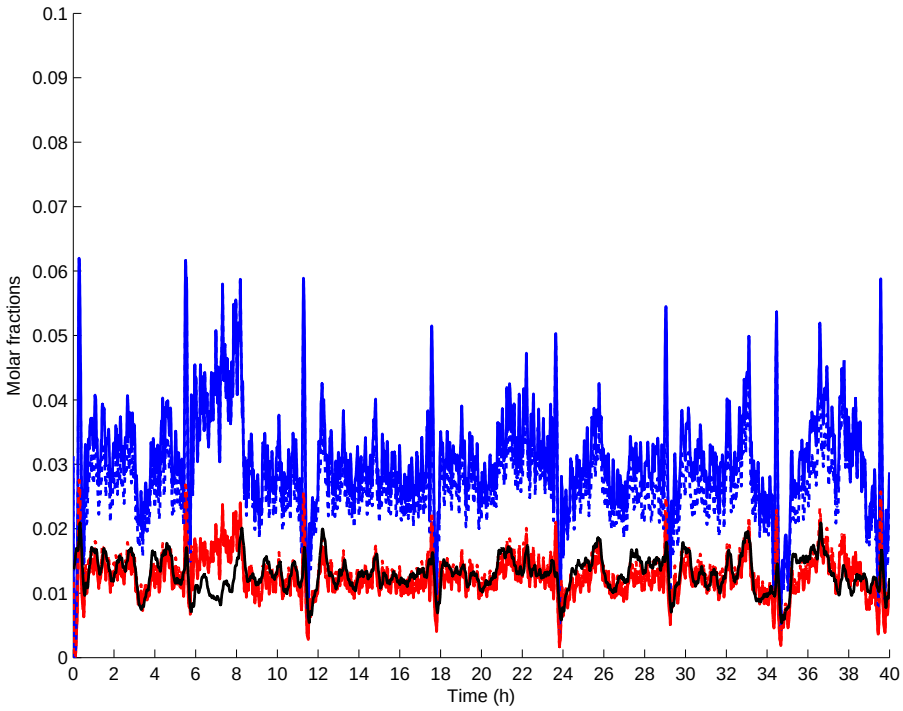

Figure 4.52: Composition estimation at the lean liquid draw point during the 40h scenario n°15 with adaptive epsilon and 40% decrease of the lean liquid draw. *Red:* $k(X)$. *Dashed red:* y. *Blue:* X. *Dashed blue:* x *Black:* analyzer.

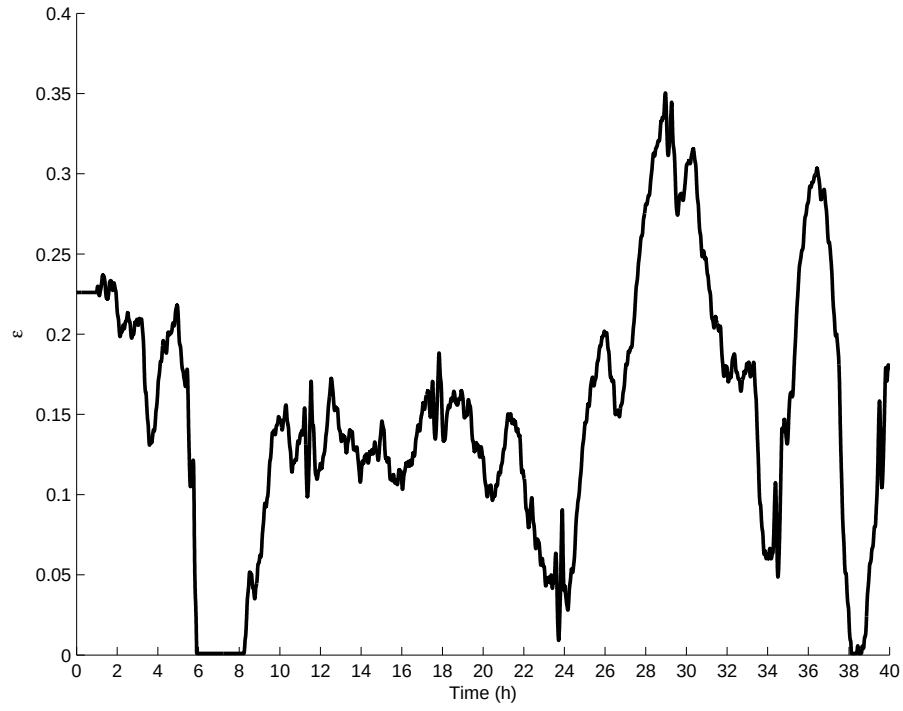

Figure 4.53: Adaptive diffusion parameter during the 40h scenario n°15 with 40% decrease of the lean liquid draw

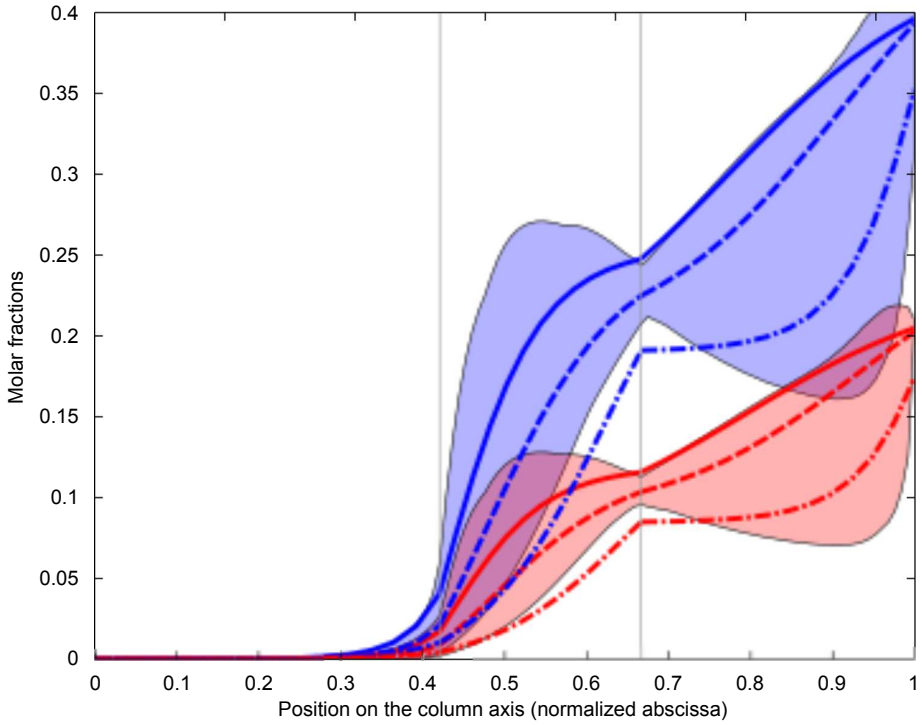

Figure 4.54: Envelope of variations of the liquid (pale blue) and gas (pale red) oxygen molar fraction profiles during the 40h dynamic scenario n°15 with adaptive ϵ and 40% decrease of the lean liquid draw. Static HYSYS profiles for cases A (solid), B (dashed), C (dash-dotted) are superimposed. Vertical gray lines indicate the junctions between packed sections.

stabilized set-point. Contrary to the simulations using the PDE model which addressed long time intervals, we focus here on shorter time periods, of the duration of a couple of oscillations.

The model is built following the chart given on Fig. 4.55. The top and bottom subsections are simulated using the downwards speed case, whereas the central subsection 2 uses an upwards speed block. The composition variation at the bottom inlet of subsection 3 is 0, since it is fed with atmospheric air of constant composition.

The 'liquid mixing block' and 'gas mixing block' respectively embed the following equations:

$$\delta x_{0,3} = \frac{\left(\overline{L}_{V03\rightarrow} + \delta L_{V03\rightarrow}\right) x_{V03\rightarrow}(p)}{\overline{L}_{V03\rightarrow} + \delta L_{V03\rightarrow} + \overline{L}_2 + \delta L_1 e^{(\theta_1+\theta_2)p}} + \frac{\left(\overline{L}_2 + \delta L_1 e^{(\theta_1+\theta_2)p}\right)\left(\overline{x}_{h,2} + \delta x_{h,2}\right)}{\overline{L}_{V03\rightarrow} + \delta L_{V03\rightarrow} + \overline{L}_2 + \delta L_1 e^{(\theta_1+\theta_2)p}} - \overline{x}_{0,3},$$

$$\delta y_{h,2} = \frac{\left(\overline{V}_3 + \delta V_{air}\right)\left(\overline{y}_{h,3} + \delta y_{h,3}\right)}{\overline{V}_3 + \delta V_{air} + \overline{V}_{V03\rightarrow} + \delta V_{V03\rightarrow}} + \frac{\left(\overline{V}_{V03\rightarrow} + \delta V_{V03\rightarrow}\right) y_{V03\rightarrow}(p)}{\overline{V}_3 + \delta V_{air} + \overline{V}_{V03\rightarrow} + \delta V_{V03\rightarrow}} - \overline{y}_{h,2},$$

where the bars indicate the set-point values and the δ the variations. The molar fractions $y_{V03\rightarrow}(p)$ and $x_{V03\rightarrow}(p)$ in the flows exiting the flashpot V03 are obtained as for the PDE model by simulating a isenthalpic flash in the pot.

Delays θ_1 and θ_2 correspond to the liquid propagation in subsections 1 and 2:

$$\theta_1 = \frac{h_1}{\mathcal{V}_{L,1}\left(\sigma_{L,1} + \sigma_{V,1}\right)},\ \theta_2 = \frac{h_2}{\mathcal{V}_{L,2}\left(\sigma_{L,2} + \sigma_{V,2}\right)}.$$

The HP column transfer functions model is tested on a different scenario than the PDE model, to be closer to a stabilized functioning. We use the scenario n°3 of our pool (see Appendix C). The whole scenario can be simulated using the linear model yet this is not its purpose. In addition, the HP column transfer model is implemented using buffer initialized with zeros; it thus yields irrelevant results for the first instants of the scenario. Moreover, we intend to compare the linear model to the PDE model, which has its own initialization time. Consequently, in the following, the first hours of the scenario are not displayed, to get rid of the initializations.

The numerical values we used for the linear model parameters are summarized in Table 4.3 and 4.4. Values in Table 4.4 correspond to input/output flows and input compositions at the beginning of the scenario. The value of ϵ and $\mathcal{V}_L$ are directly taken from the PDE model settings. Other values in Table 4.3 are directly taken from the simulation results of the PDE model at the steady-state defined by Table 4.4. In particular, $\overline{L}$ is obtained as the mean of $L(s)$ over each section in the PDE model, after stabilization. We follow the same procedure for $\overline{V}$, $\overline{\sigma}_L$ and $\overline{\sigma_V}$. G is calculated as the mean, over each section, of the s-dependent term $G_{k-1/k}$ in the PDE model, defined by (4.5).

Figure 4.56 shows variations of the input and output flows of the HP column over 10 hours of the scenario (from 2h to 12h), with respect to their initial value. In a first time, the PDE model is used with ϵ fixed ($\epsilon = 0.226$).

We are interested in the oscillations of the Lean Liquid composition, which we retrieve with our model as the small variation $\alpha_1 \delta x_{h,1}$. Short-term comparison with the measured composition is shown on Fig. 4.57. The linear model reproduces well the first oscillation (from

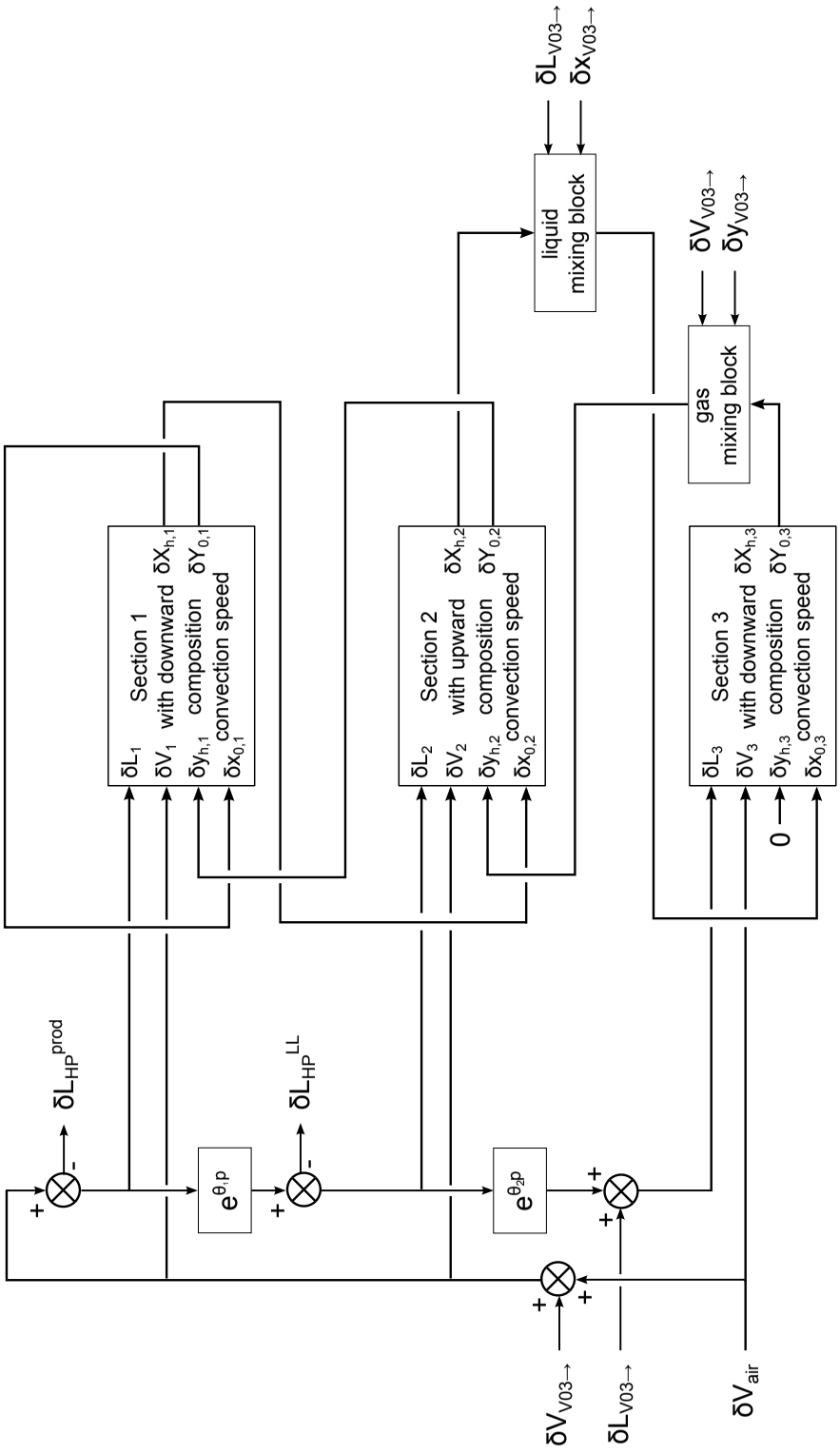

Figure 4.55: Transfer function model of the HP column

Parameter	Unit	Section 1	Section 2	Section 3
α	N/A	0.4	0.45	0.5
ϵ	N/A	0.226	0.226	0.226
G	Nm^3s^{-1}/m	16.37	9.30	16.37
$\mathcal{V}_L$	m/s	0.02	0.02	0.02
$\overline{\sigma}_L + \overline{\sigma}_V$	Nm^3/m	150	120	130
$\overline{X}_0$	N/A	10^{-7}	0.037	0.244
$\overline{X}_h$	N/A	0.037	0.244	0.4
$\overline{x}_0$	N/A	7.10^{-8}	0.031	0.243
$\overline{y}_h$	N/A	0.0195	0.1154	0.21
$\overline{L}$	Nm^3/s	25.5	12.5	17.5
$\overline{V}$	Nm^3/s	29	29	27.5

Table 4.3: Section depending parameters for the transfer functions model.

Parameter	Unit	Value
$\overline{V}_{air}$	Nm^3/s	25.73
$\overline{V}_{V03\rightarrow}$	Nm^3/s	1.77
$\overline{L}_{V03\rightarrow}$	Nm^3/s	5.24
$\overline{L}_{HP}^{prod}$	Nm^3/s	4.06
$\overline{L}_{HP}^{LL}$	Nm^3/s	13.15
$\overline{x}_{V03\rightarrow}$	N/A	0.22
$\overline{y}_{V03\rightarrow}$	N/A	0.10

Table 4.4: Global parameters for the transfer functions model.

2h to 3.5h), and the shorter bumps (for instance, between 4h and 4.5h) are reproduced in a synchronized yet amplified manner with respect to the PDE model. Since the linear model is synchronized with the PDE model, it has the same time-advance with respect to the measure. As for the PDE model, tuning the liquid speed allows modifying this time-shift; yet it also affects the interplay between the liquid and gas inputs and outputs, and can dramatically change the pattern of the simulated oscillations. There is a natural filtering effect on the measured compositions, which is not present in our linear model, since at the chosen order (order 0 in ϵ), it only comprises delayed direct transfers.

On the long term (see Fig. 4.59), a slow varying bias appears between the measure and the models. As for the PDE model, this bias can be reduced by adapting the diffusion parameter ϵ. Figure 4.60 shows the results when ϵ is injected as a time-varying parameter in the linear transfer model of the HP column. Its value is estimated in real time by the PDE model, which runs in parallel, using (4.16).

One can check that the simulated composition at the top of the column ($\alpha_1 (\overline{x}_{0,1} + \delta x_{0,1})$) is reasonable regarding its mean value (see Fig. 4.58). More interesting, the linearized tangent model approximately reproduces the oscillations estimated by the non-linear PDE model, yet with dramatically reduced amplitude and a large time-advance of about 30 minutes. The latter is problematic, since in the transfers between the inputs and the composition variation at top, there is no delay, and thus, no way to synchronize the estimations.

Using the transfer functions obtained for the subsections in the upward and downward

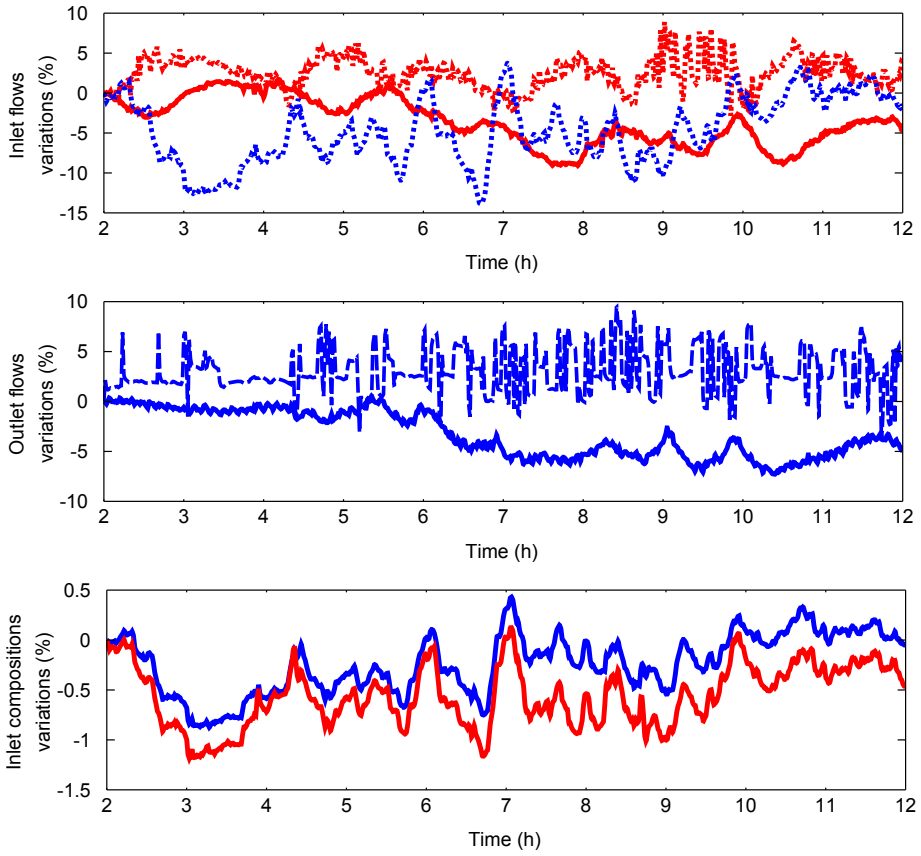

Figure 4.56: Variations of the inlet/outlet flows and input compositions of the HP column during the 10 hours scenario (from 2h to 12h), with respect to their initial value. *Top:* variations of the inlet flows (*solid red:* air inlet flows V_{air}, *dotted red:* gas flow from V03 $V_{V03\rightarrow}$, *dotted blue:* liquid flow from V03 $L_{V03\rightarrow}$). *Center:* variations of the outlet flows (*solid blue:* Lean Liquid draw L_{HP}^{LL}, *dashed blue:* liquid drawn on top for production L_{HP}^{prod}). *Bottom:* variations of O_2 molar fraction in the flows leaving the flashdrum V03 (*red:* in gas, *blue:* in liquid).

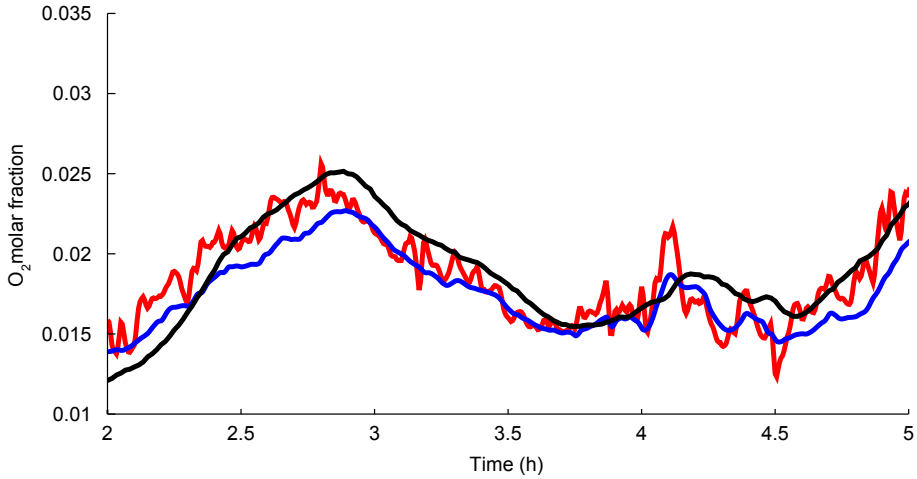

Figure 4.57: Simulated and measured composition in gas at the Lean Liquid draw location. *Blue:* according to the PDE model with $\epsilon = 0.226$. *Red:* according to the transfer functions model. *Black:* measured.

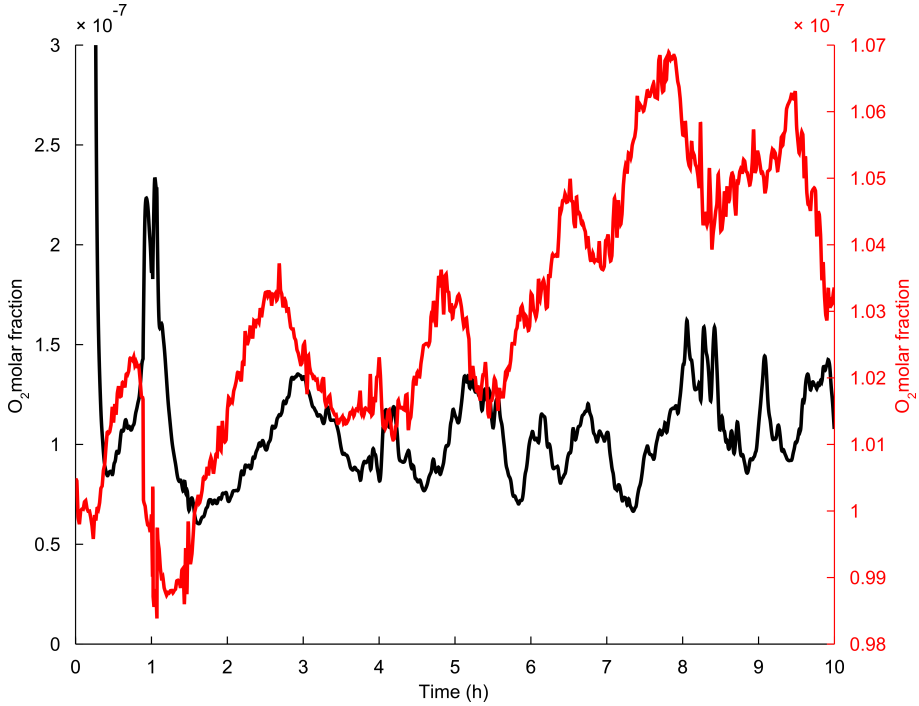

Figure 4.58: Simulated composition atop the column. *Blue:* according to the PDE model with $\epsilon = 0.226$. *Red:* according to the transfer functions model. Two composition scales are used to emphasize the similarities between the two estimations.

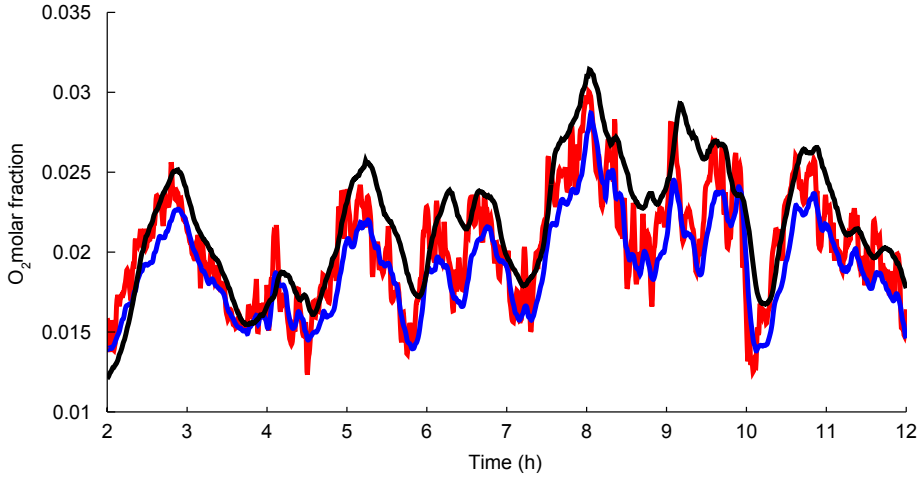

Figure 4.59: Simulated and measured composition in gas at the Lean Liquid draw location. *Blue:* according to the PDE model with $\epsilon = 0.226$. *Red:* according to the transfer functions model. *Black:* measured.

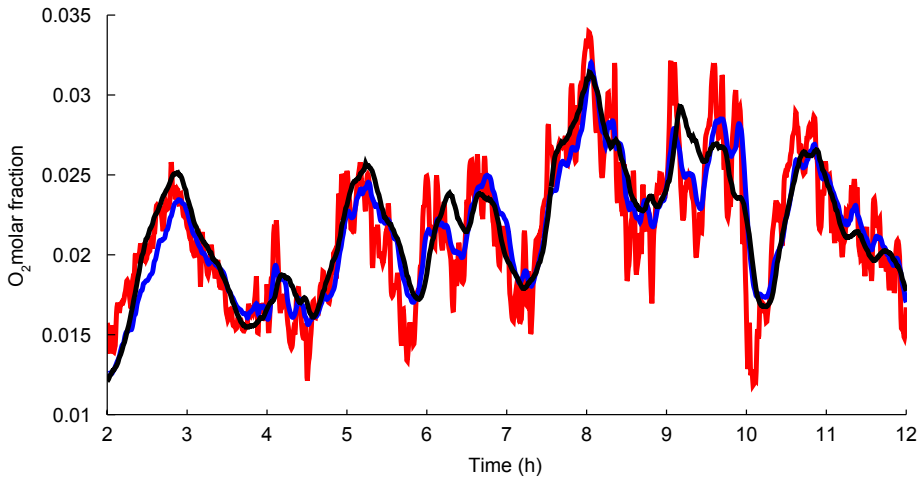

Figure 4.60: Simulated and measured composition in gas at the Lean Liquid draw location. *Blue:* according to the PDE model with adaptive ϵ. *Red:* according to the transfer functions model using ϵ from the PDE model as a time-varying parameter. *Black:* measured.

cases in Chapter 3 one can obtain the plain expression of the transfers between the inputs and outputs on Fig. 4.55. For instance, the variation of the oxygen molar fraction in the lean liquid draw reads:

$$\begin{aligned}
\delta X_{h,1} = &\left[K_a + K_b e^{-\Delta_1 p} + K_c e^{-\Delta_2 p} + K_d e^{-\theta_1 p} + K_e e^{-(\theta_1+\theta_2)p} + K_f e^{-(\theta_1+\theta_2+\Delta_2)p}\right] \delta V_{air} \\
&+ \left[K_g + K_h e^{-\Delta_1 p} + K_i e^{-\Delta_2 p} + K_d e^{-\theta_1 p} + K_e e^{-(\theta_1+\theta_2)p} + K_j e^{-(\theta_1+\theta_2+\Delta_2)p}\right] \delta V_{V03\rightarrow} \\
&+ \left[K_k e^{-\Delta_1 p} + K_d e^{-\theta_1 p} + K_e e^{-(\theta_1+\theta_2)p} + K_l e^{-(\theta_1+\theta_2+\Delta_2)p}\right] \delta L_{HP}^{prod} \\
&+ \left[K_d + K_e e^{-\theta_2 p} + K_m e^{-(\theta_2+\Delta_2)p}\right] \delta L_{HP}^{LL} \\
&+ \left[K_n e^{-\Delta_2 p}\right] \delta L_{V03\rightarrow} \\
&+ \left[K_o e^{-\Delta_2 p}\right] \delta x_{V03\rightarrow} \\
&+ \left[K_p e^{-\Delta_2 p}\right] \delta y_{V03\rightarrow},
\end{aligned} \tag{4.17}$$

where the gains $K_a, \ldots, K_p$ depend on the ASU set-point. As said above, the delays θ_1 and θ_2 respectively correspond to the dwell-time of the liquid in subsections 1 and 2. Delays $\Delta_1 = \frac{h_1}{v_1}$ and $\Delta_2 = \frac{h_2}{v_2}$ correspond to the propagation time of a composition wave, respectively in subsection 1 and 2.

Let us analyze the first line of (4.17). A small variation occurs on the bottom inlet air flow, which instantly changes the gas distribution of the whole column. According to Table 3.2, this triggers an immediate liquid composition variation at the bottom of subsection 1, hence the gain K_a. Also, this triggers a composition change at the top of the column, then a composition-change wave which travels downwards subsection 1 until it reaches the lean liquid draw location, hence the gain K_b and the delay Δ_1. In subsection 2 the composition speed is upwards, so this composition wave travels no further. The gas flow change also modifies the liquid flow in the top condenser, so a liquid flow-change wave also travels down subsection 1, hence the gain K_d and the delay θ_1. This hydraulic wave continues in subsection 2 and reaches its bottom with a delay $\theta_1 + \theta_2$. At this moment, a new reflux profile has established in subsection 2, which cause a change of the lean liquid composition, hence the gain K_e. Due to the direction of the composition wave in subsection 3, the hydraulic wave, which continues propagating downwards, has no more direct influence on the lean liquid composition. Yet, interacting with the mixing inlet flows from V03, it changes the composition of the gas leaving subsection 3 to subsection 2. Thus, a composition wave is triggered at the bottom of subsection 2, which travels upwards until it reaches the lean liquid draw point with total delay $\theta_1 + \theta_2 + \Delta_2$ (hence the gain K_f). Note that as soon as the inlet air flow has been perturbed, the mixing with gas from V03 has also been directly impacted. This has triggered an earlier upwards composition-change wave in subsection 2, which has already reached the lean liquid draw location, and is responsible for the gain K_c and the delay Δ_2.

The other input-output transfers can be interpreted the same way. Conversely, given any distillation column flowchart, one can assess the structure of the transfers by simply analyzing from Table 3.2 and Table 3.3 how the subsections respond to each other, and how hydraulic and composition traveling waves are triggered.

4.8 Conclusion

The PDE model developed in Chapter 2 has been tested against reference static simulation cases and real dynamic plant data regarding the High Pressure column. In steady-state, our model showed good agreement with the static simulations, for various operating conditions and over a wide span of compositions. Simplifying the model parameters, notably making the volatilities constant along the column axis, introduced some mismatches. Tuning the diffusion parameter ϵ allowed to restore the PDE model accuracy over the chosen section of the column. Tentative to estimate the hold-ups from simple considerations regarding the packing specific surface and the liquid speed yield unsatisfying results. The PDE model accuracy versus the static simulations was increased using a smaller liquid hold-up (comparable or inferior to the gas hold-up), which corresponds to an increased liquid speed. We had then to artificially uncouple the value of the liquid speed used for the hold-up calculation (μ_L) from the value used in the dynamic simulations ($\mathcal{V}_L$) for the flow propagation. This discrepancy between the theoretical and empirically satisfying parameters could indicate that not all the hold-up participates to the separation, or be a mirage originating from non-constant packing efficiency.

Following the validation of the model on the steady-state cases, we presented a dynamic scenario made of real data gathered from the industrial plant. We simulated the dynamics of the HP column using the PDE model in open-loop, and parameters directly borrowed from the static cases. We obtained satisfying reproduction of the Lean Liquid O_2 molar fraction, which oscillates around 2%, but the estimation was in advance with respect to the measure. The delay has been resorbed using a slower liquid speed $\mathcal{V}_L$ (the hold-ups were unchanged). The empirical value of $0.02m/s$ is about 5 times smaller than expected. The discrepancy is only partially explained by the neglected distributors dynamics and the delay induced by the measurement chain. In parallel, the estimated O_2 molar fraction at the top of the column, where it is supposed to be inferior to 1 ppm, was relevant. It was yet not possible to firmly validate the model at this location, since the corresponding O_2 analyzer on the plan operates out of its range. We have also shown that the dynamic simulation results were almost unsensitive to changes on the hold-ups preserving the liquid/gas hold-up ratio. This similarity with the steady-state may indicate that on the investigated packed column, the hydraulics largely dominates the local separation dynamics.

We have proposed a basic on-line adaption for the diffusion coefficient epsilon, based on the estimation error at the Lean Liquid draw location. This on-line tuning allows the PDE model to satisfyingly estimate the molar fractions at this location over a 40h time period.

The PDE model has then been tested on 17 scenarios, which represent 680 hours of operations, including functioning with only one of the two air compressors (results are given in Appendix C). When only one compressor is operating, the PDE model is unable to estimate the composition of the Lean Liquid. 11 scenarios are satisfying, whereas the remaining ones are at the limit (Lean Liquid molar fraction intermittently correctly estimated, and with dubious values for the diffusion parameter ϵ). It seems that the model performances decrease comes with lowered liquid and gas flows in the column; yet we were not able to propose a corrective approach.

In Chapter 3, we proposed a transfer functions model for an homogeneous packed subsection. Based on this block, we built a transfer functions model for the HP column. The goal was to reproduce the small oscillations of the Lean Liquid composition around an almost stabilized steady-state. The transfer model has been tested against real plant data. Oscillations are rendered with a small time-varying bias, without further tuning of the model.

Chapter 5

Application to LP column

Nous poursuivons dans ce chapitre la validation expérimentale du modèle EDP en l'appliquant à la simulation de la colonne Basse Pression de l'unité de séparation. Le fonctionnement de cette colonne est brièvement rappelé, et le schéma numérique pour la séparation d'un mélange binaire présenté au Chapitre 4 est complété avec les conditions aux limites adéquates. La colonne Basse Pression étant aussi le premier élément du procédé de séparation de l'argon, elle doit être considérée comme le siège d'une distillation ternaire. Aussi le schéma numérique est-il adapté pour traiter plus de deux composants. Les résultats obtenus avec le modèle EDP (pour des mélanges binaires ou ternaires) sont d'abord comparés avec les cas statiques de référence obtenus avec un modèle Hysys *à plateaux. La sensibilité de ces résultats par rapport aux paramètres et données d'entrée est évaluée. Le modèle est particulièrement sensible aux distributions internes de gaz et de liquide. Nous comparons ensuite le modèle EDP aux données réelles issues de l'ASU étudiée. Pour ce faire, nous simulons de concert les colonnes MP et BP en régime dynamique, des modèles simplifiés étant proposés pour inclure un couplage avec la première colonne argon K10. Les résultats sont satisfaisants pour la teneur en O_2 au sommet de la colonne Basse Pression. Comme attendu, un ventre d'argon apparaît durant les simulations. Du fait des grandes incertitudes sur la distribution du liquide, cette structure, de même que le principal front d'oxygène, n'est cependant pas stable sur le long terme en boucle ouverte. La simulation en boucle ouverte des compositions au niveau de la jonction K10-BP s'en trouve donc dégradée. La dernière section du chapitre utilise les équations relatives aux invariants de Riemann développées à la Section 2.6 en adaptant la théorie de la chromatographie. En nous limitant au phénomène de convection dans notre modèle, nous obtenons la carte des vitesses des fronts d'ondes de choc dans la colonne BP. Nous proposons alors une interprétation de la grande sensibilité observée pour les profils de compositions, à l'aide d'ondes de choc de vitesse nulle. Nous menons une comparaison avec la colonne Moyenne Pression, où le comportement des profils s'avère différent.*

This chapter pursues the experimental qualification of the PDE model by applying it to the simulation of the Air Separation Unit Low Pressure Column. The functioning of this column is briefly explained, and the binary-mixture numerical scheme presented in Chapter 4 is extended with the corresponding boundary conditions. Because the Low Pressure Column is also the first step of the argon extraction process, it shall be considered as the site of a ternary-mixture distillation. Thus the numerical scheme is adapted to cope with more than two components. The PDE model results (for binary and ternary mixutres) are first checked

against static simulation cases obtained with the reference HYSYS tray model. The sensitivity of the PDE model results to the model parameters and input data is evaluated. The model is found to be particularly sensitive to the liquid and gas flow distribution. The PDE model is then compared with real data from the ASU. For this, both the HP and the LP column are dynamically simulated, and simplified models are proposed to include the coupling with the first argon column K10. The results are satisfying regarding the O_2 content at the top of the LP column. A belly-shaped argon composition profile emerges as expected during the simulations. Yet due to the large uncertainties regarding the liquid distribution, this structure, as well as the main O_2 composition front, is not stable over long open-loop simulations, which impedes the open-loop simulation of the compositions at the location of the K10-LP column connection. The last section of the chapter makes use of the Riemann invariants equations developed in Section 2.6 by adapting the chromatography theory. Focusing on the convection phenomenon in our model, one obtains a map of the composition wave-fronts's speed in the whole LP column. We then propose an interpretation of the observed high sensitivity of the composition profile in terms of shock-waves with null or non-null speeds. A comparison is made with the HP column, where the profiles behave differently.

5.1 Introduction to the LP column

The Low Pressure[1] (LP) column is dedicated to the production of high-purity oxygen. The first step of the argon extraction process also takes place in this structure. The column is about 30 m high, the total packed height being about 20 m. It is subdivided into 5 packed subsections[2], whose diameter is 3 m, except for subsection n4 (counting from the top) which is narrower (about 2.5 m diameter). The type of the packing is the same as in the LP column, and is the same in each subsection. At the bottom of the column, a partial boiler recycles heat from the total condensation at the top of LP column. As in the previous chapter, we invite the reader to refer to Fig. A.3 where the tags of sensors and flows used in the following are plotted on the ASU chart.

The LP column is fed with liquid from the HP column *via* subsections 1, 2 and 3. A small amount (around 1%) of the Lean Liquid entering subsection 1 can vaporize and leave with the rest of the gas flow through the top vent. Liquid flows to enter in subsections 2 and 3 (respectively liquid air from the LP column flash-pot, and oxygen rich liquid from the bottom of LP column) first pass through flash-pots; thus the column is actually fed with a liquid-gas mixture, with significant gas/liquid ratio (about 0.15). At the bottom of subsection 4, the liquid flow is completed with the bottom liquid of the first argon column. The liquid then accumulates at the bottom of the HP column, where it partially re-evaporates, depending on the heat-flow obtained by the total condensation at the top of LP column. In parallel, liquid is drawn off the bath and constitutes the oxygen production of the plant. The evaporated fraction of the bath rises up to the bottom of subsection 4, where a large amount is deflected to serve as gas feed at the bottom of the first argon column. In this argon column, the gas is totally liquefied by the top condenser; thus an almost equivalent amount of gas is obtained by vaporization of the cooling liquid (coming from the bottom of the HP column). This gas is sent back to the LP column at the top of subsection 4 to complete the gas flow.

[1] So designated because it operates only slightly above atmospheric pressure, contrary to the HP column.

[2] Strictly speaking, there are 6 packed blocks separated by distributors; yet blocks 5 and 6 (counting from the top) are part of the same functional subsection.

Contrary to the HP column where oxygen and argon could be thought as a single pseudo-component, a significant oxygen/argon separation occurs in the LP column. At the bottom of the column, the oxygen molar fraction is almost 100%, and argon behaves similarly to nitrogen as a light component. At the top of the column, the dominating component is nitrogen (more than 95%), and argon behaves as a heavy component, similarly to oxygen. As a result, in the middle of the column, there exists a region of maximum argon concentration (up to 15-20%) known as the "bubble" or "belly". For this column, the ternary dynamic modeling is then really useful. Indeed, the goal of the process control is to simultaneously maintain a high argon molar fraction (above 10%) and a low nitrogen molar fraction (typically below 0.1 %) in the gas feeding the first argon column, while ensuring the purity of the liquid oxygen bath at the bottom of the LP column.

5.2 Numerical schemes

5.2.1 Numerical scheme for pseudo-binary simulation

The numerical scheme for pseudo-binary simulation of the LP column is similar to the one used for the HP column. The only differences lay in the boundary conditions.

LP top boundary condition

The top boundary includes a feed with a liquid/gas mixture and the venting of the entire incoming gas flow. Following the notations of the previous chapter, one has:

$$L_{in}(t)x_{in}(t) + V_{in}(t)y_{in}(t) + V_{\oplus}(t)k(X_{\oplus}(t)) + \epsilon G(X(0,t))\frac{\partial X}{\partial s}(0,t) \\ = L(0,t)X(0,t) + V(0,t)y(0,t).$$

Discretizing the equation yields:

$$X_0^i = \frac{L_{in}^i x_{in}^i + V_{in}^i y_{in}^i + V_1^i k(X_1^i) + \frac{\epsilon}{\Delta z}\left(G_{0/1} - V_0^i \sigma_{L0}^i H_{0/1}\right) X_1^i}{L_0^i + V_0^i \frac{k(X)_0^{i-1}}{X_0^{i-1}} + \frac{\epsilon}{\Delta z}\left(G_{0/1} - V_0^i \sigma_{L0}^i H_{0/1}\right)}.$$

Note that according to (4.10), this boundary condition is similar to a matching condition where $V_{\ominus}^i = 0$, i.e all the gas is "drawn off" by the vent.

LP bottom boundary condition

The LP column bottom model combines the boundary condition for the distillation equation (interface between the column and the liquid bath) and the mixing dynamics of the bath. The corresponding dynamic system reads:

$$\sigma_B \frac{dx_b}{dt} = L(h,t)x(h,t) - (L_{prod}(t) + V_B(t))x_B(t),$$
$$L_{\ominus}(t)X_{\ominus}(t) + V_B(t)x_B(t) = L(h,t)x(h,t) + V(h,t)k(X(h,t)) \\ + \epsilon G(X(h,t))\frac{\partial X}{\partial z}(h,t),$$

where σ_B stands for the amount of liquid stored in the bath, with pseudo-component molar fraction x_B, and V_B is the gas flow evaporated from the bath. L_{prod} is the liquid flow drawn off the bath for production purposes. We assume that σ_B is constant since the liquid level is tightly controlled to a constant value[3] by adjusting the production flow L_{prod}. The system reads in discrete form:

$$x_B^i = \frac{\frac{\sigma_B}{\Delta t} x_B^{i-1} + L_h^i X_h^i - \epsilon \sigma_{V}{}_h^i H_{h-1/h} \frac{X_h^i - X_{h-1}^i}{\Delta s}}{\frac{\sigma_B}{\Delta t} + V_B^i + L_{prod}^i},$$
$$X_h^i = \frac{V_B^i x_B^i + \left(L_{h-1}^i + \frac{\epsilon}{\Delta s}\left(G_{h-1/h} - \sigma_{V}{}_h^i L_h^i H_{h-1/h}\right)\right) X_{h-1}^i}{L_h^i + V_h^i \frac{k(X_h^{i-1})}{X_h^{i-1}} + \frac{\epsilon}{\Delta s}\left(G_{h-1/h} - \sigma_{V}{}_h^i L_h^i H_{h-1/h}\right)}.$$

5.2.2 Numerical scheme for ternary simulation

For the ternary simulation, the numerical scheme is intended to provide $\mathbf{X}_k^t := \left(X_{O_2,k}^t, X_{Ar,k}^t\right)^T$ for any $k \in [0, H]$ based on $\mathbf{X}_k^{t-1}$. Following the same linearization procedure than in Chapter 4, the matrix equation (2.66) rewrites in discrete form:

$$\begin{aligned}(\sigma_{L}{}_k^i I_2 + \sigma_{V}{}_k^i \mathbf{J}_K(\mathbf{X}_k^i)) \frac{\mathbf{X}_k^{i+1} - \mathbf{X}_k^i}{\Delta t} &= \frac{L_{k-1}^i \mathbf{X}_{k-1}^i - L_k^i \mathbf{X}_k^i}{\Delta s} \\ &+ \frac{V_{k+1}^i}{\Delta s} \begin{pmatrix} \frac{k_{O_2}(\mathbf{X}_{k+1}^i)}{X_{O_2,k+1}^i} & 0 \\ 0 & \frac{k_{Ar}(\mathbf{X}_{k+1}^i)}{X_{Ar,k+1}^i} \end{pmatrix} \mathbf{X}_{k+1}^i - \frac{V_k^i}{\Delta s} \begin{pmatrix} \frac{k_{O_2}(\mathbf{X}_k^i)}{X_{O_2,k}^i} & 0 \\ 0 & \frac{k_{Ar}(\mathbf{X}_k^i)}{X_{Ar,k}^i} \end{pmatrix} \mathbf{X}_k^i \\ &+ \epsilon \mathbf{G}_{k-1/k} \frac{\mathbf{X}_{k-1}^i - \mathbf{X}_k^i}{\Delta s^2} + \epsilon \mathbf{G}_{k/k+1} \frac{\mathbf{X}_{k+1}^i - \mathbf{X}_k^i}{\Delta s^2} \end{aligned} \quad (5.1)$$

where I_2 is the 2×2 identity matrix. We recall that $\mathbf{J}_K(\mathbf{X}_k^i)$ stands for the Jacobian matrix of application $\mathbf{K}$ (the thermodynamic equilibrium relation) at $\mathbf{X_k^i}$. As previously, we have:

$$\mathbf{G}_{k-1/k} = 2\left(\mathbf{G}_{k-1}\mathbf{G}_k\right)\left(\mathbf{G}_{k-1} + \mathbf{G}_k\right)^{-1},$$
$$\mathbf{G}_{k/k+1} = 2\left(\mathbf{G}_k\mathbf{G}_{k+1}\right)\left(\mathbf{G}_k + \mathbf{G}_{k+1}\right)^{-1},$$

where

$$\mathbf{G}_k = \left(\sigma_{L}{}_k^i V_k^i + \sigma_{V}{}_k^i L_k^i\right)^2 \left(\frac{\mathbf{J}_K(\mathbf{X}_k^i)^2}{\lambda_L} + \frac{\mathbf{J}_K(\mathbf{X}_k^i)}{\lambda_V}\right)\left(\sigma_{L}{}_k^i I_2 + \sigma_{V}{}_k^i \mathbf{J}_K(\mathbf{X}_k^i)\right)^{-2},$$

for any $k \in [0, H]$ according to (2.63). We obtain the numerical scheme by rewriting (5.1) in

[3] to keep the reboiler submerged and prevent the deposit of dry hydrocarbons which could catch fire in this oxygen-rich environment.

Case	Pressure (bar)	Bottom temperature (K)	Top temperature (K)
A	1.4	93.2	79.8
B	1.391	93.2	79.6
C	1.346	92.8	82.2

Table 5.1: Pressure and temperature values used to simulate the static cases with the PDE model

an implicit form:

$$\left[\frac{\sigma_{L_k}^i I_2 + \sigma_{V}{}_k^i \mathbf{J}_K(\mathbf{X}_k^i)}{\Delta t} + \frac{L_k^i}{\Delta s} I_2 + \frac{V_k^i}{\Delta s}\begin{pmatrix} \frac{k_{O_2}(\mathbf{X}_k^i)}{X_{O_2,k}^i} & 0 \\ 0 & \frac{k_{Ar}(\mathbf{X}_k^i)}{X_{Ar,k}^i} \end{pmatrix} + \frac{\epsilon}{\Delta s^2}\left(\mathbf{G}_{k-1/k} + \mathbf{G}_{k/k+1}\right)\right]\mathbf{X}_k^{i+1}$$
$$= \frac{\mathbf{X}_k^i}{\Delta t} + \left(\frac{L_{k-1}^i}{\Delta s} + \epsilon\frac{\mathbf{G}_{k-1/k}}{\Delta s^2}\right)\mathbf{X}_{k-1}^i + \left(\frac{V_{k+1}^i}{\Delta s}\begin{pmatrix} \frac{k_{O_2}(\mathbf{X}_{k+1}^i)}{X_{O_2,k+1}^i} & 0 \\ 0 & \frac{k_{Ar}(\mathbf{X}_{k+1}^i)}{X_{Ar,k+1}^i} \end{pmatrix} + \epsilon\frac{\mathbf{G}_{k/k+1}}{\Delta s^2}\right)X_{k+1}^i. \tag{5.2}$$

The compositions $\mathbf{x}_k^i$ and $\mathbf{y}_k^i$ are given by the static outputs:

$$\mathbf{x}_k^i = \mathbf{X}_k^i - \epsilon\sigma_{V}{}_k^i \mathbf{H}_k \frac{\mathbf{X}_{k+1}^i - \mathbf{X}_k^i}{\Delta s},$$
$$\mathbf{y}_k^i = \mathbf{K}(\mathbf{X}_k^i) + \epsilon\sigma_{L}{}_k^i \mathbf{H}_k \frac{\mathbf{X}_k^i - \mathbf{X}_{k-1}^i}{\Delta s},$$

where

$$\mathbf{H}_k = \left(\sigma_{L}{}_k^i V_k^i + \sigma_{V}{}_k^i L_k^i\right)\mathbf{G}_k$$
$$= \left(\sigma_{L}{}_k^i V_k^i + \sigma_{V}{}_k^i L_k^i\right)\left(\frac{\mathbf{J}_K(\mathbf{X}_k^i)^2}{\lambda_L} + \frac{\mathbf{J}_K(\mathbf{X}_k^i)}{\lambda_V}\right)\left(\sigma_{L}{}_k^i I_2 + \sigma_{V}{}_k^i \mathbf{J}_K(\mathbf{X}_k^i)\right)^{-2}.$$

5.3 Comparison with static simulation reference cases

As for the HP column, we dispose of the Hysys simulations of the Low Pressure column in the static cases A, B and C. For the sake of clarity only the figures regarding case A are included in this chapter; for case B and C, we invite the reader to refer to Appendix D. The column is modeled in Hysys using 60 equivalent trays. The flow and composition profiles obtained in Hysys are mapped to our space grid using a linear interpolation over each subsection. The pressure variation along the column is about 6.5% of its value at the top, thus it will be neglected in each case. We use a linearly varying temperature profile which interpolates the top and bottom temperatures to estimate the gas hold-ups. For each case, σ_V is estimated using (4.15) and the values of Table 5.1. The liquid hold-ups are estimated using $\sigma_L = \frac{L}{\mu_L}$, μ_L being the same for each case.

5.3.1 Pseudo-binary mixture model

Figure 5.1 illustrates the liquid and gas distribution profiles for case A (for case B and C see Fig. D.1 and Fig. D.2), together with the pseudo-binary composition profiles estimated

by HYSYS . As one can see, the LP column profiles are characterized by a huge O_2,Ar composition front in subsections 3, 4 (counting from the top). The difficulty of the PDE model fitting lays in the rendering of this front, which turns out to be highly sensitive to our model's parameters.

Using the s-depending relative volatility profile obtain with HYSYS , good fits between the tray model and the PDE model are provided by the following numerical values:

$$\overline{\mu}_L = 0.6 \text{ m.s}^{-1}, \quad \begin{cases} \lambda_L = 20 \text{ Nm}^3.\text{s}^{-1}.\text{m}^{-1}, \\ \lambda_V = 10\lambda_L, \end{cases} \quad \epsilon = \begin{cases} 0.22 & \text{for case A,} \\ 0.23 & \text{for case B,} \\ 0.23 & \text{for case C.} \end{cases}$$

The same remarks can be made about $\mu_L = 0.6m/s$ than in the previous chapter. Once again, this value shall be regarded as an empirical correlation between the liquid flow and the hold-ups. One can though notice that the ratio of the μ_L in the two columns is $\frac{0.6}{0.4} = 1.5$ which is close the section rate $\frac{1.55^2}{1.325^2} \approx 1.37$. Thus μ_L is not completely devoid of geometric meaning. Note also that the values of ϵ found for the HP column, though not directly transposable here, are reasonable guess values before a finer tuning. Figure 5.2, and Fig. D.3, D.4 in appendix, illustrate the corresponding estimated profiles, respectively for case A, B and C. The main wave-fronts are properly positioned, yet the PDE model misses the strong curvature of the profiles in subsection 4. Also, the PDE model predicts a reasonably low nitrogen molar fraction at the bottom of the column (around 10^{-7}), which is yet almost 10 orders of magnitude larger than the HYSYS estimation. Figure 5.3 illustrates the phenomenon for case A. One can though stay cautious regarding such minuscule concentrations.

Regardless of the diffusion, catching the composition fronts with the PDE model is a problem of composition waves' speed tuning. As discussed in Chapter 2 or Chapter 5, the composition waves' speed depends (in steady state) on the flows L, V and the relative volatility α. L and V being fixed, we will replace the HYSYS volatility profile by a constant α, which we will use as the wave-speed tuning parameter to render the main composition front. We obtain good performances with the following values:

$$\epsilon = \begin{cases} 0.175 & \text{for case A,} \\ 0.175 & \text{for case B,} \\ 0.175 & \text{for case C} \end{cases}, \quad \alpha = \begin{cases} 0.2763 & \text{for case A,} \\ 0.2763 & \text{for case B,} \\ 0.26175 & \text{for case C,} \end{cases}$$

the rest being unchanged. Figure 5.4, and Fig. D.5, D.6 in appendix, illustrate the corresponding results. Figure 5.5 displays the HYSYS relative volatility profiles versus the chosen constant α for each case. No particular rule for the choice of α seems to emerge, besides the fact that the s-varying profile reaches the chosen constant value in region of the main composition front.

As mentioned above, the main wavefront position is highly sensitive to the numerical values of the model parameters, in particular the constant α. Figure 5.6 shows for example the influence of a +1% variation of α in case A. A side-effect is that playing on α allows recovering the profile in subsection 3, to the expense of section 4, or *vice-versa*. The influence of ϵ exists but is less remarkable, as depicted on Fig. 5.7 for a +5% variation. The diffusion parameter ϵ playing no role in the composition wave convection speed, it affects the curvature of the estimated profile before the position of the wavefronts.

The main wavefront is also highly sensitive to the model's input data, as demonstrated for example on Fig. 5.8 (−1% variation of the gas/liquid ratio in the feed between subsections

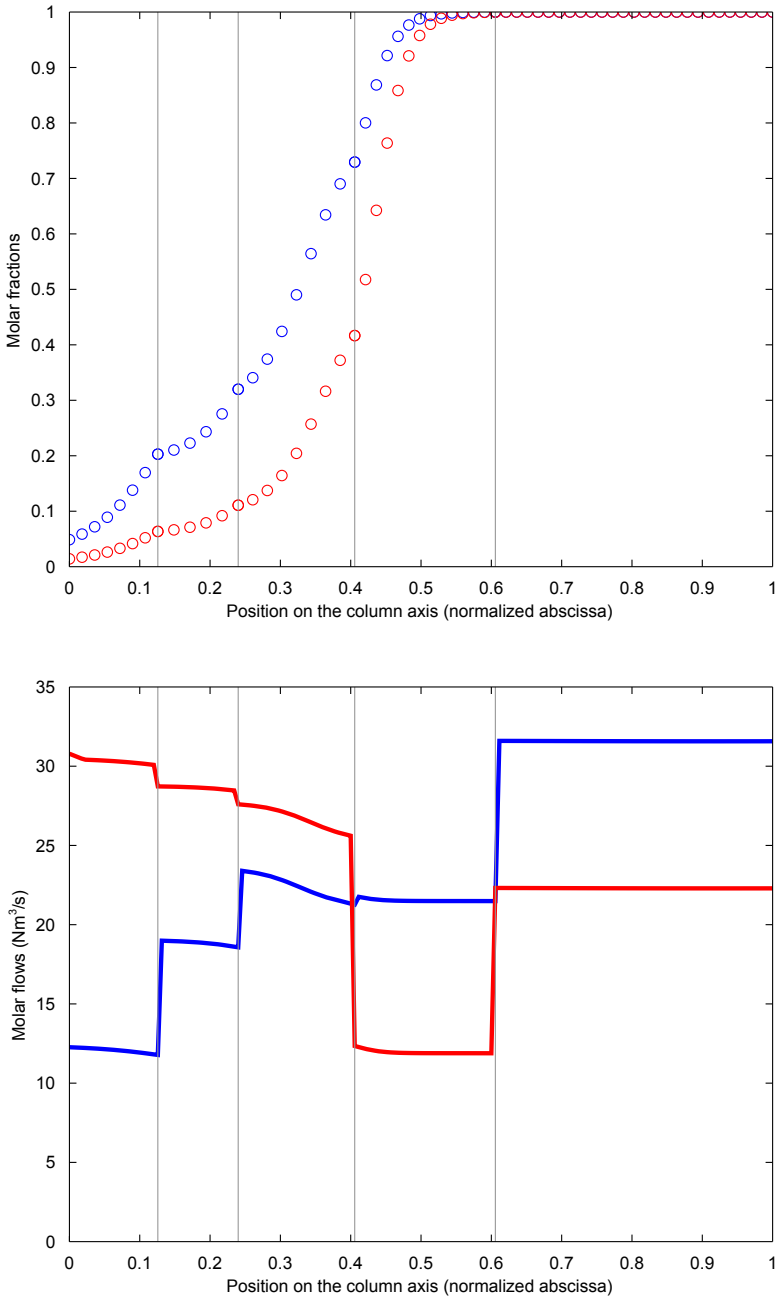

Figure 5.1: *Top:* HYSYS estimations of the liquid (blue) and gas (red) composition profiles in case A. *Bottom:* internal liquid (blue) and gas (red) flows in case A.

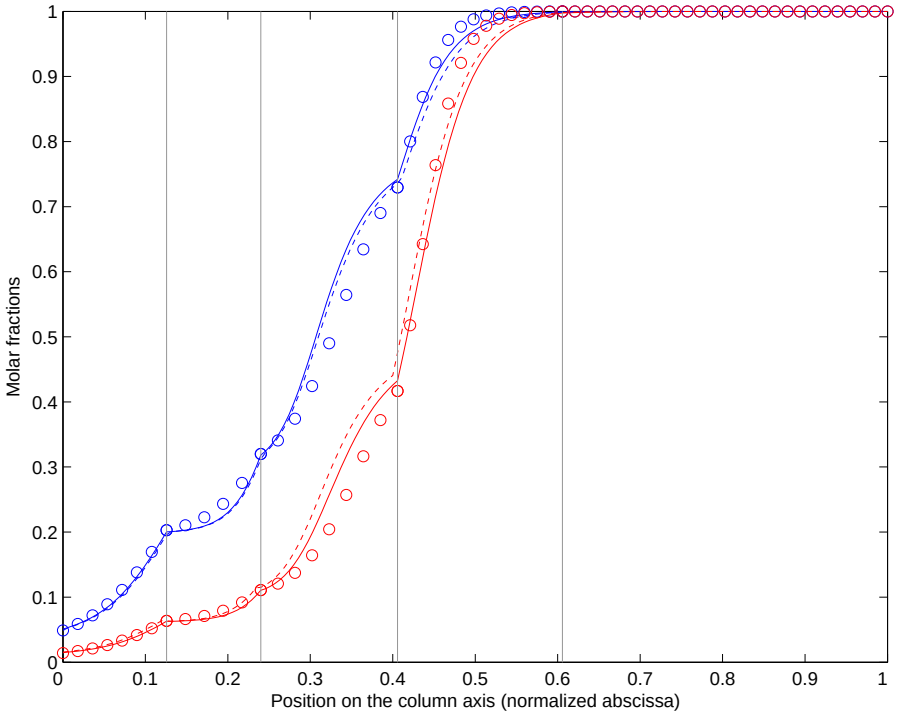

Figure 5.2: Comparison of the HYSYS and the pseudobinary PDE model composition estimations in case A with a s-varying relative volatility. *Blue circles:* HYSYS estimation in liquid. *Red circles:* HYSYS composition estimation in gas. *Blue solid line:* PDE model lumped composition X. *Red solid line:* $k(X)$. *Blue dotted line:* PDE model estimated composition in liquid (static output x). *Red dotted line:* PDE model estimated composition in gas (static output y).

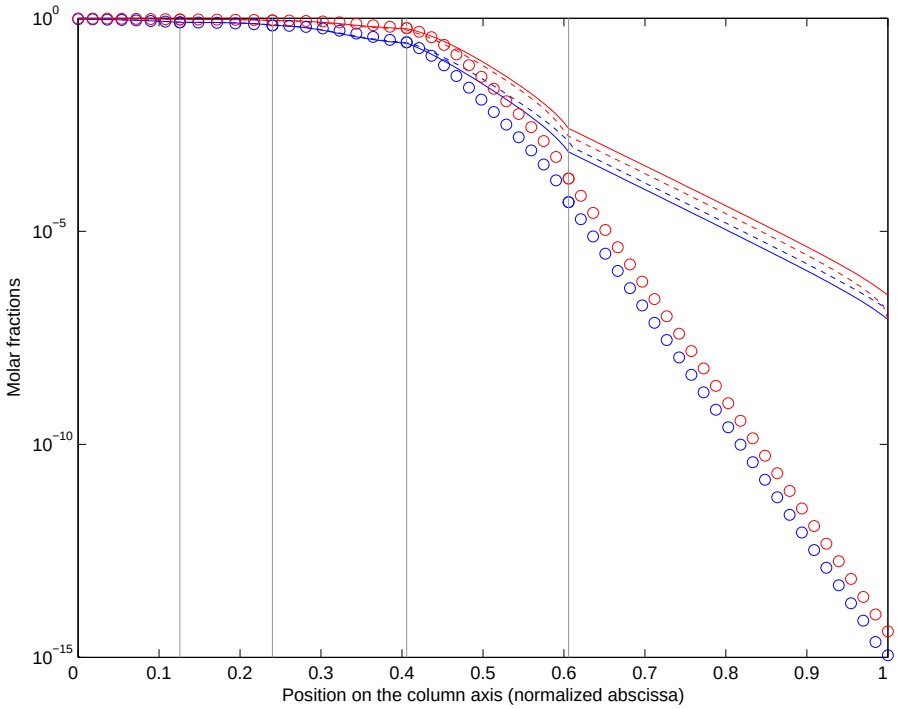

Figure 5.3: Comparison of the HYSYS and the pseudobinary PDE model nitrogen composition estimations in case A with a s-varying relative volatility, in log scale. *Blue circles:* HYSYS estimation in liquid. *Red circles:* HYSYS composition estimation in gas. *Blue solid line:* PDE model lumped composition $1 - X$. *Red solid line:* $1 - k(X)$. *Blue dotted line:* PDE model estimated composition in liquid (static output $1 - x$). *Red dotted line:* PDE model estimated composition in gas (static output $1 - y$).

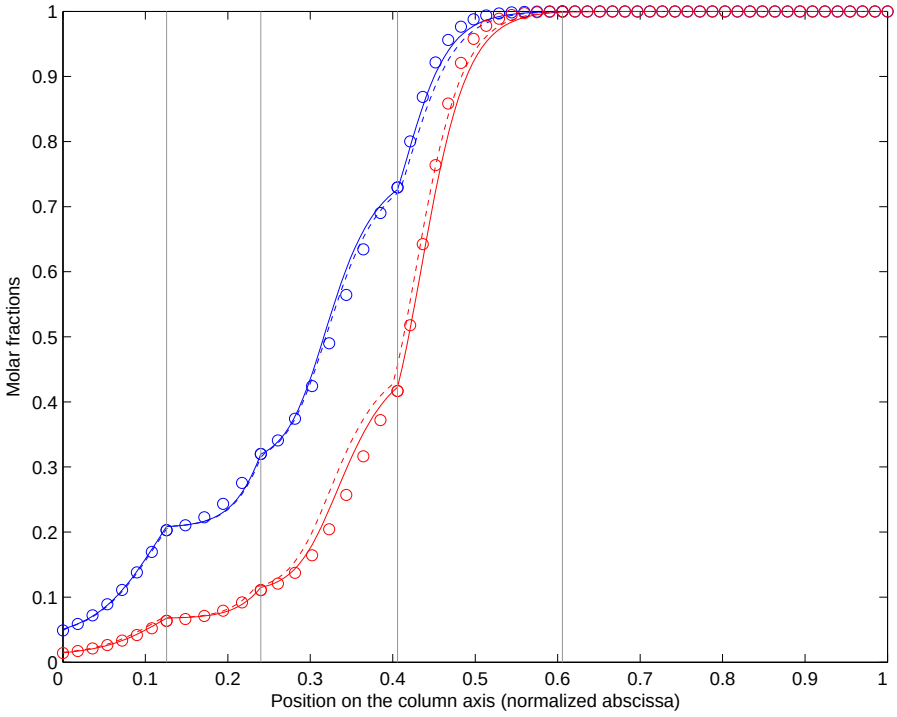

Figure 5.4: Comparison of the HYSYS and the pseudobinary PDE model composition estimations in case A with a constant relative volatility. *Blue circles:* HYSYS estimation in liquid. *Red circles:* HYSYS composition estimation in gas. *Blue solid line:* PDE model lumped composition X. *Red solid line:* $k(X)$. *Blue dotted line:* PDE model estimated composition in liquid (static output x). *Red dotted line:* PDE model estimated composition in gas (static output y).

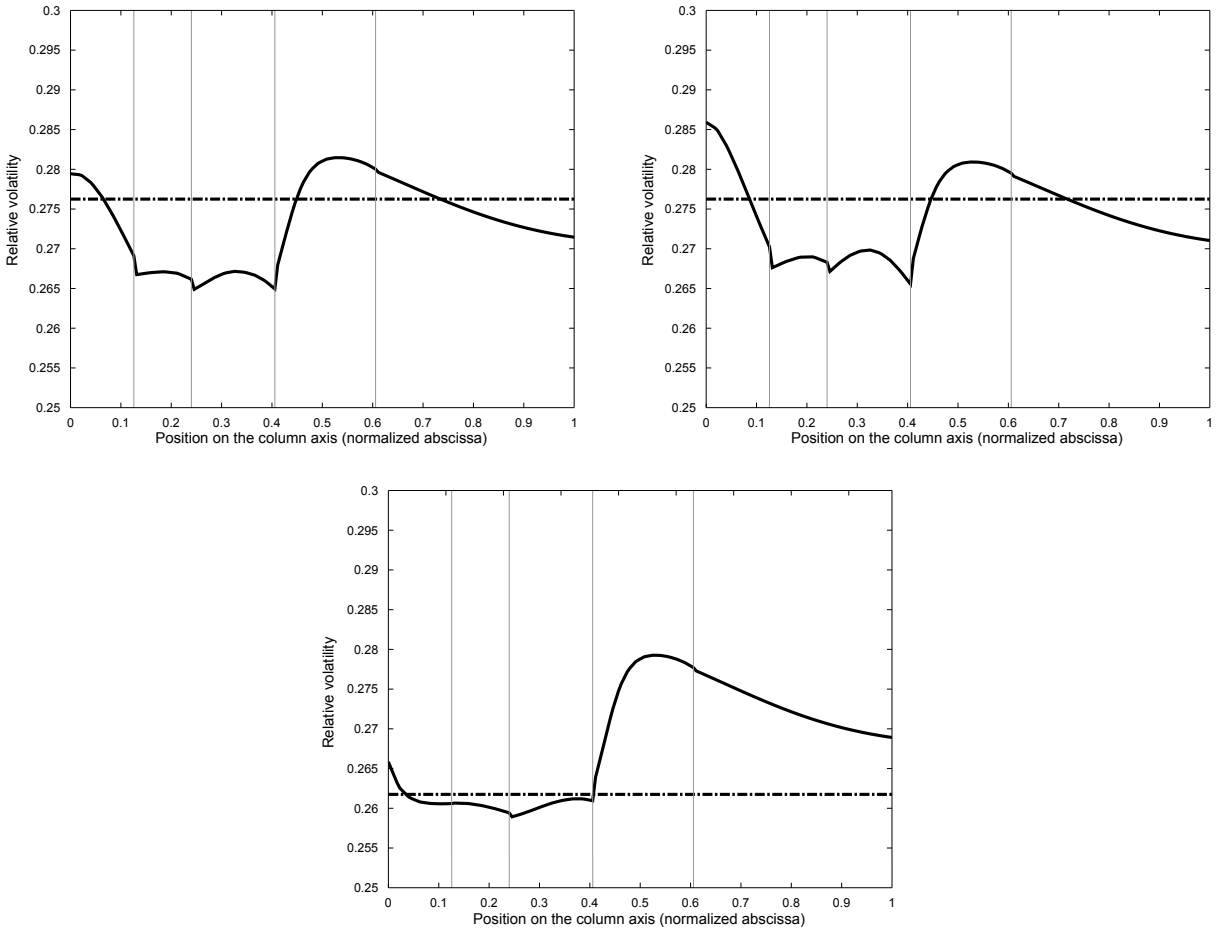

Figure 5.5: Comparison of the HYSYS profile (solid) and the optimal constant value (dash-dotted) for the relative volatility of the pseudocomponent $\{O_2, Ar\}$ versus N_2. *Top left:* case A. *Top right:* case B. *Bottom:* case C.

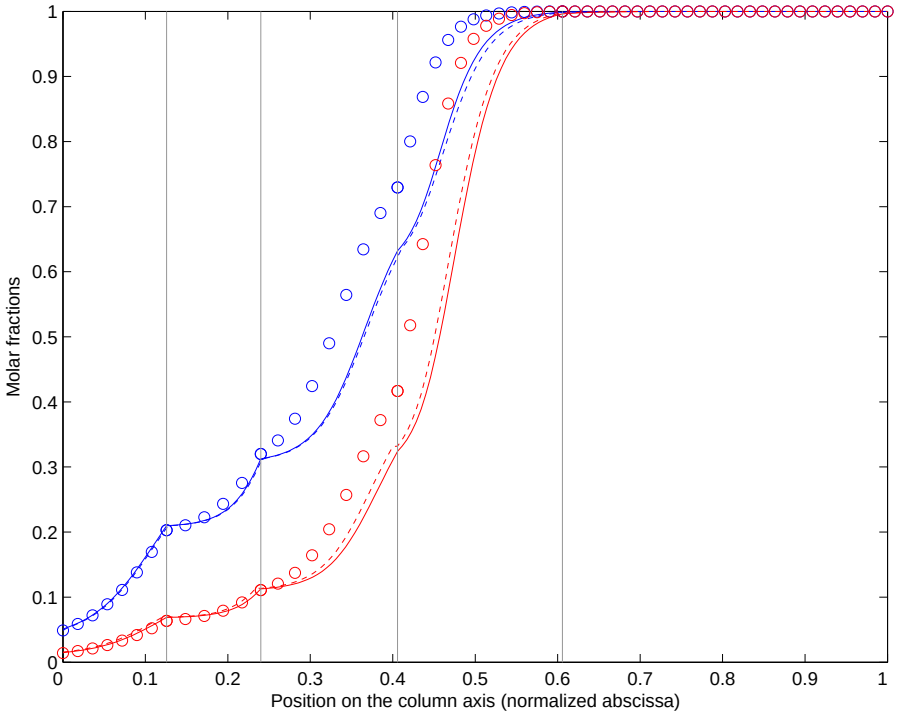

Figure 5.6: Comparison of the HYSYS and the pseudobinary PDE model composition estimations in case A with +1% perturbation on the optimal value of α. *Blue circles:* HYSYS estimation in liquid. *Red circles:* HYSYS composition estimation in gas. *Blue solid line:* PDE model lumped composition X. *Red solid line:* $k(X)$. *Blue dotted line:* PDE model estimated composition in liquid (static output x). *Red dotted line:* PDE model estimated composition in gas (static output y).

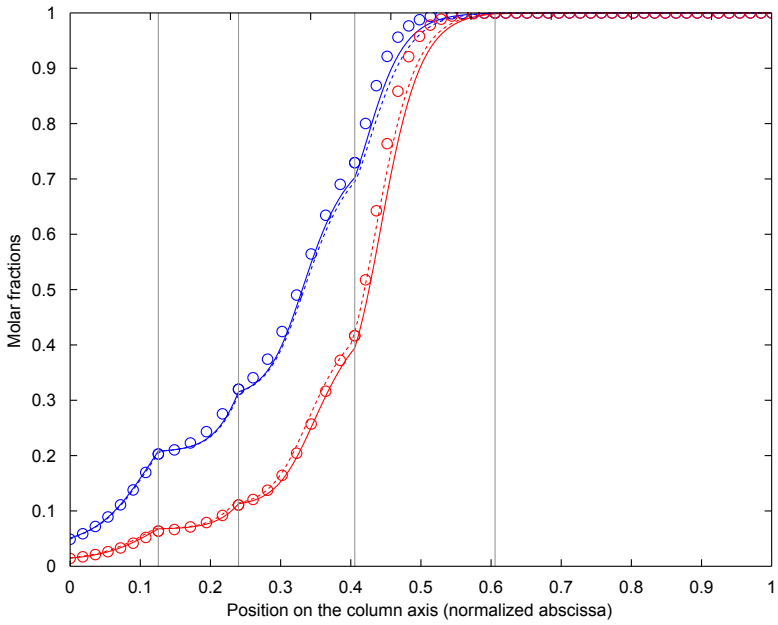

Figure 5.7: Comparison of the HYSYS and the pseudobinary PDE model composition estimations in case A with +5% perturbation on the optimal value of ϵ. *Blue circles:* HYSYS estimation in liquid. *Red circles:* HYSYS composition estimation in gas. *Blue solid line:* PDE model lumped composition X. *Red solid line:* $k(X)$. *Blue dotted line:* PDE model estimated composition in liquid (static output x). *Red dotted line:* PDE model estimated composition in gas (static output y).

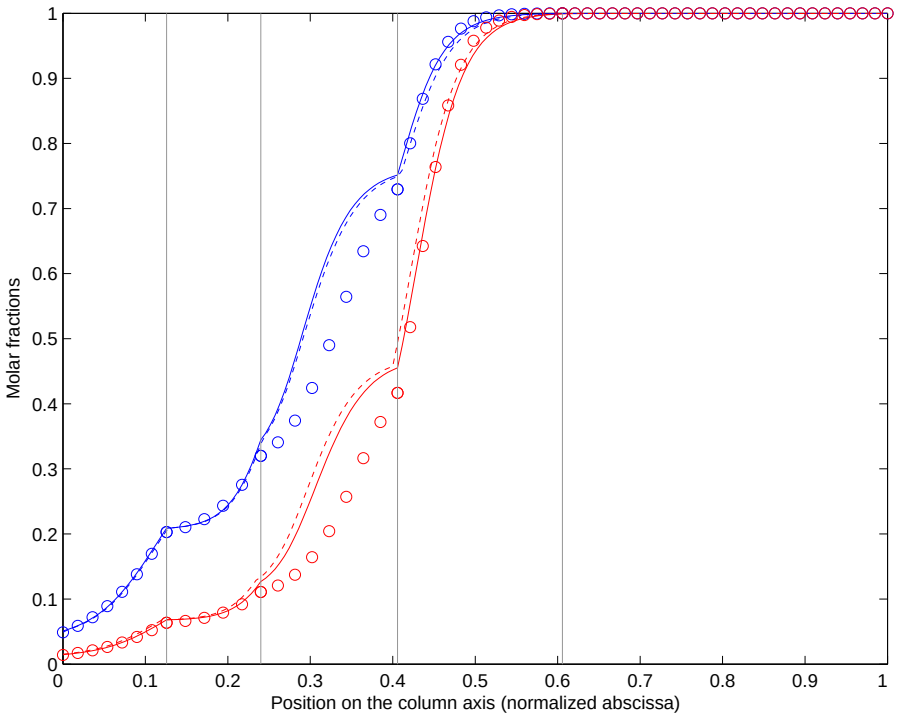

Figure 5.8: Comparison of the HYSYS and the pseudobinary PDE model composition estimations in case A with +1% perturbation on the original gas/liquid molar ratio (0.181) in the feed between subsections 2 and 3 (feed from the V04 flashpot). Original molar fractions are 0.2454 in the liquid feed, 0.1631 in the gas feed. *Blue circles:* HYSYS estimation in liquid. *Red circles:* HYSYS composition estimation in gas. *Blue solid line:* PDE model lumped composition X. *Red solid line:* $k(X)$. *Blue dotted line:* PDE model estimated composition in liquid (static output x). *Red dotted line:* PDE model estimated composition in gas (static output y).

2 and 3), and Fig. 5.9 (+1% variation of the O_2,Ar molar fraction in the feed between subsections 2 and 3). As we will see in the dynamic simulation part, this sensitivity is an effective issue for the real-life problem, where the column's inputs are poorly known. In the last part of this chapter, we give an interpretation of this sensitivity in terms of wave speeds, even for the ternary mixture problem. Illustrations of the effects of perturbations with opposite sign are in Appendix D: Fig. D.7 to Fig. D.10.

5.3.2 Ternary mixture model

With the dedicated numerical scheme, the distillation of the ternary mixture $\{N_2,O_2,Ar\}$ can be simulated in steady state in the LP column. The model's parameters set is extended with the O_2/N_2 and the Ar/N_2 relative volatilities (namely α_{O_2} and α_{Ar}). Figure 5.10, and Fig. D.11, D.12 in appendix, illustrate the results we obtain using the s-depending profiles

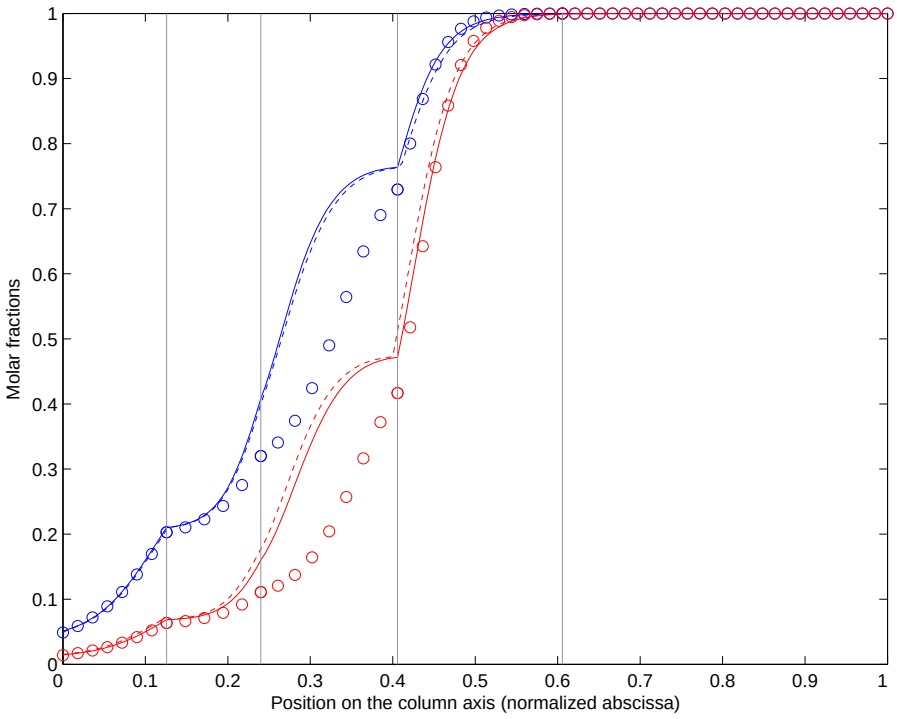

Figure 5.9: Comparison of the HYSYS and the pseudobinary PDE model composition estimations in case A with +1% perturbation on the original $\{O_2,Ar\}$ pseudocomponent molar fraction in the feed between subsection 2 and 3 (feed from the V04 flashpot). Original molar fractions are 0.2454 in the liquid feed, 0.1631 in the gas feed. *Red circles:* HYSYS composition estimation in gas. *Blue solid line:* PDE model lumped composition X. *Red solid line:* $k(X)$. *Blue dotted line:* PDE model estimated composition in liquid (static output x). *Red dotted line:* PDE model estimated composition in gas (static output y).

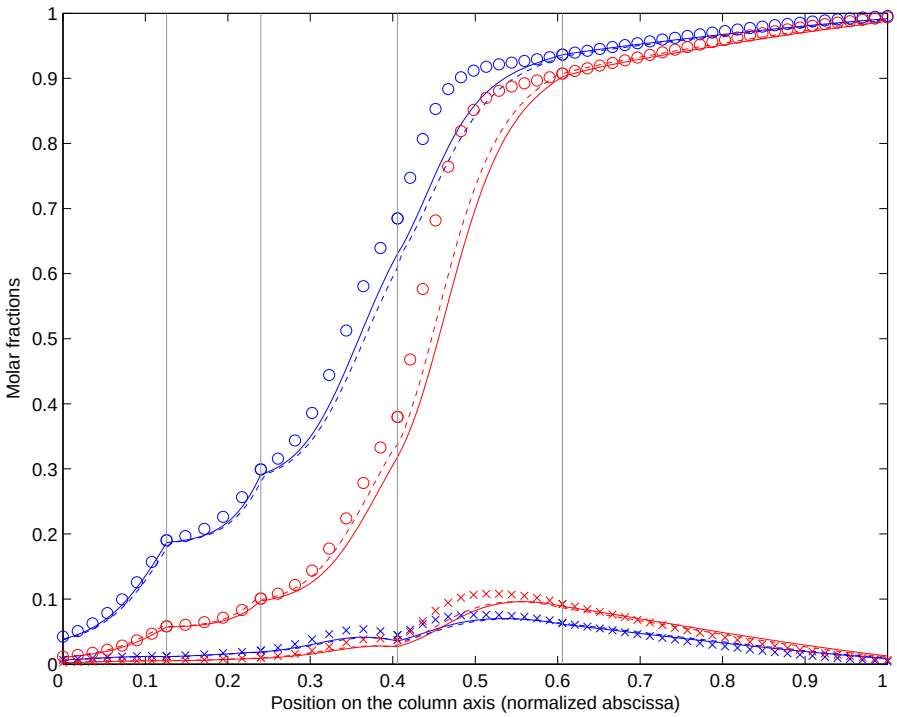

Figure 5.10: Comparison of the HYSYS and the pseudobinary PDE model composition estimations in case A with the s-dependent relative volatilities estimated using HYSYS . The monotone profiles corresponds to oxygen, the belly-shaped ones to argon. *Blue circles:* HYSYS estimation in liquid. *Red circles:* HYSYS composition estimation in gas. *Blue solid line:* PDE model lumped composition X. *Red solid line:* $k(X)$. *Blue dotted line:* PDE model estimated composition in liquid (static output x). *Red dotted line:* PDE model estimated composition in gas (static output y).

for α_{O_2} and α_{Ar} given by HYSYS and the following parameters:

$$\overline{\mu}_L = 0.6 \text{ m.s}^{-1}, \quad \begin{cases} \lambda_L = 20 \text{ Nm}^3.\text{s}^{-1}.\text{m}^{-1}, \\ \lambda_V = 10\lambda_L, \end{cases} \qquad \epsilon = \begin{cases} 0.269 & \text{for case A,} \\ 0.403 & \text{for case B,} \\ 0.211 & \text{for case C.} \end{cases}$$

One see how, in subsection 6, the steady pseudocomponent $\{O_2,Ar\}$ composition is obtained by a slow exchange of O_2 and Ar with almost constant nitrogen content. Conversely, in subsections 3 and 4, the main $\{O_2,Ar\}$ composition front in the binary mixture case shows here as the sum of a large O_2 composition front plus a small Ar contribution. The results can be improved by applying a multiplication factor m to the HYSYS $\alpha_{O_2}(s)$ and $\alpha_{Ar}(s)$, as shown on Fig. 5.11, and Fig. D.13, D.14 in appendix. We have used the following multipliers:

$$m = \begin{cases} 0.94 & \text{for case A,} \\ 0.80 & \text{for case B,} \\ 0.99 & \text{for case C,} \end{cases}$$

the other parameters being unchanged. This illustrates the high sensitivity of the ternary-mixture model to the relative volatilities of the components.

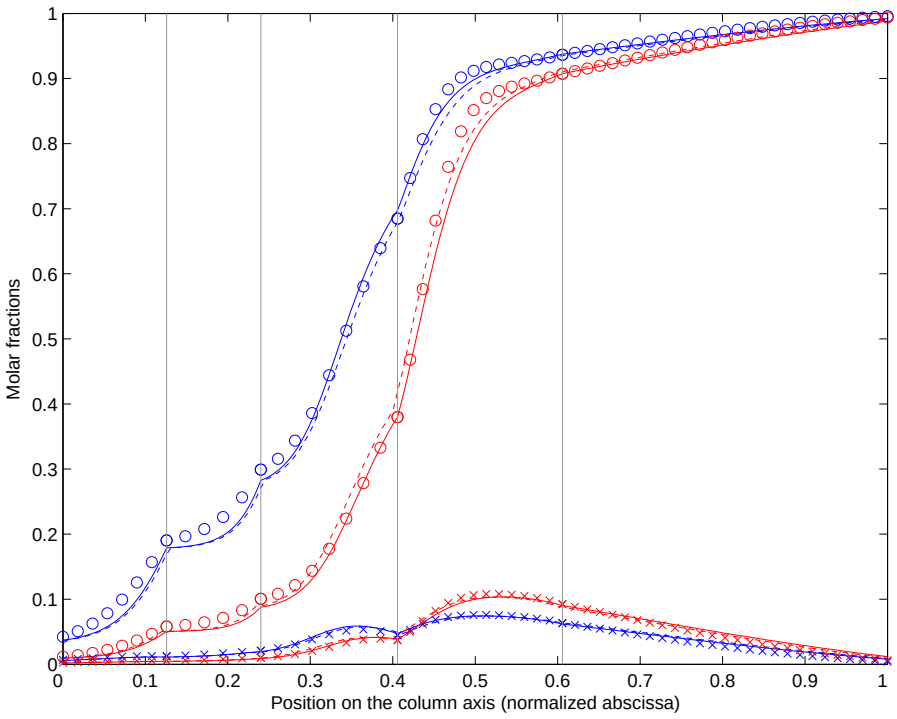

Figure 5.11: Comparison of the HYSYS and the pseudobinary PDE model composition estimations in case A with the s-dependent relative volatilities estimated using HYSYS times a multiplicative factor $m = 0.94$. The monotone profiles corresponds to oxygen, the belly-shaped ones to argon. *Blue circles:* HYSYS estimation in liquid. *Red circles:* HYSYS composition estimation in gas. *Blue solid line:* PDE model lumped composition X. *Red solid line:* $k(X)$. *Blue dotted line:* PDE model estimated composition in liquid (static output x). *Red dotted line:* PDE model estimated composition in gas (static output y).

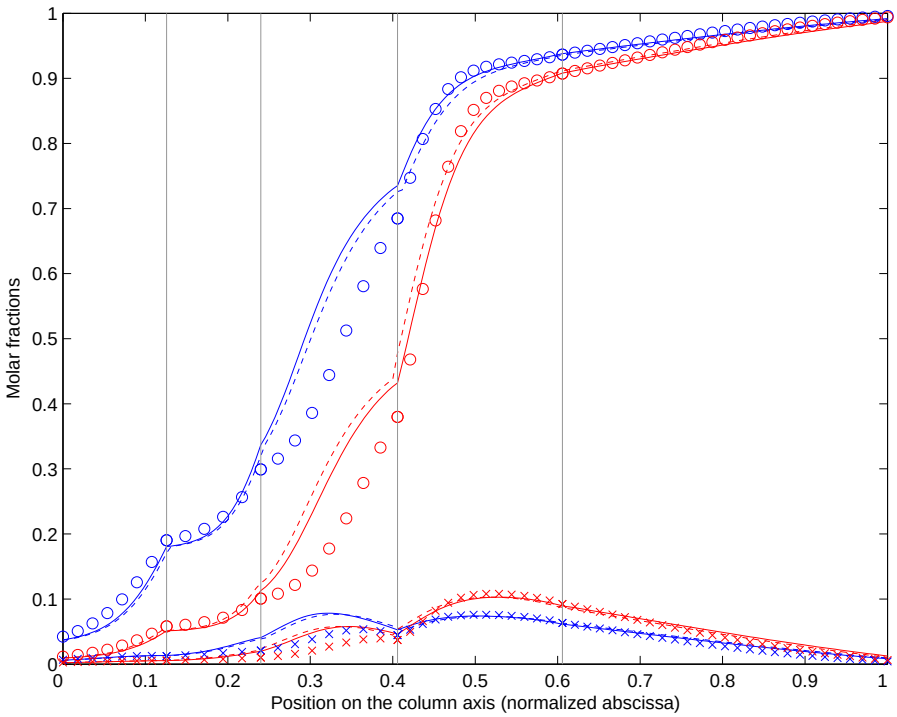

Figure 5.12: Comparison of the HYSYS and the pseudobinary PDE model composition estimations in case A with +1% perturbation on the original gas/liquid molar ratio (0.181) in the feed between subsections 2 and 3 (feed from the V04 flashpot). *Blue circles:* HYSYS estimation in liquid. *Red circles:* HYSYS composition estimation in gas. *Blue solid line:* PDE model lumped composition X. *Red solid line:* $k(X)$. *Blue dotted line:* PDE model estimated composition in liquid (static output x). *Red dotted line:* PDE model estimated composition in gas (static output y). Impact of a -1% perturbation of the gas/liquid ratio is depicted on Fig. D.15.

A high sensitivity to the liquid and gas flow distributions is still observed (see e.g. Fig. 5.12). We have seen in the binary mixture case that these sensitivities summarize as the sensitivity to the composition wave convection speed. Here in the ternary mixture case, a direct interpretation in term of wave-speed is not possible in the physical composition space. Yet we will see in the end of the chapter how we can retrieve this interpretation by the mean of the Riemann invariants equations developed in Section 2.6.

With the simplifying use of constant relative volatilities, one can still obtain reasonable approximations of the HYSYS profiles. The results depicted on Fig. 5.13, and Fig. D.16, D.17 in appendix, have been obtained with

$$\begin{array}{lll} \overline{\mu}_L = 0.6 \text{ m.s}^{-1}, & \lambda_L = 20 \text{ Nm}^3.\text{s}^{-1}.\text{m}^{-1}, & \lambda_V = 10\lambda_L, \\ \epsilon = 0.269, & \alpha_{0_2} = 0.2384, & \alpha_{Ar} = 0.3586 \text{ for case A}, \\ \epsilon = 0.3829, & \alpha_{0_2} = 0.2007, & \alpha_{Ar} = 0.3019 \text{ for case B}, \\ \epsilon = 0.211, & \alpha_{0_2} = 0.2509, & \alpha_{Ar} = 0.3774 \text{ for case C}. \end{array}$$

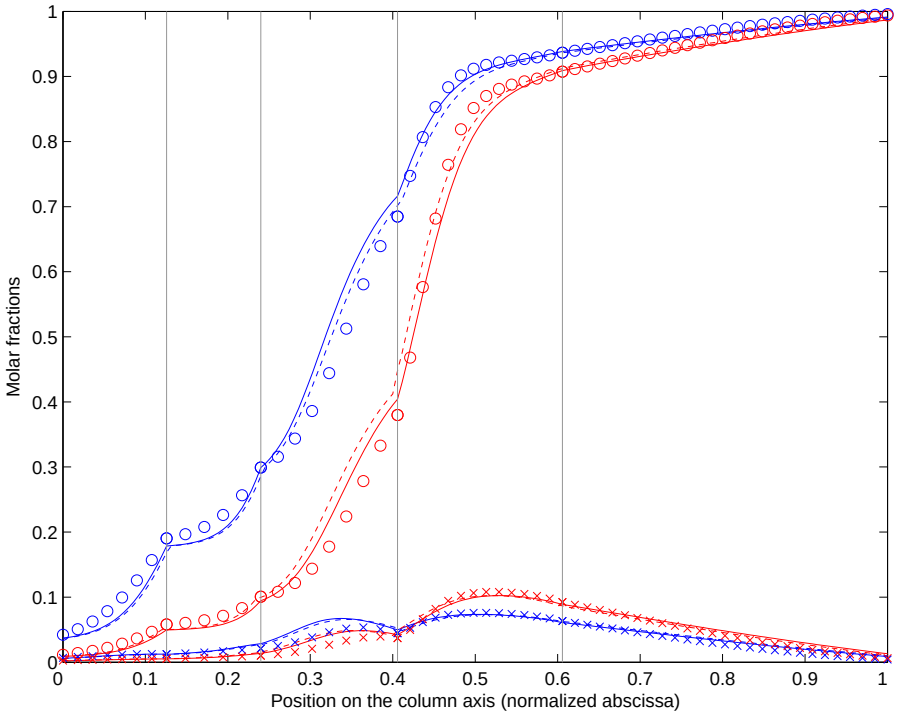

Figure 5.13: Comparison of the HYSYS and the pseudobinary PDE model composition estimations in case A with constant α_{O_2} and α_{Ar}. The monotone profiles corresponds to oxygen, the belly-shaped ones to argon. *Blue circles:* HYSYS estimation in liquid. *Red circles:* HYSYS composition estimation in gas. *Blue solid line:* PDE model lumped composition X. *Red solid line:* $k(X)$. *Blue dotted line:* PDE model estimated composition in liquid (static output x). *Red dotted line:* PDE model estimated composition in gas (static output y).

5.4 Dynamic operation scenario

The dynamic test scenario is the same as for the HP column (10 hours record of the air separation plant operation, on July 4^{th} 2011, from 10 AM to 8 PM). Figure 5.14 shows the input and output flows of the LP column during the scenario. Regarding the V04 and V02 flashpots, only the incoming mixed liquid/gas flow is known. Since the temperature of the mixture is unknown, we assume that the liquid/gas flow ratio at the output of each flashpot is the same as in the Hysys static case A. Thus we take:

$$L_{V04\rightarrow} = 0.857 Q_{\rightarrow V04}, \qquad V_{V04\rightarrow} = (1 - 0.857) Q_{\rightarrow V04},$$
$$L_{V02\rightarrow} = 0.877 Q_{\rightarrow V02}, \qquad V_{V02\rightarrow} = (1 - 0.877) Q_{\rightarrow V02}$$

For the same reason, we determine the relation between the condensed gas flow at the top of the HP column and the reboiled liquid at the bottom of the LP column based on the same static case. The same relation is established between the gas arriving at the top of the argon column K10 and the reboiled condensation liquid which feeds the LP column. We take:

$$V_{LP}^{reboiled} = 0.71 V_{HP}^{condensed}, \quad V_{K10}^{reboiled} = 1.19 V_{K10}^{condensed}.$$

Similarly to the HP column, we add a correction on the liquid and gas internal flows to account for the internal revaporization. The vaporized flow Q_{LP}^{revap} is estimated to be 10% of the reboiled flow at the bottom of the LP column $V_{LP}^{reboiled}$. Thus we artificially add a Q_{LP}^{revap} flow to $V_{V02\rightarrow}$, while we create a fictional liquid draw off Q_{LP}^{revap} at the same location. We add and withdraw the flows at the location of an existing injection, so as not to create a supplementary discontinuity in the liquid and gas distribution profiles.

The revaporization also occurs in the argon column K10. According to Hysys , we consider that 5.5% of the flow condensed at the top of K10 is vaporized during its descent. Given the height of the K10 column, and assuming that the liquid has a $0.02 m/s$ velocity, we consider a descent delay $\theta_{K10} = 0.5h$. Thus we take:

$$L_{K10\rightarrow LP}(t) = 0.945 \left(V_{K10}^{condensed}(t - \theta_{K10} - L_{K10}^{prod}(t - \theta_{K10}) \right),$$
$$V_{LP\rightarrow K10} = 0.945 V_{K10}^{condensed} + 0.055 L_{K10}^{prod}.$$

The LP column is equipped with an O_2 analyzer at top, operating in the 0-10% range. Figure 5.15 shows the measured concentration in the gas during the scenario. The O_2 concentration is also measured in gas right above the bottom liquid bath (see Fig. 5.16) and in front of the LP-K10 connection (see Fig. 5.17). These analyzers operate in the 0-100% range. A pressure transmitter gives the pressure in the residuary gas exiting the LP column at top; we will use this measure (see Fig. 5.19) as the estimated internal pressure. We will also consider a constant temperature along the column's s-axis, based on the measurement in the residuary gas (Fig. 5.18).

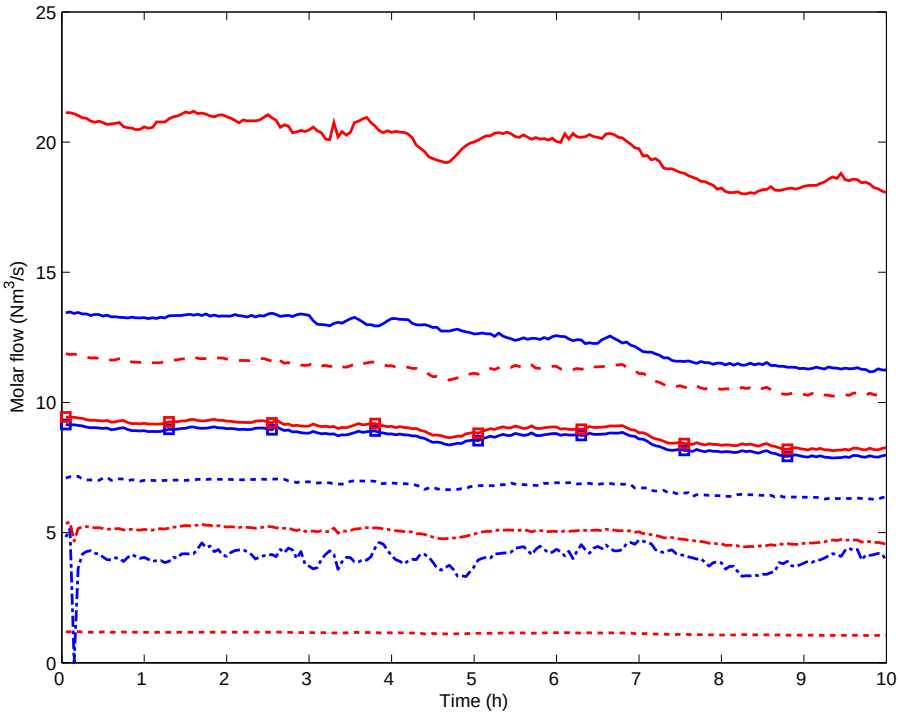

Figure 5.14: Input and output molar flows of the LP column. *Solid blue:* top reflux liquid L_{HP}^{LL}. *Dotted blue:* $L_{V04\rightarrow}$. *Dotted red:* $V_{V04\rightarrow}$. *Dash-dotted blue:* $L_{V02\rightarrow}$. *Dashed red:* $V_{K10}^{reboiled}$. *Dash-dotted red:* $V_{V02\rightarrow}$. *Squared blue:* $L_{K10\rightarrow LP}$. *Squared red:* $V_{LP\rightarrow K10}$. *Solid red:* $V_{LP}^{reboiled}$.

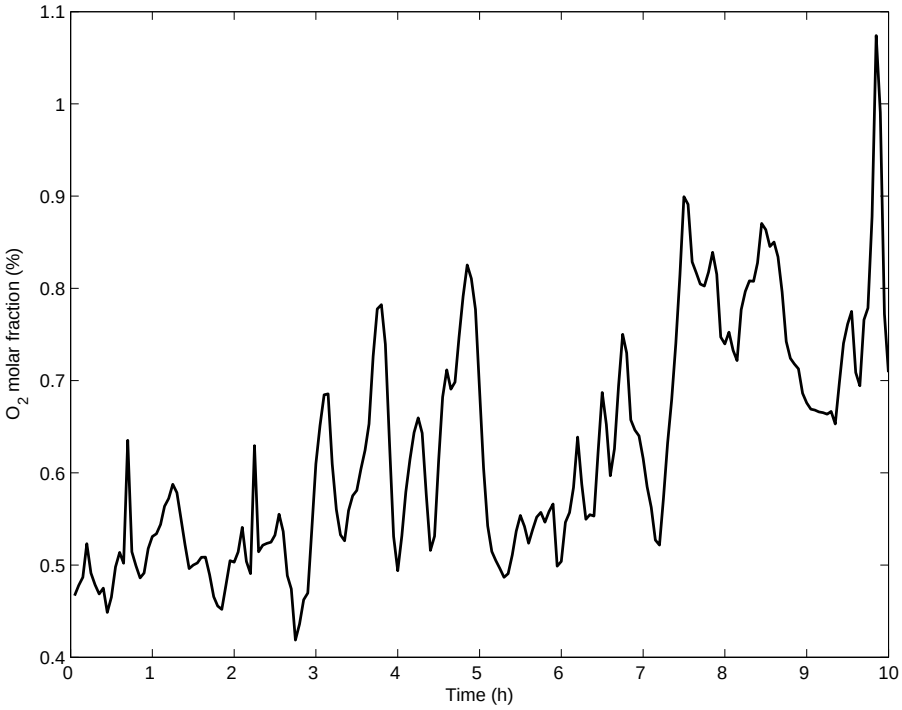

Figure 5.15: Analyzed O_2 molar fraction in the gas at the top of the LP column.

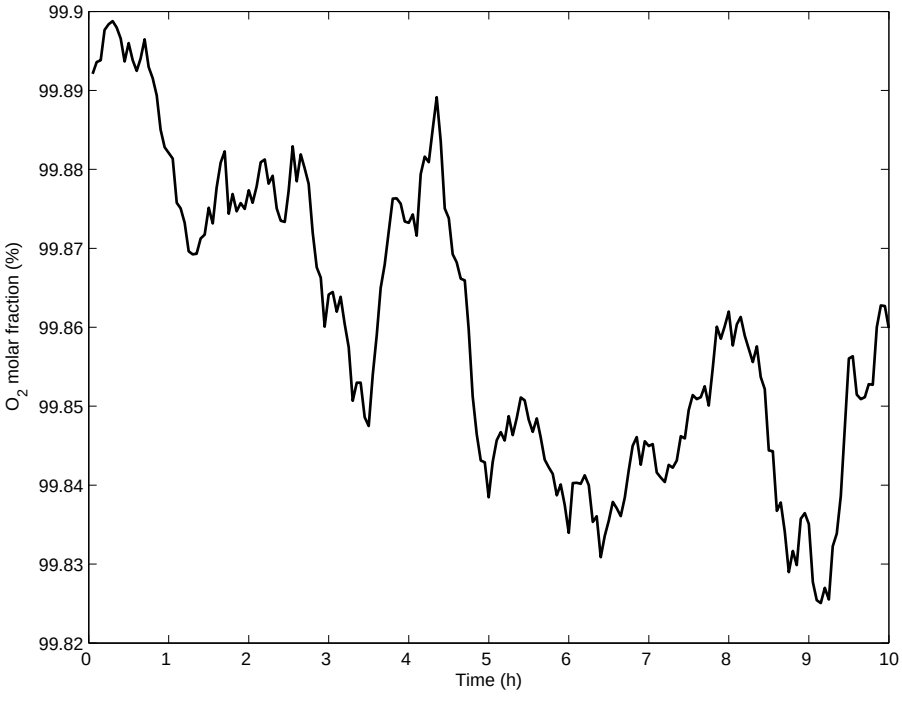

Figure 5.16: Analyzed O_2 molar fraction in the gas, over the liquid bath at the bottom of the LP column.

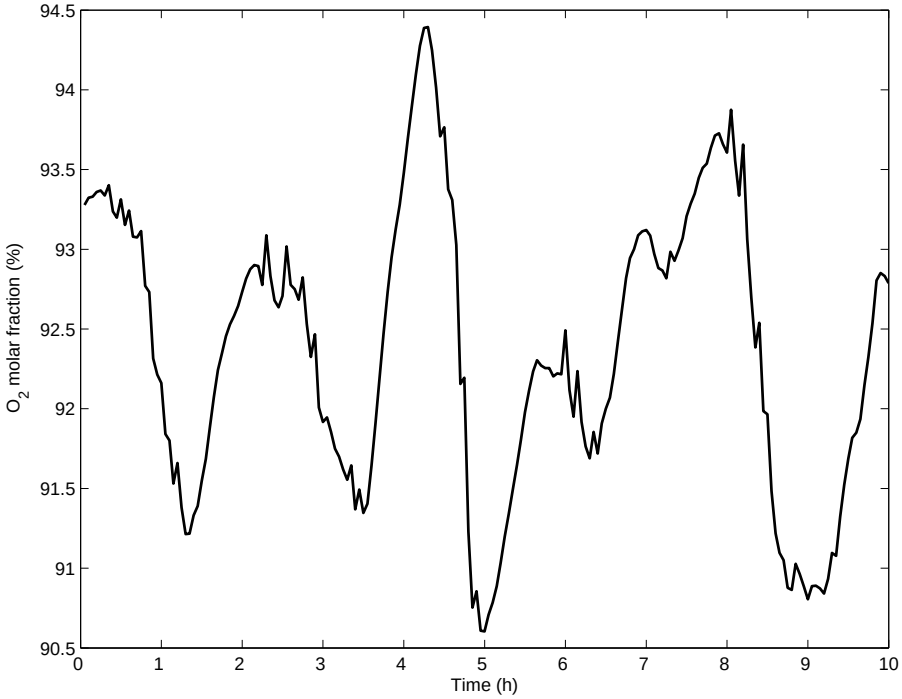

Figure 5.17: Analyzed O_2 molar fraction in the gas at the location of the connection between the LP and K10 columns.

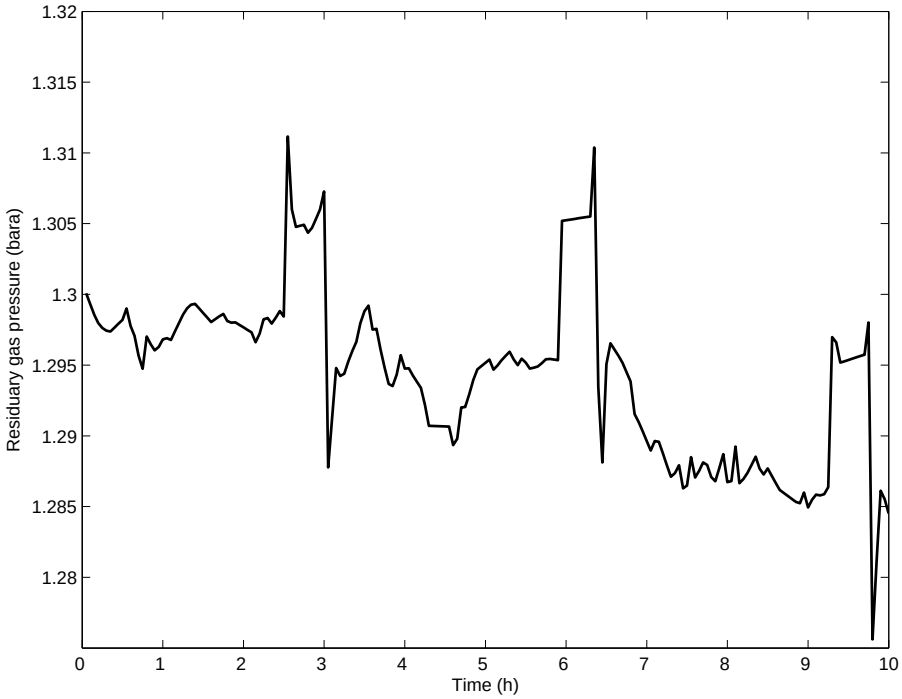

Figure 5.18: Absolute pressure in the residuary gas exiting the LP column at top.

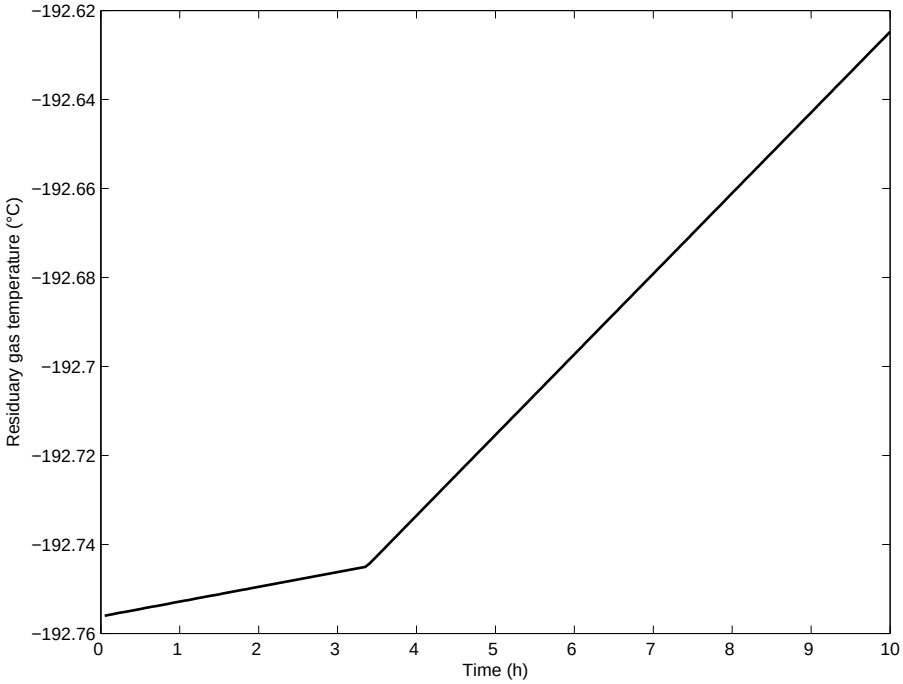

Figure 5.19: Temperature of the residuary gas. We dispose here of the long term trend only, since the corresponding sensor sampling parameters have not been modified prior to the acquisition.

5.5 Dynamic simulation

We have to simulate the HP columns dynamics to determine some of the LP column inputs. Both columns are simulated using the ternary mixture model, with $\Delta t = 0.1s$, $\Delta z = 0.1m$, and constant relative volatilities:

$$\alpha_{O_2} = 0.4, \quad \alpha_{Ar} = 0.5 \text{ for the HP column,}$$
$$\alpha_{O_2} = 0.251, \quad \alpha_{Ar} = 0.377 \text{ for the LP column.}$$

Regarding the liquid speed and hold-ups, we use $\mathcal{V}_L = 0.02m/s$ for both columns, $\mu_L = 0.4m/s$ for the HP column, and $\mu_L = 0.6m/s$ for the LP column. Regarding the diffusion, we use the dynamic adaptation of ϵ proposed in the previous chapter for the HP column; for the LP column, we take $\epsilon = 0.211$ constant, inspired by the static test case C. The liquid amount at the LP column bottom is fixed at $Q_b = 9000Nm^3$. The liquid amount at the bottom of the HP column (about 10 times smaller) is neglected here.

We focus here essentially on the simulation of the compositions in the vicinity of the argon belly.

5.5.1 Well-source argon column model

In a first time, we consider an extremely simplistic model for the argon column K10: the column behaves as a source of liquid with constant O_2 and Ar molar fraction (respectively 0.936 and 0.064), regardless of its theoretical material balance. The proposed molar fractions

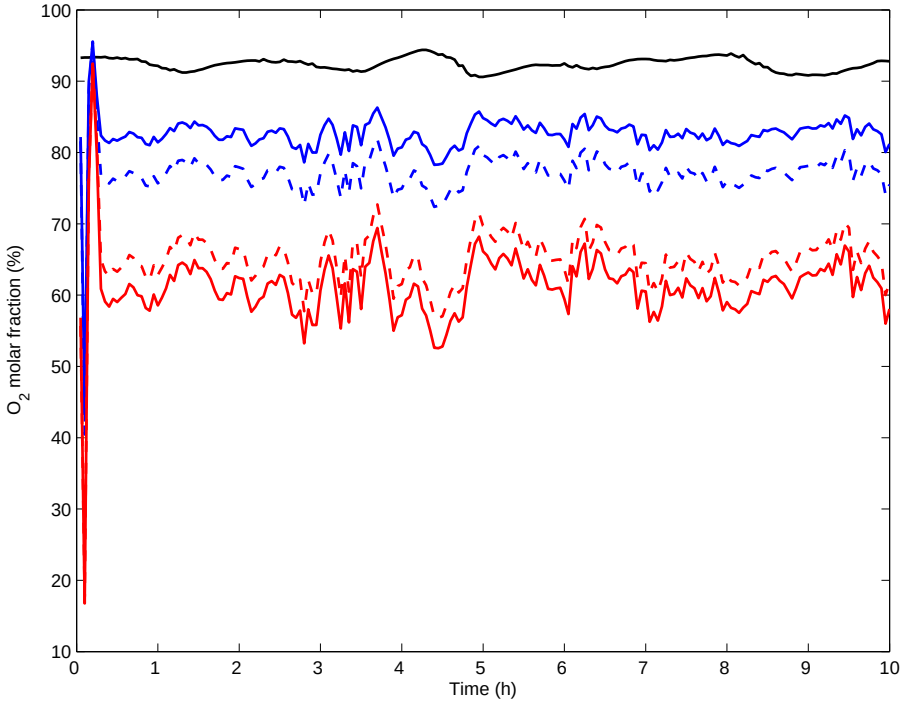

Figure 5.20: O_2 (top bundle) and argon (bottom bundle) molar fractions at the location of the LP-K10 columns connection, with $Q_{LP}^{revap} = 0.1 V_{LP}^{reboil}$. *Blue:* X_{O_2} and X_{Ar}. *Dotted blue:* x_{O_2} and x_{Ar}. *Red:* $k_{O_2}(\mathbf{X})$ and $k_{Ar}(\mathbf{X})$. *Dotted red:* y_{O_2} and y_{Ar}. *Black:* O_2 measure in gas.

are directly borrowed from the HYSYS static case A. This first approach does not introduce possibly destabilizing feedback from the column K10 to the LP column. The obvious drawback is the introduction of a favorable bias in the test, since the idealized liquid injection drives, by mixing, the simulated profiles towards the desired ones, at least in the vicinity of the LP column - K10 column connection.

Figure 5.20 shows the obtained O_2 molar fractions at the location of the K10-LP columns connection. These results are not satisfying, since the main O_2 composition front is too much repelled downwards, by a too large reflux rate.

Choosing the internal revaporized flow as the adjustment variable, we obtain satisfying results (see Fig. 5.21) regarding the compositions at the location of the K10-LP connection with

$$Q_{LP}^{revap} = 0.22 V_{LP}^{reboiled}.$$

This is a huge correction of the theoretical revaporized flow. We suppose that a portion of this correction actually compensates the estimation errors on the liquid/gas ratio in the flashpots V02, V04, which can significantly impact the liquid flows in the lower subsections of the column.

In the following, we keep the empirical $Q_{LP}^{revap} = 0.22 V_{LP}^{reboiled}$.

Figure 5.22 is a zoom on the O_2 composition at the location of the connection with K10. One can observe that the simulated composition are in advance of 30-45 min with respect to the measure. This suggests possibly lower (empirical) liquid speed in the column, since, as we will see, the time advance is smaller at the top. The amplitude of the composition oscillations

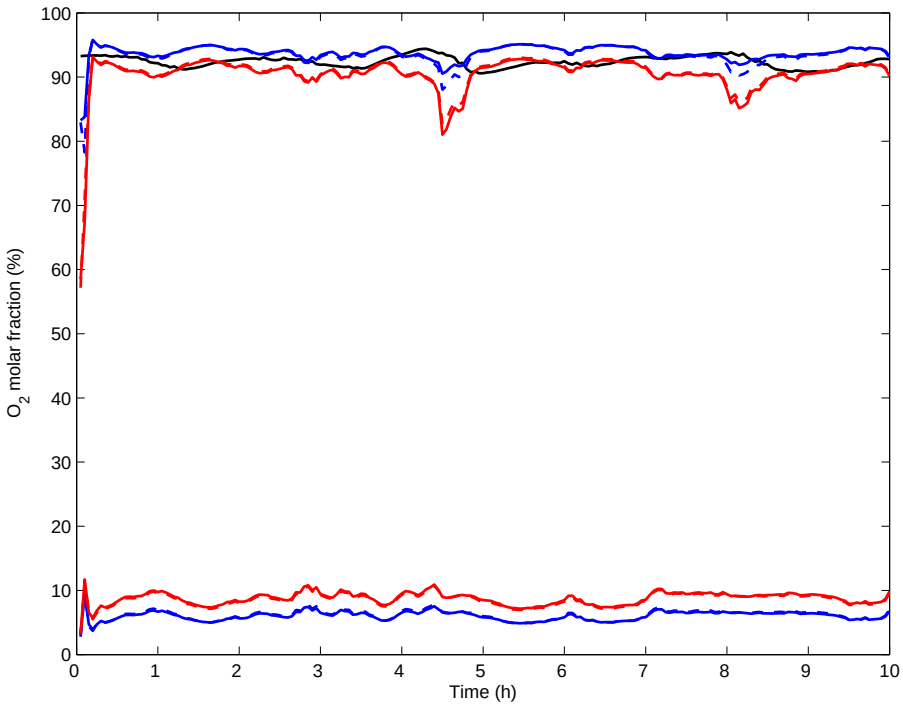

Figure 5.21: O_2 (top bundle) and argon (bottom bundle) molar fractions at the location of the LP-K10 columns connection, with $Q_{LP}^{revap} = 0.22 V_{LP}^{reboil}$. *Blue:* X_{O_2} and X_{Ar}. *Dotted blue:* x_{O_2} and x_{Ar}. *Red:* $k_{O_2}(\mathbf{X})$ and $k_{Ar}(\mathbf{X})$. *Dotted red:* y_{O_2} and y_{Ar}. *Black:* O_2 measure in gas.

is globally in good agreement with the analyzer. At $t = 4.5h$, $7h$ and $8h$, one observes large and fast decreasing dynamics. This has to be connected with Fig. 5.23, where the main O_2 front position shows unstable (and so is the location of the argon belly). We suppose that some non modeled flow dynamics compensate these drifts, such as variations of the liquid/gas ratio in the flashpots. The liquid bath at the bottom of the argon column may also play a damping role. Also, the circulation of the flows between the HP and the LP columns cause the various inputs of the LP column to be time-shifted. These shifts, not taken into account here, could lead to constructive or destructive interplay between the input flows, as pointed out in the HP column.

The simulation results at the bottom of the column are shown on Fig. 5.24. Higher concentrations could be obtained with a smaller ϵ, but this would be at the expense of the results at the LP-K10 connection location.

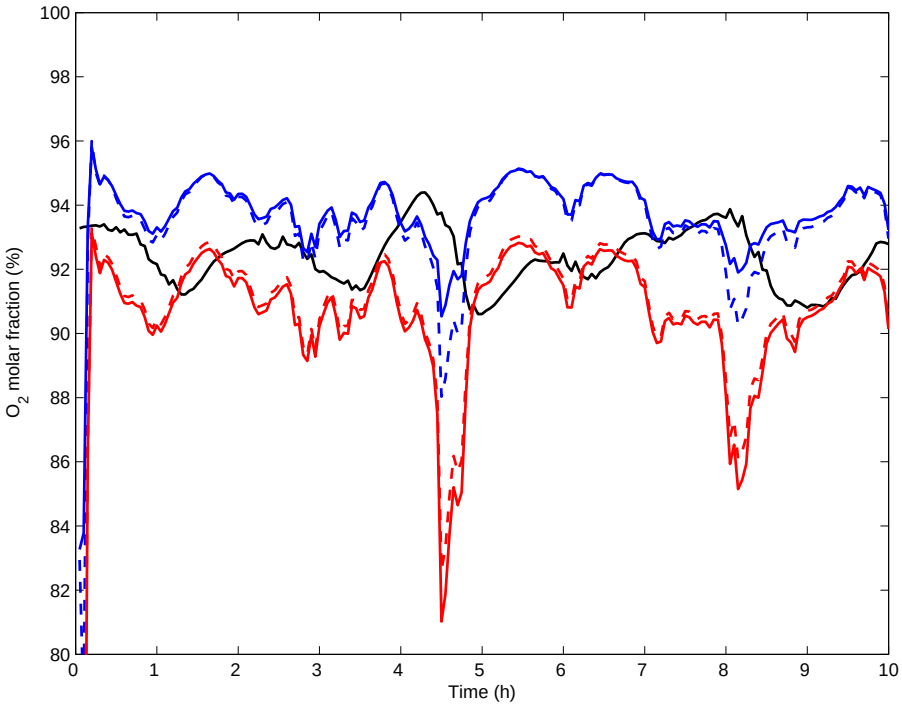

Figure 5.22: O_2 molar fractions at the location of the LP-K10 columns connection, with $Q_{LP}^{revap} = 0.22 V_{LP}^{reboil}$. *Blue:* X_{O_2}. *Dotted blue:* x_{O_2}. *Red:* $k_{O_2}(\mathbf{X})$. *Dotted red:* y_{O_2}. *Black:* O_2 measure in gas.

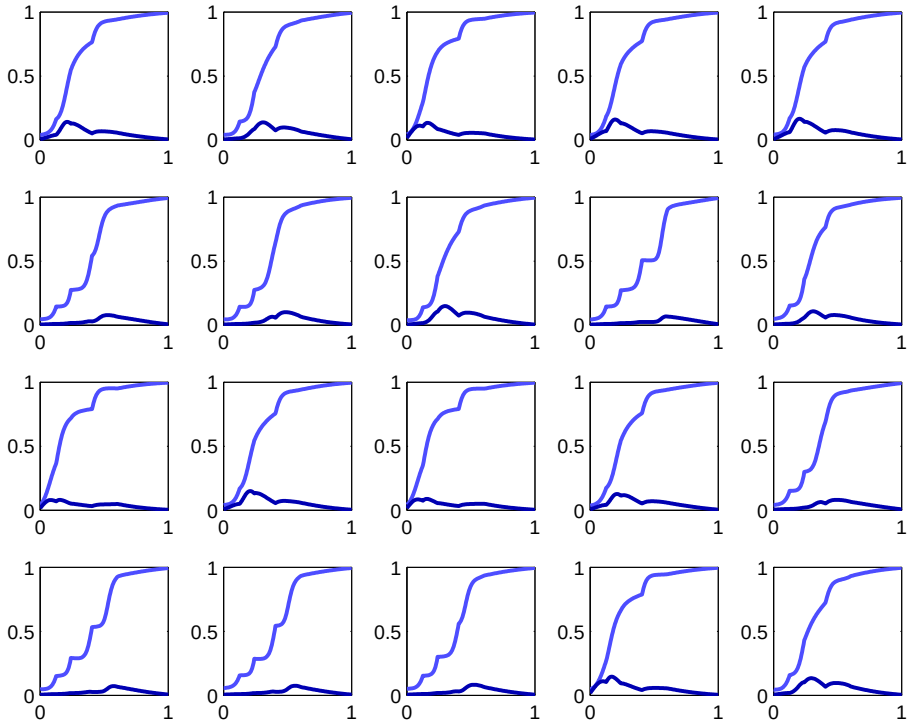

Figure 5.23: Snapshots of the molar fraction profiles during the 10h scenario. Each graph plots X_{O_2} (pale blue) and X_{Ar} (dark blue) versus the normalized column abscissa. Snapshots are taken between 30min and 10h, with 30min interval, and are ordered from left to right, and from top to bottom.

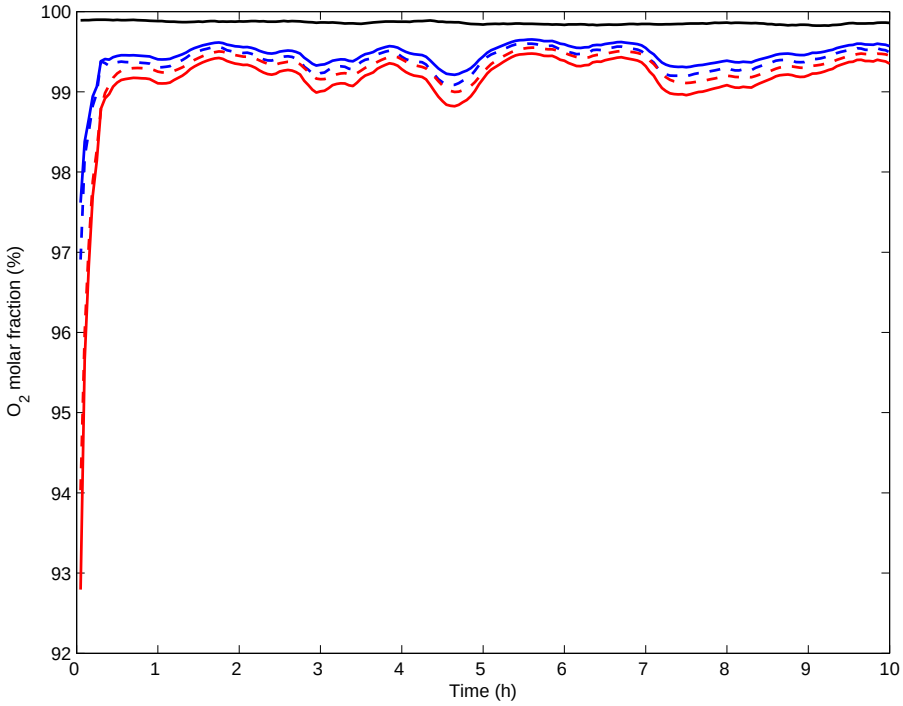

Figure 5.24: O_2 molar fractions at the bottom of LP column, with $Q_{LP}^{revap} = 0.22 V_{LP}^{reboil}$. *Blue:* X_{O_2}. *Dotted blue:* x_{O_2}. *Red:* $k_{O_2}(\mathbf{X})$. *Dotted red:* y_{O_2}. *Black:* O_2 measure in gas.

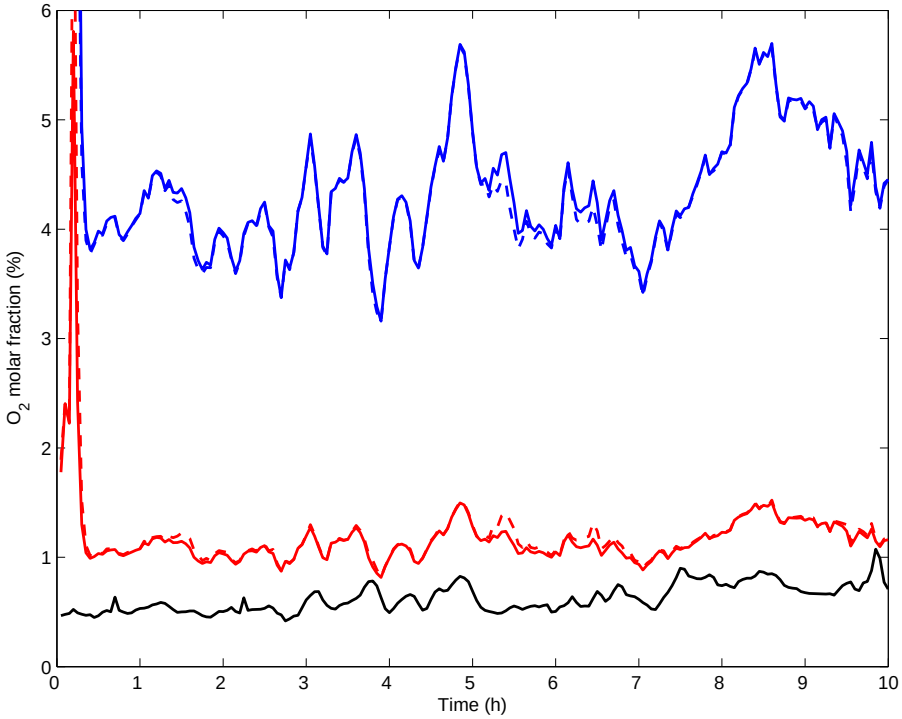

Figure 5.25: O_2 molar fractions at the top of LP column, with $Q_{LP}^{revap} = 0.22 V_{LP}^{reboil}$. *Blue:* X_{O_2}. *Dotted blue:* x_{O_2}. *Red:* $k_{O_2}(\mathbf{X})$. *Dotted red:* y_{O_2}. *Black:* O_2 measure in gas.

Results at the top of the columns are plotted on Fig. 5.25. The composition oscillations correspond with the measures, with which they are almost synchronized. The composition transport time between the HP and LP column may be responsible for the residual time-shift. The offset between the measured and the simulated gas composition is little sensitive to changes on ϵ (the column's top end induces repelling effect) or on the liquid or gas flows (provided that the changes are small enough not to move the main O_2 front up to the top of the column). We suppose that the O_2 composition in the HP column, in the drawn lean liquid, is too high (despite the good results obtained for the gas) - an error on the σ_L/σ_V ratio could explain this. The top of the LP column, where the mixing mechanism seems to dominate the separation, is thus fed with too much oxygen, which yields the observed result.

5.5.2 Equilibrium-based argon column model

The next step in the simulation of the LP column dynamics is to introduce the feedback from the argon column K10. A simplistic manner consists in stating that the liquid flowing from K10 to the LP column is at the equilibrium with the gas injected in K10. To account for the slow argon column dynamics, we take:

$$\frac{d\mathbf{x}_{K10\to LP}}{dt} = \frac{1}{T_{i,K10}} \left(\mathbf{k}^{-1} \left(\mathbf{y}_{LP\to K10}(t) \right) - \mathbf{x}_{K10\to LP}(t) \right),$$

where $\mathbf{x}_{K10\to LP}$ is the vector of O_2 and argon molar fractions in the liquid flowing from K10 to the LP column, and $\mathbf{y}_{LP\to K10}$ is the vector of O_2 and argon molar fractions in the gas

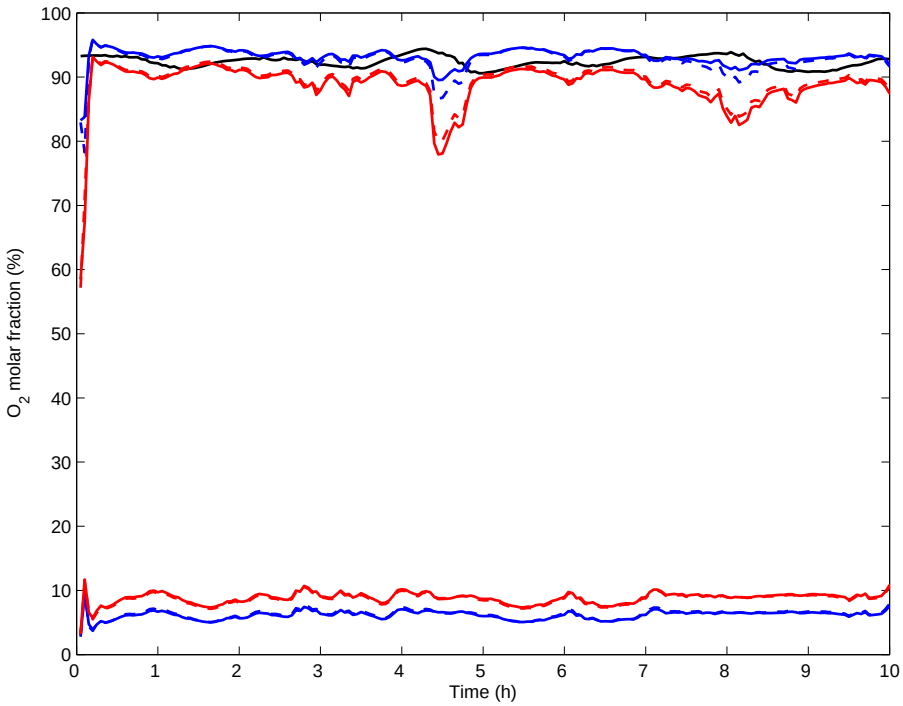

Figure 5.26: O_2 (top bundle) and argon (bottom bundle) molar fractions at the location of the LP-K10 columns connection. *Blue:* X_{O_2} and X_{Ar}. *Dotted blue:* x_{O_2} and x_{Ar}. *Red:* $k_{O_2}(\mathbf{X})$ and $k_{Ar}(\mathbf{X})$. *Dotted red:* y_{O_2} and y_{Ar}. *Black:* O_2 measure in gas.

injected from the LP column to K10. The volatilities used in the inverse equilibrium relation $\mathbf{k}^{-1}$ are the same as in the LP column, since it is almost at the same pressure that K10. In a first time, we take $T_{i,K10} = 3h$ (it corresponds to the time constant used in the linear argon column models running on the plant control system).

The performances of the model at the top and the bottom of the LP column are unchanged. Results at the location of the K10-LP connection are shown on Fig. 5.26 (oxygen and argon) and Fig. 5.27 (oxygen only). The argon content is still smaller than expected (it should be around 10-12 % according to the process documentation). Regarding the oxygen, the amplitude of the oscillations are still satisfying. Without the stabilizing influence of the well-source argon column model, the sudden changes of composition at $t = 4.5h$ and $8h$ are much larger than previously. The offset between the measured and the simulated O_2 composition seems to increase with time. This is confirmed by a longer simulation (40h, on the same scenario), as shown on Fig. 5.28, which leads us to the next argon column model.

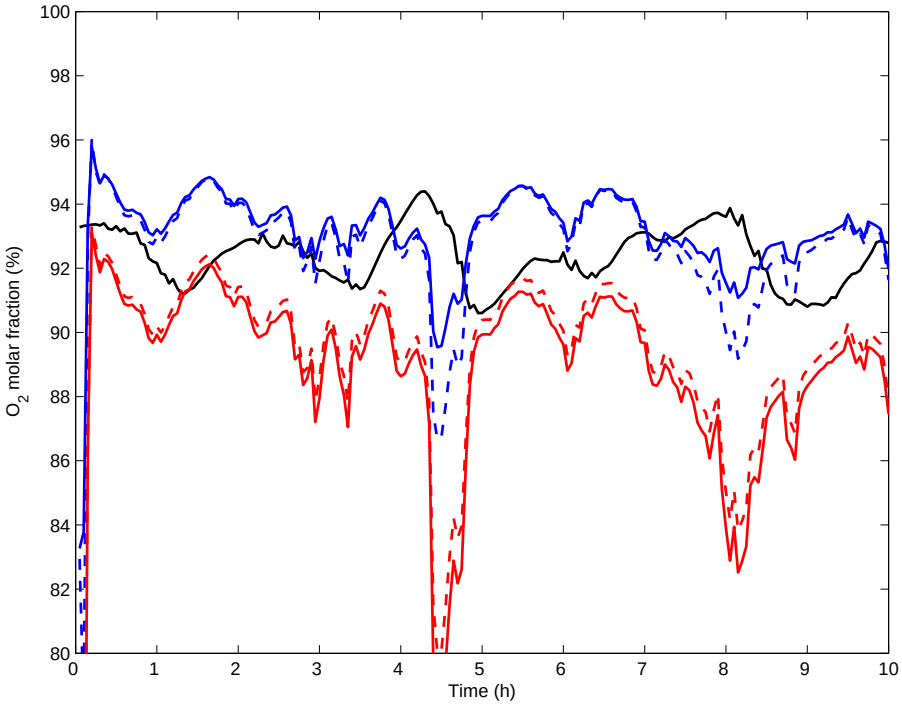

Figure 5.27: O_2 molar fractions at the top of LP column. *Blue:* X_{O_2}. *Dotted blue:* x_{O_2}. *Red:* $k_{O_2}(\mathbf{X})$. *Dotted red:* y_{O_2}. *Black:* O_2 measure in gas.

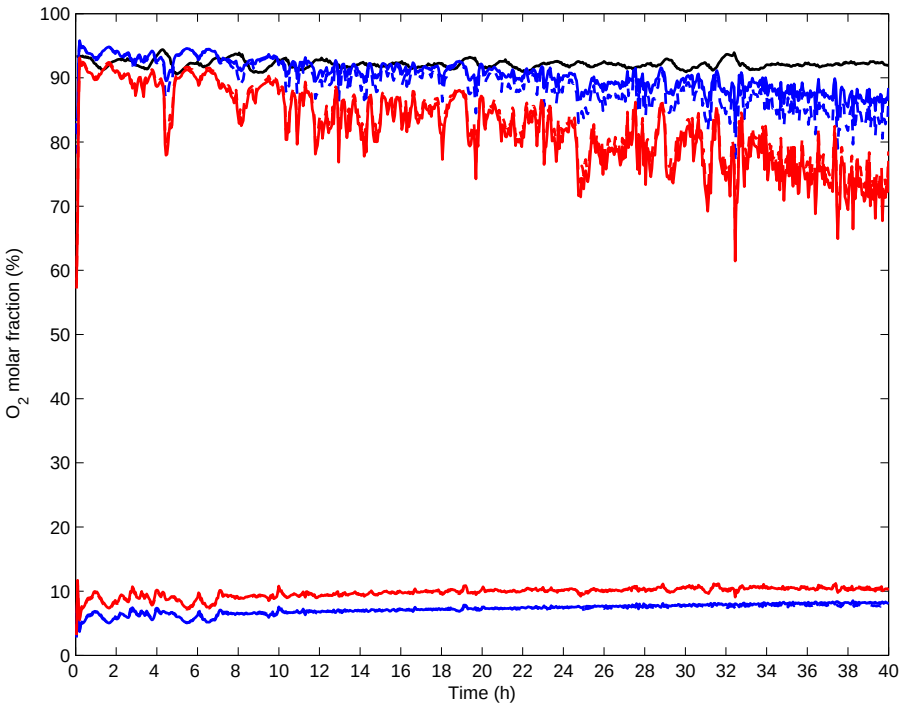

Figure 5.28: O_2 (top bundle) and argon (bottom bundle) molar fractions at the location of the LP-K10 columns connection for the 40h scenario. *Blue:* X_{O_2} and X_{Ar}. *Dotted blue:* x_{O_2} and x_{Ar}. *Red:* $k_{O_2}(\mathbf{X})$ and $k_{Ar}(\mathbf{X})$. *Dotted red:* y_{O_2} and y_{Ar}. *Black:* O_2 measure in gas.

5.5.3 Mass balance-based argon column model

The equilibrium based model does not respect the mass-balance of the argon column K10 in steady-state. To check whether the previously detected increasing offset is due to the equilibrium model, or to the change of the input and output flows on the long term (see Fig. 5.29), we propose here another simplified model for K10. In this model, the composition of the liquid re-injected in the LP column is determined by the mass balance of each component over the whole column K10. At the top of K10, both the N_2 and O_2 content are analyzed. Yet the N_2 analyzer is of no use (it indicates negative compositions). The O_2 is of some *ppm* and is negligible in the balance. In addition, we suppose that the argon content at the top of the argon column is stable. Inspired by HYSYS models of K10, we set it to 0.995. We take:

$$T_{i,K10}\frac{d\mathbf{x}_{K10\to LP}}{dt} = \frac{V_{LP\to K10}(t)\mathbf{y}_{LP\to K10}(t) - L^{prod}_{K10}(t)\begin{bmatrix} 0 \\ 0.995 \end{bmatrix}}{L_{K10\to LP}(t)} - \mathbf{x}_{K10\to LP}(t),$$

where $V_{LP\to K10}$ is the gas flow from the LP column to K10, and L^{prod}_{K10} the liquid flow extracted at the top of K10. We take $T_{i,K10} = 3h$ as previously.

The results at the top of the column are unchanged for the beginning of the scenario, and we can check on Fig. 5.30 that they hold on the long term. Regarding the compositions at the K10-LP connection location, Fig. 5.31 shows that the O_2 content keeps decreasing with time. Yet the change of argon column model has inverted the trend for the argon content. The main O_2 wavefront keeps drifting in direction of the bottom (see Fig. 5.32), with little impact on the bottom O_2 composition at the end of the scenario, as depicted on Fig. 5.33.

It is sometimes reported that the argon column has time constant larger than $3h$ (up to $8h$). We check the influence of $T_{i,K10}$ on the simulation, by taking $T_{i,K10} = 8h$. Results regarding the compositions at the K10-LP connection are shown on Fig. 5.34: the increased argon column inertia tempers the O_2 composition decrease, yet is not sufficient to stop it.

It seems thus that our current modeling of the internal flows is insufficient to stabilize the main O_2 composition front and the argon belly. In addition, the drift of the main front towards the bottom may induce a depleting of the argon column, which amplifies the drift by feedback. We could envisage to enrich the model with dynamic adaption of Q^{revap}_{LP}, the liquid/gas ratio in the flashpots, the gain of the condenser/reboileur between the LP and HP column, or the relative volatilities. Yet the delays caused on one hand by the slow liquid speed, and on the second hand by the wave-fronts own speeds, coupled with the highly non-linear gain between the stiff main front position and the composition at a given location, have made our simple attempts (slow PI, Smith's predictor) unsuccessful.

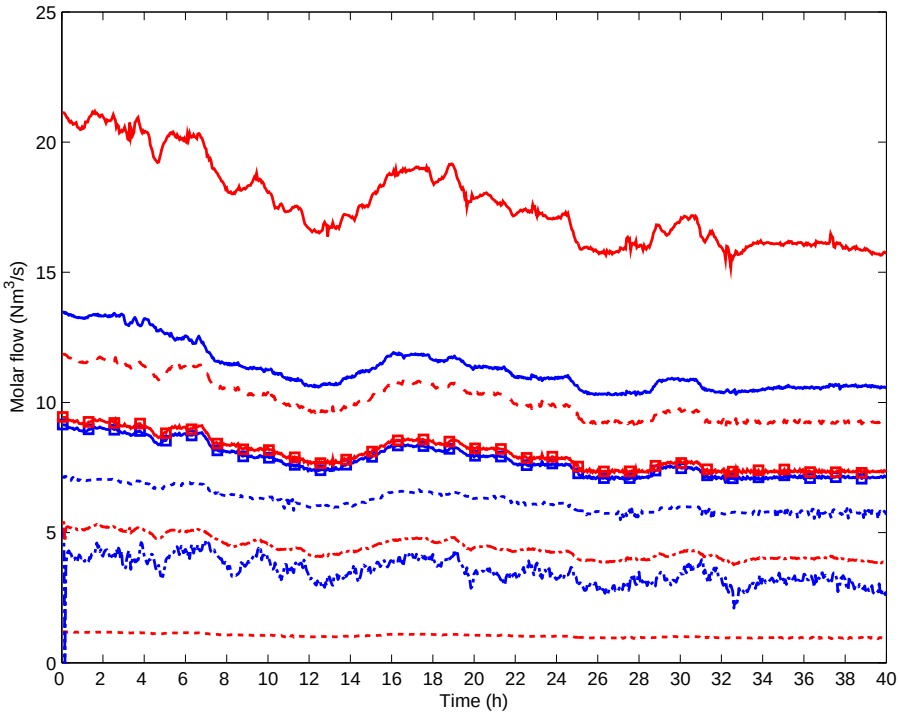

Figure 5.29: Input and output molar flows of the LP column over the 40h of the long scenario. *Solid blue:* top reflux liquid. *Dotted blue:* $L_{V04\rightarrow}$. *Dotted red:* $V_{V04\rightarrow}$. *Dash-dotted blue:* $L_{V02\rightarrow}$. *Dashed red:* $V_{K10}^{reboiled}$. *Dash-dotted red:* $V_{V02\rightarrow}$. *Squared blue:* $L_{K10\rightarrow LP}$. *Squared red:* $V_{LP\rightarrow K10}$. *Solid red:* $V_{LP}^{reboiled}$.

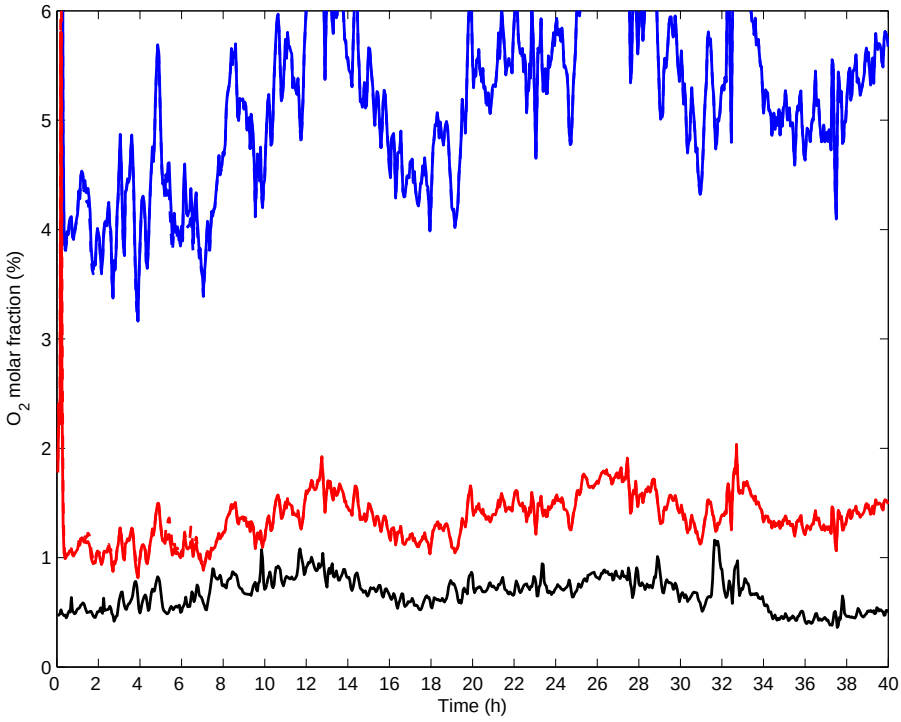

Figure 5.30: O_2 molar fractions at the top of LP column for the 40h scenario. *Blue:* X_{O_2}. *Dotted blue:* x_{O_2}. *Red:* $k_{O_2}(\mathbf{X})$. *Dotted red:* y_{O_2}. *Black:* O_2 measure in gas.

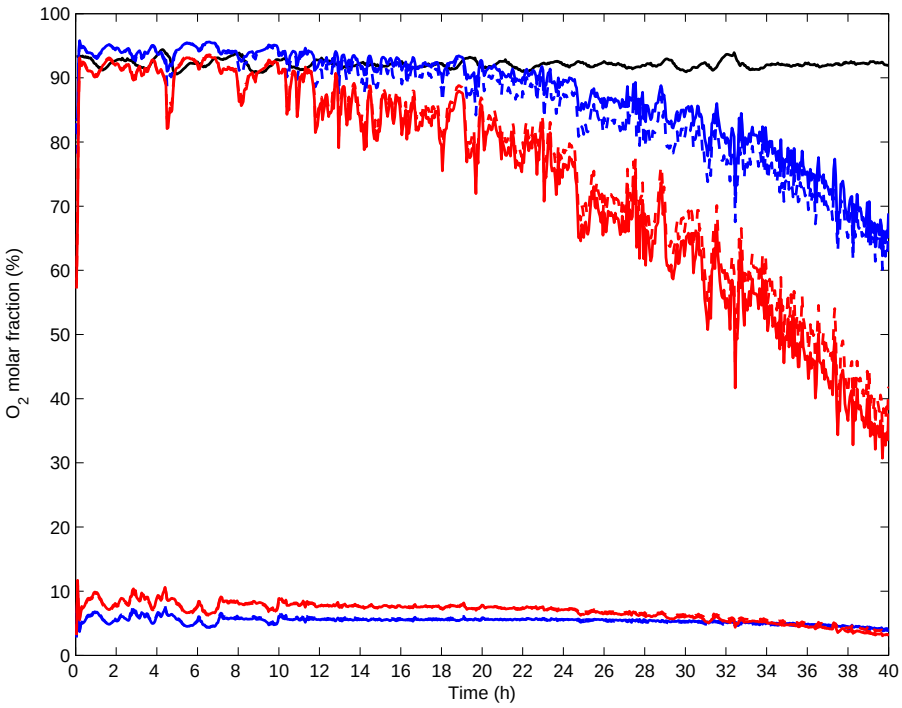

Figure 5.31: O_2 (top bundle) and argon (bottom bundle) molar fractions at the location of the LP-K10 columns connection for the 40h scenario. *Blue:* X_{O_2} and X_{Ar}. *Dotted blue:* x_{O_2} and x_{Ar}. *Red:* $k_{O_2}(\mathbf{X})$ and $k_{Ar}(\mathbf{X})$. *Dotted red:* y_{O_2} and y_{Ar}. *Black:* O_2 measure in gas.

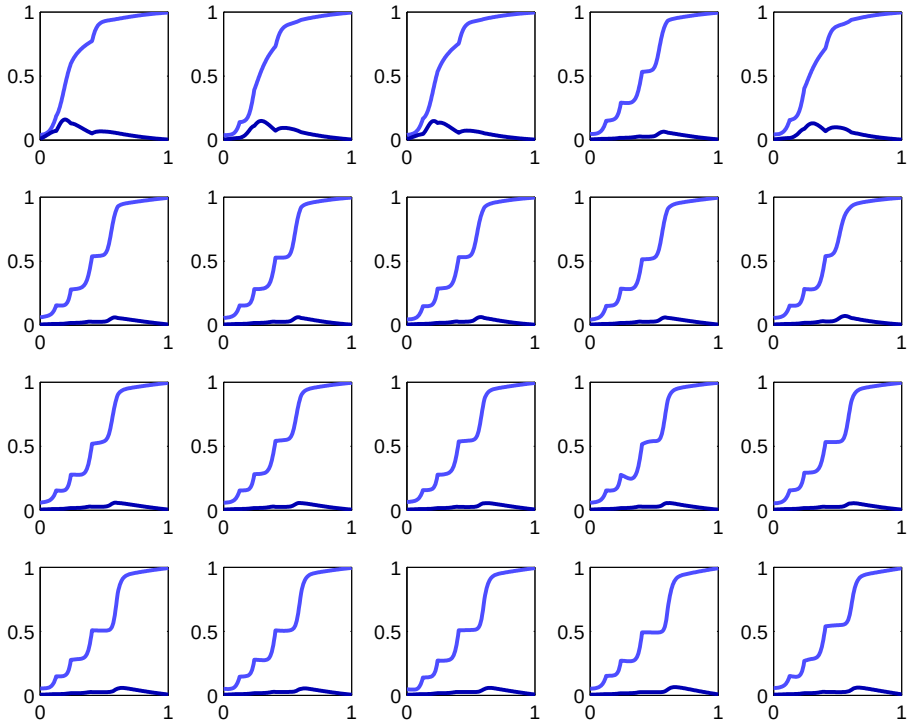

Figure 5.32: Snapshots of the molar fraction profiles during the 40h scenario. Each graph plots X_{O_2} (pale blue) and X_{Ar} (dark blue) versus the normalized column abscissa. Snapshots are taken between 2 and 40h, with 2h interval, and are ordered from left to right, and from top to bottom.

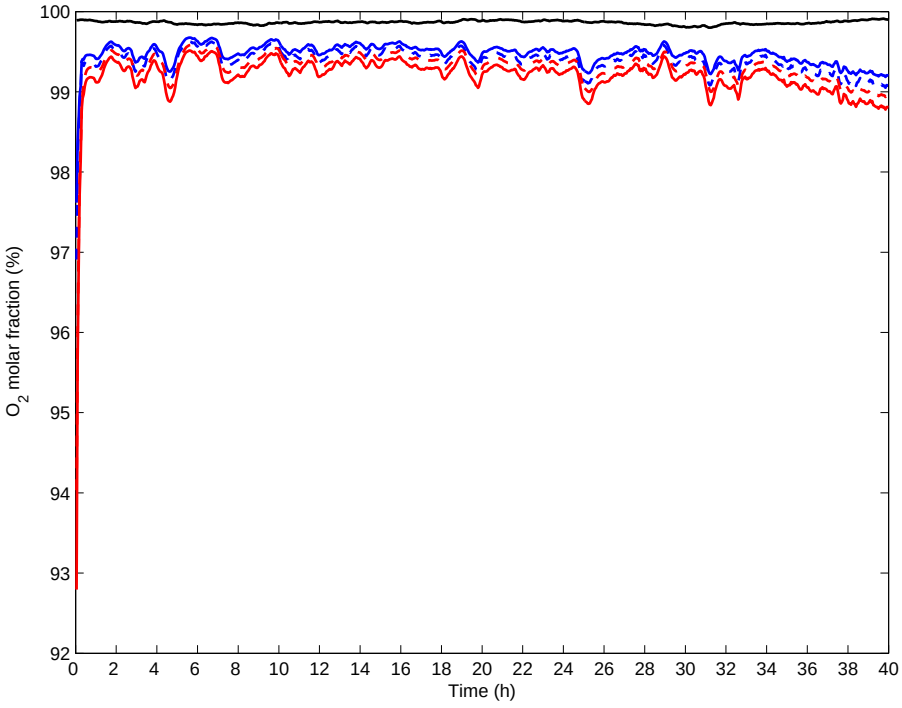

Figure 5.33: O_2 molar fractions at the bottom of LP column for the 40h scenario. *Blue:* X_{O_2}. *Dotted blue:* x_{O_2}. *Red:* $k_{O_2}(\mathbf{X})$. *Dotted red:* y_{O_2}. *Black:* O_2 measure in gas.

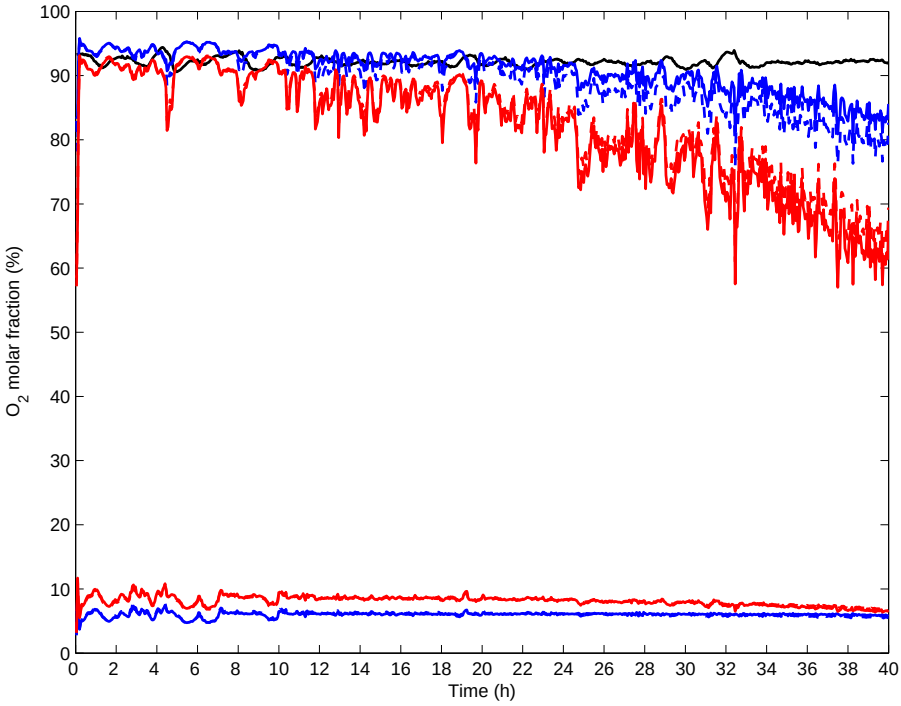

Figure 5.34: O_2 (top bundle) and argon (bottom bundle) molar fractions at the location of the LP-K10 columns connection for the 40h scenario with an 8h time constant for the argon column model. *Blue:* X_{O_2} and X_{Ar}. *Dotted blue:* x_{O_2} and x_{Ar}. *Red:* $k_{O_2}(\mathbf{X})$ and $k_{Ar}(\mathbf{X})$. *Dotted red:* y_{O_2} and y_{Ar}. *Black:* O_2 measure in gas.

5.6 Wavefronts sensitivity analysis

In this section, we study the high sensitivity of the simulated LP column composition profiles as a problem of wave-speeds. For the binary mixture case, we have seen that our (scalar) PDE model is reduced to a purely convective model if the diffusion coefficient ϵ is set to 0. In the linear case, the traveling wave reduces to a shock-wave; its velocity can be calculated by a mass balance across the shock, as illustrated by Marquardt's wave-model. For more than 2 components in the mixture, the coupling introduced by the application $\mathbf{K}$ implies that traveling quantities are necessarily bundles of several components. We have given in Section 2.6 the equations to determine these quantities in the non-linear case by the use of a non-physical space.

These equations are valid only if all the traveling waves are shock-wave, that is if

$$\frac{dD}{ds} < 0,$$

where D is defined by (2.72). Figures 5.35 to 5.37 show that this condition is fulfilled by all the HYSYS static cases.

Now let us consider one of the column's subsection. Neglecting the diffusion, we replace the HYSYS profile by a discontinuity (ensuring the matching at the boundaries of the subsection) as illustrated on Fig. 5.38(top). This is done for argon and oxygen, both in liquid and gas phase. According to the results of Section 2.6, the discontinuity will split into two shock-waves (1) and (2), as depicted on Fig. 5.38(bottom). Various configurations for the fronts' speeds are possible, yet the speeds are ordered according to (2.94).

Starting from the bottom of the subsection, the first encountered wave-front induces a switch from the initial composition state to an unknown, intermediary one. Due to the speeds' ordering, this front is necessarily front (1). Then, front (2) causes the composition to switch from the intermediary state to the input one.

Using the relation (2.80), one can compute the image of the initial and input composition states in the non-physical Ω-space. Let $\{w_{(1)}^{init}, w_{(2)}^{init}\}$ (resp. $\{w_{(1)}^{input}, w_{(2)}^{input}\}$) the coordinates of the image of the initial state (resp. input state). Let $\{w_{(1)}^{inter}, w_{(2)}^{inter}\}$ the (unknown) coordinates of the intermediary state.

Front (1) is by definition associated to the Γ-curve $\Gamma^{(1)}$. The results of Section 2.6 indicates that the $w_{(2)}$ remain constant across shock (1). Thus:

$$w_{(2)}^{inter} = w_{(2)}^{init}.$$

Front (2) is associated to $\Gamma^{(2)}$, thus:

$$w_{(1)}^{inter} = w_{(1)}^{input},$$

and one disposes of the coordinates of the intermediary state in the Ω-space. Figure 5.39 illustrates this procedure for the first LP column subsection in static case A.

Using (2.87), the compositions forming the intermediary state are deduced from $w_{(1)}^{inter}$, $w_{(2)}^{inter}$. One disposes now of the decomposition of the shocks over the two manipulated components O_2 and argon. Figure 5.40 displays the obtained shock-waves for the first LP column subsection in static case A. As indicated by Table 2.1, shock (1) is associated to an increase of both O_2 and argon composition; on the contrary, shock (2) corresponds to an increase of O_2 composition but a decrease of the argon content.

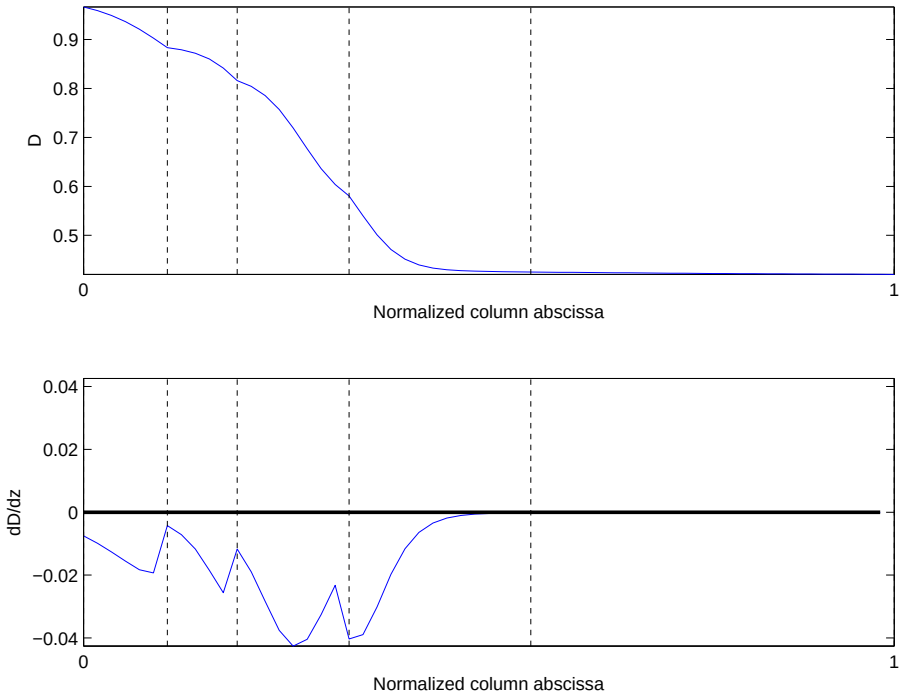

Figure 5.35: *Top:* D along the LP column for the HYSYS static case A. *Bottom:* $\frac{dD}{ds}$ along the LP column for the same case. Vertical lines indicate the subsections separations.

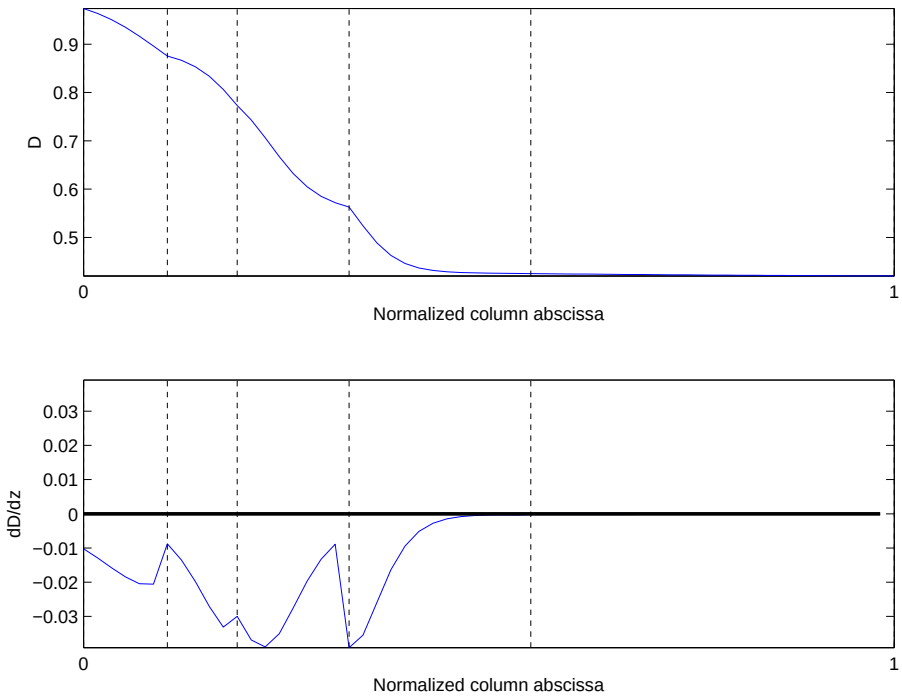

Figure 5.36: *Top:* D along the LP column for the HYSYS static case B. *Bottom:* $\frac{dD}{ds}$ along the LP column for the same case. Vertical lines indicate the subsections separations.

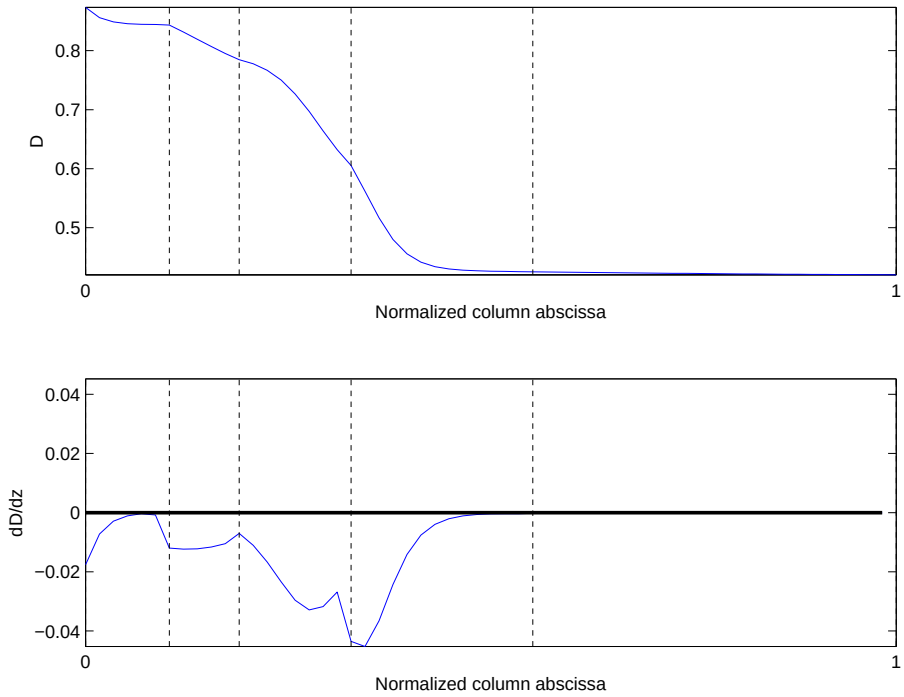

Figure 5.37: *Top:* D along the LP column for the HYSYS static case C. *Bottom:* $\frac{dD}{ds}$ along the LP column for the same case. Vertical lines indicate the subsections separations.

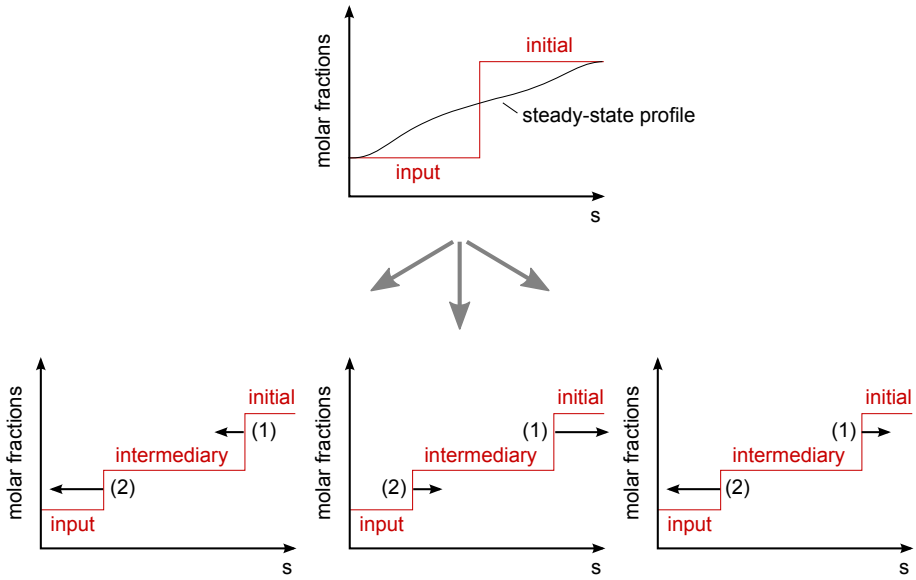

Figure 5.38: *Top:* the HYSYS steady-state profile is replaced by the corresponding discontinuous profile. *Bottom:* the discontinuous profile splits into two shock-waves with ordered speeds.

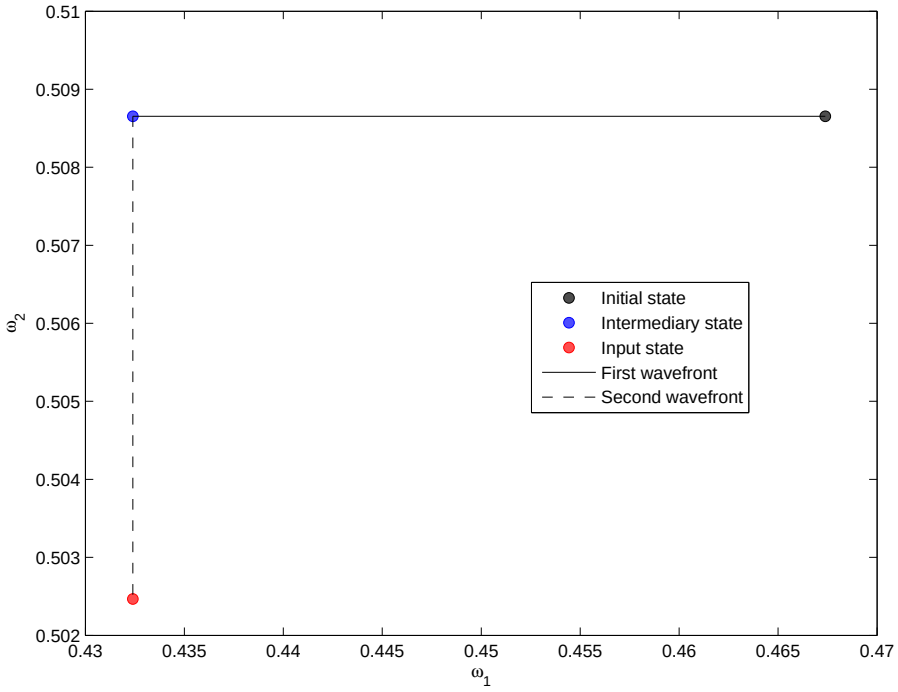

Figure 5.39: Transition from the initial state to the intermediary state, then to the input state, in the Ω-space. The trajectories maintain all the $w_{(k)}$ but one constant. LP column subsection 1, HYSYS case A.

The procedure can be repeated for each subsection, leading to a map of the O_2 and argon composition fronts along the whole column. One obtains Figures 5.41, 5.42 and 5.43, respectively for the HYSYS cases A, B and C.

We dispose of the shock velocities too, which are also depicted on the previous figures. Table 5.2 summarizes these velocities. One observes that some fronts have almost null velocity, especially in the central subsections, that is, where the profile proves particularly sensitive to estimation errors on L, V, α. Note that these speeds have been obtained by considering the mean hold-ups σ_L and σ_V over each subsection. Yet even considering the same hold-up for all the subsections still results in significantly lower shock speeds in the central subsection (see Table 5.3).

Subsection		1	2	3	4	5
Case A	shock 1	−0.0501	0.0363	0.0009	0.1409	0.0636
	shock 2	−0.0700	0.0236	−0.0233	0.0169	−0.2471
Case B	shock 1	−0.0606	0.0137	−0.0118	0.1431	0.0640
	shock 2	−0.0800	−0.0014	−0.0556	0.0089	−0.2467
Case C	shock 1	−0.2523	−0.0724	0.0254	0.1309	0.0616
	shock 2	−0.2736	−0.0885	−0.0046	0.0212	−0.2367

Table 5.2: Wave-fronts speeds (in m/s) in the LP column using mean hold-ups over each subsection.

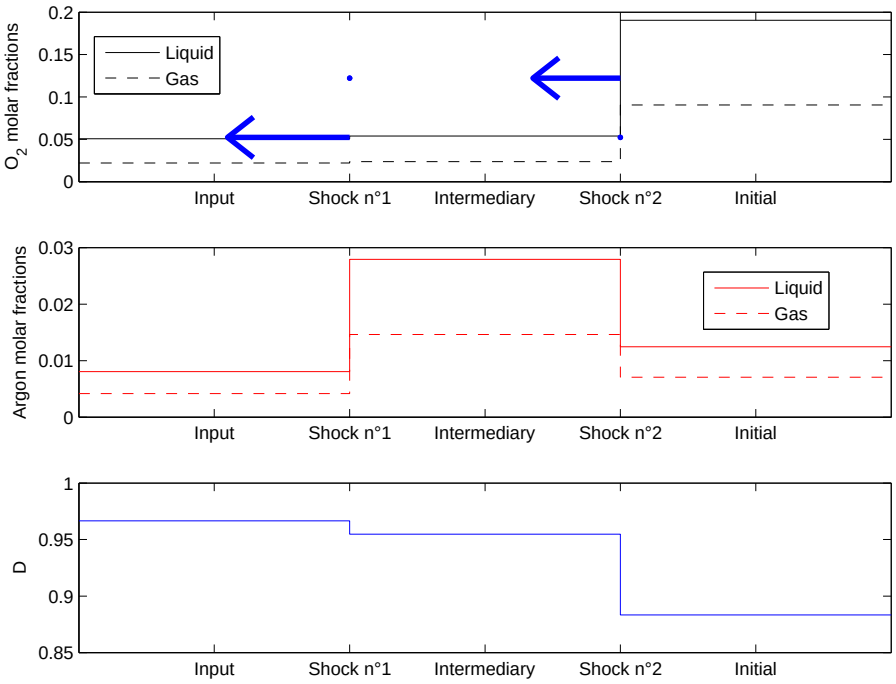

Figure 5.40: Transition from the initial state to the intermediary state, then to the input state, in the physical composition space. Arrows length is proportional to the shocks' speed. Note that the shocks' orientation is such that D is decreasing along s. LP column subsection 1, HYSYS case A.

Subsection		1	2	3	4	5
Case A	shock 1	-0.1343	0.1152	0.0032	0.3659	0.2572
	shock 2	-0.1875	0.0751	-0.0799	0.0439	-1
Case B	shock 1	-0.1599	0.0429	-0.0401	0.3703	0.2593
	shock 2	-0.2114	-0.0045	-0.1880	0.0231	-1
Case C	shock 1	-0.5677	-0.2088	0.0930	0.3613	0.2603
	shock 2	-0.6157	-0.2553	-0.0170	0.0584	-1

Table 5.3: Normalized wave-fronts speeds in the LP column using constant hold-ups along the column.

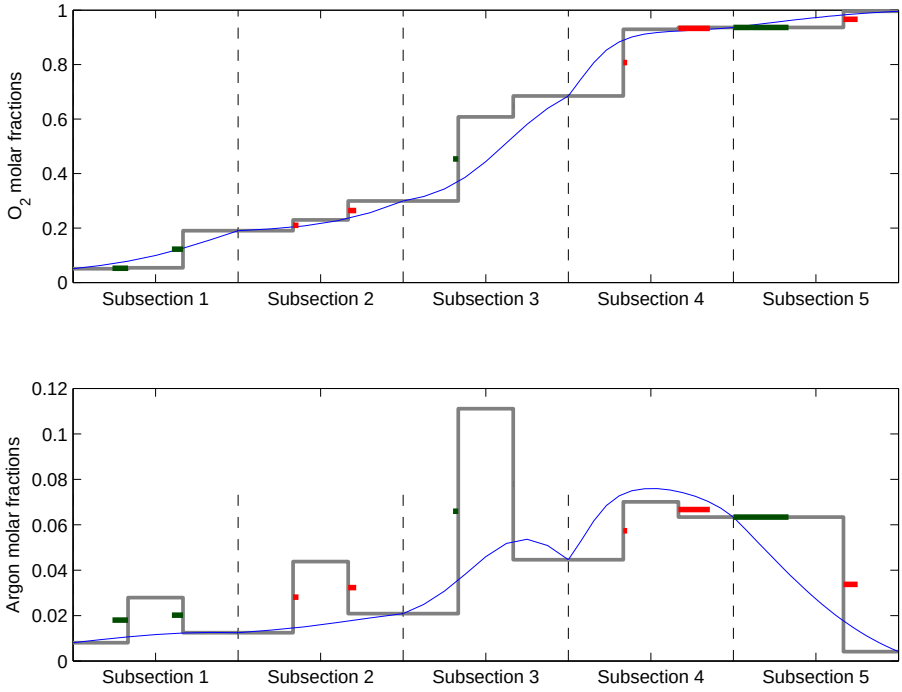

Figure 5.41: In gray, the piecewise continuous O_2 (top) and argon (bottom) composition profiles in the liquid, produced by the successive shockwaves for case A. HYSYS steady state profile is superimposed in blue. The length of the red and green markers is proportional to the corresponding shockwave speed. A red marker indicates a positive speed, a green marker a negative one.

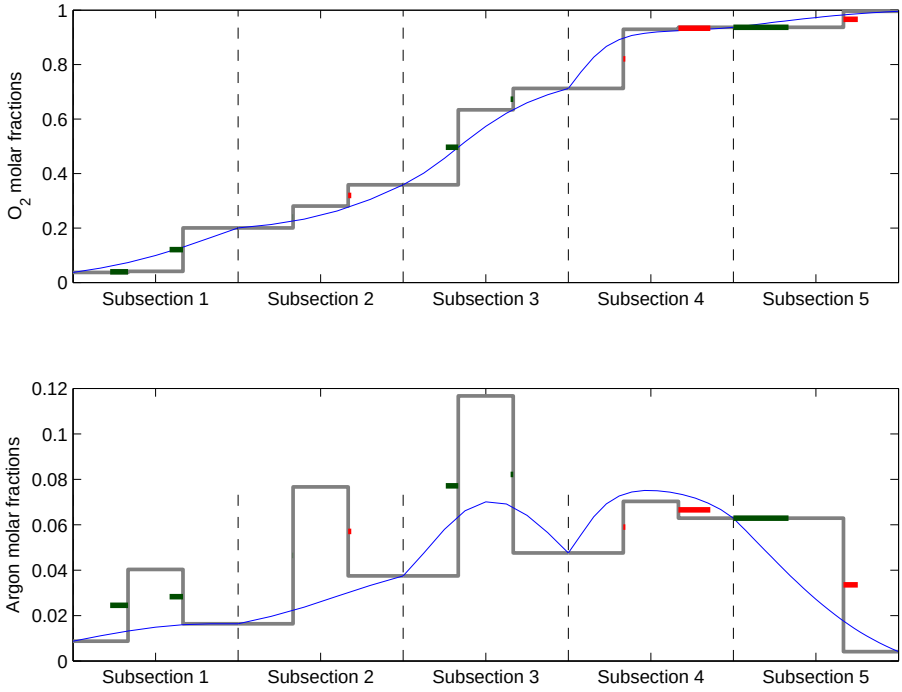

Figure 5.42: In gray, the piecewise continuous O_2 (top) and argon (bottom) composition profiles in the liquid, produced by the successive shockwaves for case B. HYSYS steady state profile is superimposed in blue. The length of the red and green markers is proportional to the corresponding shockwave speed. A red marker indicates a positive speed, a green marker a negative one.

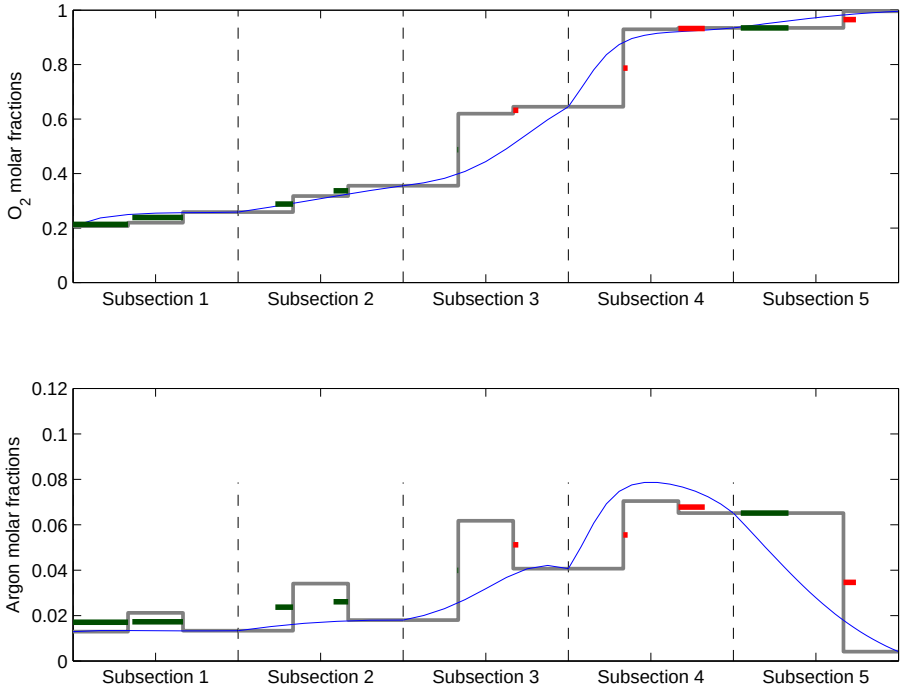

Figure 5.43: In gray, the piecewise continuous O_2 (top) and argon (bottom) composition profiles in the liquid, produced by the successive shockwaves for case C. HYSYS steady state profile is superimposed in blue. The length of the red and green markers is proportional to the corresponding shockwave speed. A red marker indicates a positive speed, a green marker a negative one.

We thus interpret the composition profiles sensitivity as follows: when a wavefront has a significantly non-null speed, it is moved towards the vicinity of a subsection boundary, where it is stopped by the interplay between the diffusion and the boundary. Small changes on L, V or α do not change the shock's velocity enough to prevent it from being pushed against the boundary, and thus little impact the resulting composition profile. On the contrary, a shock which velocity is almost null in steady-state stands far from the subsections boundaries. It behaves as an ideal Marquardt's model wave, free from the repelling end-effects. A small change on L, V or α causes this shock to drift in the direction of a boundary, and it can travel on a significant portion of the subsection before the end-effects stop it. Hence the high sensitivity of the resulting profile to small changes on L, V or α around the values that stop the shock's drift. Besides, as noticed, the diffusion coefficient ϵ will have little impact on such floating wave-front. Il will impact the regularization of the shock, thus the curvature of the profile, but its influence on the shock's localization will be negligible if far enough from the boundaries.

Now regarding the belly-shaped structures which constitute the LP column argon profile, it seems plausible that they emerge from the regularization, by the diffusion terms, of the almost still-standing creneled profile obtained by considering only the shocks. We already pointed out that the crenels result from the changing sign of the Riemann invariants for the shocks of type (1) and (2) (see Table 2.1).

Note that the situation is quite different in the HP column. Figures 5.44 to 5.46 illustrate the results of a similar analysis applied to the HP column Hysys static cases A, B and C. We were in the previous chapter focusing on the rendering of the composition at the junction between subsections 1 and 2. For the cases A and B (which, as we have seen, are close to the discussed simulation scenario), the wave speeds in these subsections are significantly non-null and oriented towards the junction. This makes the composition at this location less sensitive to errors on the wave-speeds, and more impacted by the diffusion; hence the opportunity to use ϵ as an on-line tuning parameter. Case C is different since we obtain again floating waves in subsection 2. Note that case C is characterized, amongst other particularities, by smaller liquid and gas flows; and so are the scenarios in the cluster corresponding to the functioning with one compressor only. This suggests that floating waves regime can emerge during certain operation scenarios of the HP column. For such cases, ϵ would then not be suitable for the online adaption anymore, and the simulations would become highly sensitive to the uncertainties on the flow estimations.

The wave-fronts analysis in the LP column suggests sensing and control strategies to stabilize the argon belly composition. Let us restrict ourselves to subsections 3 and 4 where the belly is essentially located. In subsection 3, shock (1) (the bottom shock) exchanges argon with oxygen, whereas shock (2) (the top shock) exchanges argon and oxygen with nitrogen, which is undesirable in the feed to the K10 column. Thus the control strategy in this subsection should be to maintain shock (1) balanced with null speed, and *a priori* close to the bottom of the subsection, so that one benefits from the argon composition increase. Automatically, shock (2) will have an upward, non-null speed which will prevent undesirable nitrogen front to reach the LP-K10 junction. Conversely, in subsection 4, one should maintain shock 2 balanced and close to the top of the subsection (then, with a small non-null upwards speed to counterbalance the end-effects), such that one rejects the last traces of nitrogen out. In parallel, shock (1) should have a non-null downwards speed, such that it enlarges the argon lobe and prevents oxygen from replacing argon in the feed to K10.

Now regarding the estimation of the composition fronts and their speed, applying the

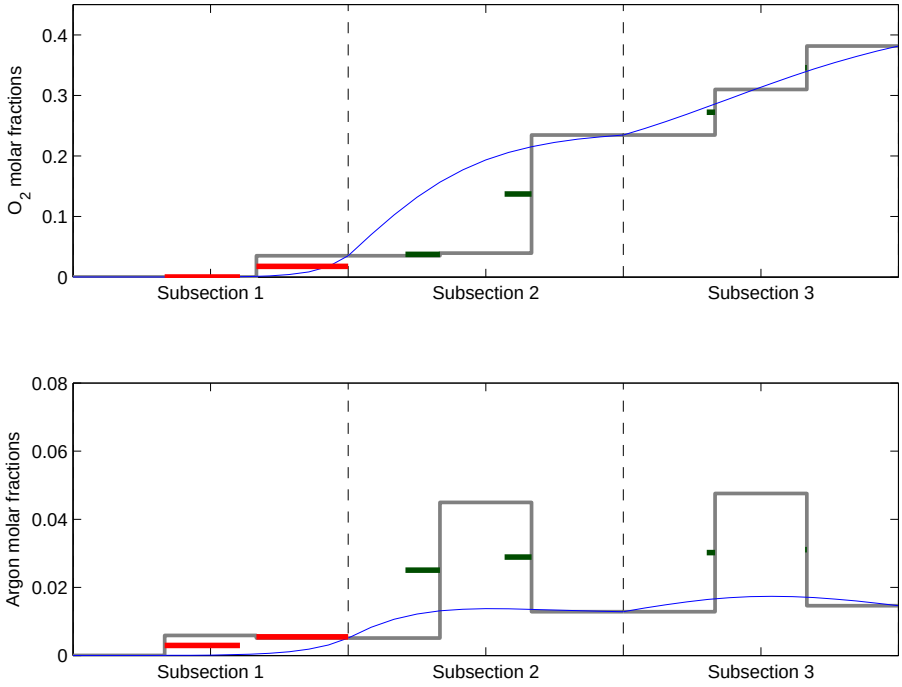

Figure 5.44: In gray, the piecewise continuous O_2 (top) and argon (bottom) composition profiles in the liquid, produced by the successive shockwaves for case A, in the HP column. HYSYS steady state profile is superimposed in blue. The length of the red and green markers is proportional to the corresponding shockwave speed. A red marker indicates a positive speed, a green marker a negative one.

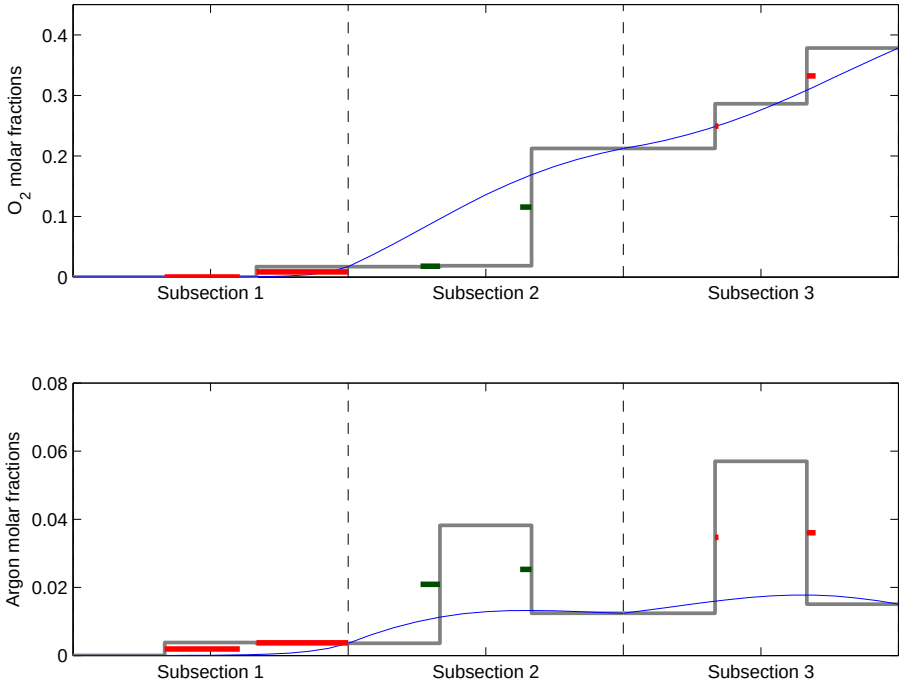

Figure 5.45: In gray, the piecewise continuous O_2 (top) and argon (bottom) composition profiles in the liquid, produced by the successive shockwaves for case B, in the HP column. HYSYS steady state profile is superimposed in blue. The length of the red and green markers is proportional to the corresponding shockwave speed. A red marker indicates a positive speed, a green marker a negative one.

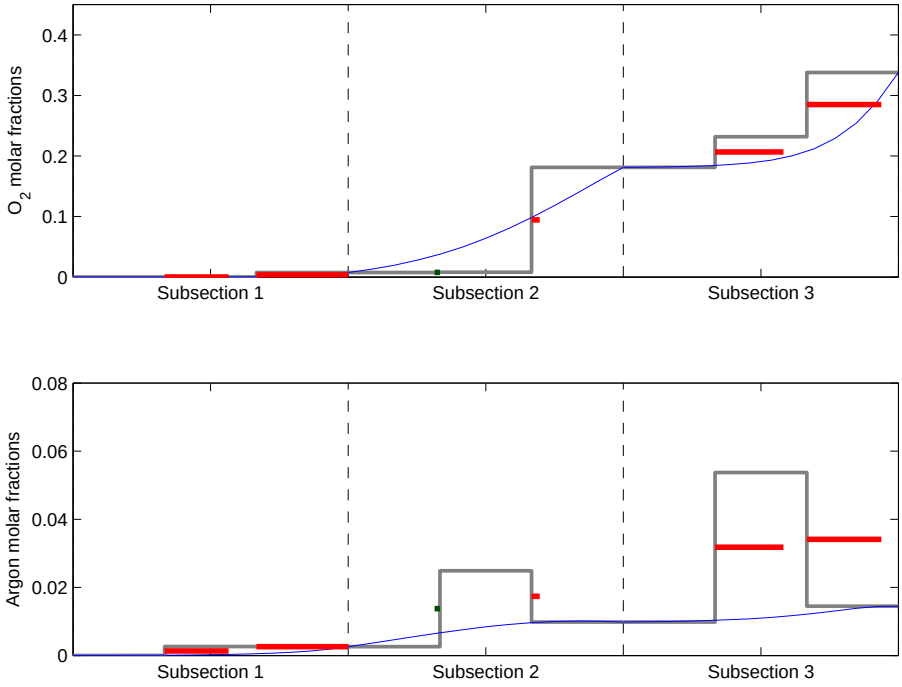

Figure 5.46: In gray, the piecewise continuous O_2 (top) and argon (bottom) composition profiles in the liquid, produced by the successive shockwaves for case C, in the HP column. HYSYS steady state profile is superimposed in blue. The length of the red and green markers is proportional to the corresponding shockwave speed. A red marker indicates a positive speed, a green marker a negative one.

wave-front analysis in subsections 3 and 4 of a real column would require three pairs of analyzers at the junctions between subsection 2-3, 3-4 and 4-5, so that one can compute the intermediary compositions, and consequently the shock speeds.

Yet note that if shock (1) is balanced in subsection 3, then shock (2) is automatically moving upwards, and if shock (2) is balanced in subsection 4, then the corresponding shock (1) is automatically moving downwards. Thus a restricted control strategy could limit itself to maintain shock (1) balanced in subsection 3 and shock (2) balanced in subsection 4. Roughly, we are now interested in detecting the drift of a composition front which can be seen as a binary exchange front: the molar fraction variation across the shock is necessarily in the same direction for two components among N_2, O_2 and Ar. Let us then consider them as only one single pseudocomponent for that shock. The key is then to detect the drift of this pseudobinary front, so now only one analyzer is required per shock. To see the front 'pass', the analyzer may now have to be located inside the subsection, where the front is supposed to stay balanced, rather than at the boundaries. The question of the one species whose concentration should be measured remains. An O_2 analyzer, as installed on the plant, seems problematic, since it would be unable to differentiate a 1-type shock from a 2-type shock: indeed, the sign of the O_2 composition variation is the same for all shocks. The same problem exists with nitrogen. Yet an argon analyzer seems well suited: one can tell a 1-type shock from a 2-type shock depending on the sign of the measured composition variation.

Of course such a strategy is purely reactive: the predictive capability of the configuration with enough pairs of analyzers to estimate the fronts' speed is lost. One can imagine to replace some of the required analyzers with soft-sensors embedding the full convection-diffusion model and adjusting their prediction based on the remaining physical measurements. We have seen yet that, due to the huge sensitivity of the system and of its model to flow estimation errors, this is hardly achievable in the LP column using only the existing analyzers.

5.7 Conclusion

In the continuity of the previous chapter, we have tested our PDE model versus steady-state Hysys simulation cases of the Low Pressure column, for the pseudo-binary mixture case. We have seen that the O_2 molar fractions profile is characterized by a large front located in the central subsections of the column. We have focused ourselves on the rendering of this front. The results we obtained show that the location of the front is highly sensitive to small perturbations on the internal flows L and V, and on the relative volatility α.

The LP column is a crucial first link in the argon separation process, for an argon belly appears in the column. In the belly, the argon molar fraction is about 10%, yet the nitrogen molar fraction can vary rapidly from 0.1% to several percents if the column is not stabilized. To ensure suitable composition of the mixture extracted from the belly to feed the first argon column, a ternary mixture model of the LP column would be useful. This motivated our tests with the ternary mixture PDE model versus the Hysys steady-state cases. We obtained satisfying representation of the bottom lobe of the argon belly, together with the main oxygen composition front. Yet the high sensitivity of the results to perturbations on L, V and α still exists.

The LP column model has been coupled with the HP column model to simulate its dynamics, versus real plant data from the air separation unit. To include the feedback effect of the first argon column K10, we have tested three simple models: a well-source model, where

the K10 column injects a mixture with ideal composition into the LP column, regardless of the argon belly composition; an equilibrium model, where the re-injected mixture composition is at the thermodynamic equilibrium with the inlet mixture of K10; and a model where the composition of the mixture injected from K10 to the LP column is determined by an approximate mass-balance over the K10 column. The main results are the followings:

- at the top of the LP column, the simulated O_2 molar fractions are well synchronized with the measurements and in agreement with them, apart from an offset which we supposed caused by an excessive estimated O_2 molar fraction in the lean liquid drawn off the (simulated) HP column;
- the oxygen concentration is much lower than expected in the liquid bath at the bottom of the LP column; this could be corrected with a significant change on the model's diffusion coefficient, but at the expense of the results at the LP-K10 connection location;
- in the argon bubble, at the LP-K10 connection location, the estimated oxygen molar fraction is globally in agreement with the measurements regarding the mean value, and the amplitude and shape of the oscillations. There is a significant time-shift between the estimation and the measure, which we suppose caused by an overestimated liquid speed in the LP column. We observe sudden O_2 molar fraction decreases, due to downwards excursions of the main oxygen front, possibly amplified by a destabilizing feedback of the K10 column. We have seen that the main oxygen front was sensitive to errors on L and V. It just so happens that the internal flows of the column are only poorly estimated in our model, notably due to a lack of measurements on the real plant. Here we can only suppose that better knowledge of the L and V flows would enhance the results. Enhancing the modeling of L and V implies taking into account the internal revaporizations caused by the differences in the components' heat of vaporization. One can also have to add the revaporization due to unperfect thermal insulation of the column (it is shown in [14], [13] on a warm column that estimated compositions can be highly sensitive to the estimation of the thermal losses).

Let us point out that our model gives access to the argon molar fractions in the LP columns, which are unmeasured on-site, especially in the bubble. Yet this information is degraded by the same phenomena that affect the main O_2 wavefront.

In an attempt to clarify the high sensitivity of the main oxygen front, and consequently of the argon bubble, we applied the result of Section 2.6 to the LP column. We have shown how, in the idealized case where there would be no diffusion, the HYSYS static profiles would split into a collection of shockwaves. It turned out that the speed of the shockwave associated to the sensitive fronts were almost null. We thus interpreted the high sensitivity of the fronts to small perturbations on L, V, α in the way of the classical wave-model: these perturbations turn a null wave-speed into a small but non-null speed, which causes the wave to drift over long distances into the considered subsection before it is repelled by diffusive phenomena in the vicinity of a boundary.

We noted a different situation in the HP column, where waves have generally significantly non-null speed in the vicinity of the lean liquid draw location. Consequently the diffusion has a predominant effect on the profile, which is 'pushed' against the boundaries: this justifies *a posteriori* that the diffusion parameter ϵ was a good candidate for the HP column model tuning.

Conclusion et perspectives (version française)

L'optimisation énergétique des procédés de séparation des gaz de l'air passe en partie par l'amélioration de leur contrôle. Des lois de contrôle améliorées devraient assurer une stabilisation plus fine des colonnes de distillation, un meilleur rejet des perturbations, et accélérer les changements de points de fonctionnement. De tels contrôleurs devraient être fondés sur des modèles de contrôle adaptés, valables pour tout point de fonctionnement et capables de décrire les dynamiques non-linéaires critiques du procédé avec le niveau de détail adéquat.

Ces considérations ont motivé la présente étude, qui s'inscrit dans la recherche de tels modèles. Nous avons restreint son cadre aux colonnes de distillations uniquement. Partant d'un élément minimal, un segment homogène de colonne, dans lequel nous avons tenté de modéliser les profils de compositions, nous avons cherché à construire, par étapes successives, un modèle de contrôle pour une chaîne de colonnes. Dans quelle mesure avons nous atteint cet objectif ?

Dans la revue bibliographique du Chapitre 1, nous avons sélectionné un modèle en particulier : le modèle d'onde. Dans celui-ci, les profils de compositions au sein d'une colonne sont modélisés par une onde de forme fixée, qui glisse le long de la colonne. À l'inverse des grands modèles à plateaux, ce modèle est concis et montre clairement le phénomène qui engendre les délais et asymétries caractéristiques de la dynamique des colonnes. Il est aussi supérieur aux modèles linéaires, calés sur un point de fonctionnement, en ceci qu'il explore, par nature, toutes les positions possibles du front d'onde de composition. Comparé aux modèles boîtes-noires, il est générateur de sens, car fondé sur une modélisation physique. Ce modèle a toutefois des inconvénients : les effets de bord y sont problématiques, en particulier à haute pureté, et l'hypothèse selon laquelle la forme de l'onde est fixée est irréaliste.

Suivant le raisonnement qui a abouti au modèle d'onde, nous avons proposé au Chapitre 2 un modèle d'équations bilans à deux fluides pour un segment homogène de colonne de distillation. En supposant que l'équilibre thermodynamique n'était pas nécessairement atteint partout dans les phases liquide et gazeuse, nous avons obtenu une expression d'un flux d'échange de matière entre les deux phases, imposé par les inhomogénéités de composition. L'ordre de grandeur de ce flux, par rapport à la convection sur l'axe de la colonne, est donné par un terme en $\frac{1}{\epsilon}$, $0 < \epsilon << 1$.

Nous avons réduit ce modèle à deux fluides en utilisant une technique de réduction variété centre. Le résultat a été, pour un mélange à $N \geq 2$ composants :

- une équation non-linéaire aux dérivées partielles, de convection-diffusion, pour la dynamique d'une variable interne X, qui est assimilée à une composition moyenne sur les

deux phases, liquide et vapeur,

- associée à des sorties statiques permettant de retrouver les compositions réelles dans chaque phase, à partir de la variable interne X.

Dans ce modèle, le terme de convection rappelle le modèle d'onde. De plus, nous obtenons un terme de diffusion dépendant de ϵ et des flux de liquide et de vapeur en chaque point de la colonne. Puisque nous pouvons relier le terme de diffusion à l'efficacité du garnissage et à la forme du profil de composition, ce que nous obtenons est en fait une forme de modèle d'onde dans lequel l'hypothèse de forme d'onde fixée est levée; la forme du profil dépend à présent des conditions d'opération de la colonne. En outre, ce terme de diffusion joue aussi un rôle dans les effets de bord, qui constituent une deuxième voie par laquelle il influe sur la forme des profils de composition.

Au Chapitre 4, nous avons vu que notre modèle EDP reproduit de manière satisfaisante des profils de composition binaires statiques dans la colonne Moyenne Pression. Nous avons également validé la dynamique du modèle, en boucle ouverte, sur la base de données issues d'une ASU réelle. Pour obtenir ces résultats, il a fallu déterminer empiriquement les valeurs de certains paramètres du modèle; elles diffèrent significativement des valeurs attendues (en particulier pour la vitesse de descente du liquide, laquelle affecte également les rétentions). Nous n'avons pu expliquer que partiellement ces écarts par des dynamiques négligées. Un point important est que de bonnes performances dans les comparaisons en régime dynamique ont été obtenues avec des valeurs de paramètres directement tirées des tests statiques. Afin d'améliorer l'accord entre le modèle et la mesure, nous avons montré qu'une simple adaptation lente du paramètre de diffusion ϵ était suffisante. Le modèle a cependant montré ses limites sur certains scénarios de test, pour lesquels nous n'avons pas pu supprimer un biais important entre les mesures et les prédictions du modèle. Cette baisse de performances semble être liée à des traffics liquide et vapeur réduits dans la colonne.

Au Chapitre 5, nous avons poursuivi les tests du modèle, en considérant cette fois la colonne Basse Pression (et en simulant nécessairement la colonne Moyenne Pression dans le même temps). Le couplage avec la première colonne d'argon a été pris en compte de façon simplifiée. Nous avons considéré tant le cas d'un mélange binaire (N_2/O_2) que celui d'un mélange ternaire ($N_2/O_2/Ar$). En comparant les résultats du modèle avec des profils statiques de référence, nous avons trouvé un bon accord, quoique moins satisfaisant que pour la colonne Moyenne Pression. Nous avons observé une grande sensibilité des profils simulés aux changements sur les flux internes de liquide et de gaz, et sur la volatilité des composants. Nous avons ensuite comparé les résultats du modèle à des données dynamiques issues de l'unité réelle, en nous focalisant sur l'estimation des compositions dans le ventre d'argon, c'est-à-dire au niveau de la jonction entre la colonne Basse Pression et la première colonne d'argon. La stabilisation de la composition du mélange à ce niveau est en effet critique pour la bonne marche du procédé d'extraction d'argon. Notre modèle reproduit assez bien la valeur moyenne de la composition O_2 mesurée à cet endroit, ainsi que certaines de ses variations. Mais du fait de la grande sensibilité constatée précédemment, et comme les flux à l'intérieur de la colonne sont mal connus, nous avons observé des divergences importantes entre l'estimation et la mesure. Notons que notre modèle EDP donne accès à la fraction molaire d'argon à cet endroit critique, concentration qui n'est nulle part mesurée. Ceci dit, les problèmes de sensibilité valent aussi pour l'estimation d'argon, et celle-ci est donc difficilement utilisable pour le contrôle à l'heure actuelle.

Concernant ce problème de sensibilité, nous voyons que le modèle EDP écrit au Chapitre 2 se réduit à un modèle de convection pure si l'on néglige la diffusion. Nous nous sommes intéressés à savoir quelles sont les quantités convectées, et de quelle manière. En adaptant des résultats issus du domaine de la chromatographie, nous montrons que pour un mélange à $N+1$ constituants, N^2 invariants de Riemann permettent de former N ensembles de constituants, dont les compositions sont propagées de façon cohérente. Nous donnons les relations permettant de lier ces ensembles aux compositions 'physiques', mesurables, dans la colonne, et *vice-versa*. Nous montrons que sous une condition suffisante, on peut décrire la propagation de ces ensembles par la propagation d'ondes de choc, et nous donnons leur vitesse. Au Chaptire 5, nous avons vérifié que la condition en question était bien remplie, tant dans la colonne Basse Pression que dans la colonne Moyenne Pression. Nous avons calculé les vitesses de convection dans la colonne Basse Pression et vu qu'en régime stationnaire, elles étaient nulles pour certaines ondes de choc. Les ondes en questions restent immobiles au milieu d'un segment de colonne. Une petite erreur d'estimation des flux de liquide ou de gaz suffit à leur donner une vitesse non-nulle, et à les faire glisser le long du segment, avant qu'elles ne soient ralenties puis stoppées par les effets de bord. Ce glissement modifie significativement les profils de composition, et explique la sensibilité constatée aux petites perturbations.

Même si cela est moins vrai pour la colonne Basse Pression, nous avons constaté que notre modèle EDP fait un observateur raisonnable pour la colonne Haute Pression. Au Chapitre 3, nous nous sommes efforcés de montrer que ce modèle a naturellement de bonnes propriétés. Sur une configuration de colonne simplifiée, et sous des hypothèses raisonnables, nous avons prouvé plusieurs de ces propriétés. Nous avons montré que les compositions moyennes X restent bien dans l'intervalle physique $(0,1)$. Nous avons démontré l'existence et l'unicité d'une solution stationnaire pour tout $\epsilon > 0$, et la dépendance monotone de cette solution en ϵ. Nous avons construit une fonction de Lyapunov pour prouver la stabilité locale exponentielle de la solution stationnaire. Nous avons aussi, sur la base de cette même fonction de Lyapunov, proposé une famille d'observateurs asymptotiques pour les profils de composition, et montré leur convergence locale exponentielle. Ces résultats sont pour des mélanges binaires uniquement. Les simulations tendent à montrer que, même si les preuves n'ont qu'une valeur locale, les propriétés seraient globales dans la pratique. Nous avons développé en parallèle, toujours au Chapitre 3, un modèle linéarisé tangent de fonctions de transfert pour un segment de colonne. Il connecte les variations de compositions en sortie, au sommet et en bas du segment, aux variations des compositions et des flux d'alimentation. Dans le domaine de Laplace, le modèle EDP linéarisé se réduit à une équation aux dérivées partielles ordinaires. Les racines de l'équation homogène associée ont une structure particulière : l'une est une série entière en ϵ, l'autre une série de Laurent en ϵ. Nous les manipulons sous forme symbolique pour écrire, via un développement asymptotique non-standard, les variations des sorties comme des séries entières en ϵ. En tronquant les expressions des racines, nous obtenons une structure de transferts en $O(\epsilon)$. Ces transferts se composent de gains et de retards purs, qui trouvent leur origine dans la convection des compositions, et l'hydraulique non-instantanée. On notera que ces transferts dépendent explicitement du profil stationnaire considéré, que l'on peut imaginer estimer à l'aide du modèle EDP. À la fin du Chapitre 4, nous avons utilisé cette structure pour construire un modèle de transfert de la colonne Moyenne Pression, et simuler les oscillations de la composition du Liquide Pauvre au voisinage d'un régime stationnaire. La comparaison avec les données réelles montre que notre modèle de transfert porte une part de l'information nécessaire.

Nous disposons donc pour la colonne Moyenne Pression d'un modèle de convection-diffusion aux performances satisfaisantes, au moins sous certaines conditions relatives aux débits internes de liquide et de gaz. La confiance dans les performances du modèle est renforcée par les propriétés démontrées au Chapitre 3. Les modèles convectifs-diffusifs, ou les modèles d'onde enrichis, semblent donc une bonne base pour des développements ultérieurs. Ceci est cohérent avec le fait que notre modèle EDP permet de dériver un modèle linéarisé, qui préserve une partie de l'information pour les petites dynamiques. D'un point de vue industriel, notre modèle EDP pourrait être implanté sur site, comme capteur logiciel estimant les compositions dans la colonne Moyenne Pression. Un tel déploiement impliquerait aussi les opérateurs de l'installation dans la recherche de bonnes pratiques d'utilisation de cette information pour le contrôle. En outre, disposer de cet outil et d'une présence sur le site de production permettrait de savoir plus rapidement et plus précisément ce qui s'y passe, à quel capteur faire confiance, quels signaux sont critiques et quels autres sont entachés d'artefacts... cette dimension est absente de l'étude, qui a été menée à distance.

La structure du modèle est inchangée pour la colonne Basse Pression ; de même, sa pertinence, *a priori*. Nous avons vu que les performances sont diminuées parce que les débits internes sont mal estimés, du fait : des revaporisations internes, des fractions liquide/gaz mal connues dans les pots de flash, et d'une modélisation rustique des bilans énergétiques dans les condenseurs et réchauffeurs. Améliorer ces performances requerrait d'intégrer des bilans énergétiques détaillés au modèle, et de coupler les modèles de colonnes à des modèles d'échangeurs thermiques. Concernant ces derniers, nous avons donné quelques pistes dans la revue bibliographique. Pour ce qui est des colonnes, nous avons envisagé de modéliser le couplage entre l'énergie et les compositions à la manière de [89], qui traite du flash adiabatique. Le modèle en question utilise explicitement des potentiels chimiques pour définir l'équilibre thermodynamique, et mène à un système de gradient qui dérive d'un potentiel (la production d'entropie, qui sert aussi de fonction de Lyapunov) et à la stabilité du flash pour un nombre quelconque de composants. Ce résultat ne peut cependant pas être étendu à une succession de flashs, puisque l'équilibre global ne correspond plus à un minimum de la production d'entropie, laquelle ne peut donc plus être une fonction de Lyapunov pour le système. Il serait intéressant de voir ce que cette approche peut amener comme résultats de stabilité dans le cas de notre système de dimension infinie. On peut aussi imaginer de récupérer une fonction de Lyapunov thermodynamique dans ce contexte, en utilisant la fonction de disponibilité thermodynamique à la manière de [44], [45].

Les différences de chaleur latente entre les principaux constituants de l'air n'est pas nulle, mais on pourrait tirer parti du fait qu'elles sont petites. Elles pourraient être prises comme petits paramètres, pour lesquels on mènerait des dévelopements asymptotiques standards pour simplifier le modèle.

Il n'est cependant pas garanti que de tels modèles enrichis, et couplés avec des modèles dynamiques d'échangeurs thermiques, soient suffisamment stables et précis pour atteindre l'objectif de modélisation des compositions dans la colonne Basse Pression. C'est peu probable en boucle ouverte, et adapter le modèle en ligne pourrait nécessiter des capteurs additionnels (rappelons que certains échangeurs ne sont pas du tout instrumentés). De la même façon, il n'est pas certain que l'on puisse développer des estimateurs satisfaisants pour les débits dans la colonne Basse Pression en couplant les débitmètres et analyseurs existants et le modèle EDP. La recommandation la moins audacieuse pour améliorer la stabilisation de la colonne Basse Pression et améliorer l'efficacité du procédé argon serait donc d'équiper la colonne de capteurs additionnels : on peut penser à des capteurs de températures qui permettraient de

voir passer le front d'oxygène principal, et/ou des analyseurs d'argon au niveau du ventre.

Au passage, la colonne d'argon a été prise en compte de façon très simplifiée dans cette étude, essentiellement parce que la simuler elle aussi par le biais d'un modèle EDP mène à des temps de calcul pénalisants. Il n'y a *a priori* pas de raison de se priver d'un modèle de convection-diffusion pour cette colonne. Des tests rapides comparés aux simulations Hysys en régime stationnaire montrent une reproduction raisonnable des profils ternaires ; la petite remontée de la concentration d'azote au sommet de la colonne est notamment bien reproduite (voir Fig. 5.47 and 5.48). Nous avons cependant observé que le principal front d'échange oxygène-argon tend à dériver lentement dans la colonne, ce qui rend son positionnement précis délicat, même en régime stationnaire. On retrouve ici le problème des ondes à vitesse nulle. Ceci dit, les modèles de convection-diffusion ne sont peut-être pas les plus adaptés pour cette première colonne d'argon. En effet, elle sépare un mélange essentiellement binaire, et l'unique front de composition est situé assez loin des extrémités de la colonne. On peut penser qu'un modèle d'onde classique, à la manière de Marquard, puisse donner des résultats intéressants.

Ceci nous ramène au modèle de contrôle linéarisé développé au Chapitre 3 et testé sur la colonne Moyenne Pression au Chapitre 4. Nous avons vu que suivant la direction de convection des compositions (vers le haut ou le bas), il nous fallait utiliser différents transferts. Mais dans la colonne Basse Pression se trouve le front d'oxygène principal, qui semble osciller lentement au milieu d'un segment, et pour lequel la vitesse de convection n'est donc orientée ni clairement vers le haut, ni clairement vers le bas. Nous pourrions imaginer ici une autre application au modèle d'onde classique : les segments extérieurs, en haut et en bas, de la colonne Basse Pression, seraient modélisés par des fonctions de tranfert, alors que leur connection serait représentée par un modèle d'onde pour le front principal. Une autre approche possible utiliserait des modèles de transfert similaire, mais appliqués à des segments fictifs de longueur variable. On utiliserait alors un transfert 'vers le bas' au-dessus du point d'inflexion du front principal d'oxygène, et un transfert 'vers le haut' en dessous. Ceci pose toutefois le problème de points d'injection et de tirage, qui feraient partie ou non d'un segment fictif en fonction de sa longueur.

Toujours à propos des applications au contrôle, on peut voir comment une stratégie de contrôle des grands transitoires pour la colonne Basse Pression se dessine, qui utiliserait tout à la fois le modèle de convection-diffusion, le modèle d'ondes de choc et le modèle de transferts (à supposer que les mesures soient en nombre suffisant pour garantir leur pertinence). Partant d'un point de fonctionnement initial, l'état initial est estimé avec le modèle EDP. Le modèle d'ondes de choc permet de calculer les changements de débits à appliquer pour démarrer le mouvement de certains fronts à vitesse contrôlée, ou pour maintenir certains fronts en place. Le modèle EDP suit en permanence la transition, de sorte que l'information est disponible pour que le modèle d'ondes de choc calcule les débits correspondants au point de fonctionnement final. La stabilisation autour de ce point est finalement assurée par le modèle de transferts.

En dehors de la conduite du procédé, on peut imaginer une utilité très différente à ce travail. La conception et le dimensionnement des colonnes obéissent en général à des considérations sur les régimes stationnaires. Les aspects transitoires sont pris en compte au niveau de l'hydraulique, par exemple pour ajuster le volume de capacités tampons. Des modèles de convection-diffusion ou assimilés, qui soient numériquement stables, concis, assez rapides et précis, pourraient constituer un outil permettant de tester un design préliminaire face à certains scénarios dynamiques (comme une panne de compresseur, un profil de demande client spécifique...). Après réglage du modèle sur un cas stationnaire simulé, il pourrait être possible

de se prononcer sur les futures performances de la colonne et de les garantir, ou encore de tester de petites perturbations du design.

On remarquera pour finir que de tels modèles, avec des capacités temps-réel, une bonne stabilité numérique et des bornes garanties, pourraient aussi trouver leur usage dans la simulation d'unités de séparation de l'air pour la formation des opérateurs.

Conclusion and perspectives

Our revels now are ended [...]

Shakespeare
The Tempest, Act IV, Scene 1

Energy optimization of air separation processes can be partially achieved by enhanced control strategies. Improved controllers shall ensure tighter stabilization of the distillation's columns, disturbance rejection, and accelerate set-point changes. Such control systems shall rely on adapted control models, independent from the set-point and catching the critical non-linear dynamics of the process with the right level of detail.

This has motivated the present study, which is part of the search for such models. We restricted its scope to the distillation columns only. Starting from an atomic element, an homogeneous packed section, in which we tried to model the compositions distributions, we aimed to build in successive steps a control model for a whole chain of columns. To which extent have we made progress ?

In the literature review of Chapter 1, we selected a model among others: the wave model. In this model, molar fraction profiles inside a distillation column are modeled as a sliding wave with *a priori* fixed shape. Contrary to the large stage-by-stage models, this model is concise and expresses in a clear manner the phenomena which engender delays and asymmetries in the columns dynamics. It is also superior to linear, set-point dependent models in that, by nature, it explores all the possible positions of the wave-front. Compared to the black-box models, since it relies on physic-based modeling, it creates sense. Yet this model has some drawbacks: end-effects are problematic, especially in a high-purity context, and the fixed shape assumption is unrealistic.

Inspired by the reasoning which yielded the wave model, we proposed in Chapter 2 a first-principles, two-flows model for a distillation column homogeneous subsection. Supposing that the thermodynamical equilibrium was not necessarily reached everywhere in the liquid and gas phase, we obtained an expression of the liquid-gas mass exchange flow, driven by concentration inhomogeneities. A term in $\frac{1}{\epsilon}$, $0 < \epsilon << 1$, scales the mass-exchange flow with respect to the axial convection flows.

We reduced this two-flows model using a Centre Manifold reduction technique. The result was, for a mixture with $N \geq 2$ components:

- a dynamic non-linear convection-diffusion partial differential equation for an internal variable X (of dimension $N-1$) which represents the lumped molar fraction over the liquid and gas phase,

- static outputs to retrieve the actual molar fraction of each component in the liquid and gas phase from the internal variable.

In this model, the convection term resembles to the wave-model. In addition, we found that the diffusion term depends on ϵ and, at each location in the column, on the internal liquid and gas flow. Since we can connect the diffusion term with the packing efficiency and the shape of the molar fraction profile, what we have obtained is a kind of wave model where the wave shape is no more fixed *a priori*, but depends on the column's operating conditions. Furthermore, the diffusion term plays a role in the column's end-effects, and also affects the profile's shape and movement this way.

In Chapter 4, we have seen that our PDE model was able to satisfyingly reproduce reference static binary mixture profiles of the HP column. We have also validated the model dynamic behavior in open loop against real plant data. To obtain these results, we had to use empirical model parameters values which significantly differ from the expected ones (especially regarding the liquid propagation speed, which also affects the hold-ups). We only partially explained the discrepancy by neglected dynamics. An interesting point is that good dynamic model performances were obtained by borrowing most of the model parameters directly from the steady-state tests. To enhance the plant-model agreement, we showed that a simple, slow on-line adaption of the diffusion coefficient ϵ was sufficient. The model has yet shown its limits on some tests scenarios, where we were unable to get rid of a large bias between the measures and the model predictions. The performance decrease seems to come with reduced liquid and gas traffics inside the column.

In Chapter 5, we went on with the model testing. This time we considered the Low Pressure column, and therefore had to simulate simultaneously the LP and the HP column. The interaction with the first argon column was handled in a simplified manner. We considered both binary (N_2/O_2) and ternary ($N_2/O_2/Ar$) mixture separation. Comparing the model against steady-state reference profiles, we obtained relevant estimated composition profiles (yet with larger errors than with the HP column). We observed that the simulated profiles were highly sensitive to small changes on the internal liquid and gas flows, and on the components volatility. We then tested the model against real dynamic data, focusing on the estimation of the composition in the argon belly, that is, at the location of the connection between the LP column and the first argon column. Indeed, the stabilization of the mixture composition at this location is important for the efficiency of the argon extraction process. We showed that our model successfully rendered the mean value of the measured O_2 molar fraction at this location, and also captured some of the composition oscillations. Yet, due to the previously observed high sensitivity, and since the columns internal flows were poorly known, we observed significant divergences between the estimated composition and the measure. Note that our PDE model gives access to the argon molar fraction at the critical location, whereas argon concentration is nowhere measured in the real column. Yet the argon molar fraction estimation is impeded by the same sensitivity issue, and thus hardly usable for control purposes as is.

Regarding this sensitivity issue, we can observe that the PDE model developed in Chapter 2 reduces to a convection model if we neglect the diffusion. We interested ourselves in finding which quantities are convected, and in which manner. Adapting results from the field of chromatography, we showed that, for an $N+1$ components mixture, N^2 Riemann invariants allow to form N multicomponent sets, which propagate in a coherent manner. We gave the equations to form these sets from the actual compositions in the column, and *vice-versa*. We

showed that under a sufficient condition, these sets propagate as non-interacting shock-waves, and gave the corresponding convection speeds. In Chapter 5, we checked that this condition was fulfilled in both the LP and the HP column. Computing the convection speeds in the LP column, we found that in steady state, some waves have null speed and stand in the middle of a subsection. A small estimation error on the internal flows or on the volatilities makes these speeds non-zero, which causes the shock wave to drift along the subsection, until it is repelled and stopped by a boundary. This significantly modifies the composition profiles, and is an explanation for their sensitivity to the mentioned perturbations.

Even if this is less true regarding the LP column, we have experimentally seen that our PDE model makes a reasonable observer for the HP column. In Chapter 3, we endeavored to show that the model has built-in good properties. On a simplified column configuration, and under a reasonable set of hypotheses, we have proved several of these properties. We proved that the estimated lumped molar fractions stays within the physical interval $(0, 1)$. We proved the existence and uniqueness of a stationary solution for any $\epsilon > 0$, and the monotone dependence of the top stationary composition on ϵ. We built a Lyapunov function to prove the local exponential stability of this stationary solution. We also proposed a family of tunable molar fraction profiles observers, which we proved locally exponentially convergent using the same Lyapunov function, even with unsteady internal flows. These results are for the binary mixture separation only. Simulations indicates that, even if the proofs are local, the properties seem to hold globally.

In parallel, we developed, still in Chapter 3, a linearized transfer functions model for a single packed subsection. This model connects the top and bottom outlet compositions variations with the variations of the top and bottom inlet flows and compositions variations. Written in the Laplace domain, the linearized PDE model reduces to an ordinary differential equation. The roots of the corresponding homogeneous equation have a particular structure: one is a power series in ϵ, the other one is a Laurent series in ϵ. Manipulating these roots via symbolic calculations, we obtained through non-standard asymptotic expansion the outputs as power series in ϵ. Truncating the roots expansion, we obtained the transfer structure in $O(\epsilon)$. The obtained transfers are composed of direct transfers plus delays, which originate from the composition convection and from the non-instant liquid propagation. Note that the obtained transfers explicitly depend on the considered steady-state profile, which we can imagine to estimate using the convection-diffusion model. In the end of Chapter 4, we used this transfer structure to build the transfer model of the HP column, and simulated the compositions oscillations of the Lean Liquid around a quasi-stationary state. Comparing the results against real plant data indicates that our transfer model indeed embeds a part of the necessary information.

We thus dispose for the HP column of a convection-diffusion model whose performances are satisfying, at least under certain conditions regarding the internal flows. Confidence in the model is reinforced by the properties demonstrated in Chapter 3. This indicates that such convection-diffusion models, or enriched wave-models, are a relevant basis for further developments. This is in coherence with the fact that our PDE model allowed to derive a linearized model, which still preserves some information regarding the small composition dynamics. From an industrial point of view, our PDE model could be implemented on-site, to serve as a soft-sensor estimating the molar fraction profiles inside the HP column. This would also involve the plant operators in finding relevant ways to use this information for

control. In addition, working on-site would allow to know quicker and more precisely what is going on on the plant, which sensors to trust, which signals are critical and which ones are artifacts... this is a dimension which was absent of this work, since all the study has been conducted in a distant manner.

Regarding the LP column, the model structure is unchanged, and so is its relevance *a priori*. We have seen that the performances are decreased because of poor estimation of the internal flows. These flows are poorly known because the internal revaporizations, the liquid/gas fractions in the flashpots, and the energy duties of the condensers and boilers have been modeled in a rough manner. Going further in this direction would require to integrate detailed energy balances into our model, and to couple the column models with heat-exchangers models. For the heat-exchangers, we have given some clues in the literature review. As regards the distillation columns, we envisaged to model the coupled energy and composition problem in the manner of [89], which is for the adiabatic flash. The model makes explicit use of chemical potentials to define the thermodynamical equilibrium and yields to a gradient system deriving from a potential (the entropy production, which also serves as Lyapunov function), which leads to the stability of the flash for any number of components. Yet the result as is can not be extended to staged flashes since the overall entropy production is non minimum at the global equilibrium, and therefore can not be a Lyapunov function. It would be interesting to investigate the stability results that could arise from such a model applied to our infinite dimension system. In addition, one could imagine to recover a thermodynamical Lyapunov function in that context using the thermodynamical availability function in the manner of [44], [45].

One could in addition take advantage of the non-null yet small differences of latent heat of vaporization between the main air components. These differences could be taken as small parameters, and the model could be simplified by classical asymptotic expansion in these parameters.

It is yet unclear whether such enriched models, coupled with heat-exchanger dynamics models, will be stable and accurate enough to achieve the modeling of the composition profiles inside the LP column or not. It is improbable in open loop, and tuning the models using plant measurement could require additional sensors (for instance, on some heat exchangers that are currently not monitored). Similarly, it is unclear whether internal liquid flows estimation strategies can be elaborated for the LP column or not, coupling the available flow-meters and analyzers and the current PDE model. The safer recommendation to improve the stabilization of the LP column and increase the efficiency of the argon process would then be to equip the column with additional sensors: for instance, temperature sensors which should allow to detect the main oxygen front pass by, and/or argon composition analyzer in the belly.

By the way, the first argon column has been handled in a very simplified manner in this work. This was essentially because simulating it using our PDE model led to penalizing computation times. Yet there is *a priori* no other reason for not using convection-diffusion models for this column. Quick tests against Hysys steady-state cases showed reasonable rendering of the ternary profile, where the small nitrogen concentration increase at the top of the column was notably reproduced (see Fig. 5.47 and 5.48). We observed though that the main oxygen - argon exchange front tends to drift very slowly along the column, which made its precise positioning uneasy even in steady state. We find here the null-speed wave issue again. This being said, convection diffusion models might not be the most suited for the first argon column. Indeed it essentially separates a binary mixture, and the unique composition front is apparently located quite far from the boundaries. We can imagine that a classical

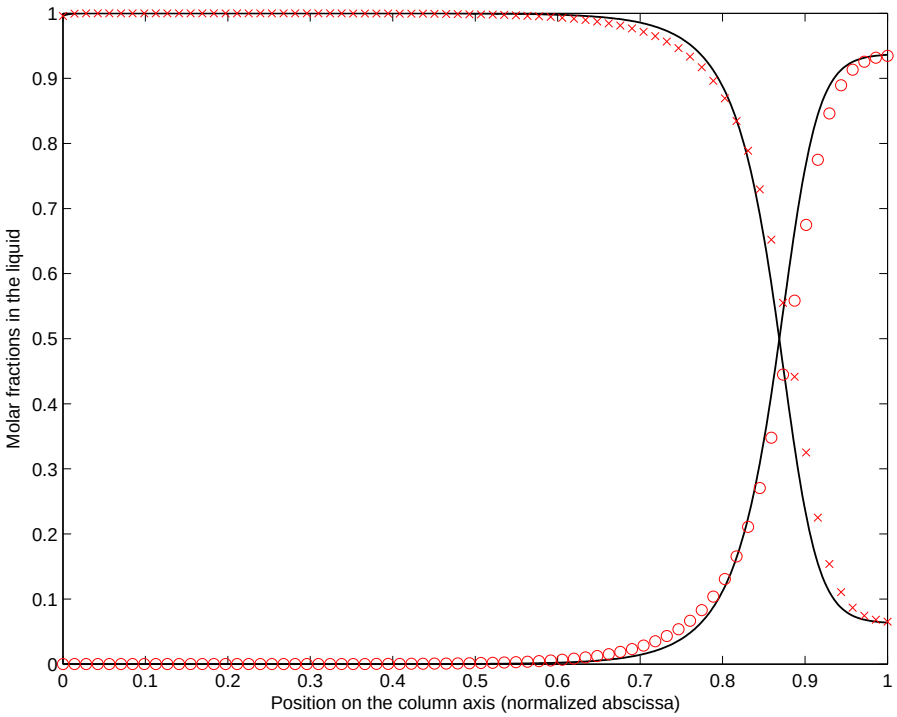

Figure 5.47: Example of a static comparison between the PDE model and and HYSYS simulation of the first argon column. HYSYS estimated liquid oxygen (red x) and argon (red circles) molar fractions, and the profiles predicted by the PDE model (black).

wave-model, in the manner of Marquardt's, could yield interesting results.

This brings us back to the linearized control model developed in Chapter 3 and tested for the HP column in chapter 4. We have seen that we have to use different transfer function, depending on the direction of the compositions convection (upwards or downwards). Yet in the Low Pressure column, we have the case of the main oxygen front, which is apparently slowly oscillating in the middle of a subsection, and for which the convection speed is neither clearly downwards, nor clearly upwards. Here we could imagine another application of the classical wave-model: the very top and bottom subsections of the LP columns could be modeled using our transfer functions; their connection would be made using a wave-model representation of the main front. Another approach would be to develop similar transfer models, yet applied to fictional subsections of varying length. One would then use 'downwards' transfers above the oxygen front inflexion point, and 'upwards' transfers below, constantly adapting the fictional subsections length with the current location of the front. These approach yet raises the issue of the column's feeds and draws, which could be part or not of a fictional subsection depending on its length.

Still regarding control applications, one can see how a transients control strategy for the LP column can take shape, with coupled use of the convection-diffusion model, the shock-wave model and the linearized model for large transients control purposes (provided notably that enough measurements are available for them to be reliable). Starting from the initial set-point, the initial state is estimated using the PDE model. The shock-wave models allows computing the flow changes required to move some composition fronts with controlled speed, or to

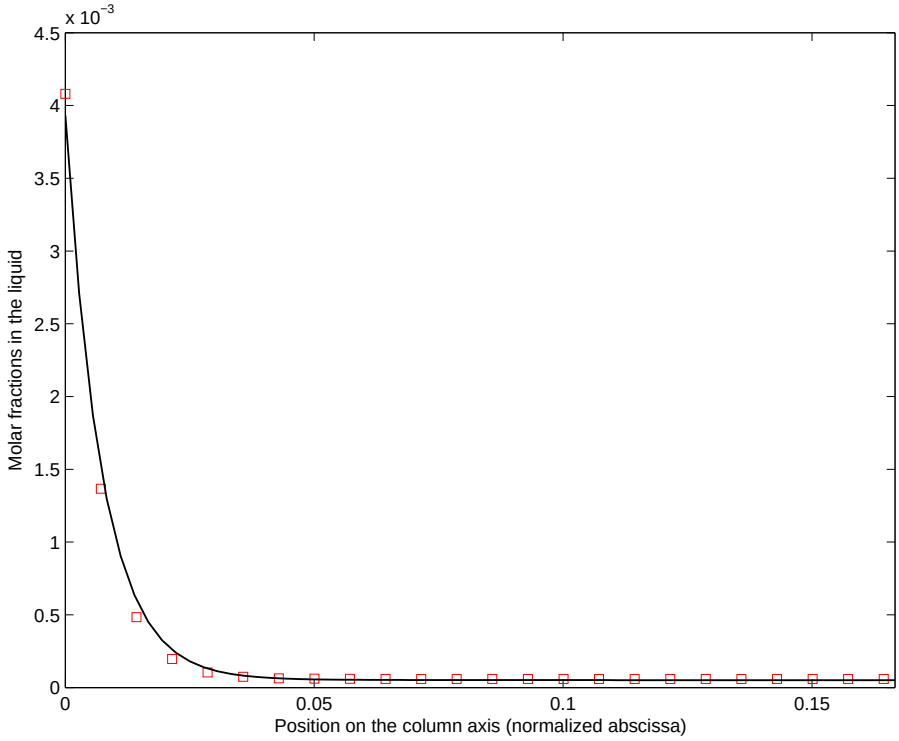

Figure 5.48: Example of a static comparison between the PDE model and and HYSYS simulation of the first argon column. Zoom at the top of the column. The PDE model (in black) renders the increase of the nitrogen molar fraction predicted by HYSYS in the liquid (red squares).

maintain other fronts unmoving. The PDE model tracks the transients, so that information is available for the shockwave model to compute the final flows for the targeted set-point. The corresponding final state is estimated using the PDE model, and final stabilization is ensured using the linearized model in the vicinity of this state.

Regardless of control application, a completely different application for this work has been imagined. The design and dimensioning of columns generally follow steady-state rules. Transients aspects are taken into account regarding the hydraulics, to adjust some buffer capacities for instance. Yet the dynamics are only loosely investigated regarding the compositions. Convection-diffusion models or similar ones, which are numerically stable, concise, quite fast and accurate, could become a tool to test a preliminary design against some dynamic scenarios (e.g. compressor failure, specific time-varying customer demand...). After tuning of the model on steady-state cases, one could thus assess and grant the future column's performances, or investigate incremental design changes.

Note also that such models with real-time capabilities, numerical stability and granted boundedness could find interesting application in air separation plants simulators dedicated to operators training.

Appendix A

Columns schemes

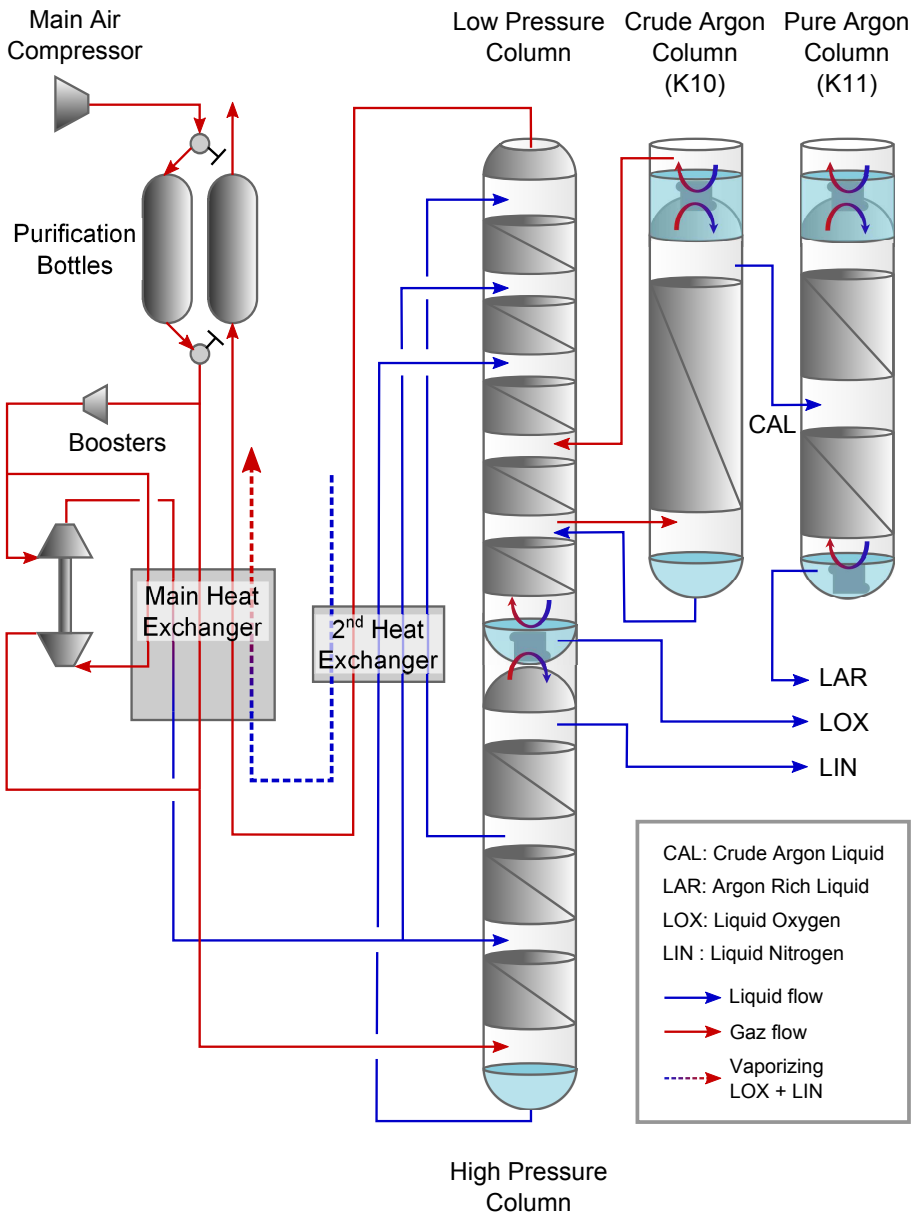

Figure A.1: Simplified flowchart of the ASU under study. Red arrows indicate gas flows, blue arrows are for liquid flows.

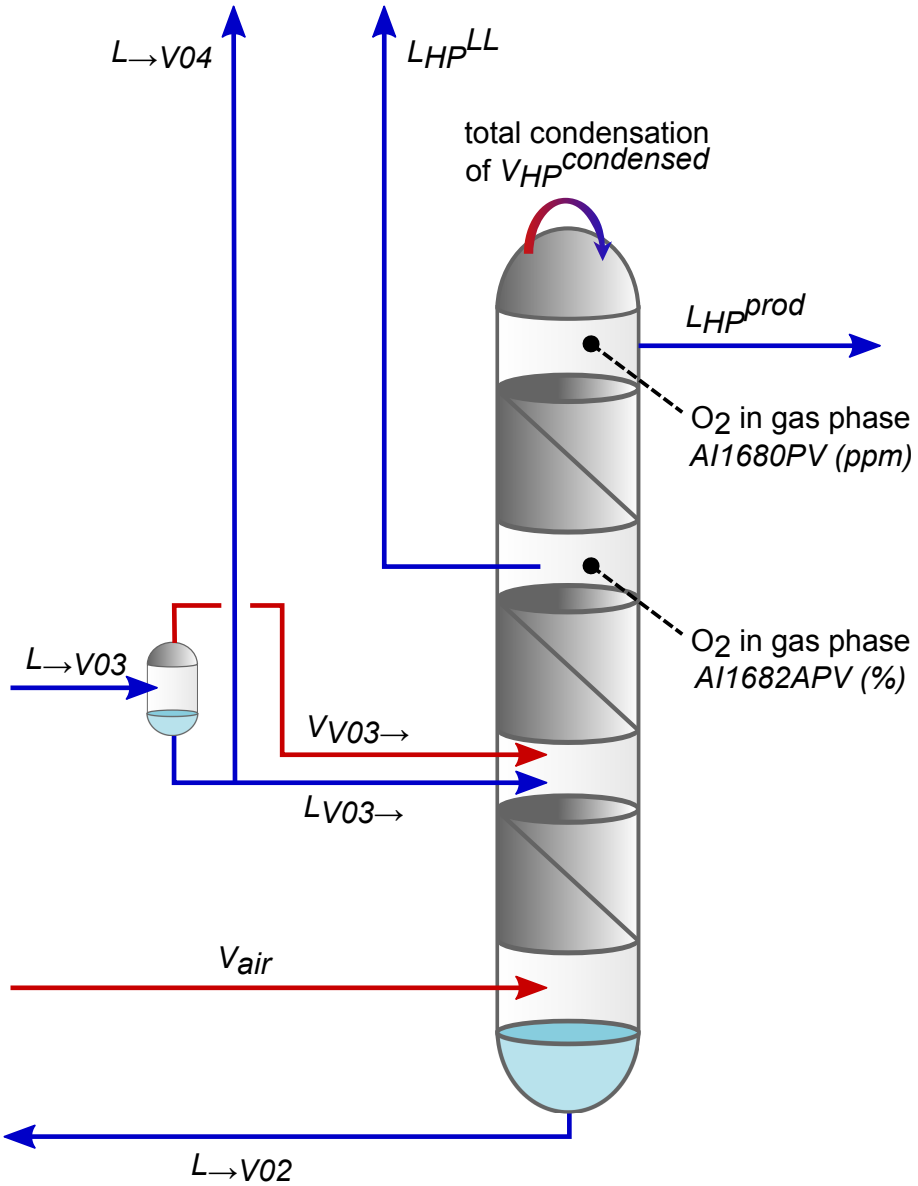

Figure A.2: Flowchart and available composition analyzers on the High Pressure column. Red arrows indicate gas flows, blue arrows are for liquid flows.

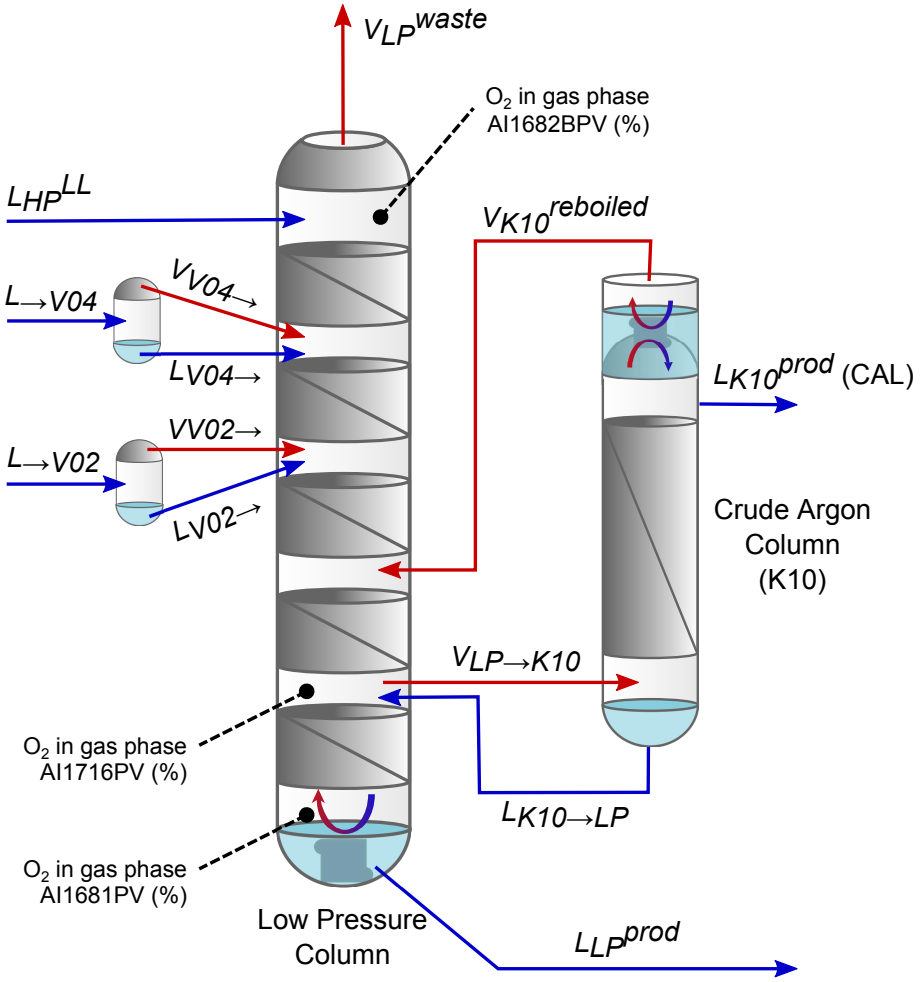

Figure A.3: Flowchart and available composition analyzers on the Low Pressure column. Red arrows indicate gas flows, blue arrows are for liquid flows.

Appendix B

Nomenclature of the tags

B.1 Tags of the HP column

V_{air} Air flow at the liquefaction point, which enters the HP column at its bottom.

$L_{\rightarrow V03}$ High pressure liquid air entering the flashpot V03.

$L_{V03\rightarrow}$ Liquid flow from the flashpot V03, entering the HP column between subsections 2 and 3.

$V_{V03\rightarrow}$ Gas flow from the flashpot V03, entering the HP column between subsections 2 and 3.

L_{HP}^{LL} Lean Liquid flow; the Lean Liquid is drawn off the HP column between subsections 1 and 2, and serves at top reflux flow for the LP column.

L_{HP}^{prod} Almost pure nitrogen liquid flow drawn off the HP column at its top; serves for the liquid and gas nitrogen production.

$L_{\rightarrow V02}$ Oxygen rich liquid flowing from the HP column's bottom to the LP column's flashpot V02.

$V_{HP}^{condensed}$ Gas flow arriving at the top of the HP column to be condensed.

B.2 Tags of the LP column

L_{HP}^{LL} Lean Liquid flow; the Lean Liquid is drawn off the HP column between subsections 1 and 2, and serves at top reflux flow for the LP column.

$L_{\rightarrow V02}$ Oxygen rich liquid flowing from the HP column's bottom to the LP column's flashpot V02.

$L_{\rightarrow V04}$ Liquid flow from the HP column's flashpot V03, entering the LP column's flashpot V04 (a part of this flow is tapped to serve for the Argon process).

$L_{V02\rightarrow}$ Liquid flow from the flashpot V02, enters the LP column between subsections 1 and 2.

$V_{V02\rightarrow}$ Gas flow from the flashpot V02, enters the LP column between subsections 1 and 2.

$L_{V04\rightarrow}$ Liquid flow from the flashpot V04, enters the LP column between subsections 1 and 2.

$V_{V04\rightarrow}$ Gas flow from the flashpot V04, enters the LP column between subsections 1 and 2.

V_{HP}^{waste} Residuary gas exiting the LP column at its top.

$V_{K10}^{reboiled}$ Gas vaporized in the argon column K10 top condenser, enters the LP column between subsections 3 and 4.

$L_{K10\rightarrow LP}$ Liquid flow from the argon column K10 bottom, enters the LP column between subsection 4 and 5, at the argon belly location.

$V_{LP\rightarrow K10}$ Gas taken out from the LP column at the argon belly location, feeds the argon column K10 at its bottom.

$V_{LP}^{reboiled}$ Gas reboiled out of the LP column's bottom liquid bath.

L_{LP}^{prod} Almost pure oxygen liquid, drawn off LP column's bottom; serves for liquid and gas oxygen production.

B.3 Tags of the first argon column K10

$V_{K10}^{reboiled}$ Gas vaporized in the argon column K10 top condenser, enters the LP column between subsections 3 and 4.

$V_{K10}^{condensed}$ Gas arriving at the top of K10 to be condensed

L_{K10}^{prod} Almost nitrogen free liquid taken out at the top of K10 to feed the second argon column K11.

$L_{K10\rightarrow LP}$ Liquid flow from the argon column K10 bottom, enters the LP column between subsection 4 and 5, at the argon belly location.

$V_{LP\rightarrow K10}$ Gas taken out from the LP column at the argon belly location, feeds the argon column K10 at its bottom.

Appendix C

HP column additional dynamic simulations

The following pages present in a condensed manner the results of the HP column simulation using 17 40h scenarios gathered from the air separation plant. The figures are all presented in the following way:

Top, left Internal liquid and gas molar flows (Nm^3/s). Solid red: gas in subsection 1 and 2. Dotted red: gas in subsection 3. Solid blue: liquid in subsection 1. Dotted blue: liquid in subsection 2. Dashed blue: liquid in subsection 3.

Center, left Internal column pressure (bara).

Bottom, left Envelopes of variation of the simulated gas (pale red) and liquid (pale blue) oxygen composition profiles. HYSYS static profiles are superimposed (Solid: case A. Dashed: case B. Dash-dotted: case C).

Top, right Estimated and measured gas oxygen content at the lean liquid draw. Black: measure in gas. Solid red: $k(X)$. Dotted red: actual simulated composition (the static output y).

Center, right Diffusion coefficient ϵ with on-line adaption.

Bottom, right Estimated compositions at the top of the column. Blue: the lumped O_2 composition X. Red: $k(X)$. Dotted red and blue: the actual simulated compositions in the liquid (blue) and gas (red), i.e. the static outputs x and y.

Simulations are made with Δt=0.1s, $\Delta s = 0.1m$, $\alpha_{O_2} = 0.395$, $\mu_L = 0.6m/s$, $\lambda_L = 20mol.m^{-1}.s^{-1}$, $\lambda_V = 10\lambda L$. The diffusion parameter ϵ is adapted according to 4.16, with time constant $T_i = 1h$. The liquid speed is $0.02m/s$.

Table C gives the day and hour of beginning of each scenario, as well as the cluster it belongs to.

Scenario	Day	Starting hour	Cluster
1	June 27^{th}, 2011	10h	1
2	July 4^{th}, 2011	10h	1
3	July 11^{th}, 2011	10h	1
4	July $18^{t}h$, 2011	10h	1
5	July 25^{th}, 2011	10h	1
6	August 1^{st}, 2011	10h	1
7	August 8^{th}, 2011	10h	1
8	August 15^{th}, 2011	10h	1
9	September 5^{th}, 2011	10h	1
10	September 12^{th}, 2011	10h	1
11	October 3^{rd}, 2011	10h	1
12	October 10^{th}, 2011	10h	2
13	October 17^{th}, 2011	10h	2
14	October 24^{th}, 2011	10h	2
15	November 1^{st}, 2011	10h	3
16	November 29^{th}, 2011	10h	3
17	May 28^{th}, 2012	10h	2

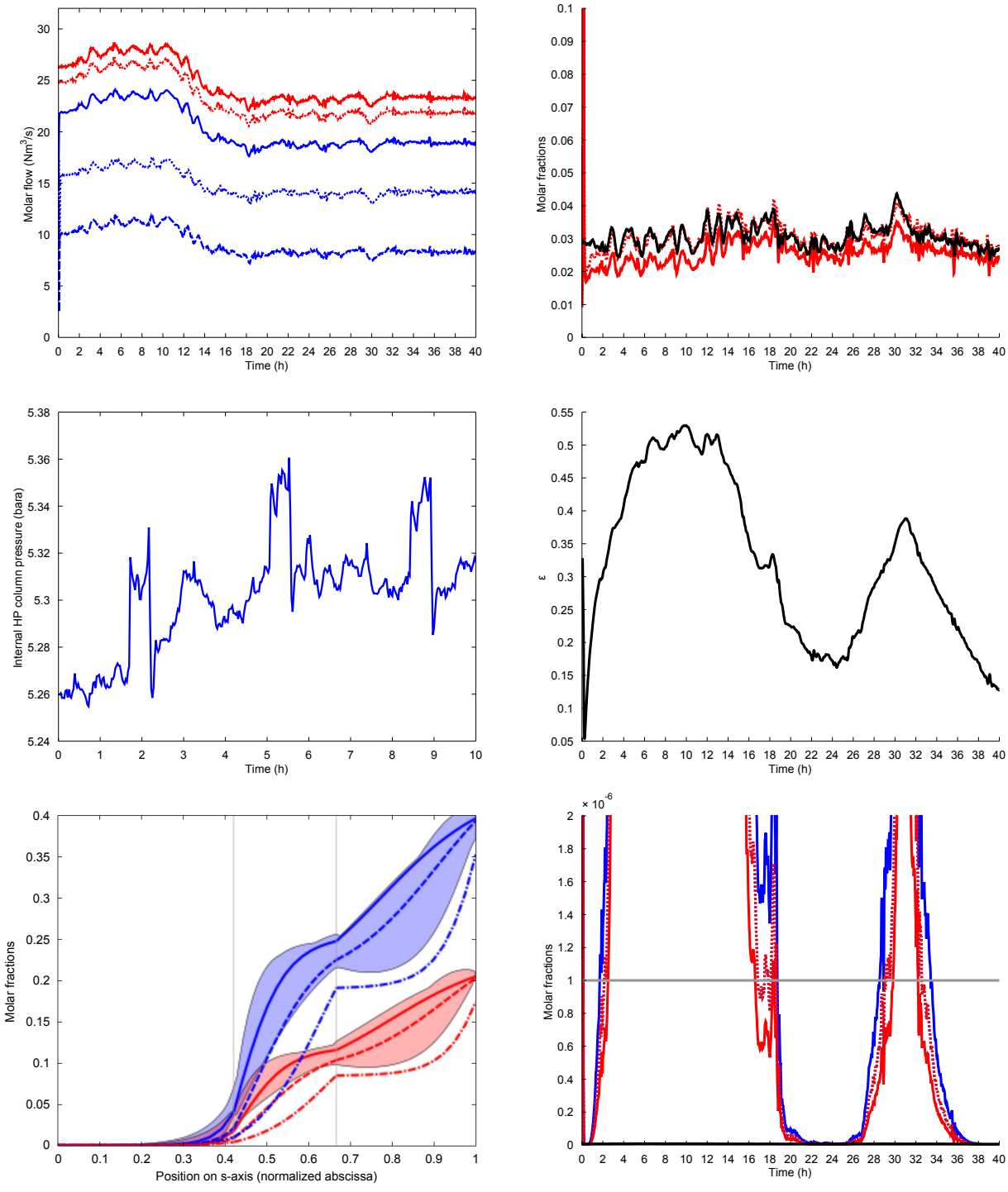

Figure C.1: Scenario n°1

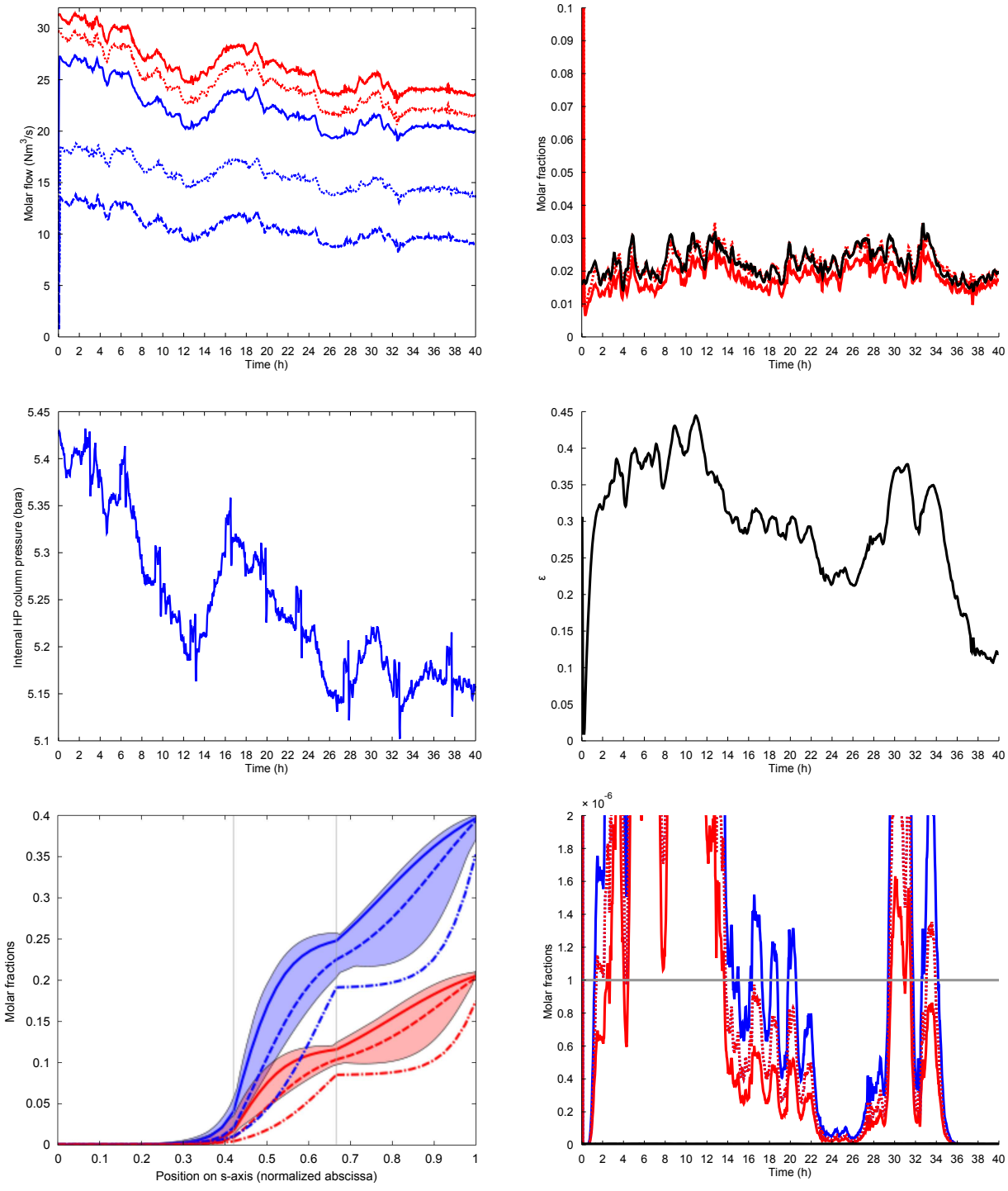

Figure C.2: Scenario n°2

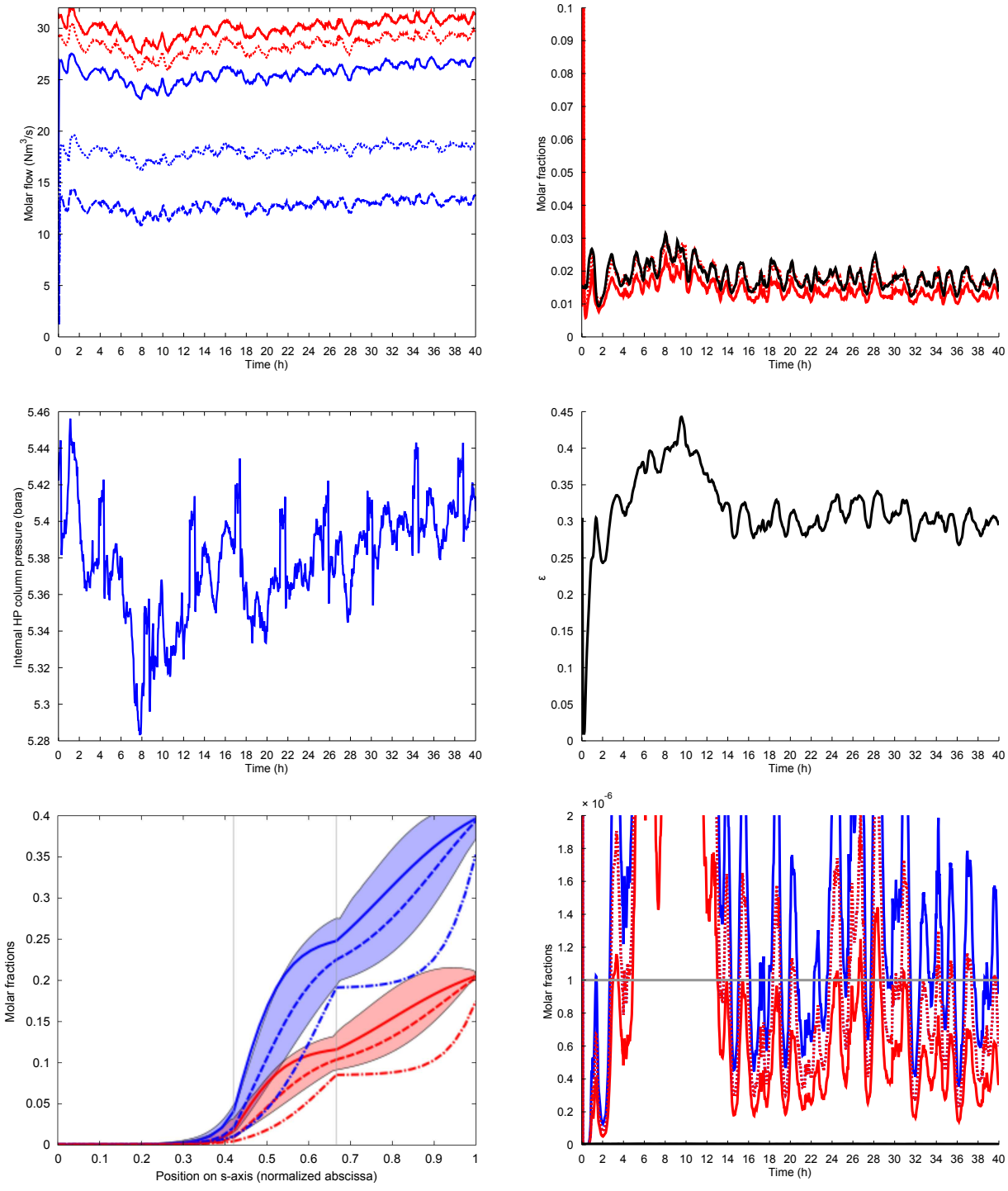

Figure C.3: Scenario n°3

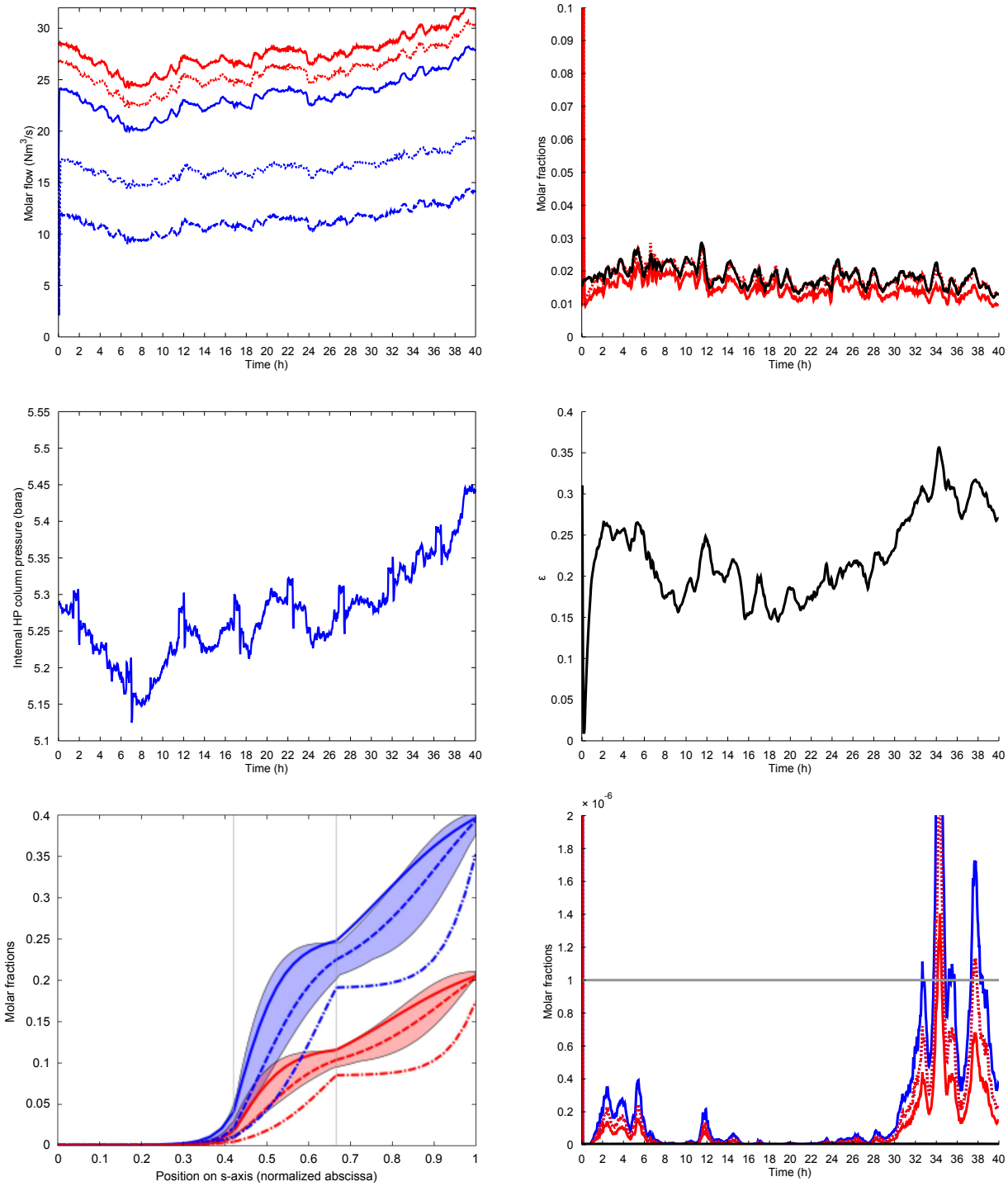

Figure C.4: Scenario n°4

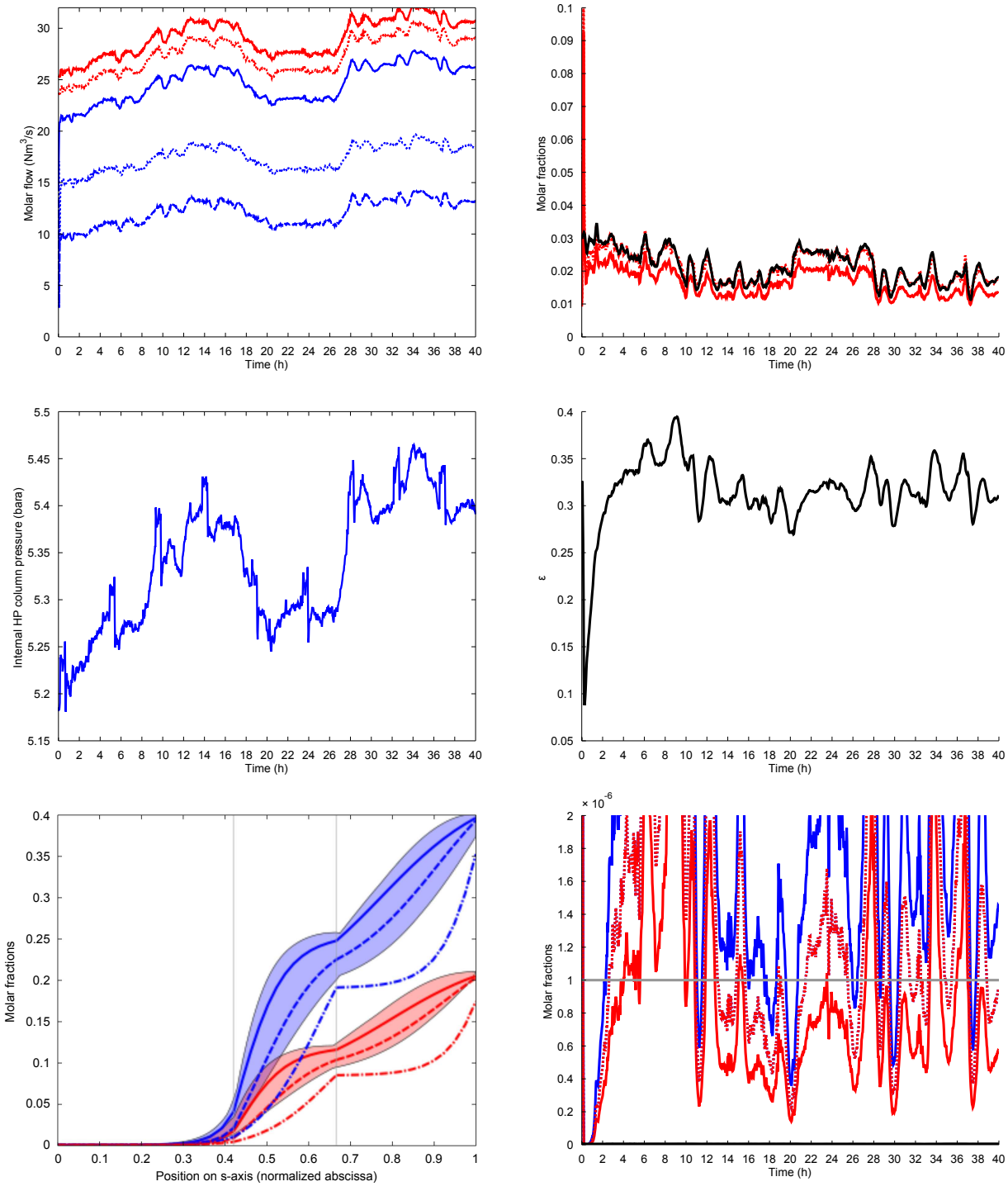

Figure C.5: Scenario n°5

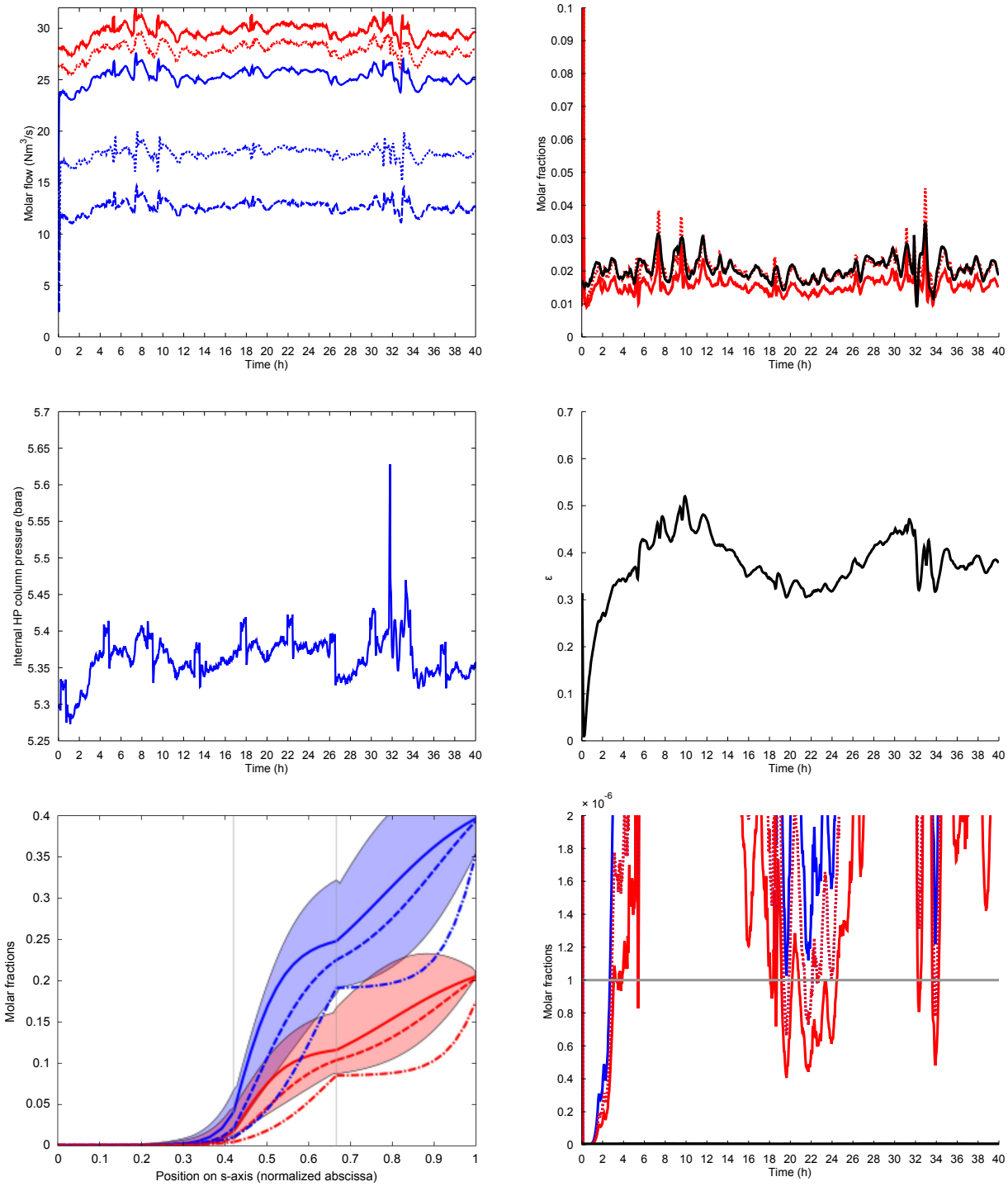

Figure C.6: Scenario n°6

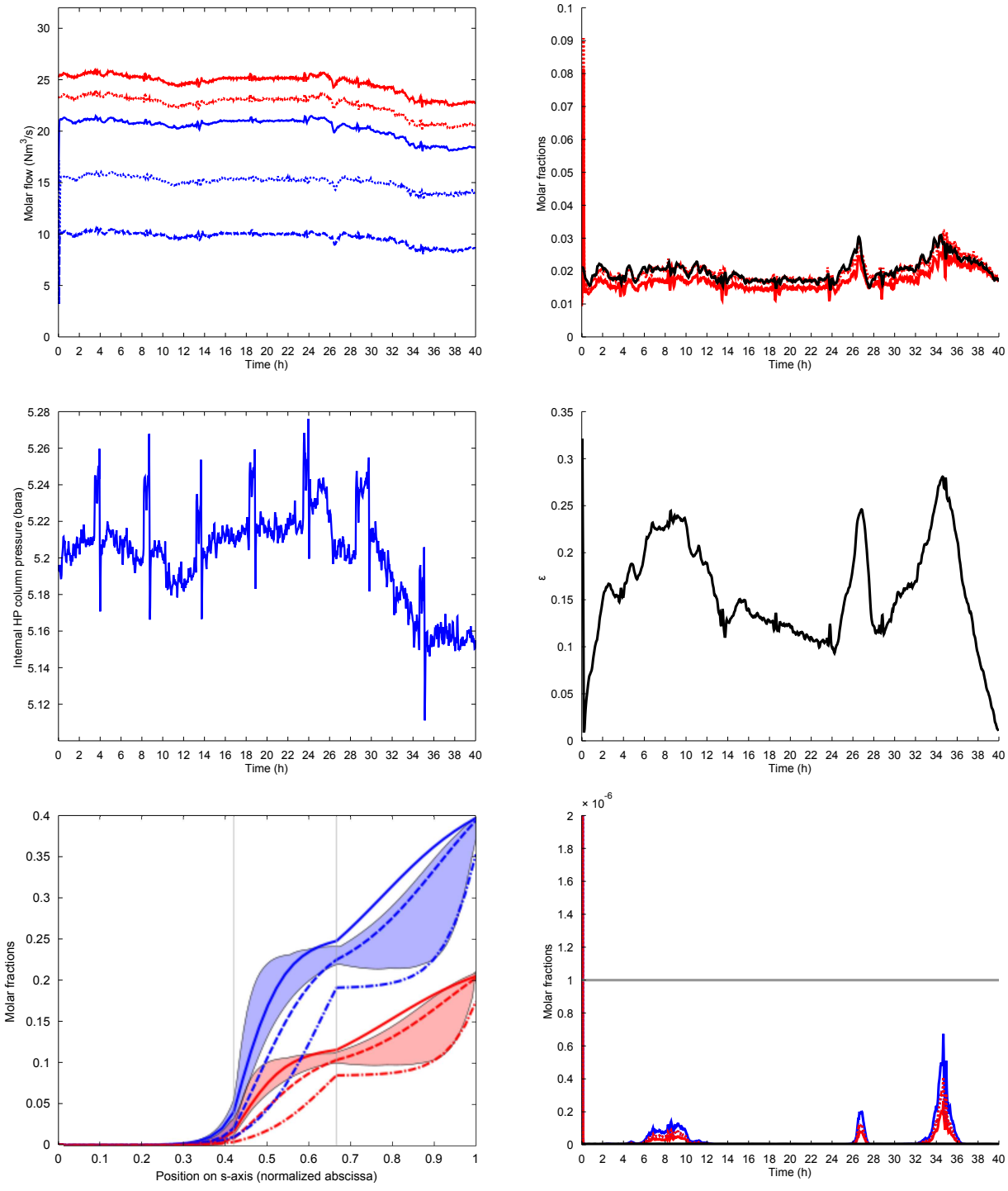

Figure C.7: Scenario n°7

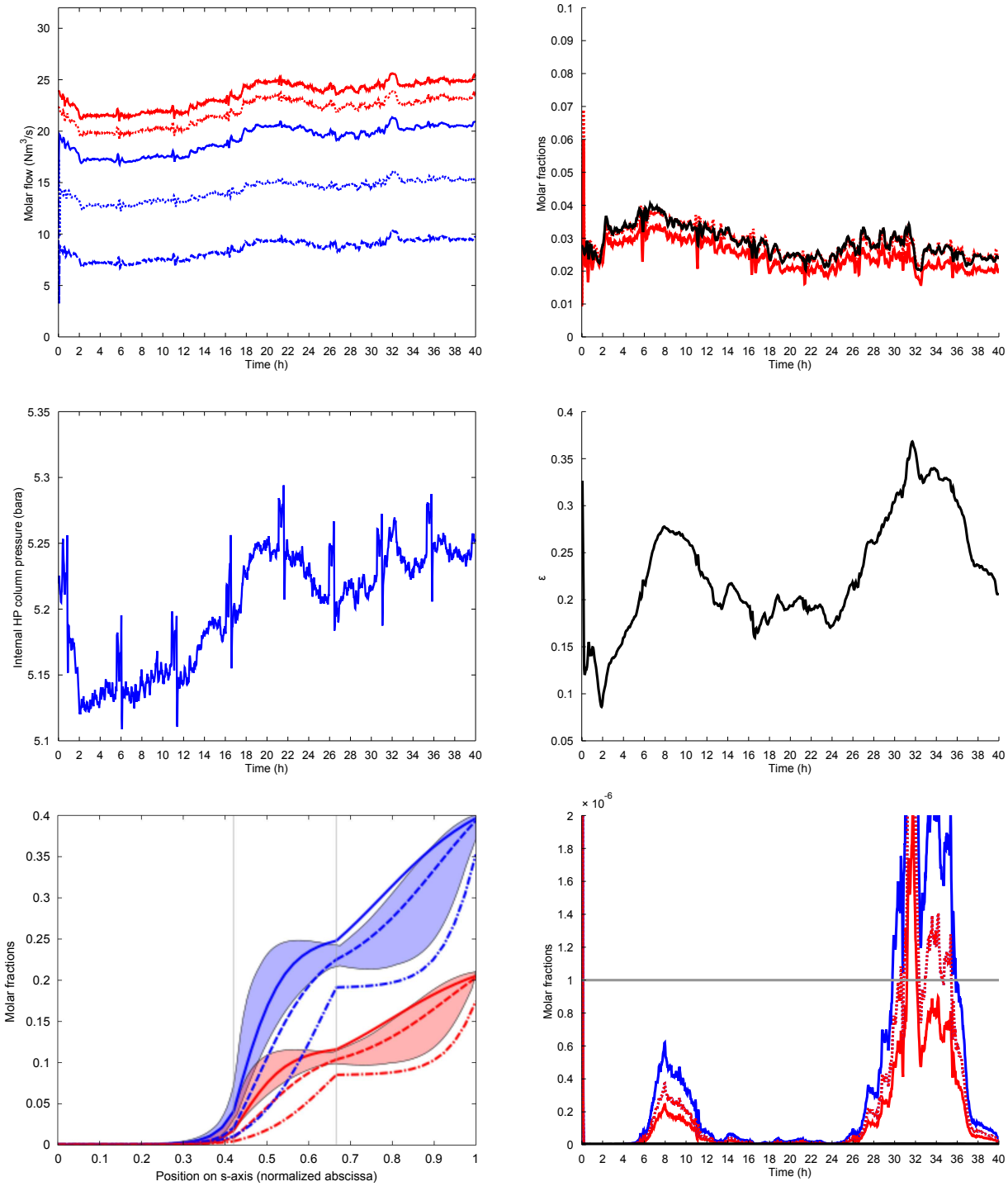

Figure C.8: Scenario n°8

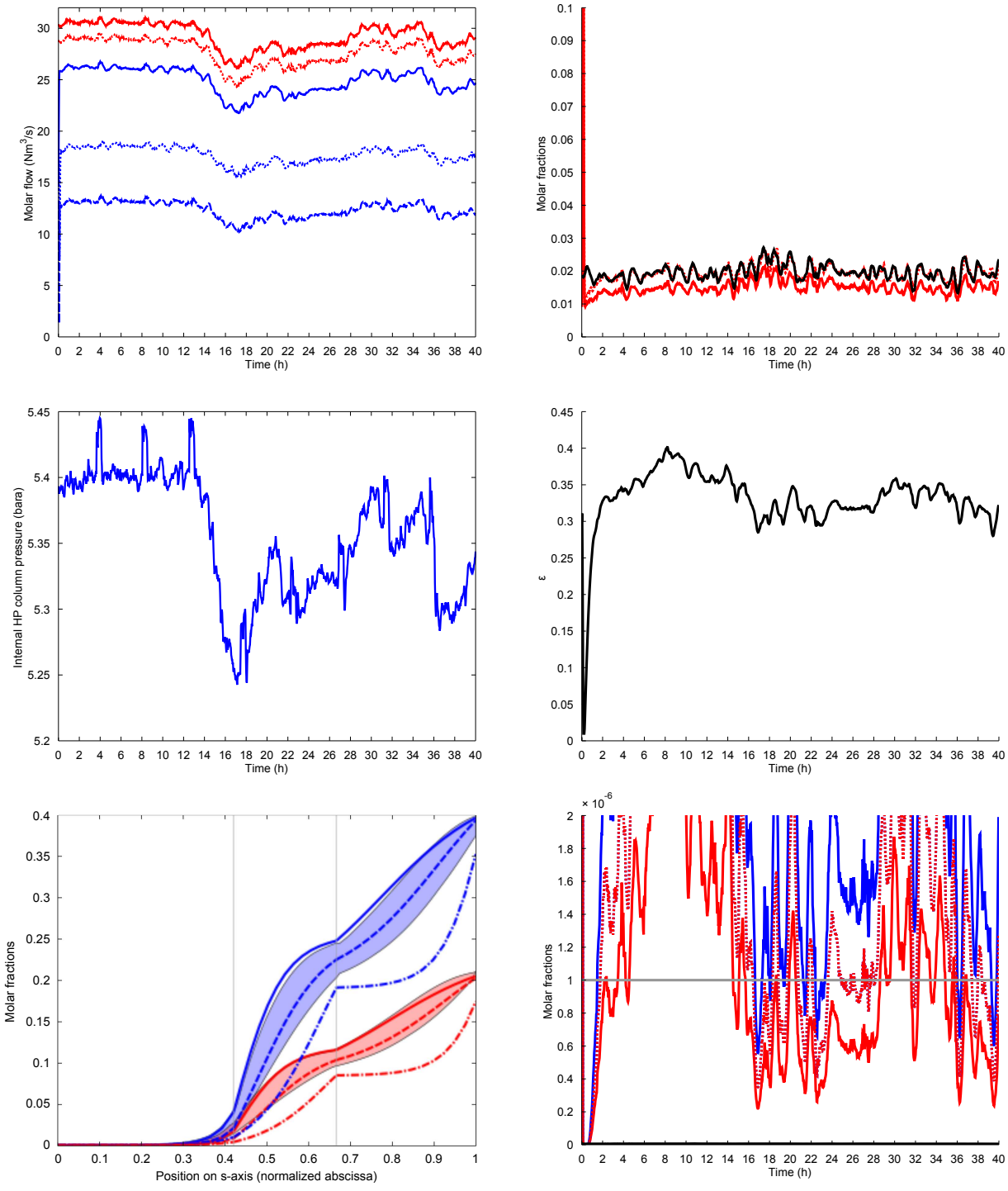

Figure C.9: Scenario n°9

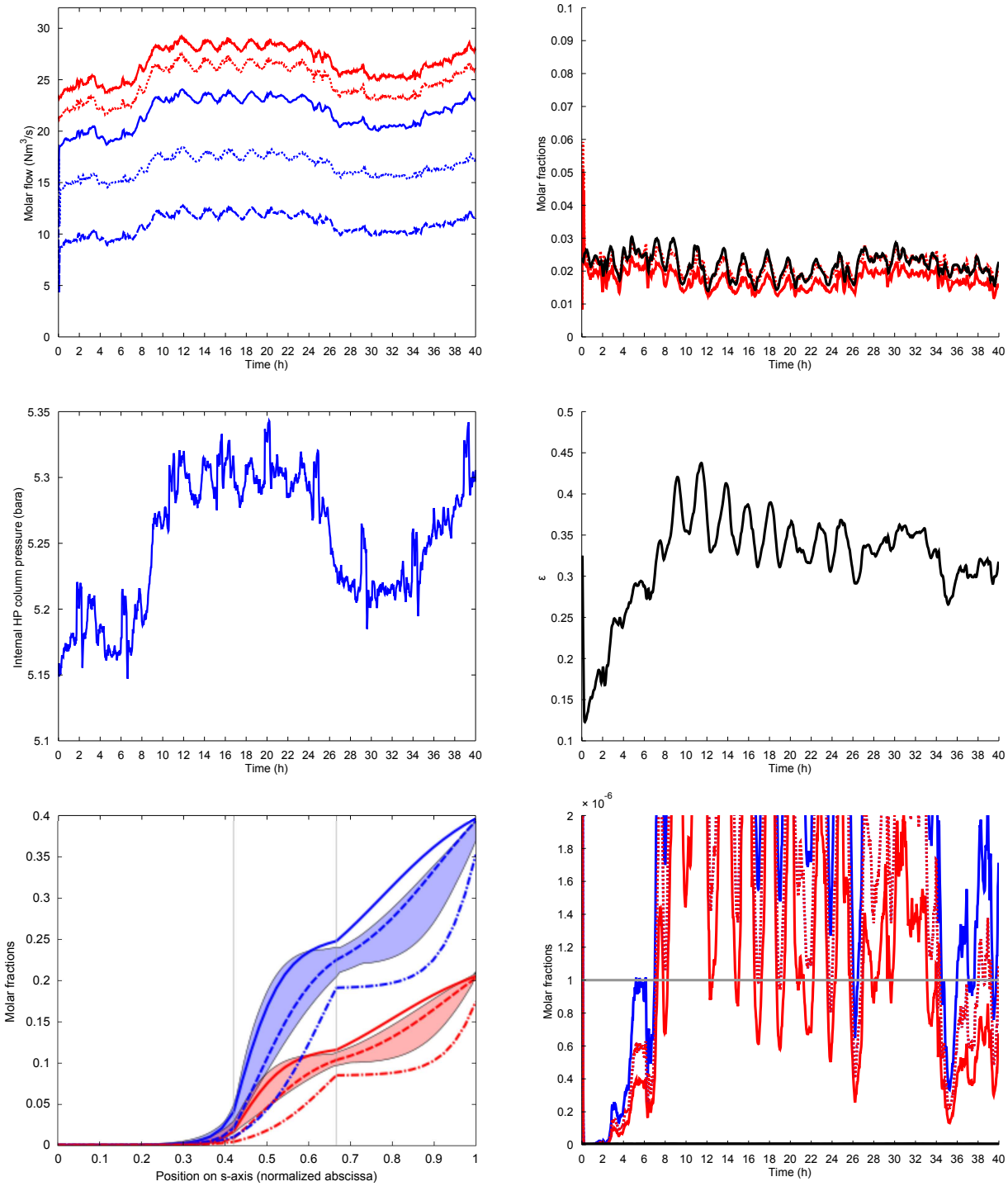

Figure C.10: Scenario n°10

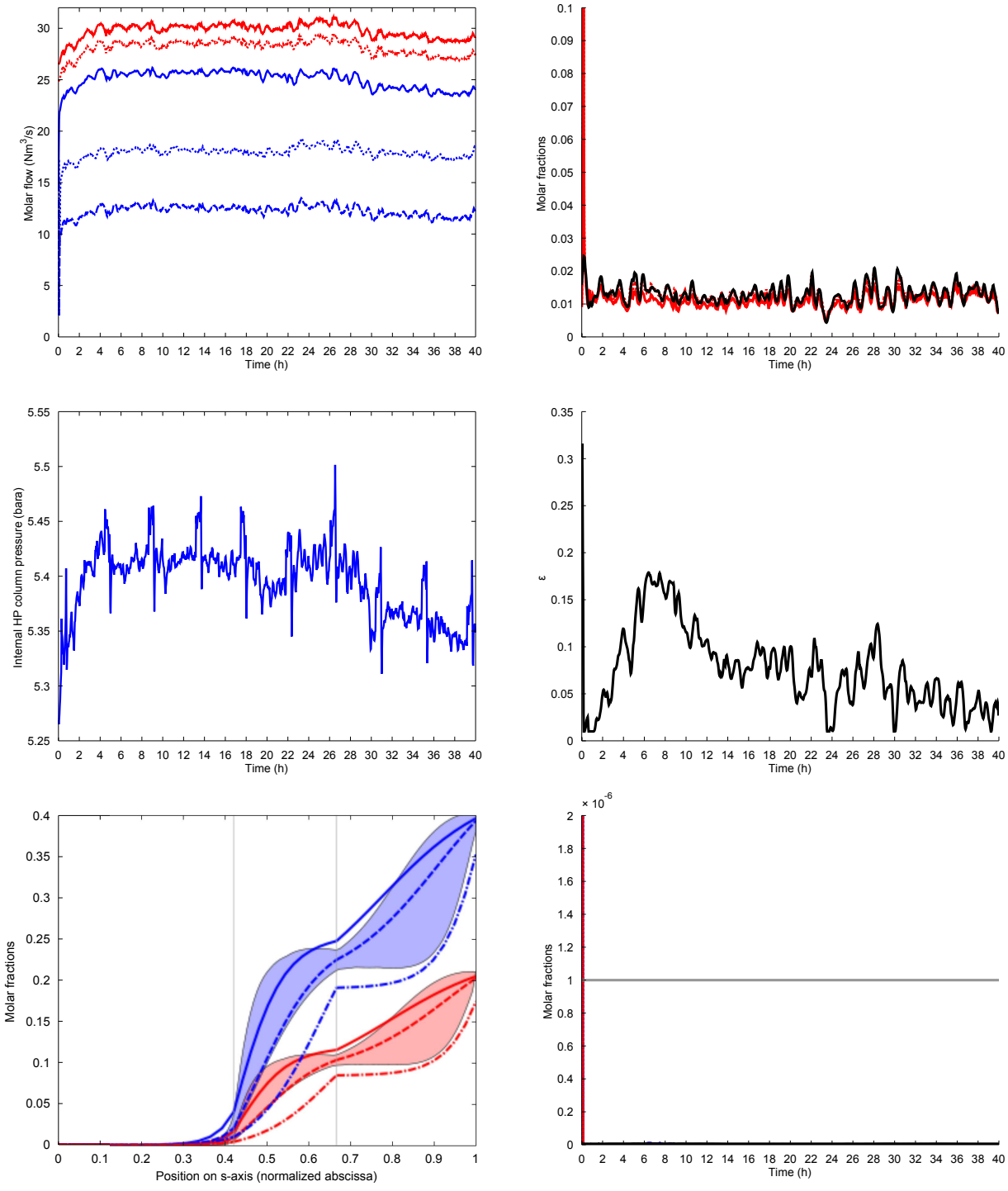

Figure C.11: Scenario n°11

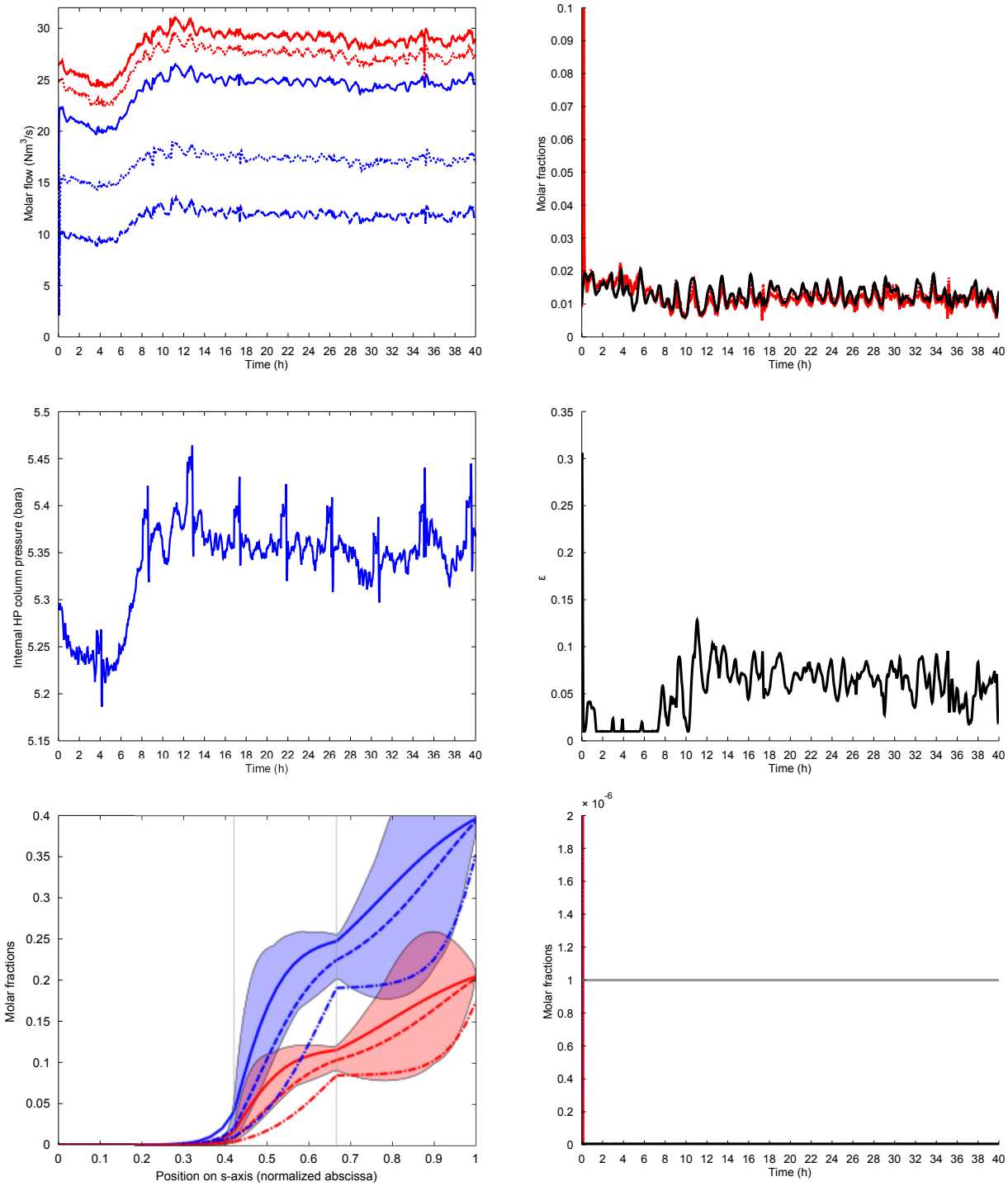

Figure C.12: Scenario n°12

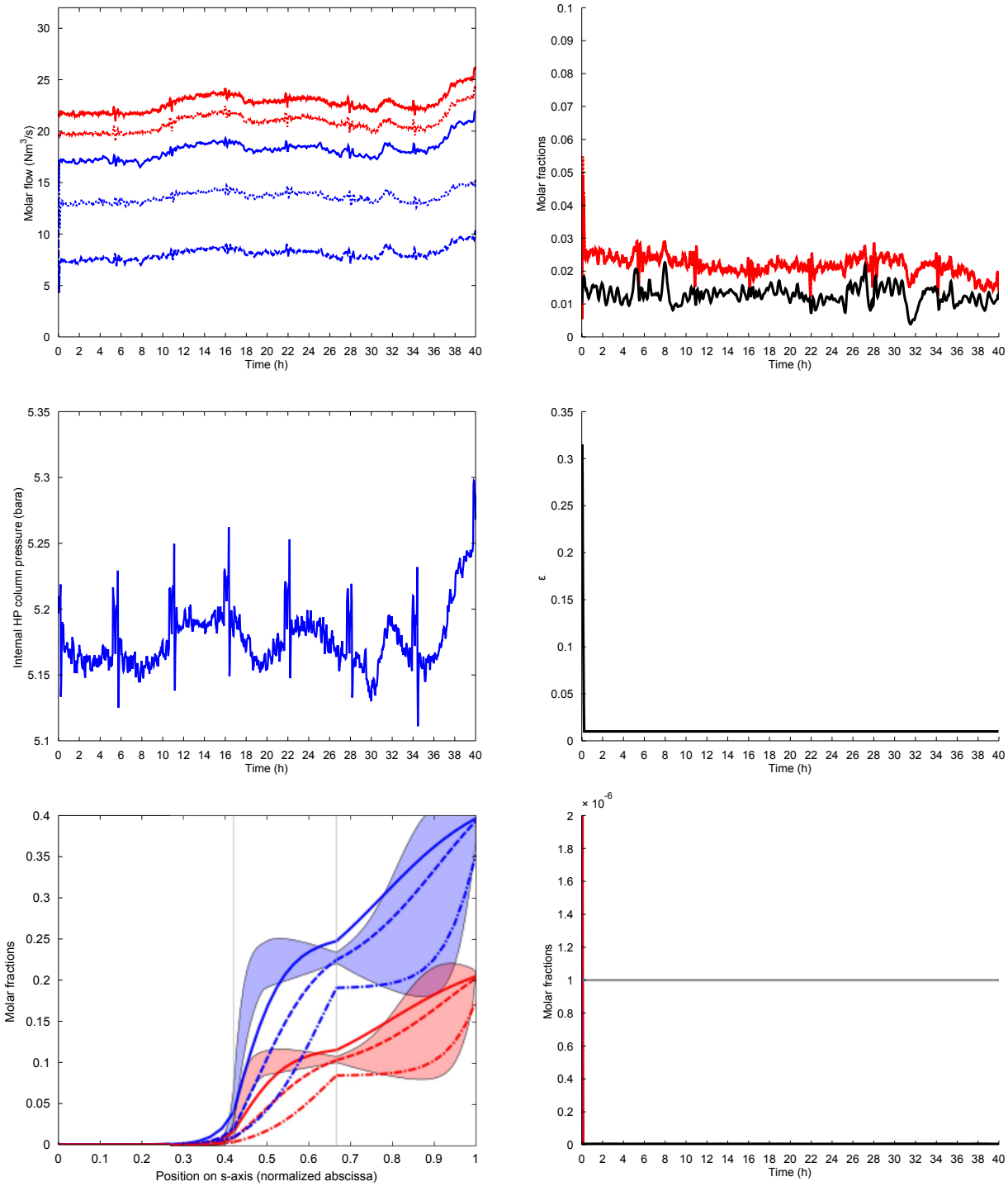

Figure C.13: Scenario n°13

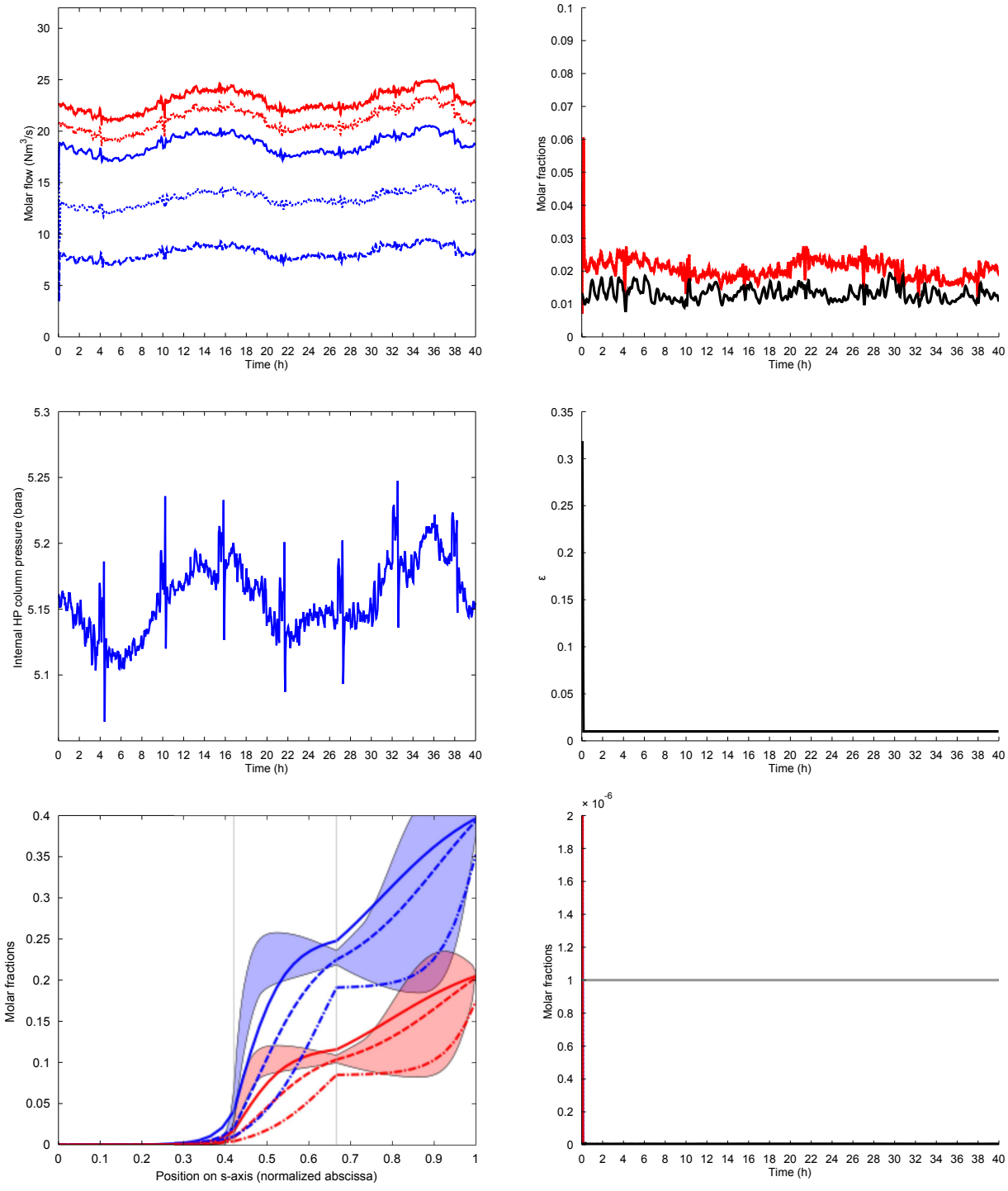

Figure C.14: Scenario n°14

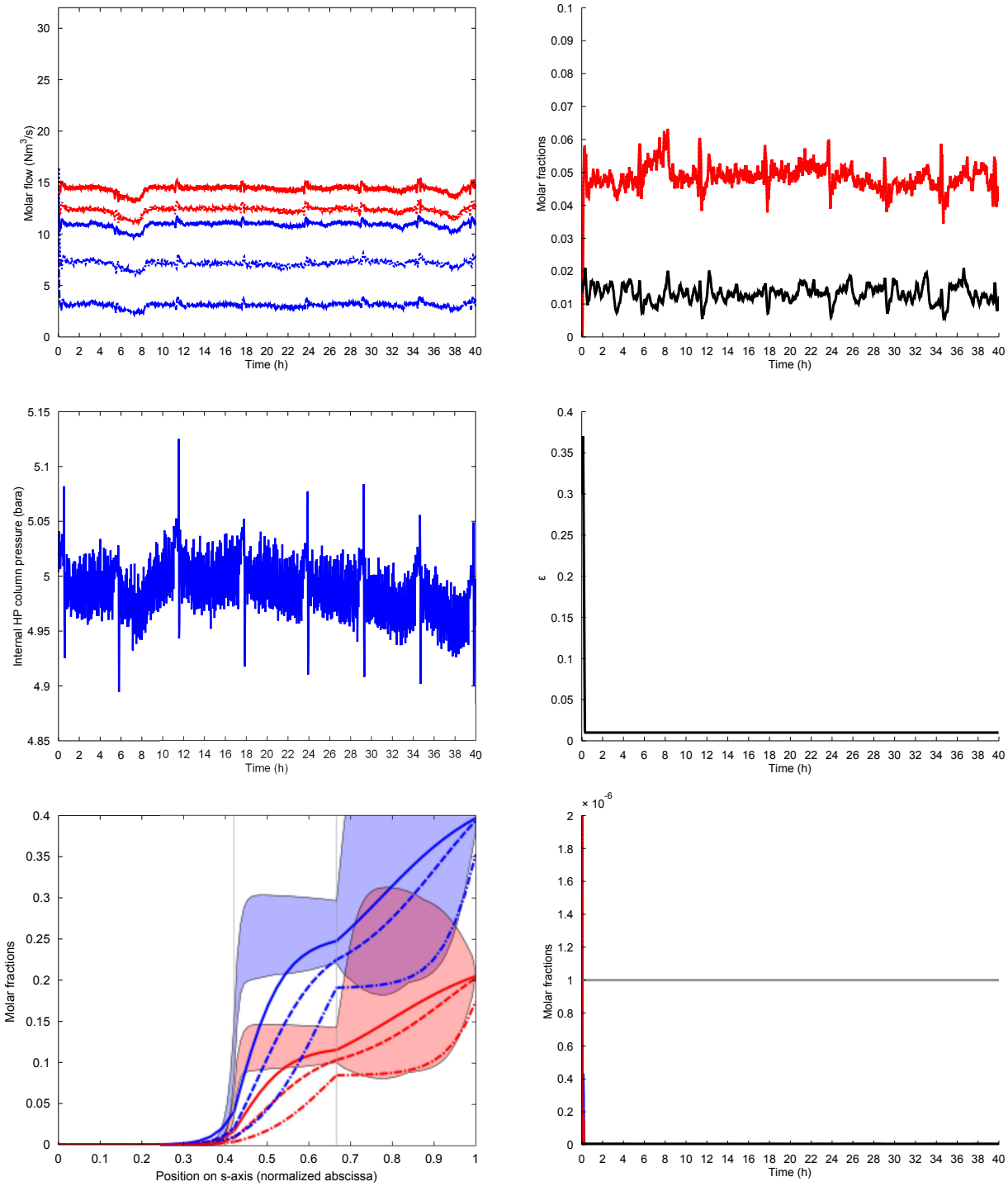

Figure C.15: Scenario n°15

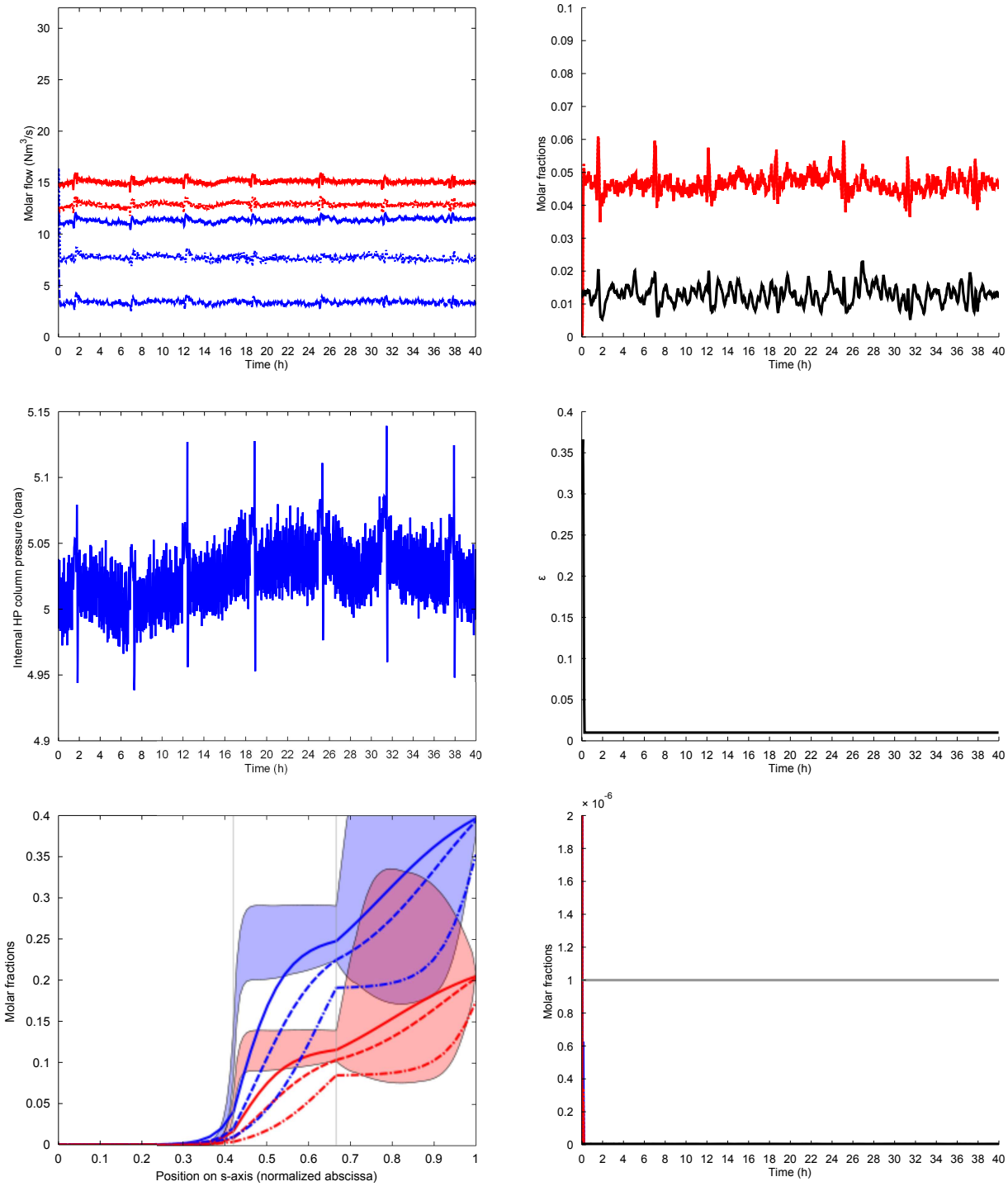

Figure C.16: Scenario n°16

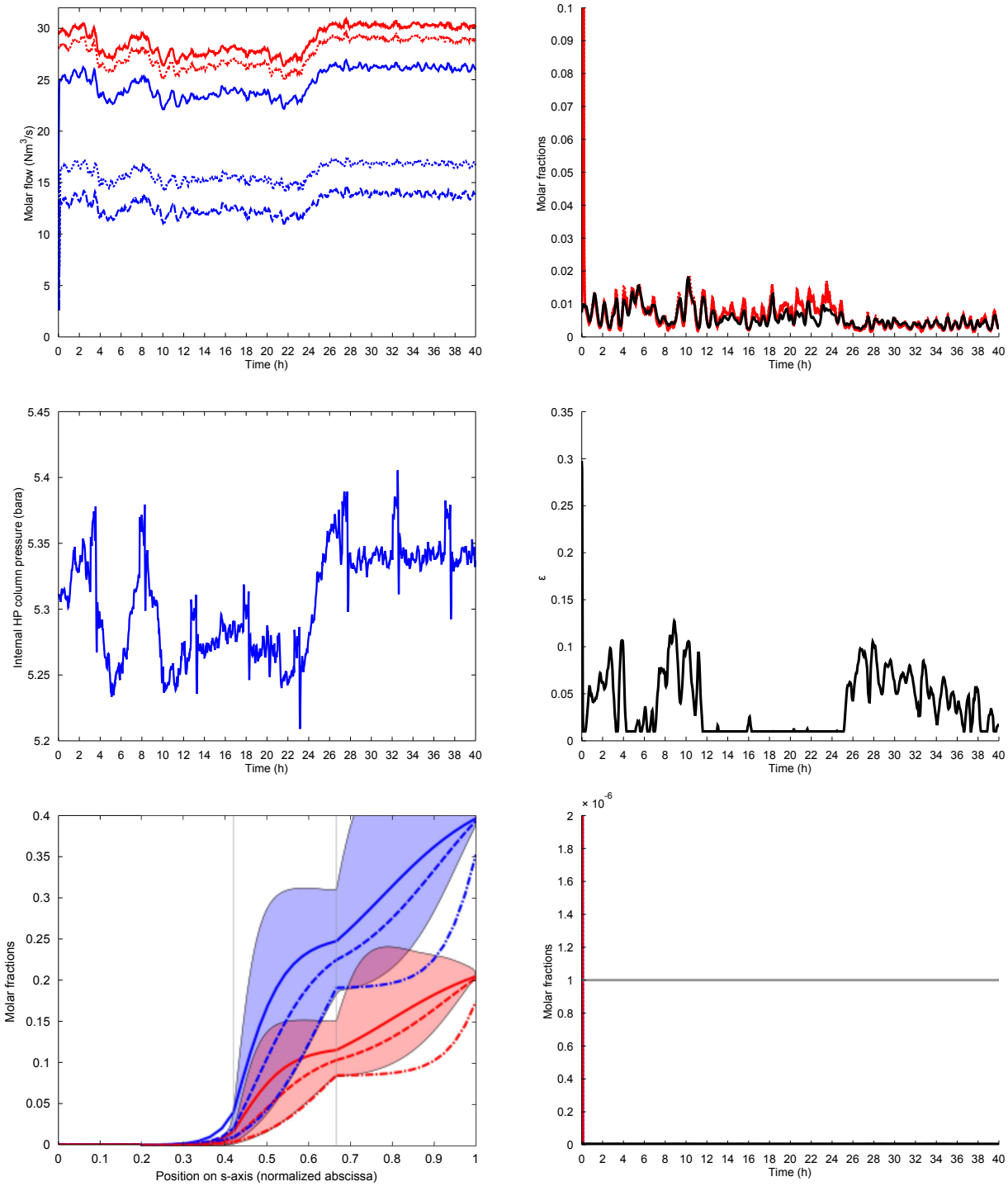

Figure C.17: Scenario n°17

Appendix D

LP column additional static simulations

This appendix contains additional static simulations results which have been taken out from Chapter 5 for the sake of brevity. These results regard static HYSYS simulation cases B and C, and sensitivity analysis of the steady-state solutions given by the PDE model.

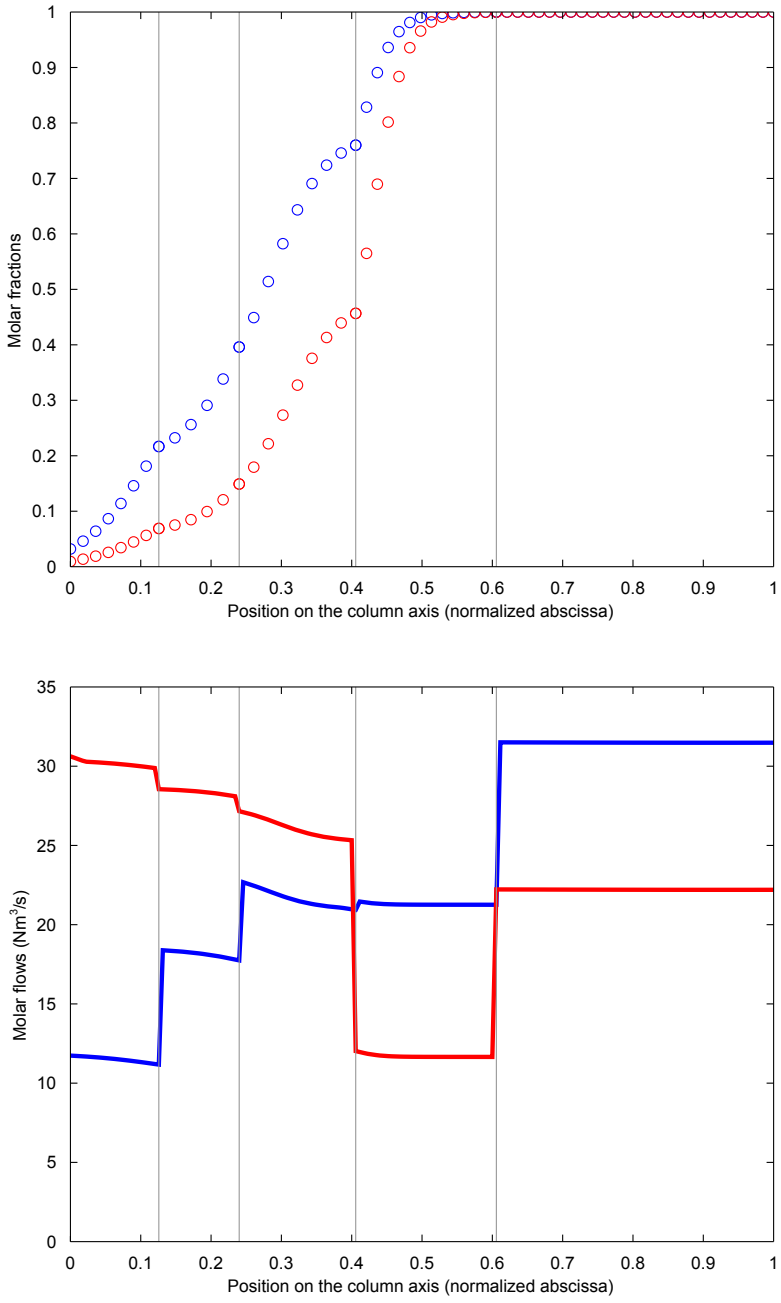

Figure D.1: *Top:* HYSYS estimations of the liquid (blue) and gas (red) composition profiles in case B. *Bottom:* internal liquid (blue) and gas (red) flows in case B. Confer Fig. 5.1.

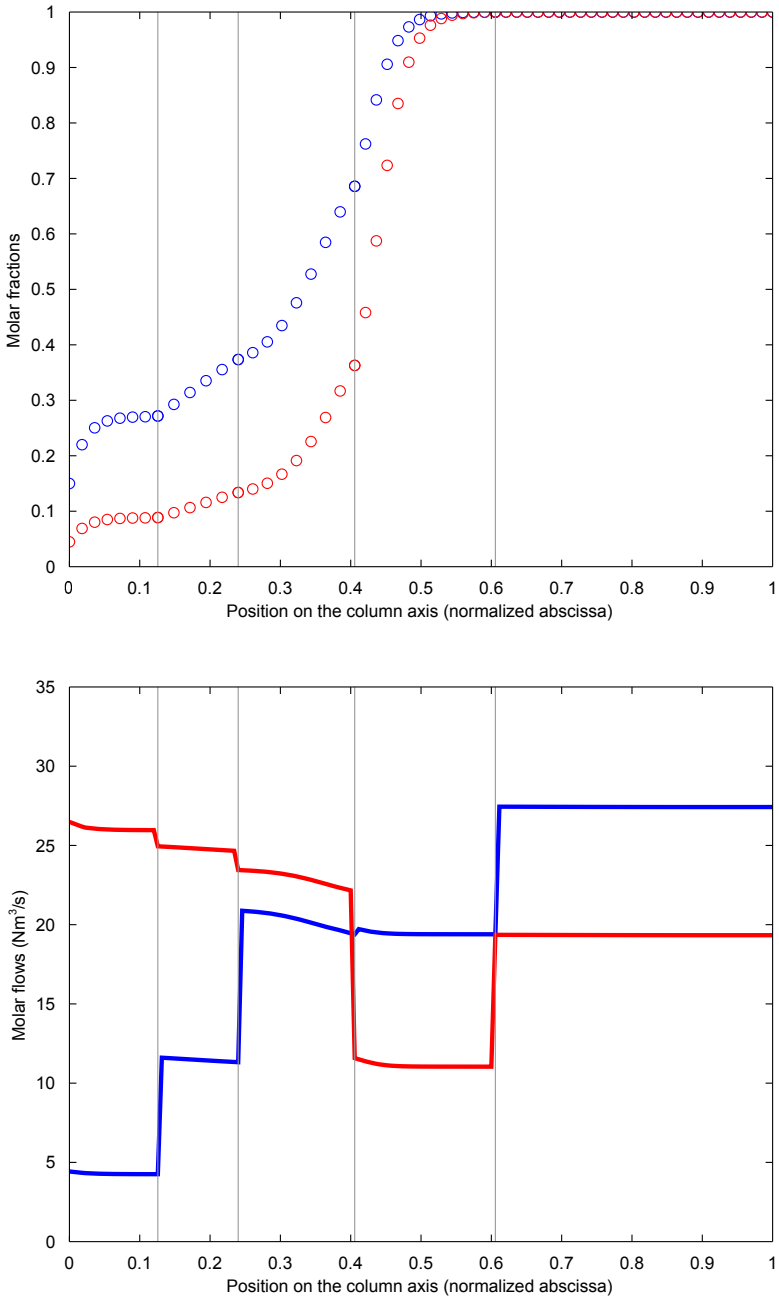

Figure D.2: *Top:* HYSYS estimations of the liquid (blue) and gas (red) composition profiles in case C. *Bottom:* internal liquid (blue) and gas (red) flows in case C. Confer Fig. 5.1.

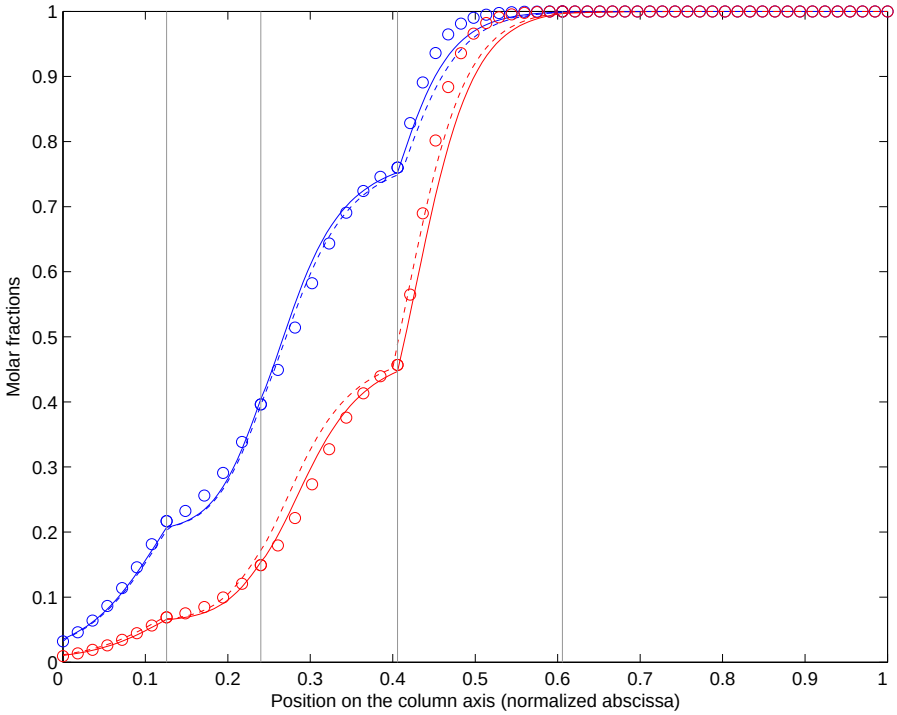

Figure D.3: Comparison of the HYSYS and the pseudobinary PDE model composition estimations in case B with a s-varying relative volatility. *Blue circles:* HYSYS estimation in liquid. *Red circles:* HYSYS composition estimation in gas. *Blue solid line:* PDE model lumped composition X. *Red solid line:* $k(X)$. *Blue dotted line:* PDE model estimated composition in liquid (static output x). *Red dotted line:* PDE model estimated composition in gas (static output y). Confer Fig. 5.2.

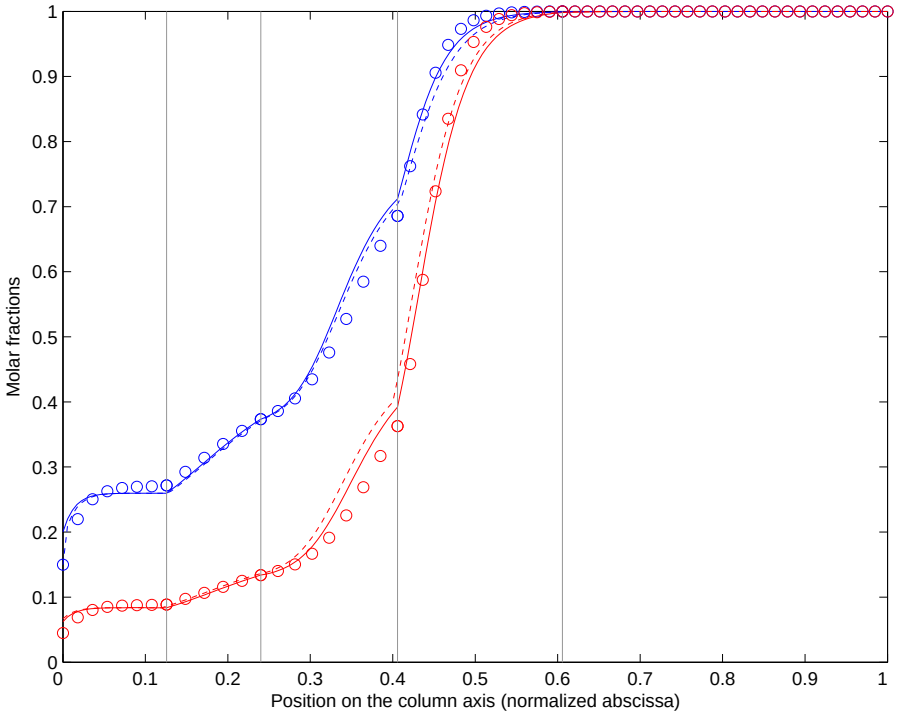

Figure D.4: Comparison of the HYSYS and the pseudobinary PDE model composition estimations in case C with a s-varying relative volatility. *Blue circles:* HYSYS estimation in liquid. *Red circles:* HYSYS composition estimation in gas. *Blue solid line:* PDE model lumped composition X. *Red solid line:* $k(X)$. *Blue dotted line:* PDE model estimated composition in liquid (static output x). *Red dotted line:* PDE model estimated composition in gas (static output y). Confer Fig. 5.2.

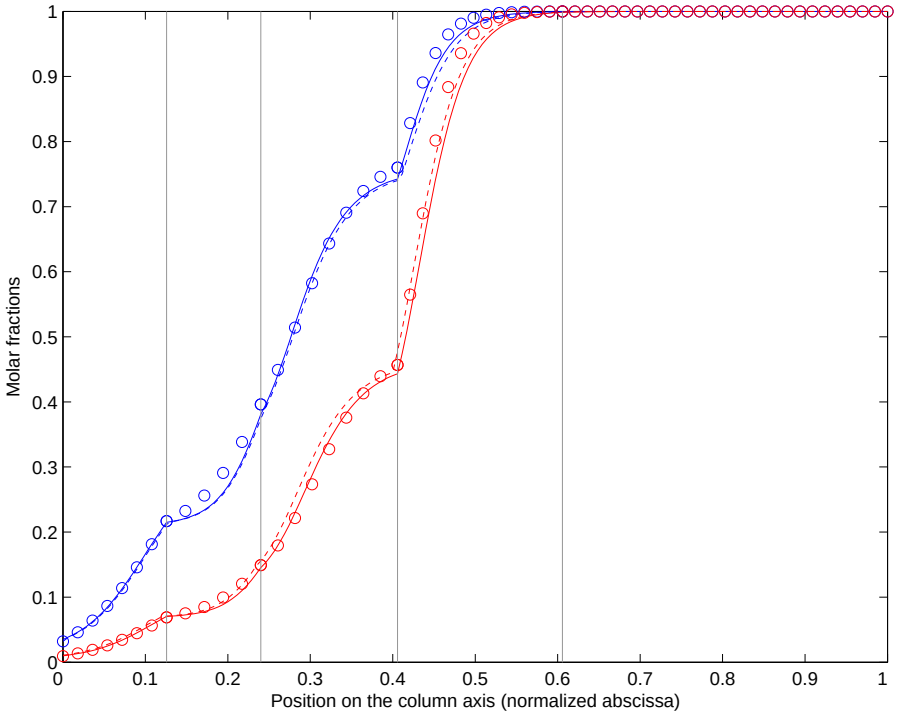

Figure D.5: Comparison of the HYSYS and the pseudobinary PDE model composition estimations in case B with a constant relative volatility. *Blue circles:* HYSYS estimation in liquid. *Red circles:* HYSYS composition estimation in gas. *Blue solid line:* PDE model lumped composition X. *Red solid line:* $k(X)$. *Blue dotted line:* PDE model estimated composition in liquid (static output x). *Red dotted line:* PDE model estimated composition in gas (static output y). Confer Fig. 5.4.

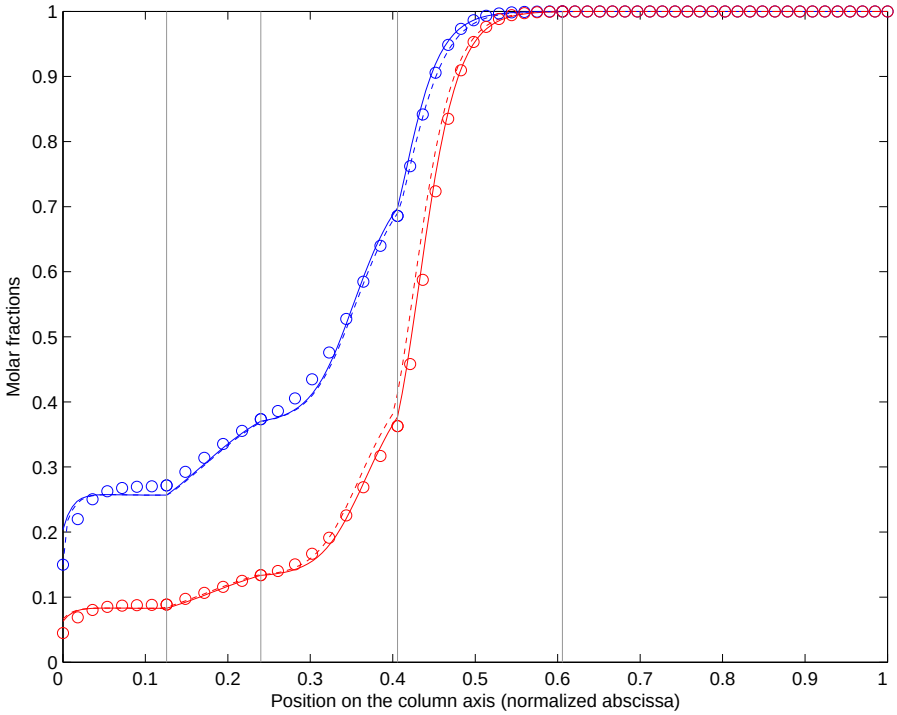

Figure D.6: Comparison of the HYSYS and the pseudobinary PDE model composition estimations in case C with a constant relative volatility. *Blue circles:* HYSYS estimation in liquid. *Red circles:* HYSYS composition estimation in gas. *Blue solid line:* PDE model lumped composition X. *Red solid line:* $k(X)$. *Blue dotted line:* PDE model estimated composition in liquid (static output x). *Red dotted line:* PDE model estimated composition in gas (static output y). Confer Fig. 5.4.

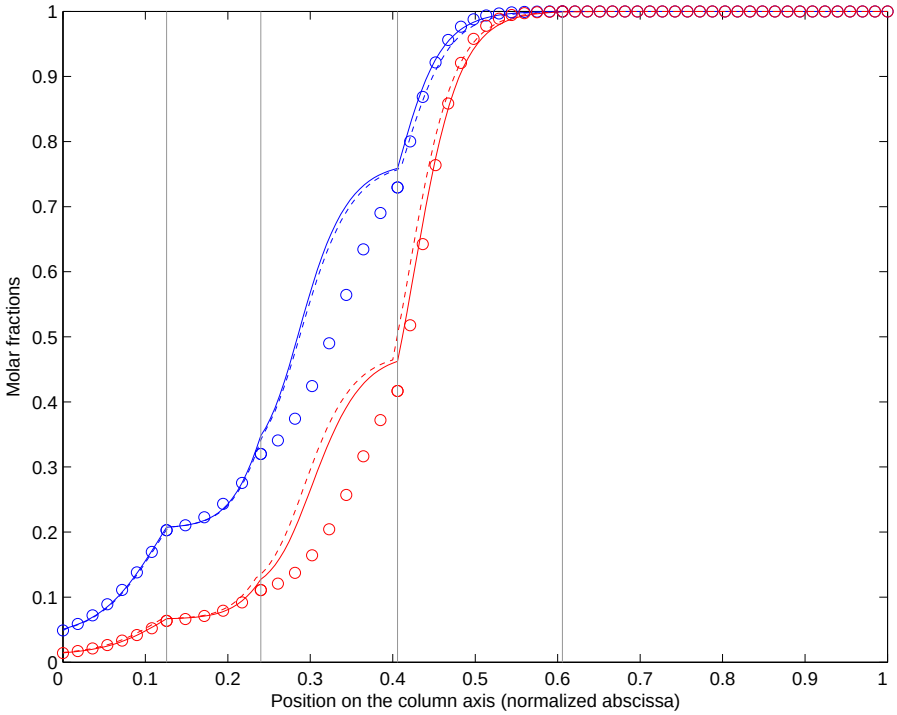

Figure D.7: Comparison of the HYSYS and the pseudobinary PDE model composition estimations in case A with -1% perturbation on the optimal value of α. *Blue circles:* HYSYS estimation in liquid. *Red circles:* HYSYS composition estimation in gas. *Blue solid line:* PDE model lumped composition X. *Red solid line:* $k(X)$. *Blue dotted line:* PDE model estimated composition in liquid (static output x). *Red dotted line:* PDE model estimated composition in gas (static output y). Confer Fig. 5.6.

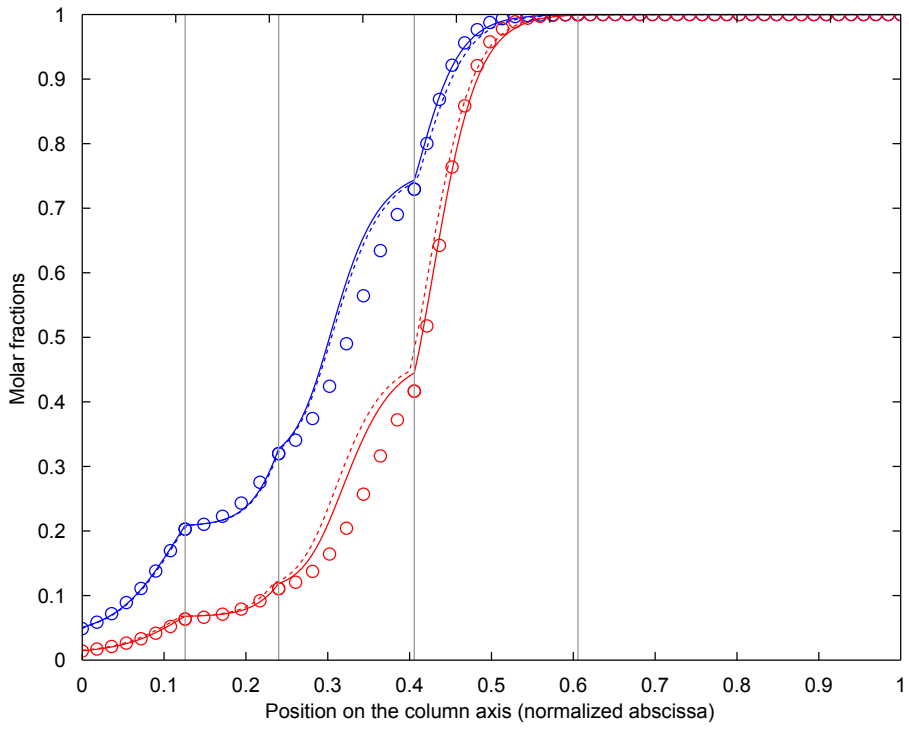

Figure D.8: Comparison of the HYSYS and the pseudobinary PDE model composition estimations in case A with -5% perturbation on the optimal value of ϵ. *Blue circles:* HYSYS estimation in liquid. *Red circles:* HYSYS composition estimation in gas. *Blue solid line:* PDE model lumped composition X. *Red solid line:* $k(X)$. *Blue dotted line:* PDE model estimated composition in liquid (static output x). *Red dotted line:* PDE model estimated composition in gas (static output y). Confer Fig. 5.7.

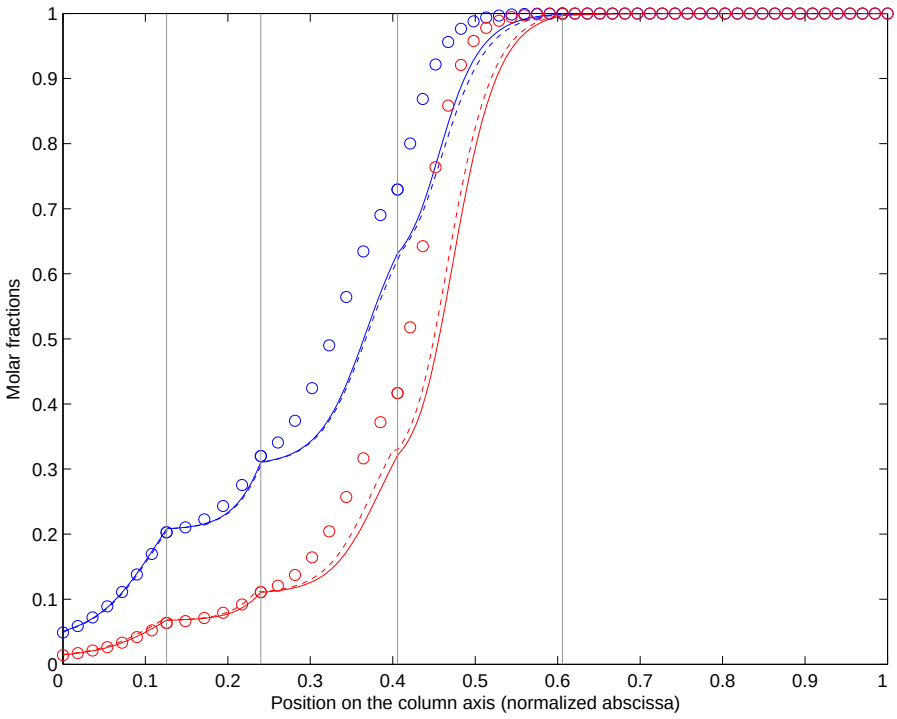

Figure D.9: Comparison of the HYSYS and the pseudobinary PDE model composition estimations in case A with -1% perturbation on the original gas/liquid molar ratio (0.181) in the feed between subsections 2 and 3 (feed from the V04 flashpot). Original molar fractions are 0.2454 in the liquid feed, 0.1631 in the gas feed. *Red circles:* HYSYS composition estimation in gas. *Blue solid line:* PDE model lumped composition X. *Red solid line:* $k(X)$. *Blue dotted line:* PDE model estimated composition in liquid (static output x). *Red dotted line:* PDE model estimated composition in gas (static output y). Confer Fig. 5.8.

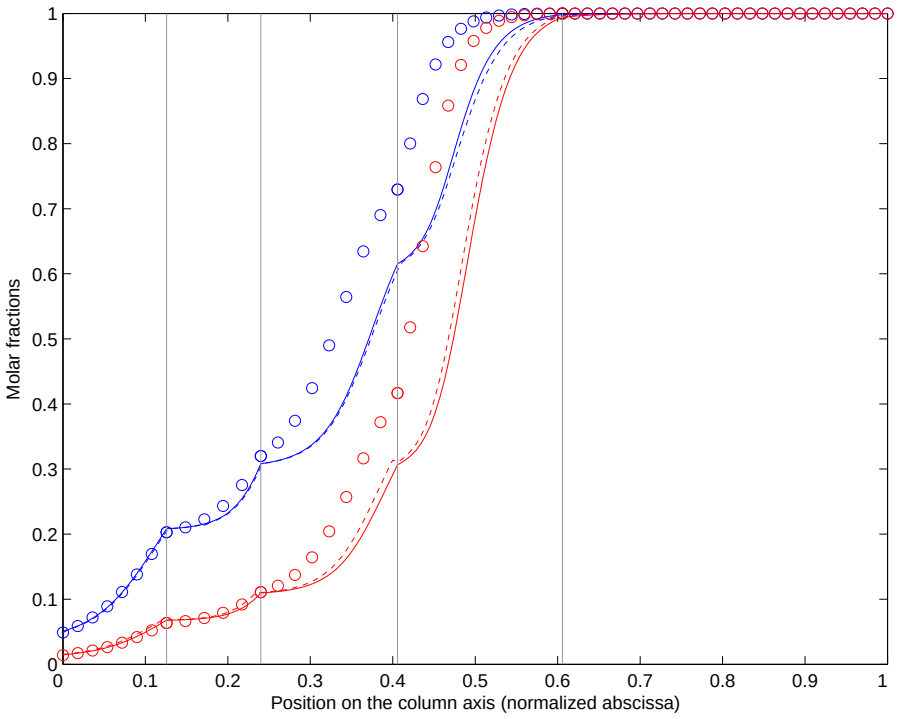

Figure D.10: Comparison of the HYSYS and the pseudobinary PDE model composition estimations in case A with -1% perturbation on the original $\{O_2,Ar\}$ pseudocomponent molar fraction in the feed between subsection 2 and 3 (feed from the V04 flashpot). *Blue circles:* HYSYS estimation in liquid. *Red circles:* HYSYS composition estimation in gas. *Blue solid line:* PDE model lumped composition X. *Red solid line:* $k(X)$. *Blue dotted line:* PDE model estimated composition in liquid (static output x). *Red dotted line:* PDE model estimated composition in gas (static output y). Confer Fig. 5.9.

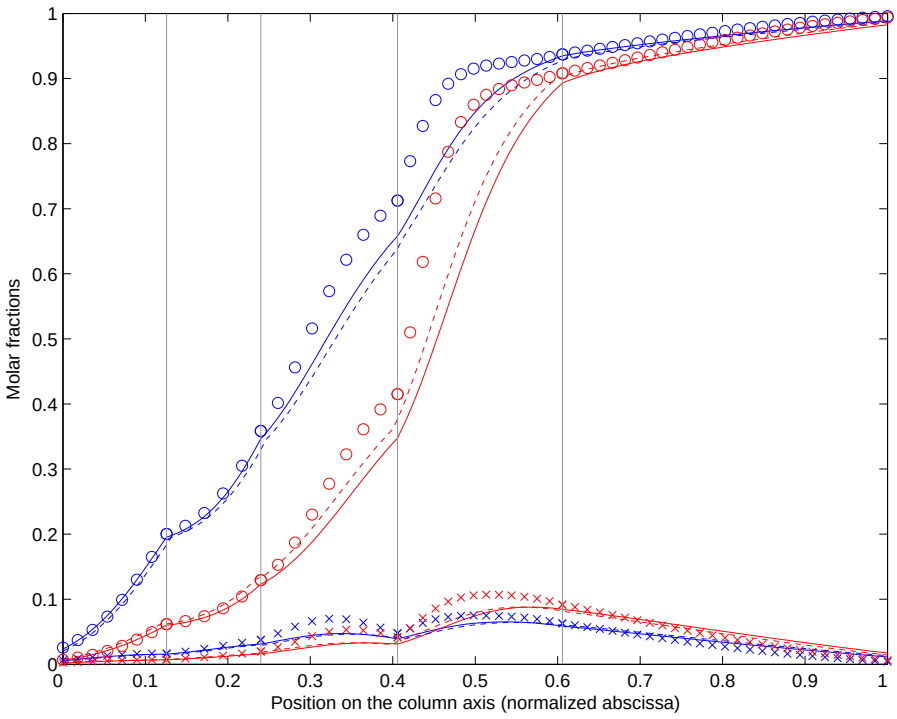

Figure D.11: Comparison of the HYSYS and the pseudobinary PDE model composition estimations in case B with the s-dependent relative volatilities estimated using HYSYS . The monotone profiles corresponds to oxygen, the belly-shaped ones to argon. *Blue circles:* HYSYS estimation in liquid. *Red circles:* HYSYS composition estimation in gas. *Blue solid line:* PDE model lumped composition X. *Red solid line:* $k(X)$. *Blue dotted line:* PDE model estimated composition in liquid (static output x). *Red dotted line:* PDE model estimated composition in gas (static output y). Confer Fig. 5.10.

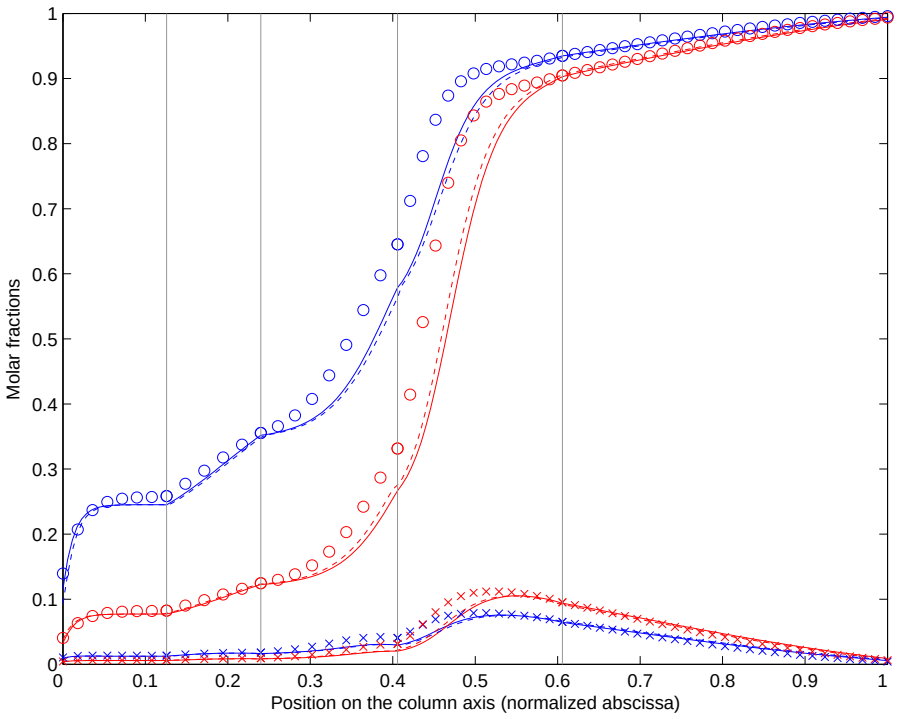

Figure D.12: Comparison of the HYSYS and the pseudobinary PDE model composition estimations in case C with the s-dependent relative volatilities estimated using HYSYS . The monotone profiles corresponds to oxygen, the belly-shaped ones to argon. *Blue circles:* HYSYS estimation in liquid. *Red circles:* HYSYS composition estimation in gas. *Blue solid line:* PDE model lumped composition X. *Red solid line:* $k(X)$. *Blue dotted line:* PDE model estimated composition in liquid (static output x). *Red dotted line:* PDE model estimated composition in gas (static output y). Confer Fig. 5.10.

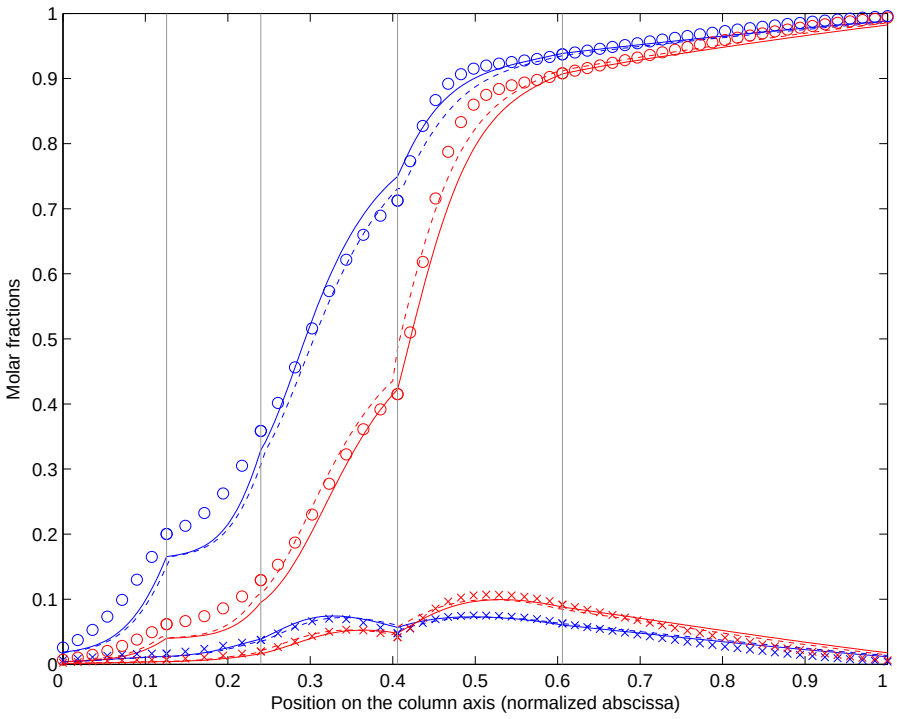

Figure D.13: Comparison of the HYSYS and the pseudobinary PDE model composition estimations in case B with the s-dependent relative volatilities estimated using HYSYS times a multiplicative factor $m = 0.8$. The monotone profiles corresponds to oxygen, the belly-shaped ones to argon. *Blue circles:* HYSYS estimation in liquid. *Red circles:* HYSYS composition estimation in gas. *Blue solid line:* PDE model lumped composition X. *Red solid line:* $k(X)$. *Blue dotted line:* PDE model estimated composition in liquid (static output x). *Red dotted line:* PDE model estimated composition in gas (static output y). Confer Fig. 5.11.

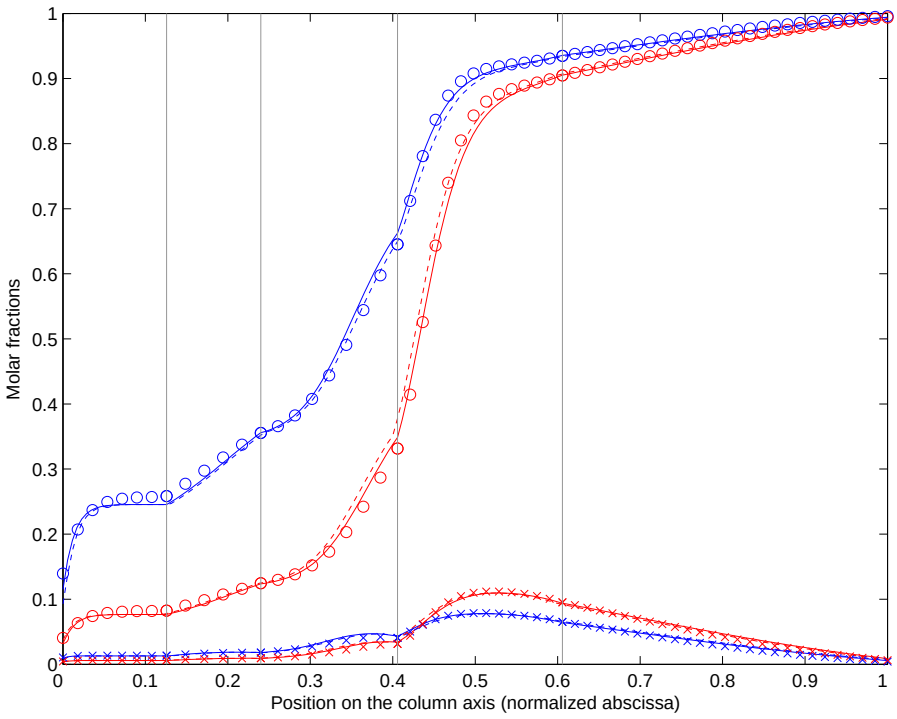

Figure D.14: Comparison of the HYSYS and the pseudobinary PDE model composition estimations in case C with the s-dependent relative volatilities estimated using HYSYS times a multiplicative factor $m = 0.99$. The monotone profiles corresponds to oxygen, the belly-shaped ones to argon. *Blue circles:* HYSYS estimation in liquid. *Red circles:* HYSYS composition estimation in gas. *Blue solid line:* PDE model lumped composition X. *Red solid line:* $k(X)$. *Blue dotted line:* PDE model estimated composition in liquid (static output x). *Red dotted line:* PDE model estimated composition in gas (static output y). Confer Fig. 5.11.

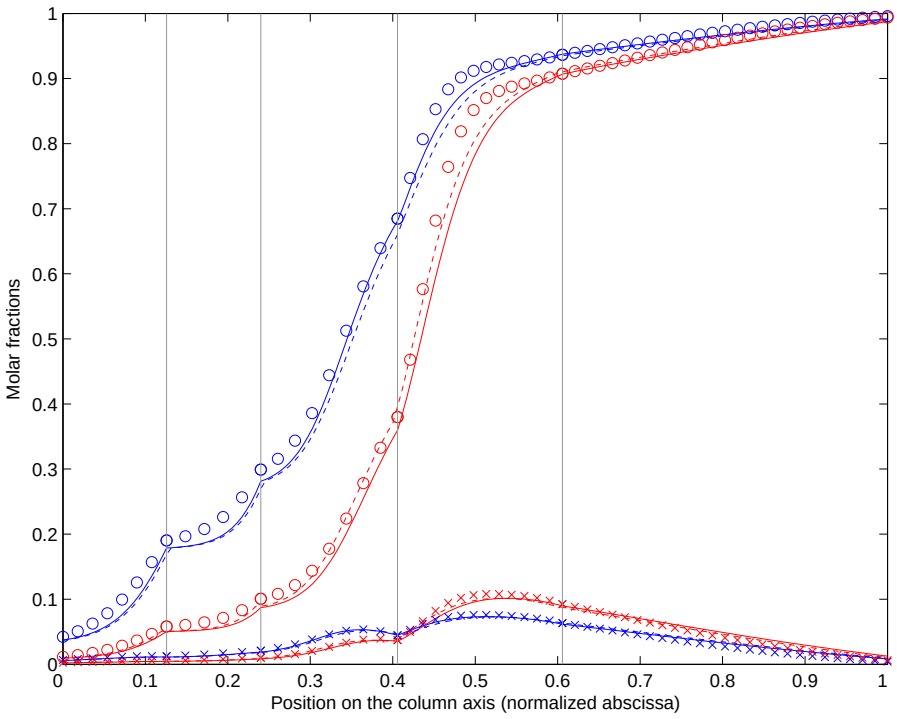

Figure D.15: Comparison of the HYSYS and the pseudobinary PDE model composition estimations in case A with -1% perturbation on the original gas/liquid molar ratio (0.181) in the feed between subsections 2 and 3 (feed from the V04 flashpot). *Blue circles:* HYSYS estimation in liquid. *Red circles:* HYSYS composition estimation in gas. *Blue solid line:* PDE model lumped composition X. *Red solid line:* $k(X)$. *Blue dotted line:* PDE model estimated composition in liquid (static output x). *Red dotted line:* PDE model estimated composition in gas (static output y). Confer Fig. 5.12.

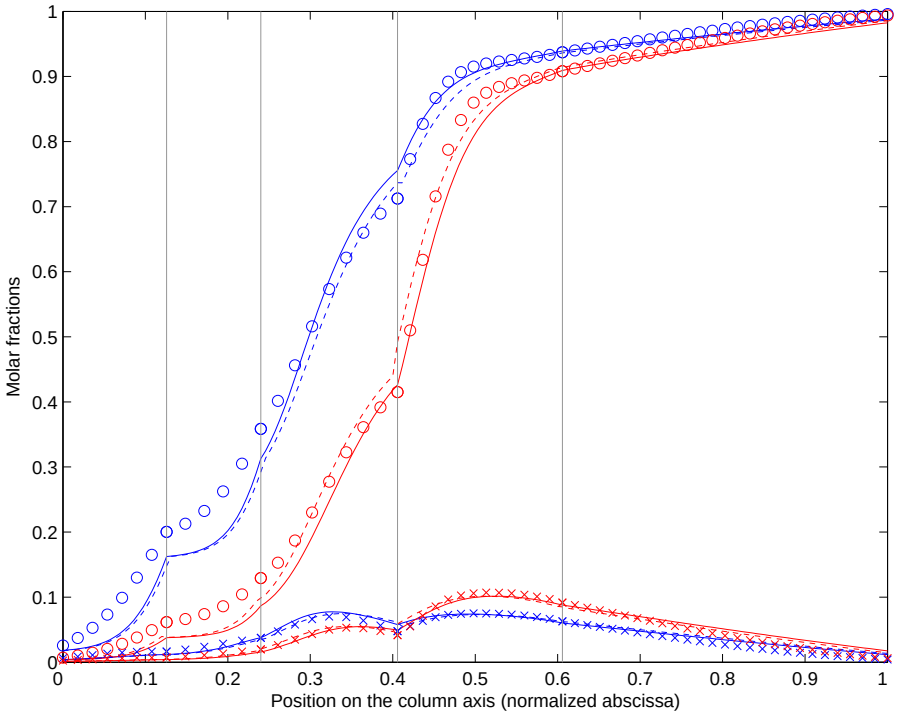

Figure D.16: Comparison of the HYSYS and the pseudobinary PDE model composition estimations in case B with constant α_{O_2} and α_{Ar}. The monotone profiles corresponds to oxygen, the belly-shaped ones to argon. *Blue circles:* HYSYS estimation in liquid. *Red circles:* HYSYS composition estimation in gas. *Blue solid line:* PDE model lumped composition X. *Red solid line:* $k(X)$. *Blue dotted line:* PDE model estimated composition in liquid (static output x). *Red dotted line:* PDE model estimated composition in gas (static output y). Confer Fig. 5.13.

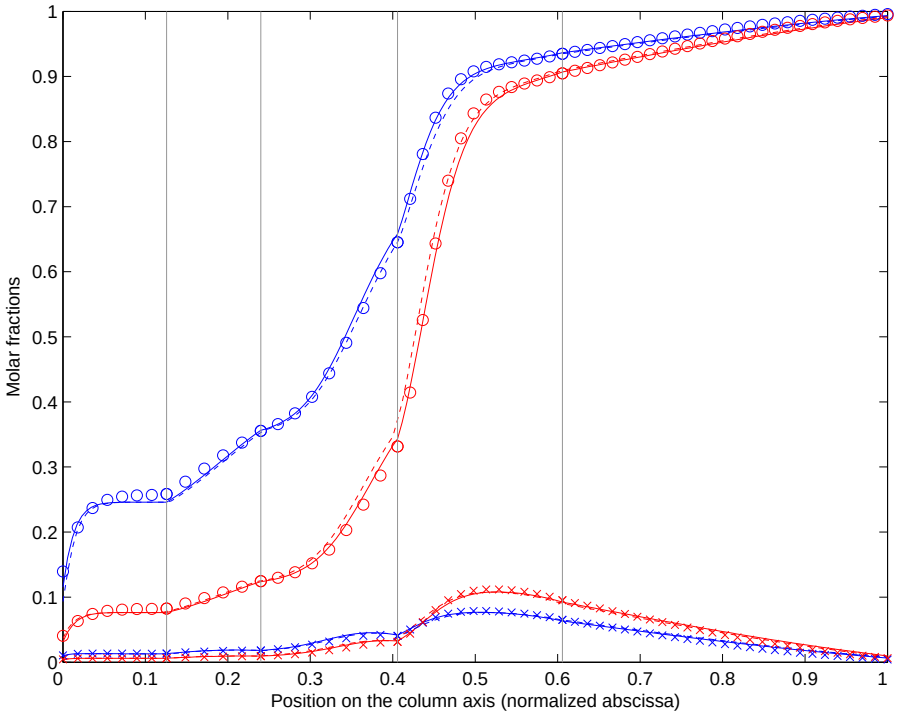

Figure D.17: Comparison of the HYSYS and the pseudobinary PDE model composition estimations in case C with constant α_{O_2} and α_{Ar}. The monotone profiles corresponds to oxygen, the belly-shaped ones to argon. *Blue circles:* HYSYS estimation in liquid. *Red circles:* HYSYS composition estimation in gas. *Blue solid line:* PDE model lumped composition X. *Red solid line:* $k(X)$. *Blue dotted line:* PDE model estimated composition in liquid (static output x). *Red dotted line:* PDE model estimated composition in gas (static output y). Confer Fig. 5.13.

Appendix E

Performances of the numerical schemes

E.1 Finite-differences scheme

The choice of a finite-differences approach, both in time and space, for the numerical simulation of the columns dynamics, is mainly for the sake of the model development convenience, rather than for computational performances. The models discretization issue is out of the primary scope of this work, and the finite-differences schemes allow agile implementation of the successive versions of our models. In addition, we have seen that turning the classical finite-differences scheme into a partially implicit scheme allows ensuring the positiveness of the results in some cases.

However, more advanced numerical techniques are certainly worth being considered. Since the distillation model comes down to conservation equations (and all the more that the scheme conservativeness is essential at high-purity), devoted methods such as Finite Elements Method (FEM) or Finite Volumes Method (FVM) are natural candidates for the numerical approximation in space (finite-difference still being used for the time domain). Note thought that, the problem being 1-D in space, FEM and FVM capability of handling complex domain geometries and meshes would not be used.

Regarding the time domain, the numerical scheme could advantageously benefit from the time-scale separation in the model. For instance, diffusion dynamics along the column being slower than convection, one could envisage to split the convection-diffusion operator in the numerical scheme. The numerical solution update from time T to time $T + \Delta t$ would then consist in convecting the initial data during $\frac{\Delta t}{2}$, then applying the diffusion once and for all (i.e. for the whole Δt), and eventually completing the convection for the remaining $\frac{\Delta t}{2}$, in the manner of [69]. A positive side-effect is that the diffusion operator, from which part of the numerical complexity arises for ternary mixtures, would have to be less frequently updated than the simple convection term.

E.2 Performances regarding the simulation of the binary HP column

Using the proposed numerical scheme to simulate the distillation dynamics of a binary mixture in the HP column requires about 10s of computation for 1h of the system time (hardware and software are described in E.4). Reduction of this computation time could be achieved in various manners, amongst which: better handling of arguments and results passing between invoked scripts and functions, specific algorithm for solving the main tridiagonal system (such as TDMA algorithm), more parsimonious writing and reading of the distributed parameters vectors (some of which are partially rewritten during instantiation)...

E.3 Performances regarding the simulation of the ternary HP and LP columns

Using the proposed numerical scheme to simulate the distillation dynamics of a ternary mixture in the coupled HP and LP columns requires about 100s of computation for 1h of the system time (hardware and software are described in E.4). This makes the numerical model as is hardly suitable for real-time control or optimization purposes, if they are to require iterative simulation during the same time step.

Apart from the fact that two columns are now simulated, this increase of the computation time can be explained notably by the fact that, to keep composition estimations between 0 and 1 (especially in the LP column), the distillation dynamics are now computed twice: once with N_2 as the unexpressed component, and once with O_2 as the unexpressed component, as said in subsection 4.2.5. In addition to the coding improvement proposed for the HP column, the second approach proposed in the latter should quicken computation.

E.4 Hardware and software

Simulation software: ..... MATLAB R2007a
Operating System: ..... Microsoft Windows XP SP3
Computer: ..... Dell Latitude E6500
CPU: ..... Intel Core2 Duo CPU (only one core is used)
CPU frequency: ..... 3.06 GHz
RAM: ..... 3.48 Go

Bibliography

[1] *ASU Operating Handbook*, volume 2. Air Liquide internal document, 2005.

[2] *ASU Operating Handbook*, volume 3. Air Liquide internal document, 2005.

[3] M. A. Abdelghani-Idrissi, F. Bagui, and L. Estel. Analytical and experimental response time to flow rate step along a counter flow double pipe heat exchanger. *International Journal of Heat and Mass Transfer*, 44(19):3721–3730, 2001.

[4] V.I. Arnold and D. Embarek. *Chapitres supplémentaires de la théorie des équations différentielles ordinaires*. Mir Moscow, 1990.

[5] David Averous. *Modélisation et simulation des échangeurs de chaleur multifluides à plaques brasées en configurations complexes*. PhD thesis, E.N.S.I.G.C. Toulouse, 2000.

[6] F. Bagui, M.A. Abdelghani-Idrissi, and H. Chafouk. Heat exchanger kalman filtering with process dynamic aknowledgment. *Computers and Chemical Engineering*, 28:1465–1473, 2004.

[7] S. Bian and M. A. Henson. Measurement selection for on-line estimation of nonlinear wave models for high purity distillation columns. *Chemical Engineering Science*, 61(10):3210–3222, 2006.

[8] S. Bian, M. A. Henson, P. Belanger, and L. Megan. Nonlinear state estimation and model predictive control of nitrogen purification columns. *Industrial and Engineering Chemistry Research*, 44(1):153–167, 2005.

[9] S. Bian, S. Khowinij, M. A. Henson, P. Belanger, and L. Megan. Compartmental modeling of high purity air separation columns. *Computers and Chemical Engineering*, 29(10):2096–2109, 2005.

[10] P. P. Biswas, S. Ray, and A. N. Samanta. Multi-objective constraint optimizing IOL control of distillation column with nonlinear observer. *Journal of Process Control*, 17(1):73–81, 2007.

[11] P. P. Biswas, S. Ray, and A. N. Samanta. Nonlinear control of high purity distillation column under input saturation and parametric uncertainty. *Journal of Process Control*, 19(1):75–84, 2009.

[12] R. Boehme, J. A. R. Parise, and R. Pitanga Marques. Simulation of multistream plate-fin heat exchangers of an air separation unit. *Cryogenics*, 43(6):325–334, 2003.

[13] J. Bonilla, F Logist, J. Degrève, B. De Moor, and J. Van Impe. A reduced order rate based model for distillation in packed columns: Dynamic simulation and the differentiation index problem. *Chemical Engineering Science*, 68:401–412, 2012.

[14] Julián Bonilla, Filip Logist, Bart De Moor, and Jan Van Impe. Parameter estimation of a rigorous rate base model for distillation in packed columns. *IFAC Proceedings Volumes*, 18(Part 1):465–470, 2011.

[15] U. Brinkmann, T. J. Schildhauer, and E. Y. Kenig. Hydrodynamic analogy approach for modelling of reactive stripping with structured catalyst supports. *Chemical Engineering Science*, 65(1):298–303, 2010.

[16] Yannan Cao. *Design for Dynamic Performance: Application to an Air Separation Unit*. PhD thesis, McMaster University, 2011.

[17] J. Carr. *Applications of Centre Manifold Theory*. Springer, 1981.

[18] Z. Chen, M. A. Henson, P. Belanger, and L. Megan. Nonlinear model predictive control of high purity distillation columns for cryogenic air separation. *IEEE Transactions on Control System Technology*, 18(4):811–821, July 2010.

[19] U. Christen, H. E. Musch, and M. Steiner. Robust control of distillation columns: μ-vs H_∞-synthesis. *Journal of Process Control*, 7(1):19–30, 1997.

[20] P. Dua, K. Kouramas, V. Dua, and E. N. Pistikopoulos. MPC on a chip - recent advances on the application of multi-parametric model-based control. *Computers and Chemical Engineering*, 32(4-5):754–765, 2008.

[21] S. Dudret. Models for dynamic control of APSA nitrogen generators. Technical report, Air Liquide R&D, 2009.

[22] S. Dudret, K. Beauchard, F. Ammouri, and P. Rouchon. Stability and asymptotic observers of binary distillation processes described by nonlinear convection/diffusion models. In *American Control Conference (ACC)*, 2012.

[23] N. Egoshi, H. Kawakami, and K. Asano. Heat and mass transfer model approach to optimum design of cryogenic air separation plant by packed columns with structured packings. *Separation and Purification Technology*, 29(2):141–151, November 2002.

[24] H. K. Engelien, T. Larsson, and S. Skogestad. Implementation of optimal operation for heat integrated distillation columns. *Chemical Engineering Research and Design*, 81(2):277–281, 2003.

[25] J. A. Fabro, L. V. R. Arruda, and F. Neves Jr. Startup of a distillation column using intelligent control techniques. *Computers and Chemical Engineering*, 30(2):309–320, 2005.

[26] Neil Fenichel. Persistence and smoothness of invariant manifolds for flows. *Indiana University Mathematics Journal*, 1971:193–226, 1971.

[27] Neil Fenichel. Geometric singular perturbation theory for ordinary differential equations. *Journal of Differential Equations*, 31:53–98, 1977.

[28] M. Fourati, V. Roig, and L. Raynal. Experimental study of liquid spreading in structured packing. *Chemical Engineering Science*, 80:1–15, 2012.

[29] K. O. Friedrichs. *Fluid Dynamics*, chapter 4, Theory of Viscous Fluids. Brown University, 1942.

[30] D. M. Grobman. Homeomorphisms of systems of differential equations. *Dokl. Akad. Nauk SSSR*, 128:880–881, 1959.

[31] F. Gross, E. Baumann, A. Geser, D. W. T. Rippin, and L. Lang. Modelling, simulation and controllability analysis of an industrial heat-integrated distillation process. *Computers and Chemical Engineering*, 22(1-2):223–237, 1998.

[32] S. Grüner and A. Kienle. Equilibrium theory and nonlinear waves for reactive distillation columns and chromatographic reactors. *Chemical Engineering Science*, 59(4):901–918, 2004.

[33] S. Gupta, S. Ray, and A. N. Samanta. Nonlinear control of debutanizer column using profile position observer. *Computers and Chemical Engineering*, 33(6):1202–1211, 2009.

[34] Jurgen Hahn and Carl Laird. Process Science & Technology Center pooled fund proposal 2010.

[35] Marian Hamdar, Maroun Nemer, and Denis Clodic. Modélisation de système de distribution de fluides, recherche d'une solution analytique. Technical report, ARMINES, Mai 2006.

[36] N. P. Hankins. A non-linear wave model with variable molar flows for dynamic behaviour and disturbance propagation in distillation columns. *Chemical Engineering Research and Design*, 85(1 A):65–73, 2007.

[37] N. P. Hankins and F. G. Helfferich. On the concept and application of 'partial coherence' in non-linear wave propagation. *Chemical Engineering Science*, 54(6):741–764, 1999.

[38] P. Hartman. A lemma in the theory of structural stability of differential equations. *Proceedings of the American Mathematical Society*, 11:610–620, 1960.

[39] P. Hartman. On local homeomorphisms of euclidian spaces. *Boletin Sociedad Matemática Mexicana*, 5:220–241, 1960.

[40] Tore Haug-Warberg. Mccabe-thiele diagrams for binary distillation. Dept. of Chemical Engineering, Norwegian University of Science and Technology, August 2005.

[41] John D. Hedengren and Thomas F. Edgar. Approximate nonlinear model predictive control with in situ adaptive tabulation. *Computers and Chemical Engineering*, 32:706–7014, 2008.

[42] Friedrich G. Helfferich. Non-linear waves in chromatography III. Mutlicomponent Langmuir and Langmuir-like systems. *Journal of Chromatography A*, 768:169–205, 1997.

[43] Friedrich G. Helfferich and Roger D. Whitley. Non-linear waves in chromatography II. Wave interference and coherence in multicomponent systems. *Journal of Chromatography A*, 734:7–47, 1996.

[44] H. Hoang, F. Couenne, C. Jallut, and Y. Le Gorrec. The Port Hamiltonian approach to modelling and control of continuous stirred tank reactors. *Journal of Process Control*, 21(10):1449–1458, 2011.

[45] H. Hoang, F. Couenne, C. Jallut, and Y. Le Gorrec. Lyapunov-based control of non isothermal continuous stirred tank reactors using irreversible thermodynamics. *Journal of Process Control*, 22:412–422, 2012.

[46] R. Huang, V. M. Zavala, and L. T. Biegler. Advanced step nonlinear model predictive control for air separation units. *Journal of Process Control*, 19(4):678–685, 2009.

[47] Rui Huang. *Nonlinear Model Predictive Control and Dynamic Real Time Optimization for Large-scale Processes*. PhD thesis, Carnegie Mellon University, Pittsburgh, PA, December 2010.

[48] Rui Huang, Lorenz T. Biegler, and Eranda Harinath. Robust stability of economically oriented infinite horizon NMPC that include cyclic processes. *Journal of Process Control*, 22:51–59, 2012.

[49] Rui Huang, Eranda Harinath, and Lorenz T. Biegler. Lyapunov stability of economically oriented NMPC for cyclic processes. *Journal of Process Control*, 21:501–509, 2011.

[50] B. Huyck, K. De Brabanter, F. Logist, J. De Brabanter, J. Van Impe, and B. De Moor. Identification of a pilot scale distillation column: a kernel based approach. *IFAC Proceedings Volumes*, 18(Part 1):471–476, 2011.

[51] Yng-Long Hwang. Wave propagation in mass-transfer processes: from chromatography to distillation. *Industrial and Engineering Chemistry Research*, 34:2849–2864, 1995.

[52] A. K. Jana, S. Ganguly, and A. N. Samanta. Nonlinear control of a multicomponent distillation process coupled with a binary distillation model as an EKF predictor. *ISA transactions*, 45(4):575–588, 2006.

[53] A. K. Jana, A. Nath Samanta, and S. Ganguly. Observer-based control algorithms for a distillation column. *Chemical Engineering Science*, 61(12):4071–4085, 2006.

[54] A. K. Jana and A. N. Samanta. A hybrid feedback linearizing-kalman filtering control algorithm for a distillation column. *ISA transactions*, 45(1):87–98, 2006.

[55] A. K. Jana, A. N. Samanta, and S. Ganguly. Nonlinear model-based control algorithm for a distillation column using software sensor. *ISA transactions*, 44(2):259–271, 2005.

[56] Christopher K. R. T. Jones. Geometric singular perturbation theory. *Dynamical systems (Montecatini Terme, 1994) Lecture Notes in Math., Springer*, 1609:44–118, 1995.

[57] Ravindra S. Kamath, Ignacio E. Grossmann, and Lorenz T. Biegler. Aggregate models based on improved group methods for simulation and optimization of distillation systems. *Computers and Chemical Engineering*, 34:1312–1319, 2010.

[58] M. Kano, N. Showchaiya, S. Hasebe, and I. Hashimoto. Inferential control of distillation compositions: Selection of model and control configuration. *Control Engineering Practice*, 11(8):927–933, 2003.

[59] E. Y. Kenig. Complementary modelling of fluid separation processes. *Chemical Engineering Research and Design*, 86(9):1059–1072, 2008.

[60] S. Khowinij, S. Bian, M. A. Henson, P. Belanger, and L. Megan. Reduced order modeling of high purity distillation columns for nonlinear model predictive control. In *Proceedings of the American Control Conference*, volume 5, pages 4237–4242, 2004.

[61] S. Khowinij, M. A. Henson, P. Belanger, and L. Megan. Dynamic compartmental modeling of nitrogen purification columns. *Separation and Purification Technology*, 46(1-2):95–109, 2005.

[62] A. Kienle. Low-order dynamic models for ideal multicomponent distillation processes using nonlinear wave propagation theory. *Chemical Engineering Science*, 55(10):1817–1828, 2000.

[63] A. Kienle, M. Groebel, and E. D. Gilles. Multiple steady states in binary distillation-theoretical and experimental results. *Chemical Engineering Science*, 50(17):2691–2703, 1995.

[64] Kirk-Othmer. *Separation Technology*, volume 1. Wiley, second edition, 2008.

[65] C. C. Klimasauskas. Hybrid modeling for robust nonlinear multivariable control. *ISA transactions*, 37(4):291–297, 1998.

[66] A. Kumar Jana, A. Nath Samanta, and S. Ganguly. Globally linearized control system design of a constrained multivariable distillation column. *Journal of Process Control*, 15(2):169–181, 2005.

[67] T. Kurooka, Y. Yamashita, H. Nishitani, Y. Hashimoto, M. Yoshida, and M. Numata. Dynamic simulation and nonlinear control system design of a heterogeneous azeotropic distillation column. *Computers and Chemical Engineering*, 24(2-7):887–892, 2000.

[68] O.A. Ladyzhenskaia, V.A. Solonnikov, and N.N. Ural'ceva. *Linear and quasilinear equations of parabolic type*, volume 23 of *Translations of Mathematical Monographs*. American Mathematical Society, 1968.

[69] C. Le Bris and P. Rouchon. Low-rank numerical approximations for high-dimensional Lindblad equations. *Phys. Rev. A*, 87(2):022125, 2013.

[70] J. Lévine and P. Rouchon. Quality control of binary distillation columns via nonlinear aggregated models. *Automatica*, 27(3):463–480, 1991.

[71] Bin Li and Andrew G. Alleyne. A dynamic model of a vapor compression cycle with shut-down and start operations. *International Journal of Refrigeration*, 33:538–552, 2010.

[72] A. Linhart and S. Skogestad. Computational performance of aggregated distillation models. *Computers and Chemical Engineering*, 33(1):296–308, 2009.

[73] Andreas Linhart and Sigurd Skogestad. An aggregation model reduction method for one-dimensional distributed systems. *AIChE Journal*, 58(5):1524–1537, May 2012.

[74] W. Marquardt. Nonlinear model reduction for binary distillation. In *Proceedings of the IFAC Control of Distillation Columns and Chemical Reactors*, pages 123–128, 1986.

[75] Jakob Munch Jensen and Hubertus Tummescheit. Moving boundary models for dynamic simulations of two-phase flows. In *Proceedings of 2nd International Modelica Conference*, pages 235–244, March 2002.

[76] K. Nandakumar and R. P. Andres. Minimum reflux conditions. Part I: Theory. *AIChE Journal*, 27(3):450–460, 1981.

[77] S. Park and C. Han. A nonlinear soft sensor based on multivariate smoothing procedure for quality estimation in distillation columns. *Computers and Chemical Engineering*, 24(2-7):871–877, 2000.

[78] Suhas V. Patankar. *Numerical Heat Transfer and Fluid Flow*. Taylor&Francis, 1980.

[79] N. B. O. L. Pettit, M. Willatzen, and L. Ploug-Srensen. A general dynamic simulation model for evaporators and condensers in refrigeration. Part II: Simulation and control of an evaporator. *International Journal of Refrigeration*, 21(5):404–414, 1998.

[80] E. N. Pistikopoulos. Perspectives in multiparametric programming and explicit model predictive control. *AIChE Journal*, 55(8):1918–1925, 2009.

[81] E. N. Pistikopoulos, V. Dua, N. A. Bozinis, A. Bemporad, and M. Morari. On-line optimization via off-line parametric optimization tools. *Computers and Chemical Engineering*, 24(2-7):183–188, 2000.

[82] Yang Qu, Lin Xu, Xiaoke Fang, Jianhui Wang, and Shusheng Gu. A new approach to heat-exchanger control based on model control. *International Journal of Information and Systems Sciences*, 2(1):31–41, 2006.

[83] K. Razzaghi and F. Shahraki. Robust control of an ill-conditioned plant using μ-synthesis: A case study for high-purity distillation. *Chemical Engineering Science*, 62(5):1543–1547, 2007.

[84] H.K. Rhee, R. Aris, and NR Amundson. On the theory of multicomponent chromatography. *Philosophical Transactions of the Royal Society of London. Series A, Mathematical and Physical Sciences*, 267(1182):419–455, 1970.

[85] C. Riverol and C. Carosi. Integration of fuzzy-logic based control procedures in cryogenic distillation. *International Journal of Soft Computing*, 1(3):187–192, 2006.

[86] M. Rodriguez and M. S. Diaz. Dynamic modelling and optimisation of cryogenic systems. *Applied Thermal Engineering*, 27(7 SPEC. ISS.):1182–1190, 2007.

[87] B. Roffel, B. H. L. Betlem, and R. M. De Blouw. A comparison of the performance of profile position and composition estimators for quality control in binary distillation. *Computers and Chemical Engineering*, 27(2):199–210, 2003.

[88] B. Roffel, B. H. L. Betlem, and J. A. F. De Ruijter. First principles dynamic modeling and multivariable control of a cryogenic distillation process. *Computers and Chemical Engineering*, 24(1):111–123, 2000.

[89] P. Rouchon and Y. Creff. Geometry of the flash dynamics. *Chemical Engineering Science*, 48:3141–3147, 1993.

[90] Pierre Rouchon. *Simulation dynamique et commande non linéaire des colonnes à distiller*. PhD thesis, Ecole Nationale Supérieure des Mines de Paris, 1990.

[91] M. Schenk, R. Gani, D. Bogle, and E. N. Pistikopoulos. A hybrid modelling approach for separation systems involving distillation. *Chemical Engineering Research and Design*, 77(6):519–534, 1999.

[92] Philip A. Schweitzer. *Handbook of Separation Techniques for Chemical Engineers - Second edition*. McGraw-Hill, New-York, 1988.

[93] J. G. Segovia-Hernández, E. A. Hernández-Vargas, and J. A. Márquez-Muñoz. Control properties of thermally coupled distillation sequences for different operating conditions. *Computers and Chemical Engineering*, 31(7):867–874, 2007.

[94] B. Seliger, R. Hanke-Rauschenbach, F. Hannemann, and K. Sundmacher. Modelling and dynamics of an air separation rectification column as part of an IGCC power plant. *Separation and Purification Technology*, 49(2):136–148, 2006.

[95] A. M. Shaw and F. J. Doyle III. Multivariable nonlinear control applications for a high purity distillation column using a recurrent dynamic neuron model. *Journal of Process Control*, 7(4):255–268, 1997.

[96] A. Shilkin and E. Y. Kenig. A new approach to fluid separation modelling in the columns equipped with structured packings. *Chemical Engineering Journal*, 110(1-3):87–100, 2005.

[97] J. Shin, H. Seo, M. Han, and S. Park. A nonlinear profile observer using tray temperatures for high-purity binary distillation column control. *Chemical Engineering Science*, 55(4):807–816, 2000.

[98] A. Singh and M. Hovd. Model requirement for control design of an LNG process. *Computer Aided Chemical Engineering*, 24:533–538, 2007.

[99] Abhay K. Singh and Juergen Hahn. Sensor location for stable nonlinear dynamic systems: Multiple sensor case. *Industrial and Engineering Chemistry Research*, 45:3615–3623, 2006.

[100] S. Skogestad. Dynamics and control of distillation columns - a critical survey. *Modeling, Identification and Control*, 18(3):177–217, 1997.

[101] S. Skogestad. Dynamics and control of distillation columns: A tutorial introduction. *Chemical Engineering Research and Design*, 75(6):539–562, 1997.

[102] S. Skogestad. The dos and don'ts of distillation column control. *Chemical Engineering Research and Design*, 85(1 A):13–23, 2007.

[103] S. Skogestad and M. Morari. Understanding the dynamic behavior of distillation columns. *Industrial and Engineering Chemistry Research*, 27(10):1848–1862, 1988.

[104] Jack Ting, Friedrich G. Helfferich, Yng-Long Hwang, Glenn K. Graham, and George E. Keller II. Experimental study of wave propagation dynamics of multicomponent distillation columns. *Industrial and Engineering Chemistry Research*, 38:3588–3605, 1999.

[105] Milton Van Dyke. *Perturbation Methods in Fluid Mechanics*. 1975.

[106] Ferdinand Verhulst. *Methods and Applications of Singular Perturbations: Boundary Layers and Multiple Timescale Dynamics*. Springer, 2005.

[107] D. R. Vinson. Air separation control technology. *Computers and Chemical Engineering*, 30(10-12):1436–1446, 2006.

[108] M. Willatzen, N. B. O. L. Pettit, and L. Ploug-Srensen. A general dynamic simulation model for evaporators and condensers in refrigeration. Part I: Moving-boundary formulation of two-phase flows with heat exchange. *International Journal of Refrigeration*, 21(5):398–403, 1998.

[109] J. Yin and M. K. Jensen. Analytic model for transient heat exchanger response. *International Journal of Heat and Mass Transfer*, 46(17):3255–3264, 2003.

[110] V. M. Zavala and L. T. Biegler. The advanced-step NMPC controller: Optimality, stability and robustness. *Automatica*, 45(1):86–93, 2009.

[111] V. M. Zavala, C. D. Laird, and L. T. Biegler. A fast moving horizon estimation algorithm based on nonlinear programming sensitivity. *Journal of Process Control*, 18(9):876–884, 2008.

[112] W. Zhang and C. Zhang. A generalized moving-boundary model for transient simulation of dry-expansion evaporators under larger disturbances. *International Journal of Refrigeration*, 29(7):1119–1127, 2006.

[113] G. Zhu, M. A. Henson, and L. Megan. Low-order dynamic modeling of cryogenic distillation columns based on nonlinear wave phenomenon. *Separation and Purification Technology*, 24(3):467–487, 2001.

[114] L. Zhu, Z. Chen, X. Chen, Z. Shao, and J. Qian. Simulation and optimization of cryogenic air separation units using a homotopy-based backtracking method. *Separation and Purification Technology*, 67(3):262–270, 2009.

[115] X. Zhu, X. Liu, and Z. Zhou. Optimization of cryogenic air separation distillation columns. In *Proceedings of the World Congress on Intelligent Control and Automation (WCICA)*, volume 2, pages 7702–7705, 2006.

[116] Y. Zhu, S. Legg, and C. D. Laird. Optimal design of cryogenic air separation columns under uncertainty. *Computers and Chemical Engineering*, 34(9):1377–1384, 2010.

Modèles de convection-diffusion pour les colonnes de distillation : application à l'estimation et au contrôle des procédés de séparation cryogénique des gaz de l'air

Résumé : Cette thèse porte sur la modélisation, pour le contrôle, des profils de compositions dans les colonnes de distillation cryogénique. Nous obtenons un modèle non-linéaire de convection-diffusion par réduction d'un modèle d'équations-bilans singulièrement perturbé. Du point de vue de l'automatique, nous nous intéressons à la stabilité des profils de compositions résultants, ainsi qu'à leur observabilité. Du point de vue du procédé, la nouveauté de notre modèle réside dans la prise en compte d'une efficacité de garnissage dépendant des conditions d'opération de la colonne. Le modèle est validé par des comparaisons avec des données de fonctionnement dynamique issues d'une unité de séparation réelle, pour la séparation d'un mélange binaire. Sur le cas plus complexe d'une cascade de colonnes séparant un mélange ternaire, le modèle montre une grande sensibilité aux erreurs d'estimation des taux de reflux. Des résultats adaptés du champ de la chromatographie nous permettent de relier cette sensibilité à des erreurs d'estimation des vitesses d'ondes de compositions cohérentes. En parallèle, nous proposons et testons également un modèle de fonctions de transfert simple (fondé sur des gains statiques et des retards purs uniquement) pour les petites dynamiques de compositions, qui dépend explicitement de valeurs mesurables ou observables sur le procédé.
Mots clés : colonnes de distillation, unité de séparation des gaz de l'air, modèle d'onde, convection-diffusion, ondes de composition, perturbations singulières, réduction variété centre, dimension infinie, observateurs asymptotiques, invariants de Riemann, capteur logiciel, lignes à retard.

Convection-diffusion models for distillation columns: application to estimation and control of cryogenic air separation processes

Abstract: This thesis addresses the problem of modeling the dynamics of the composition profiles inside cryogenic distillation columns, for control applications. We obtain a non-linear convection-diffusion model from the reduction of a singularly perturbed mass-balances model. In the control theory framework, we consider the stability of the resulting composition profiles and their observability. From the process viewpoint, we express the novelty of our model in terms of operating-conditions dependent packing efficiency. The model is validated against real dynamic plant data for a binary separation case. On a more complex, ternary separation columns cascade, the model shows highly sensitive to reflux rate estimation errors. Result adapted from the field of chromatography allows us to interpret this sensitivity in terms of erroneous coherent composition waves speeds. In parallel, we also propose and test a simple transfer functions model (based on static gains and pure delays only) for small composition dynamics, which explicitly depends on measurable or observable process data.
Keywords: distillation columns, air separation unit, wave model, convection-diffusion, composition waves, singular perturbations, centre manifold reduction, infinite dimension, asymptotic observers, Riemann invariants, soft-sensor, delay lines.

MINES ParisTech

ParisTech
INSTITUT DES SCIENCES ET TECHNOLOGIES
PARIS INSTITUTE OF TECHNOLOGY